PAUL SCHERRER INSTITUT

PSI

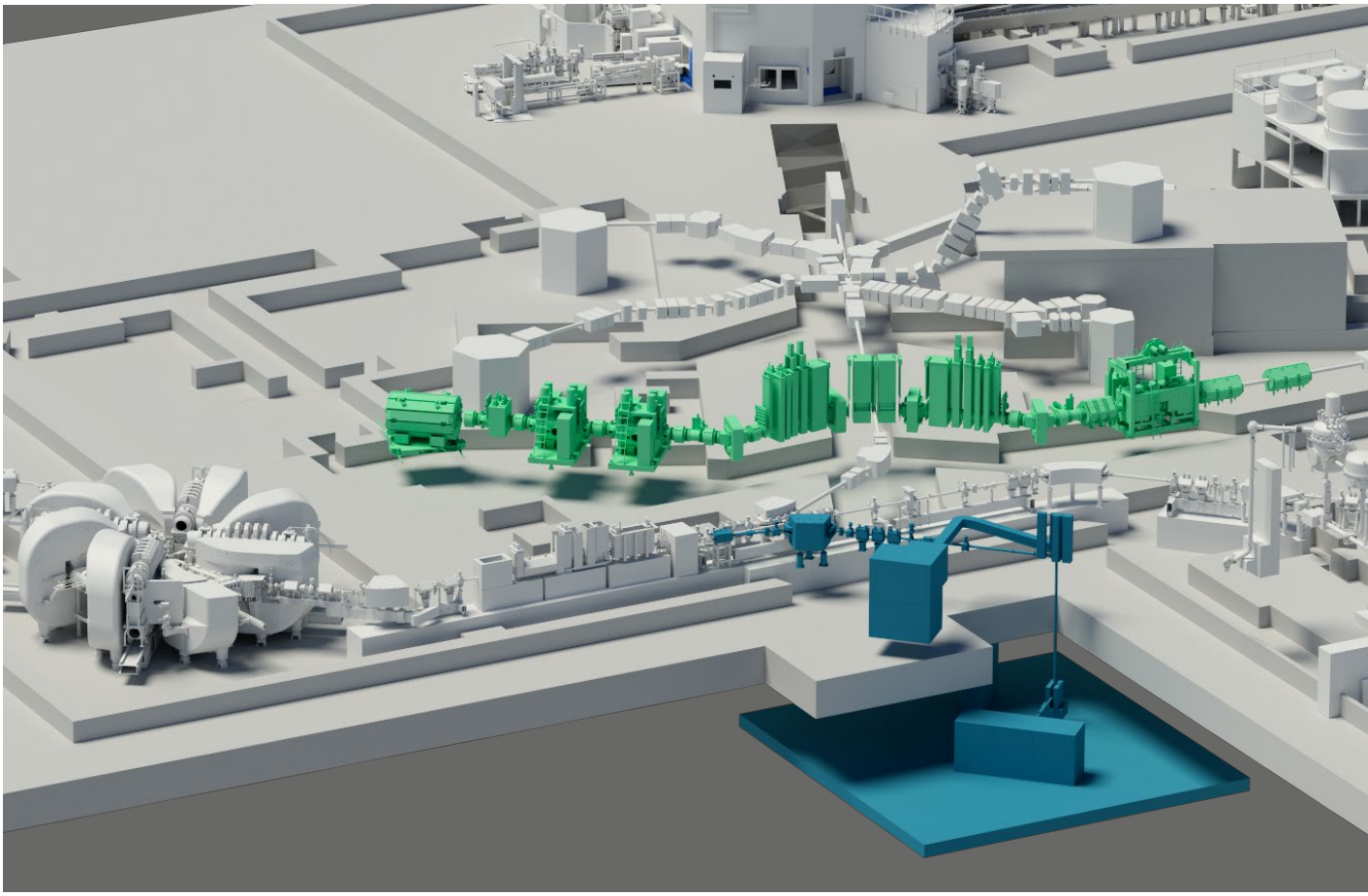

IMPACT
Conceptual Design Report

PSI Bericht Nr. 22-01
January 2022
ISSN 1019-0643

Cover page description

View of the IMPACT installations showing the HIMB production target and muon beamlines in green and the TATTOOS proton beamline, spallation target, mass separation and shielded cells for the handling of the radioisotopes in blue. The two facilities will be located at the high-power HIPA accelerator with its large ring cyclotron shown on the left. The second muon production target and the SINQ neutron source follow downstream of HIMB, while the UCN ultracold neutron source is located on the right side of TATTOOS. *Image by M. Dzambegovic.*

With contributions from:

L. Barth
C. Baumgarten
L. Caminada
J. Chang
G. Dal Maso
R. Dölling
R. Eichler
S. Forss
A. Gabard
C. Geiselhart
R. Häfeli
M. Haj Tahar
C. Harm
S. Harzmann
S. Hellmann
J. Holland
T. Höwler
E. Hüsler
A. Ivanov
M. Janoschek
A. Johayem
S. Jollet
S. Joray
M. Jörg
P. Kaufmann
P.-R. Kettle
B. Kilminster
K. Kirch
D. Kiselev
A. Knecht
A. Koschik
D. Laube
A. Macchiolo
F. Meier Aeschbacher
S. Müller
C. Nyfeler
A. Papa
L. Pedrazzi
N. Preiss
T. Rauber
D. Reggiani
D. Reinhard
S. Ritt
C. Sattler
R. Scheibl
R. Schibli
J. Snuverink
R. Sobbia
P. Steinegger
V. Talanov
N. van der Meulen
E. Valetov
A. Weber
I. Widmer
H. Zhang
E. Zimoch
J. Züllig

Acknowledgements

While the author list is limited to the people directly contributing to the document at hand, the development of the different concepts would not have been possible without the tremendous work of many other people involved. Here, we would like to thank those unnamed experts for their great efforts.
We gratefully acknowledge the support received for the project from the PSI divisions involved, as well as management in this early stage of the project. Special thanks goes to Michèle Erat for all her help and insight. We are also pleased to acknowledge support from the UZH administration, especially Thomas Trüb, for his involvement in many components of the process.
We thank the members of the HIMB External Advisory Board – Johannes Bernhard (CERN, CH), Stephen Blundell (University of Oxford, UK), Yasuhiro Miyake (KEK, JP), Rainer Wallny (ETHZ, CH), and Robert Zwaska (FNAL, USA) – for their support, comments and guidance throughout the development of the Conceptual Design Report and the international communities that have contributed to the exciting science cases developed in the context of IMPACT.
The strong support from the Swiss Academy of Sciences SCNAT and many other academic institutions and companies, as well as from the potential end users of IMPACT, is acknowledged. The large number of support letters received show that they are as excited as we are about the prospects of having IMPACT become a reality.

Contents

1 IMPACT Executive Summary

1.1 Introduction

The High Intensity Proton Accelerator complex HIPA [Grillenberger, 2021] at the Paul Scherrer Institute (PSI) plays a pivotal role in Swiss large-scale infrastructure. HIPA's Ring Cyclotron is the most powerful proton cyclotron worldwide and among the most energy efficient accelerators. It provides a world-leading 1.4 MW high-intensity proton beam of 590 MeV energy and up to 2.4 mA of beam current to target stations, simultaneously feeding 30 instruments and experiments with intense beams of low-energy secondary particles of neutrons, pions and muons for research in multiple disciplines. HIPA presently fuels three large-scale user facilities, namely, the Swiss spallation neutron source SINQ [SINQ], the Swiss Muon Source SμS [SμS], and the Swiss Research InfraStructure for Particle physics CHRISP [CHRISP]. Radionuclides are currently developed and produced at SINQ and at the IP2 beamline, fed protons from HIPA's 72 MeV Injector II cyclotron [Grundler, 2020]. When looking back at the last decade (2010-2019), more than 500 user proposals per year were submitted, about 900 individuals per year made 1700 user visits to the site and spent more than 11000 user days per year at the facilities, using more than 2800 instrument days. More than 300 publications per year resulted from this work.

The IMPACT (Isotope and Muon Production using Advanced Cyclotron and Target technologies) project, jointly proposed by PSI and the University of Zürich (UZH), aims to produce and fully exploit unprecedented intensities and quantities of muons and radionuclides at HIPA for advancements in particle physics, chemistry, material sciences and life sciences. Two new target stations, one for high-intensity muon beamlines (HIMB), and one for an online isotope separation facility (TATTOOS: Targeted Alpha Tumour Therapy and Other Oncological Solutions), will boost the existing infrastructure: HIMB will provide two orders of magnitude higher muon intensities and TATTOOS unrivalled quantities of a wide range of radionuclides.

IMPACT, combining HIMB and TATTOOS, has emerged from a bottom-up process of the Swiss research community. HIMB and TATTOOS have been put forward in the discipline-specific roadmaps of CHIPP [Wallny, 2021] and of Chemistry [Buller, 2021], respectively, in the SCNAT-coordinated process to inform the 2023 Swiss Roadmap for Research Infrastructures [SERI]. Existing and new state-of-the-art facilities at PSI, UZH (in particular, its DEMETER center, see Section 1.2.3) and the Zürich University Hospital (USZ) integrated with IMPACT, will maximize the reach of this national research infrastructure. The project partners have demonstrated records in building and operating large-scale infrastructures; in developing novel technologies for detectors, instrumentation and medical applications; and in running successful user research programs. Figure 1.1 gives an overview of the full IMPACT project.

The unprecedented muon intensities will serve new experiments and instrumentation for a broad national and international user community in particle physics and condensed matter research, at CHRISP and SμS, as documented in the recently published HIMB science case document [Aiba, 2021]. A vastly enlarged discovery potential will challenge the Standard Model of particle physics, in particular in the crucial area of charged lepton flavour violation [Baldini, 2020; Calibbi, 2018]. Together with new detector technology, completely new material science studies will become possible, e.g. concerning novel quantum materials, with much smaller sample sizes, in much shorter times, at a much broader range of conditions, in particular at very high pressures. PSI and UZH, together, will develop new instrumentation and establish new technologies for particle detection and sample environments leading to quantum leaps in muon sciences, overcoming statistical limitations and accessing a wide, uncharted parameter space. The technology developments bridge to other applications and fields, e.g. sample environments at other large-scale national and international user facilities, and detector technology for high-energy particle physics, photon science and medical applications.

The new instrumentation for TATTOOS, in conjunction with preclinical and clinical capabilities at PSI, UZH, and USZ, will provide difficult-to-obtain heavy, therapeutically interesting radionuclides to serve frontline research in radiochemistry, radiopharmacy and nuclear medicine. High radionuclide production rates will, for the first time, allow for large clinical studies of novel radiopharmaceuticals for diagnosis and treatment of patients using a theragnostic approach (what one images, is what one treats). Collaboration of the IMPACT project partners and cooperation with a

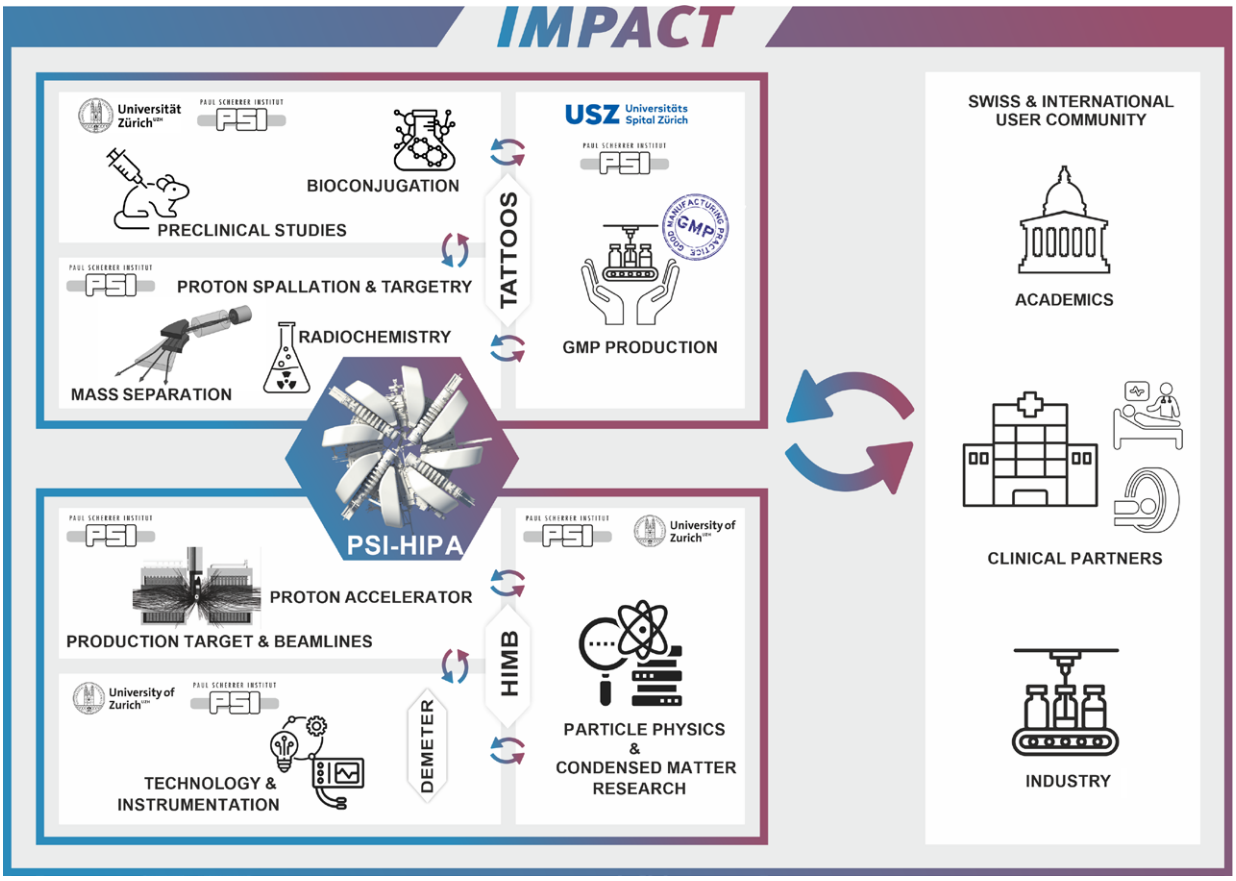

Figure 1.1: Diagram illustrating the IMPACT project.

broad national and international community, from the production of the radionuclides to the medical application, are the key to success in this 'bench-to-bedside' endeavour. Other than the main focus on medical applications, specific radionuclides for other use cases, such as materials research [Correia, 2012] or fundamental physics, e.g. [Campbell, 2016], offer exciting prospects for further research directions in Switzerland.

1.2 HIMB Science

The CHRISP [CHRISP] and SμS [SμS] facilities serve large national and international user communities of fundamental and applied research in particle physics [Signer, 2021] and solid-state physics, chemistry and materials sciences [Amato, 1997; Morenzoni, 2014; Amato, 2009; Khasanov, 2016; Guguchia, 2020a; Shang, 2021] with world-leading intensities of slow muons. IMPACT with two new beamlines HIMB, see Section 1.4, will be a sea change for breakthrough research with even higher muon rates.

The envisaged completion of IMPACT in 2028 will be matched by a next generation of muon experiments and instrumentation. As multi-experiment installation, HIMB will boost particle physics experiments, most prominently searches for charged lepton flavour violation (cLFV), and novel approaches to materials science investigations, greatly increase the formation rate of exotic atoms, in particular muonium, or, if coupled to a muCool cooling scheme and reacceleration, provide a positive muon beam of unprecedented phase-space quality and brightness for future studies. These and more opportunities, easily covering two

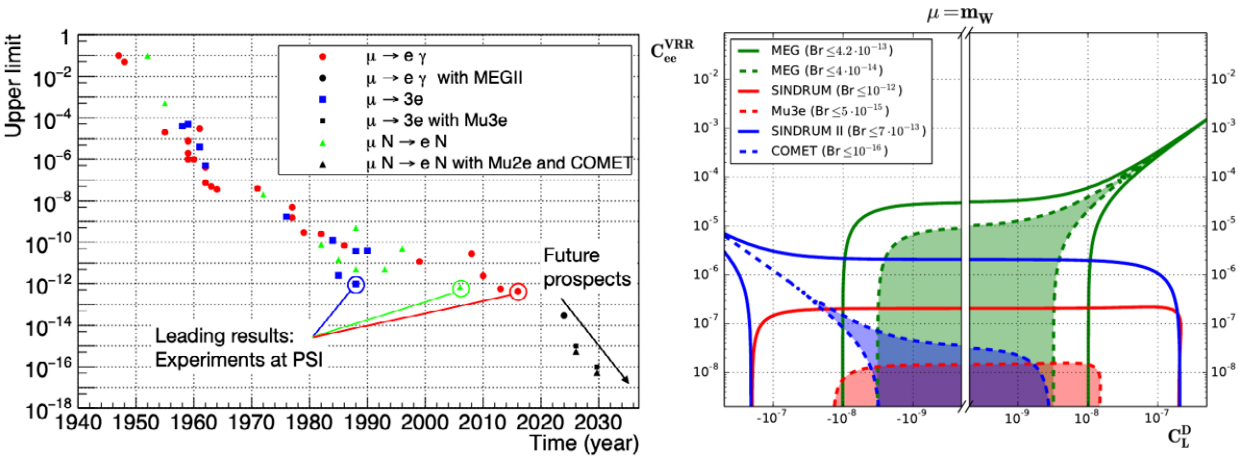

Figure 1.2: (Left) Limits on branching fractions of rare muon decays and future prospects at IMPACT and elsewhere. (Right) Two parameter projections of muon cLFV limits in an EFT approach [Crivellin, 2017].

decades of research, have recently been assembled in the HIMB Science Case document [Aiba, 2021], in a community effort.

1.2.1 Particle Physics

HIMB will be a new intensity frontier to test the Standard Model (SM) of Particle Physics, the best quantum field theory known today. Although most successful, the SM cannot be the ultimate theory. The existence of dark matter, the apparently accelerated expansion of the universe, the matter- antimatter asymmetry of the universe, the tiny neutrino masses, the seeming irreconcilability of the SM with gravity and more arguments point to the existence of physics beyond the SM (BSM). With several top-priority searches for BSM physics, muon experiments can probe energy scales of several to several hundreds of TeV, far beyond the reach of direct searches at current or future colliders. Interestingly, the presently largest tensions of particle physics experiments with the SM involve muons, in the measurement of the anomalous magnetic moment g-2 of the muon [Abi, 2021; Bennett, 2006] and in a number of unexpected asymmetries in B-physics [Graverini, 2019; Amhis, 2021; Fischer, 2021]. The SM describes our knowledge of the three flavours of leptons and quarks and their interactions. However, we have no satisfactory theory of flavour yet. Despite their different masses and Yukawa couplings, the charged leptons, e, μ and τ, are otherwise found to behave very similar. In particular, with the established neutrino flavour-oscillations, charged lepton flavour violation (cLFV) is only accidentally but very strongly suppressed due to the tiny neutrino masses. Although the suppression is of order 10^{-54}, there is no known law behind the conservation of flavour in interactions and decays, and BSM theories can produce large cLFV effects naturally. A very active theoretical and experimental research program in searches for cLFV with a huge discovery potential exists, see e.g. [Calibbi, 2018; Mihara, 2013; Raidal, 2008; Marciano, 2008]. In Figure 1.2 on the left, we show the history of experimental cLFV limits obtained with muons in the 'three golden channels' μ → eγ, μ → eee or μN → eN of neutrino-less decays. All present best limits [Baldini, 2016; Bellgardt, 1988; Eichler, 2021; Bertl, 2006; van der Schaaf, 2021] have been obtained at PSI. The projected sensitivities of next generation efforts are included. They all need major but realistically possible progress on the experiment and facility sides. In particular, progress with very thin and fast silicon-based pixel detectors is mandatory, and is a key component part of IMPACT (see Section 1.2.3). It is important to push simultaneously the different experiments in order to eventually use their signals to disentangle the underlying BSM physics. On the right of Figure 1.2, we illustrate with one of many possible examples the complementarity of the golden channels to new physics. In

an effective field theory (EFT) approach, limits on Wilson coefficients of new physics have been obtained [Crivellin, 2017] and also extrapolated to future experiments.

The result of the MEG experiment at PSI, $Br(\mu \rightarrow e\gamma) < 4.1 \times 10^{-13}$ (90 % C.L.) [Baldini, 2016] marks the strongest limit on any rare decay in physics. Next-generation experiments for all golden channels are currently under construction. They have been endorsed with high priority by international and national particle physics roadmaps, see e.g. [European Strategy, 2020; NuPECC, 2017; Wallny, 2021; P5, 2014; Japan, 2017]. The next generation of muon conversion experiments, $\mu N \rightarrow eN$, will be pursued at pulsed muon beam facilities, COMET at J-PARC (Japan) [Moritsu, 2021; Teshima, 2020] and Mu2e at FNAL (USA) [Bernstein, 2019], whereas the next round of $\mu \rightarrow e\gamma$ and $\mu \rightarrow eee$ requires continuous beams and must take place at PSI. At PSI, the experiments MEGII [Baldini, 2018; Baldini, 2021], improving sensitivity by one order of magnitude, and Mu3e (Phase-1) [Arndt, 2021; Wauters, 2021], by more than two orders of magnitude, will push the boundary of our current knowledge. However, within the next 5 years, they will exhaust their statistical reach at the current best beamline for particle physics with muons, the piE5 beam at PSI. Further progress will only be possible with much increased rates of stopped muons in the experiments. In particular, the international Mu3e collaboration with strong Swiss participation (U. Geneva, UZH, ETH Zurich, PSI) is eager to take full advantage of HIMB at PSI [Aiba, 2021].

1.2.2 Condensed Matter Physics and Materials Science

HIMB in combination with novel vertex reconstruction – based on the development of a new generation of Si-Pixel detectors (see Section 1.2.3) – will lead to a quantum leap of the μSR technique. The assignment of each positron to its muon with an attainable resolution of $\leq 1\,mm^2$ will allow overcoming the pile-up problem that limits the incoming muon rate at the quasi-continuous beams of HIPA to $\sim 4 \times 10^4$/s [Aiba, 2021].

With this new capability, the orders of magnitude higher muon rate of HIMB will become usable for μSR instruments, enabling new research directions in μSR by much faster, higher statistics and more efficient measurements (the μSR instruments at SμS are two to four times oversubscribed), by introducing lateral spatial resolution, and by being able to apply external stimuli (e.g. high pressures, DC or RF electromagnetic fields, illumination) at unprecedented levels with a tenfold gain in pressure or electromagnetic field strengths.

With HIMB, small samples of cross section $\leq 1\,mm^2$, at least twenty times smaller than currently possible, can be studied. Multiple samples can be measured in parallel, thus, for example, determining the phase diagram as a function of doping (see e.g. [Amato, 2009; Luetkens, 2009]) in one measurement. This is extremely important for the efficient and fast characterisation of novel quantum materials

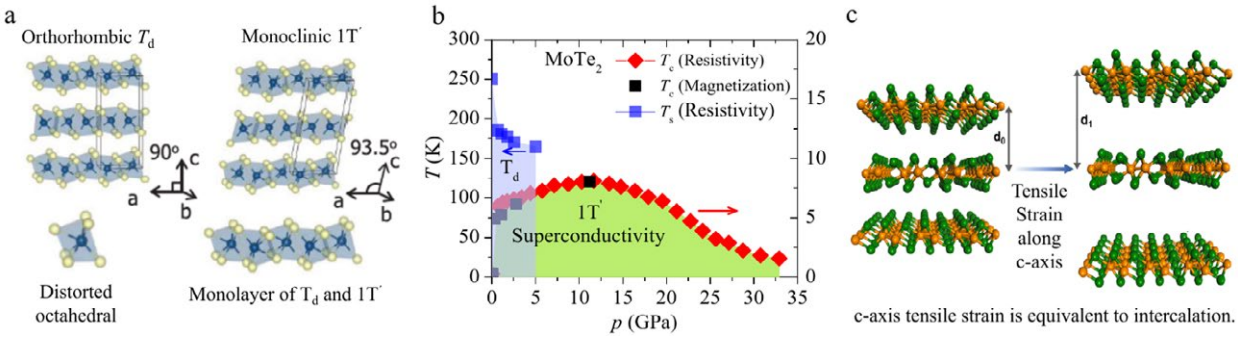

Figure 1.3: Example of the quantum material $MoTe_2$, which is a potential type-II Weyl semimetal with both topologically non-trivial bulk band structure and bulk superconductivity [Huang, 2016; Guguchia, 2017; Janoschek, 2020].
a) Crystal structures, b) temperature-pressure phase diagram, c) illustration of controlling the interlayer coupling through tensile strain. Current maximum pressure for μSR are 1 GPa (uniaxial) and 2.5 GPa (hydrostatic) [Khasanov, 2016].

(correlated electron systems, strong spin-orbit interactions, magnetic and superconducting materials, including topologically non-trivial band structures, see e.g. [Guguchia, 2017; Guguchia, 2020a; Guguchia, 2021; Das, 2021a & 2021b; Ukleev, 2021]), which can be often grown in small amounts only. Due to the significantly enhanced statistics, subtle effects can be detected, for example very slow magnetic fluctuations in quantum materials [Mendels, 2007] or ultra-weak magnetic fields in time reversal symmetry breaking superconductors [Shang, 2021; Grinenko, 2021b]. A fascinating new opportunity is the mapping of imposed lateral variation with approximately millimetre resolution of sample parameters under chemical, thermal or pressure gradients. This allows measuring extended portions of phase diagrams in one sample or stimulating gradient induced properties like time reversal symmetry breaking in superconductors by thermal gradients. With smaller samples of millimetre size, the application of about ten times larger uniaxial strain (10 GPa) and hydrostatic pressures (30 GPa) will become possible (see Section 1.2.3), allowing the exploration of so far inaccessible regions in the phase diagrams of quantum materials (see Figure 1.3).

Besides the exciting new opportunities offered by the combination of HIMB and vertex reconstruction, HIMB will enable i) novel applications in energy materials by closing the range gap between 200 nm and 200 µm, ii) new pump-probe experiments at continuous muon beams, iii) low-energy muon applications with an order of magnitude intensity gain, and iv) significantly improved applications of negative muons in non-destructive, depth-selective elemental analysis studies for energy materials and cultural heritage [Aiba, 2021].

1.2.3 Required Detectors and Target Cells

The proposed DEMETER (Detector & Matter at Extremes Test and Research) joint center at UZH for developing and producing future pixel detectors and high-pressure cells will allow the pursuit of science R&D that enables future particle physics and condensed matter research for the Swiss and international community, at HIMB and other facilities [Wallny, 2021; Abela, 2021; Rønnow, 2021]. Silicon pixel detectors provide the most precise measurements for tracking particles in future particle physics experiments, and the Advancement and Innovation for Detectors at Accelerators Horizon 2020 program (AIDAInnova) [AIDAInnova] identifies the major innovations necessary for achieving improved measurements in environments with increased data rates that are made possible by higher delivered luminosities from proposed and upgraded accelerators. The main technological goals are spatial resolutions of less than 5 µm, low material thickness for reduced scattering and therefore improved resolution, timing resolutions of tens of picoseconds that enable precise tracking in four dimensions, high interaction rates, and performance that does not degrade with irradiation at previously unexperienced doses. Highly granular, depleted monolithic active pixel sensors (DMAPS) allow for lower material thickness, and render the costly and inefficient hybridization of sensors and readout boards

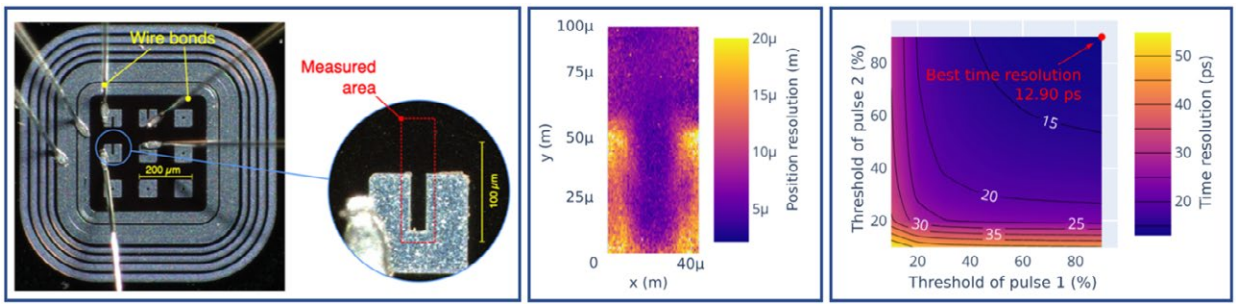

Figure 1.4: Measurements of silicon sensors at UZH. Left: sensor pixels with notches to permit measurement of fast laser pulses. Middle and right: Plot of position resolution (µm) and time resolution (ps) as a function of constant fraction discriminator. The DEMETER center will enable more precise sensor measurements.

obsolete. DMAPS can be produced in more commercially viable CMOS processes, enabling pixel detectors to provide precise tracking for larger areas at a reduced cost. Low-gain avalanche diodes (LGADs) are pixel detectors which generate precise pulses of charge that can be used to determine the time of arrival to within 30 ps of time resolution, and for which intense research is ongoing for developing small pixels of less than 100 µm in size that maintain high efficiency for hit reconstruction throughout the full pixelated sensor area, see Figure 1.4. For both LGADs and DMAPS, their application in high-rate environments depends on the development of radiation-tolerant features, which are being pursued. 3D silicon sensors, in which electrodes are inserted perpendicular to the sensor plane, can be used to make sufficiently small pixels, and overcome limitations in radiation tolerance due to the smaller drift distance of charge carriers, however, they are difficult and inefficient to produce, and can currently only be used in small detectors. Readout technologies for all sensor options should have small feature sizes, low power consumption, and be able to distribute and record signals while minimizing jitter.

The DEMETER center will also permit the investigation by condensed matter scientists of materials at the extremes of high-pressure using muon spin spectroscopy (µSR). A principle limitation in reaching high pressures is the mechanical stability of the large samples necessary for the beam spot size, muon rate, and detector size. While pressures of 100 GPa have been reached, experiments at the PSI µSR facility have been previously limited to 1 GPa and 2.5 GPa for uniaxial and hydrostatic pressures, respectively [Aiba, 2021]. The proposed HIMB will provide sufficient and focused muon rate; and with more granular pixel detectors mounted closer to the samples, all three hurdles to allow smaller, higher-pressure cell development will be overcome. In addition to the silicon research center described above, the DEMETER center will provide a facility for producing these higher-pressure cells. One route to such high pressures is a new generation of anvil pressure cells being explored by PSI and UZH scientists through an SNF R'Equip grant (ExtremeP), in which force can be applied over a much smaller area, leading to pressures of several hundred GPa. In parallel, uniaxial pressures, supplied by a hydraulic system, will also continue to be developed, which allow ultra-fast sample changes, and which provide maximum pressures exceeding the capabilities of the current µSR facility. In addition to use with muon sources, high-pressure cells can also be used with neutron and photon sources at PSI and internationally.

1.3 TATTOOS Science

The increasing demand for innovative, medically-relevant radionuclides worldwide, in particular, α-particle emitters, is the main driver behind the exploitation of alternative routes of radionuclide development and production, namely, proton-induced spallation [Catherall, 2017]. TATTOOS will address this need by complementing and significantly expanding the research opportunity with radionuclides in Switzerland and Europe through the unique capabilities of the intense, high-energy proton beam from HIPA.

1.3.1 Applied Radionuclide Sciences

At cyclotrons with proton energies of 18-70 MeV, (p,*x*n)-nuclear reactions prevail, whereas thermal neutron irradiation predominantly leads to (n,γ)-nuclear reactions. As a consequence, only radionuclides adjacent or in close proximity ($\Delta Z \leq 2$ or $\Delta N = 1$) to the line of stable isotopes can be obtained. Other radionuclides of potential interest for research and medical applications are not accessible at all or, if so, only in minute quantities. On the other hand, spallation reactions, i.e., the most common nuclear reactions occurring if high-energy, incident particles hit target material, lead to virtually any radionuclide lighter than the target material. Thus, combined with laser-ionization online mass separation, nuclear spallation addresses the shortcomings of conventional radionuclide production using cyclotrons and reactors. In this respect, CERN (ISOLDE) has performed pioneering work on targetry for spallation reactions, as well as the isotope mass separation online (ISOL) technique [ISOLDE]. The implementation of the ISOL technique is either explored or planned at several large accelerator facilities (CERN/MEDICIS; INFN/ISOLPHARM - Italy; SCK/ISOL@MYRRA - Belgium). TATTOOS, however, will join CERN by employing spallation reactions for radionuclide research, thereby, being the only facilities to manage this

			Activity [GBq]	
Isotope	Decay	$t_{1/2}$	Ta	U
^{149}Tb	α, ε	4.1 h	2390	7
^{152}Tb	ε/β^+	17.5 h	625	37
^{155}Tb	ε	5.3 d	67	39
^{211}At	α, ε	7.2 h	–	804
^{212}Pb	β^-	10.6 h	–	388
^{223}Ra	α	11.4 d	–	78
^{225}Ac	α	9.9 d	–	150
^{225}Ra	β^-	14.9 d	–	30

Table 1.1: Calculated production yields (100 µA, 590 MeV proton beam) for a selection of medically relevant radionuclides as obtained from TATTOOS using a tantalum (12 hours irradiation) and a uranium (6 days irradiation) target (see also https://www.psi.ch/en/media/71725/download).

in Europe. A similar setup is planned at TRIUMF (Canada) where a proton irradiation facility similar to HIPA exists [TRIUMF].

In order to substantially advance basic and applied sciences, it is critical to make innovative radionuclides available in sufficient quantities and at high quality. TATTOOS will address these key aspects by irradiating targets of high atomic number, namely, tantalum or uranium carbide for radionuclide development. The 50-fold higher proton beam intensity foreseen at TATTOOS (100 µA) compared to ISOLDE/CERN (2 µA) will give rise to Gigabequerel-quantities of promising and/or yet uncharted radionuclides. This corresponds to an at least 50-fold increase of ISOLDE's production capacity, under consideration of all extraction and adsorption losses as well as losses during ionization and ion transport. This will allow for extended preclinical and clinical studies (see Table 1.1 - a full list of radionuclides, including calculated yields, can be found at: https://www.psi.ch/en/media/71725/download). Technical details can be found in the further chapters of this document.

TATTOOS can build on the ample expertise of accelerator technology, beamline development, targetry (particularly up-scaling target technology) and radiochemistry, as well as knowledge regarding the thermal release properties of radionuclides from refractory target materials at PSI [Wittwer, 2011; Steinegger, 2016]. The ISOL-target technology will be coupled to resonance laser ionization (RILIS) as an element-selective ionization technique, reaching total efficiencies of up to 50 % of the calculated yields [Wendt, 2003; Fedosseev, 2017]. Whereas PSI will profit from the extensive experience of its partner institutions CERN, TRIUMF and INFN, it plans to share its leading competence in the field of radiochemical separation. During active proton beam periods (online; typically from late April to end December) ISOL/RILIS allows for the provision of virtually any desired radionuclide as requested by the research community. Meanwhile, during the annual accelerator maintenance period, TATTOOS will operate offline, serving other research purposes such as, e.g., the sample preparation for accurate half-life measurements for nuclear dating applications [Schumann, 2020].

Due to the pronounced preclinical and clinical interest in targeted α-particle therapy (TAT) of disseminated cancer, TATTOOS will put emphasis on the development of α-particle-emitting radionuclides. Research and technology will be directed towards the development of the α-emitters ^{225}Ac, ^{225}Ra (parent radionuclide of ^{225}Ac) as well as ^{211}At but also ^{149}Tb and ^{212}Pb. In all cases, the expected yields will suffice to supply multiple research and medical centers in Switzerland and abroad (see Table 1.1). Based on currently available clinical reference data and the calculated yields for ^{223}Ra or ^{225}Ac, TATTOOS could provide several hundred patient doses over a 6-day collection period. This is more ^{225}Ac than isolated at JRC (Germany), ORNL (USA) and IPPE (Russia) from their ^{229}Th-stock by anion exchange and extraction chromatography in an entire year [Morgenstern, 2020].

1.3.2 Translational Science

Currently, clinical targeted radionuclide therapy is mostly performed with β^--particle emitters (^{90}Y, ^{131}I, ^{177}Lu) on metastasized cancer. Lately, TAT has attracted attention because of the stunning clinical results obtained in patients suffering from metastasized prostate cancer after therapy with $^{223}RaCl_2$ [Parker, 2013] or ^{225}Ac-PSMA-617 [Kratochwil, 2016], see Figure 1.5 (left). There are several TAT-optimized molecules available (and under development) for other cancer types by several academic groups, as well as pharmaceutical companies, locally and abroad. However, research and clinical development is hampered because of the global

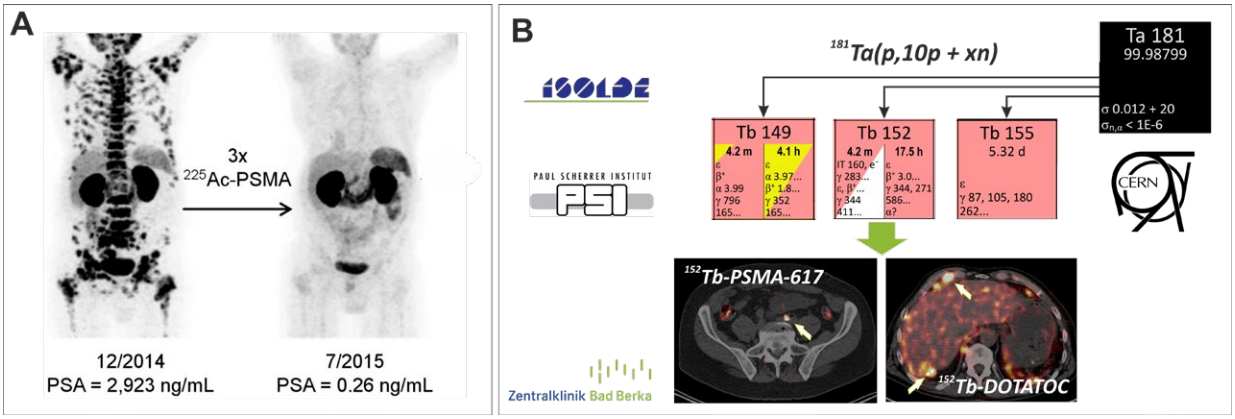

Figure 1.5: A: Successful TAT in a patient suffering from disseminated prostate cancer (picture adapted from [Kratochwil, 2016]); B: PET scans depict extensive tumor spread (black skeletal spots) pre- and post-therapy with ^{225}Ac-PSMA-617. B: ^{149,152,155}Tb produced via spallation on ^{181}Ta at ISOLDE/CERN and processed at PSI. Transversal PET scans performed at the Klinikum Bad Berka with ^{152}Tb-labelled radiopharmaceuticals targeting the prostate specific membrane antigen or the somatostatin receptor in patients suffering from metastasized (arrows) neuroendocrine and prostate cancer [Baum, 2017; Müller, 2019].

shortage of these radionuclides due to the lack of adequate sources and production capacities. At the recent PSI mini-symposium in spring 2021, with more than 300 international participants [TATTOOS, 2021], clinical key-opinion leaders also raised concerns that the current armory of therapeutic radionuclides is not sufficient to address the clinical needs. The opportunities and perspectives opened by TATTOOS has, therefore, created a lot of resonance in academia and industry. In recent years, $^{149;152;155}$Tb produced at CERN/ISOLDE and processed at PSI has been investigated preclinically at PSI in combination with various tumour-targeting molecules, among those folate conjugates [Müller, 2014], PSMA-ligands [Umbricht, 2019] and somatostatin analogues [Müller, 2019; Baum, 2017], see Figure 1.5 (right). ^{152}Tb could even be successfully evaluated in two patients. However, extended clinical studies as well as therapeutic application of ^{149}Tb has not been realized so far due to the low yields available. ^{149}Tb could have distinct advantages for TAT in comparison to ^{225}Ac for drug development and clinical indications: i) Other than ^{225}Ac, ^{149}Tb shares an almost identical chemical behavior with the radiolanthanide ^{177}Lu (the current clinical gold-standard). Thus, any tumour-targeting biomolecule currently developed for β^--particle therapy with ^{177}Lu can also be labelled with ^{149}Tb for TAT; ii) ^{149}Tb has a short half-life of 4 h and co-emits β^+-particles (7 % intensity), which can facilitate dosimetric calculations; iii) most importantly, ^{149}Tb decays by α-particle emission, whereas its daughters decay by harmless electron capture. ^{225}Ac's daughters emit several α- and β^--particles, possibly leading to unwanted side effects. Consequently, ^{225}Ac-based TAT, with the current knowledge and armory of tumour-targeting molecules, is only justified for end-stage cancer patients. ^{149}Tb could be the new generation TAT radionuclide for the treatment of patients at an earlier stage of their disease. TATTOOS will initially focus on spallation reactions on stable tantalum targets to produce particular radiolanthanides for preclinical and clinical studies (α-particle emitter ^{149}Tb, ^{152}Tb, as well as the Auger-electron emitters ^{165}Tm and ^{165}Er).

TATTOOS offers a comprehensive platform to develop and translate novel drugs labelled with innovative radionuclides from 'bench-to-bedside'. This will include platforms to optimize compounds chemically and pharmacologically using non-invasive, nuclear imaging techniques in various animal models as well as extended therapy studies. Promising drug candidates will be transferred and their synthesis established according to good manufacturing practice (GMP). The groups at PSI, UZH and USZ provide ample expertise in all aspects of radiopharmaceutical development which is un-

paralleled in Switzerland. The radiochemistry group at UZH will provide the critical know-how for the development of novel radiometal chelates and innovative bioconjugation techniques [Guillou, 2020; Patra, 2019] and will offer a state-of-the-art, preclinical imaging platform. With the support of TATTOOS, radiopharmacy at USZ/UZH will provide Swissmedic-licensed clean-room facilities and equipment to produce radioactive drugs for early Phase (0/I) clinical studies. Clinical-grade radiopharmaceuticals produced at TATTOOS will be delivered to collaborative clinical sites in Switzerland and, if possible, abroad for their characterization in patients. The concept of TATTOOS is enthusiastically embraced by the radiopharmaceutical and nuclear medical research community.

1.3.3 Prospects for Astrophysics, Materials Science and Radiochemistry

Apart from nuclear medicine applications, TATTOOS offers ample opportunities for a broader scientific community currently not available in Switzerland.

Due to nuclear spallation within the target of TATTOOS, an intense field of fast neutrons is generated. Neutrons in the energy range from 5 keV to 5 MeV are of increasing interest for astrophysical investigations. Large associated uncertainties of the neutron-capture cross sections at stellar neutron energies prevail for a large part of those radionuclides (a comprehensive figure regarding inaccurate cross section values is given in [Wiescher, 2012]). The involved data uncertainties hinder an in-depth understanding of stellar processes of nucleosynthesis. Because of the partly scarce availability of rare, but highly interesting radionuclides like ^{60}Fe, ^{93}Mo and ^{146}Sm [Lugaro, 2016], most intense fast neutron fluxes are of utmost importance. By planning a neutron irradiation position in close proximity to TATTOOS' spallation target, measurements of fast-neutron-capture cross sections may come within reach. In comparison to the existing NEAR facility at CERN, offering neutron energies in the same range, see [NTOF], a similar irradiation position at TATTOOS would translate into an increase in neutron intensity by at least three orders of magnitude (due to a roughly two orders of magnitude higher proton beam intensity as well as a closer proximity to the target), thus enabling studies with outstanding fast neutron intensities.

The availability of specific radioactive sources is also instrumental for Mössbauer-Spectroscopy (MS) and other applied physics methods employing nuclear probes [Correia, 2012]. These highly sensitive analytical methods can element-selectively probe the chemical, magnetic or electronic environment in solid samples, often complementary to μSR. Such nuclear probes serve fields of research including catalysis, solid state physics, materials research, geo-sciences, archaeology and many more. Today the scope of MS is mainly restricted to the analysis of iron- and tin-containing compounds by the limited availability of commercial MS sources (i.e., mainly ^{57}Co for ^{57}Fe or ^{119}mSn for ^{119}Sn). TATTOOS will provide a much larger inventory of radionuclides enabling the extension of MS and other nuclear probe techniques to a total of 38 chemical elements (including Ni, Ru, Sb, W, Re, Os, Ir - metals that are important in, e.g., catalysis) to investigate technologically relevant, non-iron-based compounds. Further fields of application of TATTOOS (off-line and on-line mode) concern fundamental science topics such as, for example, the chemical characterization of transactinide elements [Steinegger, 2016].

1.4 Infrastructure

Figure 1.6 shows an overview of the IMPACT installations HIMB and TATTOOS located at PSI's high-power accelerator HIPA [Grillenberger, 2021]. As can be seen in the figure, the 2.4-mA, high-energy proton beam extracted from the ring cyclotron feeds various facilities (see Figure 1.7): A proposed 100 μA will be diverted onto the TATTOOS target with the remaining beam continuing onward to the muon production targets [Kiselev, 2021b] and the Swiss neutron source SINQ. In addition, the full beam can be kicked with a duty cycle of a few percent onto a second neutron spallation target for the production of ultracold neutrons UCN.

For HIMB one of the existing target stations with its two connected beamlines will be completely dismantled and rebuilt. The new target station will feature an optimized design to maximize the production of low-energy, positive muons ideally suitable for particle physics and condensed matter research. To improve the muon rates available for experiments by up to two orders of magnitude to 10^{10} mu-

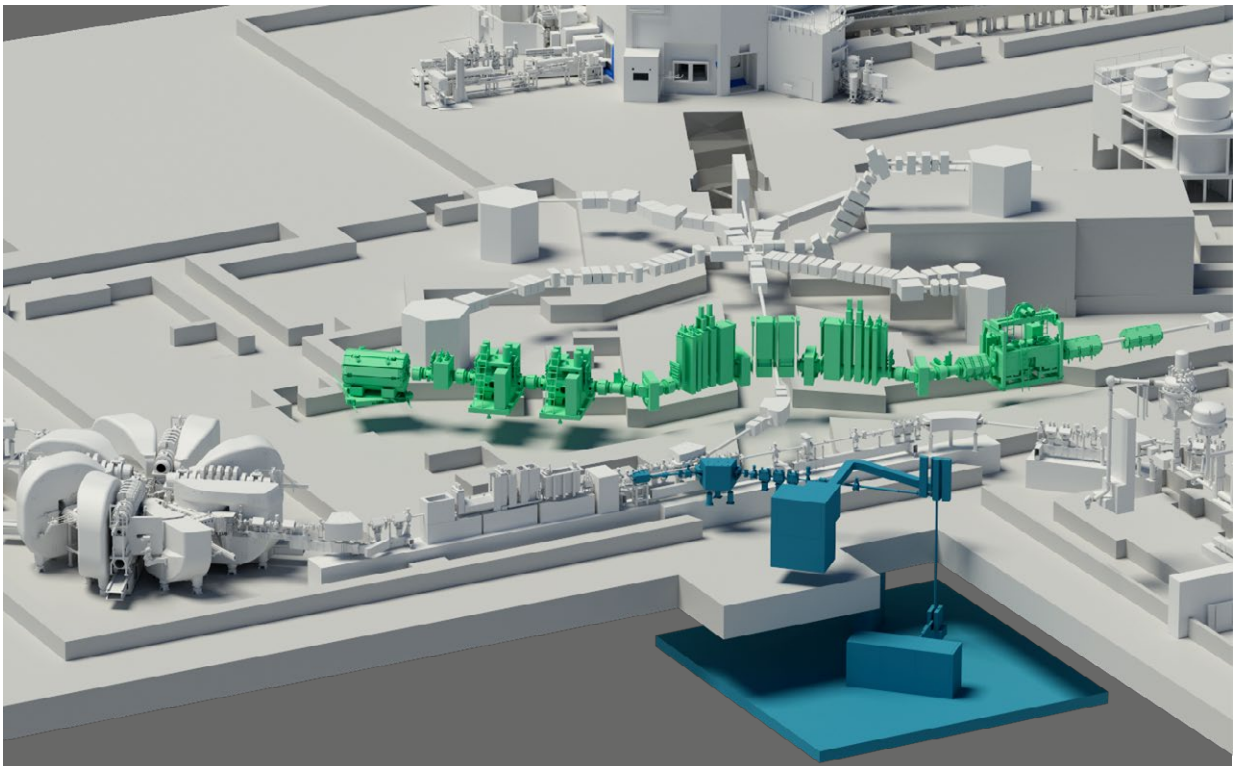

Figure 1.6: The overview shows the HIPA ring cyclotron together with the HIMB and TATTOOS installations in green and blue, respectively. The second muon production target and the Swiss neutron source SINQ are located downstream of HIMB, while the UCN ultracold neutron source is to the right of TATTOOS.

ons/s, two radiation-hard, large-aperture capture solenoids are located in close proximity on the left and right side of the production target. The following beam transport is based on large-aperture solenoids and dipoles capable of transmitting a large phase space. This combination allows to capture and transport about 10 % of the emitted low-energy muons to the experimental areas thereby greatly improving on the efficiencies of the current beamlines, which are typically at the permil level. An artist's impression on how this will look like is shown in Figure 1.8.

TATTOOS will utilize a new beamline which will divert the proton beam towards the new building housing the facility. The beamline will run into a heavily shielded area containing the target station, consisting of the tantalum or uranium carbide target where the spallation processes are induced. The system will contain heaters and an extraction system such that selected radionuclides, depending on their chemical properties, are able to diffuse out of the heated target and are either surface ionised on hot target surfaces or more selectively ionised by Laser-Resonance Ionization (RILIS). With the target held at high potential, the radioactive ions are accelerated towards a mass separator placed in the basement of the TATTOOS building for mass purification. Thus, an ion beam of pure radionuclides, with some isobaric contamination, can be collected in a suitable catcher material positioned inside a shielded cell. Subsequently, further radiochemical separation of the collected radionuclides in an adjacent shielded cell produces the desired radionuclide as a high-quality, isotopically and chemically pure product. This whole concept of online isotope separation (ISOL) was pioneered and proven by the ISOLDE facility at CERN [Catherall, 2017], upon which TATTOOS will improve by utilizing a 50-fold more intense proton beam, resulting in radionuclide productions of unprecedented quantities.

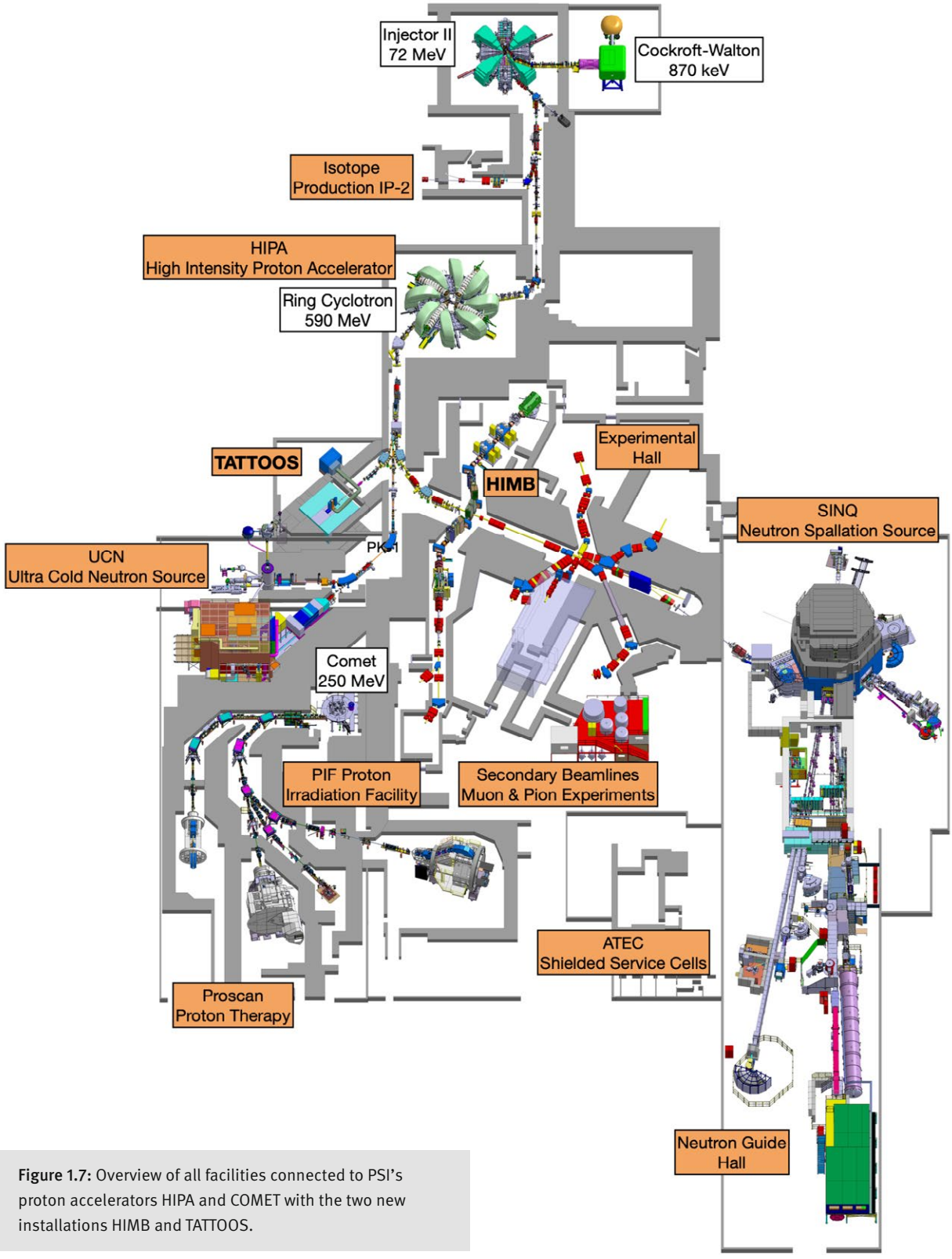

Figure 1.7: Overview of all facilities connected to PSI's proton accelerators HIPA and COMET with the two new installations HIMB and TATTOOS.

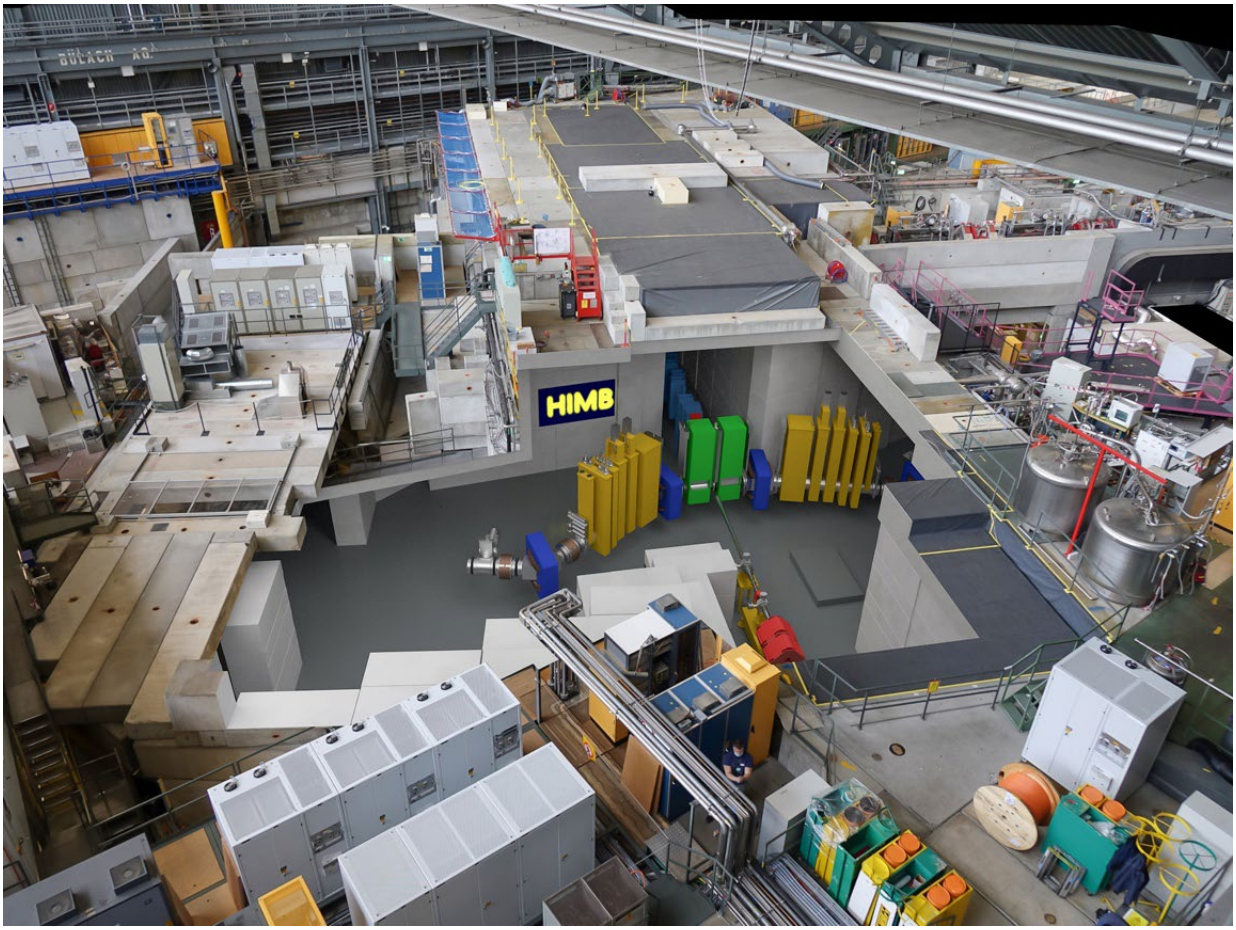

Figure 1.8: Artist's view of the new HIMB target station and muon beamlines in the experimental hall of PSI. For clarity, the shielding blocks around the target and beamlines are removed. *Image by G. Bison.*

In order to fully exploit the potential of the much higher muon rates offered by HIMB, research and development on high-rate capable pixel detectors and advanced high-pressure cells has to be intensified. While such developments will continue in the facilities of the corresponding laboratories at PSI, these efforts will be further boosted at UZH by the creation of the DEMETER facility. The DEMETER center will permit the characterization of silicon sensor solutions, such as shown in Figure 1.4, and the integration with readout electronics and data acquisition systems. Pixel-detector scientists will co-develop sensors and electronics with industrial semiconductor fabrication plants, a circular feedback system that germinates both science and industry. The pixel detector solutions discovered at the DEMETER center will be applicable to future and upgraded detectors at PSI, CERN, and beyond as described in Section 1.2. The DEMETER center will also provide a safe laboratory for producing high-pressure cells that can then be implemented in μSR experiments or at neutron and light sources. The DEMETER center will jointly house both the silicon pixel and high-pressure cell research centers, allowing a high level of integration for experiments with the PSI μSR facility that require both detector and target cells. The center will operate clean rooms and equipment for pixel detector processing, measurements, data acquisition, assembly of production detectors, and integration with mechanics, cooling, and electronics ser-

vices. The high-pressure cell center will host a state-of-the-art, computer-operated hydraulic press for load testing and assembly of pressure cells, and a large-bore cryogenic magnet for testing them, as well as for characterizing materials outside of the precious μSR beam-time environment. The department of chemistry at UZH will purchase and install a new multi-modality PET/SPECT/CT-scanner for non-invasive, preclinical, small-animal imaging and a sensitive ultra-high performance liquid chromatography system, coupled to a mass spectrometer for analysis of radiopharmaceuticals and their metabolites. The systems will be installed in the B/C type radiochemistry laboratory at Irchel campus of UZH. USZ is in the process to expand its GMP facility making it probably the largest production facility for radiotracers in central Europe, providing highest flexibility and utmost production reliability. The ground floor is reserved for the cyclotron and the clean lab GMP production of routine PET-radiotracers. For TATTOOS, on the first floor three laboratories with shielded hoods are reserved for flexible use for clinical research tracer development and production. Two laboratories are equipped with three shielded cells, connected in series, containing manipulators and different ports, will be installed. These shielded cells will contain automated synthesis modules for the production of radiopharmaceuticals. The shielded cells are connected to a processing shielded cell, in which radiopharmaceuticals can be filled into several vials and then discharged into tungsten pots below the cell chamber. Analytical chemistry equipment such as Gas Chromatography, High-performance liquid chromatography (HPLC), gamma-counters and other equipment to establish a Quality Control lab are also installed, as required for the release of radiopharmaceuticals for human use.

1.5 Users and Access

PSI provides Swiss universities and broad user communities with large-scale research infrastructures that exist only once nationally, and in some cases world-wide. With IMPACT, PSI and UZH answer the request by large research communities to provide and exploit world-leading high intensities of muons and isotopes. The need is documented in discipline-specific roadmaps [Wallny, 2021; Buller, 2021]. The science motivation was discussed in depth in community meetings [HIMB, 2021; Aiba, 2021; TATTOOS, 2021].

IMPACT will reach diverse communities from multiple disciplines. It will allow direct access for users and collaborations at CHRISP and SμS, with estimated 300 individual users and 9000 user days per year at PSI. It will serve expert users at the DEMETER center at UZH. Around 20-30 of such users per year each will work with the respective resources. Products, e.g. instrumentation developed in DEMETER, will reach thousands of users at national and international facilities. TATTOOS will be the backbone of a radiopharmaceutical drug-development pipeline together with the complementary capabilities of UZH and USZ. It will provide internal and external users and customers, such as radiochemists, radiopharmaceutical scientists and clinicians with innovative radionuclides. Dozens of researchers per year will be involved in preclinical and clinical studies, eventually identifying new and potent drug candidates and novel therapy concepts for cancer patients.

IMPACT infrastructure at PSI will be operated with the same access model as the other PSI user facilities. The PSI User Office [PSI User Office] provides a single point of contact, deals with the proposal submission processes, operates the PSI guest house [PSI Guest House], and supports users with all logistics for their stay. IMPACT infrastructure at PSI

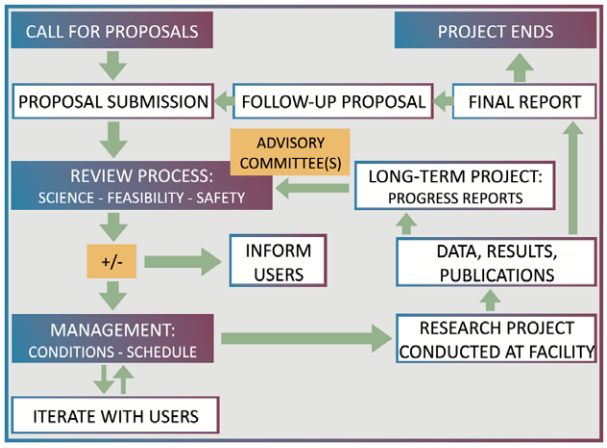

Figure 1.9: The general scheme for user access to IMPACT facilities.

and at UZH will follow the same general terms, schematically shown in Figure 1.9. Access to the user facilities, for publicly funded research, is granted based on scientific excellence of research proposals. While basic operational cost of the facility and standard instrumentation is usually not charged to these users, special requirements must be negotiated and may be charged. Options exist for proprietary research and access for industry. In such cases, facility cost is charged to the customers. Most of the user time will be given to open research.

The data produced in non-proprietary research is managed under the respective institutional data policies [UZH Data Policy; PSI Data Policy], in line with the general research-data management guidelines for publicly funded research in Switzerland. The data management follows the FAIR [FORCE11; Higman, 2019] principles. Results of the performed research will be published and openly accessible in journals and institutional repositories, such as PSI's DORA [DORA] and UZH's ZORA [ZORA]. Exceptions will apply for justified legal, ethical, privacy or security reasons, in the spirit of "as open as possible, as closed as necessary".

1.6 Planning and Timeline

The project is organized in the following phases: *planning, preparation, execution, implementation,* and *consolidation* schematically depicted in Figure 1.10. The installations at UZH are using a refitted building (DEMETER clean rooms) and are integrated into the new chemistry building and the planned extended production facility for radiopharmaceuticals. They require thus much less planning and preparation. During both the *planning* and *preparation* phases of the PSI facilities foreseen for 2022-2024, the proposed concepts will be refined and detailed Work Breakdown Structures and Workflow Schedules prepared. The design of the new target stations, the special beamline magnets, the in-depth shielding considerations and respective layouts and the required modifications of major parts of the infrastructure will be further developed and improved in the planning phase. In particular, the new building for the TATTOOS installation requires planning and permission processes to start as early as 2022 in order for construction to start on time in 2025.

The *preparation* phase will be used for building and testing prototypes of critical components, qualifying potential vendors and preparing calls for tender, in order to be able to place orders as soon as funding becomes available. In parallel, preparatory works concerning infrastructure and civil engineering construction will be carried out. Additionally, the separate, full approval of the TATTOOS building is expected in 2024. Two milestones mark the finalization of the preparation phase: By mid-2024 technical specifications have to be ready in order to prepare calls for tender and procurement and at the end of the preparation phase, the technical design report (TDR) needs to be finished. Most prominent for HIMB are the target design itself together with the large vacuum vessel, which has to house not only the target, but also the capture solenoids and the downstream collimators. Equally important are all the components forming the muon beamlines, like dipoles, solenoids, and separator, which will mostly feature new designs. At TATTOOS the proton beamline installations with a high-power moving beam splitter and a fast-ramping magnet have to be newly designed, and the choices for the cooling, media supply and handling of the spallation target have to be made. Furthermore, the design of the RILIS (Resonance Ionization Laser Ion Source) for isotope ionization and the ion optics for the highly selective mass separation has to be finalized. Moreover, the final design of the shielded cells for isotope collection and for the target exchange procedure has to be decided in this phase to prepare the tender.

Once the main technical design choices have been made and validated, the project is ready to enter the *execution* phase, which commences latest by 2025 with the start of the ERI funding period. The procurement, delivery, inspection and pre-assembly of components as well as the civil engineering construction of the new TATTOOS building will be completed by the end of 2026. In the fourth quarter of 2025 the important decision on the viability of starting the long HIPA shutdown period in 2027 has to be taken, based on the progress of procurement, preparation activities, work planning and the resource availability outlook.

Subject to a positive decision, beginning of 2027 marks the start of a 16-month shutdown period of the proton accelerator and its attached research infrastructures (IP2, SμS, CHRISP and SINQ) and the start of the *implementation*

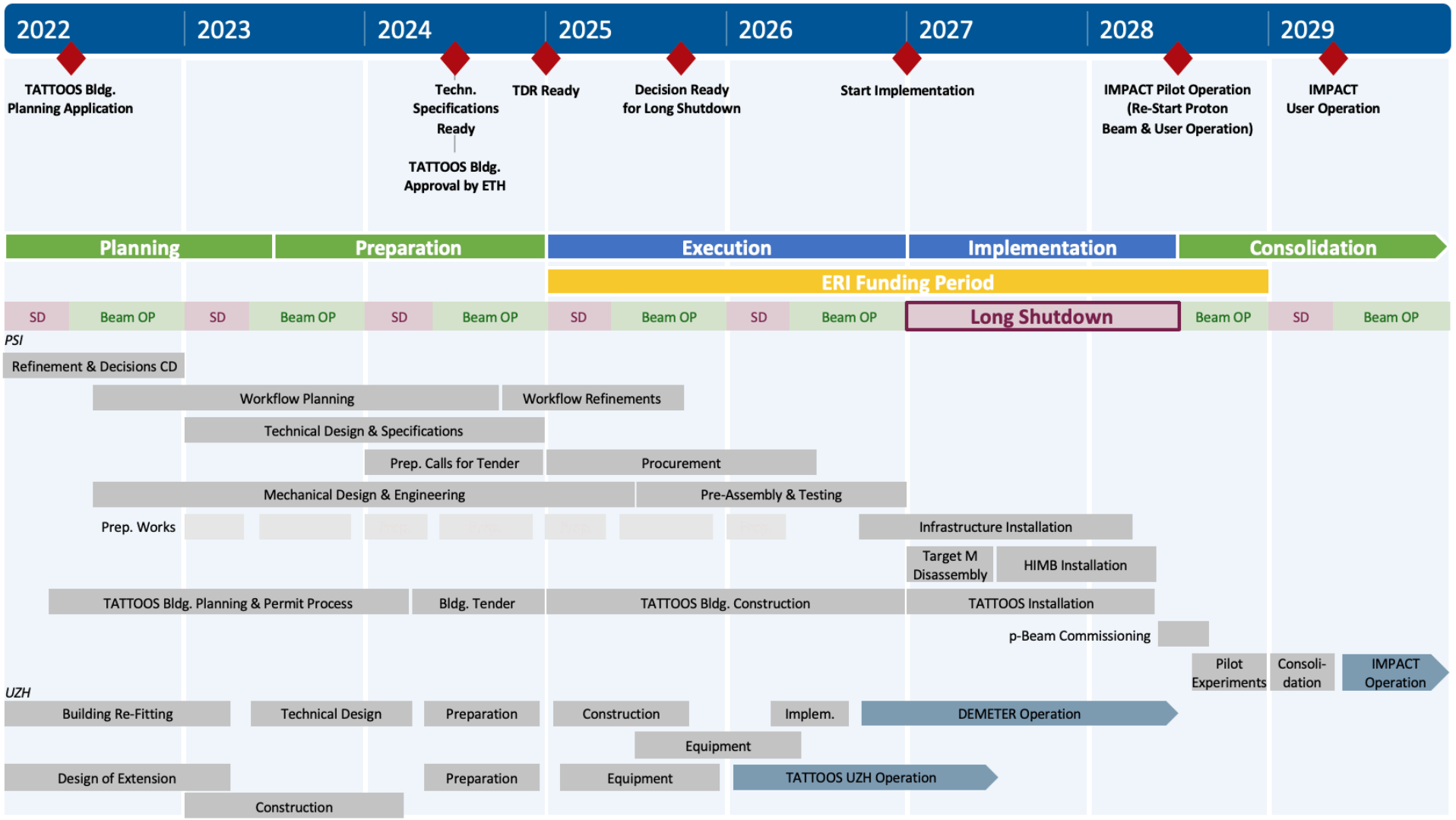

Figure 1.10: Timeline of the IMPACT project.

phase: The existing muon target station will be dismantled, the adjacent experimental areas disassembled and all infrastructure and shielding in this area removed. At the same time the infrastructure of the TATTOOS building will be prepared for the installation of components. Subsequently, the new and modified beamlines will be set up, the new shielding walls installed, the new target stations placed and the infrastructure completed.

Intensive verifications and commissioning of the new elements in the proton beamline mark the start of the *consolidation* phase. The proton accelerator will restart operation in 2028 and its connected research facilities will be able to resume normal user operation accordingly. The new facilities HIMB and TATTOOS will, in parallel, undergo beam commissioning and first pilot experiments can be performed. The regular HIPA shutdown at the beginning of 2029 will be used to optimize the installations, based on the results of the commissioning and pilot experiments, to be ready for regular user operation scheduled at HIMB and TATTOOS in May 2029.

As already alluded to earlier, the UZH installations follow a somewhat different implementation cycle compared to the HIMB and TATTOOS facilities at PSI. The planning below ensures that the installations at UZH are ready in time to fully exploit the capabilities offered by HIMB and TATTOOS as soon as they become operational.

The DEMETER facility at UZH will be located in one of the buildings on the Irchel Campus. The building will be refitted, starting in 2022. Initial workshops will be installed to explore the technical requirements. After the final preparation, the DEMETER clean rooms will be built in 2025 and fully equipped in 2026. After a short implementation phase, the DEMETER facility will be fully operational by the end of 2026.

The Institute of Chemistry moved to a brand-new, state-of-the-art building in 2021. It contains fully functional class B and C radiochemistry laboratories. To fulfill the requirements of a world-class infrastructure, additional equipment will be installed to test the safety and efficacy of new radiopharmaceuticals that will be available from the PSI TATTOOS infrastructure.

For TATTOOS, the radiopharmacy division will expand its plans for the new clean room facility in Schlieren. Apart from laboratories for the routine production (construction should be completed in 2024) of clinically approved, diagnostic radiopharmaceuticals, additional clean rooms (two fully equipped laboratories for radioactive syntheses and one for preparation and analytics) will be built for the production of radiopharmaceuticals developed within the framework of TATTOOS for early clinical studies according to Good Manufacturing Practice (GMP). Labs will be equipped with two shielded cells, synthesis modules and quality control equipment to synthesize the relevant radiotracers in 2026. The details of these GMP research laboratories will be planned in parallel to the facilities for routine production.

1.7 Organization, Governance and Management

The IMPACT project will be pursued with a governance and management model based on the experience of the previous large research infrastructure projects at PSI such as SLS, SwissFEL, Gantry 3 or SLS-2.0. The foreseen project structure based on this experience is shown in Figure 1.11 and will be used for the time period spanning from the planning until the consolidation phase. The project management is composed of people from the involved divisions and institutes with both scientific and technical background. On the PSI side, progress in the project will be regularly reviewed by a steering committee composed of the heads of PSI's involved five science and service divisions, finance, safety and radioprotection experts, the director of PSI and two representatives of UZH. In addition, two External Advisory Boards (one related to HIMB and the other to TATTOOS) will be installed that regularly meet with the project team to provide guidance and critical assessment of the project status. As also shown in Figure 1.11, the project managers will be supported by two project offices composed of experts providing support in procurement, financial reporting, risk management, and regulatory affairs. Below the project management, working groups are installed that tackle the challenges associated with the implementation of IMPACT. The project management meets monthly with the working group leaders to assess the current status and to facilitate the exchange of information and know-how across the different groups.

The project management together with the project office will continuously review the progress, schedule and financial

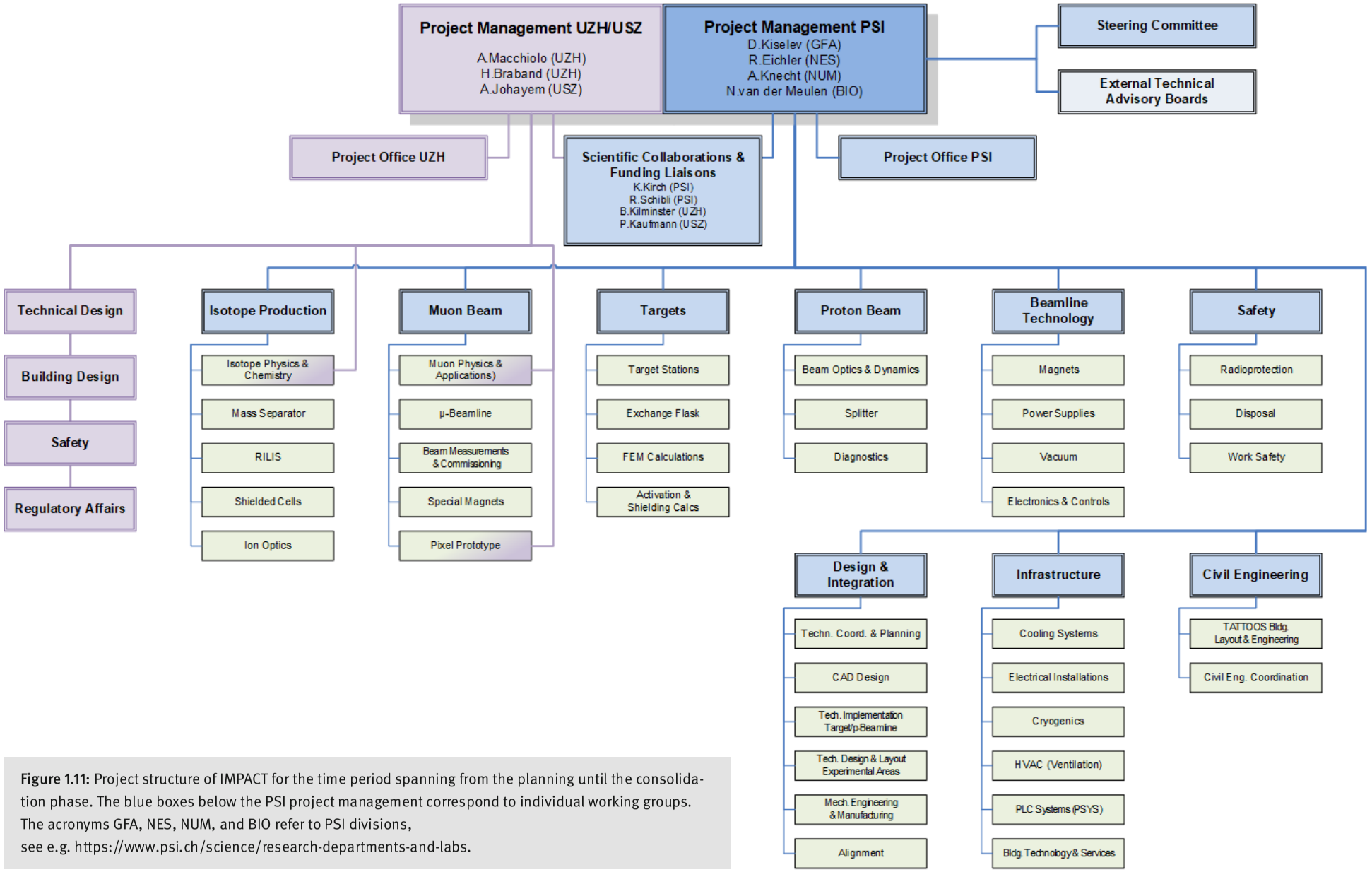

Figure 1.11: Project structure of IMPACT for the time period spanning from the planning until the consolidation phase. The blue boxes below the PSI project management correspond to individual working groups. The acronyms GFA, NES, NUM, and BIO refer to PSI divisions, see e.g. https://www.psi.ch/science/research-departments-and-labs.

reporting to identify project risks early on and find suitable mitigation measures. Additionally, a dedicated risk assessment workshop is foreseen at least once a year to review all identified risks and the corresponding measures, collect newly identified risks and update the project risks register accordingly. Of course, there are various risks involved in such a complex undertaking ranging from supply shortages and inflation, that can only be mitigated by careful and continuously adapted planning, to technical risks that need to be addressed by clever designs and innovation.

After the implementation, the two PSI facilities HIMB and TATTOOS will be part of the HIPA accelerator operation led by the division for Large Research Facilities and will be managed according to the existing models. Apart from the operational aspects, scientific advisory committees will decide on access to the infrastructure (see Section 1.5). While such scientific advisory committees already exist for the HIMB part of the project, new committees will be formed for DEMETER and TATTOOS.

1.8 Finances and Cost Estimate

The capital investment costs for IMPACT during the ERI funding period 2025–2028 amounts to 76.8 MCHF. Over this period PSI and UZH request an ERI funding volume of *64.5 MCHF* (60 MCHF for PSI and 4.5 MCHF for UZH).

The total costs for the PSI facilities HIMB and TATTOOS amount to *77 MCHF*[1]. The investment costs in the ERI funding period 2025–28 amount to 70 MCHF, prorated as follows:

- 32 MCHF for the HIMB Target & Beamlines including Infrastructure
- 38 MCHF for the TATTOOS Target, Beamlines & Radiochemistry Stations including Building and Infrastructure

We request an ERI funding volume of *60 MCHF*. PSI is investing a total of *10 MCHF* in cash contribution, consisting of 7 MCHF in the period 2022–2024 for planning activities and preparatory work and an additional 3 MCHF during 2025–2028. From our experience with infrastructure projects of this size, we presently expect to finance the remaining *7 MCHF* through other funding channels or in-kind contributions from project partners, e.g., hospitals, industry or foundations. For the successful realization of IMPACT, PSI will in addition provide in-kind manpower to the amount of 28.6 MCHF for the total period of 2022–2028 (20.7 MCHF during 2025–2028). Funding for the anticipated dismantling and disposal of the existing target station are not part of the project costs. These costs, as well as the future costs arising from the operation, dismantling and disposal of IMPACT, will be covered by ongoing annual savings contributions from the ETH Domain in accordance with the Federal Council decision of 29 April 2015 on the financing of expenses for the conditioning, interim and final storage of process waste and the decommissioning and disposal of PSI accelerator facilities.

The total costs for the UZH installations amount to *10.6 MCHF*. The investment costs in the ERI funding period 2025–2028 amount to *6.8 MCHF* with an additional *2.1 MCHF* for installation and operation. The remaining *1.7 MCHF* are investment and operation costs during 2022–2024. UZH has already invested substantially in the infrastructure of the new chemistry building, and the refitting of the building for the DEMETER facility. TATTOOS will benefit from an extension of the GMP manufacturing for radiopharmacy at the University Hospital Zurich. In essence, the DEMETER site will require capital investments of 2.0 MCHF into the building, 0.8 MCHF into the clean rooms, and 2.2 MCHF into equipment. The two TATTOOS sites at Zurich will invest 3.3 MCHF into equipment. The manpower contributions to the construction of the research platforms are not listed in the financial plan. By experience, it will encompass services worth at least 1 FTE.

[1] A first cost estimate performed and reported to the ETH board in early 2021 resulted in an amount of 66 MCHF of funding needed from 2021 to 2032 to realize IMPACT with a requested 60 MCHF of ERI funding volume for the period 2025–2028. Since then, the general concepts, the initial layout of the TATTOOS building, and overall infrastructure needs have been refined.

2 Regulations, Radiation Protection and Safety

2.1 Governance

2.1.1 General Regulatory Framework

The PSI accelerator facilities are subject to Swiss legislation. Requirements exist for all phases during the life cycle of a facility, and are not limited to e.g. actual beam operation.

With respect to ionizing radiation, the Swiss Radiological Protection Act (RPA) [SR-814.50] and Radiological Protection Ordinance (RPO) [SR-814.501] apply, as well as related ordinances by the Federal Department of Home Affairs such as SnAV [SR-814.501.51] and UraM [SR-814.554], and selected guidelines by the Swiss Federal Nuclear Safety Inspectorate, e.g. [ENSI-G12]. Regulatory body is the Federal Office of Public Health (Bundesamt für Gesundheit, BAG), for authorization as well as oversight.

Operation of each PSI accelerator facility is authorized by BAG through a licence for the facility itself. There are further BAG licences for general provisions, e.g. emissions, controlled and supervised areas, and temporary storage of radioactive waste containers. All significant changes (constructual, technical or procedural) that might impair the radiological safety must be approved by the regulator.

For regulatory oversight, PSI periodically submits various reports and statistics to BAG, e.g. on emissions, personal and ambient doses, the functional testing of safety systems, and annual summaries of activities in the facilities. Monthly meetings between BAG and PSI serve to table all kind of current topics such as ongoing projects, new regulations and incidents. BAG may also choose to perform onsite inspections to monitor specific activities, e.g. a SINQ target exchange.

Requirements for conventional safety are largely based on the labour act [SR-822.11] and related ordinances, in particular for occupational health [SR-822.113] and the ordinance on accident prevention [SR-832.30]. For installations, the product safety act [SR-930.11], the Machinery Directive 2006/42/EC and internationally agreed standards must be considered, and safety features must be state of the art.

2.1.2 PSI Safety Policy Framework

PSI has passed several policies and guidelines to support compliance with said regulations. The top-level «SGU» policy for safety, health protection and environmental protection [PSI-AW-01-07-02] outlines the PSI governance model concerning safety. There is one predominant policy each for radiation protection [PSI-AW-96-18-01] and conventional occupational health and safety [PSI-AW-96-19-176]. These policies are supplemented by various documents on subject matters, e.g. on laser safety. To facilitate access to safety-related information, «Safety@PSI» was created as an entry page on the PSI intranet for all safety topics.

Baseline controls for safely running the PSI accelerator facilities are outlined in general operating instructions [PSI-AW-81-20-434] which contain the common dos and don'ts for beam operation, maintenance and modifications and also provide pointers to the more comprehensive PSI safety policies.

2.1.3 PSI Safety Organization

Most safety related functions at PSI are centralized in the department «Radiation Protection and Safety» (ASI). As part of the «Logistics» division, ASI is separated from the research laboratories and operation of facilities This organizational setup ensures adequate segregation of duties. The groups of the ASI section «Betriebsstrahlenschutz» have a mandate to supervise the radiological situation at the accelerator facilities and the handling of potentially activated or contaminated material. Subject matter experts on various topics of conventional safety, e.g. fire protection, lasers, chemicals or cryogenic gases are either part of the ASI organization or attached to the respective line organizations. Responsibility for conventional safety lies within the line organizations. The design and build process for new or modified components must include an adequate risk assessment, according to [PSI-PB-9670-214] which is based on ISO 12100 and other standards. The line organization have appointed coordinators to assist the designers in this process and to liaise with the respective subject matter experts. Regular planning meetings are used to coordinate on site activities and to identify work related hazards.

2.2 Assessment of IMPACT

Operation of HIPA is authorized by BAG through licence AG-0444.12.001. A supplemental BAG permit authorizes radionuclide production at IP-2 on the 72 MeV beam. The facilities are supervised by the ASI group «Strahlenüberwachung Areal West». Function owners and facility specific instructions are defined in the operating instructions for HIPA [PSI-AW-81-18-01] and IP-2 [PSI-AW-22-04-01].

IMPACT consists of two constituent projects, HIMB and TATTOOS, with distinctly different challenges regarding radiological protection and regulatory approval:

HIMB is an upgrade project for an already existing beamline section and target region. It will require disassembling of infrastructure, heavy shielding and beamline components that are potentially highly activated or contaminated. Provisions for containment and radioactive waste management, a detailed storyboard and the ability to adjust to the radiological situation found locally during deconstruction will be essential. Much regulatory scrutiny is to be expected during this phase. Regulatory approval may be phased, with conditions imposed. Recommissioning of the new target and secondary beamlines will also require regulatory approval. However, as the main parameters of the primary proton beam remain unchanged, considerable less uncertainty and risk is expected for recommissioning phase.

TATTOOS is largely a new facility. Clearing of existing buildings and infrastructure to provide the necessary space is of little radiological and regulatory interest. The mechanism for diverting part of the proton beam towards TATTOOS may require a risk analysis on the final design. The main challenge, however, consists in the production and handling of alpha-emitting nuclides, which represent a new radiological hazard. Accidental release leading to contamination and unintentional incorporation must be precluded at the target and during further processing. Any emissions must be properly accounted for. The respective laboratories will need to comply with «Laboratory Type A» requirements. The design of safeguards and the respective failure analysis as stipulated in the Radiological Protection Ordinance will be the key for regulatory approval.

The two outlines presented above are further elaborated in the chapters 11 and 23 on Radiation Protection & Safety provided by the respective subject matter experts.

For both projects, conventional hazards are mainly related to construction work and the commissioning of common beamline equipment. There are no known extraordinary issues. Established procedures may be used to identify and manage risks from conventional hazards. This task will be part of the individual work streams.

2.3 Preparedness

PSI is prepared to accept the challenges outlined above. The following achievements and deliverables suggest that PSI will be fully able to cope:

a) There is much experience from regular HIPA maintenance. Each work sheet item is assessed for its radiological impact and measures defined accordingly, e.g. keeping one's distance, erecting local shielding or using personal protective equipment. Highly activated components (up to several hundred Sv/h) are routinely handled, such as target M, target E or a collimator when a replacement or repair becomes necessary. Exchange flasks (see Section 9.3.1 and Chapter 18) are docked to the beamline by crane to pull such components and to encase and shield them during transport. The ATEC facility, also located in the experimental hall, provides two service cells with telemanipulators to repair components or to dissect them for disposal.

   A preliminary concept for dismantling the target M region has been proposed, see Section 12.3.

b) The last major refurbishment of a HIPA target region was that of target E in the early 1990s, in conjunction with the construction of SINQ. Documents available on this task are carefully screened for useful information.

c) Prior to IMPACT, the project SLS 2.0 will be implemented. The project includes a complete exchange of 290 m beamline (SLS storage ring) and other refurbishment work throughout the SLS hall on an ambitious time scale. Although actual activation of components at SLS is expected to be very low, a large amount of material will need to be passed through a release process. The project will strongly depend on thorough and disciplined planning of logistics including workflow and space management. For numerous experimental stations, the conventional hazards associated with the equipment will require assessment and mitigation. In summary, SLS 2.0 will provide beneficial «lessons learned» for the subsequent IMPACT project.

d) The IP-2 facility has been in operation since the 1980s. Much expertise on how to run such a facility can be transferred to TATTOOS.

e) There is expertise within PSI concerning the design and operation of «shielded cells» as required for TATTOOS. Such cells currently exist at the Hot Lab, at IP-2 and at ATEC.

f) Functional safety systems («Person Safety Systems (PSYS)») that prohibit or allow access to an area depending on whether a serious hazard is present or not, have been designed and used at PSI for decades. The design of a PSYS for the TATTOOS target region or the upgrade of the PSYS at the Target M (Target H) secondary beamlines will be straightforward.

g) HIPA has been operating since 1974. Documentation available will be reviewed and reconciled with current realities inside the facility. This process will start in 2022, with a view to create a Safety Report comparable to those ones now required for new facilities such as SwissFEL. It will provide additional assurance that all relevant aspects of the facility are considered before IMPACT is implemented.

2.4 Conclusion

IMPACT is likely the most challenging project at the PSI accelerator facilities since SINQ with respect to radiological hazards. With existing governance structures and skills, PSI will be able to successfully manage the radiation and conventional safety issues during the project and to obtain regulatory approval.

3 Risk Assessment Strategy

3.1 Overview & Scope

The project IMPACT is a large and complex project for PSI, in terms of internal and external budget and resource requirements, duration, and its cross-departmental nature. Our institute has a track record of successfully planning and implementing similar projects, including careful preparation and management of the respective work and control of potential risks.

As part of the external funding process, IMPACT will be audited by competent bodies from the ETH domain, also with respect to risk management processes.

Risk management as a general term may comprise many different aspects. The scope of the risk assessment strategy to be pursued during the IMPACT project needs to be defined more closely, as outlined below.

We strongly rely on the recommendations by the International Project Management Association (IPMA) and the Project Management Institute (PMI), and define our goal for the risk assessment strategy as follows: Identifying potential problems and having a plan for addressing them *before they occur*, thus, decreasing the probability and impact of negative events for the duration of the project to help the project remain on track and meet its goals.

Not within the scope of the project risk management are technological risks, or hazards related to ionizing radiation, safety of machinery, and occupational health and safety. While these matters are of paramount importance, they are covered directly by corresponding regulations, policies and guidelines as described in Chapter 2. They are managed by the line organization and the respective subject matter experts, for (de)construction and installation activities during work preparation, for new or modified components during design, engineering and building. Due to the nature of the project however, radiation and work safety issues are coordinated in dedicated work packages.

The focus of our risk assessment strategy is on project risks. During the identification process, however, risks of any type may be tabled, including those described above. No restrictions will be initially imposed to allow for a broad view and brainstorming. Risk items that are covered by standard processes already implemented in PSI's line organization or project work packages will, subsequently, be deselected. The remaining, genuine project-specific risk items will be nominated and further assessed by subject matter experts, line managers and work package leaders.

Risk management is a continuous activity, to be performed during the entire lifetime of a project. Identified risks will be tracked in a risk catalogue or risk management list, which will be periodically reviewed and updated.

Section 3.2 outlines how the risk assessment strategy is implemented into the project.

3.2 Procedures & Implementation

The designated risk assessment process for the project IMPACT closely follows the IPMA and PMI standards and uses the PSI baseline definitions concerning risk management as defined in guideline [PSI-RL-11-14-01, 2014].

After an initial risk identification (brainstorming), a risk management process will be set up and periodically performed, consisting of four steps (see also Figure 3.1):

1. **Identification** (new risks) and Review (existing risks)
2. **Assessment** or Re-Evaluation (severity & likelihood of risks)
3. **Mitigation & Action** Planning (mitigation measures & strategies)
4. **Monitor & Control** incl. Reporting

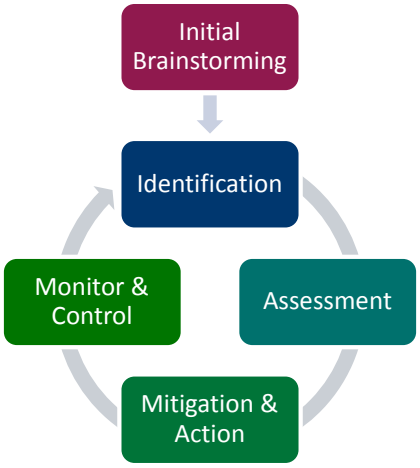

Figure 3.1: Risk management process loop, which is iterated periodically for the entire lifespan of the project.

This process will last a period of 6-12 months, depending on project phase and requirements. For each periodic iteration, it is intended to gather the project team in a workshop and go through the non-closed and new items on the risk management list. This ensures that all project members are regularly updated on project risks and kept aware of the subject.

Newly identified risks that require the immediate attention of the project team will be addressed without delay and communicated properly via the established change management process.

A bottom-up approach is promoted: risk identification, assessment and action planning are aimed to be driven by PSI subject matter experts, to fully profit from their respective expertise. Contributions from project and line managers on cross-functional, organizational and inter-disciplinary risks will complement the risk catalogue.

The design of the risk management process will be documented in the "Projekthandbuch". For registering and tracking individual risk, an appropriately prepared MS Excel-File will be used as a risk catalogue and risk management list. The file will be kept under version control on PSI's document management system. No other particular software tool is deemed necessary at this time.

The subsequent sections describe the four steps of the risk management process loop in more detail.

3.2.1 Identification & Review

The experts in the project work packages have the best technological overview of their domain and are in an ideal position to identify potential risks. Newly identified risks can be registered at any time, after consultation with line managers and work package leaders and become part of the risk catalogue, provided their project risk relevance. If necessary, immediate project management action could be triggered. No later than every workshop iteration, each work package is required to review existing risk items within their domain and brainstorm for any new additions.

Every identified risk is assigned a unique risk ID (number). Mandatory entries into the list are a description of the risk and the date of identification. Optional information would be a detailed description of the impact on the project and possible causes for the risk.

3.2.2 Assessment or Re-Evaluation

Once a risk has been identified, it is assessed in terms of severity and likelihood, as well as risk type category (dimension). As intended by the bottom-up approach, subject matter experts are the key persons to estimate severity and likelihood of a risk.

Two pre-defined six-point scales, ranging from extremely low (1) to very high (6), are used to describe likelihood and severity of a risk. The scales are defined in detail in [PSI-RL-11-14-01, 2014] and are the basis of risk ratings at PSI. The risk rating, defined as *Impact (Severity)* × *Likelihood* = *Risk Rating*, ranges from 1-36 scoring points correspondingly. According to the definitions set forth in [PSI-RL-11-14-01, 2014], commensurate mitigation measures shall be taken. Any risk rated above › 16 scoring points requires particular attention. Risks rated with less than 5 scoring points do not require any actions to be taken, but measures can be implemented if cost- and resource-neutral.

Every risk is labelled with one or multiple risk type categories (dimensions) to help classifying its impact on the project. Dimensions are also used as guidance for brainstorming during risk identification. The minimum set of dimensions to consider consists of:

- Quality-Scope
- Time
- Project Budget

Further dimensions according to [PSI-RL-11-14-01, 2014] include Financial Impact on PSI, Damage to Persons, Damage to Reputation, Damage to Business/Operation, Damage to Environment.

The risk catalogue may also contain dependencies on other major projects and on-site activities, as well as on daily operation of the accelerators and the adjacent user facilities.

3.2.3 Mitigation & Action Planning

After identification and assessment of potential risks, mitigation measures are sought and deployed, where applicable, according to the risk rating. Again, the subject matter experts are most suited to recommend effective mitigation actions. Four basic mitigation strategies are possible according to the guidelines defined in [PSI-RL-11-14-01, 2014]:

- Avoid
- Reduce

- Transfer
- Accept

Multiple measures can be defined for a given risk. A short description of the measure is recorded in the risk management list.

3.2.4 Monitor & Control

Identified risks and respective mitigation measures need to be monitored and tracked. For this purpose, the risk management list contains a responsible project member, a status field and a last review date for each risk. The status can take one of three states: Open, In Progress or Closed.
Mitigation measures that become a regular part or task of a project work package are then included in the regular progress tracking of the project. The status of the respective risk entry will, therefore, be changed to “Closed”. All other risk entries remain in status “In Progress”, or “Open” if no mitigation measures have been defined yet. Review of the risk catalogue and status checks on the implementation of mitigation measures is a continuous project management activity, which will be conducted at least once within each periodic risk workshop cycle.
At every periodic iteration of the process loop, a review of all open items on the risk management list is carried out. If no change to an entry is necessary, only the last reviewed date is adjusted. Otherwise, the entry is updated according to the required changes and a descriptive comment is made. After each periodic review, an updated list of the top rated risks is generated. It will assist project management to keep track of topics requiring closest attention, enabling them to address potential problems before they occur and, thereby, help the project remain on track and meet its goals.

I – HIMB
(High-Intensity Muon Beams)

4 Introduction & Overview to HIMB

4.1 Introduction

Muon physics covers research fields from fundamental particle physics to materials science. Muons are leptons with either negative or positive electric charge, such as electrons and positrons, but 207 times more massive and unstable. Muons are efficiently produced in weak decays of pions which are usually produced by proton beams hitting nuclei in some target material. Muons themselves decay again weakly, with a lifetime of about 2.2 µs.

Since their first discovery, muons played an important role in particle physics to help develop the theory and establish the present Standard Model. Muons are today used to perform some of the most sensitive experiments. In almost all presently existing tensions of experimental measurements with precision predictions of the Standard Model muons are involved, suggesting they might be playing a key role in exploring the landscape of new physics.

With a similarly long history, a broad range of research topics in solid-state physics, chemistry and materials science is being addressed by muon spin rotation (µSR), usually using positive muons as highly sensitive local magnetic probes.

In all these fields, the availability of low-momentum, high-intensity muon beams is a prerequisite, and technological progress from muon production to detector development and sample environments boosted reach and capabilities of the research over decades.

World-wide, several large-scale facilities provide muons to experiments and user instrumentation. They are located at RAL (UK), at J-PARC (Japan), at TRIUMF (Canada) and at PSI in Switzerland. They are all active in condensed matter research, while broader programs in particle physics are pursued mostly at J-PARC and at PSI. A dedicated program in particle physics also exists at the muon campus of FNAL (USA). Several other accelerator facilities are developing or considering a future muon physics program, among them the CSNS (China), RAON (Korea), SNS (USA), and the ESS (Sweden). Some facilities provide pulsed, others continuous muon beams, complementing each other and allowing for different kinds of experiments.

The High Intensity Proton Accelerator facility HIPA at PSI [Grillenberger, 2021] provides one of the most powerful proton beams to target stations, with 1.4 MW average beam power presently only matched by the pulsed SNS. HIPA has a 50 MHz time structure leading to quasi-continuous beams of slow muons. Many experiments today use so-called 'surface muons', positive muons generated in the decay of positive pions stopped close to the surface of a production target. These muons have well-defined momenta, are fully polarised and can be efficiently transported into secondary beam areas. The muon beams at PSI are presently leading the high-intensity frontier, with surface muon rates of order 10^8 μ^+/s, and PSI is home to world-leading research in particle physics and condensed matter research.

4.2 Goals & Scope

The HIMB project aims at providing muon intensities of order 10^{10} μ^+/s into two separate experimental areas for particle physics and materials science constituting a leap forward towards completely new experiments and measurements both in fundamental and applied physics.

This will be achieved by completely removing the existing target station TgM and rebuilding a new target station TgH optimized for the production and capture of surface muons. Two new beamlines will be connected to TgH based on large-aperture solenoids and dipoles that will capture and transport the emitted surface muons with an overall efficiency of around 10 %.

4.3 Overview & Naming Conventions

Figure 4.1 gives an overview of the full HIPA accelerator complex with its high-energy proton beamline and the two target stations and connected secondary beamlines in the experimental hall of PSI. In addition, the SINQ, UCN, and IP-2 facilities are shown, that are also driven by the HIPA proton beam, and the PIF irradiation facility and Proscan proton therapy center, which are based at the small COMET cyclotron. The ATEC shielded service cells are used (see also Section 10.4) to service any of the components from the whole complex that are too radioactive to be handled directly.

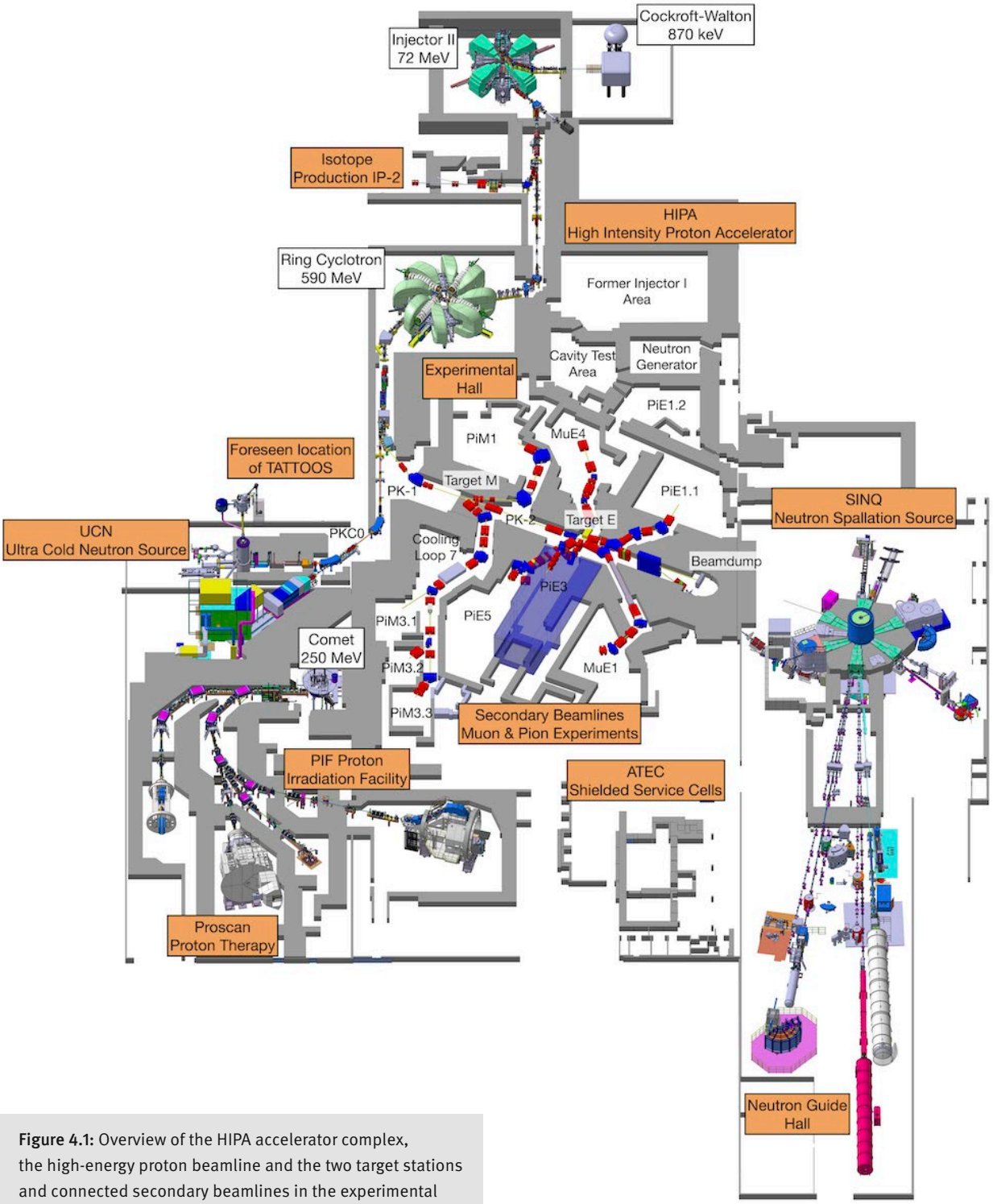

Figure 4.1: Overview of the HIPA accelerator complex, the high-energy proton beamline and the two target stations and connected secondary beamlines in the experimental hall. Additionally, the SINQ, UCN, PIF, Proscan, and IP-2 facilities are shown together with the ATEC shielded service cells.

The HIPA high-intensity proton accelerator consists of the electrostatic Cockroft-Walton accelerator delivering a proton beam at 870 keV and the two cyclotrons Injector II and Ring Cyclotron that further increase the proton energy to a total of 590 MeV and a beam current of up to 2.4 mA. This constitutes a world-record average beam power of 1.4 MW being delivered at a frequency of 50 MHz.

This high-power beam continues along the proton channel (with its different sections PK-1 and PK-2) to the two existing graphite targets TgM, which is 5 mm and TgE, which is 40 mm long. The remaining beam after these two targets is either sent to a dedicated beamdump or is bent first downwards and then again upwards to the SINQ facility reaching its spallation target from below. Additionally, the full proton beam can be kicked with a duty factor of a few percent to the UCN spallation source through the proton channel PKC0. Next to the UCN area, the new TATTOOS facility will be installed which will lead to a third leg of the proton beam in this area (see Part II TATTOOS, Chapters 13-22).

A total of 5 secondary beamlines are connected to the thicker target TgE (PiE5, PiE3, MuE1, PiE1, MuE4) while only two are located at TgM (PiM1, PiM3). They are shared between the particle physics and μSR communities and are host of a large number of muon and pion experiments every year.

The tertiary water cooling loop 7 is located just at the beginning of the PiM3 area and serves a multitude of components along the muon and proton beamlines and the production targets. As the cooling water gets heavily activated, the installation is embedded into the biological shielding. Just above the cooling loop on top of the shielding a helium liquefication plant is located providing liquid helium for the experiments and installations in the seven experimental areas and the SINQ facility.

The main work of the HIMB project will of course concentrate on the target TgM, the muon beamlines PiM1 and PiM3 and the proton beam sections PK-1 and PK-2. However, as described in the further sections of this document, infrastructure components such as the water cooling loop 7 and the helium liquefication plant will need to be moved. Additionally, in the north part of the experimental hall escape routes will be significantly improved by removing legacy installations and rearranging existing walls in the regions of the cavity test area, neutron generator, and the two experimental areas PiE1.2 and MuE4.

4.4 Structure of PART I

The remainder of the HIMB part of the document is structured in the following way: It starts with Chapter 5 that details the requirements for HIMB stemming from the science case and the user community, gives an overview of the final design parameters and details the boundary conditions for its implementation. Chapter 6 explains the detector technology and developments accompanying the project to fully exploit the high and unprecedented muon rates offered by HIMB. These more introductory sections are followed by Chapters 7 to 9 which present the various conceptual designs for the muon and proton beamlines and target station that will allow us to reach the goal of transporting 10^{10} μ^+/s into two separate experimental areas. Chapter 10 explains the complex dismantling and installation process in the challenging and highly radioactive environment. Connected to these processes are of course all aspects related to radiation protection and safety detailed in Chapter 11. The required changes to the building and infrastructure are described in the final Chapter 12 of this Part I.

5 Design Strategy and Parameter Choice

5.1 Summary HIMB Science Case

The interested national and international muon science community met for a HIMB science case workshop, April 6-9, 2021 at PSI, as a kick-off event for the work presented in [Aiba, 2021]. While this 116-page document reports on ongoing work and many aspects will be worked out over the coming years and many new, additional applications and ideas for HIMB will continue to appear, it encompasses a compelling physics case documenting unprecedented opportunities for muon science. HIMB will secure a world-wide leading position of fundamental and applied muon science at PSI and attract many national and international user groups. Specific findings of future research cannot be predicted, however, it is clear that HIMB will have great impact. Projects to be conducted on this new facility will push the limit of the known far into presently unknown territory with plenty of opportunities for ground-breaking discovery, furthering basic knowledge and understanding of nature, development of novel technologies and fertilizing spin-offs to other fields.
The HIMB project will lead, among other things, to the following unique and flagship research opportunities:

Particle physics: The hundredfold increased muon rates allow for the highest sensitivity searches for physics beyond the standard model through rare muon decay processes. In particular, new experiments on charged lepton flavor violation and lepton universality are very high up on the international roadmaps for particle physics and a necessary complement to the advances at CERN's Large Hadron Collider.

Materials science: Together with ongoing advances in detector technology, the time needed for the magnetic characterization of samples will be reduced by more than a factor of 10, allowing more detailed or expanded studies, including new research directions in quantum magnetism by applying external stimuli at unprecedented levels.

Muon beam development: HIMB will enable the long-term development of a truly exceptional reaccelerated muon microbeam that can be controlled in all three dimensions at the level of a few tens of micrometers, benefitting fundamental and applied research.

Other interesting topics in applied and fundamental physics were identified and described in the science case document that motivate the push for much increased muon rates at PSI by outlining a very strong and unique program for two decades following the implementation of HIMB.

5.2 Requirements of the Experiments and User Community

The muon and pion secondary beamlines in the experimental hall of PSI are used by the particle physics and condensed matter and materials science communities. While the experimental collaborations in particle physics typically consist of 10 to 100 people that develop and perform an experiment over several years with typically multiple weeks of beamtime every year, the teams performing condensed matter research are much smaller with typical measurements taking only a few days on one of the existing μSR instruments. The corresponding beamlines and instruments are summarized under CHRISP for particle physics and SμS for materials science.
One of the main drivers in particle physics for fully exploiting the available muon rates are the searches for rare muon decays culminating in the MEG II and Mu3e experiments that are currently occupying the PiE5 area. However, in a few years, when the ongoing experimental campaigns will be completed, these experiments will have reached their conclusion as any additional increase in sensitivity will require increased muon rates. As described in Section 5.1, the much increased muon rates offered by HIMB will allow these experiments to probe ever deeper into the realm of new physics and allow them to continue to pursue these kinds of experiments at PSI. Additional experiments and especially also exciting beam developments have been identified as described in Section 5.1, that will profit from HIMB both directly by being performed at one of the HIMB beamlines, but also indirectly by allowing such lower priority experiments to take place in a first phase in the PiE5 area, which already now offers much higher rates compared to the other CHRISP beamlines PiM1 and PiE1.
The requirements of the users of the SμS beamlines are somewhat different to the ones of the particle physics com-

munity. Here, the users require fast and thorough characterizations of their sample under a multitude of different external stimuli such as temperature, pressure or external magnetic field. HIMB together with advances in detector technology will enable a significant step forward in the application of the μSR technique for sample characterization as it will allow much faster measurements thus enabling, e.g., extended measurement series, the use of much smaller samples of novel quantum materials, or the use of multiple samples at the same time, and the application of external stimuli at so far unprecedented levels.

Of course, paramount for the success of the experimental program described in this and the previous section is the continued excellent and extremely stable performance of HIPA for the next two to three decades. In addition to HIMB, investments will thus be necessary to upgrade and refurbish parts of the accelerator in order to fully exploit the potential offered by HIMB.

5.3 Overview, Layout and Design Parameters

Figure 5.1 shows the basic layout of the new target station TgH, the surrounding target shielding block and the two attached beamlines MuH2 and MuH3. Here in this section, we would like to summarize the main design parameters that led to this layout. More details on all of these choices can be found in the dedicated sections following later in the document.

- The position of the new target TgH is at the same location as the old TgM. This is basically driven by the required extended collimation system, the existing proton channel downstream of the target (which should not be changed) and the needed length to refocus the proton beam properly onto the second production target TgE.
- Target H is designed as a slanted target with a 10-degree slant angle with respect to the proton beam and an

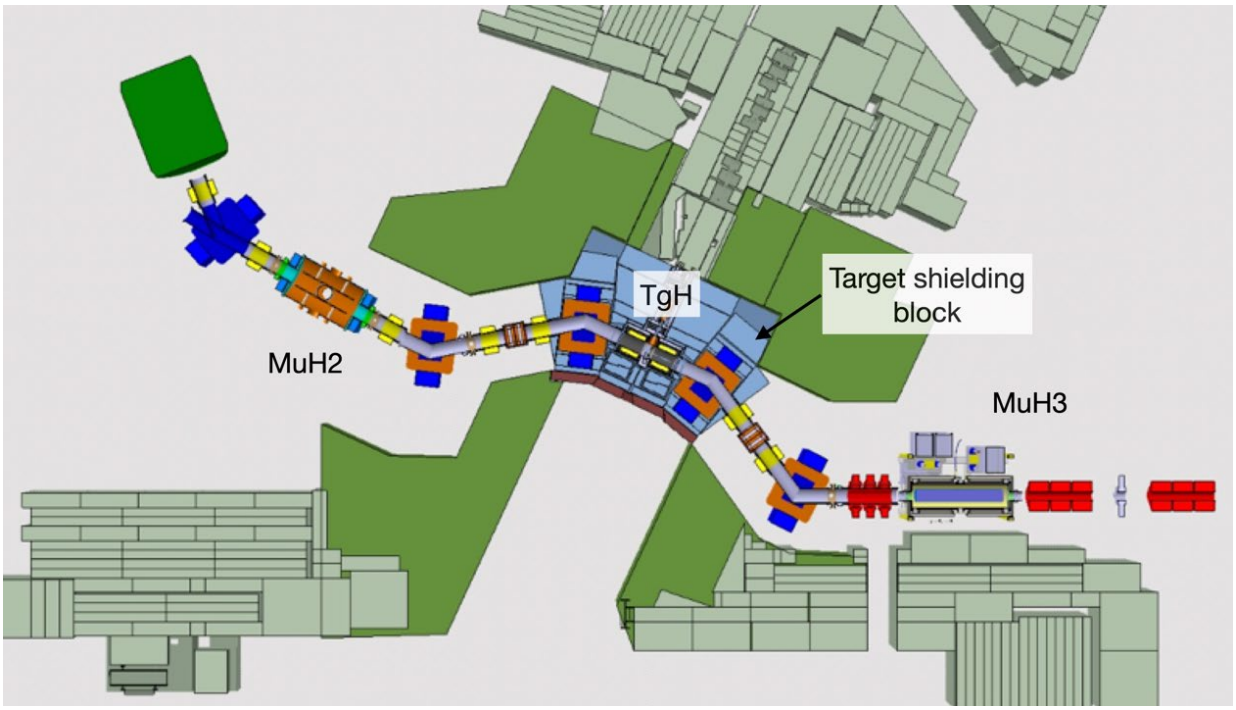

Figure 5.1: Picture of the layout of the new target station TgH with the surrounding target shielding block and with the attached solenoidal beamlines MuH2 and MuH3. Part of the new shielding is shown in green. For clarity, it is removed in the picture around the secondary beamlines.

overall slab length of 100 mm. The basic design of the target insert follows the design of the existing target TgE such that also the same, existing exchange flask can be used for the two targets.

- The two secondary beamlines MuH2 and MuH3 face the target at 90 degrees with respect to the proton beamline. The beamlines feature two dipoles of moderate deflection angles to obstruct any direct line-of-sight from the experimental areas onto the production target. Additionally, the first dipole bends the secondary beam into the upstream direction (with respect to the proton beam) to reduce the amount of radiation being transported along the secondary beamlines and to better adapt to the existing layout of the experimental areas. The muon beamlines each feature a capture solenoid located close to the target with the beginning of the coil being only 250 mm away from the proton beam.
- Two infrastructure installations are in the way of the new installations. The tertiary water cooling loop 7 is in the way of the MuH3 beamline and thus needs to be moved to a different location. Additionally, the existing helium liquefier is located on top of the shielding just above the tertiary water cooling loop 7. During the dismantling of the existing target station and shielding it has to be dismantled as well. It was decided to move it to a new and better location inside the experimental hall and not reinstall it at the previous location.
- All of the new installations will be designed and laid out for a potential upgrade of the proton beam current to 3 mA.

5.4 Realization Strategy, Boundary Conditions and Legacies

The funding for HIMB will be applied for through the 2023 Swiss Roadmap for Research Infrastructure with the funding period spanning from 2025 to 2028. Due to ongoing works related to the SLS 2.0 upgrade program at PSI, the HIMB implementation is foreseen in parallel to the TATTOOS installation during a long shutdown of HIPA and all related facilities beginning in 2027 and taking 16 months.

The careful planning of this long shutdown is of great importance and has to be completed early on as not only the meson production targets are impacted but also the SINQ and UCN facilities. With the 16-month shutdown, the facilities would in essence miss only one full beam period. Any additional delays or extensions of this shutdown would lead to additional loss in beam time at all these facilities.

The area around the existing TgM, and the experimental hall of PSI in general, is densely packed and used. Very large changes to the overall layout of the experimental hall in the design of the new target station and secondary beamlines are thus nearly impossible. However, as some changes to the experimental areas (especially for MuH2) will be needed, we use this opportunity to clean up and simplify some of the legacy infrastructure and design choices in order to improve the situation for the everyday operation in the experimental hall and to provide escape routes conforming to today's regulations and standards.

6 Detector & High-Pressure Cell Development

This chapter details the developments ongoing in parallel to HIMB at PSI and UZH on pixel detector technology and advanced high-pressure cells in order to fully exploit and profit from the increased muon rates as soon as HIMB becomes operational. Sections 6.1 and 6.2 give the current status in pixel detector and high-pressure cell technology world-wide and in Switzerland together with an outlook on the research directions followed both at PSI and UZH and the currently existing infrastructure and equipment at PSI and UZH. Switzerland already now plays an important part in this research world-wide - with IMPACT, we want to ensure this leading position. Thus, Section 6.3 introduces the new DEMETER (Detector & Matter at Extremes Test and Research) centre to be installed at UZH as part of the IMPACT programme. The centre will allow UZH and PSI scientists, as well as the Swiss and international scientific community, to fully take advantage of HIMB at PSI, by facilitating a new generation of pixel detectors for muon-decay experiments, as well as novel high-pressure devices for the study of materials with muon spin spectroscopy at the extremes of pressure. The joint DEMETER centre will provide state-of-the-art equipment to synergistically combine the expertise of detector development from the particle physics groups and high-pressure development from the condensed matter groups at the UZH Physics Institute and PSI. The centre will be accessible for Swiss and international researchers as a world-class facility with the developments being relevant not only to HIMB but more generally to high-energy physics programmes or as instrumentation for neutron and light sources.

6.1 Detector Development

6.1.1 Present Situation

The SCNAT CHIPP roadmap for particle physics [SCNAT, 2021] prioritizes the HIMB program at PSI and the particle physics it delivers. It highlights the current expertise in silicon detectors at UZH and PSI, and it points out the necessity of silicon detector R&D for improving timing and position resolution capabilities in HIMB experiments as well as at CERN in order to cope with intense particle fluxes.

The precise reconstruction of trajectories of charged particles will be a key ingredient in the physics and materials science experiments which are planned at HIMB [Aiba, 2021]. In order to carry out these experiments with an increased flux of incoming muons, highly granular detectors with excellent resolution and high-rate tolerance are needed. Silicon pixel detectors are the first choice for these applications and are foreseen to be used for track and vertex reconstruction in stopping-target experiments, for the reconstruction of particle trajectories in a muon storage ring, as active targets in muon and pion experiments, and for beam monitors and other measurement devices.

Over the past decades, pixel detectors have blossomed into many applications that have driven numerous discoveries [Damerell, 2021]. Pixel detectors come in three forms. Charge-coupled devices (CCDs), in which the charge signals are transferred from pixel to pixel to the output circuitry, were the first type of silicon pixel detectors used in precision tracking, but their applicability is limited due to long readout times and poor radiation tolerance. Monolithic active pixel sensors (MAPS), implemented in commercial CMOS technology, provide charge-detection circuitry in each pixel and can be operated at higher speeds. Hybrid pixel detectors, in which the sensor and readout electronics are separately produced in optimized processes, allow the use of complex analog and digital circuitry in each pixel. Large-area, hybrid pixel detectors have been recently used for the first time in LHC experiments, and since then have been established as the instrument of choice for particle tracking and vertex reconstruction in a high-rate environment [Garcia-Sciveres, 2018]. Their fine granularity of ~100M pixels each with a size of ~100 ×100 μm^2 and good spatial resolution of ~10 µm enables crucial measurements for a wide range of particle physics phenomena, in particular the identification of heavy quarks, tau leptons, and other long-lived particles made possible through the reconstruction of displaced tracks and secondary vertices. The high-energy physics group at PSI's Laboratory for Particle Physics has been successfully developing hybrid pixel detectors since the early 1990s, including all key technologies: sensors, readout chips, and the bump-bonding interconnection technique [Allkofer, 2008; Kästli, 2006; Meier, 2011; Brönnimann, 2006]. The group built the complete barrel part of the original CMS pixel detector [Caminada, 2009] and led the

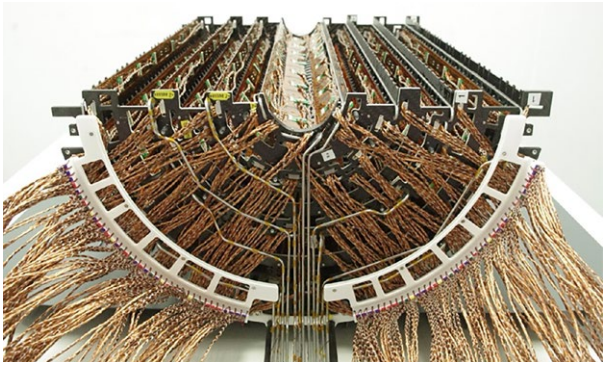

Figure 6.1: Picture of one half of the CMS Phase-1 pixel barrel detector built at PSI in 2017.

CMS phase-1 pixel detector upgrade [CMS collaboration, 2021], shown in Figure 6.1.

The generation of electron-hole pairs in silicon due to the interaction of ionizing particles with the sensor material is used as the detection principle in particle physics applications. The sensors of hybrid pixel detectors are operated in reverse-bias configuration and drifting charges are collected in potential wells at the surface of the sensor. This allows the design of fast and radiation-tolerant devices. In contrast, the early MAPS detectors [Kenney, 1994; Turchetta, 2001], which used standard CMOS processes without any modifications, were built from CMOS processes with two wells and substrates with thin epitaxial layers. The charge signal in these detectors is small and slow as charges move by diffusion. With the rise of triple- and quadruple-well CMOS technologies, it became possible to develop depleted MAPS detectors (DMAPS) with features similar to the present hybrid pixels in terms of spatial resolution, high-rate capability, and radiation hardness. Moreover, the use of DMAPS devices eliminates the need for the expensive and complex bump-bonding step in the construction of pixel detectors and opens the possibility of developing a new generation of thin, large-area pixel detectors with small pixels. Thin detectors provide less scattering and therefore more precise reconstruction of particle trajectories. This makes DMAPS detectors the most attractive choice for pixel detectors at future particle physics experiments. In fact, the pixel detector that is currently being constructed for the Mu3e phase-1 experiment is making use of a variation of the DMAPS technology called HV-MAPS [Peric, 2014].

6.1.2 Basic Considerations, Requirements, and Constraints

The Mu3e phase-1 experiment has demonstrated that DMAPS detectors, which can be thinned to tens of micrometers, have become an attractive alternative to gaseous detectors for the tracking of low energetic particles. This is especially true for high-rate applications, where the use of gaseous detectors is limited due to high-voltage stability and ageing effects. With an ultra-light mechanical design and the use of gaseous helium cooling, a thickness of about 1 per mil of a radiation length can be achieved for a silicon tracking layer [Arndt, 2021]. The use of DMAPS detectors is foreseen in different particle physics experiments at HIMB, in particular also in the Mu3e phase-2 experiment. The increased rate of incoming muons requires a redesign of the muon stopping target to achieve a similar stopping rate as in phase-1 of the experiment [Aiba, 2021]. The excellent vertex resolution provided by pixel detectors is exploited to suppress the accidental background (coincident muon decays) from the proposed long muon stopping target (about 30 cm in length in phase-2, three times longer compared to phase-1). A sketch of the experimental concept is shown in Figure 6.2. A new generation of sensors will need to be developed with improved resolution (smaller pixels with size of $< 50 \times 50\ \mu m^2$), larger area, and

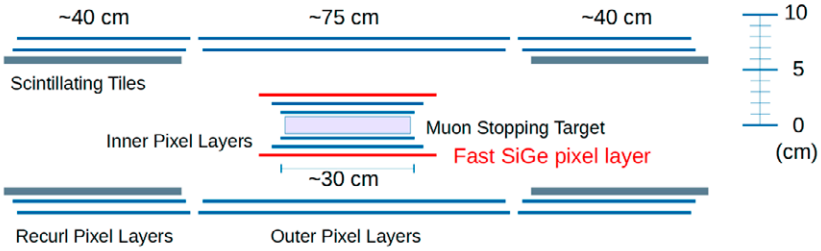

Figure 6.2: Sketch of an elongated detector design for Mu3e Phase-2 at HIMB.

advanced readout capabilities (daisy chaining of the data to minimize the need for additional readout circuitry).

In addition to track and vertex reconstruction, silicon pixel detectors are also considered as a new technological approach for time measurements in the Mu3e experiment (timing layer). The scintillating fiber detector that is used in the central region of the Mu3e phase-1 experiment cannot be operated in phase 2 because the occupancy in the fibers will be too high from the particle rates expected at HIMB. To overcome these limitations, a thin, pixelated detector with timing resolution of the order of 100-200 ps is being conceived of for timing measurements in the Mu3e Phase-2 experiment. The development of DMAPS detectors with sub-nanosecond timing resolution and sub-millimeter pixel size is an active field of research and the desired performance has been demonstrated in small prototypes [Paolozzi, 2019; Kugathasan, 2020]. Achieving such timing resolution on a large-scale chip in tracking systems will be one of the main goals of pixel detector R&D in the coming years.

DMAPS detectors also offer the possibility to be used as active targets in muon experiments in order to directly measure the muon decay position. This is particularly interesting for searches with photons in the final state as the vertex constraints significantly improve the resolution of the measurement of the particle direction and its momentum. Furthermore, DMAPS-based active targets are considered for the reconstruction of photons converting to an electron and positron. This is of high interest since the tracking of an electron and positron, together with a direct measurement of the energy loss in silicon, allows for a significantly better energy resolution compared to a calorimeter-based measurement. In order to reach acceptable conversion rates, thick DMAPS detectors are needed with a depletion region of a few hundred micrometers. Finally, the development of radiation-hard DMAPS detectors [Schöning, 2019; Bespin, 2020; Tortaiada, 2021] is also promising for high-precision real-time beam monitoring applications at HIMB.

Pixel detectors not only enable new scientific approaches in particle physics, but also in muon experiments in solid-state physics and materials science, in particular μSR. HIMB, in combination with the use of DMAPS detectors for vertex reconstruction, will lead to a “quantum leap” of the μSR technique, enabling new research directions due to the much faster accumulation of data, as well as more efficient measurements. Moreover, the envisaged spatial resolution (<1 mm) also allows for the measurement of multiple samples in parallel within the same exposure, the separation of domains with different magnetic properties in custom samples, and for new opportunities for the measurement of samples under extreme conditions of pressure and external fields.

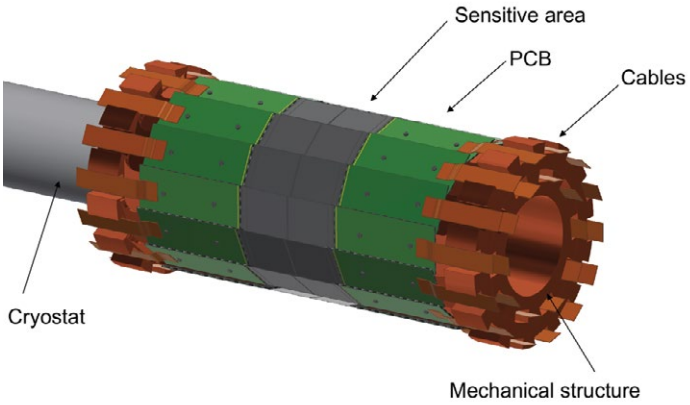

Figure 6.3: Concept of a pixel detector for a muSR instrument.

6.1.3 Pixel Detector Technology & Development

To enable pixel detectors for the next generation of particle physics experiments and other instrumentation, research and development must encompass all components of the detector, from sensors and integrated electronics to readout systems, as well as lightweight support structures and advanced cooling options. The goal is to realize detectors optimized for:

- High-precision spatial resolution (<5 μm)
- Low mass
- Timing resolution (~10 ps)
- High rate and radiation tolerance

High-precision spatial resolution and low mass detectors are of utmost importance for the development of tracking and vertexing detectors at HIMB. Rate and radiation tolerance are important factors when designing concepts for active, pixelated targets and monitors to be placed in the high-rate muon beams, while precision timing detectors will allow for the measurement of time coincidences in a high-rate environment.

An example of detector development for HIMB is the construction of a DMAPS detector for μSR. A concept for a prototype pixel detector for the General Purpose Surface (GPS) muon instrument is shown in Figure 6.3. The pixel detector is built from two concentric cylinders surrounding

a cryostat in which a sample is placed. The cylindrical axis is placed perpendicular to the muon beam. The pixel detector is used to measure the trajectory of the incoming muon and the outgoing positron, and to reconstruct the location of the muon decay vertex that is within the sample.

Due to the low momentum of the muons (‹ 30 MeV/c), the spatial resolution of the detector will be dominated by multiple scattering effects and the use of thin DMAPS sensors will be crucial. The prototype detector uses a sensor from the MuPix family [Peric, 2013] as a sensitive element. All components needed for readout, powering, and cooling for the detector are placed outside the active area. The detector performance has been studied in simulations assuming a sensor thickness of 50 µm, and the precision for reconstructing the muon decay vertex was found to be better than 1 mm. The experimental concept has been validated in a beam test in the PiE5 area in the context of the Mu3e integration run in summer 2021.

R&D is ongoing to develop an advanced detector concept that makes use of DMAPS detectors with timing resolution of less than 100 ps such that, in addition to the direction of the muon and the positron, the µSR oscillation signal can be simultaneously reconstructed.

Another area of research is to develop pixel detectors that not only precisely measure position resolutions down to several-micron precision, but also measure the transit time of the particles down to the level of 10s of picoseconds. This additional temporal measurement means that time becomes a new dimension in the tracking of charged particles. The result of such technology is that experiments can run at much higher event rates because the high-occupancy environment can be disentangled in both the space and time dimensions, so that statistically more precise measurements of particle physics processes can be achieved.The 4D tracking paradigm is based on the development of silicon sensors with internal gain, which enhances the signal amplitudes and leads to excellent performance of time resolution. An intense R&D activity is being carried out world-wide to develop fine-pitch sensors with spatially uniform multiplication in order to provide precise spatial and time resolution. This technology is being considered for future upgrades of the ATLAS, CMS and LHCb vertex detectors beyond the Phase-2 upgrades at the LHC.

Finally, a further area of development is towards more radiation-tolerant detectors. Since silicon detectors are the most precise components of an experiment, they are placed close to the interaction region, where the typical integrated fluence in the coming decade of experiments will reach 2E16 1 MeV neutrons equivalent per cm^2, yielding 10 MGy (1 Grad) of Total Ionizing Dose (TID). Radiation damage happens when the silicon lattice is permanently altered by the creation of vacancies or interstitial atoms. Depending on the accumulated fluence, the main effects on the operation of silicon detectors are: increased leakage current, an increase in the voltage required to fully deplete the substrate, and a decrease in charge collection efficiency (CCE). The damaged regions created by the radiation dose in the silicon volume act as electrically active defects with deep levels in the prohibited band of the silicon. Some lines of research focus on material engineering by adding controlled amounts of impurities to reduce the effects of radiation damage. Other R&D activities seek to modify the sensor design in order to obtain more radiation-resistant devices, for example, by reducing the active thickness in planar sensors or using 3-D structures, where the electrodes are columns etched vertically through the silicon bulk, and the drift distance of charge carriers becomes smaller.

The next generation of experiments at PSI and CERN, which have national interest from all the particle physics groups in Switzerland, as well as international interest from Europe and abroad, will require advances in the research lines above in order to produce physics measurements that significantly improve on what can be achieved today.

6.1.4 Detector Development Infrastructure and Equipment at PSI and UZH

The High-Energy physics group at PSI has conceived and built the original and current CMS barrel pixel detectors, and in this context developed radiation-tolerant readout electronics, radiation-tolerant double-sided silicon pixel sensors at the mask level, a micro-bump-bonding process for hybridization, as well as system concepts for pixel readout and control. The UZH group collaborated on this effort by developing the CMS pixel detector supply system, which provides cooling, powering, digital-optical communications, and control electronics to the detector pixel detector. Cur-

rently the PSI and UZH research groups are leading the design and construction of the extended pixel system (TEPX) for the Phase-2 upgrade of the CMS experiment and are undertaking R&D for monolithic as well as high-precision timing pixel detectors for future experiments.

In order to enable these developments, important infrastructure has been setup. At PSI, this includes a wafer probe station (for 4 and 8 inch wafers), a wire-bonding and bump-bonding machine, manual and robotic pixel detector module assembly lines, chillers and cold boxes for module

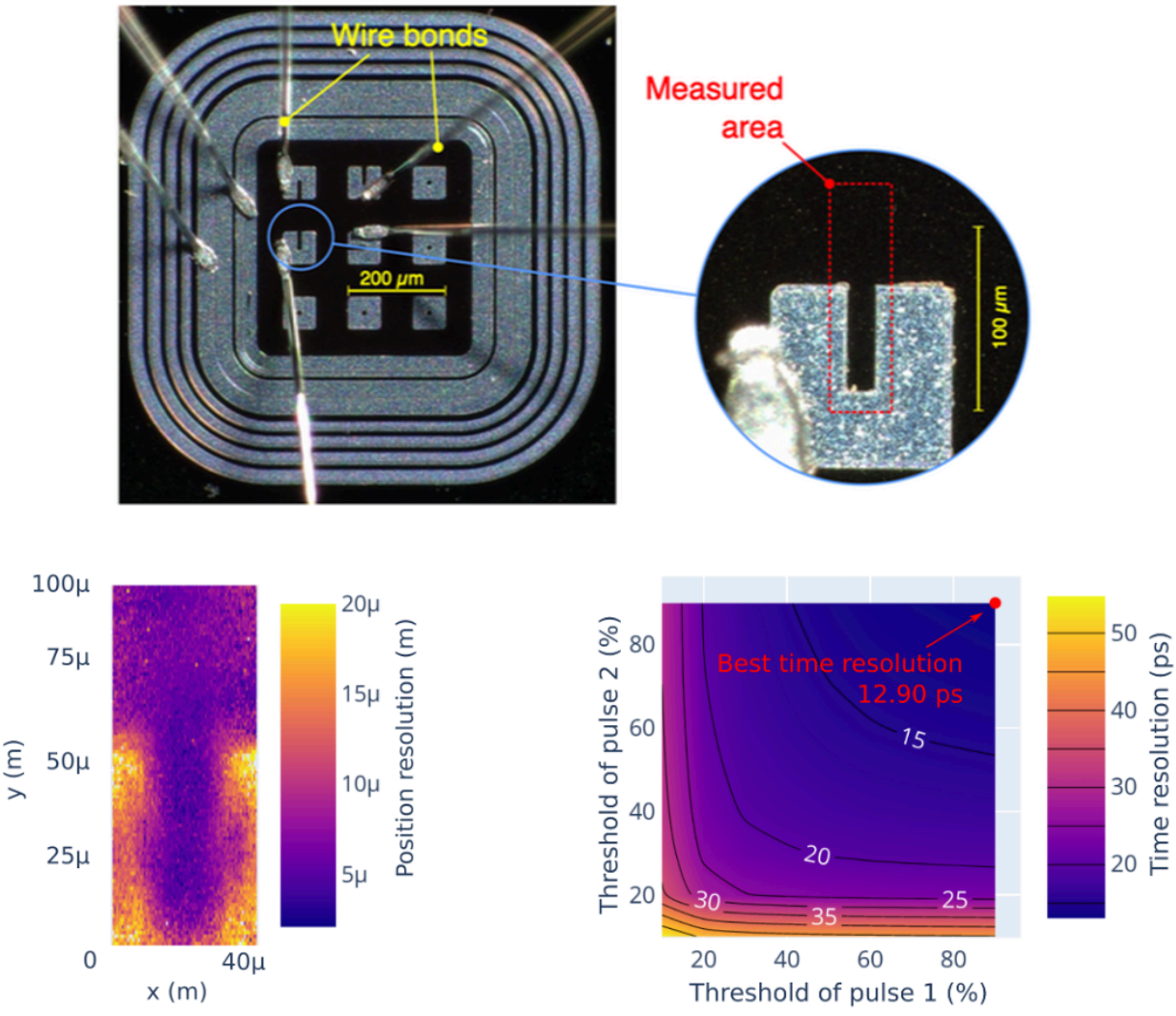

Figure 6.4: Measurements at UZH of time and space resolution of LGAD sensors using fast laser pulses. Upper left: sensors with notches to permit the measurement of fast laser pulses that are read out by wire-bonded electronics (not shown). Upper right: closeup of notched area, highlighting the measured area for one set of measurements. Lower left: Plot of position resolution of the measured area in units of micrometers in the form of a color map as a function of position on the sensor. Lower right: Plot of time resolution in picoseconds as a function of the threshold (constant fraction discriminator) above noise considered for the start (x-axis) and stop (y-axis) of the recorded ionization pulse. The new DEMETER silicon detector research facility would enable more precise sensor measurements.

testing, DAQ systems (USB, NIM, VME, uTCA), multichannel HV and LV power supplies, a digital microscope, high-speed oscilloscopes, a high-rate x-ray box, and 3D printers.

At UZH, a cold-probe sensor station (for 8 inch wafers) and device analyzer, data acquisition systems, and oscilloscopes are also being operated. Two liquid CO_2 refrigeration and two climate chambers allow for the qualification of sensors under different environmental conditions. Furthermore, a high-rate X-ray chamber for calibrating and testing detector modules has been developed and an infrared laser system designed to replicate the precise deposition of electric charge on sensors by using the Transient Current Technique is in operation. Figure 6.4 shows an example of position and timing resolution results obtained with novel low-gain avalanche diode sensors using laser pulses.

The High-Energy physics group at PSI has established close collaboration with the SLS/SwissFEL detector group in the PSD division, which is developing hybrid silicon-pixel detectors for X-ray applications. Many designs and technological advancements have been transferred to the PSD group, such as the bump-bonding technique. Furthermore, the groups share some of the infrastructure mentioned above to make better use of the equipment.

The DEMETER silicon detector facility, described in Section 6.3.1, will be an integral part in the research lines necessary for developing the next generation of pixel detectors.

6.1.5 Data Acquisition Systems, IT and Data Rate Requirement

In the framework of the Mu3e experiment, a dedicated data acquisition system has been developed using state-of-the-art FPGA technology connected to DMAPS detectors and using high speed serial links for readout [Augustin, 2021]. The Mu3e experiment will produce about 100 GBit/s of zero-suppressed data, which will be transported to a dedicated computing filter farm that uses modern Graphical Processing Units (GPUs) for event processing and filtering. The filter farm outputs about 100 MBytes/s, which can be stored and processed at PSI using a dedicated offline computing farm with about 250 CPU cores and a few TBytes of disk space. Similar systems can be used for other applications in the HIMB project. In the case of the μSR detector, individual events can be compressed online into histograms, reducing the data rate further by orders of magnitude, since only histograms need to be kept together with a subset of the raw hit data.

Raw data of all PSI experiments will be preserved for at least 10 years by the PetaByte-Archive operated by PSI in collaboration with the Swiss National Supercomputing Centre CSCS. After exploration by the collaborations, high-level data will be made publicly available under the Creative Commons CC0 waiver.

6.2 High-Pressure Cell Development

6.2.1 Present Situation

One of the major benefits of the upgraded HIMB will be the potential to carry out muon spin spectroscopy (μSR) on condensed matter systems at substantially higher pressures than currently possible [Aiba, 2021]. Due to synergetic overlap with the fields of chemistry, materials science, engineering and nano-technology, condensed matter is the most populated field of physics. Meticulous understanding of condensed matter systems has had a profound impact on present day technologies. Mastering silicon, for example, led to the invention of the transistor, and with that modern computer electronics. Contemporary condensed matter physics research with materials that surpass silicon in terms of complexity hold potential for future industrial revolutions. Our current state of understanding of the microscopic properties of condensed matter is largely owed to advanced particle probes combined with extreme environments (low temperature, high magnetic field or pressure) that allow materials to be tuned and optimized. μSR at PSI is one of the techniques that has been extremely successful in exploring microscopic properties of condensed matter at the extremes of high pressure.

The μSR user community, composed of about 300 users from more than 40 universities and research centers, makes use of about 65 % of the overall beam time available at the secondary muon beamlines, the rest being used by the particle physics community. About 40 % of the users of the PSI μSR facility originate from Swiss universities and research centers. The SμS (muon beamlines at PSI dedicated to μSR measurements) is visited every year by an average

of 230 users (Figure 6.5), highlighting that nearly the entire international community visits SμS every year. The SμS also receives about twice as many proposals as instrument days are available, again showing that μSR studies are crucial to the Swiss community. Currently, 90 % of all proposals submitted for the spectrometer GPD are high-pressure studies and comprise ~12 % of all SμS users (Figure 6.5).

However, the condensed matter community that is investigating materials at the extremes of high-pressure is much larger. For example, the European High-Pressure Research Group International Conference hosts a few hundred scientists yearly. For bulk techniques, which are more frequently used to study condensed matter at high pressure, higher pressures of more than 100 GPa can be reached. These pressures are currently out of reach at PSI's SμS source, despite it being the world leading μSR high-pressure facility [Aiba, 2021; Khasanov, 2016]. Due to limitations in beam spot size and sample size – causing problems with background of muons stopping in the pressure cells, or problems with the mechanical stability of large samples in the device for applying uniaxial pressure – the maximum pressures are 1 GPa and 2.8 GPa for uniaxial and hydrostatic pressures, respectively [Aiba, 2021].

HIMB has the potential to change this, and would automatically lead to an increase of the available community. In particular, from the increase of the muon rate from the improved HIMB target, together with the future development of pixel detectors (see Section 6.1), it is expected that the maximum pressure that can be achieved will be 10 to 100 times higher than the current state-of-the art.

6.2.2 Basic Considerations, Requirements, and Constraints

Historically and currently, PSI is internationally leading in the field of high-pressure μSR experiments [Khasanov, 2016]. Although, the bulk of high-pressure μSR experiments, as well as the development of new pressure cells, takes place at PSI, other muon facilities also offer high-pressure capabilities to their users. At the ISIS facility in the UK, high pressure experiments with up to 0.6 GPa can be carried out at the RIKEN-RAL beamline. At the Canadian TRIUMF facility, a single wall piston-cylinder pressure cell with a maximum pressure of 2.3 GPa is available at the dedicated Omni-Prime spectrometer at the M9B beamline.

The first μSR experiments under pressure were carried out at PSI in 1980, using a clamped cell with a maximum pressure of 0.7 GPa. Although a He gas pressure cell with a maximum pressure of 1.4 GPa was designed in 1986, and used until the end of the 1990ies, the current state-of-the-art in high-pressure devices are piston-cylinder cells because they not only allow higher pressures but can also be used below temperatures of 10 K, which was the lowest temperature

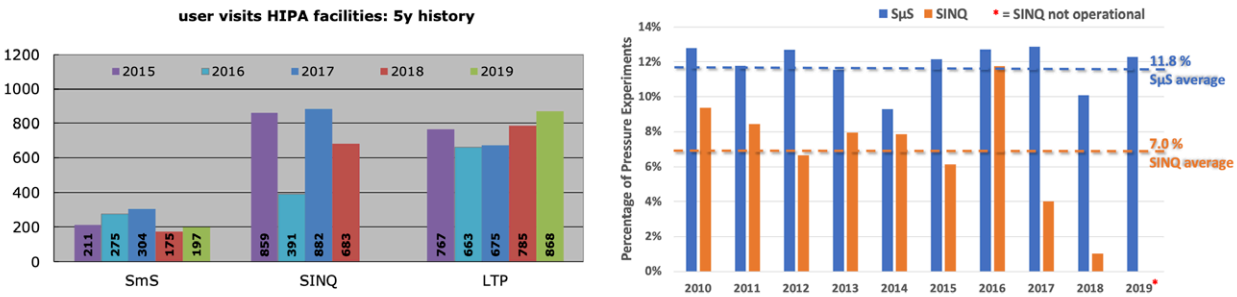

Figure 6.5: User statistics for the SINQ neutron source and SμS muon source at PSI. LTP denotes the particle physics community. (Left) Total number of visits per facility over the last five years. Note that SINQ was not running in 2019 due to a major upgrade [SCNAT Neutrons, 2021; Geue, 2021]. (Right) Percentage of accepted experiment proposals that employ high-pressure cells. The dashed lines give corresponding average values. Note that the dip in in pressure proposals at SINQ is due to various upgrade activities. All data is from the PSI user office.

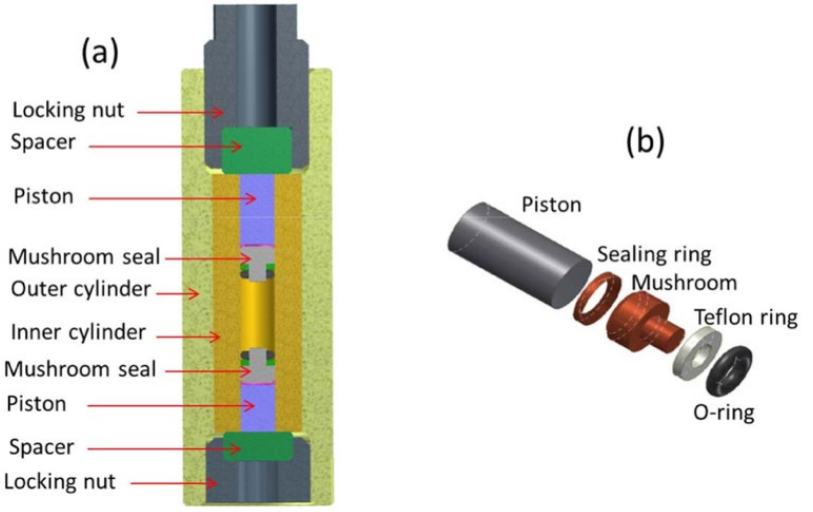

Figure 6.6: (a) Cross-sectional view of the PSI double wall piston-cylinder pressure cell for μSR; (b) Details of the pressure seal. From [Khasanov, 2016].

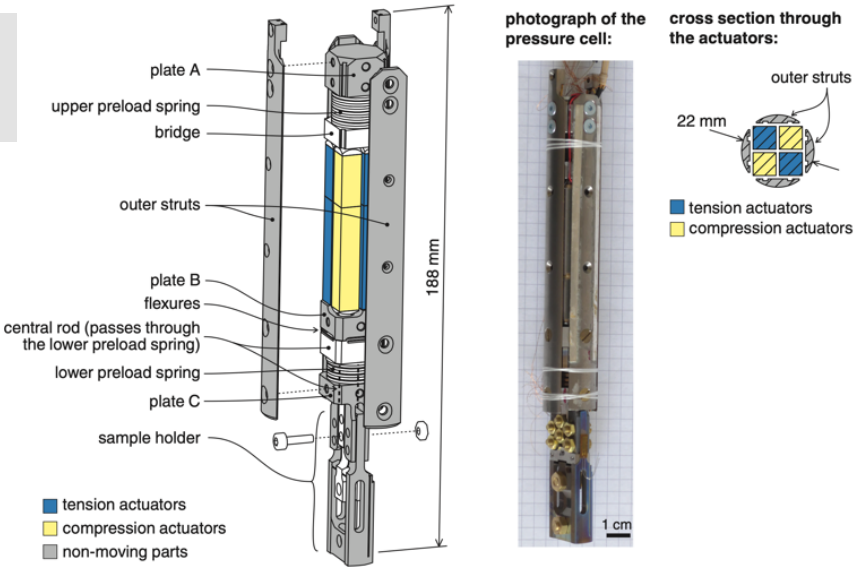

Figure 6.7: μSR uniaxial pressure cell available currently at PSI. From [Hicks, 2017].

achievable with the gas pressure cell. At PSI, measurements are now routinely done with double-layer cells with a large inner diameter of 6 mm that ensures sufficient signal-to-noise (see Figure 6.6). These cells reach maximum pressures of 2.5 and 1.8 GPa when the cells are made from MP35N/MP35N or CuBe/CuBe double layers, respectively. They can also be used down to sub-Kelvin temperatures at the GPD μSR spectrometer situated at the μE1 beamline. Using this high-pressure equipment, a plethora of high-pressure μSR experiments on quantum materials have been performed at PSI. Examples are investigations of strongly correlated electron systems, quantum criticality, unconventional superconductors, spin liquids and topological materials.

Concerning uniaxial pressure, a cell for μSR strain measurements based on a previous design for transport measurements with piezoelectric actuators has been recently developed at PSI in collaboration with Clifford Hicks (MPI Dresden). This device has been tested at the Dolly beamline at PSI and can reach strains of about 1% between 10 K and dilution temperatures [Hicks, 2017] (see Figure 6.7). First interesting results on $La_{2-x}Ba_xCuO_4$ and Sr_2RuO_4 have been already obtained [Guguchia, 2020b; Grinenko, 2021b].

6.2.3 High-Pressure Cell Technology & Development

Development of high-pressure technology for μSR experiments at the HIMB target will cover two major aspects:

1. To achieve higher pressures than currently available, a different type of pressure cell technology is required.
2. Due to substantially different geometry of the new pixel detectors to be developed for HIMB, all pressure cells need to be compatible with this geometry.

A route to achieve higher pressure beyond the realm of a few GPa is via the use of anvil cells. The use of anvils allows a force to be applied over a much smaller area, and in turn, achieves high pressures. A new generation of such anvil pressure cells is currently being developed for μSR within the SNF funded ExtremeP R'Equip project (PI Marc Janoschek, UZH and PSI, Co-PI Rustem Khassanov, PSI). A schematic of the current cell model, which is under development is shown in Figure 6.8. Currently, first tests show that this new type of cell will allow a modest increase of maximum pressure by a factor 2-3 over the piston cylinder technology currently available to SμS users.

We note that the limiting factor is not the underlying technology of anvil cells, since with the correct type of anvil material, pressures of up to several hundred GPa may be achieved. However, the current status of high-pressure experiments at PSI's muon facility remain limited to maximum pressures of substantially less than 10 GPa. The reason for this is that with currently available muon rates, relatively large samples are required, which ultimately defines the available surface area of the anvils and thus limits the achievable pressure. With the installation of the new HIMB target and in combination with new detector technology (see Section 6.1), rates that are 10-100 times higher are feasible, allowing for much smaller samples. This is an unprecedented opportunity to combine μSR with much higher pressures based on the anvil pressure cells that we have already started to develop. This will allow a completely different class of quantum materials to be researched with μSR, such as the new class of hydrogen-rich superconductors [Snider, 2020], which superconduct at room-temperature, albeit at pressures of more than 100 GPa. Achieving such extreme pressures, in combination with a spectroscopic technique such as μSR, will allow insights into quantum materials with world-wide impact.

In parallel, new developments of uniaxial pressure cells have also been pursued at the UZH Physics Institute. This new generation of uniaxial pressure cells was developed for neutron scattering [Fobes, 2017] and synchrotron experiments [Choi, 2020]. A particular strength of the newest cell (currently unpublished), a picture of which is shown in Figure 6.9, is a smart system for ultra-fast sample changes optimized for user facilities to avoid the loss of precious beam time. These cells are equally suitable for muon spec-

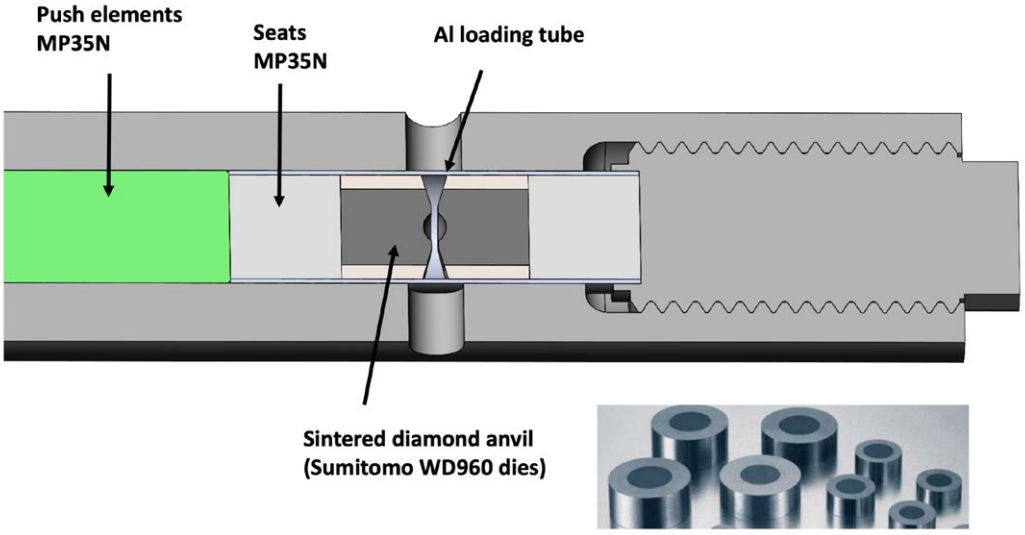

Figure 6.8: Concept of novel μSR high-pressure anvil cell currently under development within the SNF R'Equip project ExtremeP.

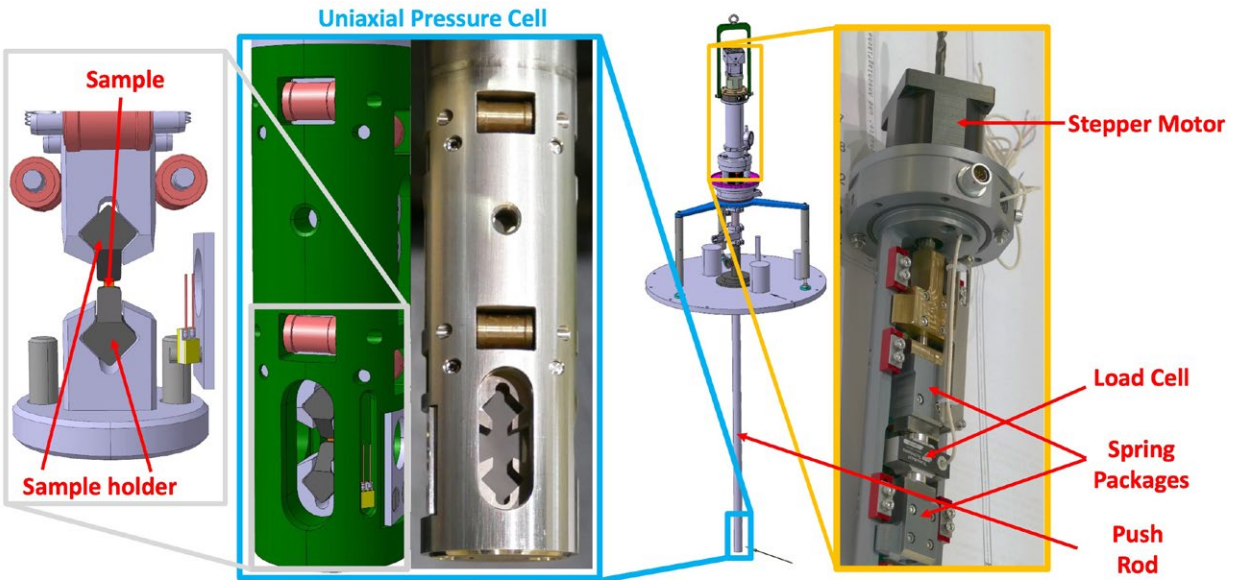

Figure 6.9: New in-situ uniaxial pressure cell developed in a collaboration by the UZH Physics Institute and PSI. The actual cell is shown in the middle blue panel. It features a sample holder (left side) that allows easy sample changes because it can be easily slides easily in the associated receptacles in the cell. The pressure is applied via a stepper motor driving a push rod through a spindle (right panels). Application of pressure in fine steps is achieved via the integrated spring packages. A load cell measures the applied force in real time.

troscopy. Notably, relying on the same sample-holder, we are already working on new uniaxial pressure cells within the SNF funded ExtremeP R'Equip project (PI Marc Janoschek, UZH and PSI) that will use a hydraulic system to apply uniaxial pressures exceeding the maximum pressure of 1 GPa possible with the current μSR setup.

To seize the opportunity of HIMB for the investigation of novel quantum matter at the extremes of high-pressure, additional efforts for the development of high-pressure equipment are required. In particular, the already high complexity of large-scale facility experiments such as those with muon spin spectroscopy, will increase further for experiments carried out at HIMB and with the developments in silicon pixel detectors. Although, our current developments in high-pressure technology taking place at PSI and UZH are an important step towards taking full advantage of the capabilities enabled by the new HIMB muon target, they are still developed for the currently world-leading high-pressure μSR instrument GPD at PSI [Khasanov, 2016]. A schematic drawing of GPD is shown in Figure 6.10. It is immediately clear that at the current GPD setup, the space available for sample environment (magnet, cryostat and pressure cells) is substantially larger than for the pixel detectors that will be required to take advantage of the higher muon rates produced by the HIMB target. Notably, these new detectors will be "wrapped" much more closely around the incoming muon beam (see Figure 6.3) and, in turn, the high-pressure devices for HIMB experiments must be developed with this detector geometry in mind. They will have to be improved towards this constrained size for a development of a new μSR high-pressure spectrometer.

6.2.4 High-Pressure Cell Infrastructure and Equipment at PSI and UZH

At PSI, and in particular, in the division for research with neutrons and muons (NUM), high-pressure expertise is distributed across three laboratories. The Laboratory for muon spin spectroscopy (LMU), the laboratory for neutron scattering and imaging (LNS), and the laboratory for neutron and muon instrumentation (LIN). Until very recently, the

currently available high-pressure equipment for both the SμS and SINQ facilities was supported via enthusiastic scientists. Pressure cells for SINQ have been obtained commercially or via scientific collaborations and have been supported by two instrument scientists (Denis Sheptiakow and Jon White). In contrast, pressure cells for SμS have been developed by Rustem Khassanov [Khassanov, 2016] with the support of less than 0.1 FTE of a technician. However, with the consolidation of most of technical expertise consolidated in LIN, the support of pressure activities is currently being consolidated in the sample environment group that serves both SμS and SINQ. A dedicated high-pressure scientist is currently being hired to support this new high-pressure strategy.

The available pressure cells at PSI and UZH are already described in Sections 6.2.2 and 6.2.3. At PSI, two laboratories (one for SINQ and one for SμS) are equipped with hydraulic presses that are used for ex-situ pressure loading of the available pressure cells. For safety reasons, the labs are equipped with shielding to protect the staff operating the presses in case of failure. There is also a compressor available for pressure loading cells that are operated with helium gas pressure. All pressure loading systems are computer controlled and allow pressure to be applied at ambient temperature in a controlled way. At UZH, currently no dedicated high-pressure laboratory is available; pressure cells have been designed in collaboration with technical and engineering staff at the Physics Institute and machined in the machine shop.

6.3 DEMETER Center at UZH

The DEMETER (Detector & Matter at Extremes Test and Research) center, to be constructed at the UZH, has the aim of harvesting the high rates of muons produced by HIMB particle physics and material science. DEMETER will allow UZH and PSI scientists, as well as the Swiss and international scientific community, to fully take advantage of HIMB at PSI, by facilitating a new generation of pixel detectors for mu-

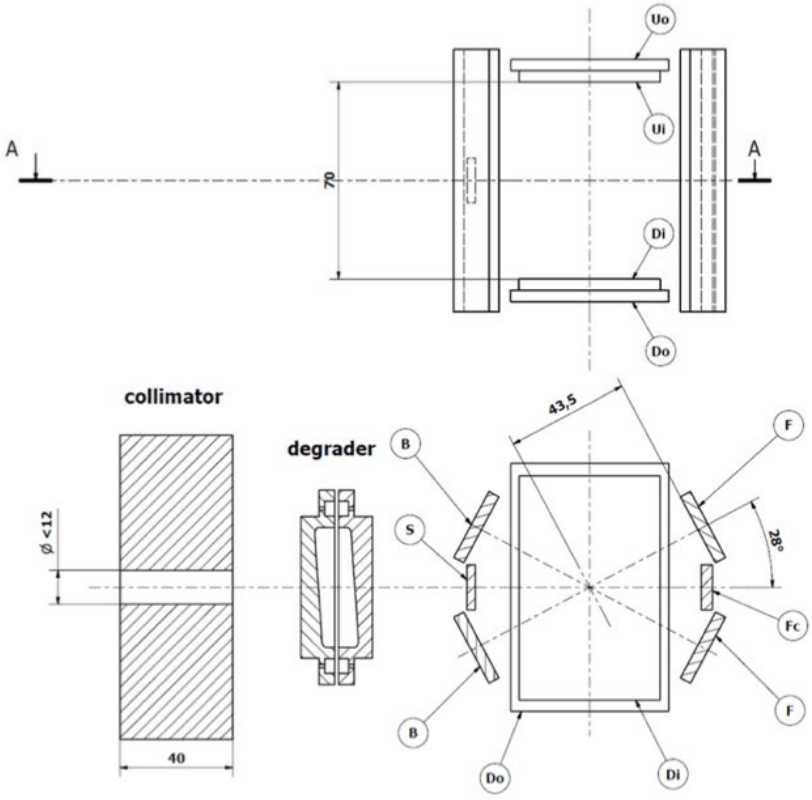

Figure 6.10: The schematic view of the detectors at the GPD spectrometer. The meaning of the detectors are: S – start, F – Forward, FC – Forward center, B– Backward, U – Up, and D –Down. The U and D detectors consist of two detectors each (i – inner and o – outer). The collimator reduces the size of the incoming muon beam. The degrader allows the momentum of the incoming muons to be decreased. Measurements are in mm. From [Khasanov, 2016].

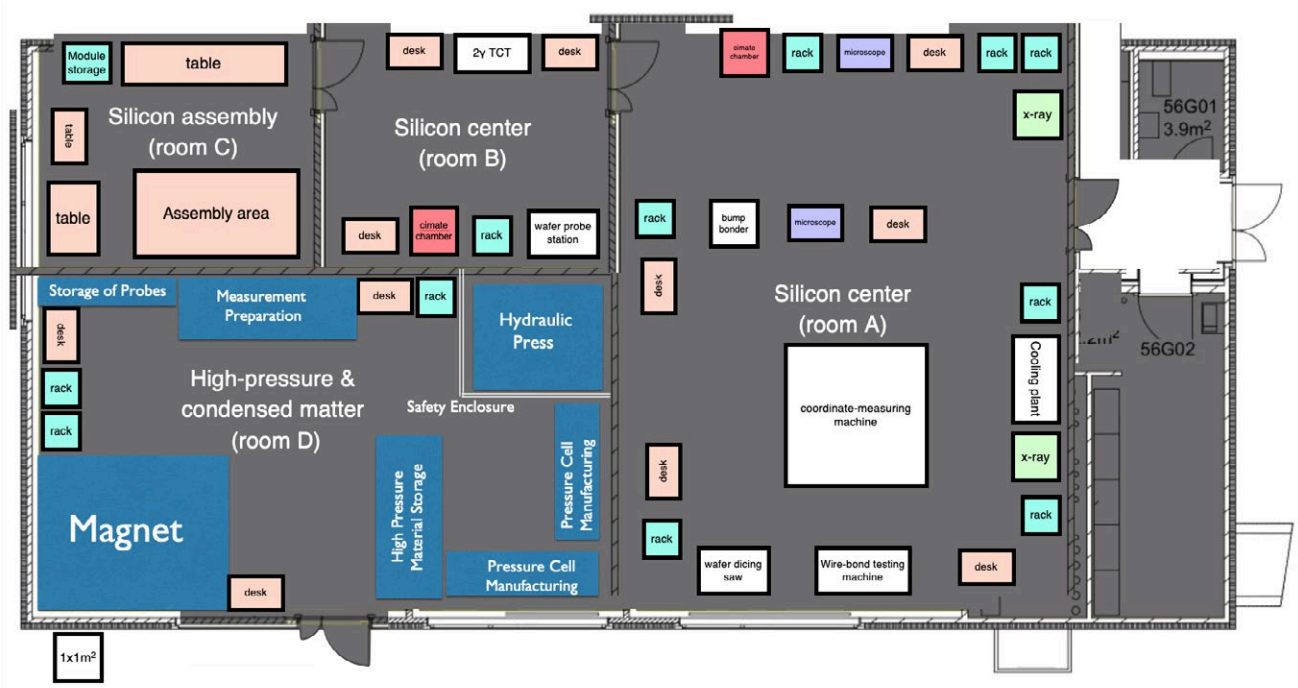

Figure 6.11: DEMETER research center at UZH for silicon detector and high-pressure cell research. The silicon center has three cleanrooms, increasing in air purity from A to C. Room A focuses on detector processing capabilities, while room B has detector measurement capabilities, and room C is for detector assembly of production modules and therefore has the strictest requirements. Room D houses the high-pressure cell development center. It will provide space for the assembly and testing of high-pressure cells, heavy duty presses, and high-pressure calibration stations. It will also allow bulk characterization measurements to be carried out at high pressure as the first stage before more advanced muon spectroscopy measurements at HIMB.

on-decay experiments, as well as novel high-pressure devices for the study of materials with muon spin spectroscopy at the extremes of pressure. The joint DEMETER Center will synergistically combine the expertise of detector development from the particle physics groups and high-pressure development from the condensed matter groups at the UZH Physics Institute. The silicon center and high-pressure center will benefit from being housed in a common center due to the high level of integration necessary between new target materials and detector components. An overview of the planned facility is shown in Figure 6.11.

6.3.1 DEMETER: Silicon Pixel Research Center

For silicon pixel detector development, the DEMETER center will host laboratory space with clean-room facilities, and equipment for R&D and detector assembly. This would mobilize existing efforts and serve as an incubator for improved detectors that would be utilized in experiments at PSI and at CERN. This new generation of detectors will have more precise time resolution and position measurements and be more commercially viable, allowing for previously unachieved 4-D measurements of charged particles such as muons at HIMB, or particles resulting from Higgs boson decays at CERN collider experiments. Such a center would benefit the Swiss particle physics community and launch new international experiments.

The silicon detector facility requires new building infrastructure to house delicate equipment and to provide clean spaces for detector handling and assembly. Humidity regulation is important since low humidity causes static discharge and fatal sparking in devices, while high humidity leads to condensation that produces electrical shorts in devices under voltage. Temperature regulation is important for several reasons. Silicon detectors, as well as the equipment that operates and tests them, generate large amounts of power, such that the heat created needs to be removed from the laboratory. The combination of temperature and humidity provides the dew point at which moisture could form on electrical equipment. Finally, knowing the temperature history of sensors allows for parametric determination of annealing properties of irradiated sensors. Dust levels must be kept to a minimum as dust can affect performance of silicon sensors or cause shorts in electrical connections. A balance between the need to have highly regulated rooms for delicate operations, while also having some applications with less strict controls, leads to a compromise in the detector facility design. A large room of cleanroom class ISO 7 clean room, such that a maximum of 10,000 particles of size ≥ 0.5 µm per cubic foot are present and the air is cycled 60 times per hour, is sufficient for most of the facility activities. Such a room should be approximately 100 m² to provide laboratory working space and store the necessary equip-

ment. Two smaller cleanrooms of ISO class 6 (maximum of 1,000 particles of size ≥ 0.5 µm per cubic foot) would provide a staging area for delicate handling of sensors and detector module assembly. These two lab rooms should each be about 30 m^2, and should be maintained at approximately 20 °C and about 40 % humidity. Electrostatic Discharge (ESD) protection and cleanroom standards for footwear, gloves, hairnets, smocks should also be observed. A dry-air (nitrogen gas) system is necessary to provide moisture-free air for ventilating cold systems to temperatures below the air dew point without risk of condensation.

New equipment will be added to the center in the context of IMPACT. A two-photon absorption laser system, where two photons are required for the creation of an electron-hole pair, would allow charge collection in sensors to be investigated with higher accuracy than the current TCT system and in three dimensions as opposed to two. This innovative TPA-TCT technique represents a breakthrough with respect to the current state-of-the-art since it allows for the generation of excess carriers on a very localized micrometric-scale voxel, enabling high-spatial resolution characterization of the new generation of semiconductor devices with small feature sizes.

To test the signals from sensors, an automatic wire-bonding machine precise enough to bond small-pitch sensor pixels to readout circuits is needed, as well as a wire-bond testing machine that verifies the strength of the connections. A coordinate-measuring machine will be used for alignment and 3D mapping of mechanical structures in order to mount silicon devices for detector integration. A wafer-dicing machine will be used to separate sensors and readout chip components from wafers, which typically have multiple projects included. In order to test the resistance to high doses of radiation of the read-out chips and monolithic active pixels sensors, an X-ray irradiation system will be available with a rate up to several Mrad/hour. An advantage of moving to monolithic or stacked devices is that the complex processes can be handled by commercial foundries that routinely produce thousands of 12-inch wafers per week. A cold-probe station capable of measuring 12-inch wafers will ensure compatibility with industry.

One technical FTE would be associated to the silicon detector center, who would be an expert in using the equipment, who could maintain lab infrastructure and a schedule of device usage, and who could provide an interface and training to the experimental groups using the facility, and also participate in detector testing and assembly.

At UZH Irchel campus, locations for the three clean rooms have been identified, and discussions with the UZH building infrastructure department have been ongoing in anticipation of the center. Such infrastructure can be outfitted in existing locations during the 2025-2028 deployment of the IMPACT proposal. The building infrastructure will be renovated to modify the interior wall space, install clean rooms, and shift services. Cleanrooms are routinely installed in the UZH campus and can be realized in a few months. It is anticipated that the purchasing and delivery of additional equipment will take less than a year, while setup and development of expertise with the equipment by the technician will take a few years before it is optimal. A plan for the DEMETER center, including the silicon research center and the high-pressure cell has already been shown above in Figure 6.11.

Being situated less than an hour from PSI, the center at UZH is convenient for detector experts who are working with experiments using PSI beamlines, as well as the UZH, ETH, and PSI groups in the immediate vicinity. The DEMETER center will provide a hub for collaborative R&D towards such detectors and can also be used for testing, assembly, and commissioning of detectors, in collaboration with scientists and facilities at PSI. Switzerland is also co-host to the international CERN laboratory, and its universities make leading contributions in detector development and physics analysis on the multi-purpose collider experiments of CMS, ATLAS, and LHCb, with silicon detector development for these experiments being a major pillar of research for U. Zurich, U. Geneva, U. Bern, EPF Lausanne, ETH Zurich, and PSI.

Particle physics is a traditionally collaborative field, and several successful models will be used for inspiration for usage of the center. UZH, PSI, and ETH have worked together on the construction of the CMS phase-1 detector, and are also collaborating on the phase-2 detector. These projects are larger than Swiss-only efforts, with many countries from Europe, Asia, and the Americas contributing. UZH and ETH have already worked together on evaluating commercial CMOS sensor options for use in CMS upgrades. UZH and PSI are working together to develop precision-timing ASICs for

silicon sensors with picosecond timing resolution. UZH and CERN are developing techniques for measuring individual irradiation defects in silicon sensors. UZH, PSI, ETH, UNIGE, and EPFL have begun workshops to generate common research lines for Future Circular Collider (FCC) detectors. The RD50 collaboration at CERN unites groups with similar research goals to produce multi-project wafer submissions, which allow resources to be combined so that progress is less expensive. The facility will provide capabilities for the major research lines necessary for silicon detector experiments at PSI and CERN in the 2030s, 2040s, and beyond.

6.3.2 DEMETER Center: High-Pressure Cell Research Center

As outlined in Section 6.2.3, the development of novel high-pressure cells for μSR experiments at HIMB is more involved because the cells must be adapted for the new pixel detectors (see Figure 6.3). Thus, the high-pressure development for HIMB will benefit immensely from close proximity to the detector development.

This is exactly the strategy pursued by the UZH DEMETER center that is proposed as part of IMPACT. The collocation of expertise with the development of muon and decay positron detectors (see Section 6.1) and high-pressure equipment at the UZH Physics Institute, makes UZH uniquely situated world-wide to reach this new frontier at the extremes of high-pressure for a muon facility. This will allow full exploitation of the proposed national investment into PSI's large-scale muon facility, and enable entirely new studies of condensed matter, which will not be possible anywhere else. Through this, DEMETER will allow careful offline testing of both detector and high-pressure components before they are deployed for μSR experiments. Naturally, this will also be done in close collaboration with PSI, where HIMB will be installed. We note that that a strong collaboration between the UZH Physics Institute and the PSI LMU and LIN laboratories already exists. The strength of this collaboration is also expressed by plans of UZH and PSI for a joint faculty position in the field of μSR that should be filled by 2024.

We note that, in addition to pure testing of technical components (pressure cells), the planned DEMETER high-pressure center will also house a flexible environment to run high-pressure characterization experiments of quantum materials. Notably, due to the high complexity of μSR experiments, it is required that materials that will be investigated at HIMB are carefully pre-characterized at the extremes of high-pressure using bulk methods such as electrical transport, thermodynamic, and magnetic measurements. This will substantially increase the success of high-pressure experiments at HIMB. This is crucial as beam time at HIMB will be limited, and this offline test will ensure that the expensive muon beam time can be used meaningfully. The condensed matter physics groups at UZH have vast expertise in studying quantum materials (Chang, Janoschek, Natterer, von Rohr), which, thus, supplies an ideal environment for these measurements as well.

First and foremost, the DEMETER center would be able to host the design and construction of a new μSR spectrometer at HIMB, in collaboration with PSI, that synergistically exploits the potential of high-pressure cells from the condensed matter groups and novel detectors developed by the particle physics groups. In addition, this new center would provide competency for Swiss scientist in carrying out high-pressure experiments more broadly. Notably, the pressure cells and techniques that will be developed for HIMB at the DEMETER center will not be limited for use only with muons. They can be easily combined with bulk measurements that are used by the entire Swiss (and international) condensed matter community. In turn, the proposed high-pressure center at UZH has the potential to boost high-pressure condensed matter research in Switzerland broadly. In addition, the pressure cells developed at DEMETER will also be suitable for neutron scattering, and in the case of diamond anvil cells for synchrotron experiments. In addition to the muon facility, PSI also operates the Swiss Light Source (SLS) and the Swiss Spallation Neutron Source (SINQ), and their user communities will directly benefit from the proposed DEMETER center. We emphasize that both communities have outlined in their recent respective roadmaps that high-pressure capabilities are a key aspect of their future science cases (SCNAT Photons, 2021; SCNAT Neutrons). As illustrated in Figure 6.5, SINQ also has substantial demand for high pressure experiments. In addition, Switzerland is, for example, a member of the European Synchrotron Radiation Facility (ESRF) in Grenoble, France, and the upcoming European Spallation Source (ESS) in Lund,

Sweden. In particular, the latter will – similar to HIMB – allow experiments on much smaller samples. This entails that the pressure cells developed at DEMETER will have a broad relevance beyond HIMB, PSI, and even Switzerland.

To fulfill this mission, the pressure center of DEMETER will host a flexible work environment with work benches to test and assembly high-pressure devices. It will further be equipped with a state-of-the-art, flexible and computer-operated hydraulic press for the application of pressure. In addition, there will be equipment required for pressure calibration such as a small Raman spectrometer for the optical determination of the applied pressure. Further, high-pressure science overlaps with materials science and mechanical engineering. Pressure-cells must tolerate forces without entering the plastic deformation regime. In the past, much of this knowledge was figured out experimentally. Modern software programs now allow pressure cell design to be simulated and, in this fashion, optimized. Such finite-element simulations are carried out using commercial software packages such as for example COMSOL or ANSYS The center, therefore will also be equipped with such computer-aided design methods. Furthermore, packages enabling compatibility with Computer-Aided Design (CAD) drawings are mandatory. Since pressure is applied through a fluid pressure medium (typically an oil), one of the packages for fluids is required. In terms of computing power, UZH infrastructure is already sufficient. Development of high-pressure equipment requires experienced personnel. Experience is mandatory both to progress according to our ambitious time plan but also to ensure that safety is never compromised. Therefore, an experienced technician or mechanical engineer with experience in this field will be employed for the day-to-day workflow. Under such experienced guidance, postdocs and PhD and master students in all condensed matter groups will contribute.

For testing the developed high-pressure cells at cryogenic temperatures, the DEMETER center will also be equipped with a flexible large-bore cryo-magnet. The large bore is required to allow for flexibility of testing, but also to additionally allow the installation of ultra-low-temperature equipment such as He3 or dilution refrigerators. This is because many of the most interesting high-pressure experiments on quantum and other interesting materials carried out at high-pressure and with μSR are also carried at the extremes of low temperatures. At the same time, this magnet provides a flexible platform to characterize materials to be investigated with μSR at HIMB at high-pressure with off-beam-line experiments at UZH. This magnet will allow a suite of valuable methods such as magnetic, thermal and electrical measurements, and at a later stage, scanning tunneling measurements that can be combined with uniaxial pressure. All of these methods ideally complement μSR measurements and will enable their successful execution.

As illustrated in Figure 6.10, a dedicated building to host DEMETER has already been identified. Building 56 is currently the only place (within the physics department) with connection to a helium recovery and the possibility to modify the floor ceiling distance, which is required for the planned activities. Figure 6.11 shows that for the high-pressure activities about 80 m^2 laboratory spaces will be available. In order to not compromise safety, it is important to have two separate laboratory spaces in the available room. One will be used for assembly and pressure application. The application of high-pressure comes with a set of safety rules to protect staff. High-pressure application equipment needs to be properly shielded and generally such equipment should not be placed in combination with office space or transition areas. In the second part of the pressure center, the cryo-magnet will be installed. High magnetic fields come with another set of safety rules. Although magnetic fields are standard, the area should be clearly enclosed with warnings to pacemaker carriers. Furthermore, this room must be kept clean from metal items due to the interaction with the stray magnetic field. Commercial cryo-magnets require a minimum floor to ceiling distance, which is provided in building 56, thus offering the possibility to install the cryomagnet in a dedicated pit. This will allow easy access to install different probes and pressure cells in the magnet bore. As the cryo-magnet will be cooled with helium, which is a non-renewable natural resource, the UZH drive towards sustainable research requires that we have a connection to the helium recovery system at the physics institute. A new and modern helium recovery system was installed recently at the Physics Institute for this purpose (2019-2020) and this system will be used.

7 Muon Beamlines

7.1 Present Situation

The experimental hall of PSI houses two target stations TgM and TgE where the high-energy proton beam of the HIPA accelerator complex passes through 5 and 40 mm of graphite respectively, in order to produce the secondary particles used by the experiments and instruments located at the ends of the corresponding beamlines. Figure 7.1 shows an overview of the facility, with the proton beam feeding the two target stations mentioned above as well as two spallation sources for the production of neutrons and the proposed, new installation TATTOOS.

Due to the high proton beam power of 1.4 MW, the rates of the secondary particles produced at the two target stations are some of the highest that can be found world-wide. Focusing on surface muons, the muons produced by pions decaying at rest at the surface of the production targets [Pifer, 1976], the two beamlines muE4 and piE5 connected to TgE currently provide 5×10^8 and 2×10^8 μ^+/s for materials science (using the muon spin rotation technique μSR) and particle physics, respectively [Prokscha, 2008; Arndt, 2021]. Due to these high achievable surface muon beam rates, their low momentum of ~28 MeV/c (with correspondingly short stopping ranges), the high degree of polarization, and the fact that the muons are delivered continuously (the 26 ns lifetime of the pions smears out the 50 MHz time structure of the proton beam), makes them the particles of choice for many of the particle physics and the majority of the materials science experiments conducted at PSI and world-wide. The shorter TgM does not offer the same intensities as the thicker TgE and features only two instead of five secondary beam lines, as in the case of TgE. Since the HIMB project is aiming to rebuild the TgM target station, we give a brief outline of the two currently attached beam lines. The channel located on the left side, piM1, is dedicated to particle physics and only offers particles with momenta higher than

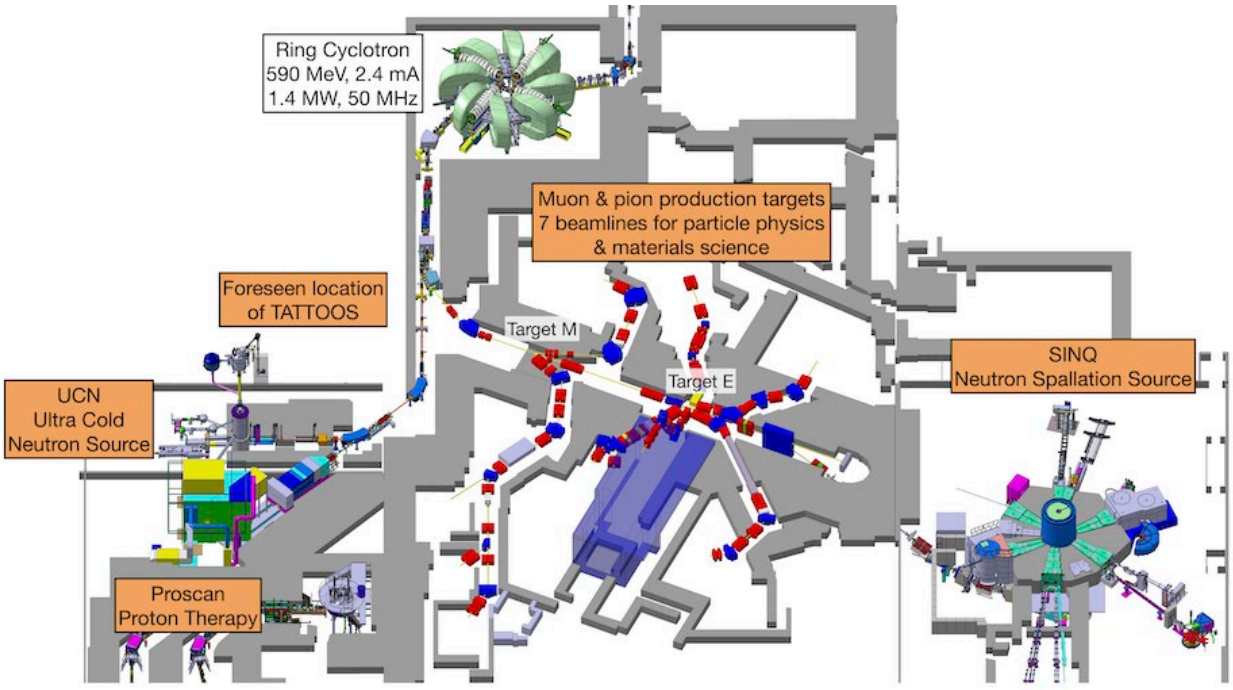

Figure 7.1: The picture shows the layout of the installations in the experimental hall of PSI. Two target stations TgM and TgE are fed by the HIPA proton beam to produce secondary particles. Also shown are the spallation neutron sources SINQ and UCN, which are driven by the same beam, as well as the location of the proposed new TATTOOS installation.

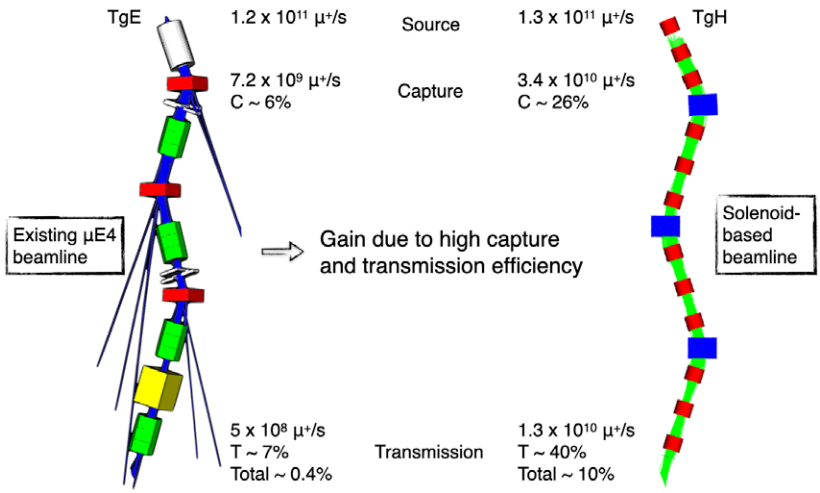

Figure 7.2: The picture compares the capture (C), transport (T) and total efficiency of the existing MuE4 beamline to a generic beamline of similar layout based on large-aperture solenoids and dipoles.

100 MeV/c. Apart from some dedicated experiments, it is mostly used for detector tests where high momenta are desirable. On the other side, piM3 is used by the μSR group to operate the two instruments GPS and FLAME [LMU, 2021] and is typically tuned to run with surface muons with a maximum beam rate close to 10^7 μ^+/s.

7.2 Basic Consideration, Requirements and Constraints

With an increasing number of proposed experiments and new facilities world-wide, interested in muon science, due to the particle's fundamental nature and clean experimental signature (Mu2e [Bartoszek, 2015], Comet [Akhmetshin, 2020], Mu3e [Arndt, 2021], g-2 [Grange, 2018] and J-PARC [Kawamura, 2018], MuSIC RCNP Osaka [Cook, 2017], FNAL [Kronfeld, 2016; Asner, 2013], CNCS [Xiao, 2016]), the HIMB Project will ensure that PSI will stay at the forefront in muon science also in the future.

Due to the muon's wide use in experiments as described above, the HIMB project focuses primarily on increasing the rates of surface muons, i.e., low-momentum particles. Based on the currently available surface muon rates at PSI and potential new experiments [Aiba, 2021], the goal was set to deliver ~10^{10} μ^+/s to the experimental areas – thus increasing the intensity by almost two orders of magnitude – with beam-spot sizes of $\sigma \lesssim 50$ mm at the final focus.

Such an increase in rate is not possible from the existing 5 mm long TgM. The length for the new target was thus allowed to increase to 20 mm because this, together with the 40-mm TgE, is a known situation from the operation of 60-mm long targets at the TgE station in the past [Kiselev, 2021b]. More details on the target design and its optimization can be found in Chapter 9. The impact that such a change in target length has on the proton beam optics is described in Chapter 8.

The new target station TgH with its optimized slanted target geometry is based on a prototype test of a slanted TgE we designed [Berg, 2016] and tested in a measurement campaign in 2019 [Kettle, 2019], where the surface muon rates at all available extraction angles were compared to predictions. The results of the measurements showed good agreement with the predicted 40 %–50 % increase in surface muon yield compared to the standard 40 mm long TgE. Since the end of 2019, the new design 40 mm slanted target has replaced the standard version at TgE.

TgH is expected to emit around 10^{11} surface-μ^+/s to either side and is thus almost as efficient in generating surface muons as the two-times-longer non-slanted TgE. In order to reach the goal of transporting 10^{10} μ^+/s to the experiments, a high and optimized capture and transport efficiency is of paramount importance – especially given the fact that for the other beamlines at PSI overall efficiencies of less than 1% are standard.

Figure 7.2 shows the concept of how this increase in efficiency is achieved compared to the existing muE4 beamline. It is based on 500-mm aperture solenoids and dipoles with the first capture solenoid being placed at a distance of only 250 mm to the target. In order to keep the transport efficiency high, the beamline continues to use large aperture dipoles and solenoids with minimized distances between the different beam elements.

While a straight and short beamline would result in the highest possible transmission, such a layout is not possible due to radiation safety issues. At least two bends are necessary along the beamline in order to avoid a direct line-of-sight from the experimental areas onto the target. In addition, having the first bend along the muon beamline in the upstream direction (w.r.t. to the proton beam direction) also helps in reducing the amount of radiation transmitted through the secondary beamline. These considerations, together with the overall structure of the existing experi-

mental areas and the development of the beam optics (see Section 7.7), resulted in the layout of the muon beamlines shown in Section 7.8.

7.3 Optimization of Target Geometry

We performed an optimization of target TgH parameters using G4beamline [Muons Inc., 2019] by simulating a proton beam impinging on the target and recording the muon counts at virtual detectors located at the upstream and downstream ends of the capture solenoids in the MUH2 and MUH3 beamlines, for various target rotations around the vertical axis. More details on the simulation program can be found in Sections 7.6.1.1 and 7.8. In this optimization, we considered a set of angles between the MUH2 beamline and the proton beamline, and, as a separate parameter, between the MUH3 beamline and the proton beamline.

The target and beamline angles mentioned above were measured from the axis of the proton beamline; in the case of the target, this was for the horizontal centerline along the length side. For the target and the MUH2 beamline, the rotation angle relative to the proton beamline was counter-clockwise, and for the MUH3 beamline it was clockwise.

In the optimization, the target length, height, and thickness in the proton beam direction were 100 mm, 150 mm, and 20 mm, respectively, unless otherwise noted. The splitting factor for both pion production and decay was 100 in the G4beamline simulations used for variance reduction.

The results of the optimization are listed in Table 7.1. This optimization study, among other things, confirms the previous results [Berg, 2016; Kettle, 2019] that a slanted target provides a higher surface muon flux than a non-slanted target. In the case of a 20-mm long target the increase in surface muon rate by slanting the target is approximately a factor 2. While of course a slab length of 150 mm and a very small target rotation of only 5 degrees would improve the amount of surface muons generated at the target, such an extreme configuration was deemed not feasible from a mechanical point of view. As rotating the beamlines did not bring significant improvements, the configuration with a 10 degree target rotation, 100-mm length, and beamline orientations at 90 degree was chosen as the baseline solution. These parameters formed the basis of the target design described in Chapter 9.

Target rotation (deg)	MUH2 rotation (deg)	MUH3 rotation (deg)	Notes on the target	Counts MUH2 capt. solenoid US	Counts MUH2 capt. solenoid DS	Counts MUH3 capt. solenoid US	Counts MUH3 capt. solenoid DS	Counts TgH MUH2 side	Counts TgH MUH3 side
5	90	90	L =150 mm	1.000	1.000	1.000	1.000	1.000	1.000
10	90	90		0.939	0.937	0.908	0.906	0.938	0.929
10	100	90		0.955	0.948	0.933	0.928	0.956	0.931
10	95	85		0.947	0.944	0.905	0.901	0.951	0.925
10	80	90		0.880	0.873	0.923	0.919	0.955	0.934
10	85	95		0.905	0.905	0.918	0.915	0.958	0.946
5	90	90		0.977	0.978	0.975	0.975	0.981	0.971
0	90	90	W = 6 mm, L = 20 mm	0.503	0.484	0.504	0.485	0.583	0.589
5	95	85		0.979	0.978	0.980	0.978	0.981	1.000
10	100	80		0.942	0.940	0.931	0.929	0.961	0.934

Table 7.1: Surface muon counts, as ratios relative to the counts for the parameters in the first row, at the upstream (US) and downstream (DS) ends of the capture solenoid in the MUH2 and MUH3 beamlines, as well as on the MUH2 and MUH3 side of target TgH, for a set of TgH rotation angles and angles between the MUH2 and MUH3 beamlines and the proton beamline. The target length L, height, and thickness in the proton beam direction were 100 mm, 150 mm, and 20 mm, respectively, unless otherwise noted. The target width W scales according to the rotation angle except for the special case of no rotation. The baseline solution is in blue.

7.4 Capture Process: Capture Solenoid

The characteristics of any beam line are governed by three main factors: beam emittance at the source, channel acceptance and channel optics. The beam emittance or phase space is a fundamental characteristic of the target design and the primary beam, whereas the channel acceptance is determined primarily by the capture properties of the most upstream element in the channel. Finally, the dominant factor determining the transmission along the channel is the optics. For a high intensity beam, such as HIMB, the channel acceptance and hence the capture properties are determined by the capture solenoids, placed on either side of the target. To understand the effect of the capture process one must also consider the particle emission spectrum, energy and the target beam emittance.

As previously mentioned in Section 7.2, the MUH2 channel will mainly serve the particle physics community with surface muons centred about 28 MeV/c as well as cloud muons, pions and electrons of both charge-sign up to a maximum of 80 MeV/c. Whereas the MUH3 side, associated with the MuSR community, will predominantly use surface muons at 28 MeV/c as well as lower energy muons of both charge-signs. The momentum spectra of both positive and negative particles produced in the target and simulated at the entrance to the capture solenoids are shown, respectively, in Figure 7.3 (left) and (right). One can clearly see the significance of surface muons, as shown in Figure 7.3 (left), which peak at about 30 MeV/c (blue curve). Not only does one achieve the highest muon yield here but it also allows the highest muon stop-densities to be obtained for stopped muon experiments due to the lower energy, which in turn allows thinner stopping targets to be used. The surface muon peak in the positive spectrum is associated with stopped pion decays at the surface of the target [Pifer, 1976] and sits on a cloud muon distribution, of lower yield, reaching to much higher momenta, which is present for both charge-signs and associated with pion decay-in-flight in and around the target.

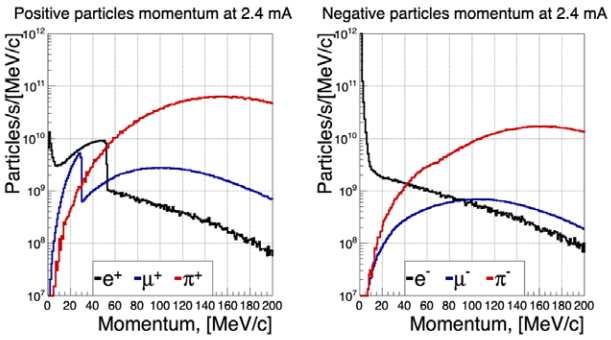

Figure 7.3 (left) and (right): The simulated momentum spectra of positive and negative particles at the entrance to the capture solenoids, respectively. The surface muon peak at about 30 MeV/c in the positive charge-sign represents the highest muon yield.

7.4.1 Target Beam Phase Space

The initial phase space at the target is defined in the simulation by a suitably dimensioned virtual detector placed centrally at 32 mm from the slanted target, parallel to the proton beam direction. The characteristics of the initial muon beam can be seen in Figure 7.4 to Figure 7.7, which show respectively the horizontal and vertical phase space (x,x' and y,y') of the beam and the divergence and polarization

Muon Beam Target Phase Space Parameters	32 mm from Target
Central Momentum P_0 / Momentum Spread σ_P (MeV/c)	23.0 / 5.3
Mean Polarization ‹PolZ›	-0.67
Horizontal Beam Centroid ‹x›/width σ_X (mm)	14.2 / 52.9
Horizontal Divergence ‹x'›/width $\sigma_{X'}$ (mr)	150.5 / 663
Horizontal Accepted Emittance $\varepsilon_X(1\sigma)$ (π·cm·mr)	559
Vertical Beam Centroid ‹y›/width σ_Y (mm)	0.2 / 52.8
Vertical Divergence ‹y'›/width $\sigma_{Y'}$ (mr)	0.7 / 676
Vertical Accepted Emittance $\varepsilon_Y(1\sigma)$ (π·cm·mr)	804
Geometric Solid Angle Ωg (mSr)	831
Full Channel Solid Angle Acceptance $\Omega_{channel}$ (mSr)	735

Table 7.2: Phase space characteristics of the initial muon beam, as detected in the simulation by a virtual detector, placed centrally 32 mm downstream of the target in the muon beam direction.

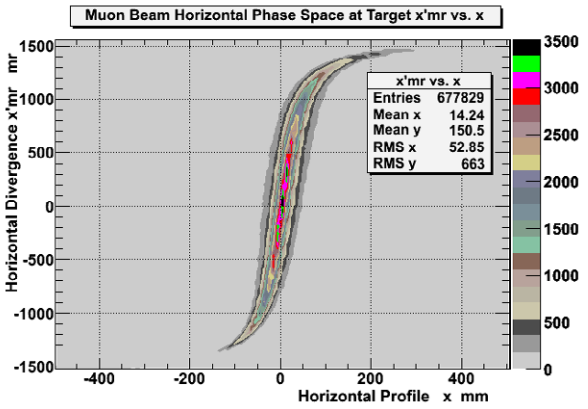

Figure 7.4: Horizontal phase space at the target (x,x').

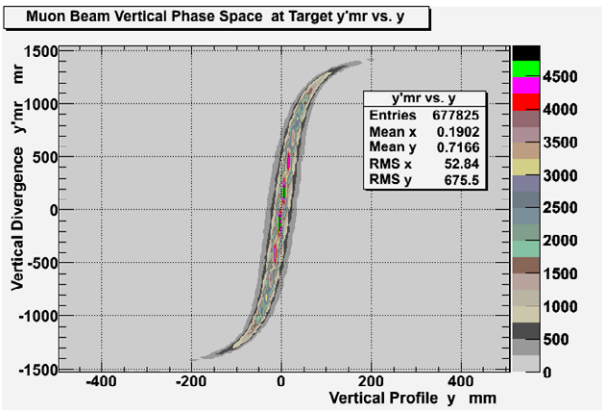

Figure 7.5: Vertical phase space at the target (y,y').

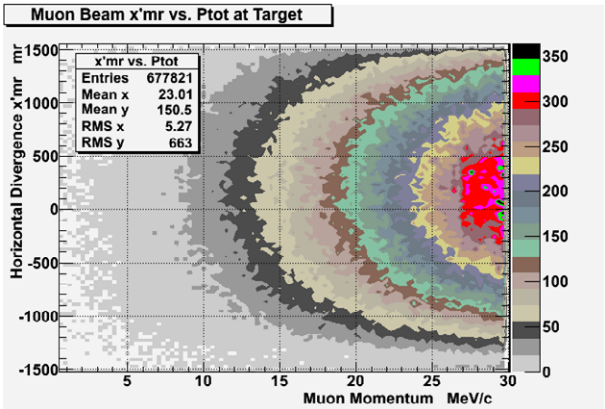

Figure 7.6: Horizontal divergence versus muon momentum at the target, showing the high momentum particles are forward-going.

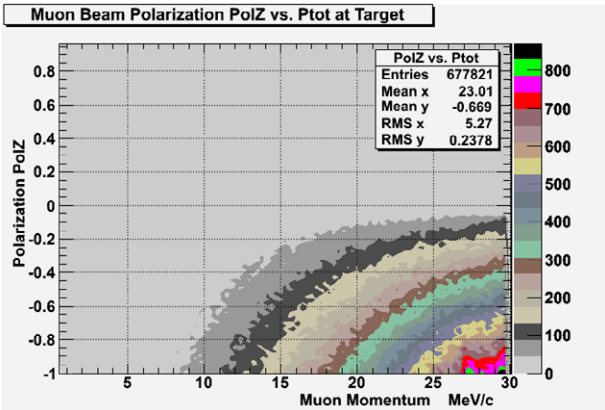

Figure 7.7: The muon polarization dependence on momentum, with the maximum polarization attributed to the high momentum, forward-going muons.

dependence on the momentum. From the latter, the high momentum particles in the beam are the most abundant and the most forward-going and hence also have the highest polarization with respect to the central beam-axis z. The phase space parameters are summarized in Table 7.2. The asymmetric filamentation of the horizontal phase space can be understood by the effect of a slanted target in the horizontal plane. This effect also accounts for the central mean-value offsets, again only in the horizontal plane.

The geometric solid angle acceptance defined by the centre of the capture solenoid and a point-source is estimated as 831 mSr.

7.4.2 Capture Solenoids

The front capture and focussing elements in HIMB are planned to be radiation-hard, iron-shielded solenoids, based on an existing design of the PSI μE4 WSX solenoid; for details see Section 7.10.1. Several new approaches to achieving large acceptance capture devices have been developed for surface muon channels over the last couple of decades, enhancing the conventional approach using quadrupole lenses, with their relatively limited solid angle and phase space acceptances [Oram, 1981; Daum, 1982; Matsuzaki, 2001]. Both normal and superconducting solenoid solutions have since been implemented with a compact

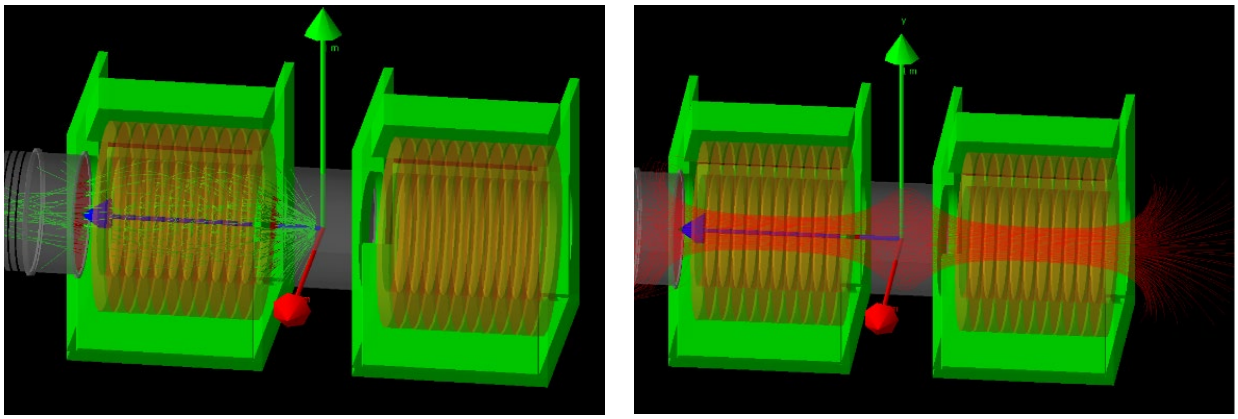

Figure 7.8 (left): Shows the G4bl model of the "new long" capture solenoid, showing some muon trajectories from the target.
Figure 7.8 (right): Shows the same model though with magnetic field lines in and between the two solenoids, the axes origin being the target.

"all-in-one" superconducting axial-focussing channel Dai Omega at KEK, Japan [Miyadera, 2006] and a normal conducting mixed/hybrid channel at PSI [Prokscha, 2008]. The most recent advances based on new facilities such as J-PARC MUSE U/H-Lines in Japan [Kawamura, 2018] use radiation-hard solenoids, whereas MuSIC at RCNP Osaka, Japan [Cook, 2017] and the Chinese Spallation Source CNSC [Xiao, 2016] make use of primary targets placed inside the capture solenoids for continuous and pulsed primary beams.

The capture solution chosen for HIMB must not only consider the spatial constraints imposed by the target vessel but also the radiation environment and the influence of the magnetic field on the proton beam itself as well as the proton beam optics to the downstream Target E and the SINQ spallation neutron source. Since a large acceptance solution is sought – a normal conducting solenoid with Mineral Insulated Conductor (MIC) coils was chosen. Also, to enhance the solid angle and phase space acceptance a distance of only 250 mm between the coil and the target was chosen. Iron shielding was also included to reduce the fringing field influence on the proton beam and surroundings. Furthermore, the choice of a solenoid reduces the axial space needed, which enhances transmission, since as a focussing element it has the advantage of being rotationally symmetric and simultaneously focussing in both planes, unlike a quadrupole doublet or triplet which require significantly more space.

Two initial solutions were examined, a so-called "long" version of 784/589 mm total/coil length with an aperture of 500 mm and a "short" version of 498/373 mm total/coil length with the same aperture. A recent "new long" version with modified coil configuration, with better thermal coil properties was designed, having 810/650 mm total/coil length. 3D field maps were generated for all three types and the capture and transmission properties compared using the simulation package G4beamline (G4bl) with muons generated from the equivalent of 10^{11} proton interactions in the slanted target. The basic G4bl model of the "new long" capture solenoid is shown in Figure 7.8 (left) with some muon trajectories and Figure 7.8 (right) with magnetic field lines present. The axial and transverse magnetic field characteristics are shown in Figure 7.9 and Figure 7.10 for a central magnetic field of 0.375 T. The axial distance shown on the plots is from the centre of the target (z=0) to approximately 1.5 m downstream. A Gaussian fit to the central part of the distribution gives the correct centre of the solenoid.

A comparison of the transmission properties of the three different types of capture solenoid are shown in Figure 7.11. Here the absolute transmission T_{abs}, defined as the number of muons detected by a virtual detector on the downstream side of the solenoid, compared to the number of muons emitted into the forward hemisphere around the target is plotted against the central magnetic field of the solenoid. The limit of 0.45 T is taken as the limiting magnetic field due to the MIC coils for the current designs. Both "long" types show similar characteristics, with a clearly favourable "short" version yielding a 19 % higher relative transmission

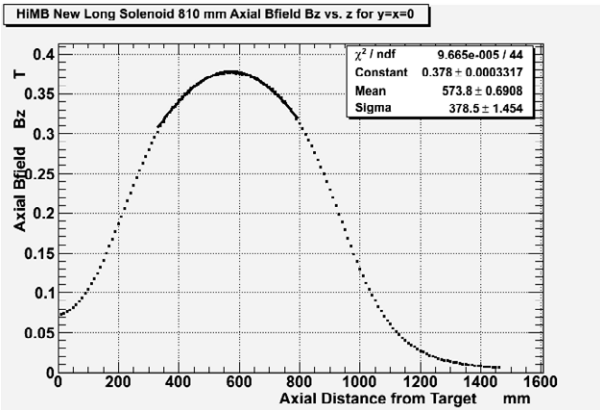

Figure 7.9: Shows the axial magnetic field B_Z versus the axial distance from the target centre. The Gaussian fit to the central region gives the correct centre of the magnet.

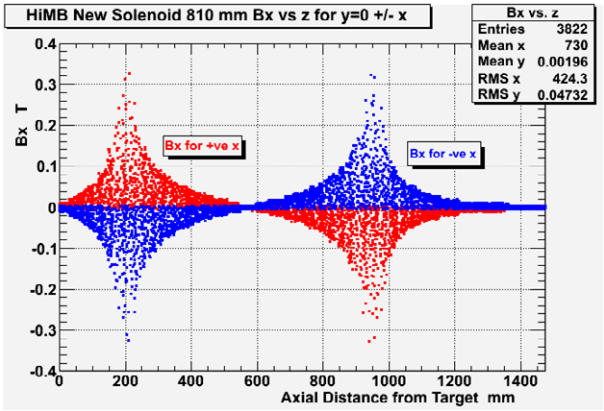

Figure 7.10: Shows the transverse field B_X for Y=0 along the z-axis of the solenoid with +ve x-values in red and -ve x-values in blue.

at the maximum field strength. The absolute transmission of the "Short" solenoid is 31% with a relative transmission (downstream detector compared to upstream) of 51%. However, since the focusing-power scales with the integral of $B^2 \cdot dl$, the equivalent field for the "long" version would be even lower, leading to an even larger loss. The simulation is made with the same two types of solenoids placed on either side of the target and having a +/+ polarity configuration. This field configuration enhanced the transmission for non-shielded solenoids, whereas for the iron-shielded version virtually no difference was seen.

7.4.3 Solenoid Acceptance

The solenoid accepted phase space was determined by selecting those events which make it to the downstream side detector of the solenoid and comparing their initial parameters in the target emittance file with those of all particles in the emittance file. The horizontal and vertical phase space distributions of all target-emitted events compared to target-emitted events which make it to the downstream detector of the capture solenoid are shown in Figure 7.12 (left) and (right). The capture solenoid also plays a significant role in increasing the polarization of the beam

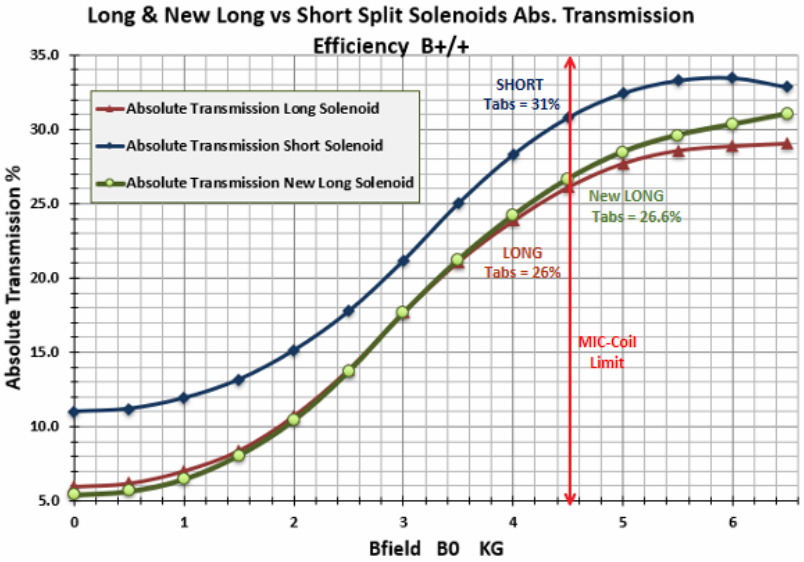

Figure 7.11: Comparison of the absolute transmission of the three capture solenoid types. A significant 19 % relative transmission enhancement is seen for the "short" version.

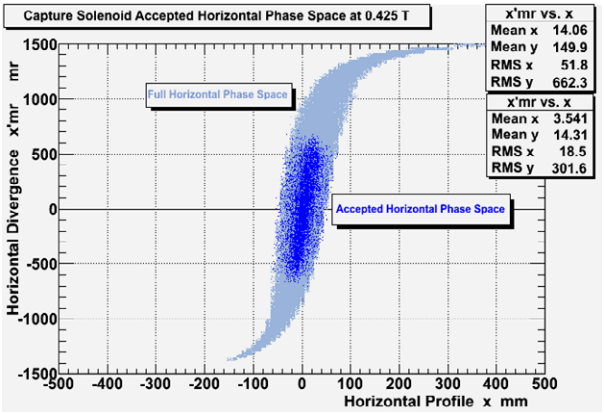

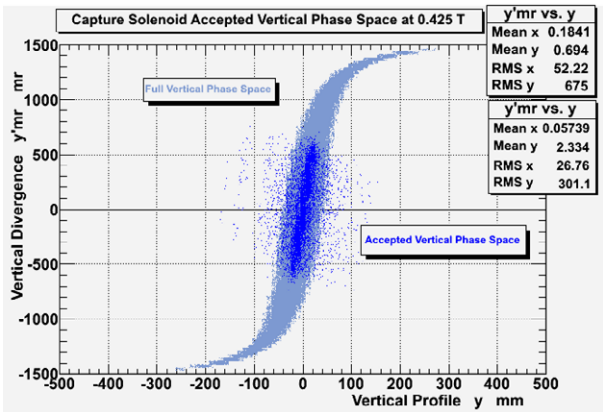

Figure 7.12 (left): Horizontal phase space at the target (light blue events), together with the accepted phase space at the target for events which make the downstream acceptance of the capture solenoid (dark blue events).
Figure 7.12 (right): The equivalent vertical phase space distributions.

by reducing both the vertical and horizontal divergence. This is demonstrated in Figure 7.13, which shows the distributions of muon polarization versus muon momentum at the target for all events (blue distribution) and for those events which make the acceptance of the capture solenoid (red distribution). The solenoid enhances the polarization of the muons, with respect to the beam axis, from 67 % to 91 %.

7.5 Particle Separation Process: Separator and Spin Rotator

As can be seen from Figure 7.3 (left) and (right), there are substantial backgrounds associated with muon beams in the momentum range to be accessed by HIMB, up to 80 MeV/c. For the low momentum range, around 30 MeV/c, associated with surface muons and that of sub-surface muons (surface muons from deeper within the target) approximately (5–26) MeV/c, the dominant background is from positrons of similar yield, while the pion contamination is

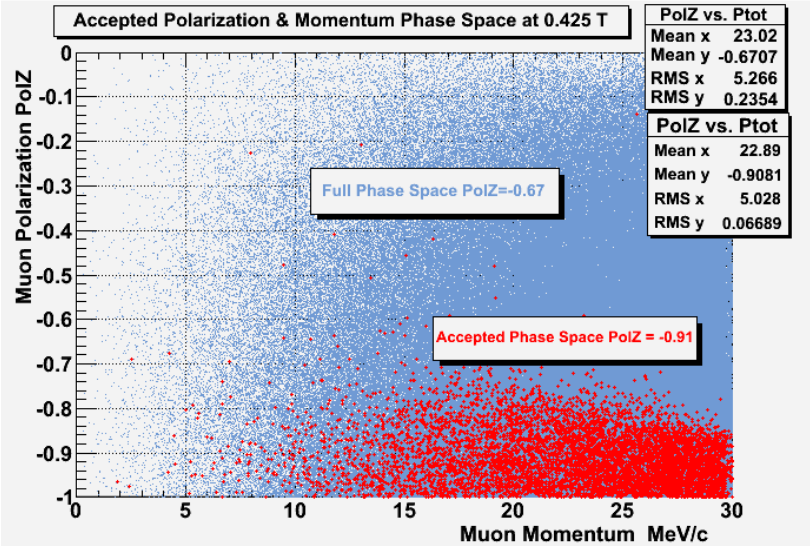

Figure 7.13: Shows the polarization distribution as a function of muon momentum for all target muons (blue distribution) and for those target muons that are accepted by the solenoid (red distribution). The polarization with respect to the beam axis PolZ is enhanced from 67 % to 91 % by the solenoid.

comparatively negligible being more than 2-orders of magnitude lower. For the negative charge-sign below 30 MeV/c the electron contamination is 2-orders of magnitude higher, whereas the pion contamination is comparable. Above 30 MeV/c for both charge-sign muons, the pion contamination increases to about a factor of 10 times the muon yield at 70 MeV/c.

7.5.1 Background Separation Techniques

Three main methods to separate the beam-related background are applicable to HIMB and under study:

- *Differential energy loss* – the use of a degrader foil, placed at an intermediate focus to reduce multiple scattering, in conjunction with a downstream dipole magnet. This technique relies on the particle-types in the beam having very different energy losses dE/dX in the degrader material, hence inducing a momentum difference between the particles which is then exploited in the downstream dipole magnet by removing the unwanted particles from the central trajectory. This technique was successfully used in the first surface muon channel at PSI, PiE3 [Daum, 1982]. A MYLAR foil thickness of 380 μm gave a clean separation of muons and positrons, though with the consequence of a factor of 2 loss in muon intensity and a lowering of the beam momentum.
- *Time-of-flight separation* – At PSI's HIPA facility the radio-frequency signal (RF) of 19.750034 ±0.000002 ns period from the proton accelerator can be used as a precise clock to measure the time-of-flight (TOF) of particles from the target to a detector in the experimental area. A raw oscilloscope trace of such a TOF-spectrum taken for a negative pion beam at 85 MeV/c is shown in Figure 7.14 (left). The top trace is the 50 MHz RF-signal from the accelerator, triggered on a scintillation pill-counter in the experiment, showing the relative TOF within the modulo 19.75 ns of the 50 ns time window displayed. The respective muon, pion and electron signatures can clearly be seen repeated after 19.75 ns. The bottom trace is the TOF-spectrum with the clearly separated e^-, π^- and μ^- peaks shown running from right-to-left. The corresponding triple Gaussian fit to the TOF-spectrum is shown in Figure 7.14 (right). Furthermore, the above particles also have different energy losses (dE/dX) in the detector material which also allows further discrimination due to pulse-height. In the case of surface muons, the situation is more complicated, as the muons have no time structure

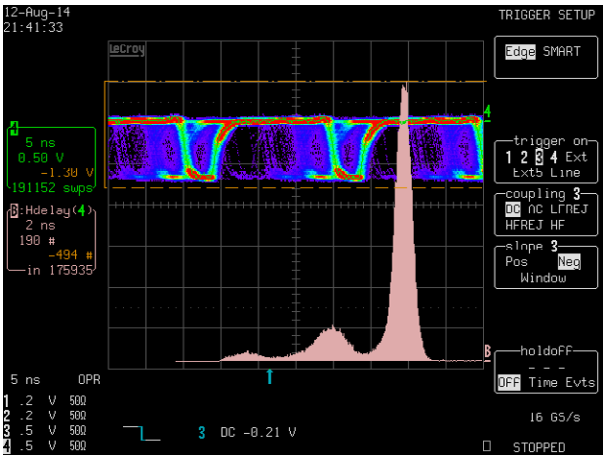

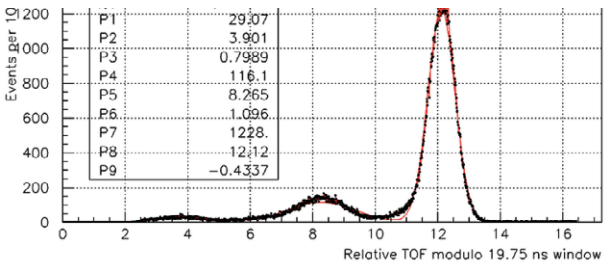

Figure 7.14 (left): shows raw oscilloscope trace of a TOF measurement at 85 MeV/c. The top trace is the 50 MHz RF-signal from the accelerator triggered on the signal from a pill scintillation detector in the experiment, showing the modulo 19.75 ns TOF measurement within the 50 ns time window of the display. The bright distribution is from beam electron contamination in the pion beam. To the left of the e^- are the π^- and μ^-. **Figure 7.14 (right):** shows the fitted data of the TOF-spectrum with the e^-, π^- and μ^- peaks running from right-to-left.

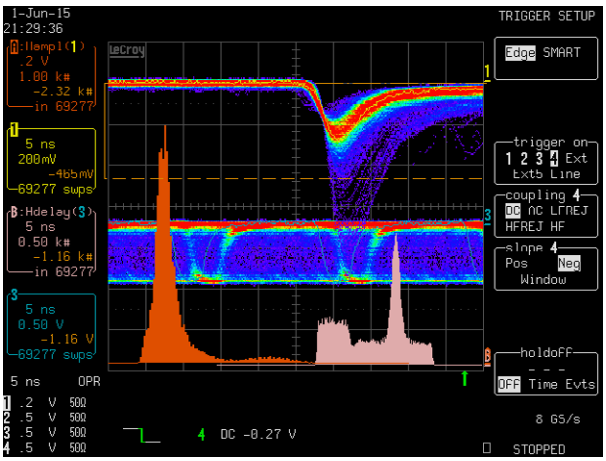

Figure 7.15: The TOF and pulse-height situation for surface muons at 28 MeV/c. The top oscilloscope trace shows the scintillation detector output signal, triggered just below the beam positron distribution (hence the faint higher muon line). The centre trace is again the RF-signal triggered on the counter, showing clearly the modulo 19.75 ns correlated beam positron signal. The bottom two spectra are (orange) pulse-height spectrum with positron (low pulse-height) on the left muons (high pulse-height) on the right side. The pink TOF-spectrum shows a clear correlated signal due to beam positrons sitting on a flat spectrum of muons and Michel positrons. (The box-like structure on the left of the spectrum is a wrap-around artifact of the oscilloscope; ½ of this box should be added to the end of the spectrum).

with respect to the RF-signal and produce a flat timing spectrum and since they also decay, the Michel positrons from their decay also have a flat timing spectrum, predominantly being produced in the detector. Though other beam-related backgrounds such as beam positrons or pions are correlated with the RF, being produced directly from the proton interaction in the target. Hence, the beam positron peak in the timing spectrum sits on a flat background. This can be seen in Figure 7.15 (bottom right-hand spectrum). Hence when placing an anticoincidence window on the beam positron peak, a certain percentage, in the above case approximately 20%, of the flatly distributed muon events will also be cut. However, here also the difference in pulse-height of the different signals can be used.

- *Wien-filter/Spin Rotator*

  A Wien-filter is a crossed-field separator, employing a magnetic field placed perpendicular to an electric field and both perpendicular to the central beam-axis. The device is essentially a velocity filter and due to the orthogonality of the fields the Lorentz force acting on a particle of charge q is $F = q(E+v\times B)$. This will have the separate forces opposing each other, so that only particles with a velocity $v = E/B$ will be undeflected and stay on the beam-axis, all other velocities will be deflected. Wien-filters used as separators are only useful in the low-energy realm below ‹40 MeV/c, as the separation quality above this value, especially for large emittance beams, becomes marginal. The Wien-filter can also be used to rotate the intrinsic spin polarization of the muons, with respect to their momentum vector, required for some μSR techniques. Here the goal is not only the removal of background but the rotation of the spin which requires much larger field integrals. For a 45° to 65° rotation a length of some 3 m is needed. This is sometimes split into two or more separate lengths with focusing elements between to enhance the transmission [Ikedo, 2013].

7.5.2 HIMB Wien-filter & Spin Rotator

For HIMB the Wien-filter solution was primarily investigated, though a combination is not ruled-out. On the MUH3-side the recently built Spin Rotator 1, outlined in Table 7.3 and described in Section 7.10.3 will be used, whereas on the MUH2-side a new Wien-filter will be needed. The initial design is based on modifying the existing Spin-Rotator 1 to accommodate a larger diameter beam transport system, hence increasing the plate separation from 200 mm to 500 mm and decreasing the plate length from 3 m to 2 m. This gives an overall length including associated vacuum ports and shutters of 4.2 m, for a single 1 m plate length version the overall length would be 2.9 m (c.f. Section 7.10.2). Simulations were made for this 4.2 m long version using three simultaneous particle beams of pions, muons and positrons using G4beamline for momenta of 28, 40 and 70 MeV/c. The separation quality was studied as a function of beam size, divergence and reduced high voltage, as well as the influence on the polarization. The Wien-filter parameters used are given in Table 7.3.

Wien-filter Parameters	MUH2	MUH3
Plate Length	2.0 m	3.0 m
Plate Gap	0.5 m	0.2 m
Max. HV / Nominal HV	± 300 kV / ± 280 kV	± 300 kV / ± 275 kV
Max. E-field / Nominal E-Field	1.2 MV/m / 1.12 MV/m	3 MV/m / 2.75 MV/m
Nominal B-field (Muons 28 MeV/c)	145.7 G	358 G
Total Length / Filter length	4.2 m / 3.2m	4.3 m / 3.6 m
Nominal Muon Spin Rotation Angle	17.3°	63.7°

Table 7.3: Simulation values used for the modelling of the Wien-filter.

The formulae for the respective electrostatic θ_E and magnet θ_B deflection angles are given in Eq. 1 and Eq. 2 (Frosch, 1995)

$$\theta_E[mr] = \left(\frac{V\ L_{Eff}}{d\ P_0\ \beta}\right)\ [kV, m, MeV/c] \qquad -(1)$$

$$\theta_B[mr] = \left(\frac{30\ L_{Eff}\ B}{P_0}\right)\ [G, m, MeV/c] \qquad -(2)$$

where V is the voltage between the plates, L_{Eff} is the respective effective length of the electrostatic field or the magnetic field, d is the plate separation, P_0 is the central momentum, β is the particle velocity and B the magnetic field, with the appropriate units shown. The corresponding magnetic field B to centre the respective particle type is given by Eq. 3 and the nominal spin rotation angle ϕ with respect to the muon momentum vector is given in Eq. 4 (Frosch, 1980).

$$B[G] = \left(\frac{\theta_E\ P_0}{30\ L_{Eff}}\right)\ [mr, m, MeV/c] \qquad -(3)$$

$$\emptyset\ [rad] = \left(\frac{30\ B\ L_{Eff}}{P_0\ \gamma}\right)\ [KG, m, MeV/c] \qquad -(4)$$

The deflection angles, angular separation quality and the required magnetic field B for the three momenta 28, 40 and 70 MeV/c for each of the three particle types are shown in Table 7.4 below.

The G4beamline model of the MUH2 separator is shown in Figure 7.16 (left) with the parameters set to transmit surface muons (green tracks) at 28 MeV/c, with pions (blue tracks) and beam positrons (red tracks) of equal number shown. The particle separation at the end of the Wien tank, 2.6 m from the start of the HV electrodes is shown in Figure 7.16 (right) for beam spot sizes of 30 mm (1σ) and 3 % Δp/p. As can be seen the beam e^+ are deflected beyond the diameter of the beam-pipe, whereas in reality, at 28 MeV/c there are no measurable pions in the beam. The action of the Wien-filter on the muon spin is given by Eq. 4 this leads to a muon spin rotation at 28 MeV/c, calculated from φ of 4.53 % so for a 100 % polarized beam one would expect a polarization of – 0.9547 in the beamline direction after the separator, which is confirmed by the simulation as shown in Figure 7.17. For beams with a large emittance at the entrance to the filter or having large divergences in the bending plane a significant

P=28[MeV/c]	θ_E [mr]	B(θ_E= θ_B) [G]	Δθ wrt μ [mr]
π	406.7	198.8	+94.4
μ	312.3	145.7	0
e	80.0	37.3	-232.3

P=40[MeV/c]	θ_E [mr]	B(θ_E= θ_B) [G]	Δθ wrt μ
π	203.3	135.5	+45.1
μ	158.2	105.5	0
e	56.0	37.3	-102.2

P=70[MeV/c]	θ_E [mr]	B(θ_E= θ_B) [G]	Δθ wrt μ
π	71.4	83.3	+13.5
μ	57.9	67.6	0
e	32.0	37.3	-25.9

Table 7.4: Momentum dependence of deflection angles, angular separation quality and equivalent required magnetic field to centre the respective particle type for the 3 simulated momenta 28, 40 and 70 MeV/c.

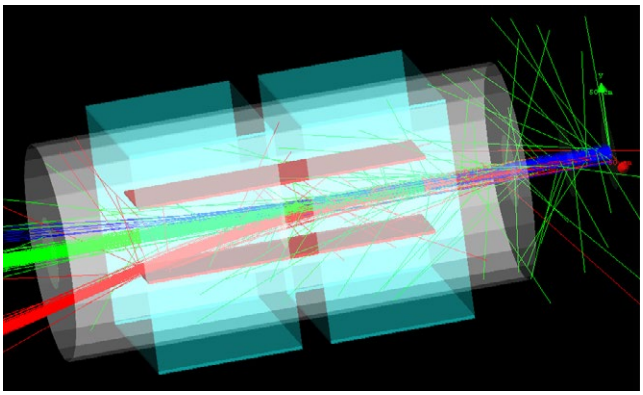

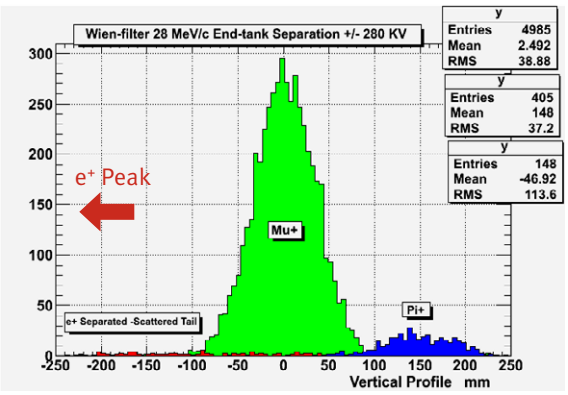

Figure 7.16 (left): G4beamline Wien-filter model with 3 simultaneous beams of muons (green), pions (blue) and beam positrons (red). The parameters are set to transmit surface muons of 28 MeV/c and the beam positron peak is off-axis in **Figure 7.16 (right)**, while it should be noted that at 28 MeV/c there are no measurable pions in the beam.

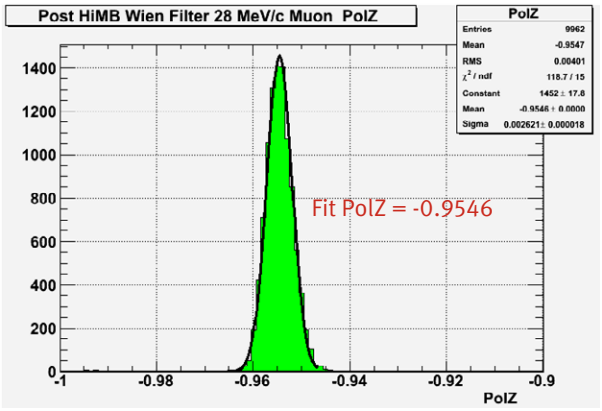

Figure 7.17: Shows a fit to the muon polarization distribution downstream of the Wien-filter for surface muons at 28 MeV/c. The fit results correspond exactly to the calculated rotation effect derived from Eq. 4.

reduction in the separation power can be expected. This can be seen from Figure 7.18 (left) and (right) which show the case for 28 MeV/c surface muons having a 1σ beam-spot of 80 mm, totally filling the beam tube and the case of a divergence of 100 mr in the bending plane. For 28 MeV/c a good separation quality is still achieved for larger beam-spots, though for divergence in the bending plane the quality is ruined. For divergence in the non-bending plane the separation quality is unchanged, only the transmission is reduced. Finally, the momentum dependence of the separation quality is shown in Figure 7.19 (left) for 40 MeV/c particles and Figure 7.19 (right) for 70 MeV/c particles, both for small beam-spot sizes (σ=30 mm) as in Figure 7.16 (right). At 40 MeV/c a satisfactory separation is still achieved but only for small spot-sizes, for beam-spots that fill the aperture, the distributions start to merge. At 70 MeV/c no separation can be achieved even for small spot-sizes.

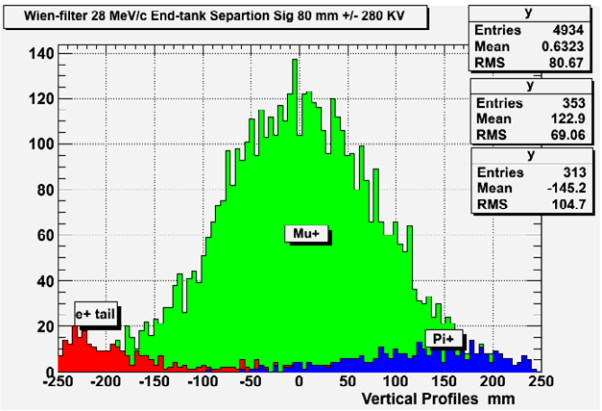

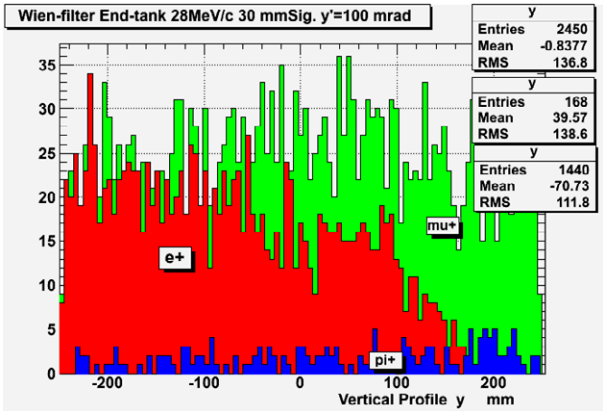

Figure 7.18 (left): Separation quality at the end of the Wien-filter tank for a beam-spot that fills the aperture at 28 MeV/c showing the separation is still satisfactory. **Figure 7.18 (right):** Shows the situation for a divergent beam of 100 mrad in the bending plane for a small beam-spot (σ=30 mm). For equivalent bending in the non-bending plane no separation quality difference is seen, only a reduction in transmission. The figures should be compared with Figure 7.16 (right).

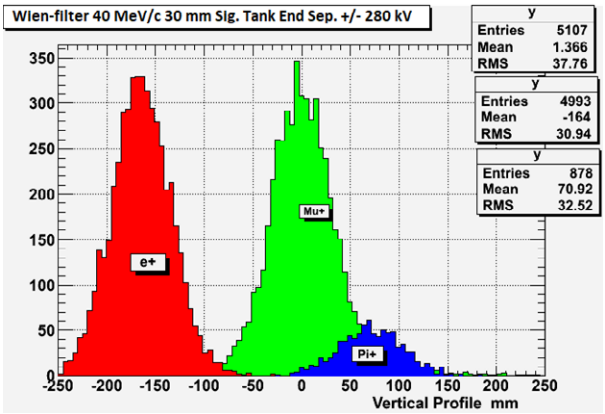

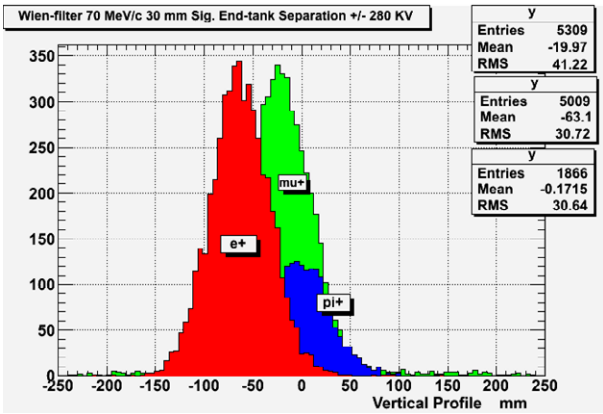

Figure 7.19 (left): The end-of-tank separation quality for a small beam-spot of σ=30 mm for 40 MeV/c particles. The quality is still acceptable, though for spot-sizes equivalent to fill the aperture the distributions start to merge.
Figure 7.19 (right): The same situation for 70 MeV/c particles. Clearly there is no separation possible, even for small spot-sizes.

7.5.3 Current Separation Conclusions

The current HIMB status concerning particle separation can be summarized as follows –

On the MUH3-side, the Spin Rotator 1 will be kept along with the downstream μSR facility elements and the new MUH3 solenoid channel will couple to these.

For MUH2, a new Wien-filter option was investigated. However, it seems that a single long element of 4.2 m in length, although achieving the separation quality, at least for momenta ‹40 MeV/c, cannot be used due to the low relative transmission of 26 % for the filter. A more complex solution using two Wien-filters with intermediate focussing is now under study, this together with the first two background separation techniques is expected to bring a satisfactory solution.

7.6 Simulation Programs

We perform particle transport simulations and beam optics optimization mainly using the codes G4beamline [Muons Inc., 2019], TRANSPORT [Rohrer (TRANSPORT)], and TURTLE [Rohrer (TURTLE)]. Additionally, some beamline model development and optimization are carried out using *COSY INFINITY* [Berz, 2006a]. Below we briefly describe the different programs.

7.6.1 G4beamline

G4beamline is a program by Muons, Inc. for particle transport and physics processes based on the Geant4 toolkit [Agostinelli, 2003]. We use a custom build of Geant4 4.10.05.p01 and G4beamline 3.06, with parameterized pion production cross sections and event biasing for pion production and decay [Berg, 2016]. Figure 7.20 shows an example of a G4beamline model for HIMB particle transport studies.

G4beamline uses conventional integration of the equations of motion for each simulated particle and Monte Carlo simulations of physics processes. It does not use or calculate a transfer map, a transfer matrix, or dispersion functions. The advantages of G4beamline are that it accurately simulates the production of surface muons from the target and includes particle decay and beamline apertures (including slits) in the simulation. As a result, realistic muon distributions are generated along the beamline.

For optimization of multiple beamline parameters such as field strength and element positions, we perform optimization on a computing cluster using the asynchronous Bayesian optimization package DeepHyper [Balaprakash, 2018], where the custom build of G4beamline is deployed as a Docker / Singularity image. For one-parameter optimization, we also use grid scans.

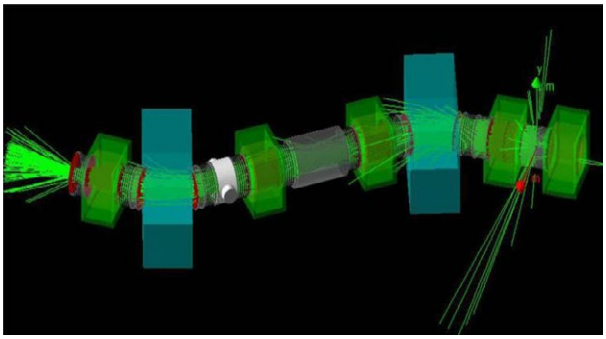

Figure 7.20: System plot of a G4beamline model for HIMB particle transport studies.

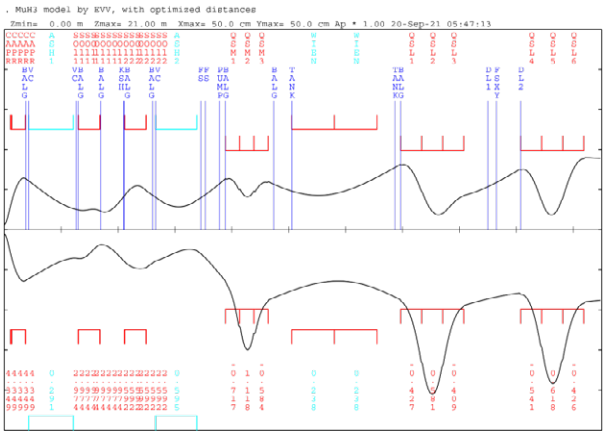

Figure 7.21: First order beam envelope plot for a TRANSPORT model for HIMB beam optics studies.

7.6.2 TRANSPORT

TRANSPORT is a transport-matrix based beam optics program dating back to 1963. Its development and maintenance were carried out at CERN, SLAC, Fermilab, and most recently at PSI. TRANSPORT includes first and second-order calculations and fitting.

TRANSPORT calculates various essential beam optics values such as the transfer matrix, beam envelopes, and dispersion functions. Fitting is performed efficiently, for a set of parameters specified in the beamline definition using vary codes and with objective functions specified as transfer matrix elements or beam sigma matrix elements.

It is often more straightforward to fit a beamline to, e.g., a desired transfer matrix element or Twiss function values, as opposed to statistical properties of particle distributions generated using Monte Carlo simulations in G4beamline. Moreover, the kinds of beam optics outputs generated by TRANSPORT are standard for procedures such as matching the beam between different parts of a beamline. Figure 7.21 shows an example of a beam envelope plot by TRANSPORT for HIMB beam optics studies.

7.6.3 TURTLE

TURTLE is a code for simulation of charged particles occupying a small phase space volume through a beam transport system, where rays are propagated using first and higher-order transfer matrices. The original version of TURTLE was developed by D.C. Carey at Fermilab. The version we use is DECAY TURTLE, which was developed at CERN and later at PSI, and which includes particle decay simulation capabilities.

TURTLE has a mixed order approach to accounting for aberrations; for example, transfer matrix elements for chromatic aberrations in quadrupoles and sextupoles are exact to all orders, but in bending magnets, chromatic effects are calculated only to second order, which is usually sufficient considering the relatively weak focusing effects of bending magnets. Geometric aberrations are evaluated locally to second order but provide higher-order terms by accumulation.

A TRANSPORT input deck can be used for TURTLE with minor modifications. TURTLE augments TRANSPORT's functionality by simulating an ensemble of rays with particle decays, effects of slits and apertures, and higher-order effects.

7.6.4 COSY INFINITY

COSY INFINITY is a scientific computing code by Martin Berz and Kyoko Makino (Michigan State University) with specialized packages including a beam physics simulation and analysis package COSY.FOX. Beam physics computations are performed using Differential-Algebraic (DA) transfer maps of arbitrary computation orders. A transfer map of order *n* is essentially composed of all aberrations from the zeroth to the *n*th order. In practice, orders up to 7 or 11 are typically used.

There are several fringe field modes in *COSY INFINITY*, where the most accurate fringe field mode considers the transverse offset of the reference orbit due to the fringe field in bending elements, compared to not performing fringe field calculations. *COSY INFINITY*'s particle optical elements include arbitrary field maps, and simulations of particle decays and physical apertures are possible. Figure 7.22 shows an example system plot for HIMB beam optics studies.

COSY INFINITY's packages include a rigorous global optimizer COSY-GO [Berz, 2006b]. It is possible to add a genetic optimization algorithm to COSY-GO. Both COSY-GO and genetic optimization have been used successfully to solve nontrivial beam and spin dynamics problems.

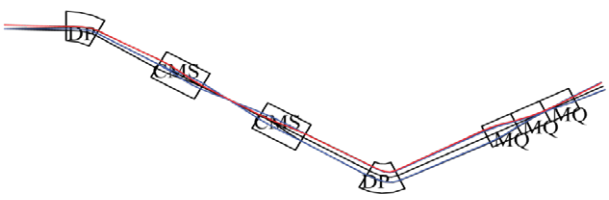

Figure 7.22: System plot of a COSY INFINITY model for HIMB beam optics studies.

7.7 Beam Optics MUH2 & MUH3

7.7.1 Beam Optics MUH2

The HIMB concept for a beam transport system is based on a large acceptance capture solenoid at the target followed by a normal conducting solenoid channel with the same aperture of 500 mm. The MUH2 beam line will sit on the left-hand-side of the target station in the proton beam direction, with the distance to the capture solenoid's first coil being only 250 mm. The beam line should be designed for maximum transmission leading to a final achromatic focus either in a solenoidal detector such as the Mu3e solenoid [Arndt, 2021] or a non-solenoidal final focus for other types of particle physics experiments. Designing for maximum transmission with a solenoidal channel means a compact design compared to a classical quadrupole channel since a solenoid is rotationally symmetric and focusses in both planes simultaneously, as opposed to a quadrupole. However, this also means that emittance-growth due to the coupling between planes must be considered. Furthermore, a direct line-of-sight to the target must be avoided due to the significant radiation field and neutron flux at the target. Hence a double dipole version is envisaged with bending angles of about 40° leading to a stretch Z-layout. Depending on the final Wien-filter solution a further dipole might be needed to fit the area layout.

7.7.1.1 Simulations

The simulation tools used for the design of the transport system were already described in Section 7.6. For MUH2 we used mainly the matrix-based code Graphics Transport [Rohrer (TRANSPORT)] for the initial optical model. This was then studied and refined using G4beamline release 3.06 [Muons Inc., 2019]; as a cross-check the charged particle ray-tracing program Graphics Turtle [Rohrer (TURTLE)] was also used.

As a starting point for MUH2 a straight solenoidal channel of equivalent length was investigated to look at various optical configurations and compare them with G4beamline. Examples of different modes for both Transport (left) and G4beamline equivalents (right) are shown in Figure 7.23. From this study the Pt-›Pt (point to point) optics in the capture solenoid followed by a Pt-›//-›// (point to parallel to parallel) optics for the remaining transport solenoids and ending in a //-›Pt optics for the last focusing solenoid was found to have the highest transmission with a relative transmission of 34 % for the capture solenoid, 32 % for the transport solenoids giving a total absolute transmission of 11 % over the 12 m channel.

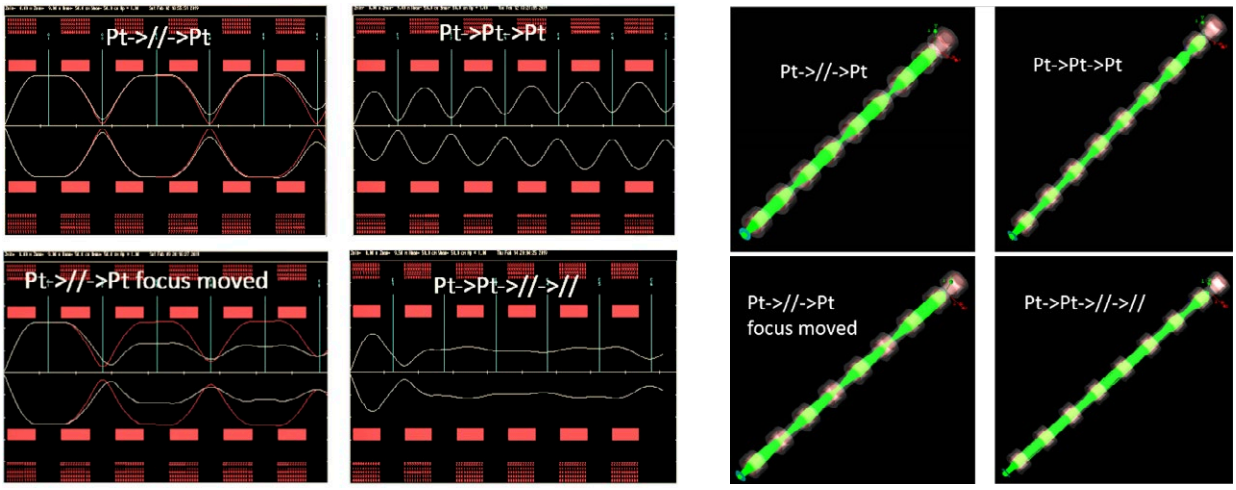

Figure 7.23: Shows examples of different optical models for a straight solenoidal channel in Transport (Left) and the equivalent beam trajectories in G4beamline (Right). They differ in the sequence of focussed (Pt) and parallel (//) beam transport through the solenoids.

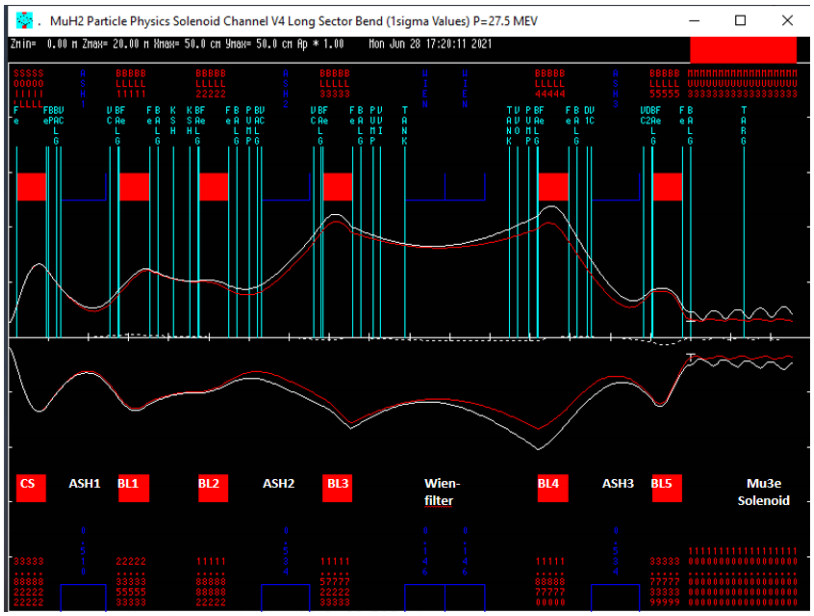

Figure 7.24: Shows a Transport calculation of the vertical and horizontal beam envelopes along the beam-axis for the original MUH2 full beam line with the large Wien-filter and Mu3e solenoid. See the main text for an explanation.

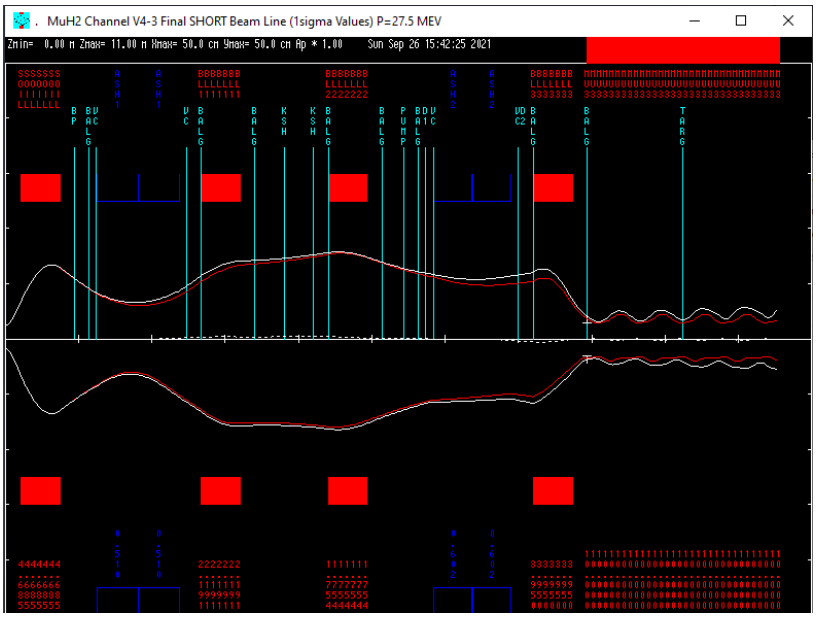

Figure 7.25: MUH2 optical model from Transport, without a Wien-filter and ending with the Mu3e solenoid. The envelopes shown in red are 1st-Order, while those in white are 2nd-Order. Upper envelopes vertical, lower horizontal.

The optical model for the original full layout of MUH2, including the large Wien-filter and the Mu3e solenoid, is shown in Figure 7.24. The Transport output shows the 1st-order (red trace) and 2nd-order (white trace) beam envelopes for the vertical plane (top half) and the horizontal plane (lower half) along the horizontal beam-axis. The vertical and horizontal scales are different. The red elements are the capture (CS) and transport solenoids (BL1-5), as well as the large Mu3e solenoid, while the blue are dipole magnets (ASH and Wien-filter). The barely visible dotted line close to the axis is the dispersion trajectory for 1% off-momentum particles. The optics follows the outlined plan above, with a Pt-to-Pt transformation for CS followed by double beam waists placed at the centre of the dipoles. The dispersion is made to go to zero after the final dipole, producing an achromatic focus. The matching to the Mu3e solenoid is not perfect as can be seen by the nodal fluctuation in the 2nd-order envelopes.

The current MUH2 setup, without a Wien-filter, is shown in Figure 7.25 for the final focus at the centre of the Mu3e solenoid. Here the 1st-order, 1σ beam-spot sizes at the centre of the solenoid are $\sigma_X = 33$ mm and $\sigma_Y = 31$ mm. Whereas in second order they grow to $\sigma_X = 41$ mm and $\sigma_Y = 36$ mm.
The final non-solenoidal focus is shown in Figure 7.26, for both versions the optics are similar to that described above. Here the final focus beam-spot sizes are $\sigma_X = 34$ mm and $\sigma_Y = 35$ mm in 1st-order and $\sigma_X = 36$ mm and $\sigma_Y = 39$ mm in 2nd-order. The rms emittances derived from Transport for both versions compared to the source emittance are shown in Table 7.5 below.

7.7.2 Beam Optics MUH3

The MUH3 beamline (see Figure 7.27) is designed for μSR applications and does not require the full ~10^{10} muons/sec as the MUH2 beamline, where high statistics are necessary

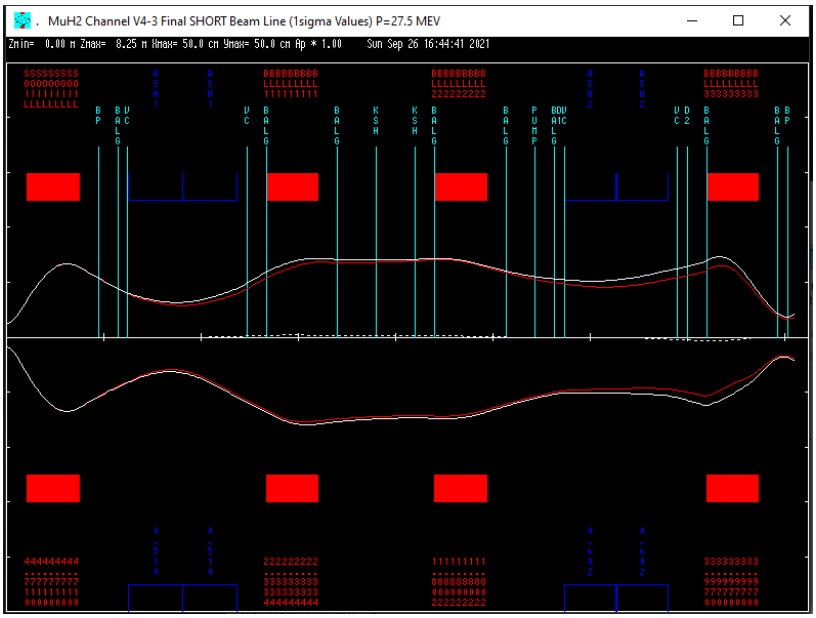

Figure 7.26: Transport optical model for the compact MUH2 version without a Wien-filter showing the vertical and horizontal beam envelopes along the beam-axis in both 1st-Order (red) and 2nd-Order (white). Upper envelopes vertical, lower horizontal.

Model	Initial rms Emittance ε_X / ε_Y [π·cm·mrad]	Final Focus Emittance ε_X / ε_Y [π·cm·mrad]
Mu3e Solenoid Focus	559 / 804	986 / 820
Non-solenoidal Focus	559 / 804	815 / 998

Table 7.5: Shows the initial and final focus rms horizontal and vertical emittances ε_X and ε_Y for the short MUH2 optical models without a Wien-filter, for both the Solenoidal and non-solenoidal focus.

for particle physics experiments. As in the MUH2 beamline, solenoids are used instead of quadrupoles for focusing in the first two straight sections (transporting ~10^{10} muons/sec to the start of the experimental area). However, conventional quadrupole tuplets are used from the beginning of the third straight section to the experimental installations. The role of the part of the MUH3 beamline with solenoid focusing is the same as in MUH2: to provide the highest possible transmission while shielding the downstream parts of the beamline from radiation emitted by the target station. The part of the MUH3 beamline with quadrupole focusing has a conventional design, and its role is to transport the surface muons to the experiments.

7.7.2.1 Capture Part

The capture part of the MUH3 beamline (mainly the target and the capture solenoid, apart from the target rotation sense) is mechanically mirror-symmetric to the MUH2 beamline relative to the target TgH. The difference between the two capture parts that breaks the mirror symmetry is that the fields of the capture solenoids in MUH2 and MUH3 are co-directional, in a way that the fields of these solenoids

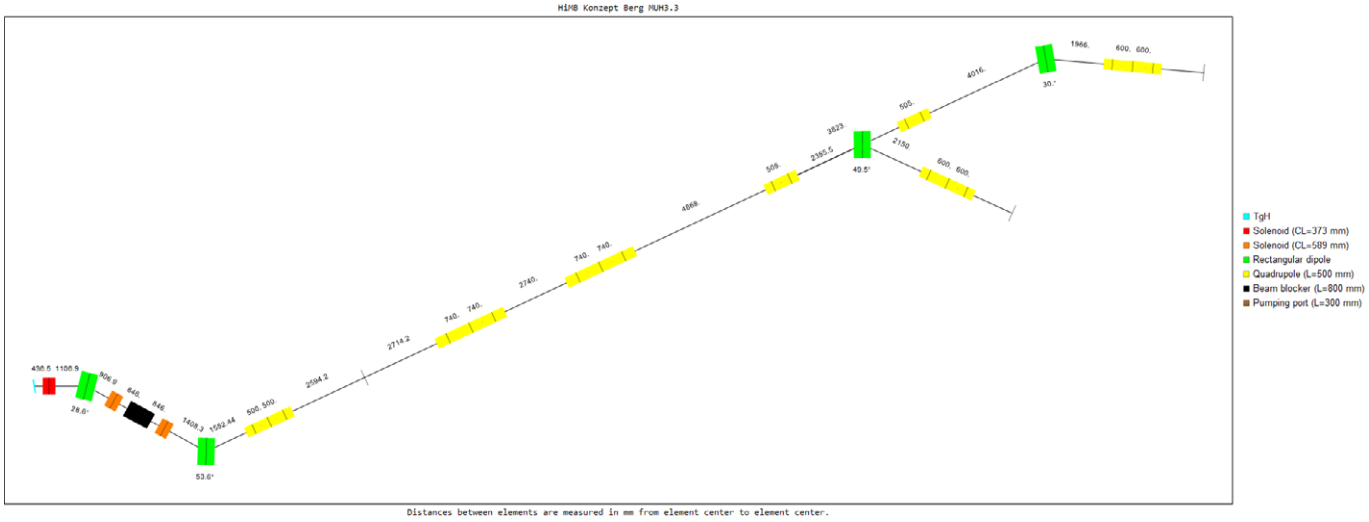

Figure 7.27: System plot of the MUH3 beamline, from the target TgH (cyan) to the final foci of the MUH3.2 and MUH3.3 branches.

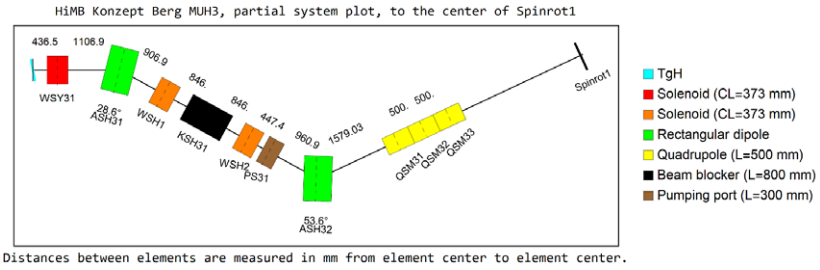

Figure 7.28: A partial system plot of the MUH3 beamline, from the target TgH (cyan) to the center of the spin rotator Spinrot1. The distances in the plot are between the centers of the elements, measured in mm.

do not cancel out at target TgH. However, as described above (see Section 7.4) having the two field directions of the capture solenoids opposite to each other does not have any impact on the capture efficiency when using solenoids with an iron return yoke.

This difference also does not have a significant effect on the beam optics, and the same beam optics and muon transmission considerations apply to the capture sections of both MUH2 and MUH3 beamlines. In particular, even though the transmission to the downstream end of the capture solenoid peaks at or above 0.5 T, in a combined optimization beyond the first dipole ASH31 the optimal field of the capture solenoid does not exceed 0.45 T. Also, in a study comparing downstream transmissions for capture solenoids with 373 mm and 589 mm coil lengths, we found that shorter solenoids tend to provide a higher transmission rate, which is why we use a capture solenoid with 373 mm coil length in the MUH3 beamline, just like in the MUH2 beamline.

7.7.2.2 Solenoid Focusing–Based Transport Part

The lengths of the first two straight sections and the distance between the second dipole ASH32 and the first quadrupole triplet QSM31-QSM32-QSM33 (see Figure 7.28) are optimized to maximize transmission and are thus close to as short as possible while allowing for the necessary beamline elements, including the beam blocker KSH31 and the pumping port PS31.

Dipole magnet field strengths and translational offsets are optimized for the reference particle to pass through the beamline's centerline and parallel to it at a set of beamline intersections.

A first-order beam envelope obtained using TRANSPORT [Rohrer (TRANSPORT)] for a part of the MUH3 beamline from the target to the downstream of the third quadrupole tuplet QSL4-QSL5-QSL6 is shown in Figure 7.29.

7.7.2.3 Quadrupole Focusing–Based Transport Part

We are working on the beam optics of the MUH3 beamline from the first quadrupole triplet QSM31-QSM32-QSM33 to the beamline branches MUH3.2 and MUH3.3. For fitting of the final foci of MUH3.2 and MUH3.3, we developed a *COSY INFINITY* model that was verified to match the particle transport in G4beamline. We apply *COSY INFINITY*'s built-in optimizers, such as the simulated annealing algorithm and the LMDIF optimizer, to fit the final foci using objective functions in terms of transfer matrix elements and aberrations, or standard deviations of the tracked muon beam. The existing TRANSPORT models for the PiM3 beamlines can be reused with appropriate modifications for the quadrupole focusing—based part of the MUH3 beamline.

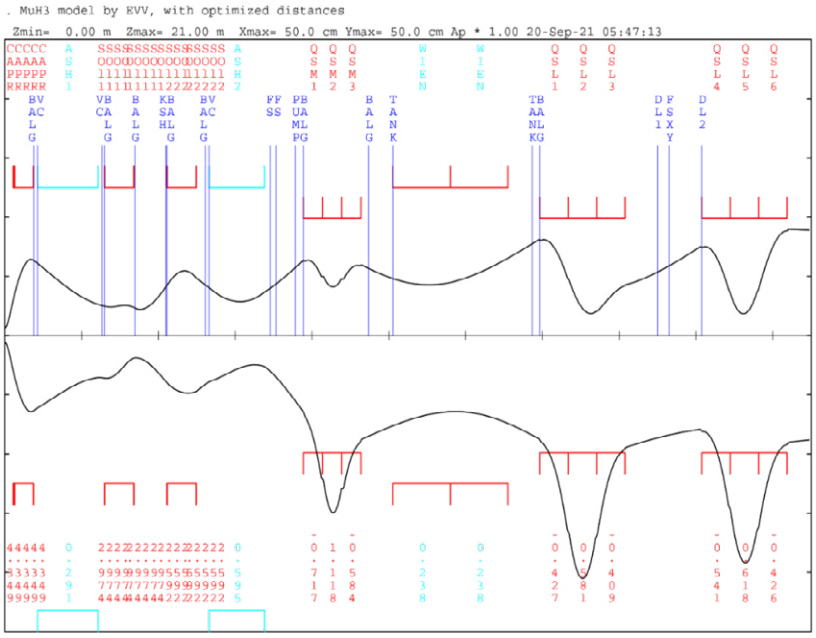

Figure 7.29: First order beam envelope plot from TRANSPORT for the MUH3 model.

7.8 Particle Transport Simulations: Surface Muons

The particle transport simulations, as well as the muon beam generation, were performed using the Monte-Carlo (MC) G4beamline program package [Muons Inc., 2019], based on GEANT4 [Agostinelli, 2003]. The simulation studies involved a sequence of steps based on a basic layout concept of transporting a high-intensity muon beam from a new target station placed at its old original site to existing, though modifiable, experimental areas MUH2/MUH3, corresponding to the current PiM1/PiM3 areas at PSI. The concept of a frontend high acceptance capture solenoid followed by a solenoidal transport channel with at least two dipole magnets, to not only fulfill the "no-direct line of sight" to the target station safety requirements but also to satisfy the directional requirements, led to the initial layout scheme for both channels.

The next step in the simulation procedure was to define the transport elements and their characteristics. However, in order to perform realistic simulations, a realistic muon source was required. The muon beam generation was based on an impinging proton beam, having the beam characteristics of the HIPA 590 MeV cyclotron, on a slanted graphite target TgH. The target is characterized by a slant angle of 10° relative to the proton beam axis, with a length of 100 mm and a thickness of 3.5 mm. A custom physics list in G4beamline was used based on our own developed π^+-cross-sections [Berg, 2016], giving more precise estimates than the default GEANT4 cross-sections, which vary by up to a factor of 10 compared to experimental data. In order to achieve sufficient statistics, various MC variance reduction techniques were used, including using a splitting factor of 100 for both pion production and decay. Generally, large splitting factors (e.g., ten or larger) are not advisable [Mokhov, 2021]; in this case, however, it is justifiable due to the point-like production region compared to the channel acceptance area.

In total the equivalent of 10^{11} proton interactions were simulated and the produced muons written to a beam file. From the total number of muons in the file, a muon/proton ratio of $6.77819 \cdot 10^{-6}$ leads to a total target muon yield of $1.01673 \cdot 10^{11}$ μ^+/s at a proton current of 2.4 mA. The initial phase space parameters and plots are given in Section 7.4.1.

7.8.1 Particle Transport Simulations MUH2

The initial channel layout on the MUH2 side is shown in Figure 7.30 (see figure caption for explanation). The above-mentioned concept of a high acceptance capture

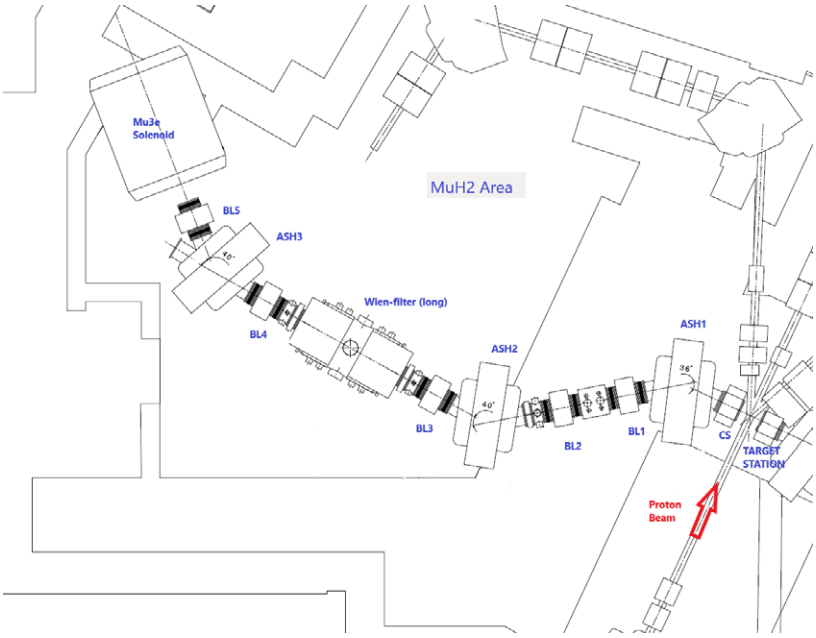

Figure 7.30: Shows the initial layout scheme for the MUH2 channel and area. The incoming proton beam is shown in red, CS the front-end capture solenoid, while BL1-5 are the transport solenoids. ASH1-3 are dipole magnets, the remaining elements are infrastructure, such as a beam-blocker system.

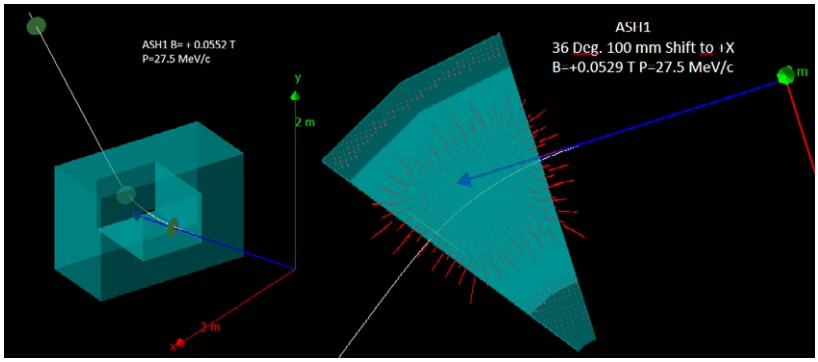

Figure 7.31: shows the tuning of the 3D field map versions of the rectangular dipole design (Left) and the sector dipole design (Right) for muons with a central momentum of 27.5 MeV/c (white track).

section, followed by a solenoidal transport/dipole section and ending in a final focus section, though with an interleaved beam background cleaning section was realized.

7.8.1.1 Beam Element Studies

This involved taking or constructing generic elements in G4beamline, such as solenoids, sector/rectangular dipole and steering magnets, Wien-filters and studying and optimizing their individual characteristics and suitability as MUH2 beam elements. See e.g., Section 7.5.2 concerning the Wien-filter and Section 7.4.2 for the choice of solenoids. Next, realistic elements needed to be designed and magnetic field maps produced for inclusion in the simulation. Figure 7.31 shows an example of the testing of the rectangular and sector dipole versions with the inclusion of their 3D field maps. Although their generic focussing is different, the sector being in the horizontal plane for off-axis particles while the rectangular is in the vertical plane for all particles due to the pole-face rotation angles, a comparison showed little difference from the transmission point-of-view. Since the rectangular form can be used for different bending angles, one standard design can satisfy all required dipoles.

7.8.1.2 MUH2 Channel Layout

The initial full channel version with the long Wien-filter using rectangular magnets is shown in Figure 7.32, ending with the Mu3e solenoid; this corresponds to the layout in Figure 7.30 above. However, due to the low relative transmission of 26 % in the long Wien-filter, a new shorter channel version without a Wien-filter is currently the baseline solution. Parallel to this both, improved injection studies to the separator as well as a short double separator version with an

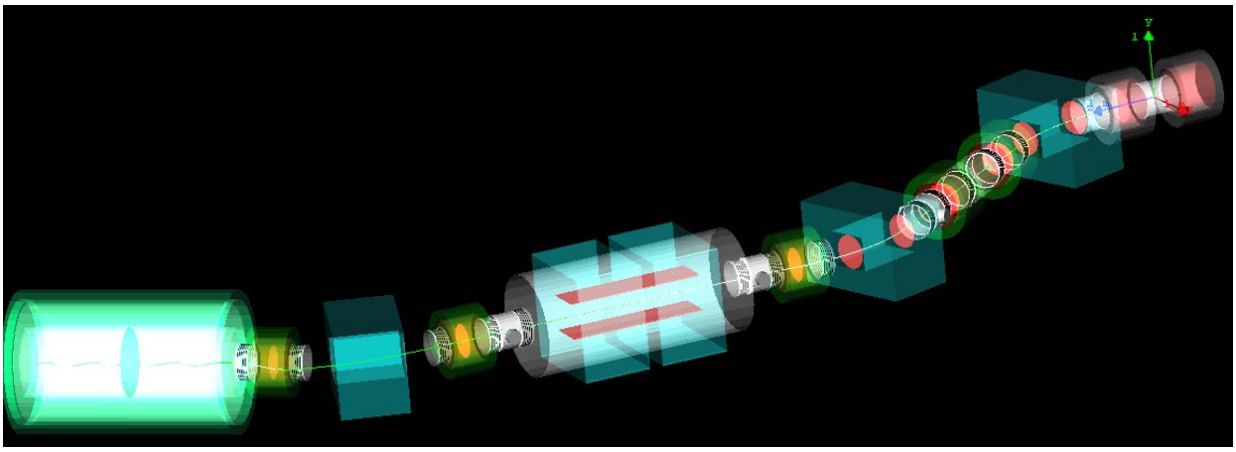

Figure 7.32: The full initial long Wien-filter version of the MUH2 channel, using rectangular magnets and ending in the Mu3e solenoid.

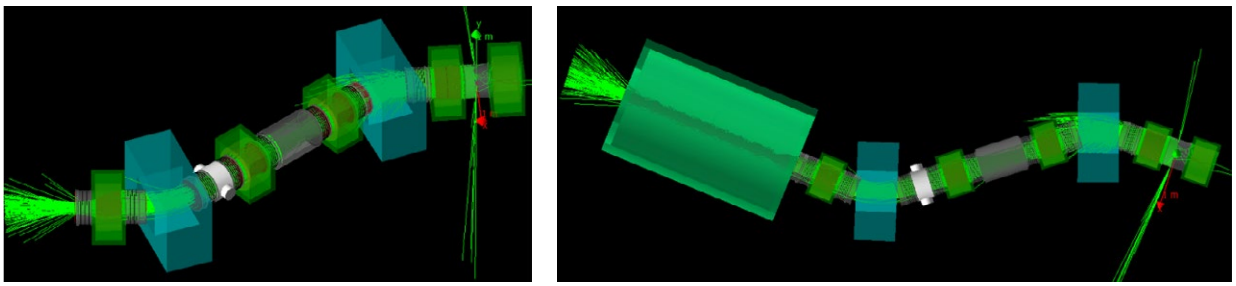

Figure 7.33: Shows the two focal versions of the new short MUH2 channel. A muon yield of $1.22 \cdot 10^{10}$ μ^+/s and $1.19 \cdot 10^{10}$ μ^+/s at 2.4 mA proton current are obtained respectively.

intermediate focussing element solution is under investigation, this would also allow the third dipole and last transport solenoid to be spared.

Alternative solutions to the Wien-filter are also mentioned in Section 7.5.1. The new short versions of the channel are shown in Figure 7.33 for both focus types.

The transmission for both versions is relatively high being in absolute terms 12 % and 11.7 % which translates into a muon rate of $1.22 \cdot 10^{10}$ μ^+/s and $1.19 \cdot 10^{10}$ μ^+/s at 2.4 mA proton current. Both versions were also re-run introducing the new long solenoid mentioned in Section 7.4.2; however, this has a significant impact on the final transmission as can be seen from Table 7.6. A new short solenoid version is now under design. Two-channel versions with the new long solenoid were also explored, the first with all solenoids replaced by this type and the second version with only the capture solenoids replaced. The relative transmission losses compared to the short solenoid are 33 % and 24 %, leading to final muon rates of $8.2 \cdot 10^9$ μ^+/s and $9.3 \cdot 10^9$ μ^+/s at 2.4 mA proton current respectively. Hence the shorter version is required. The geometric solid angle acceptance of the centre of the capture solenoid and based on a point-source is

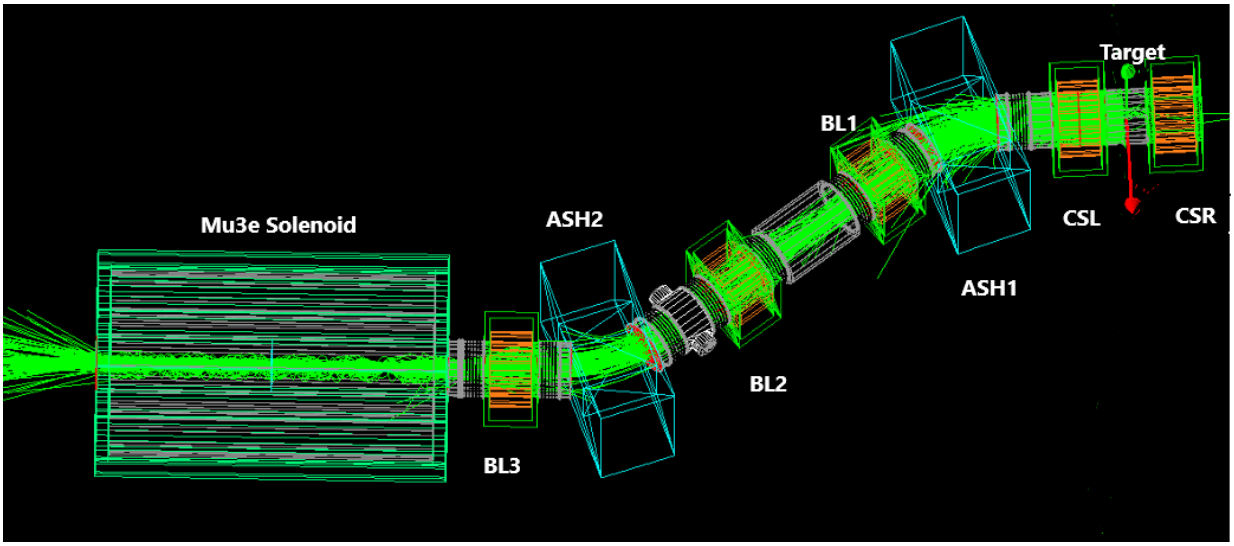

Figure 7.34: Current baseline solution for the MUH2 channel showing the main components, here including the Mu3e solenoid.

Channel Version	Non-Solenoid Final Focus			Mu3e Solenoid Final Focus		
	Muon Rates/s at 2.4 mA I_P	spot sizes σ_X/σ_Y mm	Polarization	Muon Rates/s at 2.4 mA I_P	spot sizes σ_X/σ_Y mm	Polarization
Short Channel	$1.22 \cdot 10^{10}$	40/42	-0.95	$1.19 \cdot 10^{10}$	37/39	-0.88
Baseline All Short Solenoids	$1.19 \cdot 10^{10}$	38/42	-0.96	$1.16 \cdot 10^{10}$	36/38	-0.88
All Long Solenoids	$8.2 \cdot 10^{9}$	45/53	-0.99	–	–	–
Long Capture Solenoids, Short Transport Solenoids	$9.3 \cdot 10^{9}$	39/42	-0.96	$9.1 \cdot 10^{9}$	35/35	-0.91

Table 7.6: Shows the characteristics of the MUH2 Channel variations studied for 2 focal versions.

831 mSr, whereas the total channel acceptance $\Omega_{Channel}$ = 735 mSr based on the full transmission to the final focus.
The final simulation layout with short solenoids is shown in Figure 7.34 together with a simulated muon beam. The final beam-spot size and polarization at the centre of the Mu3e magnet are displayed in Figure 7.35, while the survey layout of the channel is shown in Figure 7.36. A final muon yield of $1.19 \cdot 10^{10}$ μ^+/s and $1.16 \cdot 10^{10}$ μ^+/s at 2.4 mA proton current is achieved for the two different focal versions.
Finally, the characteristics of the main channel versions studied, showing final muon rate estimates, beam-spot sizes and beam polarization P_Z with respect to the beam-axis, for both focal versions are given in Table 7.6.

In conclusion, a high-intensity muon channel MUH2, with a channel acceptance of 735 mSr, has been designed for maximum transmission, based on a large acceptance front-end capture solenoid followed by a solenoidal channel with a double dipole solution, using a single design rectangular magnet. Currently, the originally planned single long Wien-filter, for background suppression, is not incorporated due to the impact on the transmission. Various solutions mentioned previously are under study, both with and without a Wien-filter, all leading to a shorter version than the original design. The baseline solution presented here fulfils the sought intensity goal with $1.19 \cdot 10^{10}$ μ^+/s and $1.16 \cdot 10^{10}$ μ^+/s at 2.4 mA proton current for the non-solenoidal final focus and the

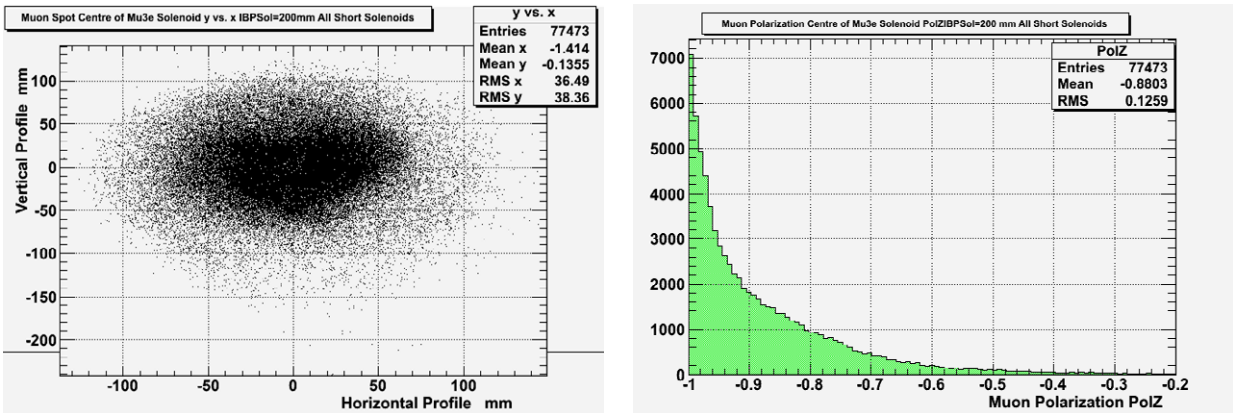

Figure 7.35: Beam-spot size and polarization at the centre of the Mu3e solenoid for the baseline solution of MUH2.

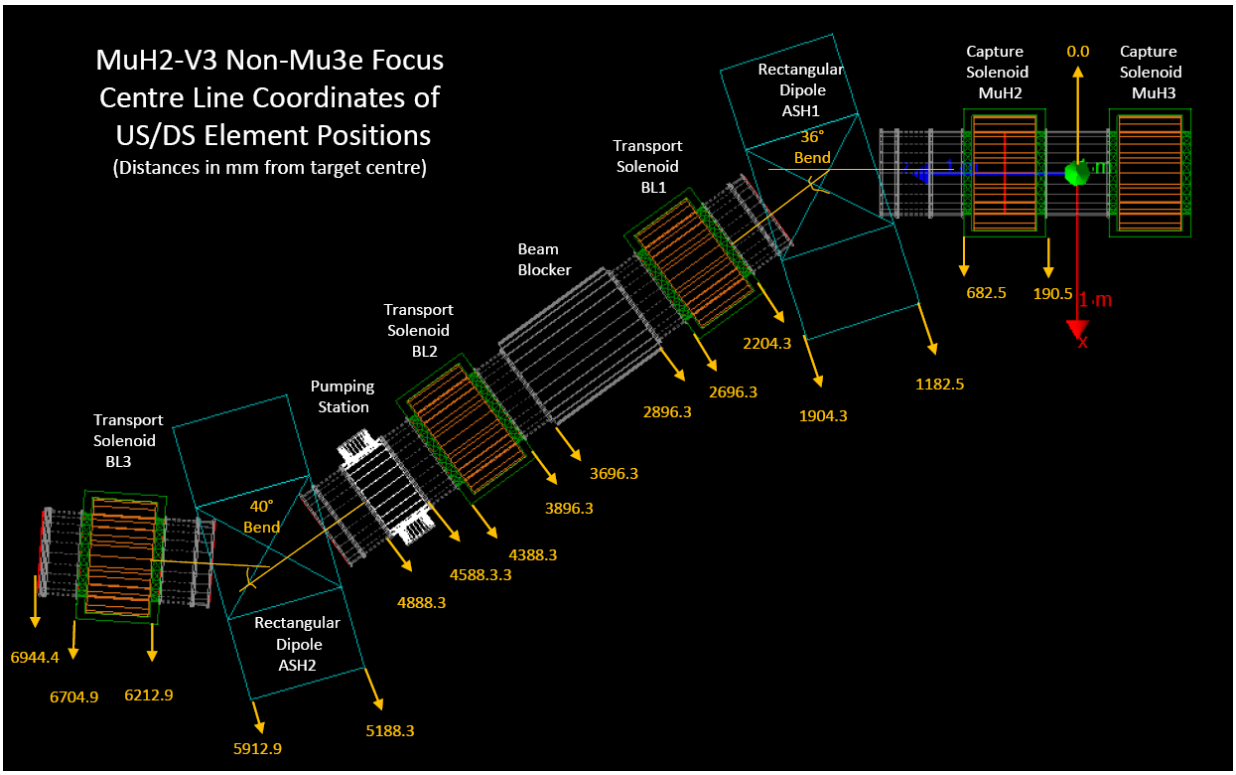

Figure 7.36: MUH2 survey layout with dimensions in the system of centre line coordinates.

Mu3e focus respectively. Final beam-spot sizes of the order of 36-42 mm (1σ) are smaller than the starting emittance equivalent values of around 55 mm (1σ) and polarization values of 96 % and 88 % for the two focal versions (see Table 7.6) are achieved.

7.8.2 Particle Transport Simulations MUH3

7.8.2.1 Particle Optical Element Representation

We started our particle transport studies with a G4beamline model composed of G4beamline's built-in elements, which is generally a good starting point, as built-in elements require less computing resources in optimization, and also built-in elements can be used to cross-check with field map element representations.

We gradually added field maps for particle optical elements, subject to their availability. The current G4beamline model uses field maps for solenoids, first and second dipoles, and quadrupoles by default. We performed individual studies of the field maps; for example, for the dipole field maps we computed the effective length (Figure 7.37).

7.8.2.2 Muon Transmission

At a proton beam current of 2.4 mA, the transmission based on G4beamline simulations of the MUH3 beamline to a focus point located 1.5 m downstream of the last quadrupole QSE304 of the quadrupole tuplet in the MUH3.3 branch is around 3×10^{8} muons/sec, as Figure 7.38 shows. For the MUH3.2 branch, the transmission is similar. An additional optimization is expected to result in an increased transmission to the MUH3.2 and MUH3.3 branches.

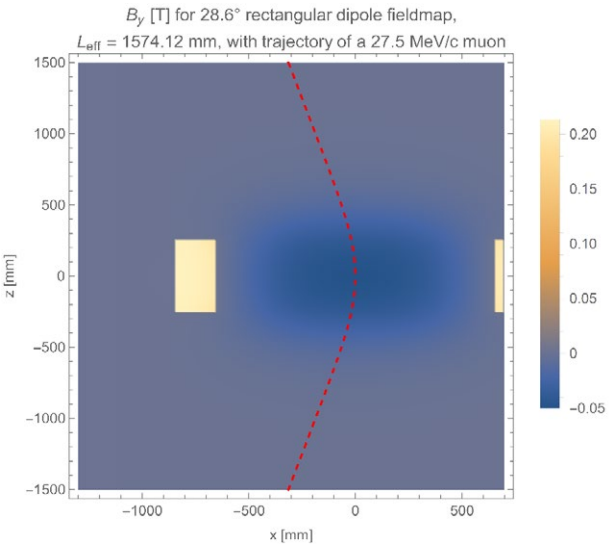

Figure 7.37: Plot of the central horizontal cross section of the 28.6-degree rectangular magnetic dipole ASH31. The reference trajectory is denoted by the red dashed line. The effective length of the dipole was computed as 1574 mm.

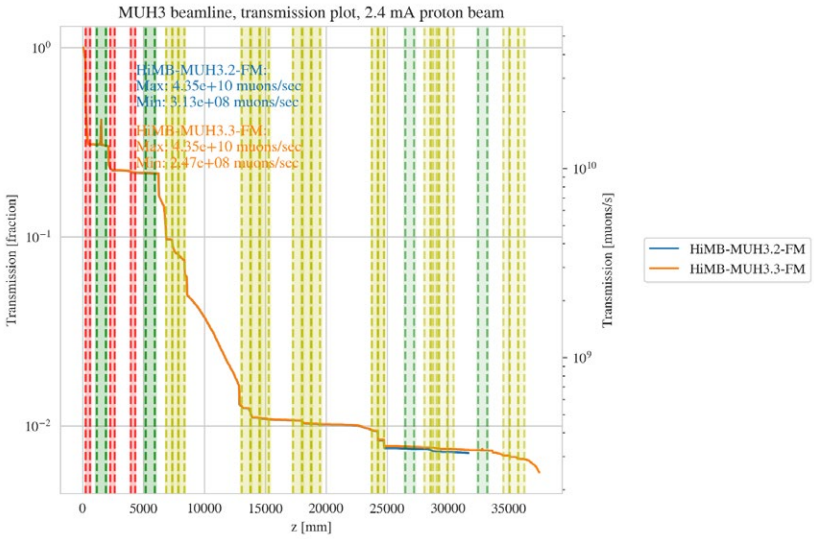

Figure 7.38: Muon transmission from the target to the final foci of the MUH3.2 and MUH3.3 branches of the MUH3 beamline as a function of the distance along the beamline's centerline from the center of the TgH target. The transmission is expressed as a fraction of the muon flux through a beamline cross section relative to the flux at 31.7 mm from the target center, and also in muons/sec. Regions denoted by red denote solenoids, green regions denote magnetic dipoles, and yellow regions denote quadrupoles.

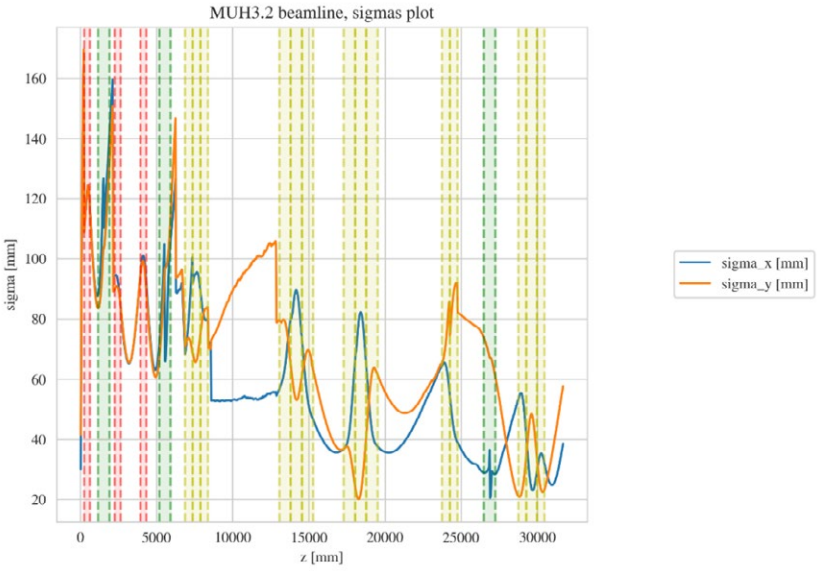

Figure 7.39: Beam size computed as r.m.s. from the target to the final focus of the MUH3.2 branch of the MUH3 beamline as a function of the distance along the beamline's centerline from the center of the TgH target. The final focus was not optimized for the smallest beam spot.

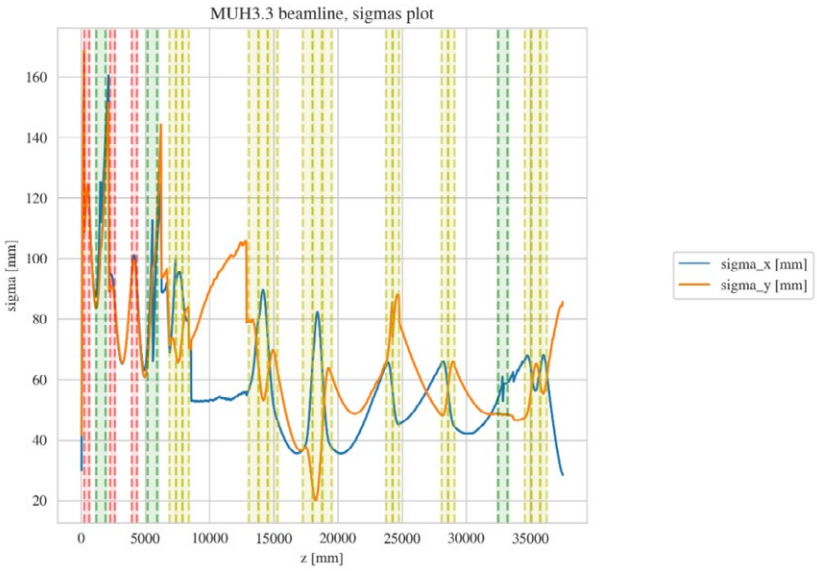

Figure 7.40: Beam size computed as r.m.s. from the target to the final focus of the MUH3.3 branch of the MUH3 beamline as a function of the distance along the beamline's centerline from the center of the TgH target. The final focus was not optimized for the smallest beam spot.

The largest muon beam losses are in the capture section due to a high beam divergence, in the spin rotator because of the length of the device, and in the section between the third and fourth quadrupole tuplets, which contains a septum magnet and a kicker for extraction into the MUH3.2 branch. Figure 7.39 and Figure 7.40 show the beam sizes for the MUH3.2 and MUH3.3 branches of the MUH3 beamline, respectively.

7.8.2.3 Momentum Spectrum

With an optimized set of solenoid, dipole, and quadrupole currents in the MUH3 beamline, the momentum spectrum 1.5 m downstream of the center of quadrupole QSE304 in the MUH3.3 branch is shown in Figure 7.41. The peak of the spectrum of 27.91 MeV/c is approximately in the center of the momentum bite of 25.38 MeV/c to 29.79 MeV/c. For the MUH3.2 branch, the momentum spectrum is similar.

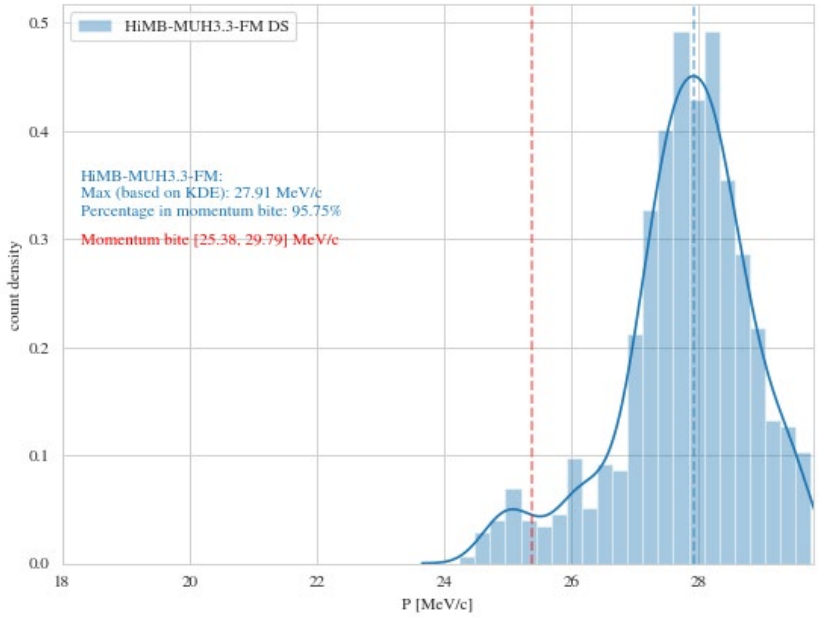

Figure 7.41: The muon momentum spectrum 1.5 m downstream of the quadrupole QSE304 in the MUH3.3 branch.

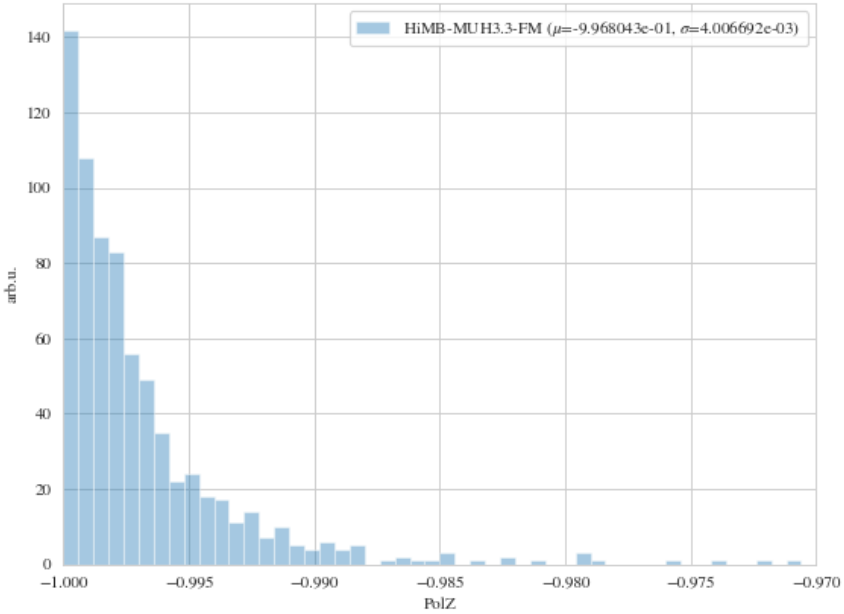

Figure 7.42: A muon spin histogram 1.5 m downstream of the quadrupole QSE304 in the MUH3.3 branch.

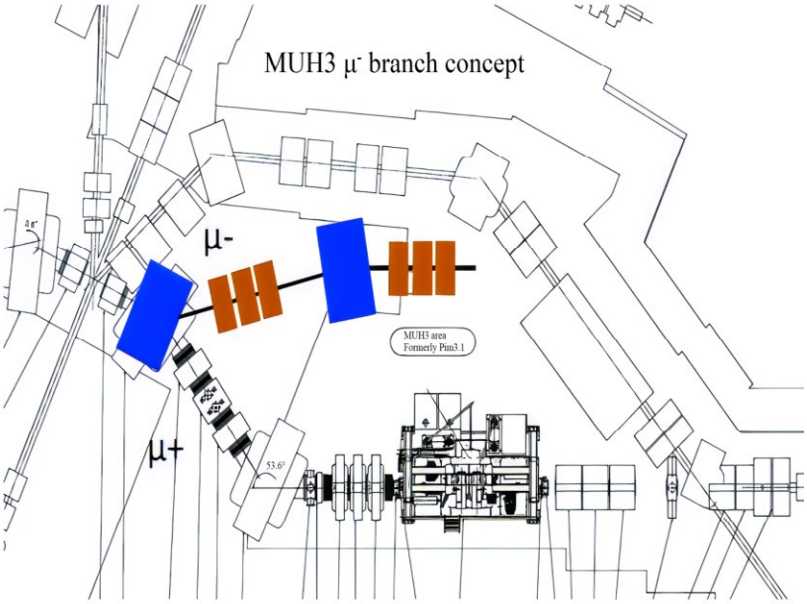

Figure 7.43: Sketch of a possible negative muon branch of the MUH3 beamline. The dipoles are denoted by blue color, and the quadrupoles are denoted by red. The branch starts from the ASH31 dipole.

7.8.2.4 Muon Polarization

The MUH3 beamline maintains excellent muon spin polarization. At 1.5 m downstream of the center of quadrupole QSE304 in the MUH3.3 branch, the muon spin histogram is as shown in Figure 7.42, yielding a value of -0.997.

7.8.2.5 Parasitic Negative Muon Beam

We considered the possibility of a parasitic negative muon branch for the MUH3 beamline, with two straight sections after the first dipole ASH31, where the bend at ASH31 is naturally in the opposite direction of the bend for positive muons (see Figure 7.43). This branch would use quadrupoles only for focusing. This branch could provide up to ~10^7 muons/sec at a proton beam current of 2.4 mA. Further studies will need to be performed to fully assess the feasibility of such a parasitic beam.

7.9 Particle Transport Simulations: Other Particles

As described previously, the secondary particles are produced by bombarding a graphite target with the high-energy proton beam provided by HIPA. While the main interest lies in low-energy muons, many other particles are created in addition. Figure 7.44 shows the momentum spectra of positive and negative electrons, muons and pions at the entrance of the capture solenoids. The solenoidal beamlines will feature good transmission up to about 40 MeV/c. Above that the overall transport efficiency will start to drop off as the solenoids cannot be powered any higher. The dipoles will be designed to operate up to 80 MeV/c.

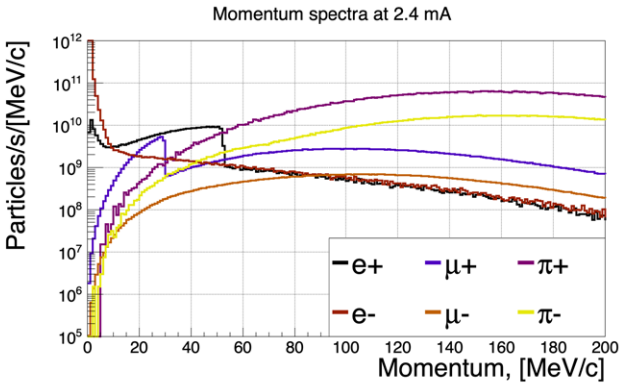

Figure 7.44: Momentum spectra at the capture solenoid entrance (fields off) for the different particles produced at TgH.

While the main focus lies on surface muons, the other particles are also used in dedicated experiments as detailed shortly below:

- sub-surface muons (p < 26 MeV/c): for fixed-target experiments, where shorter stopping ranges are required than

for surface muons, or for μSR measurements probing different depths in the sample

- negative muons (up to 40 MeV/c): negative muons can, for example, be used for muon-to-electron conversion experiments or for experiments studying muonic atoms
- negative pions (~70 MeV/c) and Michel positrons (‹53 MeV/c): both are currently used as calibration beams. See, e.g., [Baldini, 2018].

In the following sections we present the first estimates for the transport of these particle beams through the MUH2 and MUH3 beam lines, as they were presented in the previous sections.

7.9.1 MUH2

The MUH2 beam line has been designed for particle physics related experiments: currently at PSI surface and sub-surface muons are used for a number of experiments. Among them the MEG II and Mu3e experiments that rely specifically on high-intensity surface muons: due to the high intensity in a small momentum bite, they are ideal for high-intensity stopping target experiments. However, a possible limitation linked to this feature is that a change in momentum bite strongly affects the intensity of the muon beam. When designing the MEGII experiment, it was considered as an option to use subsurface muons instead, to reduce the thickness of the target [Baldini, 2018]. This would have led to a reduced straggling and an enhanced vertex reconstruction, but the loss in intensity was too high.

With a beamline such as MUH2, sub-surface muons become competitive for such experiments, with, e.g., a concept based on stopping sub-surface muons at momenta as low as 10 MeV/c with sufficiently high intensity. Currently, the

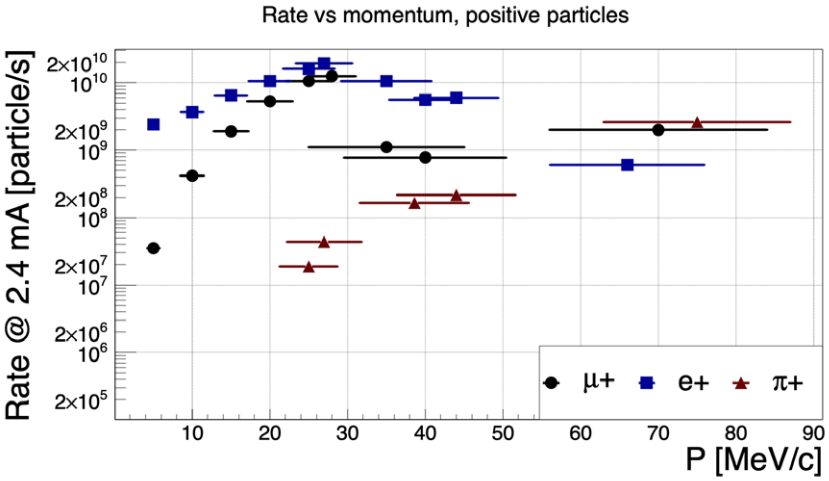

Figure 7.45: Positive particle rates at 2.4 mA proton current vs the selected momentum as delivered by the MUH2 beam line, at maximum acceptance settings (slits fully opened).

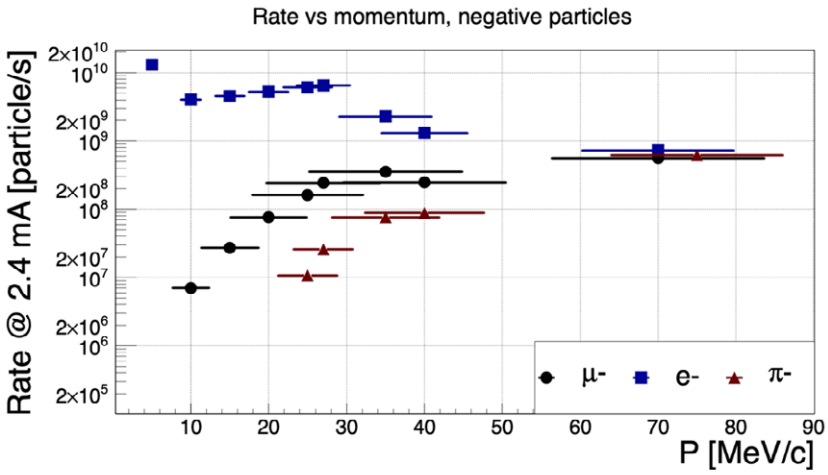

Figure 7.46: Negative particle rates at 2.4 mA proton current vs the selected momentum as delivered by the MUH2 beam line, at maximum acceptance settings (slits fully opened).

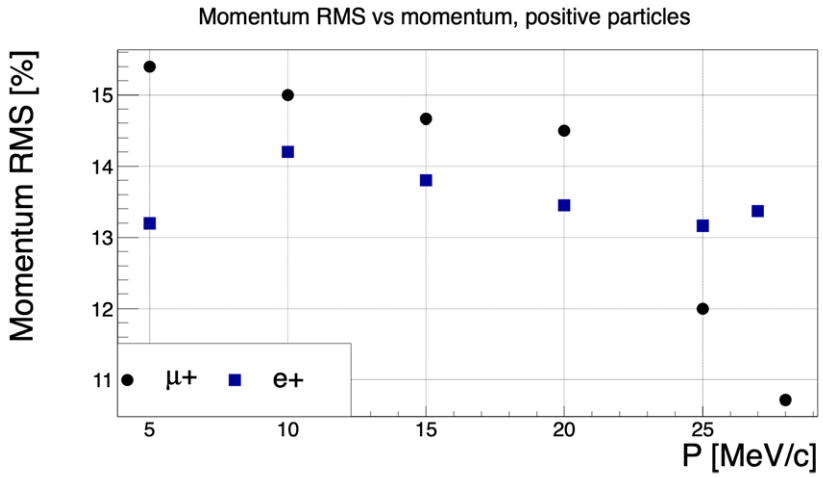

Figure 7.47: Momentum RMS at maximum acceptance settings (slits fully opened) vs selected momentum of the different positive particle beams as delivered by MUH2.

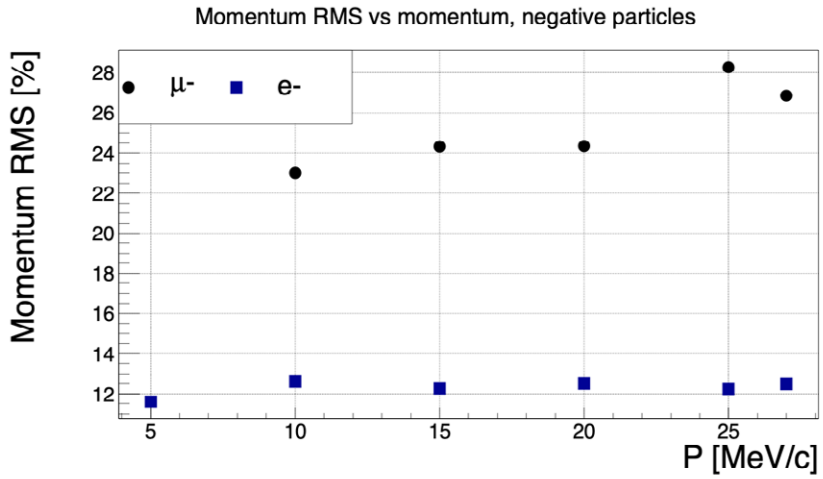

Figure 7.48: Momentum RMS at maximum acceptance settings (slits fully opened) vs selected momentum of the different negative particle beams as delivered by MUH2.

MEGII collaboration aims at stopping rates as high as 7×10^7 μ^+/s. Thinking about an upgrade, the rate can be as high as $4\ 10^8$ μ^+/s at 10 MeV/c (see Figure 7.45), reducing the range of the muons from 1 mm to ~20 µm in mylar.

Typically, in the context of searches for rare muon decay, not only muons beams are used, but also beams for calibration purposes: for example, in the MEGII experiment a negative pion beam is used, at a momentum of ~70 MeV/c, for the calibration of the LXe calorimeter through the charge exchange reaction and a 50 MeV/c positron beam is used to calibrate the drift chamber through Mott scattering measurements. The MUH2 beamline would be able to deliver ~ 6×10^9 e^+/s at 45 MeV/c (see Figure 7.45), and ~6×10^8 π^-/s at 75 MeV/s (see Figure 7.46). Such rates can be reached considering the limits in the current of the solenoids for the baseline version of MUH2.

Negative muons are also interesting in the context of high-rate experiments. cLFV experiments such as muon to electron conversion are based on negative muons. Additional interest is coming from muonic atom experiments. Here HIMB could deliver such beams from low momenta (~5 MeV/c) up to 40 MeV/c with the highest intensity of 2.4×10^8 μ^-/s reached at 28 MeV/c.

Finally, we show the momentum RMS dependence on the selected momentum for electrons and muons with p ‹30 MeV/c (see Figure 7.47 and Figure 7.48). Up to this value, the optimization and the scaling down of the fields, optimized for surface muons, work very well and result in reliable predictions. For higher momenta, however, the current limits on the solenoids do not allow to maintain a high transmission, and scaling up the elements is non-trivial. The optimal beam settings for momenta higher than 30 MeV/c are currently still being investigated.

It is important to point out that the rates and the RMS values shown in this section are obtained without including the slit systems along the beam line: this leads to poor momentum selection, especially for cloud muons. While up to 30 MeV/c the width of the momentum distribution of positive muons is defined by the width of the surface muons distribution, for higher momenta the major contribution comes from cloud muons that can be generated by pions decaying in flight away from the target: the higher the momenta the deeper inside the capture solenoid they will be accepted. In the case of negative muons there are no surface contributions and the momentum distribution at the end of the beamline is always wide, on the level of 25–30 % of the

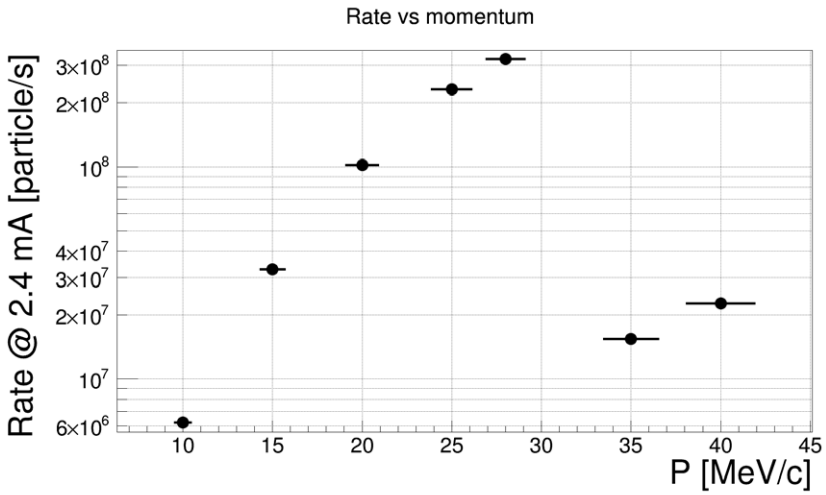

Figure 7.49: μ^+ rates at 2.4 mA proton current vs the selected momentum as delivered by the MUH3 beam line, at maximum acceptance settings (slits fully opened).

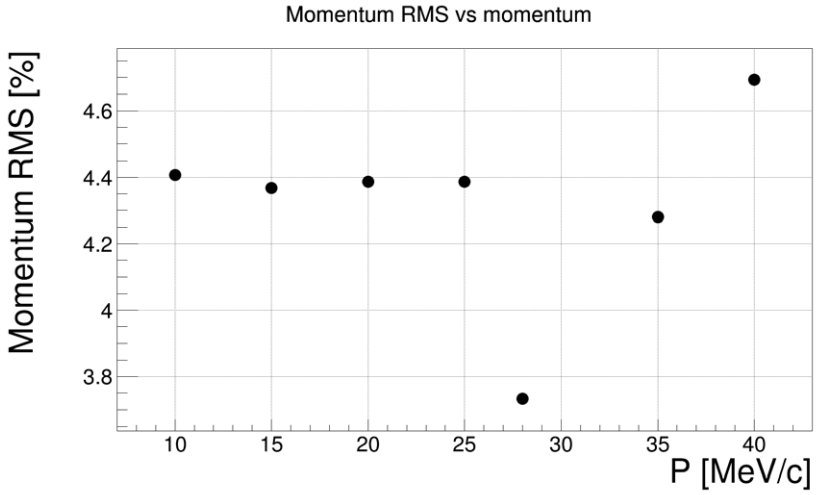

Figure 7.50: Momentum RMS at maximum acceptance settings (slits fully opened) vs selected momentum of μ^+ as delivered by MUH3.

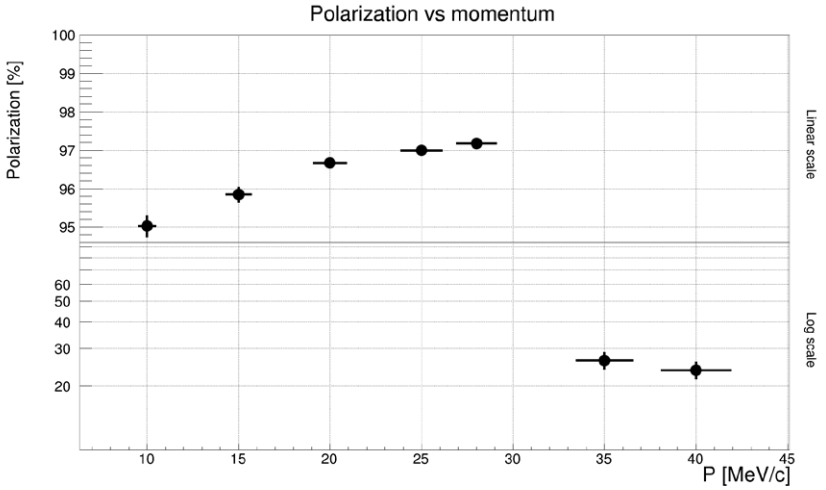

Figure 7.51: Polarization of μ^+ at the end of MUH3 at maximum acceptance settings (slits fully opened) vs selected momentum.

central momentum. The quality of the beam can be improved using slit systems along the beam line (see Section 7.10.7) and their positioning and optimization are currently under study.

7.9.2 MUH3

The MUH3 beam line has been designed for μSR measurements. This technique allows the use of muons to probe the magnetic properties of materials. The depth that can be investigated in a material depends on the initial momentum of the muons.

So far there has been a gap in the depth that could be probed, in the range corresponding to sub-surface muons. Measurements are usually made using either surface muons at 28 MeV/c (KE ~4 MeV), or moderated to very low energies, lower than 30 keV (LEμ), but in the subsurface region the rates are too low to be used for such a purpose.

Within the HIMB project, the MUH3 beam line would allow the delivery of sufficient numbers of muons to cover this gap and provide higher LEμ rates, as the moderation process is very inefficient ($< 10^{-5}$).

It would be possible for example to deliver up to 6×10^6 μ^+/s at 10 MeV/c (KE ~0.47 MeV, see Figure 7.49), which corresponds to a few μm in the range in copper, lying within the empty gap.

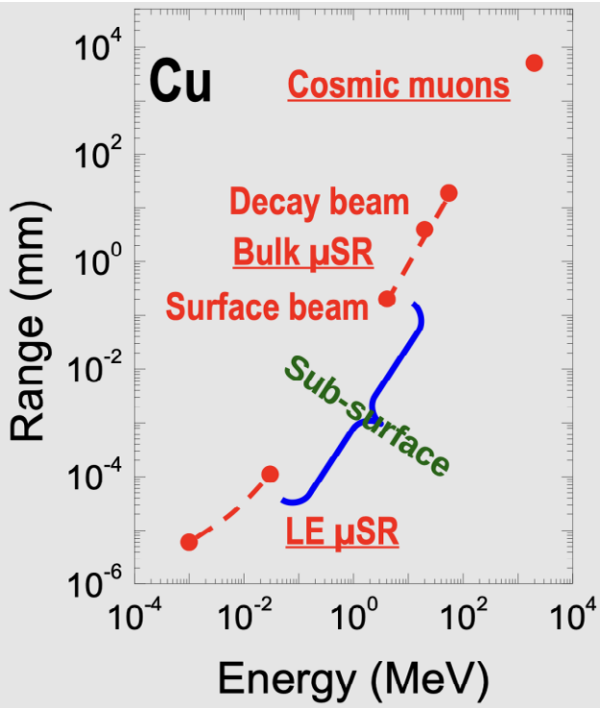

The momentum RMS is ~4 % of the selected momentum, for all the considered cases (see Figure 7.50). The polarization is high for surface and sub-surface muons, with the maximum at 25 MeV/c, and it decreases for higher momenta (see Figure 7.51).

In this section as well the simulations were run without slit systems.

7.10 Beamline Components

7.10.1 Capture Solenoid

This section describes the capture solenoid and all its magnetic and mechanical aspects. The high radiation load prevalent in this area of the beamline requires the solenoid to be made of radiation resistant materials. Additionally, the magnet will be operated in vacuum in order to place it as close to the target as possible. These two requirements make the capture solenoid the most challenging item in the muon beamline.

7.10.1.1 Magnetic Design

The prerogatives for the calculation of the capture solenoid were as follows:

Variable	Value
Aperture	500 mm
Length	Max. 400 mm
Field	0.4 T
Distance from target	250 mm

Table 7.7: Operating data for the capture solenoid.

Using these values and a current density based on previous experience, a first design was established and carefully checked with beam dynamics requirements.

The results then had to be aligned with mechanical requirements. This proved to be a challenge since the magnet and its coils must withstand high radiation levels (see Section 7.10.1.5 for details). After several iterations, a first functioning solution was found. The model used in the FEM simula-

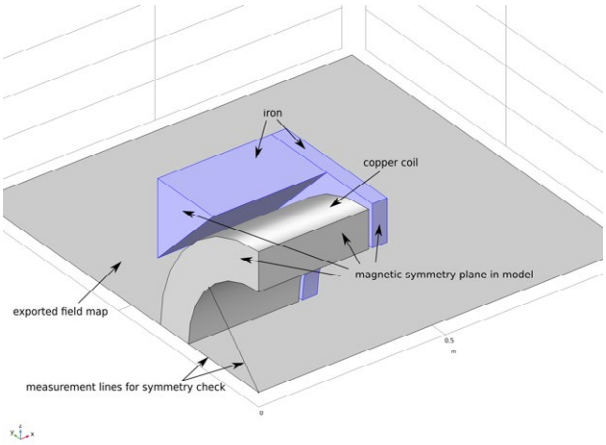

Figure 7.52: First FEM model for magnetic field calculations.

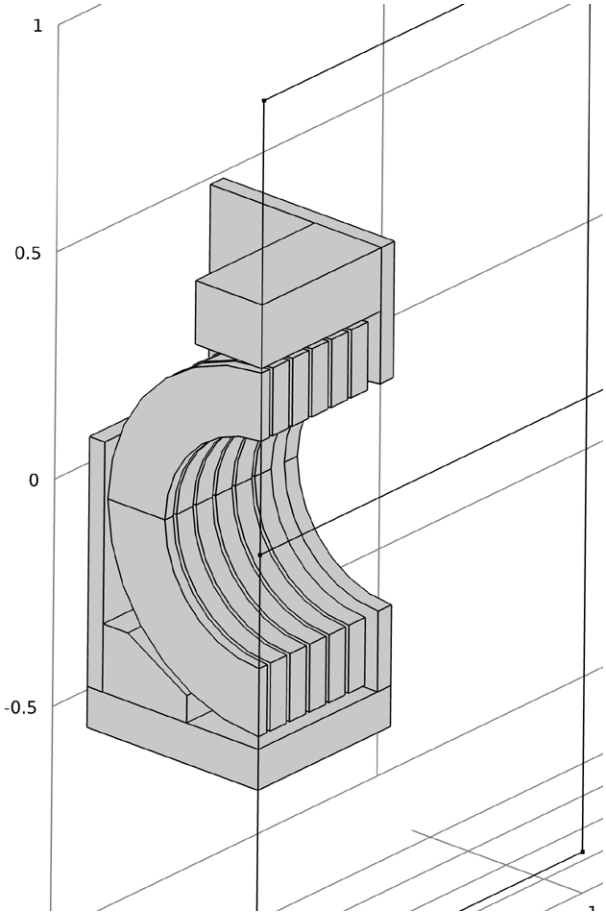

Figure 7.53: Final model after mechanical design.

tions is shown in Figure 7.52 with the mechanical model shown in Figure 7.53.

7.10.1.2 Mechanical Concept

Due to the requirement of radiation hardness, no organic materials can be used as they quickly disintegrate during the exposure to radiation (see Figure 7.54).

Based on several decades of experience at PSI, a design with radiation hard components was developed. The conductor itself is made of plain copper insulated with magnesium oxide powder, all of which is seated inside a copper sheath. See Figure 7.55 for a cross section.

While seemingly being an attractive option, the conductor with an internal cooling channel is not suited for this application. Based on experience, PSI avoids at all cost to have directly cooled copper conductors in a radioactive environment. Otherwise, due to the interaction between the radiation and water [U.S. DOE, 1993], the copper is attacked and

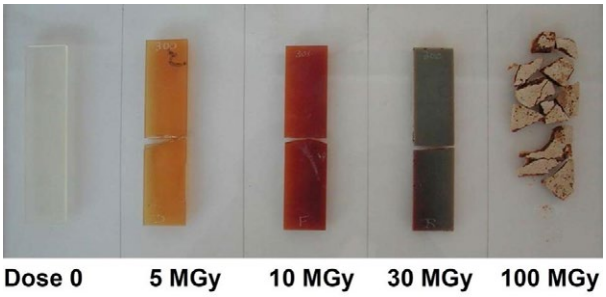

Figure 7.54: Deterioration of epoxy resin in a radioactive environment (CERN).

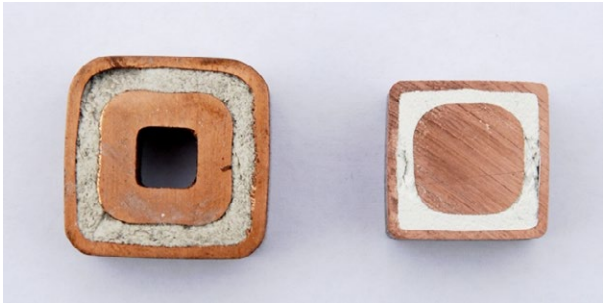

Figure 7.55: Cross section of a Pyrotenax conductor with and without cooling channel.

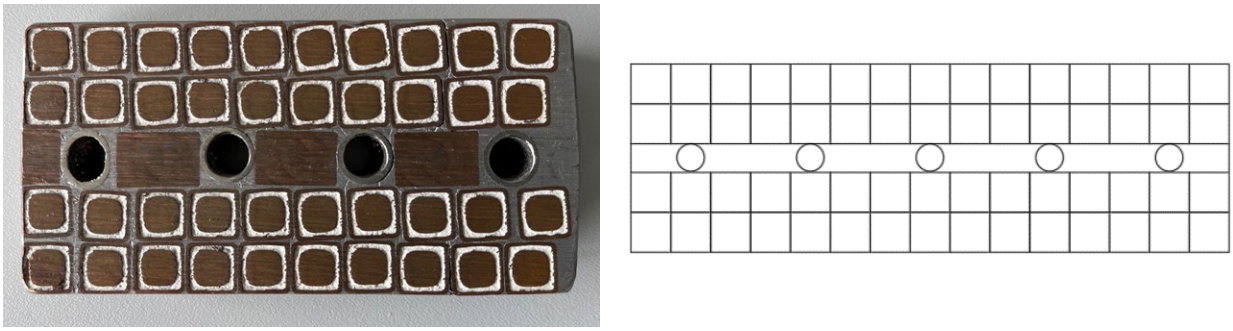

Figure 7.56: Example of an actual coil cross section (left) and coil concept (right) for radiation hard magnets at PSI.

will corrode, forming copper oxide. This in turn will accumulate inside the cooling channel and create blockages, leading to magnet failure (overheating) due to blocked cooling channels. Therefore, the PSI concept for radiation hard magnets is based on indirect cooling and will use the plain conductor without cooling channel.

The best layout known to PSI for a coil cross section is shown in Figure 7.56. Two double pancakes are wound separately and assembled into a unit with a layer of cooling channels in between. The cooling channels are made of stainless steel, helping to avoid any corrosion issues. After assembly, the whole unit is potted in soft solder for rigidity and better heat transfer. Copper pieces between the cooling channels are inserted to additionally improve heat transfer.

Therefore, each coil unit consists of two double pancakes with a cooling layer in between. Several of these units are manufactured individually and then assembled in a row to form a long solenoid. This approach has shown to be beneficial in the past since there is always a risk building coils with this type of conductor; the outer sheath of the conductor is rather fragile and slight misalignments or mechanical influences can create a short to ground inside the unit. Should this be the case, scrapping one single unit is less of a waste in terms of material and cost than scrapping a large coil.

Figure 7.57 and Figure 7.58 give an overview of the complete mechanical concept and how the coils are placed inside the magnet yoke.

7.10.1.3 Cooling the Current Leads

While the coil body is sufficiently cooled in the current design, a problem remains: The leads that carry the current

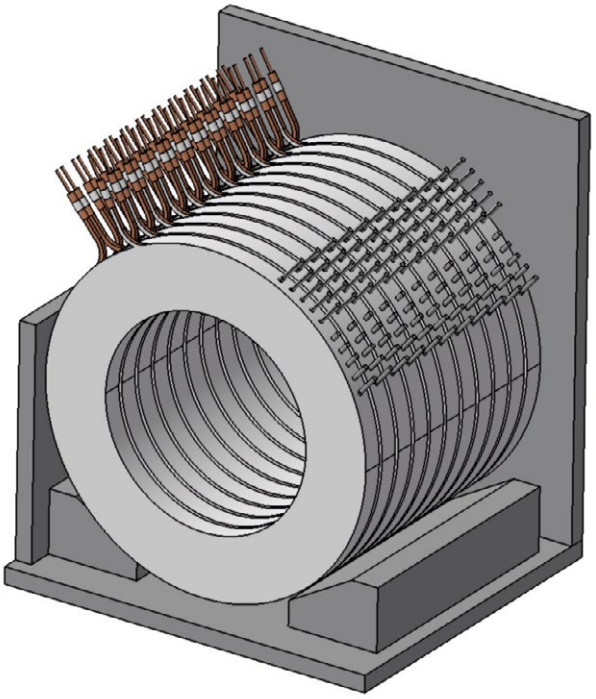

Figure 7.57: Assembly of the coil units inside the magnet yoke.

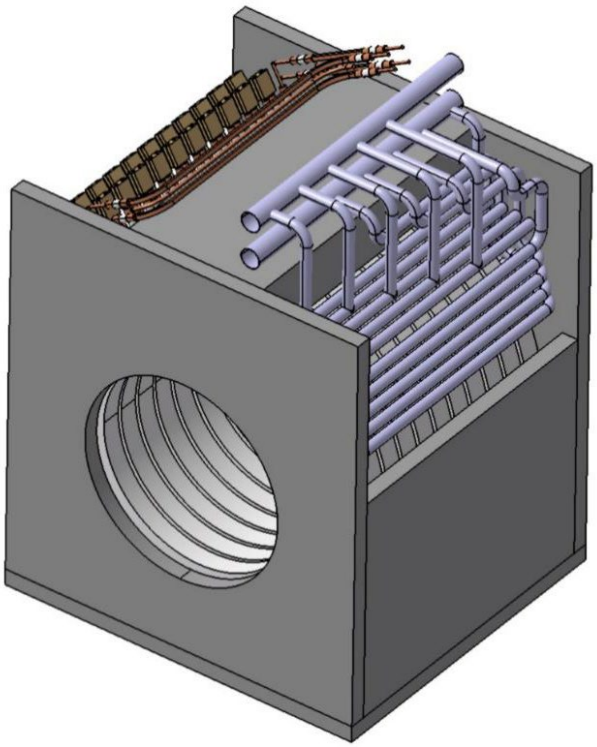

Figure 7.58: Capture solenoid, mechanical concept.

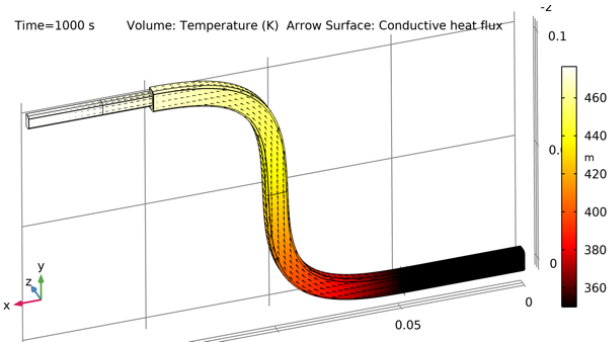

Figure 7.59: Numerical estimation of current lead heat dissipation. A temperature gradient of about 100K was found over the length of the modeled geometry.

into and out of the coils are exposed and without cooling; since operation of the solenoid takes place inside vacuum, there is no air cooling available to mitigate this problem. Figure 7.59 shows a simulation of the heating effect on the uncooled current leads due to the dissipated heat inside the conductor.

Therefore, a solution was chosen where these current leads are water cooled as shown in Figure 7.60. This concept has to be refined to allow for thermal expansion of both the coil units and the cooling channel.

7.10.1.4 Exchange Concept

As discussed above, in contrast to all other magnets used at PSI the two capture solenoid magnets are designed to be operated in vacuum due to the two following requirements: 1) distance of 250 mm from the beam axis to the front of the capture solenoid and 2) a possibility to remove the magnet without dismantling the whole secondary beamline.

In addition to the description of the magnet at the beginning of Section 7.10.1, a massive metal block is placed on top of the magnet, which acts as shielding. All the supplies for the capture solenoid will be guided through two gaps in this shielding block from the top of the target vacuum chamber to the magnet. A sketch of this shielding and the supplies is shown in Figure 7.61.

Because the capture solenoid magnets are located very close to Target H, they get activated to very high dose rates of several Sieverts. The best way to handle such activated components is to use a shielded exchange flask, similar to the ones used for the exchange of the graphite targets like the present Target E and Target M (see also Section 9.3.1). For the capture solenoids, it is planned to design and build a simple exchange flask. This flask will look like a bell, but with a sliding door at the bottom. Inside, it will feature a hoist drive with a gripper, which attaches to the top of the local shielding of the magnet. The following steps will have to be performed to exchange a capture solenoid magnet:

1. Switch off the water cooling and the electrical power of the magnet
2. Switch off the vacuum pumps and vent the system with dry nitrogen
3. Remove the concrete shielding on top of the beamline to the service level
4. Switch on the beryllium and tritium venting system
5. Disconnect the water and electric housing and cables

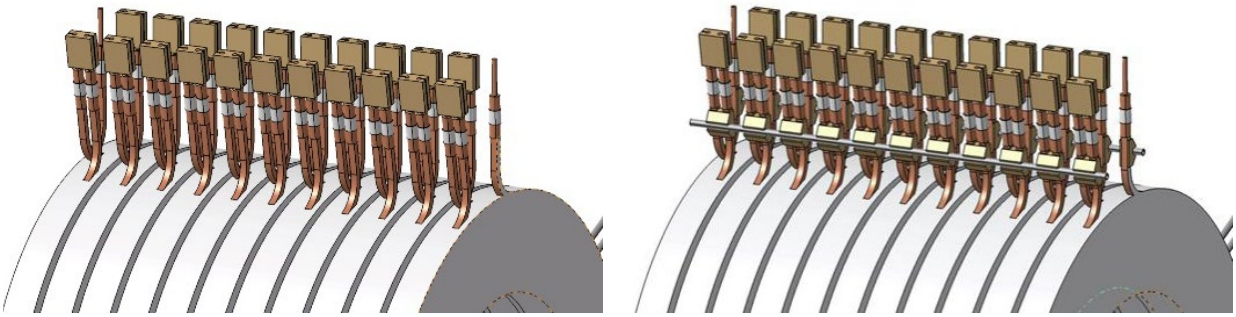

Figure 7.60: current leads without (left) and with water cooling (right).

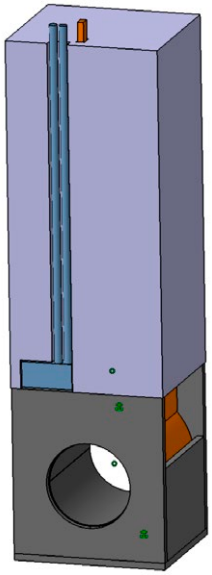

Figure 7.61: Sketch of the capture solenoid with shielding block.

6. Remove the vacuum flange
7. Add a simple contamination protection around the magnet (for an example see Figure 7.62)
8. Connect the big hose of a mobile venting system to the contamination protection
9. Mount the gripper attachment on the magnet
10. Install a support centered to the magnet for the exchange flask
11. Put the exchange flask on the support with the big hall crane, make sure that the gripper is in the right position
12. Drive down the gripper and attach it to the magnet
13. Drive up the gripper including the magnet into the exchange flask
14. Close the sliding door at the bottom of the flask
15. Hook the hall crane to the exchange flask and bring it to the required place like ATEC to repair it or into a parking cell to store the magnet
16. Load the exchange flask with the repaired or a spare magnet and bring it back to the proton beam channel
17. Perform steps 17 to 1 in reverse to re-install the magnet

Figure 7.62: An example of KHE2 contamination protection.

7.10.1.5 Dose Rate & Energy Deposition

Energy deposition in the coils of the solenoids during the target operation was estimated by an MCNP version 6.1 [Pelowitz, 2013] simulation of the secondary particle fluxes using the reference HIMB geometry model. To capture the longitudinal distribution of the deposited energy, the coils of the solenoids were segmented along the X-axis into five cylindrical parts. Figure 7.63 gives the distribution of the energy deposited in the parts of the target station and the solenoidal magnets, calculated using MCNP on the Z-X plane for 1 proton incident on the target.

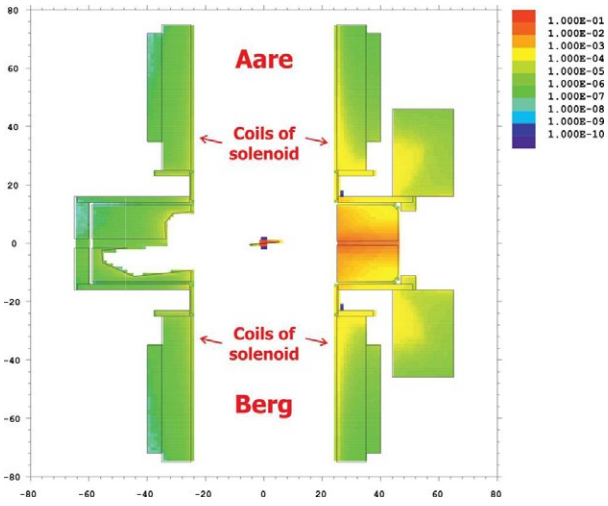

Figure 7.63: Distribution of the deposited energy (MeV per 1 proton on the target) in the elements of the target station and neighboring solenoidal magnets.

As Figure 7.63 shows, in the coils of the solenoids most of the energy is deposited in the "downstream" corner of the coil. The reference HIMB geometry model used for the calculations did not have the mirror plates between the target and the solenoids that were designed later to shield the coils of the solenoids. As the shielding provided by the mirror plates will certainly reduce the loads on the coils, the presented estimates of the levels of the deposited energy are conservative.

The total energy deposition in each part of the solenoid coils for the proton beam current of 2 mA is given in Table 7.8.

Solenoid, Aare side			
X_min	X_max	E_dep	%
25	35	0.96	57.38
35	45	0.36	21.37
45	55	0.18	10.93
55	65	0.11	6.37
65	75	0.07	3.95
	Total	**1.67**	

Solenoid, Berg side			
X_min	X_max	E_dep	%
−75	−65	0.07	3.99
−65	−55	0.11	6.32
−55	−45	0.18	11.04
−45	−35	0.36	21.46
−35	−25	0.95	57.18
	Total	**1.66**	

Table 7.8: Energy deposition (kW/2 mA) in five segments of the coils of the solenoids on the left ("Aare") and right ("Berg") sides of the target station.

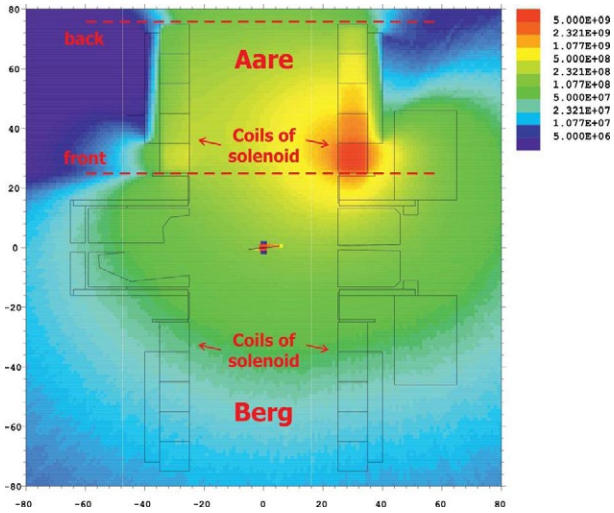

Figure 7.64: Distribution of the remnant dose rate (pSv/s) around the elements of the target station and neighboring solenoidal magnets.

This table also gives starting and ending X coordinates of the cylindrical parts of the coils. Table 7.8 shows that the amount of energy deposited in the coils rapidly decreases with the increase of the distance from the target. The distribution of the deposited energy is symmetrical with respect to the target position, and almost 60 % of the power, which is about 1 kW, is deposited in the first 10 cm thick part of the coil.

To estimate the remnant dose rate at the coils of the solenoids after irradiation during target operation, the residual nuclei produced in particle interactions in the materials and neutron spectra with energies below 20 MeV were scored in the MCNP simulation. The output of the MCNP simulation has been processed by the Activation Script [Gallmeier, 2007], and the nuclide inventories in the parts of the coils have been calculated using FISPACT [Forrest, 2007]. The inventory calculation assumed that the target station has been in operation for 20 years at a beam current of 3 mA, followed by one month of cooling time.

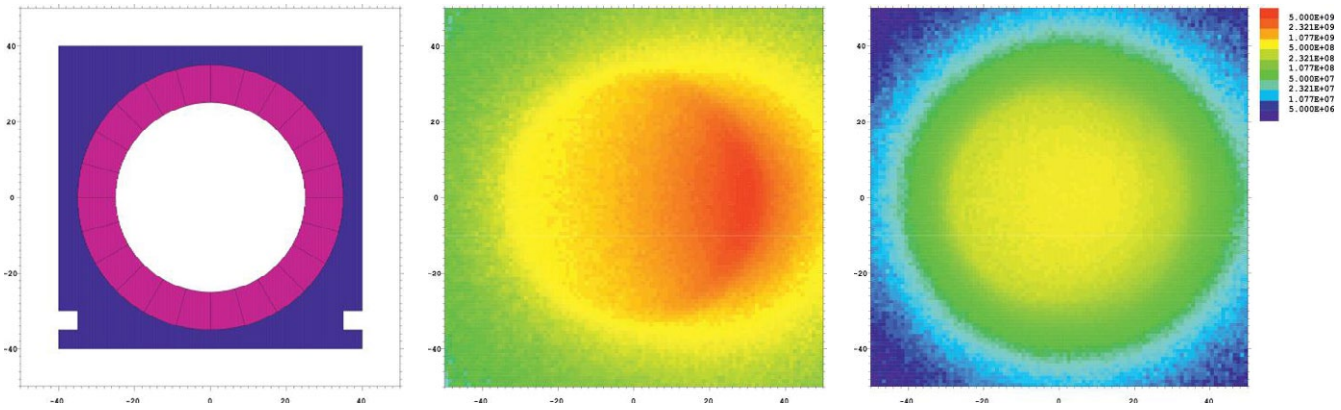

Figure 7.65: Left: MCNP model of the coil segmented for the activity calculations in the sectors of 15 degrees. Middle: distribution of the remnant dose rate (pSv/s) on the Z-Y plane at 3 cm from the "front" surface of the coil. Right: same as the middle plot, but at the "back" surface.

The spectra of the secondary gammas from the produced unstable nuclides were used as a source for another MCNP simulation, in which the distribution of the remnant dose rate has been calculated. Figure 7.64 shows the map of the remnant dose on the Z-X plane at the target station for the case of the solenoid coil at the Aare side as a source. As in the calculation of the deposited energy, the hottest spot is in the “downstream” corner of the solenoid coil.

Two transverse distributions on the Z-Y plane have been taken from Figure 7.64 for the numerical analysis, at the locations of 3 cm from the “front” and “back” surfaces of the coil. These distributions are shown in Figure 7.65. The calculated maximal dose rate on the “front” surface under the assumed conditions of irradiation and cooling is 15.7 Sv/h, while the maximal dose rate on the “back” surface is factor 10 lower, 1.8 Sv/h.

7.10.2 Separator

As discussed in Section 7.5, a separator is ideally needed along the MUH2 beamline in order to separate out the positrons from the muon beam by means of crossed electric and magnetic fields.

The development of a separator for the large-aperture MUH2 beamline is certainly a challenge. As a starting point a device with 2000-mm long electrodes and a gap of 500 mm was designed. Figure 7.66 shows how such a separator could look, and it was used as the input for the beamline simulations described above in Section 7.5.

As the transmission through the separator with the 2-m long electrodes (resulting in an overall length of 4.2 m), is unacceptably low, a new concept was developed that relies on two shorter separators with a 1-m long electrode each. In between the two separators a solenoid would be placed that

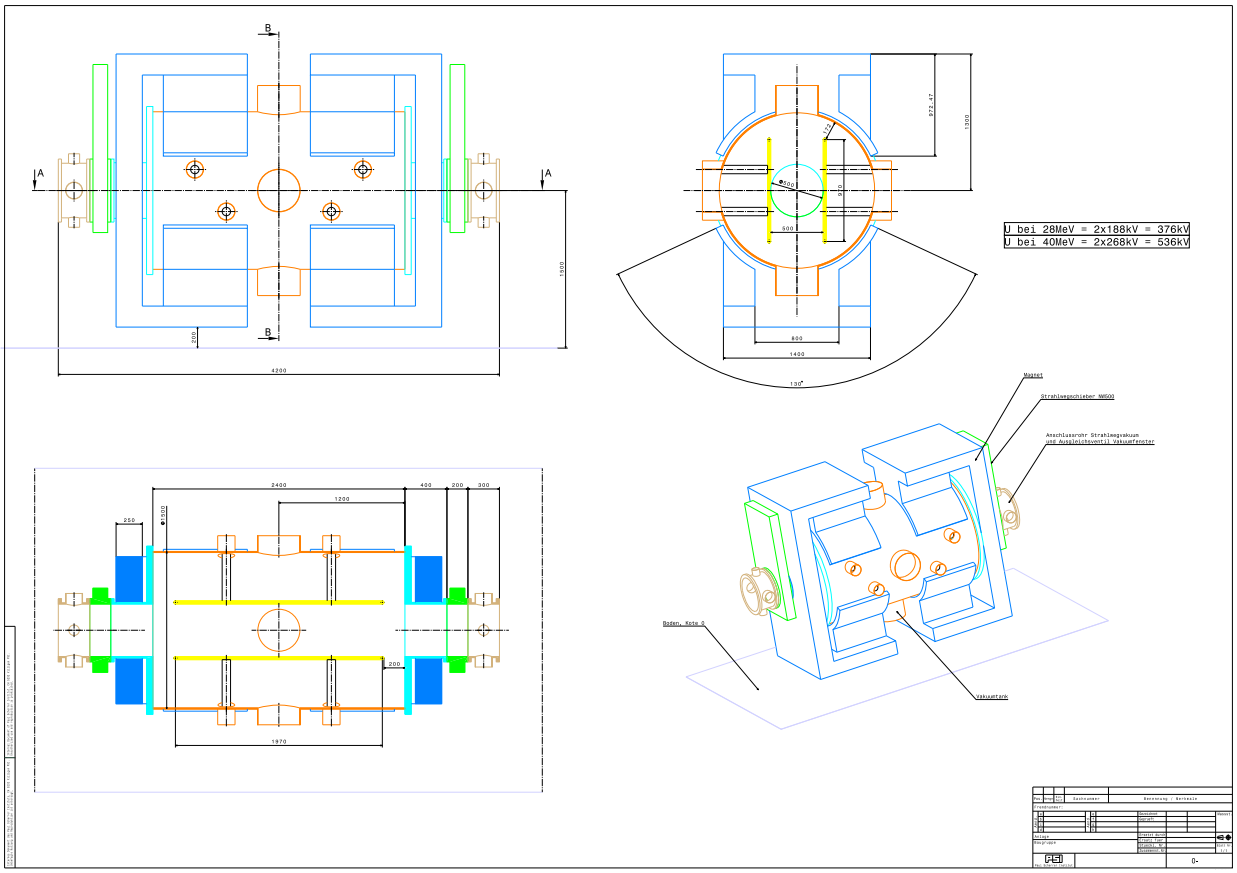

Figure 7.66: Sketch of the separator with 2 m long plate.

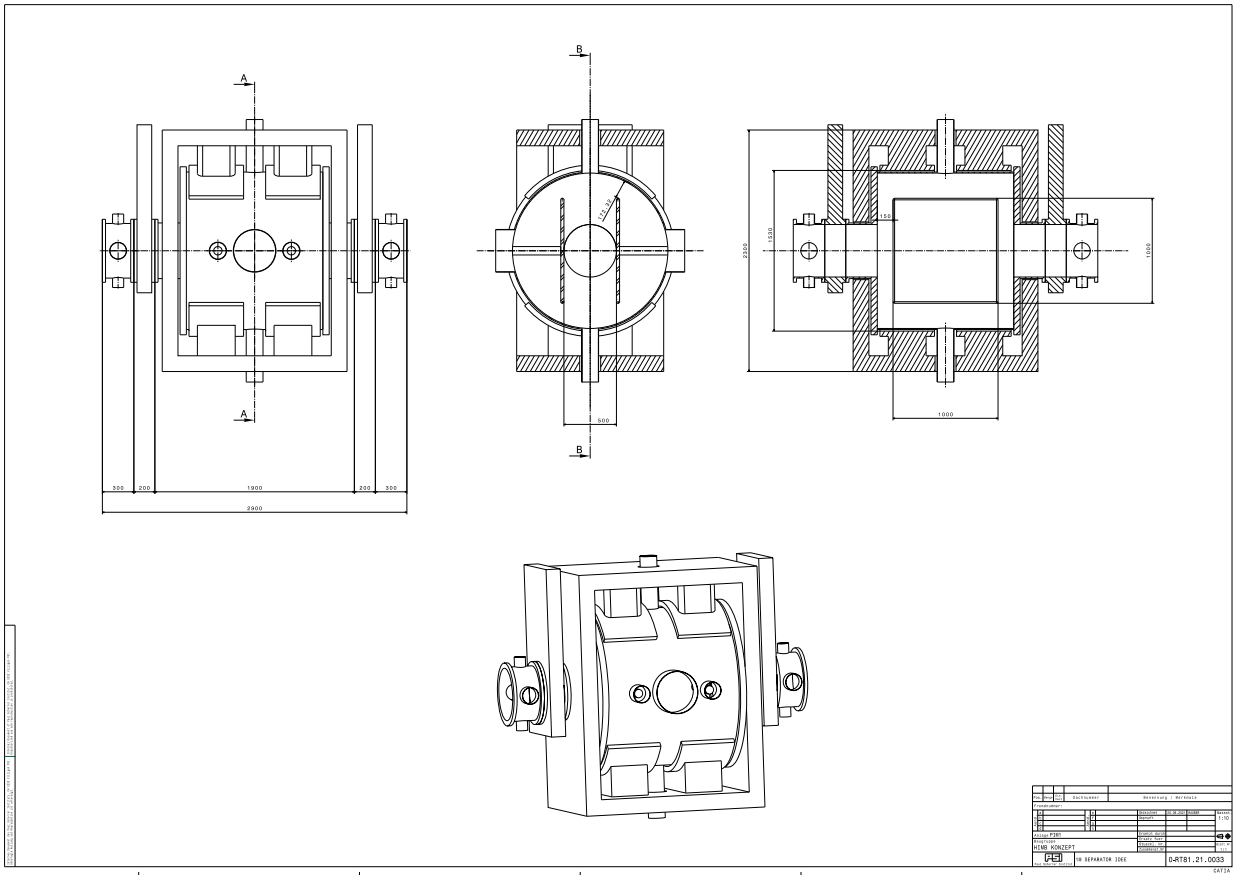

Figure 7.67: Sketch of the separator with 1 m long plate.

allows one to refocus the beam through the second solenoid thus increasing the overall transmission. Figure 7.67 shows the layout and overall dimensions of such a shorter separator. These dimensions are currently being implemented in the muon beam simulations to study the performance of this separation concept.

Table 7.9 shows and compares the design parameters of the two separator concepts with 2-m and 1-m long electrodes. The nominal parameters for its operation are based on the experience with various similar systems being used at the secondary beamlines of PSI and on how they are operated on a daily basis.

7.10.3 Spin Rotator

The MUH3 beamline will reuse the existing "spin rotator 1", which was built in 2017 and has since been operated in the piM3 beamline. As the piM3 beamline serves two μSR instruments, it is built as a spin rotator in order to not only

Design parameter	2 m version	1 m version
High voltage for muon beams of 28 MeV/c	+/-149 kV	+/-149 kV
High voltage for muon beams of 40 MeV/c	+/-213 kV	+/-213 kV
Separation at 300 kV up to beam energy of	56 MeV/c	28 MeV/c
Spin rotation separation mode	10°	5°
High voltage maximum	+/-300 kV	+/-300 kV
Electrode length	200 cm	100 cm
Gap between electrodes	50 cm	50 cm
Magnetic field integral	0.032 Tm	0.016 Tm
Gap between magnet poles	153 cm	153 cm
High voltage field orientation	horizontal	horizontal
E-field maximum	12 kV/cm	12 kV/cm
E-field integral at 28 MeV/c	1170 cm kV/cm	578 cm kV/cm
E-field integral at 40 MeV/c	1672 cm kV/cm	826 cm kV/cm
E-field integral maximum at 600 kV	2364 cm kV/cm	1164 cm kV/cm

Table 7.9: Design parameters for the separator concepts with 2-m and 1-m long electrodes.

Design parameters for 28 MeV/c	
High voltage separation mode	+/-30 kV
Spin rotation at 60kV	7.7°
High voltage spin rotation mode	+/-275 kV
Spin rotation at 550kV	70.7°
High voltage maximum	+/-300kV
Spin rotation at 600kV	77.1°
Electrode length	300 cm
Gap between electrodes	20 cm
Magnetic field integral	0.12 Tm
Gap between magnet poles	86cm
Beam transmission	70%
High voltage field orientation	vertical
E-field maximum	30 kV/cm
E-field integral at 60 kV	900 cm kV/cm
E-field integral at 550 kV	8250 cm kV/cm
E-field integral at 600 kV	9000 cm kV/cm

Table 7.10: Operational parameters of the existing spin rotator 1 device being operated at the piM3 beamline.

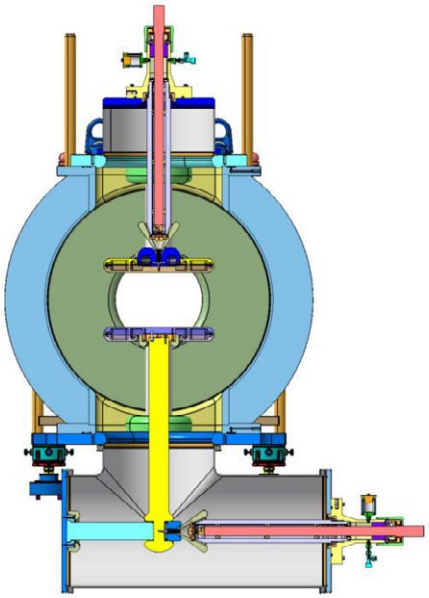

Figure 7.68: CAD cross section of the spin rotator 1 showing the inner parts of the device.

remove unwanted positrons from the beam, but also to rotate the intrinsic spin direction of the muons. It therefore features a very long electrode of 3 m in order to achieve a sufficient degree of spin rotation.

Figure 7.68 and Figure 7.69 show a CAD cross section and picture of the spin rotator. Its operational parameters are given in Table 7.10.

Figure 7.69: Picture of the spin rotator 1 mounted on the crane in the experimental hall of PSI.

7.10.4 Magnets

7.10.4.1 Dipoles

The dipoles are used to bend the muon beam along the designated beam path. To maximize the particle transfer, a vacuum chamber of a height of 500 mm was chosen, setting the aperture of the dipoles to 550 mm. Spatial constraints dictated that the dipoles be as short as possible.

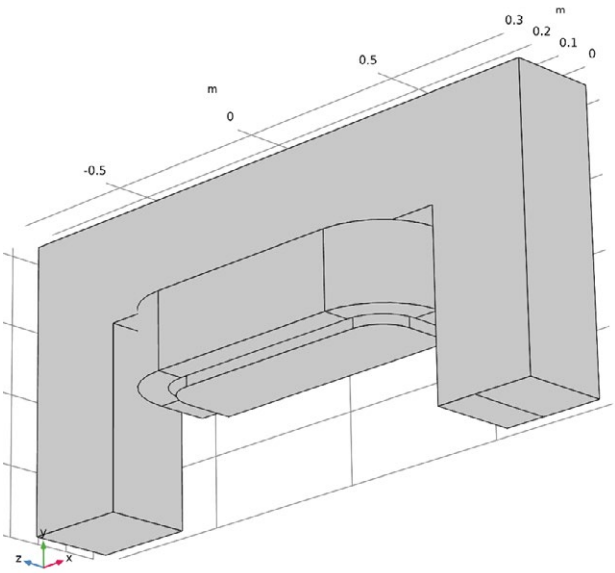

Figure 7.70: Dipole FEM model.

7.10.4.1.1 Beamline Dipoles

Using a current density based on previous experience and yoke dimensions designed to keep the field inside the iron at an acceptable level, yoke and coil were designed and checked by FEM calculation (see Figure 7.70).

While the dipoles with smaller deviation angles could have been made smaller, it was decided to use the same dipole at all bending points for manufacturing reasons.

The total length of the dipole was defined to be 700 mm for the current design; a possible shorter version will have to be investigated later.

Based on the calculation, a simple 3D model was created as shown in Figure 7.71. It does not yet take into account the power and cooling connections, however since there is enough room in transversal direction of the beam, accommodating these connections will not be an issue.

7.10.4.1.2 Radiation-hard Dipole

The first dipole behind the capture solenoid will be subjected to a relatively high radiation dose. Just as the capture solenoid, this dipole will be realized as a radiation-hard dipole, only using non-organic materials and components - see Section 7.10.1 above for details.

The goal is to use the same yoke as for the standard dipoles combined with a radiation-hard coil with indirect cooling and radiation-hard components for the connections.

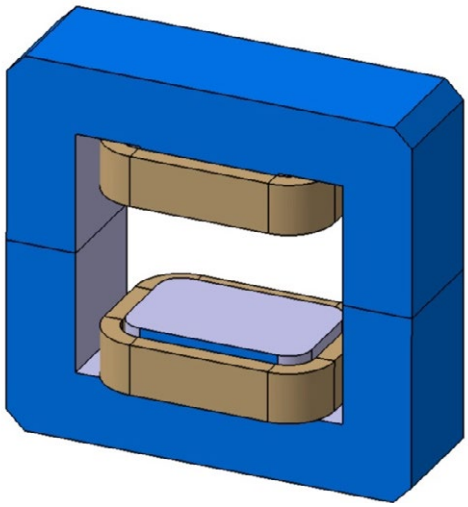

Figure 7.71: 3D CAD model of the beamline dipole.

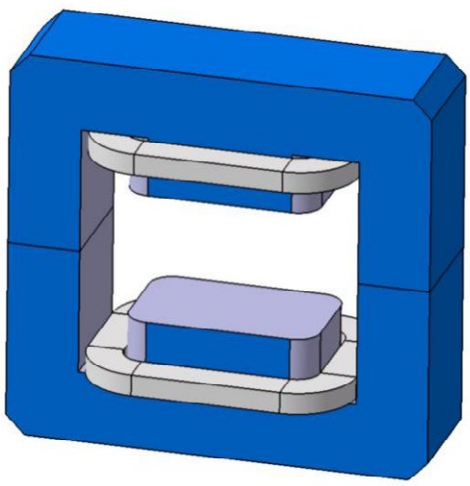

Figure 7.72: Dipole with radiation-hard coils.

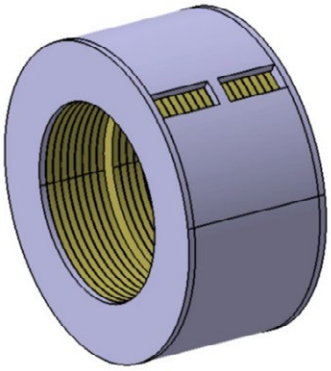

Figure 7.73: 3D CAD model of the transport solenoid.

A first design was created and a simple 3D model established as shown in Figure 7.72. Further details will be defined later based on past experience; especially the coil dimensions will most certainly change.

7.10.4.2 Transport Solenoid

The transport solenoid has the same operating parameters as the capture solenoid, but the requirements regarding radiation resistance are much lower. In this case, a normal magnet concept can be used, namely a directly cooled copper conductor impregnated with epoxy resin.
Based on the given geometry, a simple 3D model as shown in Figure 7.73 was created.

7.10.5 Vacuum System

The vacuum system for the two new beamlines will follow the standard installations that can be found along the secondary beamlines of PSI with the corresponding adjustments in terms of the pumping speeds in order to cope with the large diameter of the beamline vacuum tubes. Typical vacuum levels reached in the secondary beamlines are around 10^{-6} mbar, which is sufficient to not interfere with the passage of the particle beams.

7.10.6 Power Supplies

PSI has been and still is, pursuing a program to renew the power supplies used by the various beamlines. In this process the power supplies that still mostly date back to the start of the accelerator operations are being replaced by modern power supplies that were developed in-house. For both of the current beamlines piM1 and piM3, this upgrade has already happened. It is thus foreseen to reuse these power supplies, which mostly are specified as 160 V/500 A, also for the two new beamlines MUH2 and MUH3. The magnet design takes these boundary conditions into consideration in order to not exceed the available current and voltage limits. As in the case of the new beamlines, solenoids are used for focusing and replace either a quadrupole doublet or triplet, such that the number of available power supplies is more than sufficient.

7.10.7 Slit Systems

Slit systems are typically used along the secondary beamlines in order to shape the size and divergence of the beam, adjust its intensity and tune the momentum acceptance. We foresee three new slit systems: two along the MUH2 beamline and one in the new part of the MUH3 beamline. The first slit system will be installed in both beamlines in the straight section after the first bending magnet. The exact location will still need to be specified. This slit system will allow one to control the intensity and shape the momentum accept-

Figure 7.74: Photograph showing one of the slit systems used in the secondary beamlines of PSI during construction.

ance. However, it should be noted that due to the very high acceptance and transmission of the solenoidal channel, with limited momentum resolution, only a very limited tuning of the momentum acceptance will be possible. The second slit system will be located at the end of the MUH2 beamline and allow one to adjust and shape the beam spot upstream of the final focus.

The design of the slit systems will follow the existing designs used at the other secondary beamlines adapted to the larger aperture of MUH2 and MUH3. Figure 7.74 shows an example of such a system. It is made from a 50 mm thick tungsten alloy plate close to the beam and a 50 mm thick copper plate further outside (see also the change in color in the picture). An actuator is installed to precisely adjust the position of the two plates.

Figure 7.75: Picture showing one of the beam blockers used in the secondary beamlines of PSI during its construction. It is constructed as a sandwich of 90 mm copper, 120 mm stainless steel and another 90 mm copper.

7.10.8 Diagnostics

Secondary beams at PSI generally do not feature fixed beam diagnostics installations. Typically, dedicated scanners are only installed at the end of the beamline (or at more upstream positions if possible) to optimize the rate and beam shape for the experiments.

As part of the HIMB project, we are investigating whether a retractable beam scanner (e.g., a grid of scintillating fibers read out by silicon photomultipliers (see also Section 7.11.1) could be realized and installed directly at the beginning of the experimental areas such that the experiments would have a standard tool with which to tune the first part of the beamline.

7.10.9 Cooling System

Cooling water for all the magnets along the beamline will be provided by the cooling loop described in Section 12.4 and will follow the standard installation procedure used in the existing beamlines. Compared to the existing beamlines piM1 and piM3, the amount of heat to be cooled away is estimated to be roughly the same as the same power supplies will be used (see above).

7.10.10 Control System

Several control systems will be in place to allow for a safe operation of the beamline. The vacuum control system will monitor the status of the vacuum along the beamline and control the corresponding vacuum gate valves in order to protect the overall facility from erroneous manipulations. This is, of course, standard at the existing beamlines, and its design will follow those implementations as also described in Section 8.5.7.

The magnet control system will also follow the existing implementations at PSI and allow the experimentalists to operate and tune the power supplies and thus the currents through the electromagnets within safe limits. Each magnet features a temperature interlock that immediately switches off the power supply should its temperature exceed a predetermined limit.

An additional control system will be in place for access to the experimental areas and the safe operation of the secondary beam by the experimentalists. This PSYS control system is described in Sections 11.2 and 12.8.

7.10.11 Beam Blocker

Two large 300-mm thick beam blockers made of copper and stainless steel will be installed after the first dipole in order

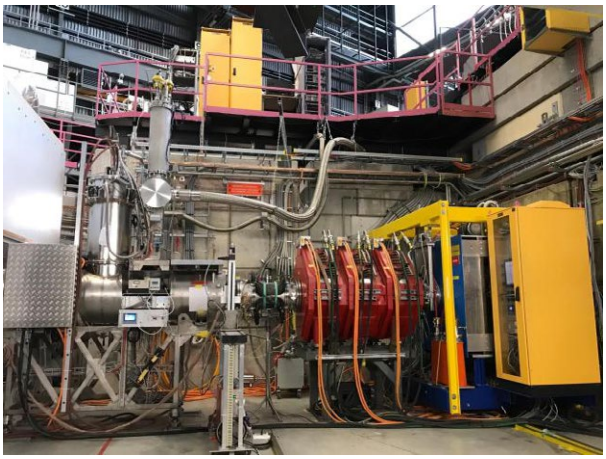

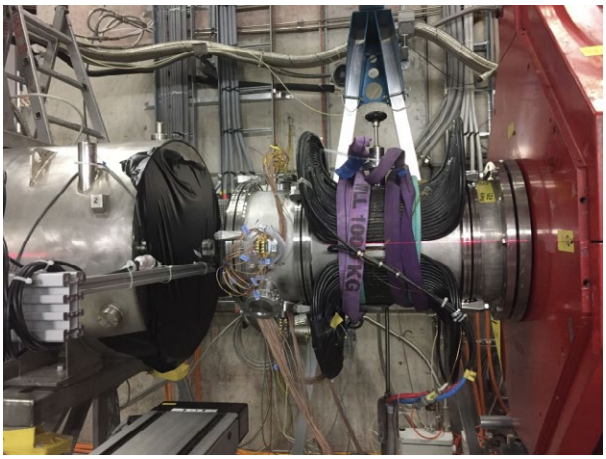

Figure 7.76: The pill detector mounted along the piE5 beamline. The scanner system is also visible.

to completely stop the transmission of any radiation down the beamline thus allowing safe access to the experimental areas. The two independently controlled beam blockers that directly follow each other provide the required redundancy for the safe operation of the beamline under any circumstances.

The beam blockers will be designed based on the existing installations adapted to the larger aperture sizes of the MUH2 and MUH3 beamlines. Figure 7.75 shows an example of such a system.

7.10.12 Support Structures

Support structures will be designed in order to lift and position the different magnets, slit systems and beam blockers to the appropriate places along the beamline. Much experience exists in this regard from all the existing installations, and many standard solutions exist at PSI that only need small adaptations for these new beamlines.

7.11 Commissioning and Operation

The commissioning of the two new beamlines will foresee several measurements of the beam profile and rate, as well as the evaluation of the beam divergence in a few strategic positions along the channels. Those measurements will assess the actual beam rate and properties to validate the Monte Carlo simulations.

Different beam detectors at the same position along the beam lines will be used in order to have independent measurements and keep under control systematic effects. Some of the main challenges of performing such measurements is to have detectors that will be able to sustain the expected high particle fluxes, performing particle identification (either directly, i.e. exploiting differences in particle energy deposition where possible, or indirectly, i.e. using time-of-flight techniques), working in the presence of high magnetic fields, and being vacuum compatible where needed.

Several detectors have been developed and used along the piE5 beam line. They operated up to a flux of a few x 10^8 muons/s, and some of them even up to a beam intensity of ~10^9 particles/s (positron beam). A short summary of these detector characteristics and performances is given below. Ongoing R&D is also mentioned.

7.11.1 Beam Detectors

Pill detector. This detector consists of an NE-102A scintillator, 1 mm in radius and 2 mm in length, coupled to a miniature Hamamatsu R9880U-110 photomultiplier. It is connected to a scanner system that allows a “raster” scan to

Figure 7.77: An example of the Pill signal at the oscilloscope. The high amplitude waveforms are associated with the muons while the low ones with the positrons (in this case cut by the trigger threshold). The separation between the two particle types is very clear.

be made with the possibility of having a few mm pitch and a 2D fine grid size allowing up to a thousand measured points per scan in a region of 160 ×160 mm^2 with a pitch of 5 mm. The system is read-out by a 4-channel waveform digitizing board (the so-called DRS4 evaluation board) and fast electronics, with a LabVIEW-based acquisition system. This detector is operated in air; it allows for a clear separation between minimum ionizing particles and stopping muons, and it can be used only in low magnetic field regions to avoid compromising the functionality of the photomultiplier. Due to the setup, the impact on the beam is destructive. Thanks to the small active area of the detector, the high particle fluxes, even those expected at HIMB, can be measured without significant rate saturation.
Figure 7.76 shows a picture of the Pill detector, while Figure 7.77 shows some detector signal results.

APD detector. This detector is an avalanche photodiode of 1.5 mm active area radius, with a 130 µm depletion layer (SPL4419 Hamamatsu). It is the depletion layer that is the sensitive part of the detector. Since the depletion layer is relatively thick, it allows for a remarkable clear separation between minimum ionizing particles and stopping particles. A single detector coupled with a scanner, as described for the Pill detector, allows one to perform both X- and Y- beam profile scans, as well as 2D fine grid profile scans. The main advantage of the APD over the Pill is that it is insensitive to the magnetic fields, and can be used in high magnetic field environments, in our case deployed up to 1.25 Tesla. The front-end electronic board provides the first amplification stage and the proper bias delivery. The output signal is used, as in the Pill detector case, as an input to a DRS4 evaluation board and fast electronics and manipulated to extract the beam profile and rate measurements.
A new generation of highly depleted APDs will be used for HIMB, with a similar detector size and a depletion layer of 145 µm (S12453 Hamamatsu).

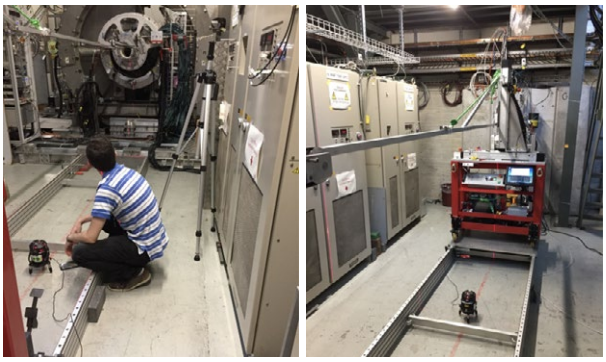

Figure 7.78: APD experimental setup as used in MEGII, with the detector connected to the scanner.

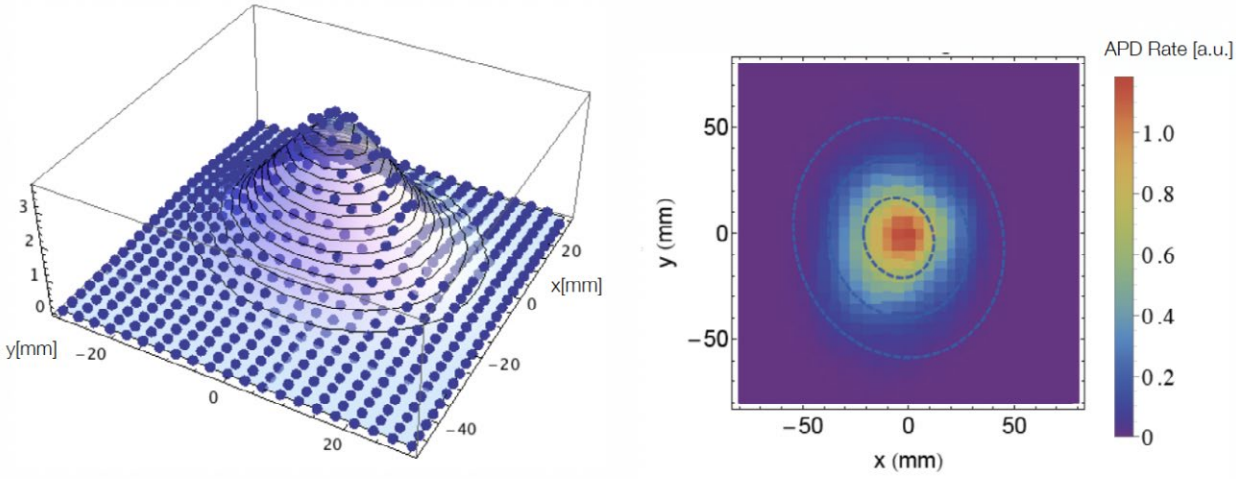

Figure 7.79: Muon beam profile at the center of the MEGII magnet. The picture shows the collected measured points in “raster” scan mode.

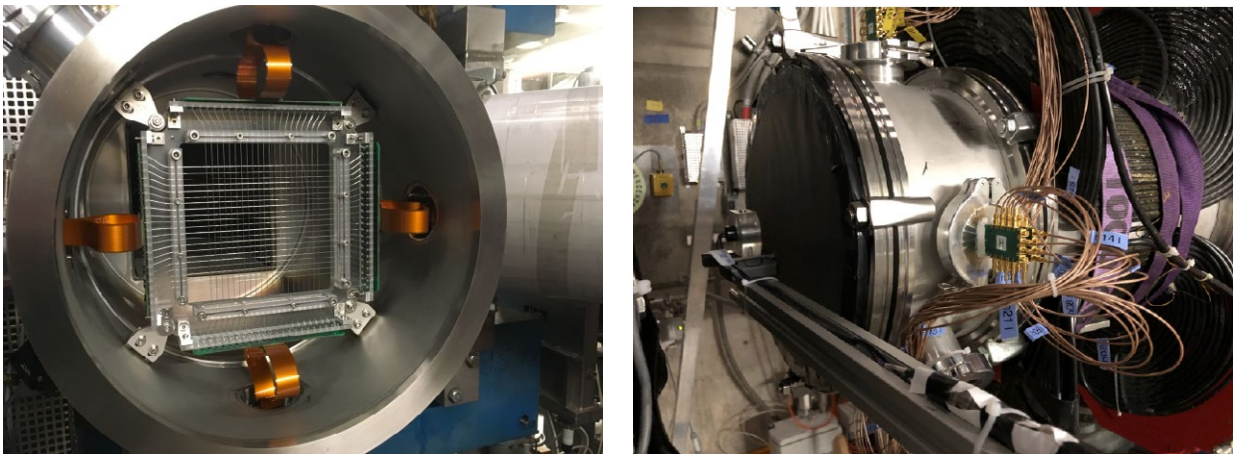

Figure 7.80: Two pictures of the SciFi detector (vacuum version) showing how it looks inside (left) and outside (right) the beam pipe.

While the current setup is used in air, we will investigate the possibility of having it compatible with a vacuum environment.
Figure 7.78 shows a picture of the APD detector, while Figure 7.79 shows some results.

SciFi detector. This detector is a quasi-non-invasive, high-rate sustainable beam monitoring tool, able to provide beam rate, profile measurements and particle identification in real time. It is based on scintillating fibres (SciFi) coupled to MPPC (SiPMs). It consists of a grid of two orthogonal fibre layers: one with the fibres running along the x-axis and the other with the fibres along the y-axis. Each fibre is independently coupled at both ends to MPPCs. A vacuum compatible version has been built and used while a movable configuration is now under construction.
Two detectors have been built and tested, the only main difference between the two being the type of mounted fibres (Saint-Gobain multi cladding BCF-12, 250×250 μm^2 and 500×500 μm^2) while in both cases S13360-1350CS MPPCs from Hamamatsu Photonics have been used (with an active area of 1.3×1.3 mm^2 and a pixel size of 50×50 μm^2). The relative distance between adjacent fibres mounted in the same layer is 4.75 mm, a pitch that satisfies the requirements for a precise measurement of the beam profile and rate. Furthermore, a large detector transparency T > 92 % (where 1 – T = particles hitting the fibres/total incident particles) is achieved with a relatively small number of channels (≈ 100). In fact, for these detectors, we mounted 21 fibres per layer, giving a total number of 84 channels. The readout system is based on the WaveDAQ boards developed at PSI and the trigger boards of the MEGII experiment. It also includes the pre-amplifier and the voltage power for each MPPC. The system allows for the digitization of the waveform of each channel up to 5 Gigasamples per second. This feature

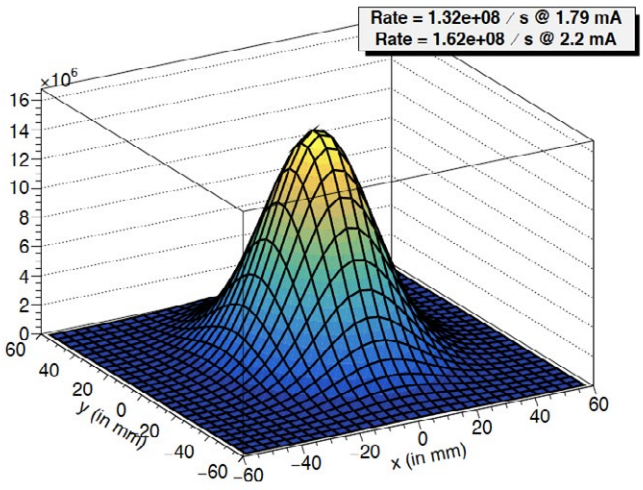

Figure 7.81: Muon beam profile as measured by the SciFi detector at the piE5 beamline.

is mainly useful during the setup of the detector. Normally, the beam profile and rate are extracted based only on the single fibre rate (for independent X- and Y- profiles) and the coincidence between fibres of different layers (to extract possible beam profile correlation. This feature has been proven to work with one of the two detectors (500 µm fibre detector-version) for a rate up to 7×10^7 muons/s.

A full Monte Carlo (MC) simulation code has been written, based on GEANT4. It also includes the response of the photosensors, going through the full electronic chain up to the waveform digitization, with a standalone code based on C++.

Figure 7.80 shows a picture of the matrix detector, while Figure 7.81 shows some results.

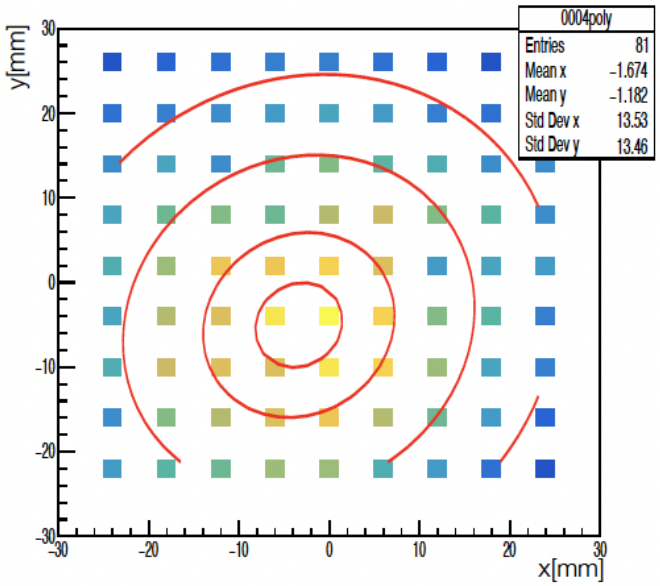

Figure 7.83: First test of the MatriX detector's capability along the piE5 beamline.

MatriX Detector. The currently optimized version of this detector is made of a matrix of 9×9 independent elements that act as a single detector, with a 6 mm pitch. Each element is made of 2×2×0.2 mm^3 BC400 plastic scintillator, followed by a 2×2×2 mm^3 plexiglass (light guide/MPPC protection) coupled to a S13360-1350PE (soon S13360-1325PE is to fully exploit the pixel dynamic range) Hamamatsu MPPC. The readout system is based on the WaveDAQ boards developed at PSI and the trigger boards of the MEGII experiment, following a similar approach to the one for the SciFi detector. The sensitive area coverage, the number of channels and the pitch can be optimized based on the expected beam characteristics. The main advantages associated with this detector are as follows. 1) A one-shot 2D grid scan from which both the beam profile and the rate can be extracted, as well as any beam correlations. The exposure to the beam will be just a few seconds, similar to the SciFi detector, and

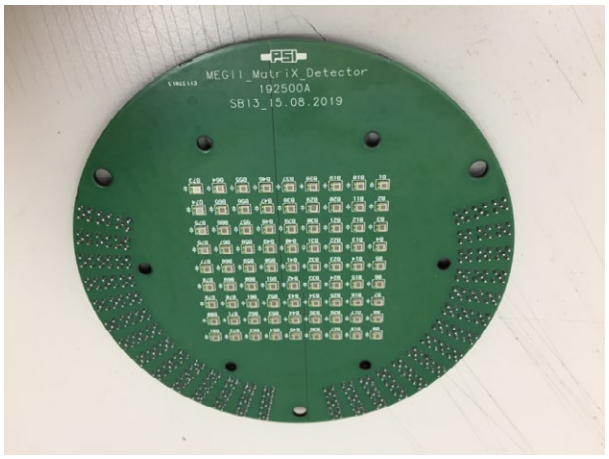

Figure 7.82: A picture of the MatriX detector prototype during the assembly stage. The MPPC matrix is on the left and BC400 scintillators are on the right.

different to the Pill/APD scan that could require up to several hours, depending on the amount of requested measured points. 2) A detector compatible with both magnetic fields and vacuum. 3) A detector able to perform particle identification. The detector itself is beam-destructive. A movable version to operate it on demand and reduce the exposure to radiation to a minimum, allowing for a longer detector lifetime, is foreseen.
A full MC simulation code is also available for this detector. It is based on GEANT4 and it extends to the response of the photosensors, going through the full electronic chain up to the waveform digitization, with a standalone code based on C++.
Figure 7.82 shows a picture of the matrix detector, while Figure 7.83 shows some results.

Luminophore detector system. Based on scintillation light imaged by a CCD camera system, the ultra-thin 3 μm thick PET-foil substrate has a CSI(Tl) layer of around 5 μm deposited on it using a thermal vapour deposition technique. An initial 130 mm diameter imaging foil was developed for use in high-intensity secondary beams of muons, pions and electrons, allowing both non-destructive and accurate beam profile imaging and together with a one-off independent intensity measurement, also allows beam intensity variations to be followed in real-time. Figure 7.84 shows the

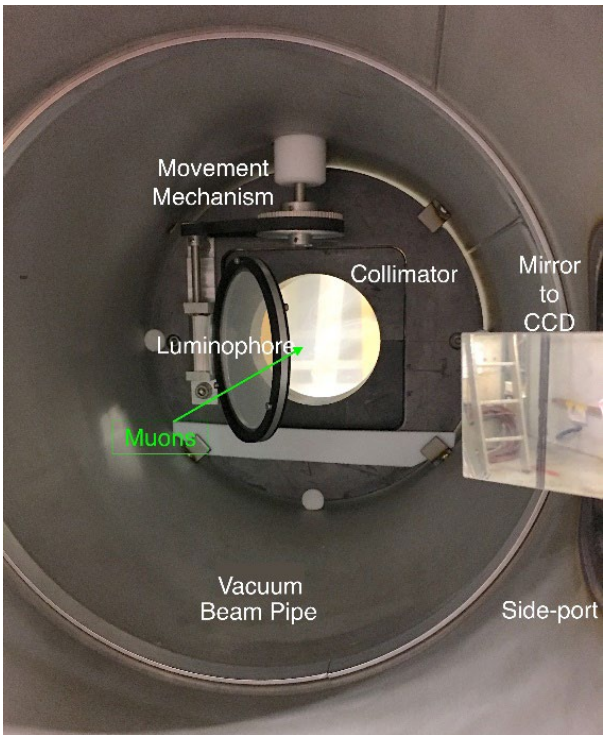

Figure 7.84: Luminophore setup used in the MEG II and Mu3e experiments. The foil is placed in the vacuum-pipe and can be moved in and out of the beam. It is imaged by a CCD camera system viewed via a side-port from outside of the vacuum system.

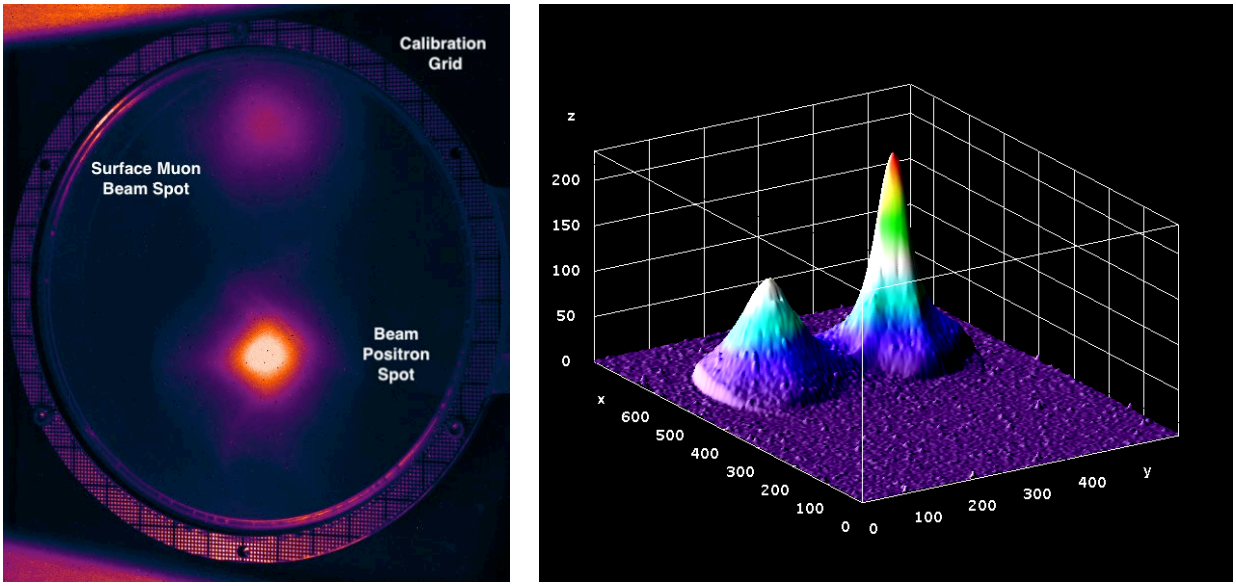

Figure 7.85: The surface muon beam spot and beam positron spot at an intermediate focus position downstream of the Wien-filter is shown, with reduced high-voltage so as to see both spots in the same frame (left). The light-yield/beam profile data plotted are given as well (right).

system developed for in-situ vacuum measurements developed for the MEG II and Mu3e experiments.

A calibration grid on the frame of the luminophore, which can be illuminated by an upstream UV-LED allows a pixel-to-mm ratio to be determined, as well as, allowing a perspective transformation to be made when viewing the foil off-axis. A beam profile image typically comprises of five consecutive exposures and five dark frames, taken with the beam-blocker closed, to produce a background subtracted image of the beam, using the high-resolution thermoelectric/water cooled 16-bit QSI RS-9.2S camera with a Canon EF-S 18-200 mm f/3.5-5.6 IS lens. The spatial resolution of the system has been measured to be better than 540 μm with a linear light-yield response over two-orders of magnitude in intensity reaching above 10^8 particles/s, only limited by the available beam [Berg, 2020]. Comparative measurements with the pill-scanner system show comparative profile measurements to within 100 μm. The radiation hardness has also been tested up to 75 kGy.

Figure 7.85 (left) shows a measurement made with reduced separation-power of a Wien-filter to clearly show the separated muon and intense beam positron spots in the same field of view, also shown is the calibration grid. Figure 7.85 (right) is the associated light-yield/beam profile distribution.

Future detector developments. While the detectors described in the previous section can work at the expected HIMB intensities, with a fine-tuning of material thickness and size, as well as the number of channels, future beam tools based on different technologies, such as silicon devices, will be considered and investigated as well. In fact, one of the main limitations of the scintillator coupled to MPPC based detectors is the effect of radiation hardness, which strongly affects the lifetime of the detector itself. Furthermore, "transparent"/ "super-thin" devices that could be permanently installed along the beamline would simplify the monitoring and operation of the beam line itself.

7.11.2 Beam Measurements

Here we describe the beam measurements expected to be performed along the MUH2 beamline (Figure 7.34). A similar approach will also be followed for the MUH3 beamline. After the installation and commissioning of both beam lines, in the case of the MUH2 beamline, outlined here, two measuring stations will be assessed for annual/monthly beam checks; for the first commissioning of the MUH2 some extra measurement points will be considered. The two default measuring stations will be (a) after the separator (depending on the available space before/after the BL4 element) and (b) at the end of the beamline, after the BL5. In collaboration with Mu3e we expect to perform also some measurements at the center of the Mu3e magnet.

8 Proton Beamline

8.1 Present Situation

After being extracted from the 590 MeV main ring cyclotron with an efficiency better than 99.98 %, the beam is transported in three different stages to impact three different targets: *The first stage* of the proton beamline delivers the beam to Target M: its transfer line consists of a 43 m long channel containing 5 bending magnets, 12 quadrupoles, 12 steering magnets and 22 profile monitors (see also Figure 4.1). After impacting Target M, the beam is transported in a *second stage* to Target E. This section of the beamline is 18 m long and consists of 2 quadrupoles triplets that we will refer to as "Triplet 1" and "Triplet 2", 12 profile monitors (6 horizontal and 6 vertical) as well as 2 horizontal and 2 vertical steering magnets. In the *third and last stage*, the remaining primary proton beam is directed towards the SINQ target for neutron production: this section is 55 m long and its components are 4 bending magnets, 12 quadrupoles, 9 profile monitors (horizontal and vertical), 5 horizontal steering magnets, 7 collimators and 3 pairs of slits: KHNY21, KHNX22 and KHNY30. KHNY30 was introduced at the dispersive region to block the unwanted beam, with large energy spread, missing Target E and to trigger an interlock / for machine protection [Rohrer, 2002], [Rohrer, 2004].

In the present situation, the effective thickness of Target M is 5 mm only. Interactions with Target M therefore reduce the average kinetic energy of the 590 MeV beam only minimally by 2 MeV. For the secondary particles, muons and pions, there are two beamlines under 22.5° in forward direction. For comparison, in the target station E, a 40 mm or 60 mm graphite wheel-like target can be inserted.

8.2 Basic Considerations, Requirements and Constraints

The purpose of the transport channels is to transport the high power beam with minimum losses towards each target and to produce optimum matching conditions suitable for both the primary and the secondary beamlines. As discussed in previous chapters, one of the major changes in the IMPACT project consists in replacing the 5 mm Target M with the slanted 20 mm Target H. Such a thicker target will thus increase the beam divergence, lower the beam energy and alter the downstream optics. Regarding Target H and Target E impact locations, the proton beam shall be focused to a waist ($\sigma'_x = \sigma'_y = 0$) with typical spot sizes of $\sigma_x = \sigma_y = 1$ mm. A much more focused beam could damage the target due to overheating, and a larger and more divergent beam could lead to large losses on the subsequent collimators. Furthermore, tails and halo of the beam might miss Target E, whose standard width is 6 mm only. The consequences could be locally higher, potentially damaging current densities at the SINQ target. In addition, upstream of Target H, the goal is to reduce the power depositions to a level below 1 W/m equivalent to a fractional beam loss of ‹1.7 nA/m for hands-on maintenance.

Although the nominal beam current for HIPA is 2.2 mA, an increase to 3 mA is considered. We aim to design the new target station for a future, possible increase. Beam studies showed that the size of the beam is increasing with current as it is shown in Figure 8.1. The beamline has to tolerate such variations, other imperfections and alignment errors. This indicates the need for a sensitivity study to assess the respective impact on power depositions along the beamline. Results will assist designing beam components such as collimators or profile monitors that are resilient enough to withstand the power depositions induced by such a high power beam (1.8 MW at 3 mA).

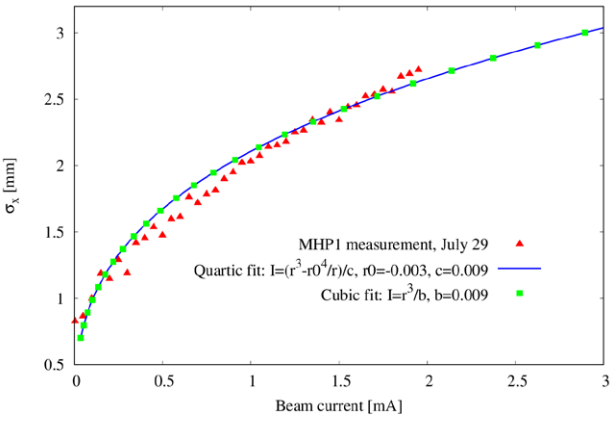

Figure 8.1: Beam size versus current at the location of the first profile monitor of the beamline after the 590 MeV ring cyclotron. The projected beam size at 3 mA is also shown.

Furthermore, the density of the target material made of graphite might increase in the future, if one extrapolates from the experience in the past. The first polycrystalline graphite target used at PSI in 1985 had a density of 1.7 cm^3 whereas the analysis performed between 2019 and 2021 on the manufactured targets showed that the density is lying in the range [1.80:1.82] g/cm^3. This is still far from the value of 2.26 g/cm^3 for natural graphite, however, it shows the progress in the manufacturing process achieving higher densities by decreasing the size of the crystals of about 10 µm nowadays. A density of 1.84 g/cm^3 is chosen as the reference value for all our simulations including the secondary beamline calculations, however, the influence on the optics due to an increase of the density, which we might expect in the future, is studied as well in the sensitivity analysis.

8.3 Simulation and Calculation Tools

All above considerations lead to the need to perform particle tracking simulations in electromagnetic fields and to simulate the accurate interaction processes with the beamline components to infer the power depositions in all subsystems. This unique combination implies that the beamline geometry, particularly the one surrounding the target, shall be accurately implemented. In addition, flexibility of the simulation tool is needed in order to optimize the beamline optics and redesign the collimators. This has led to the choice of the Beam Delivery Simulation (BDSIM) as the reference program for all calculations [Nevay, 2020]. BDSIM combines particle accelerator tracking routines with the standard high energy physics code Geant4 [Agostinelli, 2003].

However, when handling several processes interacting simultaneously, it is highly beneficial to benchmark each simulated process individually against standard calculations or other dedicated simulation tools. Namely, the optics shall be benchmarked against TRANSPORT (see Section 8.3.1 regarding the benchmarking and Section 7.6.2 for more information about the tool), MAD-X [Deniau, 2021] and ZGOUBI [Méot, 1999] while the interaction processes shall be benchmarked against MCNP [Goorley, 2017] and TURTLE [Brown and Iselin, 1974].

Last but not least, a start-to-end simulation of the beamline will be performed and the present optics benchmarked against the beam profile measurements in Section 8.3.1. This is the first time that a single code is handling beam tracking and interactions all the way from the ring cyclotron extraction channel to the SINQ target. Figure 8.2 displays the new simulated model starting from TgH and leading to SINQ.

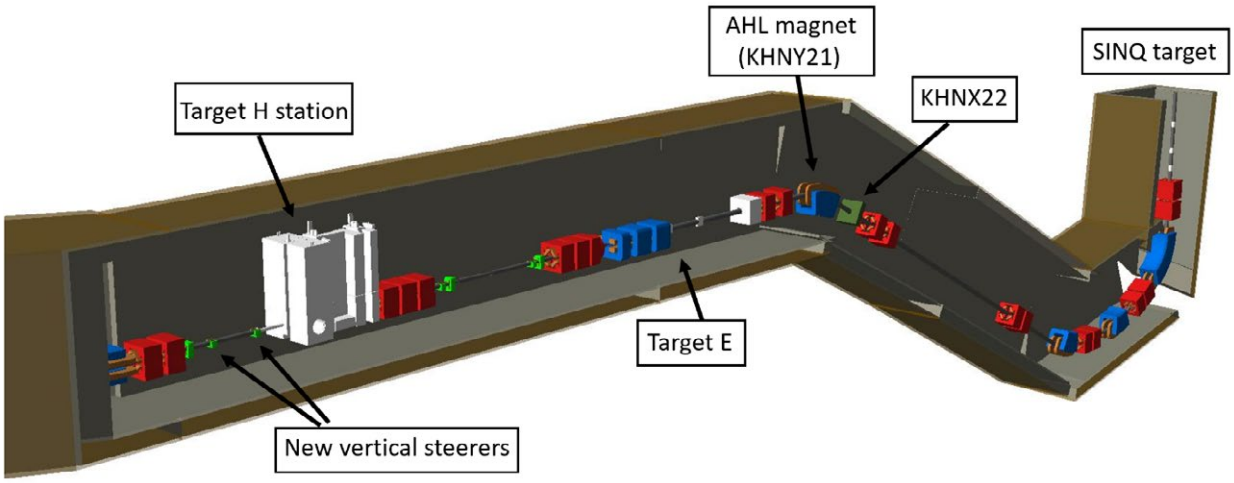

Figure 8.2: New optical layout of the TgH region displaying the quadrupoles (red), bending magnets (blue), steerers (green) and TgH region along with its collimators (white). The vertical slits KHNY21 are located inside the AHL magnet.

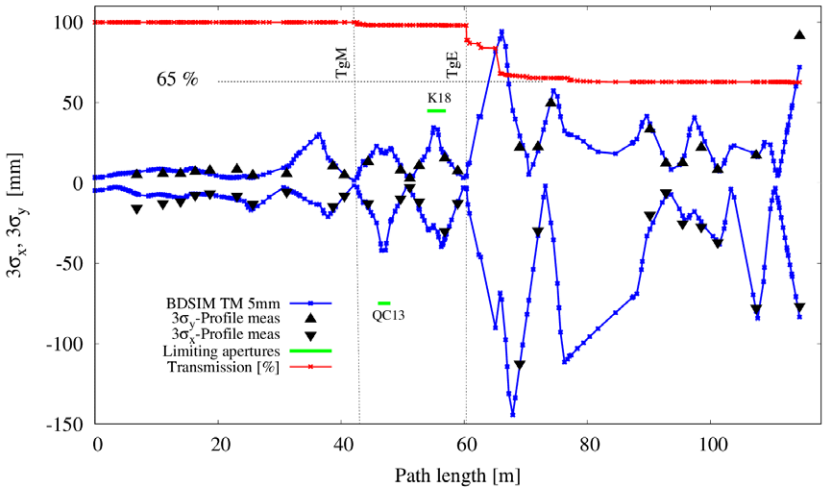

Figure 8.3: Transverse beam envelopes obtained from tracking in BDSIM and comparison with the measurements. The upper-pointing triangles display the vertical beam size from the profile monitors measurement and vice-versa.

8.3.1 Benchmarking with Present Beamline Optics

The benchmarking with the present beamline optics was performed in two stages: In the first stage, the optics was validated by comparing the Twiss functions calculations both in BDSIM and MAD-X. The initial lattice files for the SINQ beamline were obtained from TRANSPORT along with the initial beam conditions. The latter are intensity-dependent, i.e. evolve with the incoming beam current from the cyclotron: For the purpose of the benchmarking, the initial beam conditions assumed are the same. Tracking is performed in BDSIM, TRANSPORT and comparison of the transverse beam envelopes with the profile monitors measurements up to Target E is shown for the 2 mA current in Figure 8.3. An excellent agreement is obtained between the simulated and measured values except at the first part of the beamline i.e., before TgM. In order to solve such a discrepancy TRANSPORT code is exploited: Owing to its built-in fitting capability, TRANSPORT can determine the initial beam conditions that matches the beam sizes to the measured values. Such matching conditions are subsequently fed into BDSIM and comparison of the obtained envelopes with the different simulation codes displayed in Figure 8.4. Note that the TRANSPORT results are based solely on fitting the beam initial conditions at the ring extraction and at the exit of TgM using the measurements at the profile monitors. In order to account for the beam interactions at the target, TRANSPORT is combined with TURTLE where the beam conditions at the entrance of TgM are used as input for TURTLE thenceforth completing the tracking to the entrance of TgE.

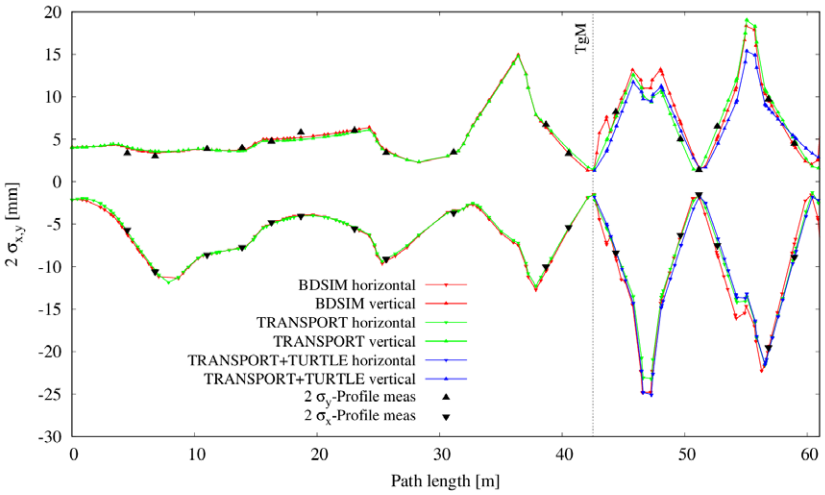

Figure 8.4: Transverse beam envelopes obtained from tracking in BDSIM, TRANSPORT as well as TURTLE and comparison with the measurements. The upper plots depict the vertical plane and vice-versa.

8.3.2 Benchmarking with Power Depositions

In order to benchmark the power deposition calculations in BDSIM and MCNP, the idea is to perform both simulations by relying on the same geometry, the same beam parameters and last but not least the same material composition. To facilitate the task, both codes start from the same step file generated by CAD software and containing the complex geometry. Using the appropriate tools, the geometry is then converted into the format suitable for tracking (GDML format in BDSIM). The material composition is then assigned to each volume and the initial beam generated: A pencil beam is chosen for this task since it reduces the uncertainties with beam generation methods. A comparison of the power deposition calculations for a 2 mA pencil beam impinging on TgH is finally shown in Table 8.1 where a good agreement can be observed. The small differences are mainly due to the differences in the physics models.

The benchmarking effort was particularly rewarding and helped fixing one major bug in the built-in geometry model of elliptical collimators in BDSIM.

	Target H	Coll KHM0	Coll KHM1	Coll KHM2
BDSIM	17.9	22.9	7.8	0.9
MCNP	18.7	20.3	8.8	1.3

Table 8.1: Comparison of power depositions calculations in kW between BDSIM and MCNP. A 2 mA pencil beam is assumed.

8.4 Proton Beam Transport with Target H

One of the major questions to answer is how the beam transmission towards each target will be impacted when replacing Target M with Target H. Furthermore, the power deposition on particular components is an important issue, which shall be clarified. For this reason, a start-to-end simulation is performed. The layout of the model is shown in Figure 8.2 and different aspects of the optimized model will be discussed next.

8.4.1 Correction of the Fringing Field at Target

The fringing field produced by the solenoids surrounding TgH does alter the primary proton beam trajectory. Given that the main magnetic field component of the solenoid is in the x-direction i.e. perpendicular to the momentum direction of the primary beam and in the median plane as illustrated in Figure 8.5, the only noticeable impact will be a vertical beam deflection that, if uncorrected, reaches its maximum of nearly 30 mm at the location of the 1st quadrupole triplet downstream the target. The horizontal beam motion is unaffected.

In order to cure such an effect, two methods are employed: *the first one* consists of adding mirror plates adjacent to the solenoid entrances in order to reduce the fringing field extent i.e. the field integral seen by the primary beam. Figure 8.6 displays the impact of different mirror plates thicknesses on the field profile: above 40 mm, the plates are not saturated anymore and a further increase in thickness reduces the

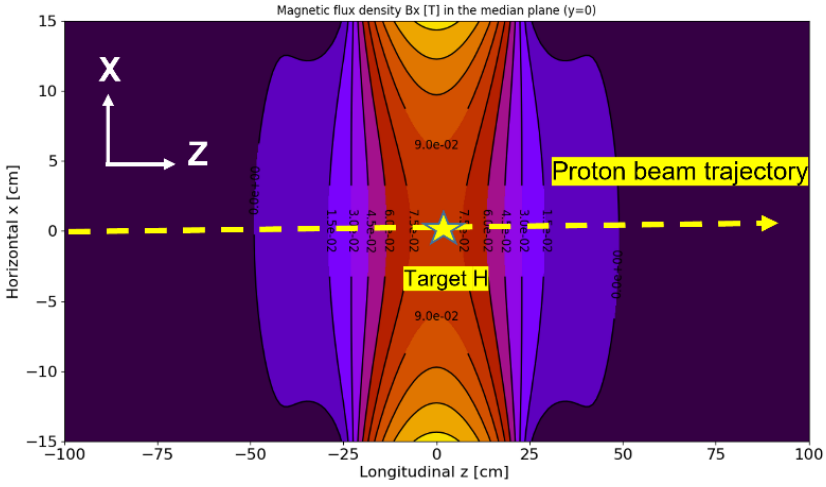

Figure 8.5: Horizontal magnetic field component (Bx) along the primary proton beam trajectory.

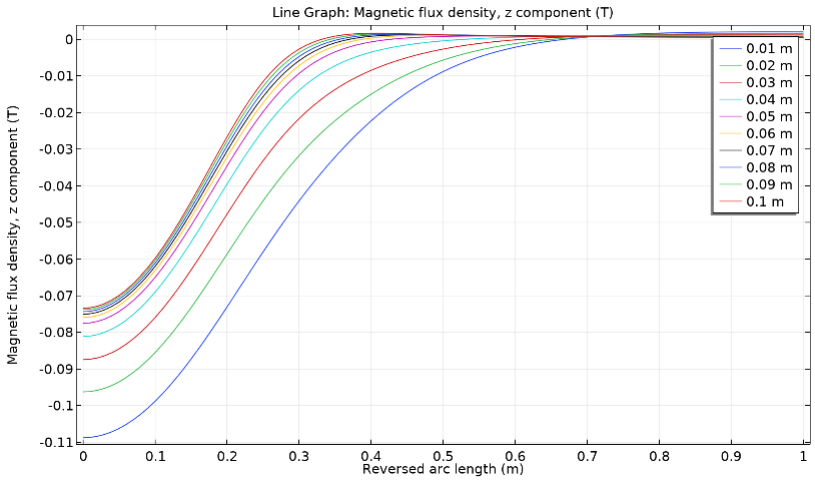

Figure 8.6: Magnetic field falloff as a function of the mirror plates thicknesses at TgH region. The x-axis denotes the longitudinal position starting from TgH impact location while the vertical axis denotes the horizontal field component.

effectiveness. Given the space constraint in the target region, a 40 mm thickness is retained. The effective extent of the fringing field can be limited to ±1 m around the target and its peak value, where the beam impacts TgH, amounts to 0.88 kG. *The second method* consists in canceling the impact that the remaining fringing field will have on the primary proton beam trajectory after the target. The idea is to modify the incoming beam trajectory towards the target by applying two vertical deflections that will compensate for the fringing field. Since the matching conditions required are for the beam to be back on axis after the target i.e. Y = Y' = 0, only two vertical steerers are needed for the correction. The horizontal beam motion as well as the focusing of the beam in the vicinity of the target are unaffected. However, the latter is strictly valid when hard edge models are employed for the steerers i.e. if the fringing field of the steerers is neglected. At a later stage of the design, realistic field model of the steerers shall be implemented into the simulation. The location of the two steerer magnets are optimized in order to ensure the beam trajectory remains as close as possible to the ideal one and to utilize the lowest field strength for such magnets. Figure 8.7 displays three different steering magnet settings along with the matched beam trajectory. The solution retained is shown in green where the last steerer is located 1.6 m away from the target, precisely at the exit of "bunkerwand". The steering magnets are 20 cm in length and shall produce an integrated magnetic field of 31.77 kG.cm and -62.89 kG.cm.

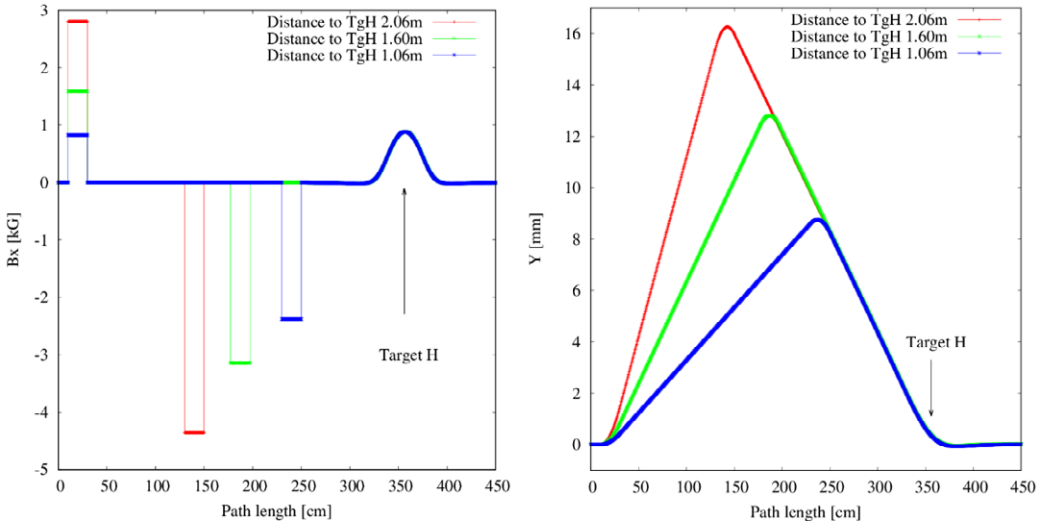

Figure 8.7: ZGOUBI simulations of the corrected proton beam trajectory upstream of TgH. The position of the second steerer magnet is varied and the newly matched solution computed accordingly.

The matching conditions at the location of the target, which are imposed by the fringing field strength only, are as follows: Y = 0.3 mm and Y' = -3.9 mrad. This has minor impact on the secondary beamlines. However, the above conditions are dictated by the settings of both solenoids: The present scenario is the worst possible case in which both solenoids have the same polarity so that their magnetic fields add-up and the required correction fields are maximized. In case the polarity of one of the solenoids is inverted, their magnetic fields shall cancel to the extent that the symmetry is well fulfilled. However, in all possible scenarios, with partial or full cancellation of the fringing fields, the correction scheme can be implemented by adjusting the field strength of the steerer magnets. The latter shall be newly designed given that the required strength is nearly five times above the limit of the existing ones in the beamline. This should not pose a problem. The additional steerer could also be extended above 20 cm or placed into the shielding, if there is not enough space in front of the shielding. Note in addition that the field map tracking results have been benchmarked in two codes: ZGOUBI and BDSIM. An excellent agreement was achieved.

8.4.2 Target Protection Collimator

In order to protect the vacuum chamber from a badly mis-steered beam, a protection collimator is placed at the entrance towards Target H. Its apertures are chosen such as to accommodate for various fringing field strengths, thus for various vertically deflected beam trajectories compensating for it, as well as for possible beam size variations. The latter lies in the range 1 mm $< \sigma_{(x,y)} <$ 2 mm. Thus, allowing a safety margin of few millimeters, the apertures are chosen as follows: $r_x = 10$ mm and $r_y = 15$ mm.

8.4.3 Optimization of the Collimator System after Target with Respect to Power Deposition

The collimator system is one of the most important elements of the high power beamline. With the anticipated beam intensity upgrade of the cyclotron complex in the years to come, the new collimators shall be able to withstand the power depositions produced by the 3 mA beam. In addition, the collimators act both as local shielding and as absorbers by reducing the beam halo that might deposit its energy in some critical parts of the beamline downstream that are not sufficiently protected against high radiation levels. In doing so, the collimators should also not be very sensitive to beam misalignment errors of sub-millimeter level in order not to trigger frequent interlocks of the machine. The design of the collimators is driven by the beam simulation including power deposition calculations on the component and its shielding. As a general rule of thumb, 2/3rd of the power depositions shall go into the collimators and 1/3rd to the surrounding

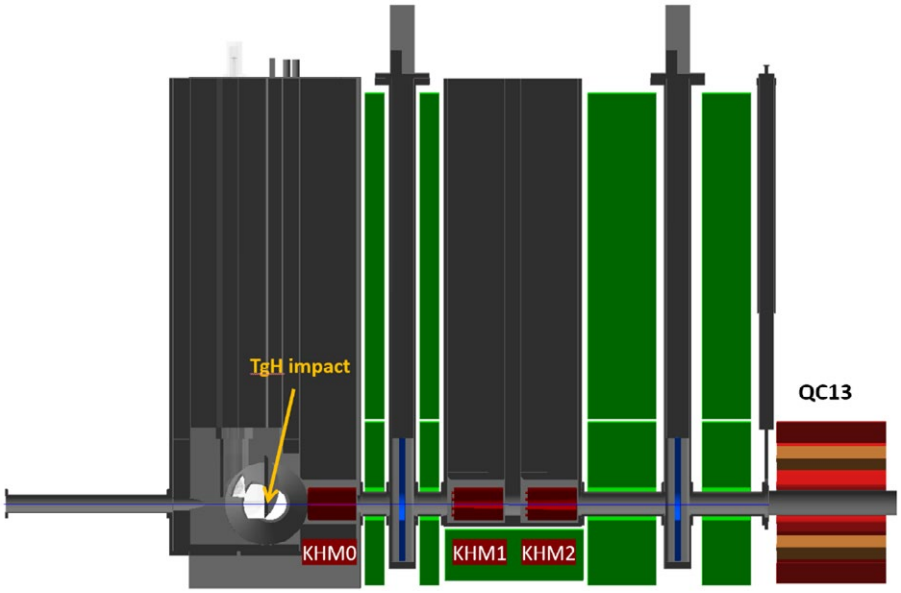

Figure 8.8: Layout of the TgH region up to the first quadrupole downstream, i.e. QC13. The added shielding is displayed in green while the profile monitors made of aluminium are in blue.

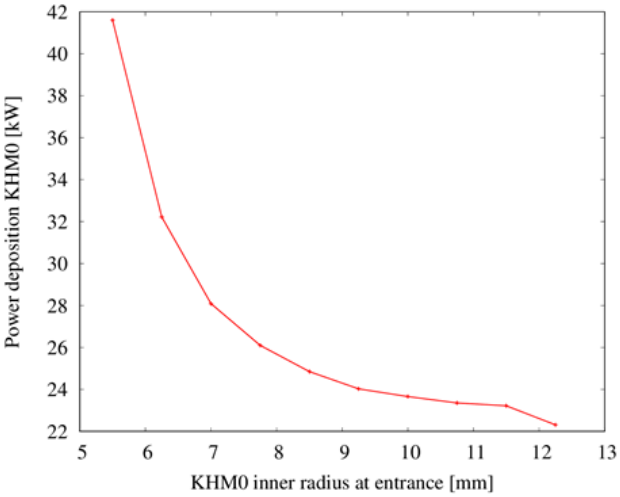

Figure 8.9: Power deposition for KHM0 collimator as a function of its entrance inner radius. A 2 mA proton beam is assumed.

shielding. Aside from the protection collimator which is upstream of the target, the remaining region to optimize starts 25 cm downstream of TgH impact point i.e. at the entrance to the first collimator denoted KHM0, and extends to the entrance of the first quadrupole denoted QC13 as can be seen in Figure 8.8. Since the aim is to use the same previous optics layout from QC13 onwards, the available space to place the new collimators along with the diagnostic elements is 2.9 m long.

Since QC13 is defocusing in the horizontal plane, the divergence of the already divergent beam from TgH will be increased. If the beam is not properly collimated beforehand, QC13 can receive a high power deposition. For this reason, the collimators were optimized by having an elliptical shape that cuts a larger fraction of the beam in the horizontal plane than in the vertical one. The only exception is KHM0 which acts as a shielding for the wide angle scattered particles from the target and has a conical shape with an inner circular cross section.

First, the aperture of KHM0 is varied in order to assess the optimum values that do not intercept the core of the primary beam and reduce the power deposition to the level where it is not very sensitive to missteered beams. This is illustrated in Figure 8.9 where we can see a plateau at around 11 mm. The corresponding power deposition is around 23 kW for a 2 mA beam which, to first order, amounts to ~35 kW for the aimed 3 mA beam. Keeping in mind that one of the collimators behind Target E is designed to stand more than 100 kW, the power deposition for KHM0 should not pose a problem. In addition, the shielding shall receive 8 kW from the 2 mA beam. In order to determine the optimum apertures of KHM1 and KHM2 collimators, parametric studies are performed whereby the ratio of the exit/entrance apertures of each collimator is varied as well as their relative openings as illustrated in Figure 8.10. The aim is to infer the parameters suitable for

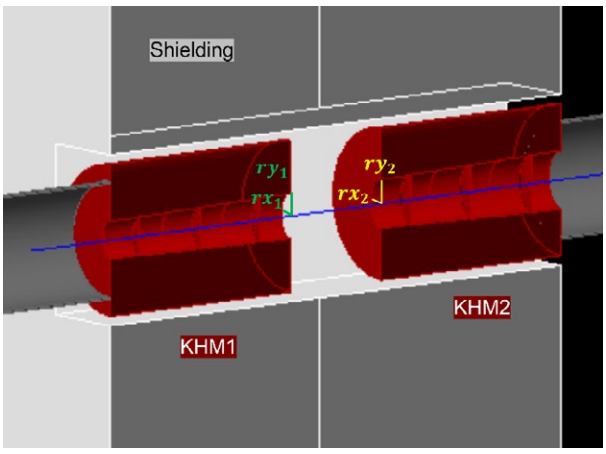

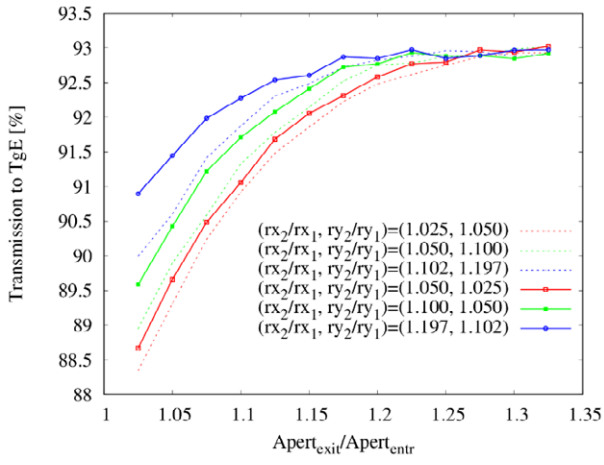

Figure 8.10: Parametric study of the collimators aperture suitable for a stable beam transmission. Left: Cross section of the collimators 3D models with labels. Right: Transmission to Target E as a function of the collimators aperture.

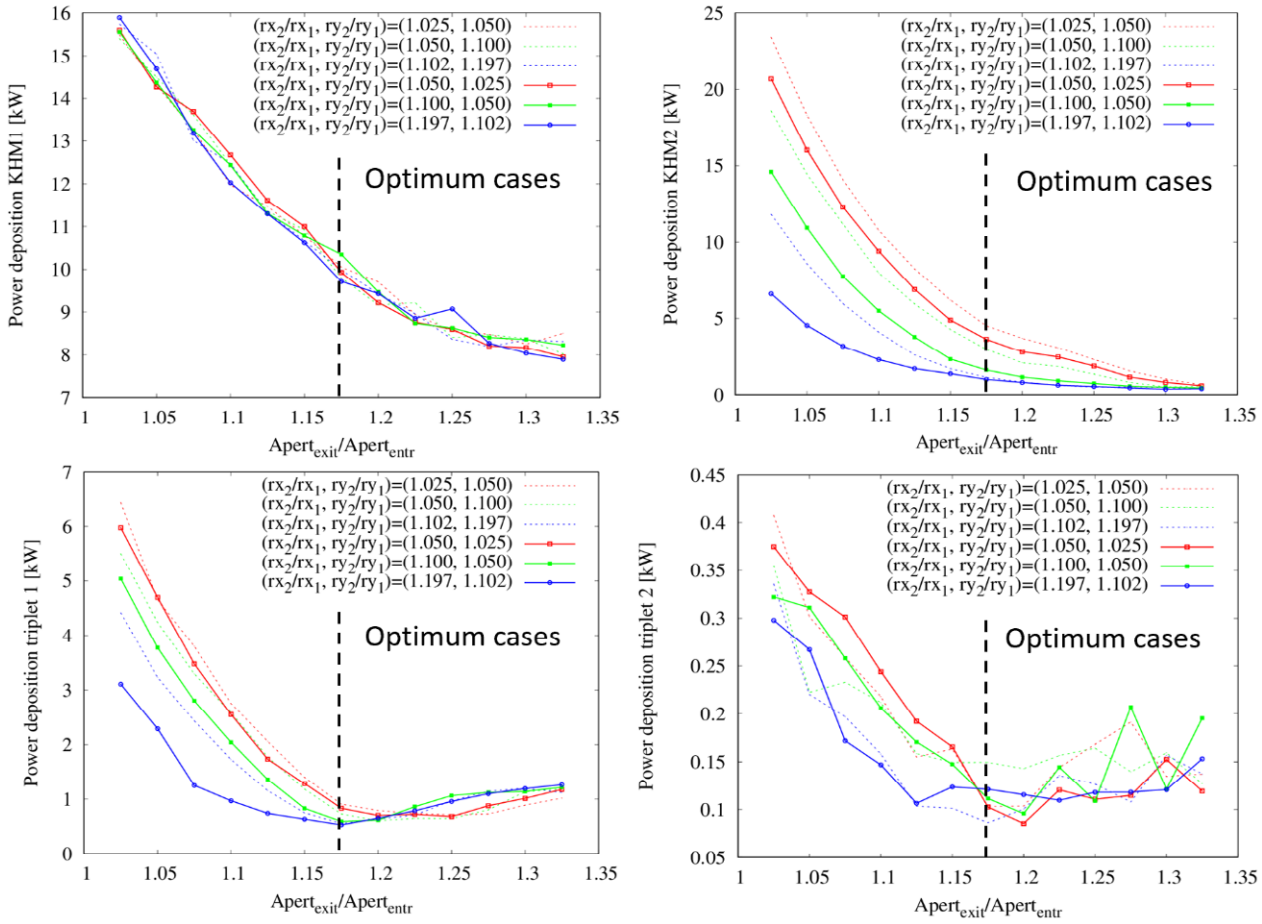

Figure 8.11: Parametric studies of the impact of the collimators aperture on the power depositions along the TgH-TgE beamline, assuming a 2 mA beam. The optimum case is shown in solid blue lines.

maximum stable transmission towards Target E while reducing the losses downstream. With the new Target H, the fraction of the beam arriving towards Target E represents 93.2 % of the incoming beam from the cyclotron. This represents a decrease of nearly 5 % from the 98.3 % transmission with the existing Target M. The result is summarized in Figure 8.10.

At the same time, the optimum apertures of KHM1 and KHM2 are the ones yielding the lowest power depositions on the quadrupoles triplets 1& 2 and guaranteeing a low sensitivity against possible sources of imperfections. To achieve this, two steps are necessary:

1) First, the optics between Target H and Target E are adjusted by changing the gradients of all 6 quadrupoles in between, namely QC13 to QC18. The changes aim to reduce the beam size at two critical locations of the beamline (without displacing any of the elements): QC13 which defocuses the beam in the horizontal plane so that the x-plane limits the beam transmission. And K18, which is the collimator partly located inside QC18 with a limited aperture of ± 45 mm in both planes. The required gradient changes represent at maximum 30 % departure from the values currently utilized in operation and are largely within the reach of the existing magnets as has been verified and tested in the control room. In addition, the beam matching conditions at Target E are well fulfilled with the new optics.
2) The second step consists in performing parametric scans of the collimators aperture and determining the region with lowest power deposition on triplets 1& 2 as it is shown in Figure 8.11.

	KHM0	KHM1	KHM2
Horizontal aperture entrance [mm]	11.5	15.5	21.80
Horizontal aperture exit [mm]	14.65	18.21	25.62
Vertical aperture entrance [mm]	11.5	25	32.37
Vertical aperture exit [mm]	14.65	29.37	38.04
Longitudinal position entr [cm]	25	115	160
Longitudinal position exit [cm]	55	145	190

Table 8.2: Optimum collimators apertures for TgH region, displaying half the total width of the collimator. The longitudinal positions are with respect to the target impact location.

From Figure 8.11, it can be seen that the power depositions on both triplets can be reduced below 0.5 kW. Triplet 1 is the bottleneck of the beamline between TgH and TgE and its entrance shall be properly shielded although the power depositions are almost evenly distributed inside. In the present situation, it is estimated that the power deposited inside is 0.1 kW which is nearly five times lower than with Target H. As mentioned earlier, due to presence of the defocusing quadrupole at the entrance of triplet 1, a larger fraction of the beam is cut in the horizontal plane than in the vertical one to enable a larger beam transmission to TgE. Nevertheless, given that all magnets for both triplets are radiation hard, this shall not pose a problem. However, it must be verified that the present cooling system can stand the 0.5 kW power deposition from the 2 mA beam which will reach 0.75 kW at 3 mA.

In summary, the optimized collimators apertures are listed in Table 8.2. All these elements are made of copper which is a high Z material that can absorb particles efficiently. In addition, the outer width of the collimators was chosen to contain at least 2/3rd of the power depositions in its immediate surroundings. The position of the elements is yet another parameter that had to be optimized. In order to leave enough space for the profile monitor preceding QC13 and for the shielding to be effective in protecting the quadrupoles, the optimum choice was to place KHM1 & KHM2 in the same vacuum chamber nearly midway between TgH and QC13 entrance. This design is similar to the already existing one (KHE2 and KHE3) in Target E region. More details regarding the geometry layout can be found in Section 8.5.3. The power deposited on KHM1 and KHM2 amounts to 9.9 kW and 1.2 kW for the 2 mA beam as is shown in Figure 8.11.

Regarding the profile monitor, the power deposited in the aluminum part (shown in blue) amounts to ~70 W in the vicinity of the target. The vacuum chamber on the other hand shall withstand power depositions amounting to ~400 W/m which requires adequate cooling quite similar to the already implemented one in the vicinity of Target E.

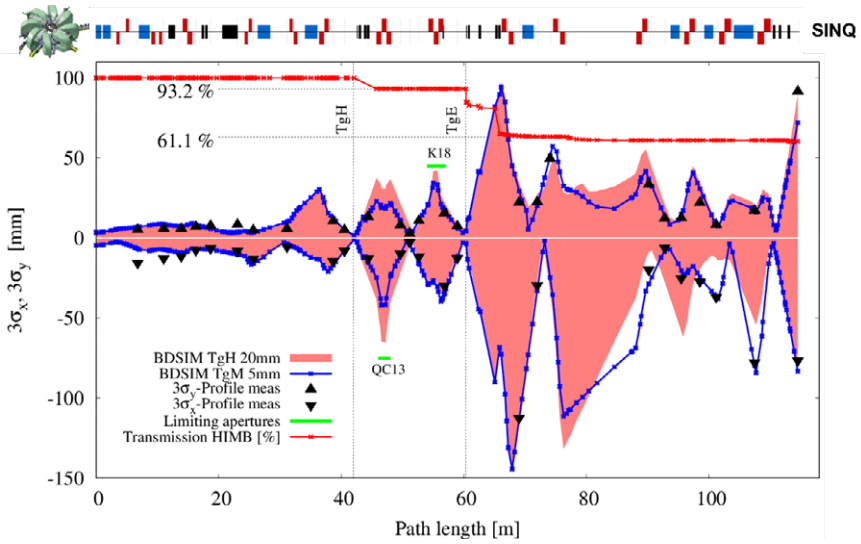

Figure 8.12: Comparison of the transverse beam envelopes obtained with the slanted TgH and with the standard TgM.

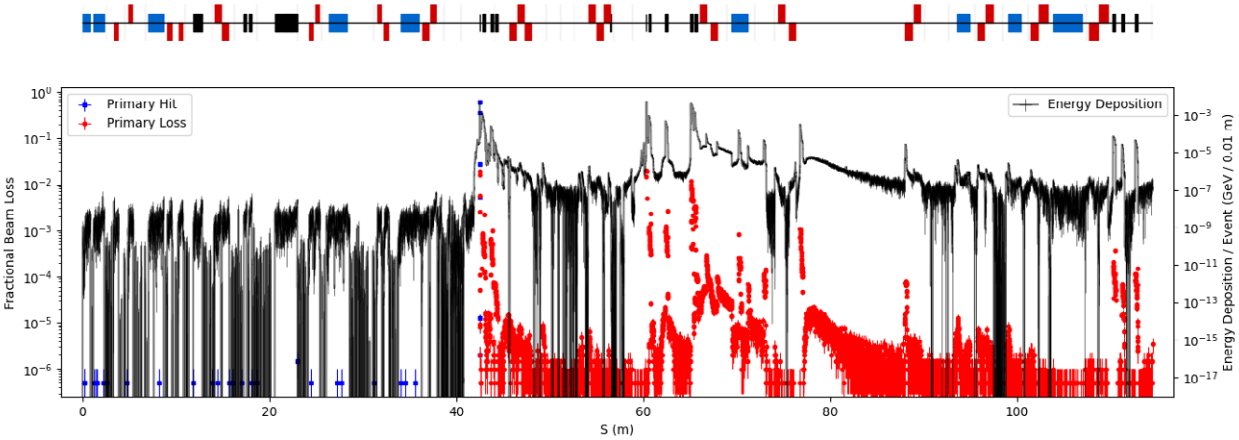

Figure 8.13: Energy deposition and beam losses chart from the ring cyclotron to SINQ target.

8.4.4 Beam Envelopes and Transmission

The main consequences of the new Target H on the part of the beamline following Target E are:

1) The beam loses 8.45 MeV of its energy after impacting TgH in comparison with the 2 MeV energy loss with the existing Target M. Such an additional energy loss shall be corrected by lowering the bending fields of all magnets downstream of Target E. The field change amounts to -0.7 % and is a necessary condition for the beam to reach SINQ.
2) For the same extracted current from the cyclotron, the fraction reaching Target E is 5 % lower with TgH in comparison with TgM.

Since the beam matching conditions are almost identical at Target E, both consequences imply that the absolute beam losses and the power depositions on Target E and its set of collimators will be lower with the new Target H. Nevertheless, the beam energy spread with TgH is nearly a factor of two higher than with TgM. Thus, the optics start to differ after the first bending magnet following Target E, namely AHL, as is illustrated in Figure 8.12. This impacts the power depositions on the slits KHNY21 and KHNX22 which may need to be opened slightly more: KHNY21 is placed inside the first magnet bending the beam vertically, namely AHL, while KHNX22 is located right afterwards as is shown in Figure 8.2. In addition, it should be verified that those slits can with-

	Target M		Target H	
	Primary beam losses [%]	Energy depositions [kW]	Primary beam losses [%]	Energy depositions [kW]
Target E	8.2	41.7	7.7	39.22
KHE0	1.86	27.55	1.82	26.34
KHE1	1.90	16.99	1.62	14.44
KHE2	13.3	137.25	10.50	107.40
KHE3	3.7	31.98	2.84	23.94
1st doublet QG21-22	1.074	8.49	0.92	7.79
1st bend AHL	0.77	6.28 (5.31 to KHNY)	1.76	16.92 (15.11 to KHNY)
KHNX slits	0.09	0.82	0.33	2.84
2nd doublet QG23-24	0.001	0.006	0.0049	0.092

Table 8.3: Power depositions comparison in the SINQ beamline following Target E assuming a 2 mA proton beam.

stand a few kW of additional power deposition. Given that those slits were originally introduced to protect the beamline from the possible fraction of the beam that could scatter off Target E collimators and deposit its energy in the subsequent elements, it is important to keep this aspect in mind during the commissioning. Since it is envisaged to use a slanted target type in the Target E station, which already demonstrated an increase of the surface muon rate of 30–50 %, the beam positioning on the target is more relaxed. In addition, a new development with grooves on the inner and outer side of the target, will certainly help to immediately detect a beam offset from the target center with high sensitivity [Kiselev, 2021a].

The complete layout of the optics along with the beam transmission and energy deposition is summarized in Figure 8.12 and Figure 8.13 where we can see that the fraction of the beam reaching SINQ target amounts to 61% of the total incoming beam from the cyclotron. This represents a downgrade of 4 % only in comparison with the existing TgM. The reason lies in the fact that the newly introduced collimators after TgH will cut a large fraction of the halo beam that would have been cut otherwise by Target E collimators. Figure 8.12 also gives a comparison of the optics with the present 5 mm TgM and the 20 mm TgH. In Figure 8.13, the losses along the beamline are shown. A comparison of the power depositions of the most absorbing or critical components is given in Table 8.3.

8.4.5 Sensitivity Studies to Misalignment Errors, Beam Size and Density Variations of the Target

One of the important questions to tackle is how sensitive the beam losses are to different sources of imperfections in the beamline. To answer this, each element of the beamline is transversely (horizontally and vertically) shifted randomly using a Gaussian distribution with a standard deviation σ_{err} and a cutoff at $\pm 2\sigma_{err}$: for each misalignment error σ_{err}, 30 different patterns are generated and a source of imperfections is assumed. For instance, the beam transmission from ring cyclotron to SINQ is illustrated in Figure 8.14 where the source of imperfection is due to horizontal beam size variations σ_x at injection: With reasonable misalignment errors $\sigma_{err} \leq 1$ mm, the transmission is essentially unchanged. However, the latter is more sensitive to the horizontal beam size. An increase of 40 % of σ_x drops the transmission by about 1%. This proves that, under realistic misalignment errors, none of the existing or newly designed elements in the beamline will be intercepting a substantial fraction of the primary beam, which is crucial to avoid frequent interlocks of the machine.

Figure 8.15 shows the power depositions on two of the most sensitive elements of the beamline: Collimator KHM1 and triplet 1. The trend is quite similar to the beam transmission. However, the sensitivity to the horizontal beam size variations at injection is more pronounced: An increase of 40 % of the horizontal beam size yields an increase of ~20 % of

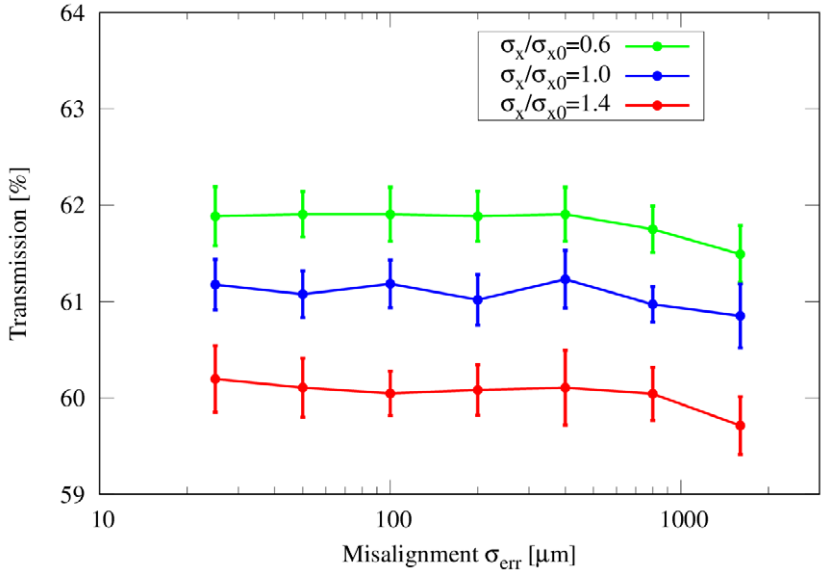

Figure 8.14: Total beam transmission to SINQ as a function of the random transverse misalignment errors. The three cases correspond to different horizontal beam sizes at injection i.e. at extraction from the main ring. The reference case, in blue, corresponds to the beam conditions at injection that matches with the 2 mA beam profile measurements.

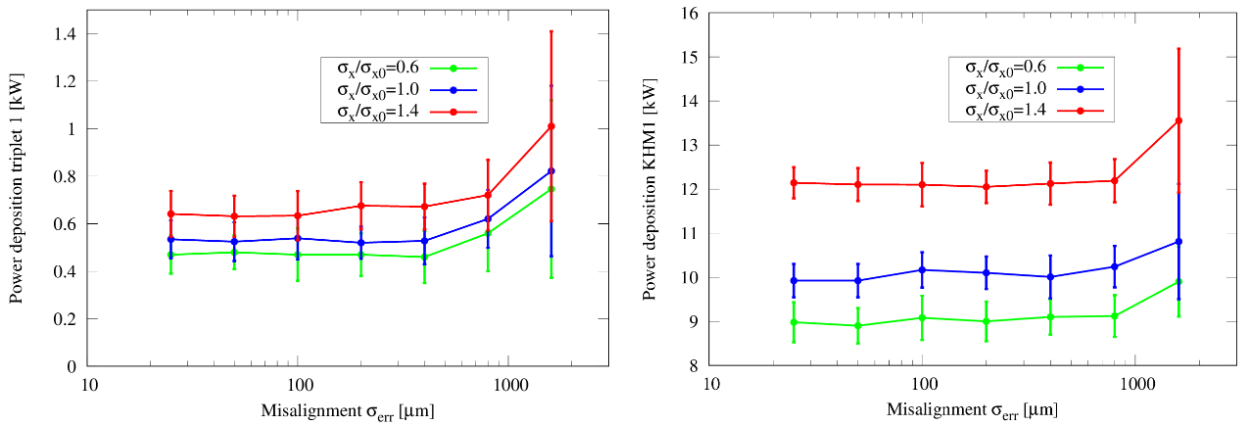

Figure 8.15: Total power deposition on KHM1 (left) and triplet 1 (right) as a function of the random transverse misalignment errors. A 2 mA beam is assumed.

the localized power depositions. This is expected since KHM1 is designed to cut a fraction of the horizontal beam halo that might deposit its energy on the first triplet (see Figure 8.11). In addition, the misaligned quadrupoles kick the beam transversely, which can enhance the losses. This problem can be further alleviated once the steering magnets are activated to correct the motion of the beam centroid and the focusing of the quadrupoles adjusted to reduce the beam sizes. However, in order to maintain the power deposition on triplet 1 below the 0.5 kW level with the 2 mA beam, the misalignment errors shall remain below ± 0.8 mm (which is equivalent to $\sigma_{err} < 0.4$ mm) as is shown in Figure 8.15.

The same analysis is repeated where the initial vertical beam size, the initial energy spread as well as the density ρ of the target material are varied.

In order to assess the impact of each source of imperfection on the losses, the relative change of the power deposition P for a specific element of the beamline can be expressed as follows:

$$d\ln P = \frac{\partial \ln P}{\partial \ln \sigma_x} d\ln \sigma_x + \frac{\partial \ln P}{\partial \ln \sigma_y} d\ln \sigma_y + \frac{\partial \ln P}{\partial \ln \sigma_E} d\ln \sigma_E + \frac{\partial \ln P}{\partial \ln \rho} d\ln \rho + \cdots$$

where we assume no correlations between the different variables. The above expression can be rewritten in the following simpler form:

$$\frac{dP}{P} = A_x \frac{d\sigma_x}{\sigma_x} + A_y \frac{d\sigma_y}{\sigma_y} + A_E \frac{d\sigma_E}{\sigma_E} + A_\rho \frac{d\rho}{\rho} + \cdots$$

where the coefficients A_i measure the strength of the imperfection. A similar expression can be defined for the total beam transmission T_r to SINQ:

$$\frac{dT_r}{T_r} = B_x \frac{d\sigma_x}{\sigma_x} + B_y \frac{d\sigma_y}{\sigma_y} + B_E \frac{d\sigma_E}{\sigma_E} + B_\rho \frac{d\rho}{\rho} + \cdots$$

The above coefficients are then calculated for each element of the beamline and the results listed in Table 8.4 for the most sensitive elements: Clearly, the most sensitive elements are the ones between TgH and TgE. As discussed earlier, any beam size imperfection originating from the injection shall be cut by the set of collimators belonging to TgH and thus will not reach the elements downstream TgE. In addition, the sensitivity to vertical beam size variations is negligible. However, such is not the case with the horizontal beam size and the energy spread at injection, which nearly have the same influence on the power depositions. This stems from the fact that the horizontal apertures are lower than the vertical ones (see Table 8.2) to protect the triplets downstream. However, to further reduce the coefficients A_x and A_E, it may be of advantage to aim for an elliptically shaped transverse beam spot on TgH such as an increased vertical size and a decreased horizontal one.

Furthermore, it is of particular interest to notice that the density of the target material plays the most important role in determining the power depositions at all locations as well as the beam transmission to SINQ as illustrated in Figure 8.16: This can be explained by the fact that the spread of

	P [kW] @ 2 mA	A_x	A_y	A_E	A_p
TgH	18.9	~0	~0	~0	1.1
KHM0	22.9	0.006	0.006	0.006	1.14
KHM1	9.9	0.50	~0	0.48	2.13
KHM2	1.2	0.52	~0	0.57	1.23
Triplet 1	0.5	0.43	~0	0.61	0.48
Triplet 2	0.1	0.29	~0	0.56	2.01
TE	39.2	~0	~0	~0	1.03
KHE0	26.3	~0	~0	0.003	0.82
KHE1	14.4	0.10	~0	0.031	2.18
KHE2	107.4	0.12	~0	0.058	1.17
]QI26, KHN31[	0.9	~0	~0	~0	0.51

Table 8.4: Sensitivity of the power depositions to beam size variations, momentum spread and target density variations. The first column lists the reference values where no imperfections are assumed.

	B_x	B_y	B_E	B_p
Transmission	-0.043	-0.001	-0.026	-0.94

Table 8.5: Sensitivity of the SINQ beam transmission to beam size variations, momentum spread and target density variations.

the beam escaping from the target is proportional to the square root of the density. All losses downstream are subsequently following the increase/decrease of the losses on target. Although it is of major advantage to enhance the target thickness in order to gain more surface muons, our design of the collimators is based on the assumed graphite density of 1.84 g/cm^3 that is slightly above the measured ones. This shall be checked again once the new targets are manufactured since an increase of the density can be expected in the future. In particular, it is important to recall that the bending magnets as well as the focusing quadrupoles after each target are set up for a specific average beam energy. This implies that any change in the target thickness and/or material density shall be compensated by adjusting the optics for the new beam energy. In case of substantial change, the thickness of the target can be reduced to compensate for the increase of its density and vice-versa.

Another effect regarding the target is the deformation of the segment due to the thermo-mechanical stress induced by the high power beam on the target: As shown in Section 9.2.4, the thermal response of the target to an impinging 2.5 mA proton beam leads to a bending of the long sides of the target segments of ± 0.15 mm and a 10 times smaller effect on the centre of the segment. This corresponds to an increase of its thickness from 2 mm to 2.015 mm which slightly reduces the density of the target material. However this effect is negligible.

In summary, the expected transmission to SINQ is stable under realistic misalignment errors and beam size variations as shown in Table 8.5.

Target misalignment is yet another important imperfection that needs to be accounted for. A leading source of misalignment is the angular deviation between the incident proton beam trajectory and the target axis from the ideal one. Such an effect dominates when the angular deviation is around the Y-axis as illustrated in Figure 8.17 since it alters the effective thickness d of target material that the beam will travel

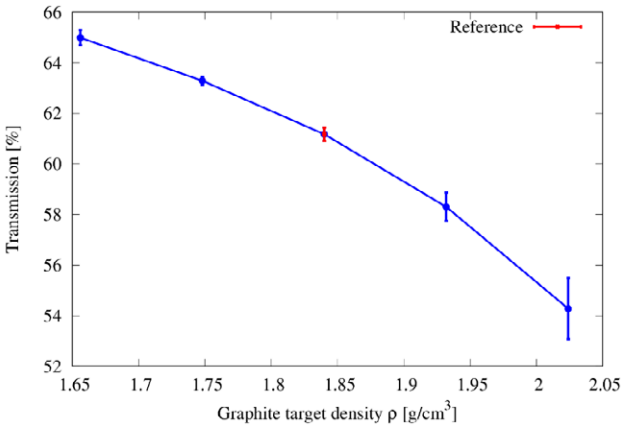

Figure 8.16: Total beam transmission to SINQ as a function of the density of target material (TgH + TgE). The reference value used for all calculations is shown in red.

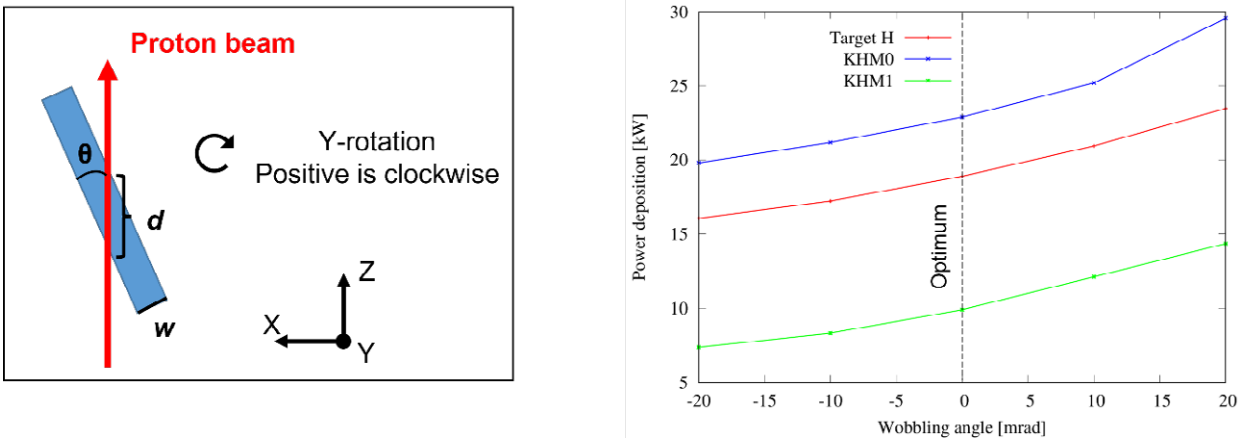

Figure 8.17: Impact of the wobbling angle on the power depositions. On the left hand side, a simplified schematic depicts the slanted target configuration where the wobbling angle is defined as the deviation from the ideal slanted angle θ.

through. From basic trigonometric rules, it can be shown that $d = w/\sin(\theta) \sim w/\theta$ where w is the target thickness and θ is the slanted angle which is approximately equal to 104 mrad in the present design. As a consequence, the effective thickness is inversely proportional to θ and any imperfection due to coherent horizontal oscillations or to the deviation of the target axis from the ideal one can yield larger or lower losses depending on the sign of the deviation. An additional effect is the bending/deformation in parts of the target segment due to thermo-mechanical stress issues as described earlier. Such an effect leads to the wobbling/fluttering of the power deposition as well as the beam transmission. Defining the wobbling angle around the most sensitive Y-axis as $d\theta = \theta - \theta_{ref}$, the impact of such an imperfection on the power deposition is calculated for the first three elements of the TgH beamline. As shown in Figure 8.17, the change is nearly linearly scaling with the wobbling angle such as:

$$\frac{dP}{P}[\%] = \frac{d\theta}{\theta}[\%] \approx d\theta[\text{mrad}]$$

This implies that, in order to adjust the power depositions variations due to beam and/or target wobbling to the levels between ±5 %, the angular deviations around the vertical axis shall be controlled to the levels between ±5 which is set as our constraint.

8.4.6 Intensity-dependent Effects

As established earlier, the impact of the vertical beam size variation on the beam losses is negligible. Thus, in order to assess the predicted power depositions for the 3 mA operation, it is crucial to estimate the expected horizontal beam size increase from 2 mA to 3 mA. For this reason, the radial beam size extracted from the 590 MeV ring was measured at various currents in order to infer a simple law to extrapolate it to 3 mA. The result is shown in Figure 8.1. A simple quartic fit of the beam size versus the current shows that, when extrapolating from 2 mA to 3 mA, the horizontal beam size shall increase by ~15 %. This is in agreement with the much simplified model that, under matching conditions, the space charge dominated beam occupies a sphere whose volume is nearly proportional to the current i.e. $\sigma_x \alpha I^{1/3}$. This is valid for the 72 MeV injector 2 cyclotron [Stammbach, 2001], [Baartman, 2014], [Kolano, 2018]. Although the beam is subsequently accelerated in the 590 MeV ring and transported towards the different target stations, the previous scaling law still applies for the final acceleration stage as is shown in Figure 8.1. To first order, one can also assume that the beam energy spread shall increase due to the longitudinal space charge forces. Such an increase is non-trivial to predict given that the power of the RF cavities of the main ring will be renewed for the 3 mA case in order to achieve less turns to the same final energy, compatible with larger turn separation, which at the same time reduces beam

losses and consequently activation. In addition, the flattop cavity shall be replaced and tuned to compensate for the linear energy spread. However, we can pessimistically assume an increase by 15 % as well. This finally yields for the energy depositions in the different parts of the beamline:

	P [kW] @ 2 mA	*P* [kW] @ 3 mA
TgH	18.9	28.4
KHM0	22.9	34.4
KHM1	9.9	17.0
KHM2	1.2	2.1
Triplet 1	0.5	0.9
Triplet 2	0.1	0.2
TE	39.2	58.8
KHE0	26.3	39.5
KHE1	14.4	22.0
KHE2	107.4	165.4
]QI26, KHN31[	0.6	0.9

	2 mA	3 mA
Transmission [%]	61.1	60.7

Table 8.6: Comparison of the power depositions and transmission for 2 mA and the 3 mA case.

Furthermore, the SINQ transmission reduces by nearly 0.5 % when increasing the beam current from 2 mA to 3 mA.

8.4.7 Required Diagnostics for Safe Operation

The protection of the beamlines, the target stations as well as the collimators from the high power proton beam is of utmost importance. At 590 MeV, it takes about 10 ms to cause a meltdown of the beamline components with a missteered beam having a transverse distribution comparable to the ones at Target M and Target E [Dölling, 2005]. This could result in about 1 year of shutdown, if there is no spare part. Therefore, a fast and redundant interlock system, called machine protection system (MPS, see Section 8.5.8) is in place to detect such losses and switch off the beam fast enough. Based on the PSI experience acquired over more than 40 years of operation [Rohrer, 2005], [Dölling, 2005], [Reggiani, 2020], several types of diagnostic elements will ensure the safe and reliable operation with the new TgH station:

- *Beam profile monitors* (see Section 8.5.4.1): They are used temporarily to tune the optics and also improve the understanding of the beamline, e.g. when comparing to simulations.
- *Beam position monitors (BPM)* (see Section 8.5.4.2): The new profile monitors are combined with a BPM. The BPM's at both target stations are used for automatic centering the beam on Target E, i.e. they are part of the proton beam trajectory control loop.
- *Current monitors* (see Section 8.5.4.4): They serve to determine the beam transmission at the different target stations. Such elements are regularly calibrated and of particular importance to prevent the possibility of having a fraction of the beam bypassing the target. An interlock is generated whenever the losses deviate significantly from the usual ones. All current monitors are already in place, i.e. no additional one is necessary.
- *4-segment aperture foil* (see Section 8.5.4.3):A thin four-sector aperture foil with measurement of the secondary emission currents is provided at the entrance of several collimators. An overly offset beam can be detected from the sector signal current ratios. By comparing the sector signal currents to a measurement of the full beam current, an overly focused or defocused beam can be detected. Aperture foils are in use for several of the collimators and beamdumps in HIPA.

The following diagnostic elements will be installed for safe operation of the Target H beamline, i.e. protection of all components from damage:

Upstream of the Target H:

- The two new vertical steering magnets are each followed by a horizontal/vertical BPM/profile monitors system. If a steering magnet fails or the capture solenoid current is changed accidentally, there will be an interlock, i.e. immediately (within ms) the beam is switched off. There are two systems for redundancy, if one fails: Monitoring the magnet current and the beam losses on the four-sector aperture monitor shall allow this.
- An aperture foil to protect the target chamber in case of missteered beam will be installed close to the entry of the chamber.

At the Target H:

- A very narrow collimator embedded in the target cooling plate and preceded by a 4-sector aperture foil. This collimator is not only equipped with thermocouples but also measures the secondary emission current created by the beam passing through it, which can trigger a fast interlock.

Downstream of the Target H:

- A set of three copper collimators (KHM0-2) shields the following beamline components and reshapes the beam after scattering off the Target H. KHM0 is a fully new element whereas KHM1-2 replace the existing ones at different positions. Each collimator is preceded by a 4-sector aperture foil and equipped with at least four thermocouples to protect the collimator from damage.
- Two BPM/Profile monitor sets currently developed by the proton diagnostic group (information and pictures can be found in: [Dölling, 2019]) will be installed between Target H and the first triplet as is shown in Figure 8.8. The first set represents a new diagnostic element and will be located between KHM0 and KHM1. The second new set that shall be installed after KHM2 will replace the currently existing one MHP/MHS23-24. Two devices are installed for redundancy and check of the profile before the KHM2&3 and after it, where the beam is cut by the elliptical aperture. Those elements will be useful to tune the optics whenever the fringing field of the solenoids changes due to the needs of the secondary beamlines. Due to their proximity to the targets, the power depositions on the profile monitors were calculated for later adequate cooling (see Section 8.4.3). With the two BPM's a tilt of the beam can be easily detected online and corrected with the steering magnets. After Target E the second one is missing, which makes it more difficult to align the beam.

In addition, the machine protection system will get the signal coming from the beam loss monitors as well as magnet currents (see Sections 8.5.4 and 8.5.7). By properly setting the interlock thresholds, one will be able to avoid damaging the vacuum pipe and/or any other beamline element in case of failure. In addition, including the BPM in the interlock system is under consideration.

A similar situation occurs in the vicinity of Target H where the new steering magnets compensate for the fringing field emanating from the capture solenoid. Since those magnets are correlated, their current cannot be set-up independently. Should the field of one or both capture solenoids change for some reason (like changing the muon momentum in one or both of the secondary beamlines), then the fields of both vertical steerers will be changed along in a well prescribed way. This will be done by means of a so-called "Super knob" similar to the one in use in the Target E region which correlates the fields of AHU, AHV and AHSW41 magnets. Thus, their current will be monitored constantly.
More details regarding the diagnostic elements and the machine protection system of the proton beamline can be found in Section 8.5.4 and 8.5.8.

8.5 Beamline Components

With the new graphite Target H about 5 m of the beamline will be replaced and therefore will require some new elements.

8.5.1 Magnets

The only new magnets needed for the proton beamline are two steerers that will be installed upstream of Target H. The main purpose of these new elements is to compensate for the vertical beam tilt introduced by the fringing field of the muon capture solenoids. The first of them will replace the currently installed SHA11Y, whereas the second will have to be installed at 1.6 m distance from Target H, just upstream of or inside the shielding block. Since the strength of this magnet will be larger than the one provided by common HIPA steerers (see Section 8.4.1), these magnets will have to be designed from scratch. Besides providing the compensation for the capture solenoids fringing fields, these steering magnets will also be part of the proton beam trajectory control loop. This system relies on the information provided by BPMs at different beamline locations in order to feed the steerers with the correct current and keep a stable beam trajectory.

Figure 8.18: Beam Dump 1 hanging on the 60 t crane.

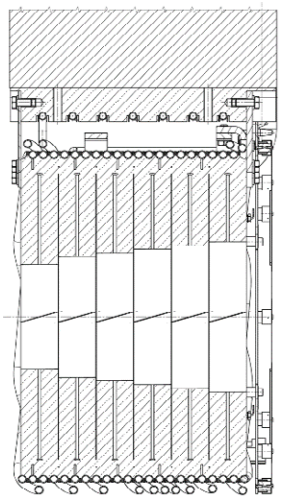

Figure 8.19: Drawing of a cut along the beam dump BHE1.

Figure 8.20: Beam Dump 1, assembling of the aperture.

8.5.2 Powering

The difference in power consumption between the present and the future situation is expected to be negligible.

8.5.3 Collimation System

8.5.3.1 Collimation System after Target H

The collimator system is designed like other collimators or beam dumps which have been used in the proton beamline for many years. The design is shown in the following Figure 8.18, Figure 8.19, Figure 8.20.

8.5.3.2 Technical Design & Manufacturing

The heart of the collimator is the copper block, which is positioned in the beam. This part is made out of six copper disks (see Figure 8.19), which are later brazed to each other. The copper is produced according to a detailed specification, which describes mainly how the copper has to be forged and thermally treated.

After each disk is pre-machined, they are pulled together with a threaded rod. Then the helix grooves for the cooling tubes are milled into the surface. Holes were drilled in order to hold the brazing wires in position (see Figure 8.21 and Figure 8.22).

After the milling, the disks are cleaned and the cooling tubes are wound around in the helix grooves (see Figure 8.23). The cooling tubes are made from stainless steel 316L and coated with a thin copper layer (thickness 20 µm). This layer is required to make sure that the brazing material properly moistens the tubes.

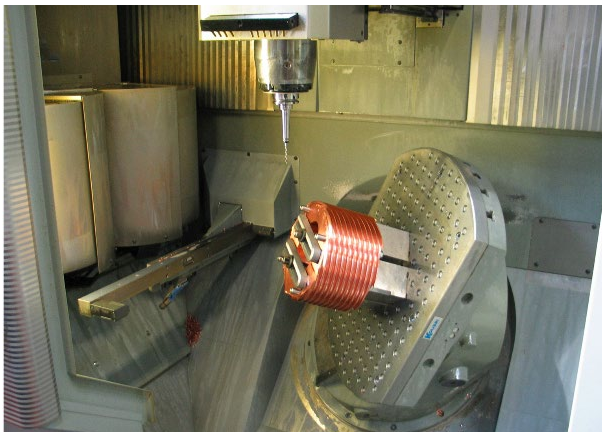

Figure 8.21: Milling of the helix grooves into the mockup collimator.

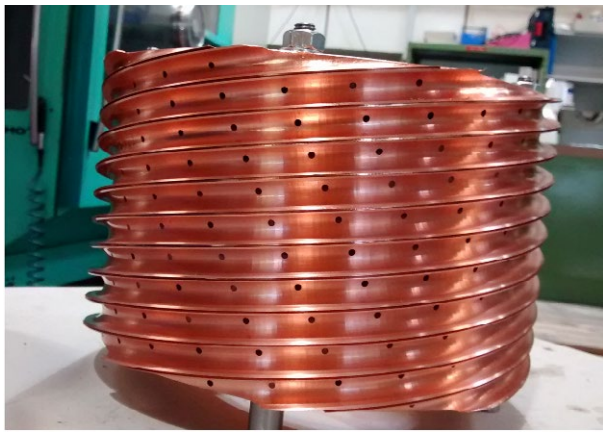

Figure 8.22: Mockup collimator with brazing holes.

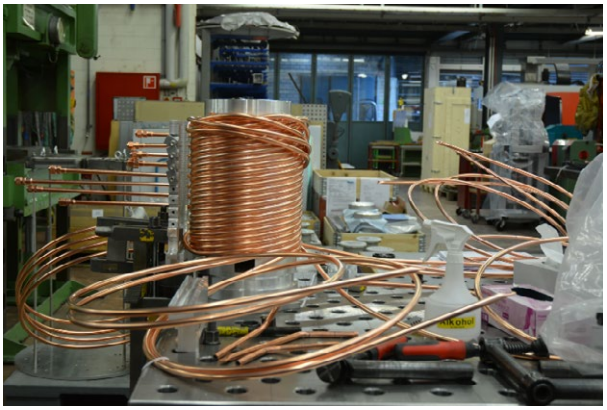

Figure 8.23: KHE2 copper block after winding.

Figure 8.24: Mockup collimator in the vacuum oven after brazing.

The brazing is done in a vacuum oven above 800 °C (see Figure 8.24). The sheet metal provides a homogenous distribution of heat in the oven during the brazing process.
After the vacuum brazing the cooling efficiency, i.e. how fast a hot copper block is cooled down with a certain cold water flux, is measured. At the same conditions an ANSYS simulation is performed assuming an ideal thermal contact between the tubes and the copper block by brazing. A deviation of the measurement from the simulation then indicates how well the brazing is done. This is used as quality assurance.
After confirmation of sufficient thermal contact by the measurement (see Figure 8.25), the tubes are welded to the collector tube (see Figure 8.26). At the same time the cooling plate will be connected via the large collector tube to tubes of the copper cylinder.
After welding the tubes, another thermal measurement will be done, like it was done for the cupper bloc. This is the final measurement and a function test to be sure that all thermocouples work fine.
After that, all other parts of the insert like the shielding and 4-segment aperture foil are assembled (see Figure 8.20). The aperture foil is a diagnostic element, which helps determinig the beam position (see Section 8.5.4.3).

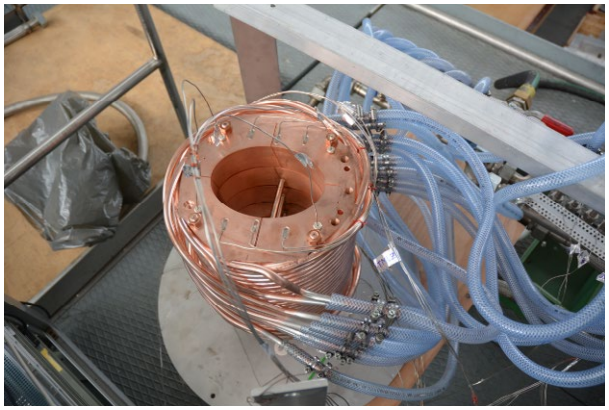

Figure 8.25: KHE2.3 copper block, thermal measurement.

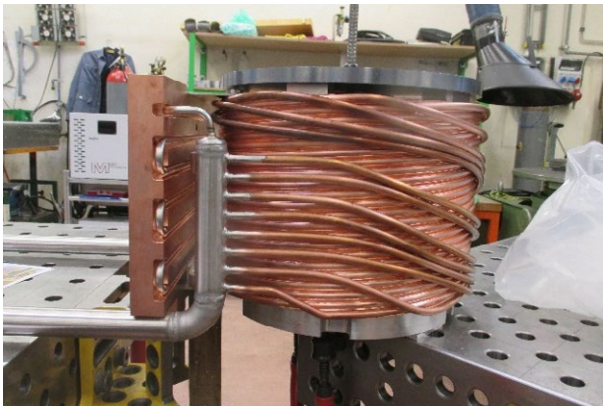

Figure 8.26: Beam Dump, with welding completed.

8.5.3.3 Design with respect to cooling

In 2014, the ANSYS software package was used to determine whether the design of the KHE2 and KHE3 collimators could be improved to withstand a 3 mA proton beam thermally. Simulations were performed in steady-state configuration with an imposed convective heat transfer coefficient and the material properties for non-irradiated oxygen free copper (OFE). The optimization procedure briefly described in section will also be implemented for the thermal design of KHM0, KHM1 and KHM2.

8.5.3.3.1 KHE2 and KHE3 geometries

Downstream of Target E and before the bending magnet (AHL), four collimators are located. KHE0 and KHE1 mainly absorb the scattered secondary particles produced by the proton beam hitting Target E. KHE2 and KHE3 with their elliptic opening are responsible to shape the optimal beam profile for low loss beam transport to the neutron spallation source SINQ. Each collimator is 30 cm long and constructed of six OFE disks, each with a thickness of 50 mm and connected together with four bolts (see Section 8.5.3.2 for details). Each collimator is actively cooled by water. The collimator system composed of KHE2 and KHE3 absorbs approximately 14 % of the total proton beam power, with KHE2 receiving the highest power load of more than 100 kW from the divergent beam.

8.5.3.3.2 Material properties

All material properties used in simulations are for non-irradiated oxygen free copper (OFE). The OFE mass density was assumed to have a constant value of 8'960 kg m^{-3}. Isotropic thermal conductivity and specific heat capacity at constant pressure have a temperature-dependent behavior. Values originate from an experimental investigation performed at PSI and a survey of literature [Deutsches Kupferinstitut, 2005] [CDA, 2010].

8.5.3.3.3 Thermal equation and boundary conditions

The source term in the heat conduction equation, $\dot{g}$, can be expressed as:

$$\dot{g}(x,y,z) = \frac{dE}{dz}(z) \left[\frac{I_0}{2\pi\sigma_x\sigma_y} \; e^{-\frac{(x-x_0)^2}{2\sigma_x^2}} \; -\frac{(y-y_0)^2}{2\sigma_y^2} \right]$$

where $\frac{dE}{dz}$ represents the power deposited in the solid by the protons per unit length per unit current along the beam path and the term in square brackets is the current density of the proton beam, which has the typical double Gaussian distribution. A proton current, I_0, of 3 mA on Target E was used in simulations with a transmission factor of 0.88 due to 40 mm graphite and the beam parameters $\sigma_x = 29.5$ mm and $\sigma_y = 26.3$ mm corresponding to the beam parameters measured during the 2008 running period. In order to estimate the term $\frac{dE}{dz}$ and the divergence of the beam at each mesh node an APDL script was implemented based on former calculations [Heidenreich, private comm.]. A Monte Carlo simulation was done on a flat and horizontal volume of OFE and imported in ANSYS. The ANSYS script estimates the penetration of the beam in the solid in Z direction assuming that Target E location is far away and the beam traversing the solid can be thought to be parallel to the Z axis. In Figure 8.27, the sketch of the cross section of 2 disks in a quarter of the geometry is presented. The beam path through the

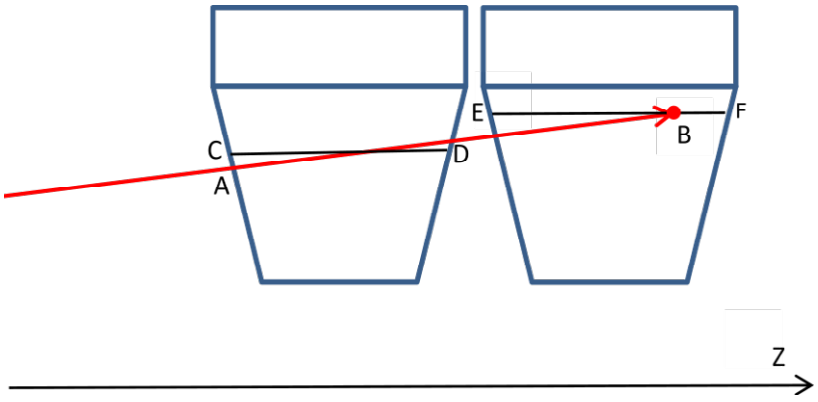

Figure 8.27: Sketch of the cross section of 2 disks in a quarter of the geometry. Beam path, in red, impinging on mesh point B.

solid body, from point A to point B, is approximated by the sum of the linear segments CD and EB using trigonometric relations. The divergence of the beam from Target E to point B is taken into account by scaling-up σ_x and σ_y at the front of the target to the location of the mesh node B.

When the effective penetration length of the beam through the solid body, z_{eff}, is known, the term $\frac{dE}{dz}(z_{eff})$ can be obtained by looking at the corresponding value in the Monte Carlo input data. If needed, a 1D interpolation is performed on two neighboring data points.

An effective convective heat transfer coefficient corresponding to 8 m/s at 118 mm radius inside the body was used instead of the convective heat transfer coefficient on the internal surface of the pipes. In this way, the pipes were not included in the simulation, which dramatically reduces the mesh size and computation complexity. The total pipe length around one collimator is 4 meter. The effective convective heat transfer coefficient for the water flow conditions relevant to KHE2 and KHE3 was taken from reference [Heidenreich, 2009].

8.5.3.3.4 Numerical implementation and mesh

The starting point was to simulate the thermal response of the collimators geometry in operation in 2014 for a proton beam current of 3 mA. Since the maximum temperature reached a too high value, see next section, a so-called "Goal Driven Optimization" was performed. ANSYS is capable of optimizing a given geometry by iteratively changing input parameters such as angles and lengths in order to achieve certain goals, e.g. maximum temperatures in some specific locations. OFE can undergo phase transition, from α phase to β phase, which will reduce its ductility. Half of the melting temperature in Kelvin (homologous temperature) was decided to be the upper temperature limit during the optimization procedure, which is 405 °C. An initial mesh of about 972'362 elements was used and dynamically adapted to each geometry through the optimization process.

8.5.3.3.5 Results

In Figure 8.28 the temperature field at 3 mA proton beam current of the original design and the thermally optimized configuration, the latter with aligned and misaligned beam of 1 mrad, are presented in a cross section plane parallel to the beam direction for a quarter of the full collimators. The

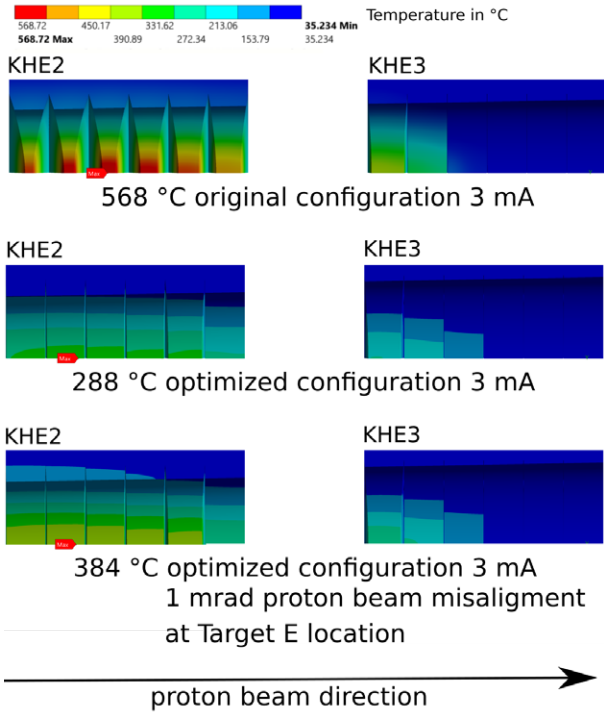

Figure 8.28: Temperature field at 3 mA proton beam current of the original and thermally optimized configurations, the latter with aligned and misaligned beam of 1 mrad, in a cross section plane parallel to the beam direction for a quarter of the full collimators.

misalignment is assumed at Target E location. The optimized configuration is a converging in KHE2 and diverging in KHE3 shape configuration. When the ellipsis front side half-minor axis is larger than the ellipsis back-side half-minor axis, the configuration is called convergent configuration. The opposite case is called divergent configuration. Moreover, the optimized configuration has the back side ellipsis area of KHE3 26.6 % larger than the original one. The original configuration clearly exceeds set temperature limit of 405 °C. The optimized configuration does not exceed the threshold temperature even accounting for 1 mrad proton beam misalignment at Target E location.

8.5.3.4 Power distribution on the collimator system after Target H

In addition to the results obtained with BDSIM/Geant4 (see Section 8.4.3) the energy deposition in the KHM0,1 and 2

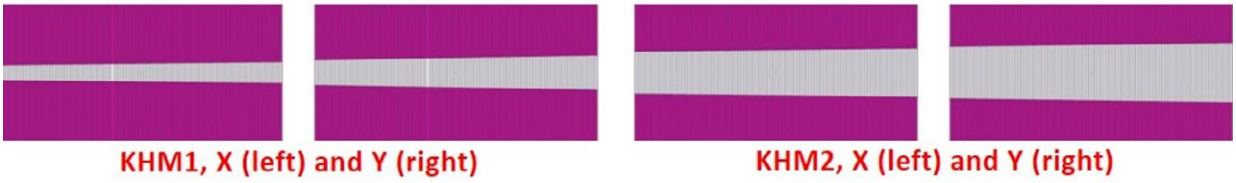

Figure 8.29: MCNP model of the elliptical openings of the KHM1 (left) and KHM2 (right) collimators in the X and Y planes. X is the horizontal plane and Y is the vertical one.

collimators at the target station was estimated by the MCNP version 6.1 [Goorley, 2017], since this is the simulation the design of the cooling will rely on. To this end, the simulation of the secondary particle fluxes relied on the reference HIMB geometry model. The KHM1 and KHM2 collimators have been simulated as having elliptical conical openings in both X and Y planes. Figure 8.29 shows the implementation of the elliptical collimators in the MCNP model. Table 8.2 gives the dimensions of the opening for all three collimators KHM0, 1 and 2.

Figure 8.30 shows the distribution of the energy deposited in the components of the proton beamline including KHM0, 1 and 2 collimators, calculated with MCNP on the Z-X plane for 1 proton incident on the target. Out of three collimators the largest amount of the energy is deposited in the KHM0. For the proton beam current of 2 mA it is 20.3 kW. For the next collimators KHM1 and KHM2, the amount of the deposited energy is significantly lower, 8.8 kW for KHM1 and 1.3 kW for KHM2, respectively. In addition, 8.4 kW is deposited in the local shielding surrounding the KHM0. The MCNP results are in good agreement with BDSIM/Geant4 energy deposition calculations as is shown in Section 8.3.2 and Table 8.6.

8.5.4 Diagnostics Elements

Beam diagnostic elements installed in the proton channel provide information on beam size, position, current and losses. This information is of utmost important during beam commissioning and the set up. Moreover, the delivered signals are employed by the Machine Protection System (MPS) to trigger a machine interlock in case one or more parameters exceed some predefined threshold.

The diagnostic devices already installed are BPMs, beam profile monitors, segmented aperture foils, beam loss monitors and beam current monitors. With few modifications, these elements will keep playing a central role also during the commissioning of the HIMB beamline.

8.5.4.1 Beam Profile Monitors

The proton channel is equipped with 54 Beam Wire Profile Monitors (27 for each transverse plane). They are present in all beam line sections, including the SINQ beam line.

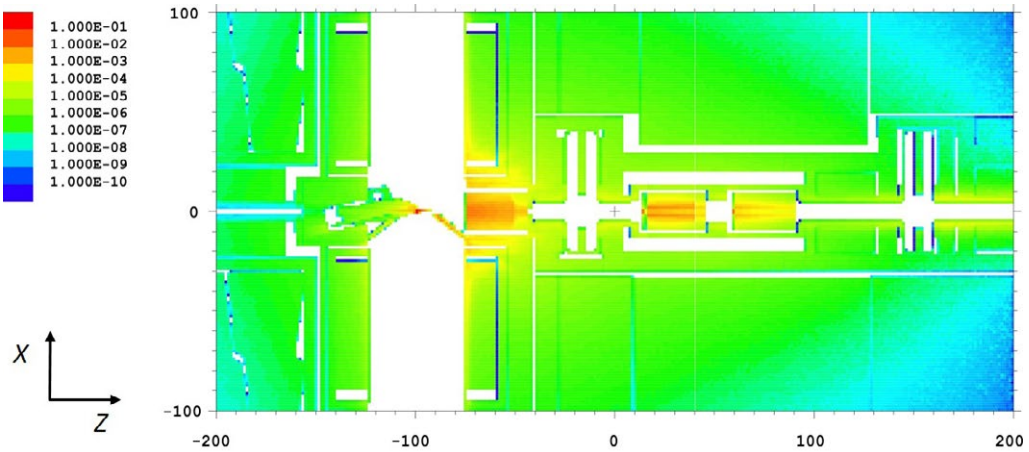

Figure 8.30: Distribution of the deposited energy, (MeV per 1 proton on the target) on the Z-X plane in the components of the proton beamline.

Profile Monitors are very useful during commissioning, set up and tuning since they can be used to determine the beam optics through envelope reconstruction. On the other hand, Profile Monitors are not useful for the Machine Protection System since they are run "on demand" and cannot provide therefore constant information.

8.5.4.2 Beam Position Monitors (BPMs)

Currently, 32 BPMs are installed in the proton channel between the Ring Cyclotron extraction and Target E, 16 for each transverse plane. They use inductive pick-up loops with an aperture of 100 mm and working frequency of 101.26 MHz (two times the bunch repetition rate of 50.63 MHz). Their resolution at 2.0 mA is in the order of 0.2 mm [Keil, 2006]. BPMs are key components of the beam centering system which monitors the beam trajectory and apply corrections whenever needed. In the proton channel this is an essential tool since it ensures that the entire beam goes through the very narrow Target M and Target E. If even a very small portion of protons (in the percent level) missed Target E, this could have very serious effects on the SINQ target since the un-scattered protons would still reach SINQ and build an hot-spot which could lead to a mechanical damage of the target itself. At PSI each BPM pair is embedded in the same enclosure containing a Profile Monitor pair. A new modular concept is being developed [Dölling, 2020] which will be employed also for the two BPM/Profile Monitors to be installed downstream of Target H. A drawing representing the device under development is shown in Figure 8.31.

8.5.4.3 Aperture Foils

Segmented aperture foils are made out of thin-sheet metal of nickel and located at the upstream end of collimators. These annular-shaped foils, usually divided into four sectors, detect protons impinging on the foil via secondary emission electrons, i.e. electrons, which are produced by the protons in interactions, mainly by ionization. They provide qualitative information about beam width and position and the delivered currents can be correlated to the temperatures measured in the corresponding collimator sector. Their signals are employed by the Machine Protection System. On one hand, an overly off-axis beam can be detected from the sector signal current ratios. On the other hand, by comparing the sector signal currents to a measurement of the full

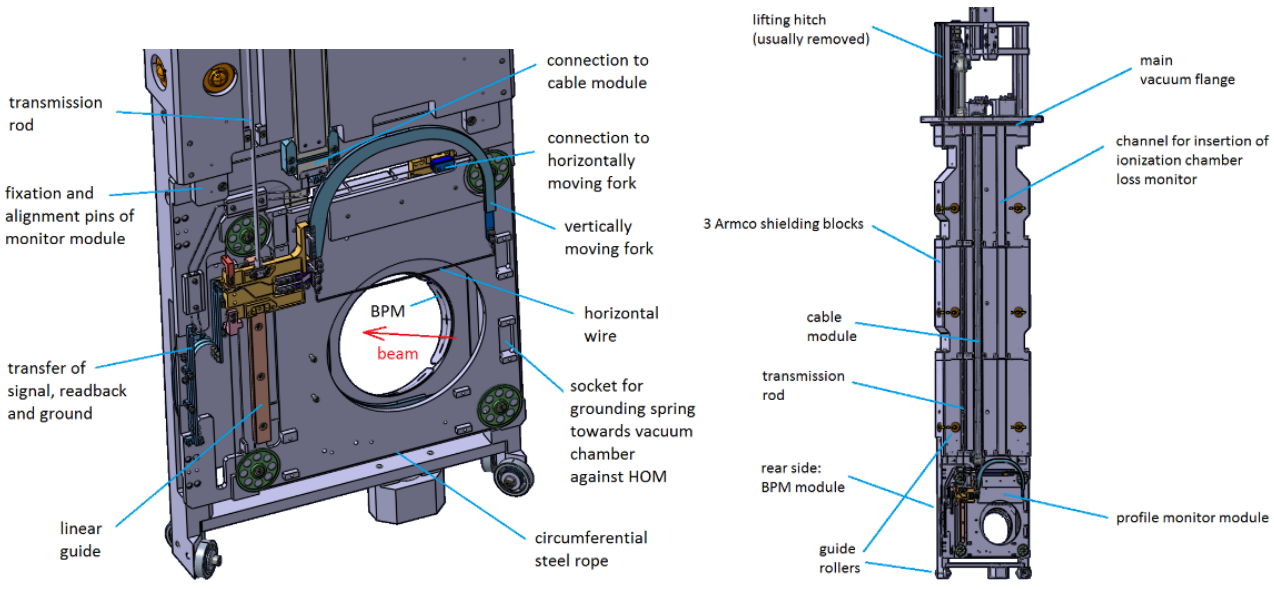

Figure 8.31: Profile monitor module.

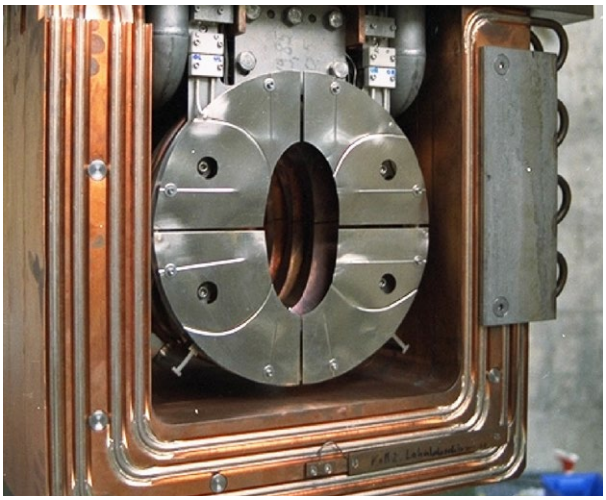

Figure 8.32: Aperture foil MHB6 installed at the upstream end of collimator KHE2.

beam current, an overly focused or defocused beam can be detected. The aperture foil of one of Target E collimators is displayed in Figure 8.32.

8.5.4.4 Beam Current Monitors

The proton channel is equipped with eight beam current intensity monitors. Six of them (MHC1-6) are fast resonators which need frequent calibration whereas two are current transformers (MHC2b and MHC6b) providing an absolute intensity measurement used to calibrate the resonators. At full current of about 2 mA, the resolution of the beam current monitors is 1 µA. The accuracy of the current transformers is 5 µA. Signals delivered by current monitor pairs can be combined in order to evaluate the beam transmission through a certain beamline section, especially through Target H and Target E. This measurement is particularly important in order to ensure that no protons are missing the targets. The design of the HIMB proton beam line does not foresee any change of the beam current monitors.

8.5.4.5 Beam Loss Monitors

Beam Loss Monitors (BLMs) are ionization chambers filled with air and placed in the vicinity of the beam tube. Around 50 BLMs are installed in the proton channel. BLMs are very fast devices (response time of the order of 2 ms), hence their signals are employed by the MPS in order to trigger a machine interlock as soon as one or more thresholds are exceeded. Since the beam losses depend on the beam current, the MPS provides dynamic windows for the loss threshold. This ensures the beam losses to stay within the allowed range (neither too high nor too low) during beam ramp up or whenever the beam current needs to be changed. No new beam loss monitors are planned for HIMB.

8.5.5 Cooling System

All components close to the beamline like the three new collimators KHM0-2 will be cooled by water. The cooling will be provided in a similar way as in the present system. The cooling water is supplied from a central station (see Section 12.4) with a maximum pressure of 11.1 bar and reduced by a diaphragm usually in front of the component to the desired flux. In case of very low pressure, the diaphragm can be also installed behind the component to avoid cavitation. Components like collimators with high power deposition and therefore high water flux have their own water circuit, others like the local shielding are connected in series. The water flow is controlled by a flow switch.

In order to prevent overheating from beam energy deposition, the whole beam pipe up to the upstream end of the quadrupole triplet QHTC13-15 will be also cooled by water. This differs from the present situation, where no cooling has been foreseen due to the tiny effect on the beam emittance given by the 5 mm thick Target M. All vacuum chambers are cooled as well.

8.5.6 Vacuum System

Concerning the vacuum system, no conceptual changes are expected with respect to the present situation. Flanges, which are in the shielding, are connected by an inflatable seal, also called pillow seal. Once placed between two flanges by remote handling, the pillow seal is inflated by means of compressed air until its two metal foils get pressed onto the down- and upstream flange respectively.

8.5.7 Control System

The control system presents a central part of all large facilities. Its main task is to integrate the autonomous controllers that are distributed throughout the facility into one coherent

infrastructure. The control system provides an abstraction layer between hardware and the operators, and creates the environment that allows scientists to carry out their experiments. It also enables the technical support groups to compare previous data with current one in order to enhance the performance of their systems. Guidelines for the design of the control system are ease of use, reliability, and security. Beyond its pure functionality, the maintainability of the whole system and the portability for new developments in computer science are basic requirements.

All of these basic design features can be achieved by the setup of a framework that covers both hardware and software parts. Inside the framework, single components of the Control System can be optimized and thoroughly tested to reach a high reliability. The expandability is coupled to the clear definition of interfaces between the parts of the framework. The maintainability of the control system can be optimized when there is an agreement on the use of standardized components for both hardware and software. In addition, the interfaces provide means to adapt to new technologies in the future.

The main challenge of the IMPACT project for the control system is the integration into the existing control systems of the proton accelerator on the one hand and the new requirements and technical progress on the other hand. Therefore, the IMPACT control system will be rooted in the existing system while at the same time providing the capability to grow in order to accommodate new possibilities and developments.

8.5.7.1 The EPICS Framework

The control system will use the EPICS (Experimental Physics and Industrial Control System, described on https://epics-controls.org/) toolkit. Using a standard software toolkit will allow us to make the best use of in-house know-how and to consolidate technical support services. Due to its collaborative nature, using EPICS enables us to take advantage of work done at other laboratories. The Controls group will develop EPICS further to adapt the well-known system to the new challenges and possibilities of modern computer hard- and software.

Control system applications must be designed to enable future upgrades and easy maintenance. Well defined interfaces to support the modular upgrade and replacement of code is a key component of this requirement. The EPICS architecture used at PSI provides such interfaces, from the connection to the hardware, over network protocols, up to the unified access to process variables. The software used to implement High Level Applications will attempt to accomplish the same level of modularity.

8.5.7.2 Software Environment

The architecture of the control system software infrastructure will be based on experiences from other PSI accelerator facilities like the existing HIPA setup and the new developments of SLS 2.0 but it will be adapted to the new needs of IMPACT.

The basis for operator applications will be the Python programming language and the caQtDM display manager. To integrate the new systems seamlessly into the existing HIPA control system, we will upgrade the general software tools to include the new devices.

The expert groups, e.g. the beam dynamics and diagnostics team or the experiment scientists, will provide application software which requires a deep understanding of either accelerator physics or the experiments. Where applicable, automated procedures will relieve the user from administrating the software manually.

8.5.7.3 Hardware Strategy

At the proton accelerator HIPA the hardware controllers are still exclusively based on VME. This concept has been revised already for other facilities at PSI and is replaced by a toolbox approach. The changes in computer technology result in different classes of devices that will be handled each by a different approach:

- A hardware toolbox will be provided for both
  - Simple devices that need no real-time capabilities and no connection to a global timing and event system.
  - Moderate to demanding devices that need real-time capabilities or connection to a global timing and event system.
- Devices that come with a network or serial interface like vacuum gauges and PLC systems will be integrated by using dedicated network protocols communicating directly with EPICS servers running on virtual machines in the server room. This group of devices has grown substantially

over the last decade and increases both the required number of network ports and the overall network traffic.
- Highly demanding devices are developed for IMPACT according to specific and unique requirements. For the later integration of such devices into the control system, the controls experts will accompany the developments already during the design phase.

In addition, a timing and event system will be needed to handle the beam transport to TATTOOS. The basic concept will be based on the experiences with the UCN facility.
The machine protection system of HIPA will be expanded to include both parts of the IMPACT project and ensure a safe operation of the facility. Access to radiation protection areas and person safety is handled independently from the control system by a dedicated Person Safety System (PSYS) that solely grants read-only access to all other systems.

8.5.8 Machine Protection System (MPS)

The philosophy of the MPS will not differ substantially from the one already implemented [Mezger, 2010]. For the HIMB beamline particular care must be paid to the protection of the Target H chamber as well as the graphite target itself since in this region the beam is extremely narrow and can melt stainless-steal in about 10 ms time. Moreover, the beam path towards the target wheel is hindered by two main constraints:

- The beam vertical trajectory is strongly affected by the fringing field of the two muon capture solenoids. The strength of their field depends on the required particle momenta in the secondary beamlines.
- The beam path will go through a narrow aperture in the cooling plate located upstream of the interaction point where a Densimet® protection collimator will be placed. An aperture foil at the upstream end of the collimator will provide the signal for the MPS. In addition, the collimator temperature as well as the electric current flowing through it will be monitored. Both these parameters shall be minimized during beam operation and thresholds shall be implemented above which the MPS would trigger a machine interlock.

The MPS generates a beam interrupt in case the beam trajectory deviates significantly from the ideal case. For example, the aperture foils attached to each collimators (the one upstream plus the three downstream of the Target H) deliver signals for the MPS. An additional aperture foil could be installed upstream of the target chamber. Simulations are being carried out in order to assess the need for it.
The beam trajectory control system, making use of BPMs and steering magnets will be in charge of keeping the beam position stable within 0.2 mm tolerance.

8.6 Commissioning and Operation

Before starting the beam commissioning, the interlock thresholds of all relevant parameters will be set to very conservative values in order to prevent damage of machine components due to wrong beam setting.
The commissioning of the HIMB proton beam line will be carried out in steps of increasing beam intensity starting at very low current (around 20 µA). The capture solenoids shall be ramped to their nominal values for surface muon production.
The first thing that must be carefully checked is that beam optics and trajectory are such that the beam safely crosses Target H and Target E and reaches the SINQ target with the proper footprint. The optics in the beam sections between Target H and Target E as well as between Target E and SINQ shall be reconstructed by fitting beam profile measurements with tools like TRANSPORT [Rohrer (TRANSPORT)] and MINT [Baumgarten, 2021], both available in the control room. If necessary, the beam optics and the interlock thresholds will be adjusted.
At this point, the beam current can be slowly increased to around 100 µA. During this ramping, beam transmission and losses shall be constantly monitored. At 100 µA, optics and trajectory must be checked again. Once all parameters are considered to be acceptable, the current can be slowly ramped further to 200 µA, where a new optics/trajectory check will be carried out. This procedure shall be repeated in steps of 100 µA until the nominal beam current will be reached.

9 Target Station

9.1 Present Situation

The original design dates back to 1985. The 85-cm steel shielding plug is placed upstream of the target and is not accessible during beam operation. The rim of the target is about 2-cm wide with a thickness of 2 mm. As the beam passes through the rim at an angle of 22.5°, its effective thickness is 5.2 mm (see Figure 9.1 left). The power deposition is about 2.4 kW/mA and the target operates at around 1100 K, mainly cooled by thermal conduction. The target insert is mounted horizontally, which has the advantage that the rotating shaft is long and the two bearings are well shielded. This results in bearing lifetimes of several years. In 2012/13 a new target insert was designed and installed in the beamline (see Figure 9.1 right). To increase the bearing lifetime by improving the cooling, an additional water-cooled copper plate was attached to the front of the shielding plug close to target and beam. The rotating shaft is made of low conducting material, titanium-vanadium, to reduce the heat flux from the target to the bearings. In the 2013 design, the bearings can be exchanged without changing the target by pulling the shaft through the shielding plug. Further improvements in the maintenance and handling of the vacuum seal at the rear of the target insert were implemented in the new design.

As Target M has a much smaller thickness, and the bearings are far from the beam and placed in the shielding, the irradiation environment is much less challenging than for Target E and the future Target H.

9.1.1 Activation and Dose Rates

Activation and remnant dose rates at the existing target station were estimated by the MCNPX version 2.7.0 [Pelowitz, 2011] simulation of the secondary particle fluxes using a detailed CAD model that includes the target station, two quadrupole triplets, the downstream drift space to target E and the concrete shielding around the proton beamline [Kiselev, 2015a]. Figure 9.2 shows the 3D view of this model. Figure 9.3 shows the cross-section of the CAD model of the target station as implemented in MCNP. In the MCNP simulation the produced residual nuclei and spectra of the neutrons with the energies below 20 MeV were scored. The output of the MCNP simulation has been processed by the Activation Script [Gallmeier, 2007] and the nuclide inventories of the components of the target station have been calculated using FISPACT [Forrest, 2007]. To estimate the dose rate present at the time of dismantling the target station M it is assumed that the present target station is in operation until the year 2026 at an averaged beam current of 2 mA. Two subsequent cooling periods were assumed, of 1 month and of 6 months, two different realistic start days of the dismantling process after the shutdown.

MCNP simulations for the following four configurations/ cases of the components of the target station have been performed to estimate the remnant dose rates at the target station from the produced unstable nuclides:

1. No dismantling: all the components stay on place
2. Partial dismantling, excl. vacuum chamber: the insert of the target M and collimators are taken out, the vacuum chamber of the beamline stays on place

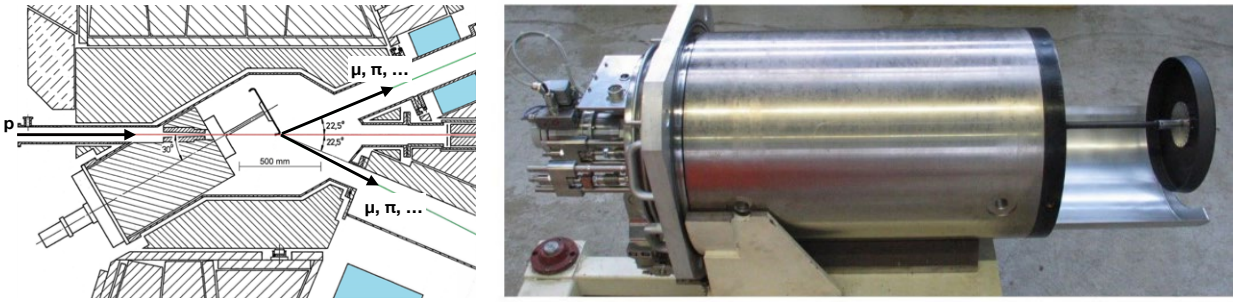

Figure 9.1: Left: Schematic view of the Target M insert at beam height. Right: Target M insert, new design.

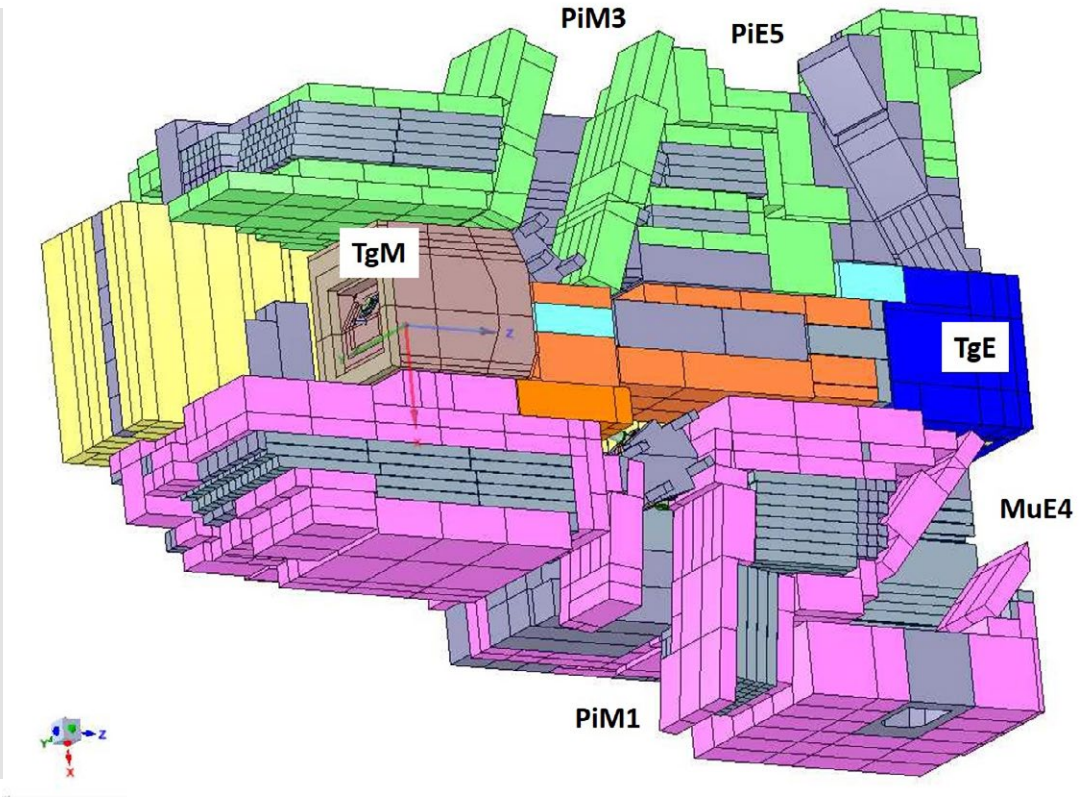

Figure 9.2: 3D view of the CAD model of beamline components and shielding of the proton channel PK2 from Target M to Target E (bottom view from the side of Target M). Beam moves in z-direction.

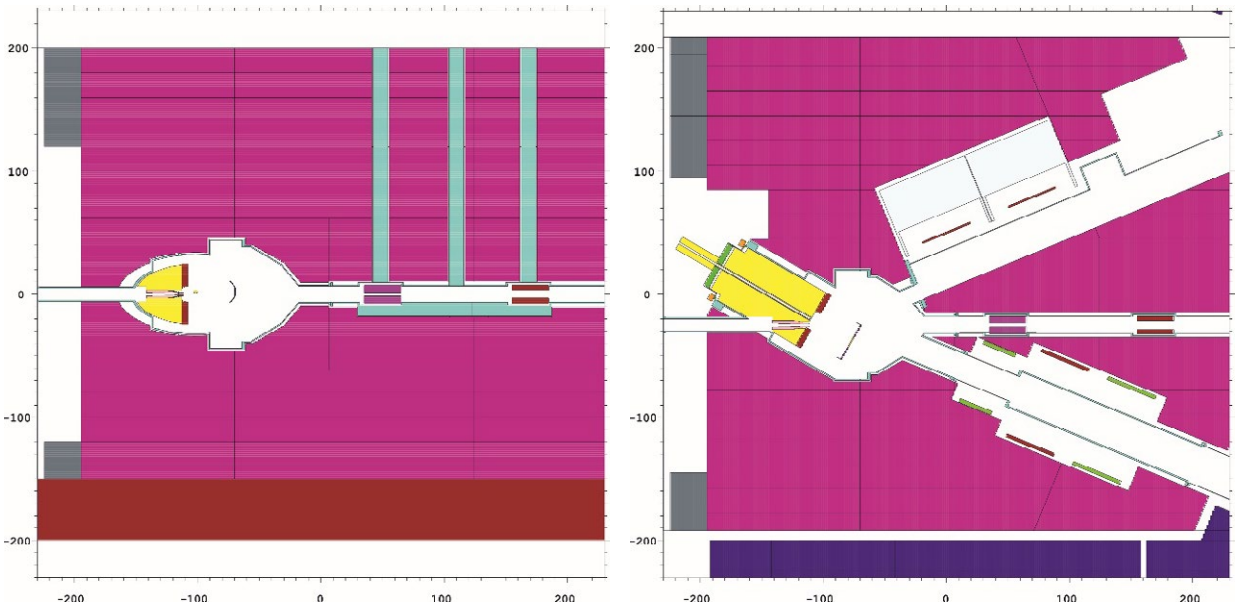

Figure 9.3: Vertical in Z-Y-plane (left) and horizontal in Z-X plane (right, view from the bottom) cross-sections of the MCNP model of the target station. Coordinate scale in cm.

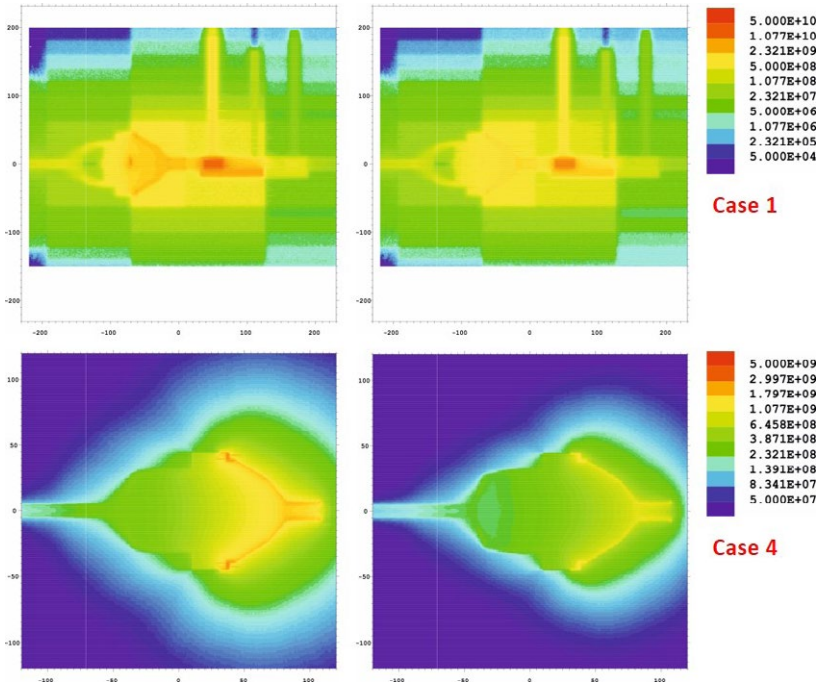

Figure 9.4: Remnant dose rate (pSv/s) on the vertical Z-Y-plane centered at the position of the beam for two cooling times of 1 month (left) and 6 months (right), for the case 1 (top) and for the case 4 (bottom). Coordinate scale in cm.

3. Partial dismantling, incl. vacuum chamber: only the iron shielding (purple blocks in Figure 9.3) stays on place
4. Vacuum chamber only: additionally the dose rate from the fully retracted vacuum chamber of the target insert has been estimated

Figure 9.4 shows a comparison of the remnant dose rate at the target station between the case 1 and the vacuum chamber only configuration (case 4). Maximal dose rates at the target station for all four cases are given in Table 9.1. After partial dismantling, including vacuum chamber, the dose rate becomes a factor of 10 smaller. Waiting for another 5 months of cooling allows for obtaining the remnant dose rate lower by 30 % at least and by almost a factor of 2 in some cases.

Figure 9.5 shows a comparison of the remnant dose rate at different heights along the target station for the cases 1, 2 and 4. Maximal dose rates for three considered cases are given in Table 9.2. The activated shafts of the collimators define the remnant dose rate on the top of the target station at the height of 3.5 m as Figure 9.5 shows. This shall be considered an artefact of the simulation, since the region of the shafts were not segmented, i.e. the average dose rate is shown independent of the distance from the beamline.

Case	Cooling time	
	1 month	6 months
No dismantling	39.2	21.9
Partial, excl. vacuum chamber	10.7	5.8
Partial, incl. vacuum chamber	4.0	2.9
Vacuum chamber only	8.8	4.9

Table 9.1: Maximal dose rate (Sv/h) on the vertical Z-Y plane for four calculated cases and two cooling times.

h (m)	No dismantling	Partial, excl. vacuum chamber	Partial, incl. vacuum chamber
1	3.67	3.68	6.06
1.5	39.17	10.30	4.18
2	4.29	4.25	6.00
2.5	4.14	4.13	0.26
3	4.12	4.11	0.09
3.5	1.02	1.01	0.08

Table 9.2: Maximal dose rate after 1 month cooling time (Sv/h) on the horizontal Z-X plane at the various height, for three different configurations of the component of the target station.

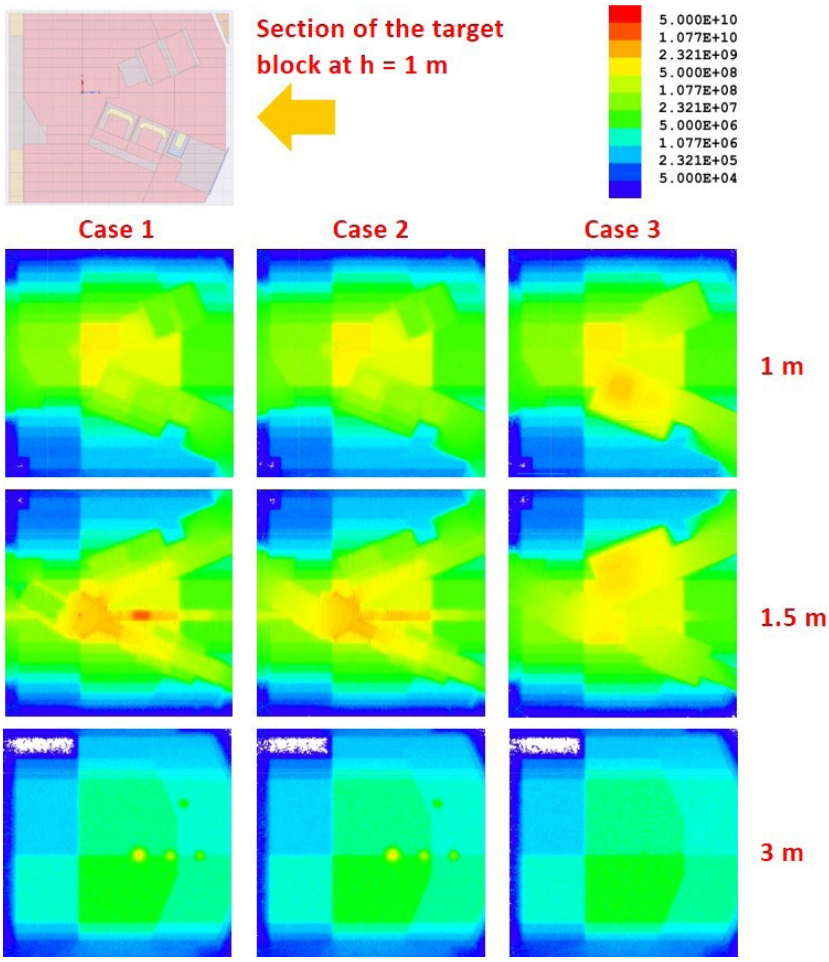

Figure 9.5: Remnant dose rate after 1 month cooling time (pSv/s) on the horizontal (in Z-X-plane) section at the various distance from the bottom of the target station, for three different configurations of the components.

At the same time, Table 9.2 shows that at the height of 3.5 m which is at the top of the target station the remnant dose rate is less than 3 % of the maximal dose rate. Going deeper inside the target station the maximal dose rate in the "full" and "partial" cases remains almost the same of 10 % of the maximal dose rate until one reaches the height of the beam plane at 1.5 m where the highly activated components of the proton beamline and secondary beamlines are located.

A separate MCNP simulation has been performed to estimate the dose rate at the floor of the experimental hall, after the target station will be shut down and completely dismantled. Under the same assumption of the operation of the target station until the year 2026 as above, the maximal dose rate at the floor at the shutdown equals to 21 mSv/h and drops to 55 µSv/h and then to 44 µSv/h after 1 month and 6 months of the cooling time, respectively.

For a detailed personal dose rate planning (Section 11.1) for the dismantling and handling of the radioactive components and shielding blocks, the actual dose rates according to the dismantling plan will be calculated as well.

9.1.2 Radioactive Waste

The amount of the radioactive waste at shutdown has been estimated for the whole HIPA facility, for the present layout of the facility (at year 2014), assuming operation until the year 2058 at the maximal beam charge per year of 10 Ah followed by 10 and more years of cooling time [Kiselev, 2015a]. It has been found that the components of the target station M will inevitably become radioactive waste. Figure 9.6 illustrates this conclusion.

The components of the target station that will become radioactive waste can be broken into following categories:

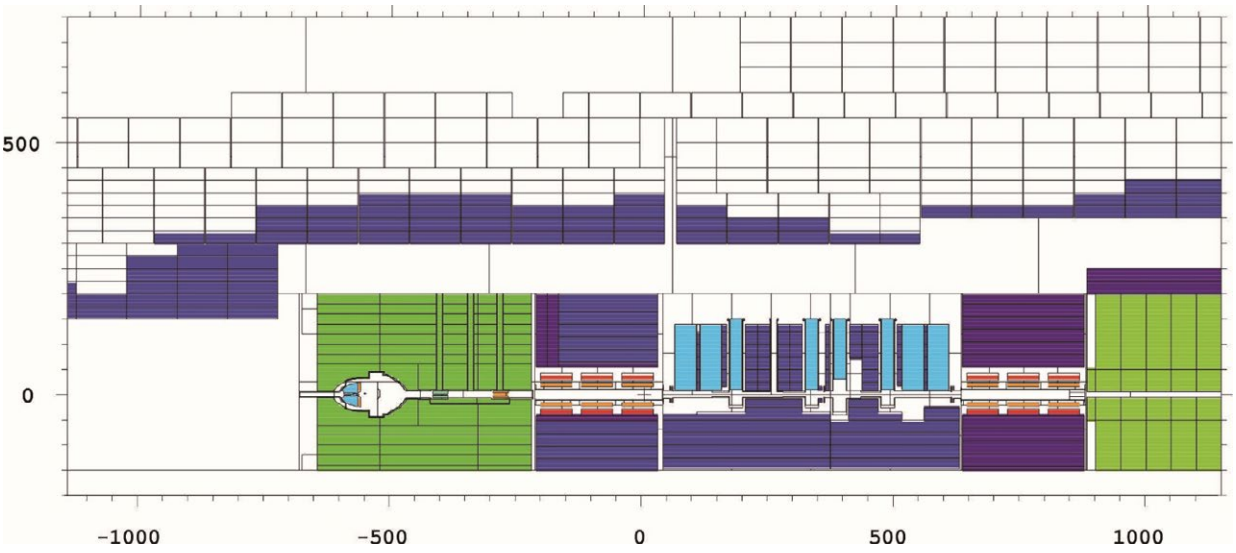

Figure 9.6: Example of the distribution of the radioactive waste at the target station and downstream beamline, assuming operation until year 2058 followed by 40 years of cooling time: vertical Z-Y section of the MCNP geometry where only the cells that will be considered as radioactive waste are shown in color. Coordinate scale in cm.

1. Marble, the last layer of the shielding downstream from the target
2. Iron, of the shielding blocks around the target and of the shielding inside the vacuum chamber of the collimators
3. Iron, of the yokes of the magnets that are inside the shielding of the target station
4. Stainless steel, from the vacuum chamber, the beamlines and the vacuum chamber of the collimators
5. Copper, of the coils of the magnets and of the collimators

As can be seen from Figure 9.6, the whole target block will be radioactive waste.

9.1.3 Disposal

As can be seen from the previous section, all shielding blocks and components, which cannot be reused, have to be disposed as radioactive waste. Therefore, the aim is to reuse as much as possible already activated shielding blocks. The components, which cannot be reused, are the two collimator inserts, the profile monitor, two target inserts (see Figure 9.1 right), all vacuum chambers and six magnets as well as specially shaped shielding blocks. Magnets with a reasonable dose rates, could be saved as spares in the active storage, WAKA, at PSI.

The highly activated collimator blocks made of copper with a dose rate of about 100 Sv/h will require a primary lead-shielded canister. Such a concept is already in preparation for the old collimator KHE2 with a few 100 Sv/h. The lid of the canister will be welded with a welding equipment, which can be handled in the shielded service cell ATEC at PSI by manipulators. This concept is similar to the disposal of SINQ targets – except that the SINQ targets are poured with LBE for shielding purposes in addition. As PSI has still a stock of lead ingots, they can be filled in the canister in case of a too high dose rate, however, this case is not expected. The lower part of the profile monitor located after Target M consists of a thick piece of copper, which was recently taken out and measured to a dose rate of 0.5 Sv/h.

The vacuum chambers consists of stainless steel. Some of them, the target chamber and the first collimator KHM1, are cooled with water tubes made of stainless steel. The tubes are fixed using melted Aluminum, which was sprayed around them. This Aluminum cannot be removed from the surface. However, NAGRA, the SWISS agency responsible for the final repository, poses a limit of 24 kg Aluminum per waste container. The mass of Al on the surfaces is around 7–16 kg/m^2. For the target chambers 40–80 kg Al, for the KHM1

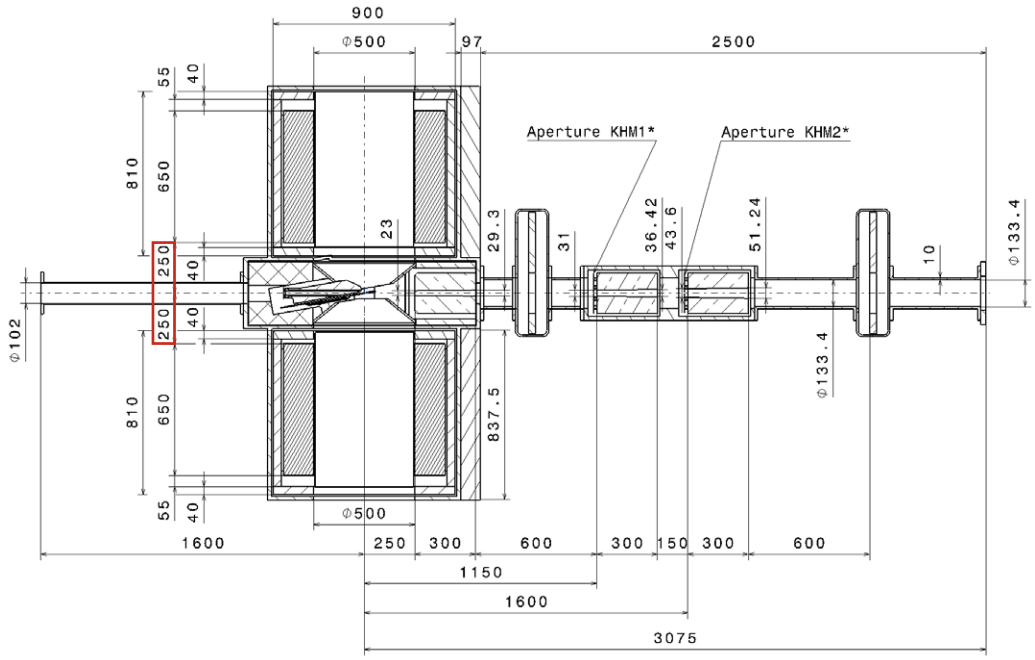

Figure 9.7: Target station from the top at beam height.

chamber 15–25 kg are estimated. More accurate estimates can be performed, when the chambers are inspected in ATEC. Difficult to reuse are shielding blocks with special shapes. Some are made of a stainless steel canister, which was filled with waste of pieces from steel of the former Target M station.

From the measurement of contamination with ^{124}Sb on the working level it is expected that lead sticks between the shielding blocks were used to block the air flow from outside keeping the required underpressure in the target block. Lead does not pose a problem for the disposal.

In summary, all waste belongs to the usual category of operational waste from the accelerators. PSI has large experience in disposing such waste and with the shielded service cell ATEC the necessary infrastructure on site. In addition, a new plant for conditioning PSI waste containers with mortar is planned at the location close to ATEC. It is supposed to be operational in 2023; related activities are currently on schedule.

9.2 Layout of the Target Station H

The target station design is driven to a large extent by the requirement that the distance between the capture solenoid magnets and the graphite target must not exceed 250 mm (see red lined value in Figure 9.7). Because of this small distance, the magnets have to be put in the same vacuum chamber to save the additional wall as well as the flange with the inflatable seal (see Section 8.5.6). Further, the mirror plate has to be reduced to 40 mm to keep the distance of 250 mm.

It should be noted that in the present design there is no additional seal planned for the 4.6 m long proton beamline including the vacuum chambers for the inserts. This means that after manufacturing of the parts, everything has to be aligned with the help of surveying and then welded to one large piece. The stability, alignment and handling during installation need to be checked. The design of the target E region demonstrates that such a construction should work. In case of doubts, an inflatable seal could be inserted. However, exposure of the seal to the harsh radiation environment close to the target chamber should be avoided. Although being fully made from metal, continuous movement of the seal due to thermal expansion and contraction by large power deposition would lead to scratches and later to increasing leakages.

The target station contains the mainly following components (see Figure 9.8):

position	quantity	notation
1	2	capture solenoid magnet
2	1	Target insert inclusive graphite target and Densimet collimator
3	3	Copper collimator, KHM*0, KHM*1, KHM*2
4	1	Metal inflatable seal
5	2	Beam monitors

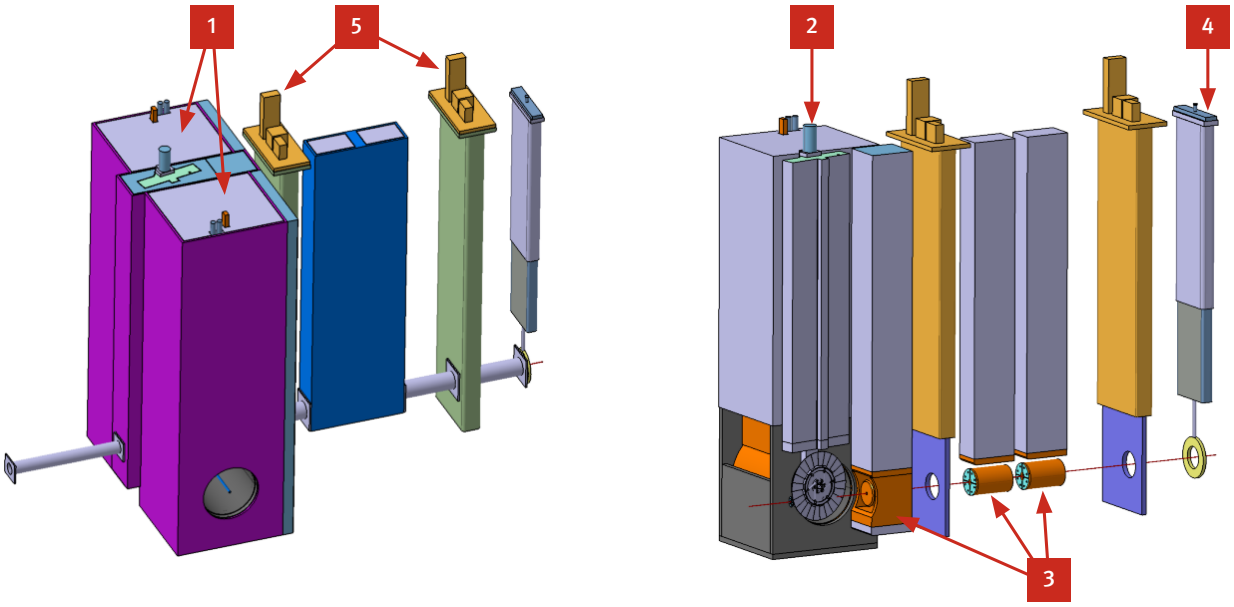

Figure 9.8: Target station with vacuum chambers and beam tube. Right: Target station with view of the beam components.

9.2.1 Tolerances and Alignment

Alignment and tolerances are very important. In the worst case, deviations of individual beamline components could add up and result in such a large misalignment that the beam might hit for example the Densimet collimator inside the target insert (opening in horizontal of 20 mm)[1]. For this reason, the beamline components need to be positioned very precisely, about +/– 0.5 mm in tolerance. Another example is the graphite target, which has a thickness of 3.5 mm and is positioned with an angle of 10° to the beam axis. A change of the angle or the thickness of the target would change the transmission of the proton beam (see Section 8.4.5).

[1] This would cause an interlock for the beam due to a current sensitive collimator (see Section 8.4.7)

9.2.2 Target Insert and Operation

The HIMB target H insert (see Figure 9.9) is to a large extent a copy of the already existing target E (see Figure 9.11) insert. This insert is equipped with a steel shielding block, copper cooling plate (s. the round orange disk in Figure 9.10), turning mechanics and the graphite wheel. The shielding block is the biggest part and every component is attached and fixed to it.

One obvious difference between target E and H insert is the size and shape of the shielding block (see Figure 9.12 and Figure 9.13) due to the small space available. A comparison of the graphite wheel of target H and E is shown in Figure 9.14 and Figure 9.15. The other parts, particularly the rotating mechanism, are adapted from the target E insert.

The version V2, shown in Figure 9.14 and in the next section, is judged by the manufacturer less problematic, since it is

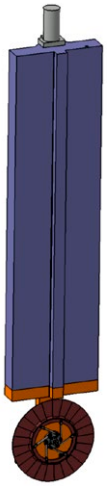

Figure 9.9: Target H insert.

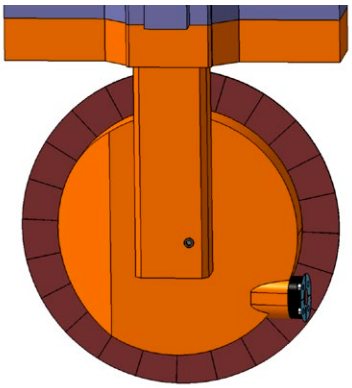

Figure 9.10: Lower part of the target insert with the graphite wheel and the copper cooling plate.

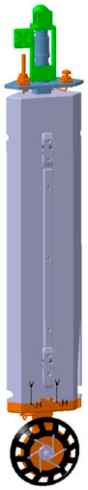

Figure 9.11: Target E insert.

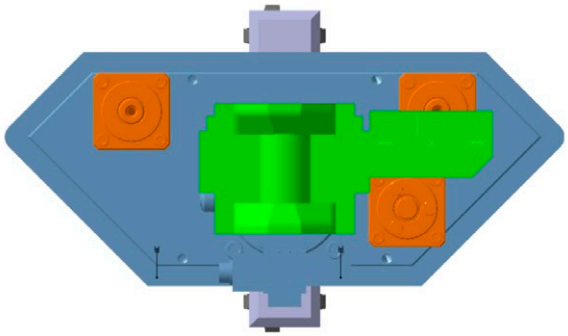

Figure 9.12: Target E insert, view from top.

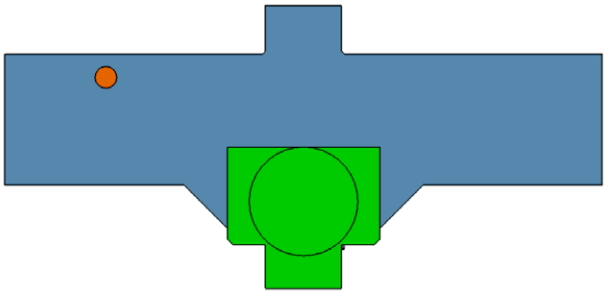

Figure 9.13: Target H insert, view from top.

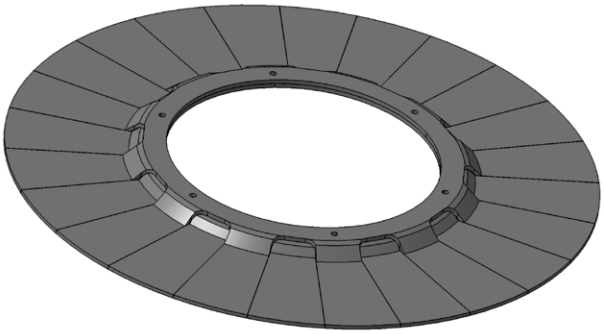

Figure 9.14: Target H.

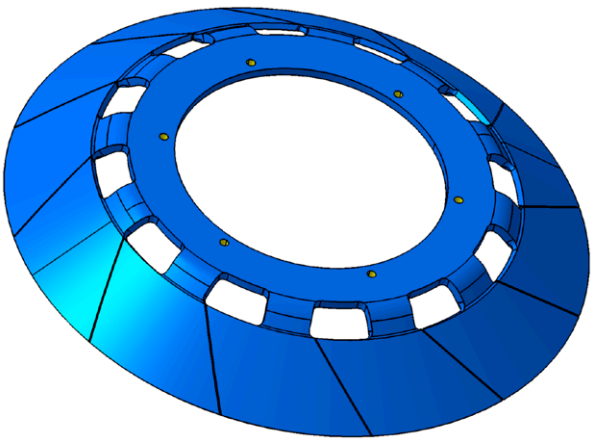

Figure 9.15: Slanted target E.

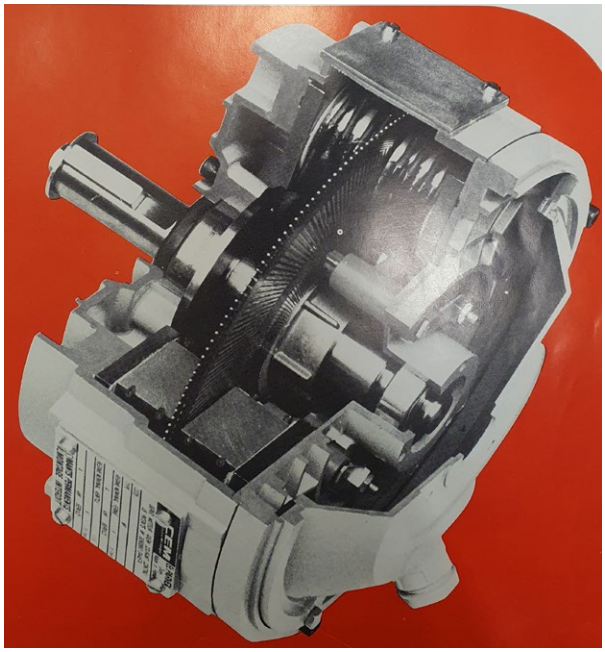

Figure 9.16: Servomotor (picture of an old brochure from the company ABB).

Figure 9.17: DC disc rotor servomotor.

made mainly from a flat disk. This has the advantage that not so many layers are crossed, which makes the wheel more stable against deformations. Further, it is easier to manufacture.

The target H graphite wheel is designed to rotate with 1 Hz like target E and M. It is driven by a DC disk rotor servomotor (see Figure 9.16 and Figure 9.17), which is located on top of the shielding to avoid radiation damage. Via a magnetic clutch, the motion is transferred to the vertical drive inside the vacuum chamber. There, an angular gear changes the direction to the horizontal shaft, onto which the graphite wheel is mounted. Important components are the three bearings as they ensure that the drive transmission has little friction. The challenge is that the bearings have to operate without grease due to the harsh irradiation environment. In addition, the bearings are exposed to temperatures of above 100 °C and therefore require additional clearance. These are not ideal conditions and shorten the lifetime of the bearings to a few months. When a bearing jams, an exchange of the insert with the spare is needed. The exchange requires approximately two days of work. The broken bearings are later exchanged in the shielded service cell ATEC at PSI by remote handling. Since late 2020, a set of new bearings from the Japanese company KOYO used at J-PARC has been mounted on the target in the beamline. Results look promising. The goal is to have a target exchange just once a year during shut down.

9.2.3 Target Design Options

Six different target designs with an effective target thickness of 20 mm for the beam were proposed and evaluated. For an optimized large surface muon production rate the proton beam needs to hit a target wheel with a large rim under a small angle (see Section 7.3). In general, as larger the rim and as smaller the angle, as larger is the effective surface muons could be emitted and therefore as larger is the muon production rate. However, manufacturing of the wheel and space limitations poses restrictions on the choices. Two realistic parameter sets which were considered, are a flat angle of 5 degrees and 1.8 mm graphite thickness, or an angle of 10 degrees and 3.5 mm graphite thickness. Due to concerns about the stability of a graphite wheel of less than

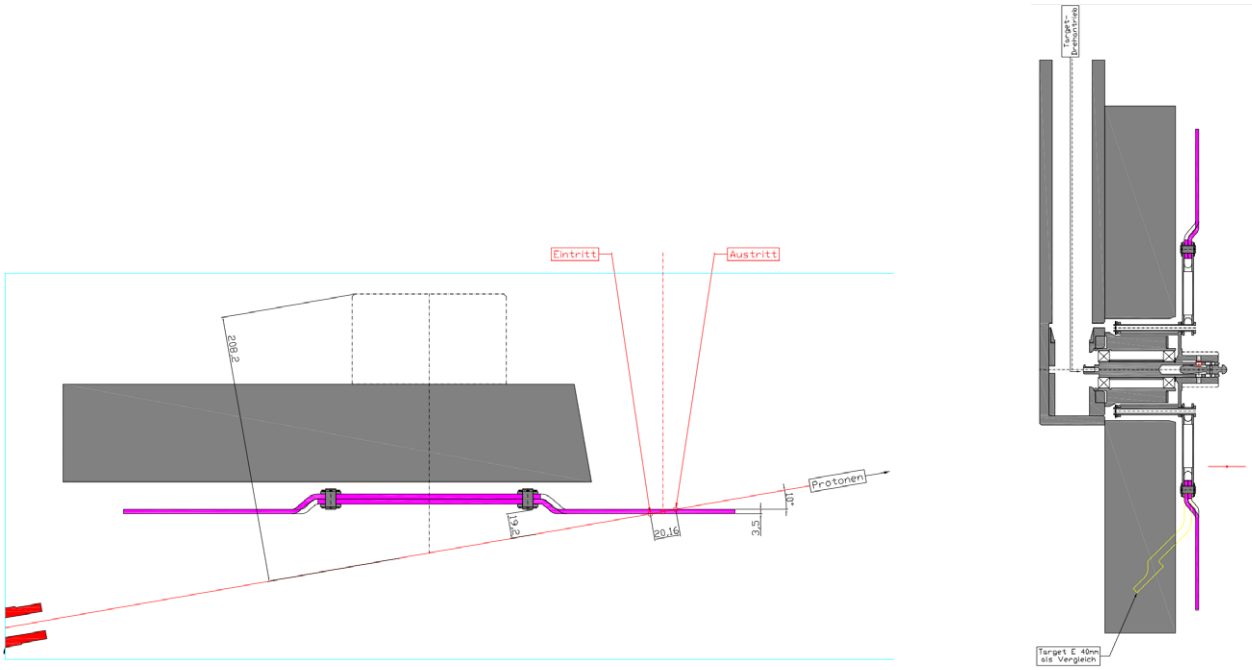

Figure 9.18: Beam in front of target, left view from top, right side view.

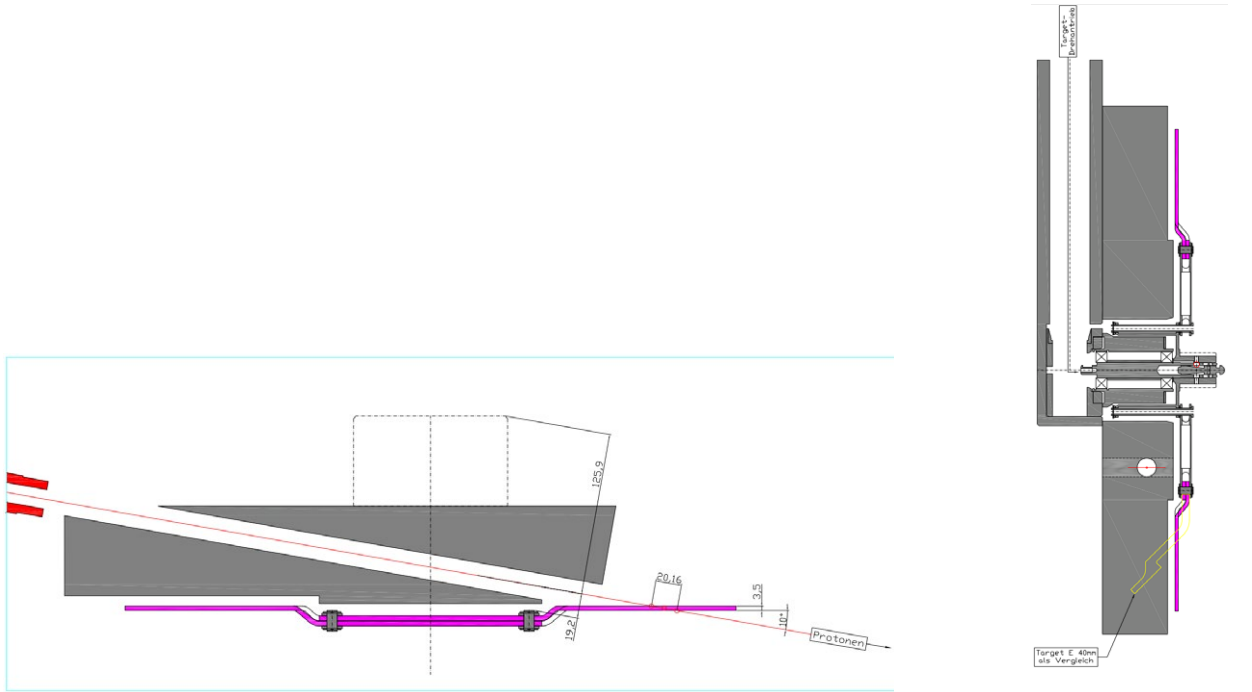

Figure 9.19: Beam through target cooling plate, view from top, right side view.

2 mm thickness, it was decided in favor of an angle of ten degrees, a thickness of 3.5 mm and a rim of 100 mm. According to Table 7.1 less than 10 % of the surface muons is lost with respect to the thinner version and 150 mm rim. The larger rim would have not fit into the existing exchange flask for Target E, which is intended to be used for Target H as well.

Another decision had to be taken, if the beam passes in front of the target wheel or in the back, where the cooling plate is located. (see Figure 9.18, Figure 9.19). Because of space

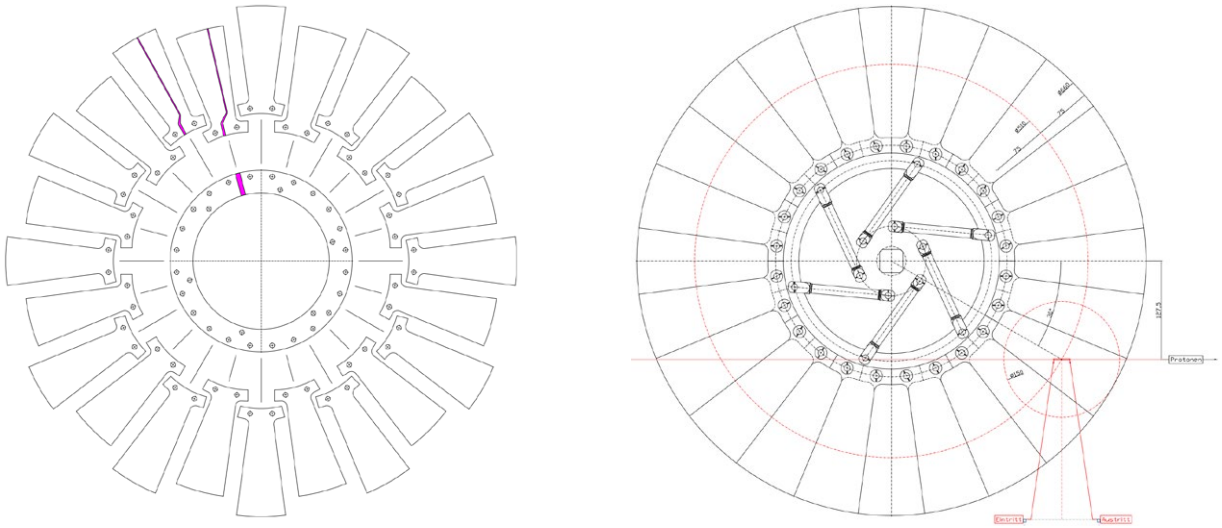

Figure 9.20: Target H version V1.

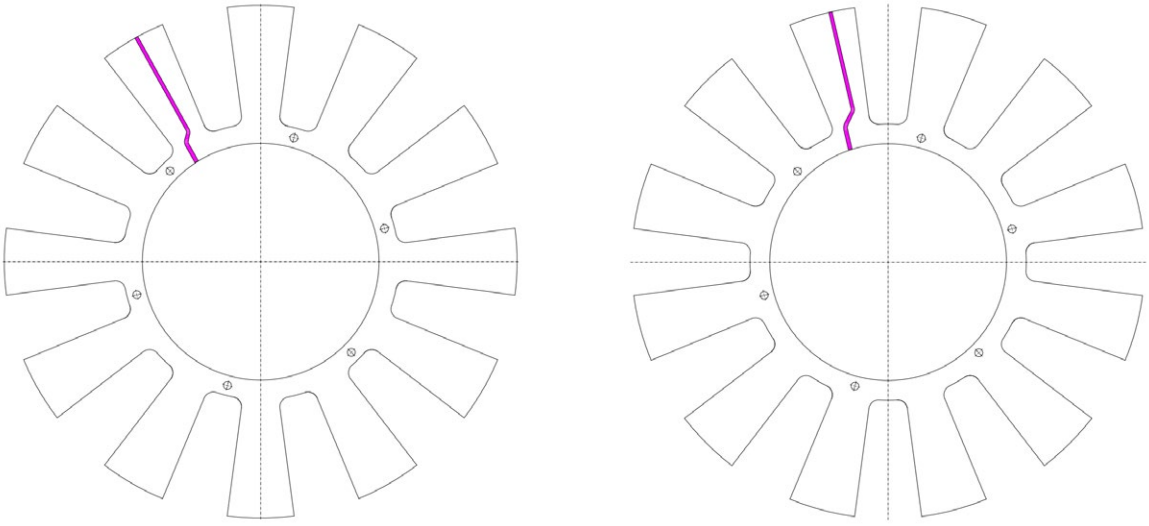

Figure 9.21: Target H version V2, left disk 1, right disk 2.

restrictions, it was decided to pursue a version with the beam passing through a duct located inside the target cooling plate. Accident scenarios such as an overheating of the cooling plate or a damage of its water pipe by mis-steered beam can be avoided by redundant beam diagnostics. Therefore, a Densimet collimator was designed with a 4-segment aperture for monitoring the beam position. Such a solution requires that the rotation axis of the target wheel is positioned above the beam-axis, otherwise the beam would hit the rotational mechanic. This also helps to keep the effective diameter of the wheel smaller at beam height but the thermal impact, i.e. the energy density on the graphite increases (see Section 9.2.4). The angle chosen in the following designs is 30 degrees measured from the centre (s. Fig. 9.20 right), which is a compromise. The design of target version V1 is based on a support ring, onto which 24 graphite blades are mounted with bolts and

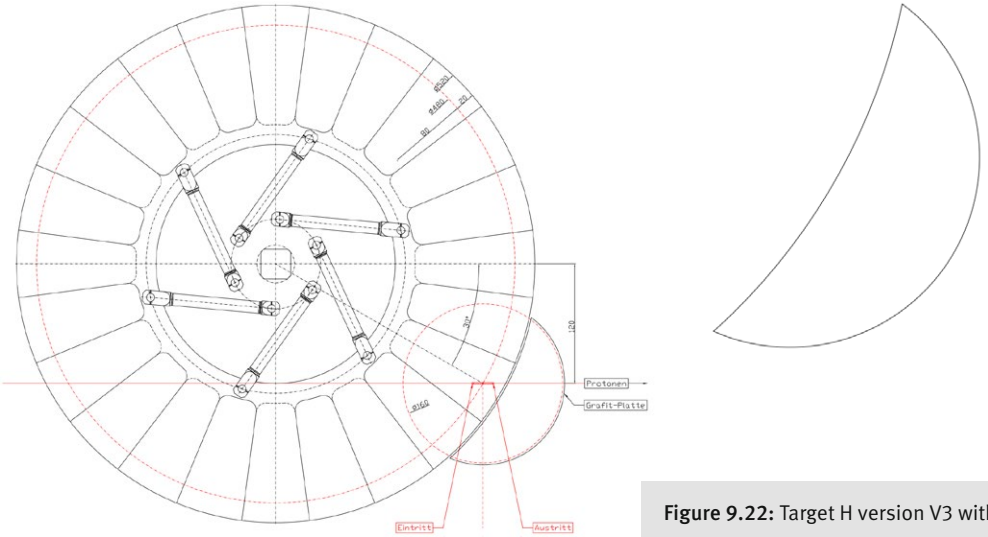

Figure 9.22: Target H version V3 with a moon.

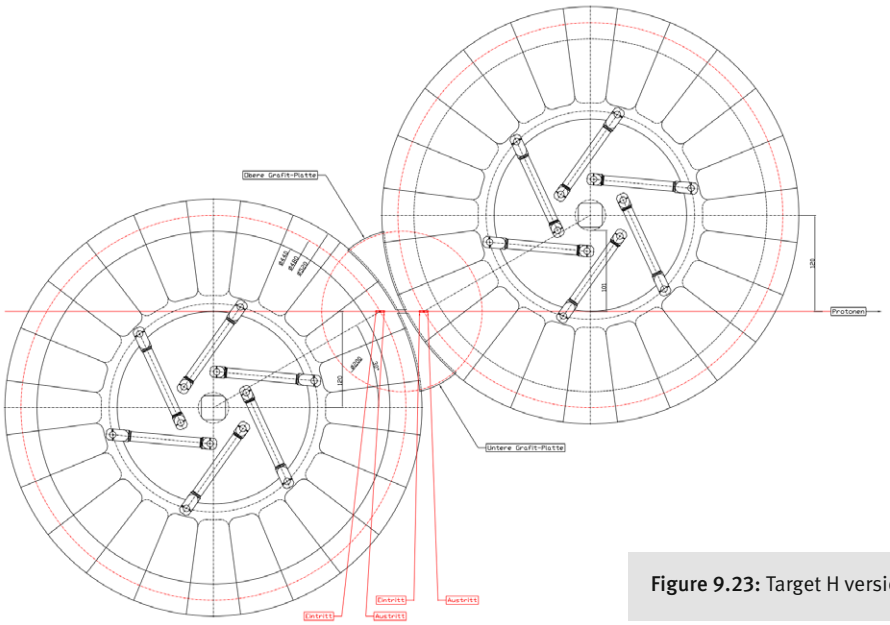

Figure 9.23: Target H version V5.

kept in position with springs (see Figure 9.20). Because of the many parts, which might untighten themselves from the main body, this version is considered delicate. In addition, as the segments are from different parts of the graphite block, they might respond differently to thermal heat.

Target version V2 is designed using two different disks (see Figure 9.21) of thickness 3.5 mm and a rim of 100 mm, for an angle of 10° against the beam. The two disks are overlaid on each other and attached with bolts to the rotation spokes. This version has much less parts than V1 and seems to be a viable option for target H.

Target version V3 is the same like version V2, but in addition with a graphite piece at the location, where the beam hits the target. This moon-shaped piece should help to extend the graphite field resulting in a higher surface muon rate. However, such a construction imposes several problems,

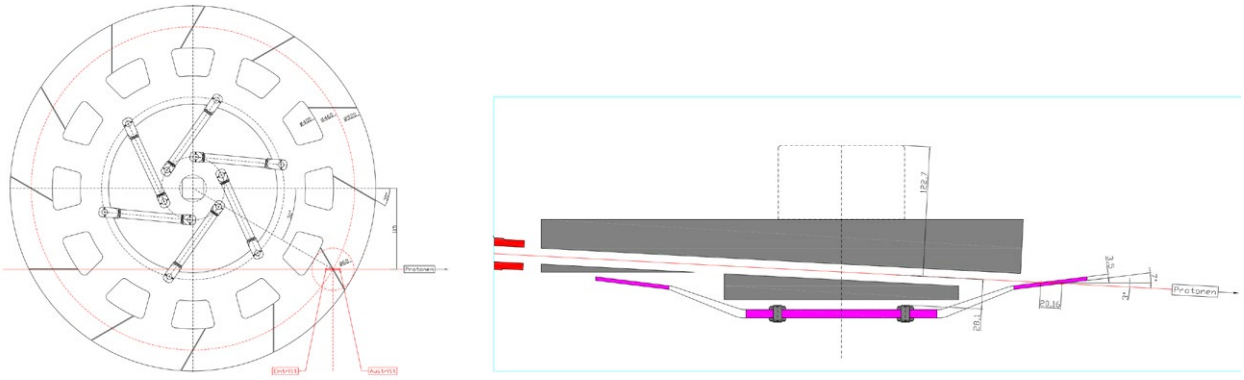

Figure 9.24: Target H version V6.

e.g. that the beam must not hit the graphite "moon" as it is uncooled. Further, due to thermal expansion the rotating wheel could touch it. Therefore, this version has been abandoned as too risky.

Version V4 is the same design like V3, but positioned with an angle of 5° to the beam axis and thus a thickness of only 1.8 mm. Version V5 (see Figure 9.23) consists of two wheels of version 4 to elongate the rim for increasing the surface muon rate. This version would take too much space and is considered prone to defects because of two rotating hubs.

Version V6 resembles the design of a target E wheel, but with a thickness of 3.5 mm. It is cut from one part, with 12 slits in the rim for thermal expansion. The shape of the target looks like a bent plate. If a different angle is needed in the future, it should be possible to replace the wheel for another design with a different bend angle of the outer rim.

Target designs V2 and V6 were shortlisted, since they promised the best mechanical and thermal stability. A further analysis performed with the manufacturer of Target M and Target E revealed that V2 is likely less sensitive, because of less stress in the material during manufacturing and less mechanical deformations during the milling. Such prestresses could lead to large deformations during beam operation, where the graphite is heated up to about 1500 °C. Therefore, V2 is the first choice for target H.

9.2.4 Thermal and Stress Simulations

ANSYS software package was used to simulate the thermal response of the graphite target wheel V2 to the power deposited by the proton beam, and to determine the induced thermo-mechanical stress. Simulations were performed in steady-state configuration, using the material properties of non-irradiated polycrystalline graphite.

9.2.4.1 Planar equivalent ANSYS geometry of version V2

Instead of dealing with the curved shape of one segment of version V2, an equivalent planar shape was used. The beam hits the rim under an angle of 30° measured from the center of the wheel, see Figure 9.20, and it enters the rim with an angle of 10°. The additional simplification made for ANSYS calculation is to ignore the 30° angle and to recalculate the entry angle and beam path through the solid. Since the volume swept by the beam is reduced, the power density should be rescaled in order to have the same total power as described later in Section 9.2.4.3.

9.2.4.2 Material properties

All material properties here reported are for non-irradiated polycrystalline graphite. The graphite mass density was assumed to have a constant value of 1'850 kg m^{-3}. The temperature-dependent isotropic thermal conductivity and the specific heat capacity at constant pressure are taken from [Kiselev, 2015b] [Poco Graphite, 2001]. In order to study the structural response of the target, the thermal expansion coefficient, the Young modulus and the Poisson ratio have to be defined. The thermal expansion coefficient depends on temperature, and the Young modulus and the Poisson ratio have fixed values respectively of 1.30E+10 Pa and 0.3

[Cost, et al., 1968] and the thermal emissivity is set to 0.7 [Kiselev, 2015b].

9.2.4.3 Thermal equation and boundary conditions

The first step in the present analysis consists of a thermal calculation to establish the temperature field, which will lead to thermal stress and deformation. The source term $\dot{g}$ in the heat conduction equation can be expressed as:

$$\dot{g}(x,y,z) = \frac{dE}{dz}(z) \left[\frac{I_0}{2\pi\sigma_x\sigma_y} e^{-\frac{(x-x_0)^2}{2\sigma_x^2} - \frac{(y-y_0)^2}{2\sigma_y^2}} \right]$$

where $\frac{dE}{dz}$ represents the power deposited along the beam path by the protons per unit length per unit current and the term in square brackets is the current density of the proton beam, which has the typical double Gaussian distribution. A total current I_0 of 2.5 mA was used in the present simulation and rescaled to one segment with the beam parameters $\sigma_x = 0.9\,mm$ and $\sigma_y = 0.6\,mm$. Since we perform a steady-state simulation, the proton beam has been smeared along the rotation path, y, considering a constant distribution of value a. The previous equation of $\dot{g}$ for one segment reduces to:

$$\dot{g}(x,z) = \gamma\beta \frac{dE}{dz}(z) \left(\frac{I_0}{\sqrt{2\pi}\,\sigma_x} e^{-\frac{x^2}{2\sigma_x^2}} \frac{a}{a \times d} \right) = \frac{dE}{dz}(z) \frac{I}{\sqrt{2\pi}\,\sigma_x} \frac{1}{d} e^{-\frac{x^2}{2\sigma_x^2}}$$

where β is the current rescaling factor, $a \times d$ is the normalisation factor being d the sweeping path of the proton beam on one segment, equal to 55 mm. The 30° slanted beam angle was ignored by scaling the power by a factor γ to take into account the reduced volume through the segment. A similar implementation was already successfully used in the design of the slanted version of Target E, which is presently thermally stable and in operation with an increased surface muon production up to about 50 % with respect to the previous geometry [Kiselev, 2021b]. As initial thermal condition, a constant temperature of 22 °C is imposed everywhere. The thermal boundary conditions are set as radiative boundary conditions with emissivity equal to 0.7 [Kiselev, 2015b]. The remaining surfaces are adiabatic surfaces also to represent thermal symmetry conditions.

9.2.4.4 Structural equation and boundary conditions

When the temperature field is known, a steady-state structural analysis can be performed. In steady-state the structural equation in matrix form for the unknown nodal displacement vector, $\{u\}$, reads:

$$[K]\{u\} = \{F\}$$

with the applied load vector, $\{F\}$, representing the steady-state thermal excitation and the stiffness matrix, $[K]$, taking into account the elastic response of the structure. The boundary conditions consist of symmetry planes and fixed supports.

9.2.4.5 Numerical implementation

The solver used to simulate both the thermal and structural response of the structure is ANSYS Mechanical [ANSYS]. The power deposition described in the Section 9.2.4.3 was implemented via an APDL script linked to the main solver (distributed sparse matrix direct solver). Frictionless supports on both base sides of the segment were imposed to account for structural symmetry and a fixed support was enforced on a single line in the middle of the geometry to constrain the global movement of the structure giving the freedom to thermally expand. Simulations were performed in a CISCO M5 blade with 4 Intel Xeon-Gold 6140 CPUs running at 2.3GHz, each with 18 Cores and a total RAM of 1.5 TB type DDR4-2666.

9.2.4.6 Mesh

The segment was subdivided in 4 bodies to better resolve the thermal gradients. The chosen mesh element is SOLID90 for the thermal analysis, which has 20 nodes with temperature degree of freedom at each node. SOLID186 elements, 3-D 20-Node structural solid, was selected for the structural analysis. This produced about 181'600 elements and 766'639 nodes.

9.2.4.7 Results

Due to the lower power deposition and stress values with respect to the slanted version of Target E already in operation, it is envisaged that this configuration will be thermally and structurally stable as proven by the following simulation outcomes. In Figure 9.25 the temperature field is presented showing a maximum temperature of about 1322 °C, well below the melting point of about 3'500 °C. The power deposited by the proton beam in 1 segment is about 0.41 kW

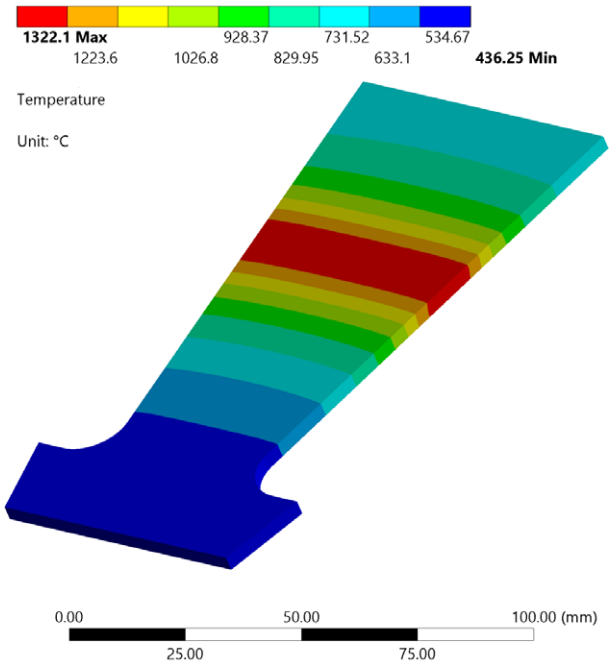

Figure 9.25: Temperature field in °C.

per mA, which gives about 1 kW for a current of 2.5 mA in 1 segment and about 25 kW for the whole geometry composed of 24 segments. In comparison, the total power during operation deposited in Target E slanted 40 mm thick for the same current is about twice this value [Kiselev, 2021b].

In Figure 9.26 the von Mises stress with a maximum value of about 23 MPa is shown for the upper part of the segment, which is not affected by the stiff part used as structure constrains. Modelling the full geometry will give the correct stress results at the base of the tile. The maximum value of about 23 MPa is lower than the typical ultimate tensile strengths for un-irradiated polycrystalline graphite, which ranges from 34 to 69 MPa [Poco Graphite, 2001].

The lateral, X axis, and vertical directional, Z axis, deformations are shown in Figure 9.27. The lateral deformation has a maximum value of about 0.16 mm and the vertical deformation has a maximum value of about 0.015 mm on the top surface.

Even considering the lower limit of 34 MPa as strength before failure, the safety factor is always above 1 indicating that no failure is expected, see Figure 9.28.

The slanted version of Target E receives in operation at the same power density about twice the power than the target envisaged for the current project for the same proton beam current. The simulated maximum temperature and von-Mises stress of one planar segment of the slanted version of Target E and the present configuration are respectively about, 1460 °C versus 1322 °C and 26 MPa versus 23 MPa. The slanted version of Target E is successfully in operation since 2019 and it is expected that also the present target will operate without major problem. The main differences, which

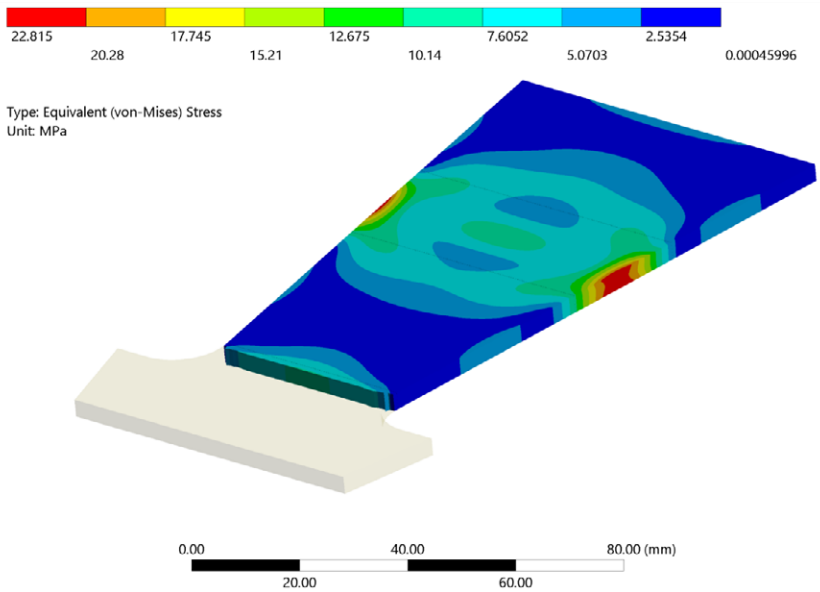

Figure 9.26: von-Mises stress in MPa for the upper part of the tile.

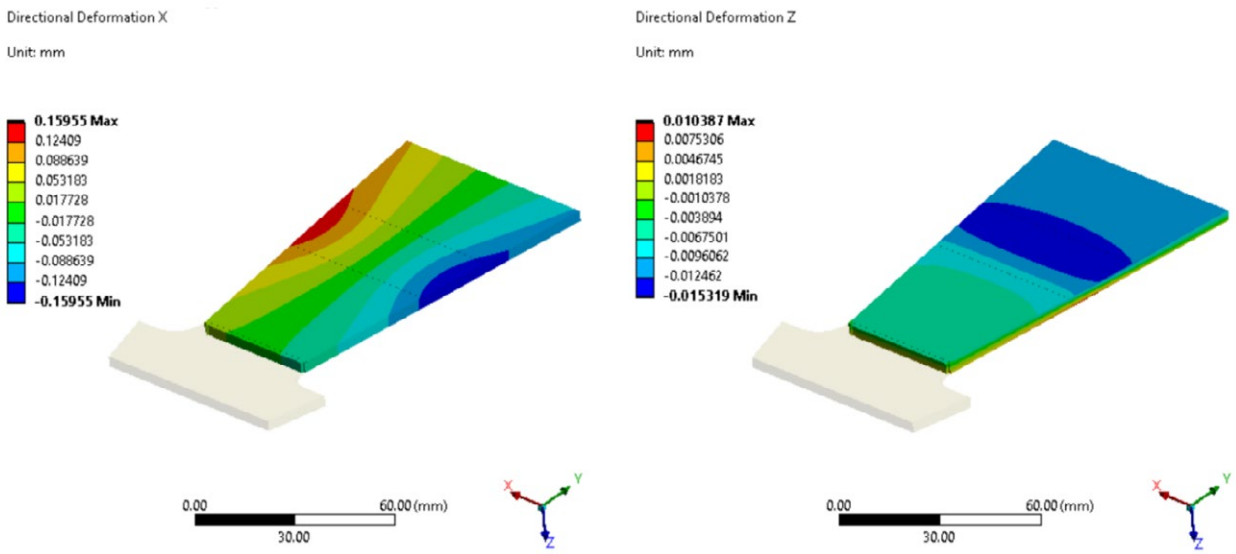

Figure 9.27: Lateral and vertical directional deformations on the upper part of the tile in mm. On the right hand side, the positive deformation on the back surface is not visible.

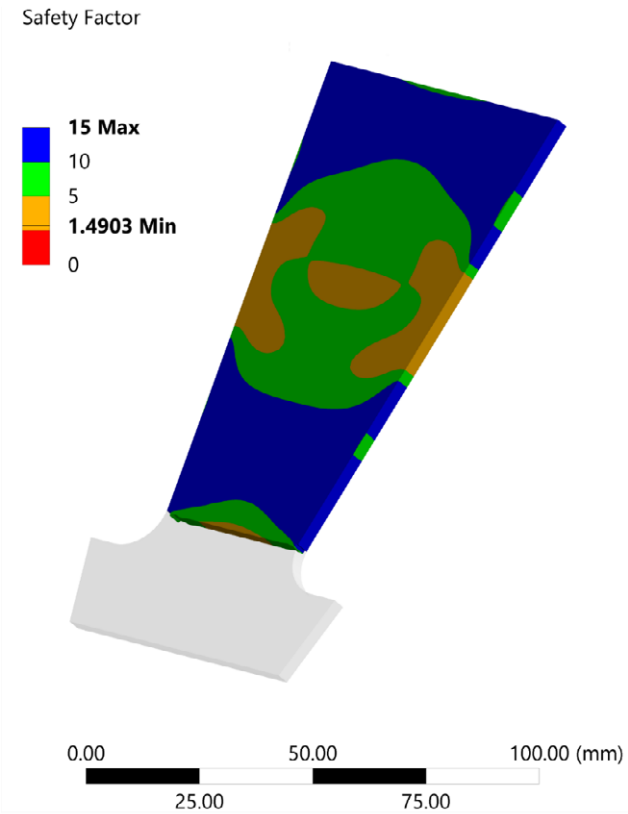

need to keep attention, is the larger rim (100 mm instead of 82.7 mm for the slanted version target E) and 3.5 mm instead of 5.57 mm.

9.2.5 Cooling

A proven concept for the cooling of components in the proton beamline, is the cooling by water. In the following the concepts for the cooling of the target, the mirror plate of the solenoid as well as the vacuum chambers with its local shielding will be provided.

9.2.5.1 Cooling of the target

Due to its high temperature of about 1500 °C (see Section 9.2.4) and the large emissivity of graphite of 0.7 the target wheel is cooled by thermal radiation, in which case the Stefan-Boltzmann law applies. The total heat from the target is absorbed in a step like arrangement of cooling systems:

Figure: 9.28: Safety factor with respect to the ultimate tensile strength of 34 MPa.

- The so called cooling plate behind the target wheel.
- The local shielding inside of the vacuum chamber of the target station
- The vacuum chamber of the target station

The cooling plate consists of cooper with steel tubes brazed on. Such a plate is already successfully used for target E for many years and will be designed very similar to it.

Since vacuum chambers are usually made from austenitic steel, the amount of power deposition, which can be dissipated, is limited as will be shown in the next section. Therefore, parts of the chamber, which are close to the target, have to be protected by local shielding, which is made from thick Cu plates. Considerations about their cooling is shown in Section 9.2.5.3. In both cases it is anticipated that the power deposition in the material thickness is close to a homogeneous distribution. On a material like copper with a large thermal conductivity the heat is fast distributed.

9.2.5.2 Cooling of thin plates like vacuum chambers, far from the thermal heat source

48 different cases were calculated to be applied for vacuum chambers or beam tubes: 3 different models (see Figure 9.29), 4 different homogeneous power densities ranging from 1'000 to 10'000'000 W/m^3 and 4 distances between the cooling tubes from 50 mm to 300 mm.

The model a) is derived from the design of the vacuum chambers as they are presently in operation in the proton beamline. They are made from austenitic steel with water tubes, which are thermally connected by aluminum. In a special procedure the molten aluminum was sprayed on the tubes. Model b) is thought to be an alternative for manufacturing a vacuum chamber. However, it requires more machining. Model c) is a thin copper plate of 20 mm with water tubes, which are brazed on the copper like on the cooling plate of the target. The water tubes are made from stainless steel to avoid erosion at high water fluxes.

The conclusion is as follows: Model a) and b) are thermally equivalent. Copper can be cooled much better, however, it is too soft for the construction of the vacuum chambers. Therefore, collimators and local shielding have to protect the vacuum chambers. The wall thickness of the vacuum chambers should be minimized in areas with high energy deposition.

From the BDSIM simulation, the beamline behind KHM0 gets a power deposition of 400 W/m. According to the results from this study, this leads to a spacing of the tubes of 10 cm. In fact, it is the spacing, which is realized at locations close to the loss point in the present proton beamline.

9.2.5.3 Cooling of thick plates like local shielding, far from the thermal heat source

36 different cases were calculated: 3 models, 3 homogeneous energy deposition ranging from 100'000 to 10'000'000 W/m^3 and 4 plate thickness 30, 40, 50 or 60 mm.

The 3 models used are shown in Figure 9.30. In model a) the plate is made of copper with two redundant water tube loops, where only one is in operation. Model b) is similar to a) but there is just one water loop. Model c) is like model a) but using mild steel instead of copper.

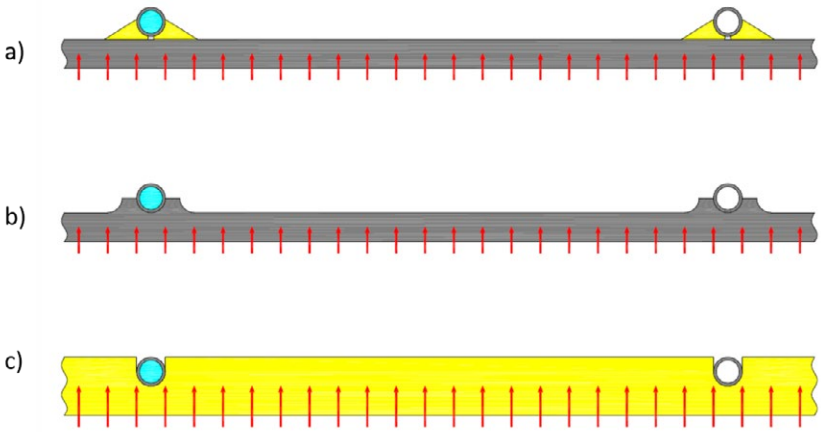

Figure 9.29: 3 models for the case of cooling thin plates: a) model derived from the presently used vacuum chambers in the proton beamline. b) Alternative model to a). c) model made from copper (395 W/(m*K)) instead of austenitic steel (15,5 W/(m*K)).

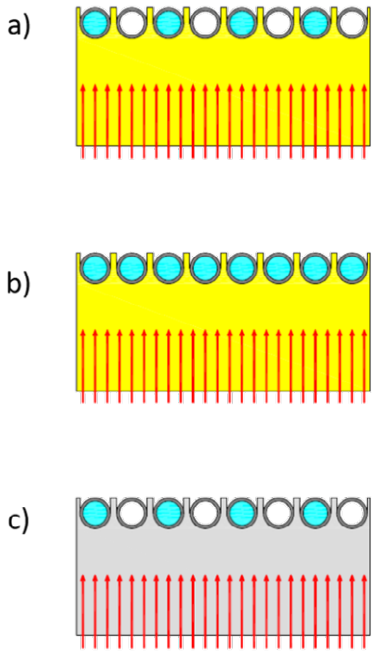

Figure 9.30: 3 models for the case of thick cooling plates: a) copper plate with one spare non-used cooling tube. b) same as a) but without redundant tubes. c) same as a) but from mild steel (40 W/(m*K)).

The conclusion is as follows: Local shielding made of copper is perfect. The copper temperature is always low. Model b) helps at large power depositions. Model c) could be applied for the mirror plate of the solenoid for the part of the power deposition, which is homogeneous, i.e. from nuclear reactions. Since the mirror plate is made of pure iron (Armco) with a much lower thermal conductivity of 70 W/(m K) compared to copper (395 W/(m K), hot regions on the mirror plate are expected. Since the power deposited by nuclear reactions is mainly forward peaked, the water cooled collimator KHM0 and its local shielding should help to dissipate and shield the heat. The power deposition on the mirror plates due to nuclear reactions is shown below.

The distribution of the deposited energy in the local shielding of the capture solenoidal magnets at the secondary MuH2 and MuH3 beamlines was estimated by the MCNP version 6.1 [Pelowitz, 2013] simulation of the particle fluxes from the proton beam interaction with the target. The reference HIMB geometry model was used in the MCNP simulation, in which a plate made of pure iron (density 7.874 g/cc) was placed between the solenoid and the target. The so called mirror plate reduces the magnetic field at the target but at the same time also decreases the flux of the secondary particles to the coil of the magnet. Each plate had dimensions of 55 × 45 cm^2 in (Y, Z), thickness of about 4 cm and a radius of the inner opening of 25 cm.

Figure 9.31 shows calculated profiles of the density of the deposited energy in these two mirror plates in front of the capture solenoid at the MuH2 and MuH3 beamlines. At the MuH3 beamline an additional conical heat shield is present between the target and the mirror plate, that smears and makes more radially uniform the forward-peaked distribution of the deposited energy, leading to the increase of the density in the upstream ($-Z$) part of the plate and decreasing the density in the downstream part ($+Z$). The maximal density of the deposited energy is less affected by the presence of the heat shield and both at MuH2 and MuH3 was found on the beam plane ($X = 0$) at the first 1 cm radial bin of the scoring mesh, that means at $r = 25.5$ cm, in the downstream part of the plate. In the mirror plate at the MuH2 beamline, the maximal density equals to 0.94 W/cm^3, and

Figure 9.31: Calculated Y-Z distribution of the density of deposited energy (MeV per 1 proton on the target) in the mirror plates at the MuH2 and MuH3 beamlines. Coordinate scale in cm.

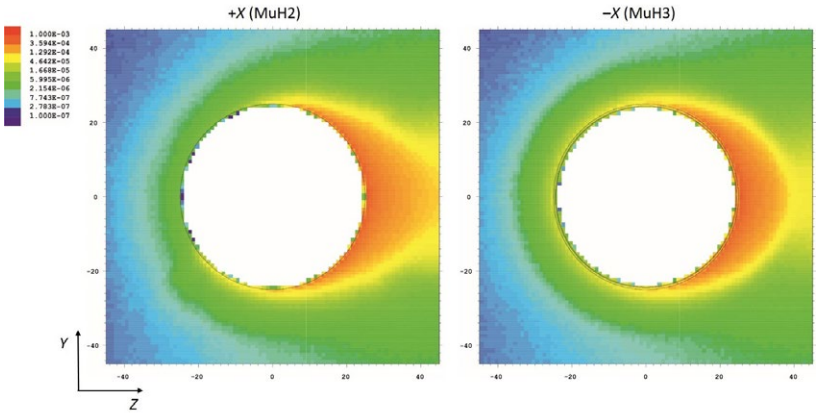

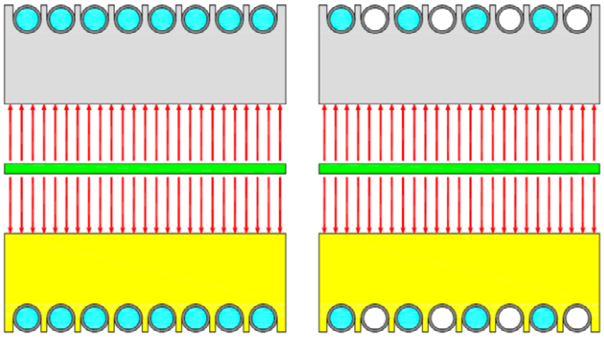

Figure 9.32: Illustration of the cases studied with direct thermal irradiation from the graphite target.

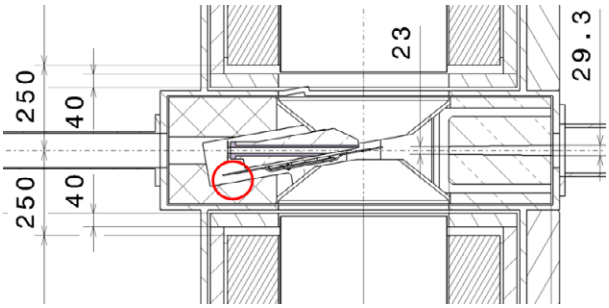

Figure 9.33: Cut from the CAD drawing of the Target H environment. The red circles marks the closest distance of the graphite wheel to the mirror plate.

in the mirror plate at the MuH3 beamline the maximal value of 0.9 W/cm^3, that means lower by 4 % only, has been found, for the proton beam current of 2 mA. In the upstream part of the plate the maximal density of the deposited energy is by at least a factor of 10 lower.

9.2.5.4 Cooling in case of thermal radiation from the graphite target

The thermal radiation irradiates the surface of the surrounding materials – contrary to the case of nuclear irradiation, which heats the material homogeneously. For medium thick plates this is a good approximation. First, the thermal irradiation from the 1500 °C graphite target has to be estimated. Some simple and conservative assumptions are made:

- Energy deposited in the graphite target is emitted by thermal radiation only.
- Thermal radiation is emitted from the graphite surface in perpendicular direction only.

16 different cases were calculated: Thermal emission were irradiated from 20 or 100 millimeters wide rings on the graphite surface. Then plates with thicknesses of 30 or 60 mm made of copper or mild steel were considered. Water tubes with or without redundancy were assumed. The cases are illustrated in Figure 9.32.

The conclusion is as follows: There must be more than two water tubes on the plate to avoid water boiling on the tube wall.

The mirror plate of the solenoids is made of mild steel and will have a hot spot if it is facing the graphite target. The critical location of the closest distance between graphite wheel and the mirror plate is illustrated in Figure 9.33.

The opposite side of the wheel is already protected by the cooling plate and therefore the adjacent mirror plate is less critical. For the opening needed for the path of the muons, pions etc. to the secondary beamlines, a cooled cone will protect the mirror plate. The critical location marked in Figure 9.33, could be protected by an additional copper plate on the mirror plate. A second cooling plate might be also considered, however, it would need to be dismantled, when the bearings need to be exchanged in the shielded service cell at PSI. However, such a construction using two cooling plates is foreseen at GSI for the graphite target at the Super-FRS in the new FAIR facility.

9.3 Lifecycle Considerations

The lifecycle of target H is expected to be similar to the lifecycle of target E, since the same rotating mechanism as described in Section 9.2.2 is used. During shutdown, the bearings of the target E wheel are exchanged as preventive maintenance. Up to now, the bearings last a few months, and often one target exchange is needed during user operation. Work is going on to improve this situation (see Section 9.2.2). The graphite wheel of target E endures up to four years; after this time deformation become unacceptable. While a thinner target is likely to have a shorter lifetime, a life span of at least one year is anticipated for the graphite

wheel of target H. As the bearings will be exchanged yearly anyway, this does not pose an operational concern. However, the number of disposed graphite targets would increase. Since the slanted version is not as sensitive to deformation as the slab target with a width of +/−3 mm, the limits for maximum acceptable deformation, nowadays +/−1 mm, could be more relaxed.

Components in need of maintenance are mainly the bearings. In our experience, the electric motor runs at least for 10 years. The lifetime of a collimator is not exactly known, but expected to be similar to a beam dump. Beam-Dump no. 1 was running at HIPA for 26.5 years (1991 to 2017) and had to be exchanged because of a water leak. This indicates that the lifetime of a collimator may be around 25 years, depending on how much charge the device absorbs. The inflatable seal has also a very long lifetime. Up to now, only once an inflatable metal seal was not tight after removing and reinstalling after 20 years of service. For the beam monitor a long lifetime may be expected as well. For example, monitor MHP45/46 broke after 25 years, due to a problem in the control unit cause by a water leak in the service area. To conclude, operational experience suggests that the usual life span of beam components is more than 20 years, which is the anticipated operation time of target H station. Nevertheless, the design of each component must allow removal by an exchanges flask so that the component can be moved to the ATEC service cell for repair by manipulators or disposal.

9.3.1 Remote Handling and Exchange

Installation, removal and transport of activated beamline elements will be performed remotely by means of exchange flasks, which are shielded by up to 40 cm steel. Figure 9.34 and Figure 9.35 show the exchange flask, which can lift target E and a couple of other components. This exchange flask is also designated for the handling of target H and the inserts shown in Figure 9.8. In addition to the exchange flask, a bridge for precise positioning of the flask (see Figure 9.36 and Figure 9.37) and a control unit (see Figure 9.38, Figure 9.39 and Figure 9.40) for remote operation is needed. The following steps will have to be performed for exchanging the HIMB target H:

1. Switch of the water cooling and the electric power of the target
2. Switch of the vacuum pumps and vent the vacuum system with nitrogen
3. Remove the concrete shielding on top of the beamline up to the service level
4. Switch on the special air extraction system , which provides an underpressure to avoid spreading of contamination and outgassing of Tritium
5. Disconnect the water and electric housing and cables

Figure 9.34: Exchange flask target E on the bridge.

Figure 9.35: Exchange flask lifted by the 60t crane.

Figure 9.36: Bridge lifted by the 60 t crane.

Figure 9.37: Bridge on the proton beam channel.

6. Remove the vacuum flange
7. Mount the gripper rack on the target
8. Bring the bridge by the big 60t crane and position the opening centered above the target
9. Insert a contamination protection into the opening of the bridge
10. Put the exchange flask on the support with the big hall crane, make sure that the gripper rail is in the right position
11. Bring the control unit for the exchange flask and connect it with the exchange flask
12. Drive down the gripper and grip the rack of the target
13. Drive up the gripper including the target into the exchange flask
14. Close the sliding door at the bottom of the flask
15. Disconnect the control unit of the exchange flask
16. Connect the hall crane with the exchange flask and bring it to the required place like ATEC to repair it or into the parking slot to store the target
17. Load the exchange flask with the repaired or spare target and bring it back to the proton beam channel
18. Repeat the steps 15 till 1 in the reverse order

The remote handling of the exchange flask is performed by the control unit, which is realized by a Siemens S7 PLC control system. The control unit is operated by means of a touchscreen (see Figure 9.40). On the screen is a schematic representation of the components, which are currently handled and the present parameters for the component to be lifted are shown. The operator also receives information

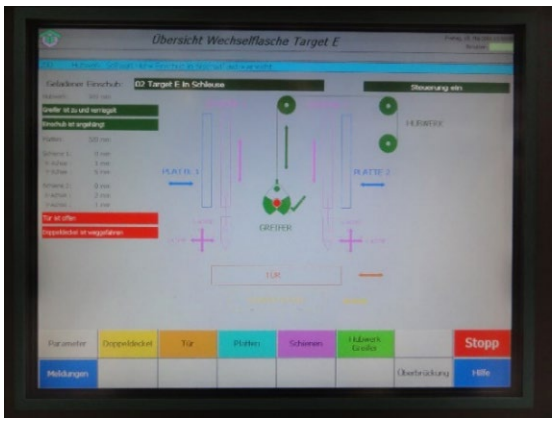

Figure 9.38: Control unit of the exchange flask.

Figure 9.39: Control unit of the exchange flask side view.

Figure 9.40: Touchscreen of the control unit.

Figure 9.41: Target E contamination protection.

about the current situation by updated images and values in real-time.

The contamination protection device prevents the spread of radioactive particles into the surrounding area. The device is connected to a mobile air extraction system, which is connected to the central filtering system of exhausted air. The contamination protection has a special lid, which can be operated remotely by the exchange flask during target exchange.

9.3.2 Spare Part Policy

For both target stations E and M, a second target is kept available as a spare. The same strategy will be followed for target H. Since the spare part is activated and contaminated, it is stored in a parking slot, i.e. a shielded cell equipped with a vacuum system and two guide bars (see Figure 9.42 and Figure 9.43). The target insert is sliding with rolls in the slide bar, this makes sure that it will be guided safety and stay in correct position. This is in fact the same technique as it is used in the proton beamline. The vacuum is needed to avoid moisturizing of the bearings, which would destroy the coating. On top of the parking slots a lid will be installed like the one in Figure 9.41 to avoid contamination.

Although the target M parking slots would not be needed anymore, there is not enough space for the vertical parking slots of target H. If the target H insert would fit into the target E parking slot, this would be the best option as only three parking slots would be required. However, this has to be carefully checked. Another option would be to build new parking slots, potentially in the former Injector-1 bunker (see Figure 9.44 and Figure 9.45, green field), as the ATEC area is already crammed with parking slots and storage room for exchange flasks. Figure 9.42 shows two parking slots which can be used for various beamline inserts like collimators. These parking slots do not contain a vacuum chamber.

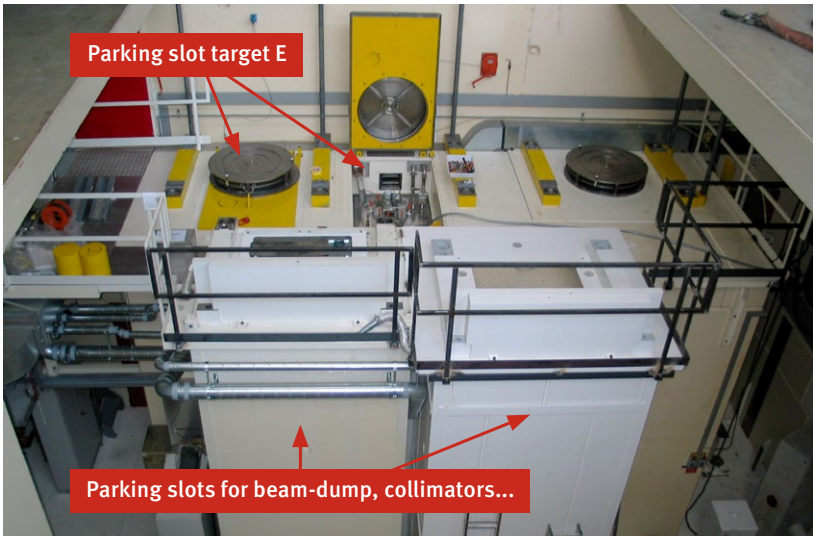

Figure 9.42: Parking slots at ATEC.

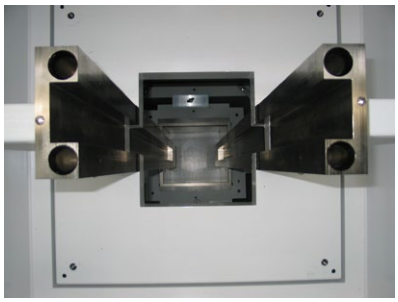

Figure 9.43: Parking slot from inside.

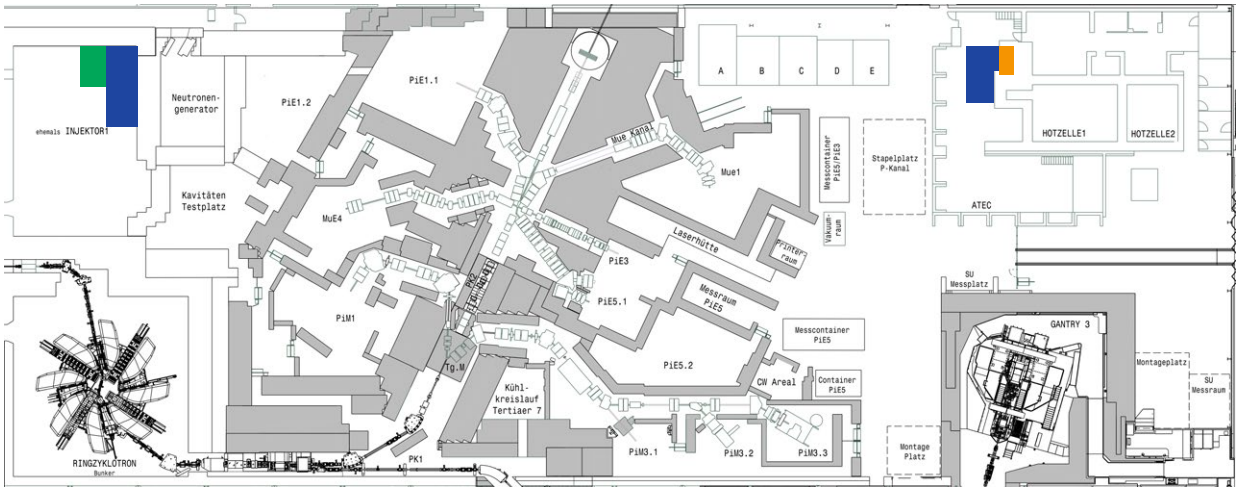

Figure 9.44: Map of the experimental hall. The locations of existing parking slots are marked in blue (KHE2, BHE) and orange (TgE), the location of the proposed new parking slots is marked in green (TgH).

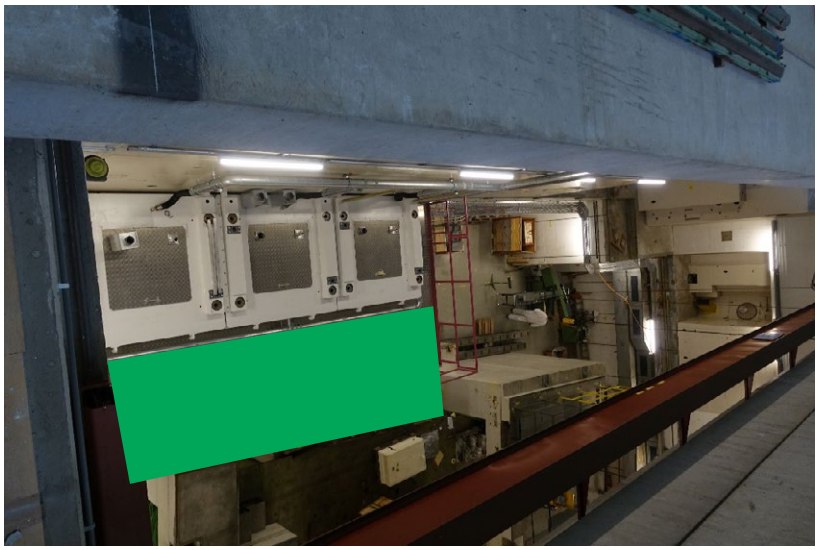

Figure 9.45: Possible location for target H parking slots, see green field.

No spares exist for other beamline components (KHE, BHE….), because the lifetime or maintenance interval is much longer than 20 years.

9.4 Shielding

The prompt dose rate around the target station can be considered to scale, in the first approximation, linearly with the increase of the losses, i.e. with the increase of the target thickness, which is a factor 4. To ensure the operation of the new target complies with the radiation safety requirements, the concept of the upgraded radiation shielding at primary and secondary beamlines is discussed in the present and following sections.

The main requirement concerning the shielding upgrade is to meet the guidance value of 10 µSv/h for the prompt dose rate outside the shielding, i.e. in the accessible parts of the experimental hall (see Chapter 11). Various shielding configurations were evaluated with respect to this criterion in

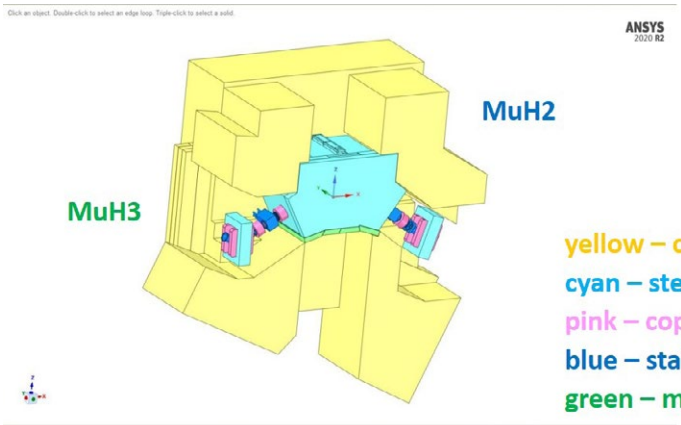

Figure 9.46: CAD model of the target station and secondary beamlines, with upgraded steel and concrete shielding.

a numerical study. Monte Carlo simulation with MCNP version 6.1 [Pelowitz, 2013] were used for the beam losses on the target and for the resulting secondary particle fluxes in the vicinity of the target station.

Figure 9.46 shows the resulting configuration of the shielding at the target station. The height of the steel shielding on top of the target station has been increased by 50 cm, to the total height of 2.5 m, counting from the beam plane. The same steel thickness of 2.5 m has been applied in the horizontal beam plane radially from the target in the downstream region. Upstream from the target station the thickness of the steel shielding has been left unchanged. The thickness of the outer concrete shielding has been also increased by 50 cm, to the total thickness of 3.5 m. There is a gap on top of the steel shielding between the steel and the concrete shielding which will continue to be used for necessary infrastructure like ventilation and vacuum pumps. The width of the gap will remain unchanged at 1 m. Same thickness of the concrete shielding of 3.5 m has been used on top of the target and also in the region of the proton channel upstream from the target station.

9.5 Prompt Dose Rates

The distribution of the neutron flux through the steel and concrete shielding at the target station on the vertical plane simulated with MCNP6.1 is shown in Figure 9.47. The proposed configuration of the shielding effectively reduces the neutron flux in the direction towards the top of the roof of the proton channel. Three dominating streaming paths of the flux are observed. The first one lies in the direction at 90° from the target, where the secondary neutrons encounter the lowermost layer of shielding. In the downstream region, the next streaming path lies at 60°, the maximum of the angular distribution of the secondary neutron flux

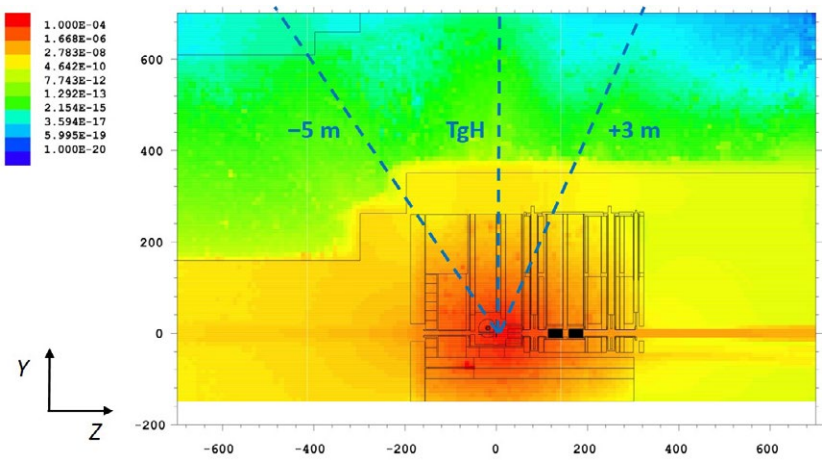

Figure 9.47: Neutron flux at the target station (n/cm2 per 1 proton on the target) on the vertical Z-Y beam plane. Proton beam points to the Z direction. Coordinate scale in cm.

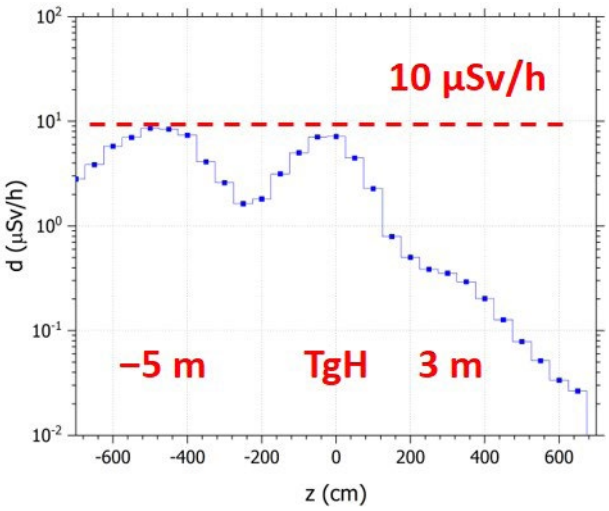

Figure 9.48: Dose rate (µSv/h per 3 mA) at X = 0 at the top of the concrete shielding, at h = 7 m from the beam plane (8.5 m from the floor of the proton channel). Proton beam goes in the Z direction.

from the steel shielding of the target. The most pronounced is the maximum of the neutron flux in the upstream region. There, the thickness of the concrete is radially kept equal to 3.5 m but the thickness of the steel and marble shielding rapidly decreases in direction to the upstream beamline, allowing more secondary particles to escape from the target station and to enter the concrete shielding.

The profile of the prompt dose rate at the top of the concrete shielding above the target along the beamline calculated with MCNP6.1 is shown in Figure 9.48. At two positions along the beam, directly above the target and in the upstream region, the calculated dose rate is close to the limiting value for a 3 mA beam. This local increase of the dose rate can be mitigated by an additional single 50 cm concrete block.

To estimate the amount of steel and concrete shielding needed at the secondary beamlines MuH2 and MuH3 to comply with radiation protection requirements, the approach of the "hermetic" shielding has been applied. From the CAD model shown in Figure 9.31 the components of the secondary beamlines after the bending magnet were taken out and the remaining space was filled by steel and concrete blocks as shown in Figure 9.49 . The thickness of the steel blocks is 2 m and the concrete blocks 3 m, counting along the direction of the secondary beam. Separate MCNP simulations have been performed, to estimate the dose rate after the steel shielding block, at +/− 7 m from the target, and at +/− 9 m, after the block of the concrete shielding.

The distribution of the neutron flux through the steel and concrete shielding at the secondary beamlines on the horizontal planes simulated with MCNP6.1 is shown in Figure 9.50. In the downstream region, the uniformly radially distributed steel shielding effectively reduces the secondary flux into the concrete shielding. In the upstream region the backscattering from the target station creates a significant secondary source of the particles in the concrete shielding. This source is suppressed by additional concrete shielding blocks. However, there is certainly room for improvement,

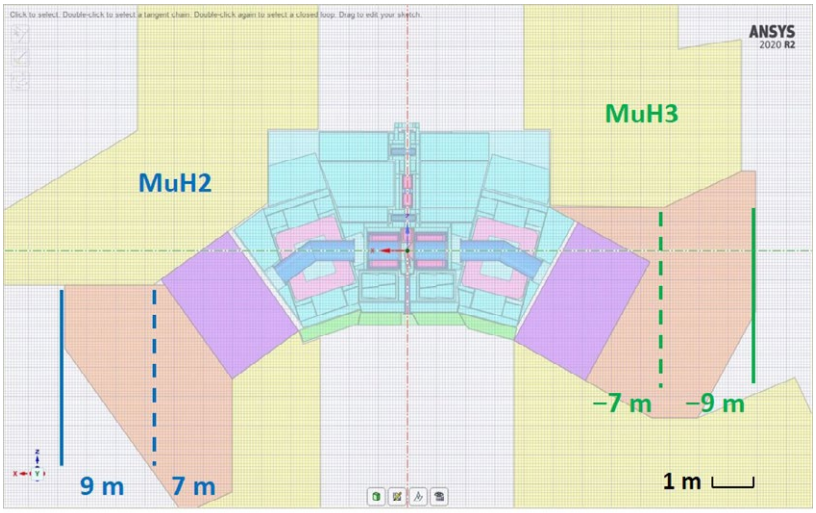

Figure 9.49: CAD model of the target station with steel (pink) and concrete (orange) shielding blocks at the secondary beamlines MuH2 and MuH3.

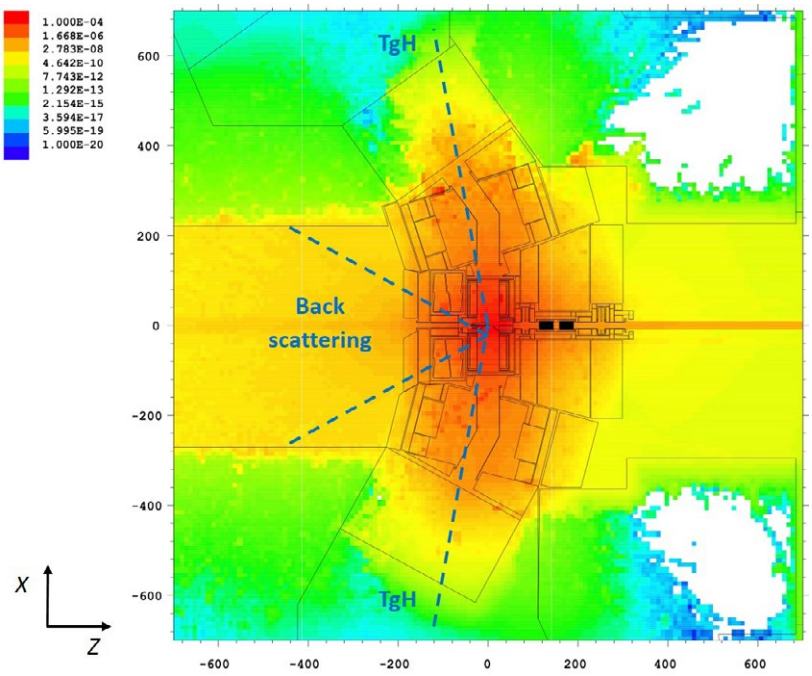

Figure 9.50: Neutron flux at the target station (n/cm² per 1 proton on the target) on the horizontal Z-X beam plane. Proton beam goes in the Z direction. Coordinate scale in cm.

e.g. elongating the steel shielding upstream of the target to decrease the particle flux at the source. The main contribution to the dose rate after the shielding at the secondary beamlines are from the particles that were produced by primary interactions in the target. These particles are observed at large distance from the primary beamline because of the direct line of sight from the target through the large aperture of the secondary beamline.

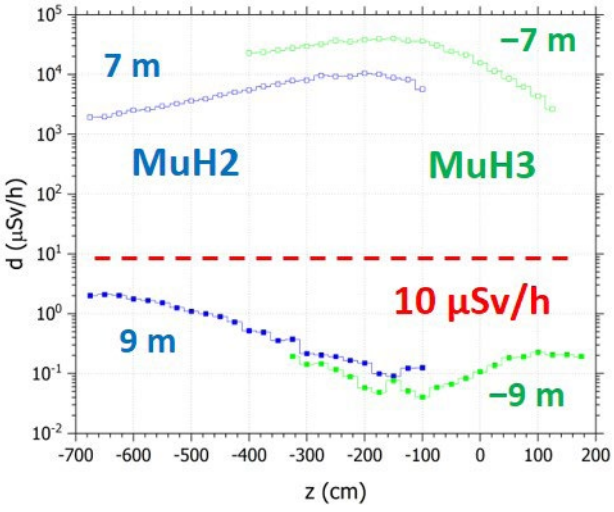

Figure 9.51: Dose rate (µSv/h per 3 mA) at the beam plane (Y = 0) at the secondary beamlines MuH2 and MuH3, after the steel (at +/− 7 m) and concrete (at +/− 9 m) shielding. Proton beam goes in the Z direction.

The profile of the prompt dose rate after the steel and concrete shielding blocks at the secondary beamlines MuH2 and MuH3 is shown in Figure 9.51. With the steel shielding only, the dose rate after the shielding is still a factor of 100 higher than the limit of 10 µSv/h. Introducing 3 m of the concrete shielding next to the steel shielding is a kind of "warranty" for the dose rate to comply with the safety requirement and at the same time leaves room for further shielding optimization.

9.6 Remnant Dose Rates

Another MCNP simulation was used to estimate the remnant dose rate at the top of the steel shield of the target station, which is the so called working platform and accessed by people during maintenance. Neutron spectra and production rates of the unstable nuclides calculated by MCNP were processed by the Activation Script [Gallmeier, 2007] and build-up and decay of the nuclides have been calculated by

Height of steel	Cooling time				
	6 h	12 h	18 h	24 h	1 month
2 m	48.5	16.9	10.4	9.0	5.3
2.5 m	0.63	0.21	0.13	0.10	0.064

Table 9.3: Remnant dose rate (mSv/h) at the top of the steel shield after the stop of the target operation, for different cooling times.

the nuclide evolution code FISPACT [Forrest, 2007]. From the FISPACT calculation, the value of the contact dose rate for the different parts of the steel shield was obtained, assuming the target operation for 20 years at the beam current of 3 mA.

Two cases have been considered: current height of the shield of 2 m from the beam plane and the proposed increased thickness of 2.5 m. The maximal values of the dose rate at the top of the steel shield calculated for each of these two cases and for the cooling intervals within one day, and also for 1 month, are given in Table 9.3.

From Table 9.3 it can be concluded that the additional 50 cm of steel is necessary for planned maintenance work, as dose rates above 10 mSv/h are unacceptable. In addition, from the experience gained by former comparisons between simulation and measurement the measured dose rate is usually a factor of 2 higher due to gaps between shielding blocks and particularly around a component and its vacuum chamber. Locally, hot spots just above such gaps are observed exceeding the average dose rate by factors of 5 to 10.

9.7 Activation and Waste

Activities of the residual nuclides in the target station and in the shielding were calculated. A MCNP6.1 simulation of the particle fluxes in the target station was followed by a build-up and decay calculation using the nuclide evolution code FISPACT. Target operation for 20 years at the beam current of 3 mA and 10 years + 30 years of cooling time were assumed.

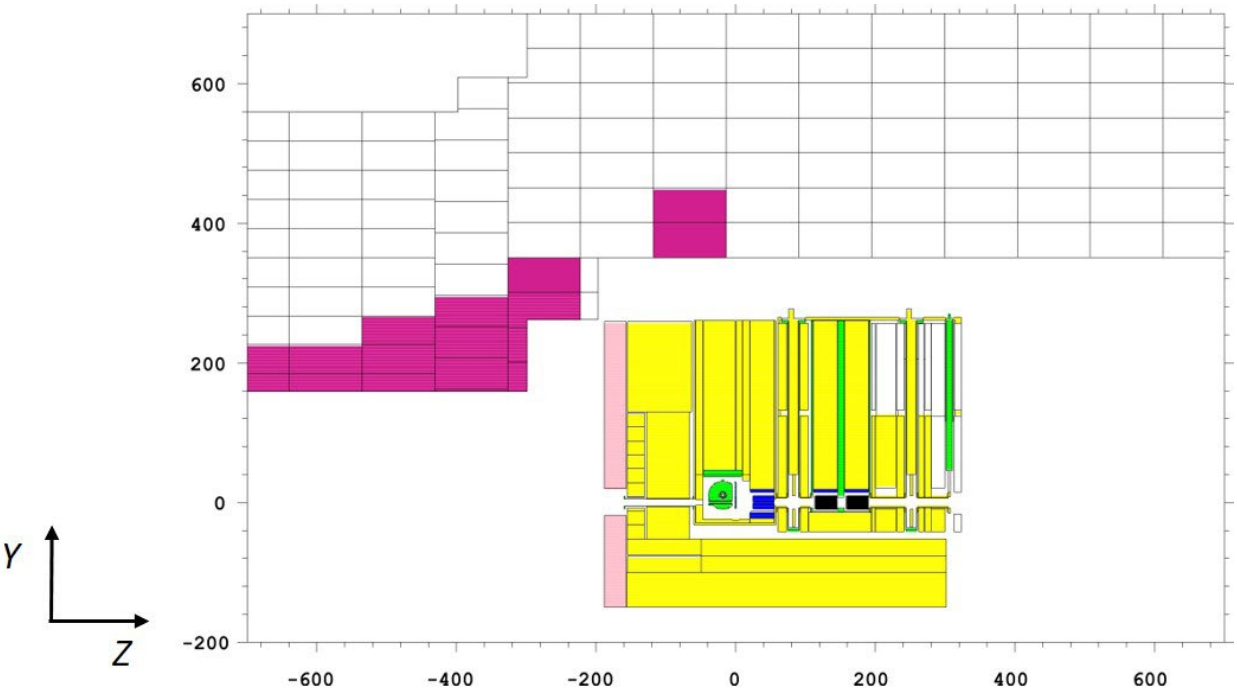

Figure 9.52: Distribution of the radioactive waste on the vertical Z-Y beam plane. Only the cells of the geometry that have the value of the LL index of the nuclide inventory larger than 1 are colored. Coordinate scale in cm.

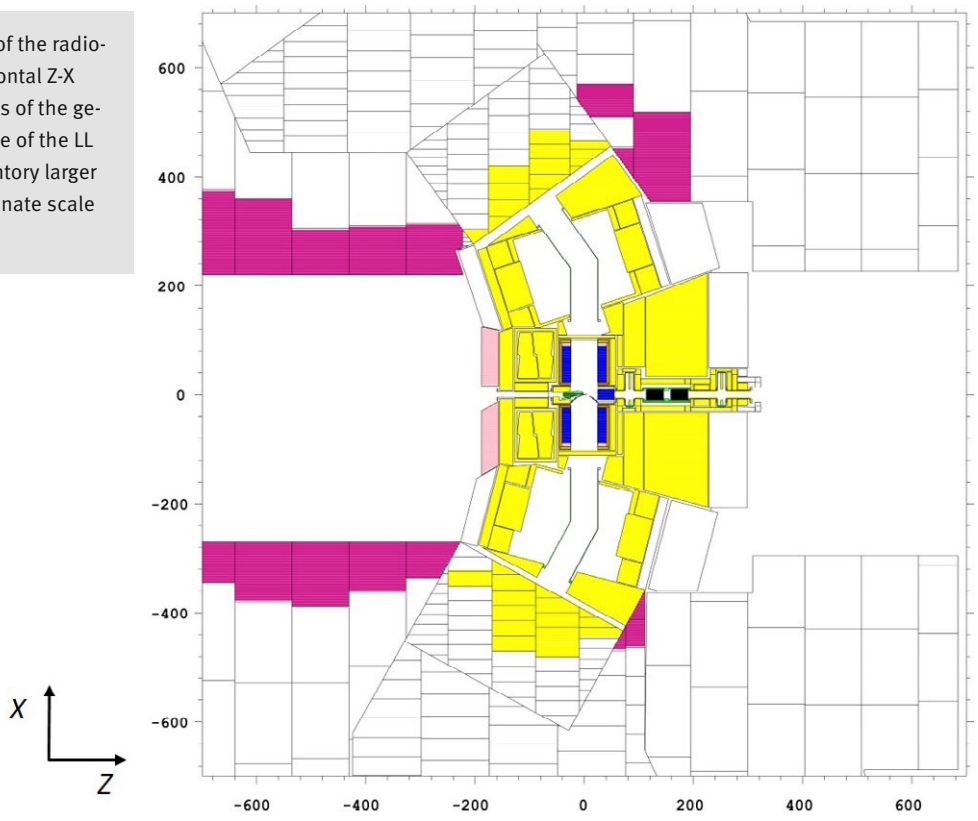

Figure 9.53: Distribution of the radioactive waste on the horizontal Z-X beam plane. Only the cells of the geometry that have the value of the LL index of the nuclide inventory larger than 1 are colored. Coordinate scale in cm.

Steel and concrete shielding from the reference CAD model shown in Figure 9.31 were segmented into individual geometry cells and the LL index for the nuclide inventory of each cell was calculated. The distribution of the produced radioactive waste is illustrated by the cuts of the MCNP geometry shown in Figure 9.52 and Figure 9.53.

The following components will become radioactive waste under the assumed conditions of operation:

1. All components of primary and secondary beamlines: sections of the vacuum chamber, collimators and magnets, and corresponding inserts
2. Most of the steel shielding of the target station, including the additional 50 cm thick top shielding plate
3. Two of four blocks of the marble shielding upstream from the target
4. About one third of the steel of the shielding at secondary beamlines MuH2 and MuH3
5. Innermost part of the concrete shielding upstream from the target and first blocks of the concrete shielding above the target insert

As discussed in Sections 9.4–9.6, the additional steel shielding at the target block is needed to moderate the increase of the secondary particle flux and particularly the dose rate on top of the shielding. The increased flux is due to the thicker target, 20 mm for TgH instead of 5 mm for TgM. However, adding more steel to the shielding will increase the amount of the future steel waste. The total increase is about 20 %, relative to the volume of the steel waste produced in the proton channel between targets M and E. This increase is not only due to the thicker target but also due to the conservative assumption of a constant beam current of 3 mA during the year, corresponding to 26 Ah instead of 10 Ah per year, which was used for the calculation presented in Figure 9.6 and so far is the maximum charge per year provided by HIPA.

The amount of the additional concrete waste can be estimated as marginal, comparing distributions of the waste in Figure 9.6 with Figure 9.52. This is the result of the attenuation of the neutron flux on top as well as downstream from the new target, thanks to the additional steel shielding of the target block.

10 Integration, Implementation, Planning & Logistics

This chapter is concerned with the planning of the dismantling of the existing Target M station, the installation of the new target station and secondary beamlines, and the required modifications to the experimental areas and overall layout of the experimental hall.

As a lot of the conceptual designs have only been completed in the process of compiling this CDR, the planning of the installation process is somewhat less detailed as the dismantling steps. After the description of all the relevant details, this chapter finishes with a timeline showing how all the work can fit into a single 16-month long shutdown of the proton accelerator.

10.1 Present Situation

Figure 10.1 shows a picture of the Target M region in the experimental hall of PSI. As can already be seen from this picture, it is a complicated area that has historically grown over the past five decades since the start of proton beam operations in 1974.

The elements of the Target M region are shown separately and more clearly in Figure 10.2. They consist of the following items:

1. **Target M:** The Target M is mounted in a steel vacuum chamber and fully encapsulated by the target shielding block.
2. **Beamline PiM1:** Two secondary beamlines are connected to the Target M in the forward direction with an angle of 22.5°. PiM1 is located on the left side of the proton beam channel.
3. **Beamline PiM3:** See (2). PiM3 is located on the right side.
4. **Target shielding block:** The target shielding block ($4.5 \times 4 \times 3.5\ m^3$) is constructed like a puzzle from several steel blocks with irregular contours.
5. **Main shielding:** The main shielding is a tunnel made of many concrete and iron blocks with a width of 5 m and a height of 4.5 m. The thickness of the side wall of the tunnel is 3 m on one side and 4.5 m on the other. The roof itself has a thickness of 4.5 m.
6. **Tertiary water cooling loop 7:** In this room, the water cooling installation for many of the nearby components

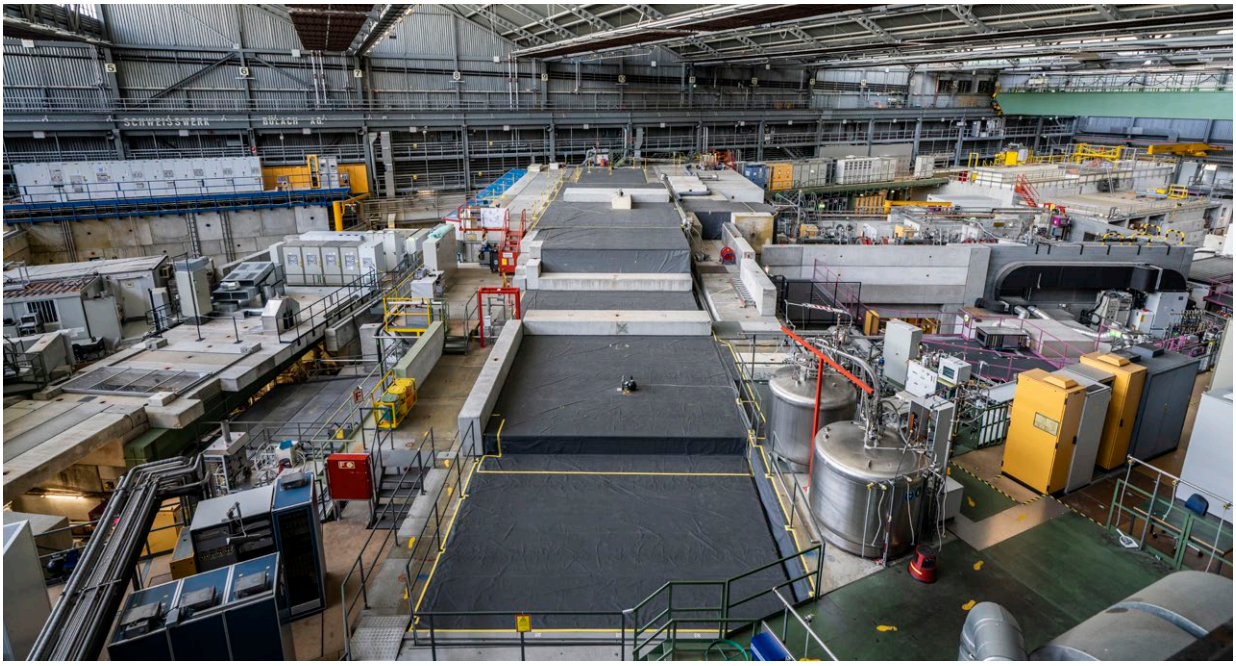

Figure 10.1: Image of the Target M region located slightly below the centre of the picture and the helium liquefaction plant shown in the bottom right part.

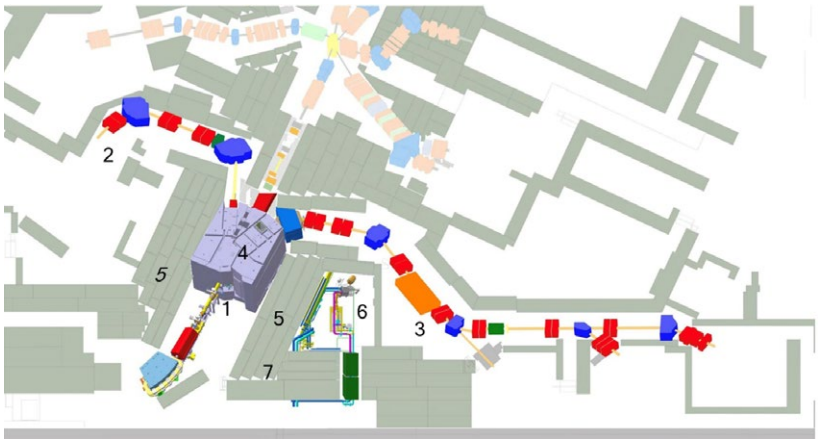

Figure 10.2: Elements in the Target M region: (1) Target M, (2) PiM1 beamline, (3) PiM3 beamline, (4), target shielding block, (5) iron and concrete main shielding, (6) tertiary water cooling loop 7, and (7) helium liquefaction plant (on top of main shielding).

is located. As the cooling water gets activated, this installation is embedded into the main shielding.

7. **Helium liquefaction plant:** The helium liquefaction plant is located on top of the main shielding as shown in Figure 10.1.

10.2 New Layout in the Experimental Hall

HIMB comprises a new target station and two new secondary beamlines. However, the new beamlines do not fit into the existing floor plan of the experimental hall. The beam area currently known as PiM1 will be given up to make space for the new MuH2 area.

An initial analysis showed clearly that major modifications are unavoidable. Figure 10.3 shows a concept for these modifications at the ground floor level. It is clear that additional planning and design is needed as, e.g., the layout of the upper floor has not yet been undertaken. The space formerly occupied by the injector 1 (1973-2011) and the adjoint low energy beamlines can be reclaimed for new purposes. The legacy arrangements for the current Target M beamlines can be given up. What is known today as the PiM1 beamline will become MuH2 (left arm in Figure 10.3). The right arm will be called MuH3 and will connect to much of the existing beamline currently known as PiM3.[1]

Two major infrastructure areas will be affected by this change. First, the bunker housing the water cooling loop "tertiary 7". This will need to be shifted away and will reclaim some of the space of the current PiM3 beamline that will no longer be used. More details on this can be found in

[1] To avoid confusion with existing beamlines carrying the identifier "1" in their names, the enumeration starts with 2.

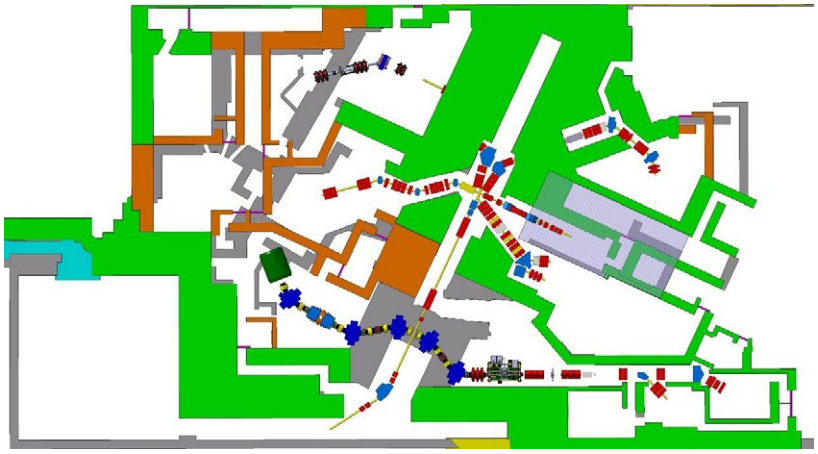

Figure 10.3: New layout superimposed on the current layout of the experimental hall. The concrete shielding walls shown in green remain unaltered. Grey walls will be removed and replaced by the new walls, shown in brown. Note: shielding around the new Target H is not shown for clarity.

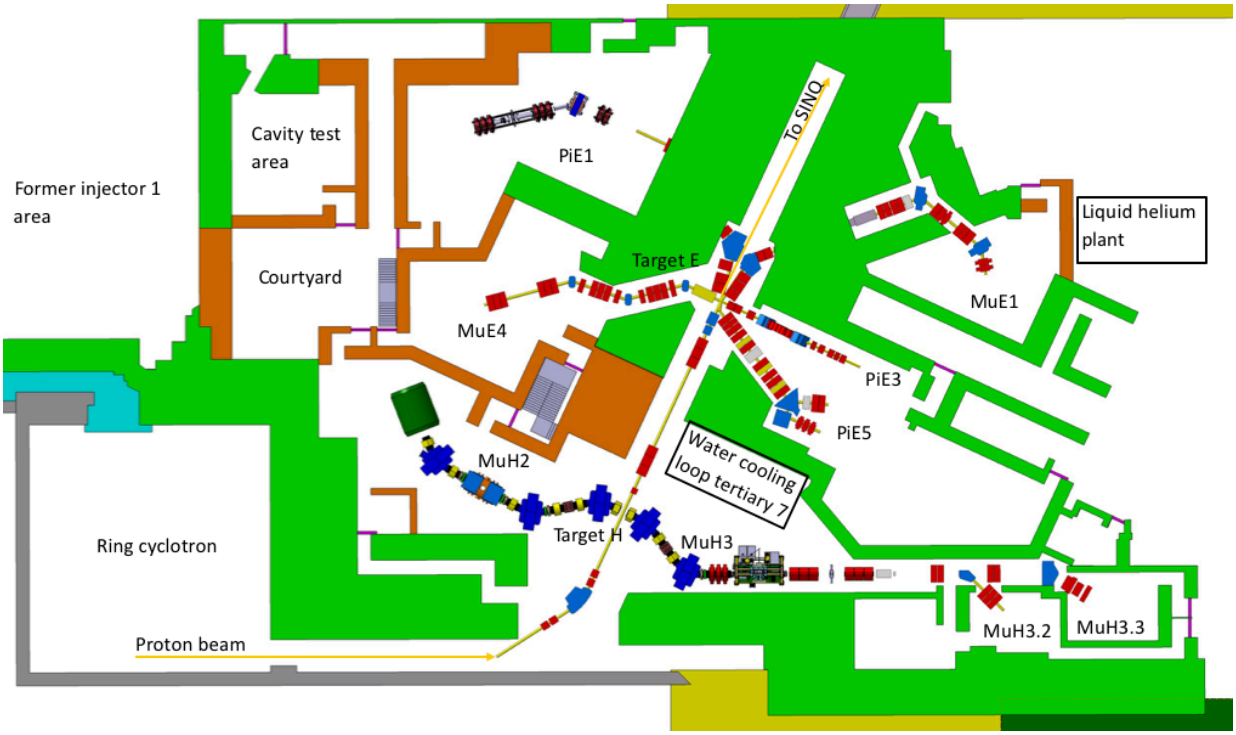

Figure 10.4: Situation in the experimental hall after the HIMB installation and with the cooling loop and liquid helium installation moved. The two new areas formed on the left of the PiE1 and MuE4 areas are used as an access courtyard and for the tests of accelerating cavities.

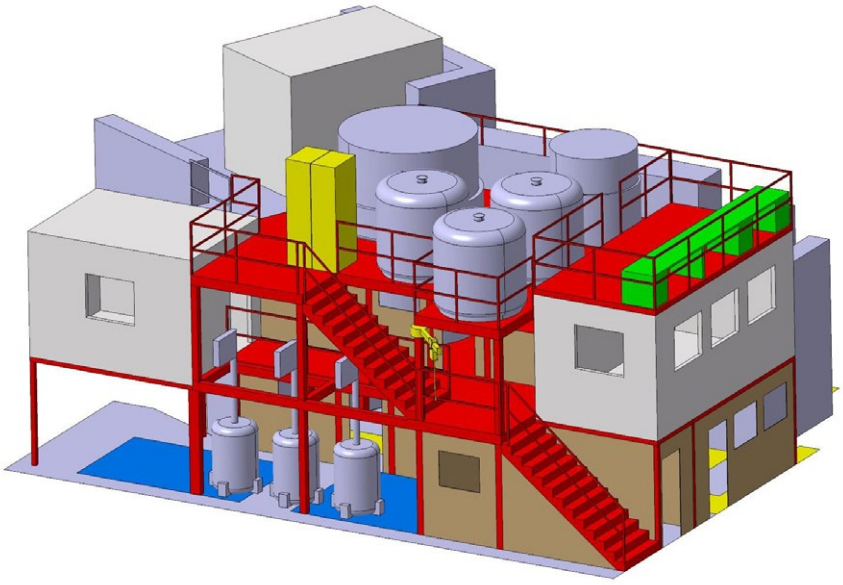

Figure 10.5: CAD rendering of the new helium liquefaction plant. The three vessels on the ground floor indicate the location of the filling stations for movable dewar vessels.

Chapter 12. Second is the helium liquefaction plant, which needs to be moved away. It is currently located on top of the tertiary 7 bunker. This plant provides liquid helium for the cooling of the muon channel in the MuE1 area, the superconducting magnet of the MEG experiment in the PiE5 area, and for helium supply handled by movable dewar vessels for general use. The solution found is described in the next section and further details can also be found in Chapter 12. The situation after the change and with these two infrastructures moved is shown in Figure 10.4.

10.2.1 New Location for the Helium Liquefaction Plant

The current location has the disadvantage that all dewar vessels for general use have to be craned from the platform to the respective areas, where it will be used. The proposed new location shown in Figure 10.4 has the advantage that the filling stations are on the ground floor. Figure 10.5 shows the general concept of this new installation. It does not only feature the filling of the liquid helium dewar vessels at ground floor, but also features additional work space for the maintenance of cryogenic equipment and integrates control rooms for the experiments taking place in the PiE3 and PiE5 areas. Refilling the dewar vessels will no longer require craning them down from the top of the shielding around TgM for most of the users, which is a clear advantage and a cost-saver.

10.3 Work Safety Enhancements

Many passageways in today's experimental hall have grown historically over the years and do not comply with current safety codes. Today, escape routes need to be at minimum 1.2 m in width and the total length to a safe place shall not be longer than 50 m.

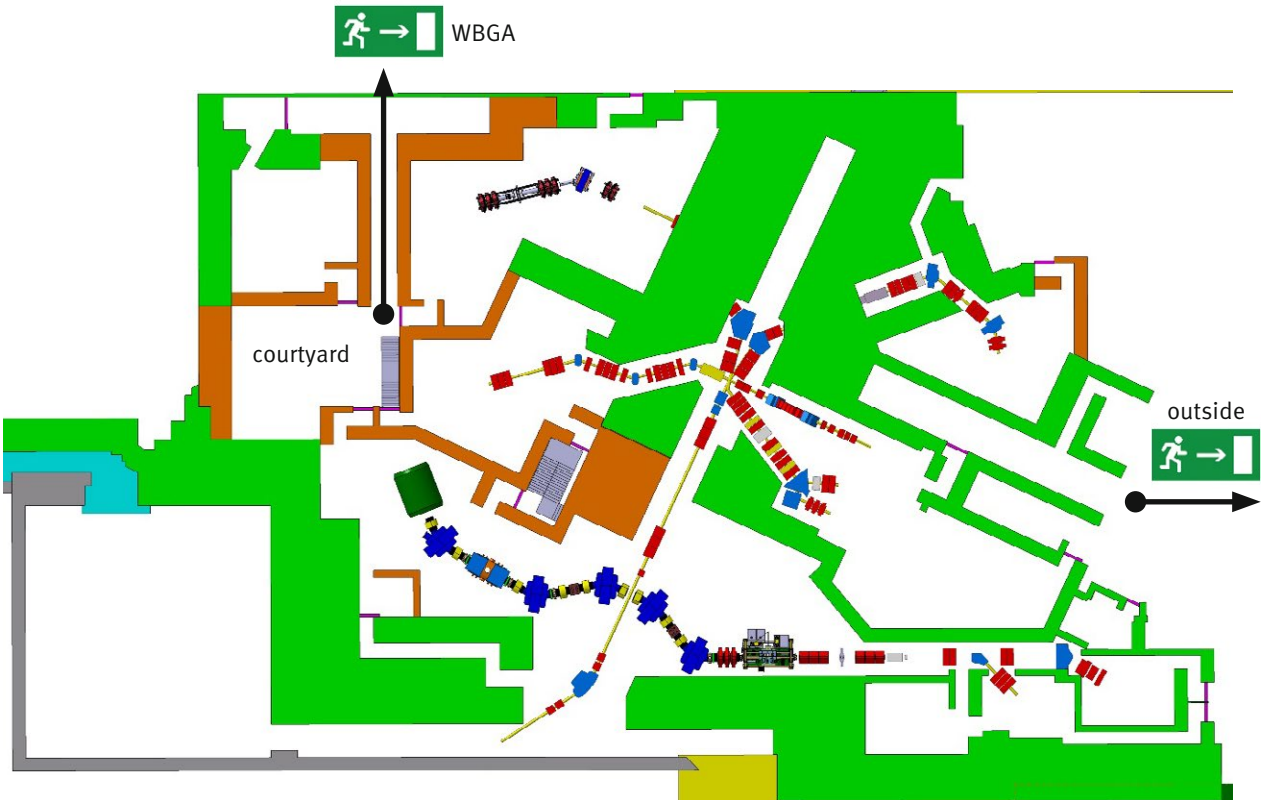

Figure 10.6: Overview of the escape routes in the experimental hall. A new escape route will be formed to lead from the central courtyard at ground level to the neighbouring building WBGA.

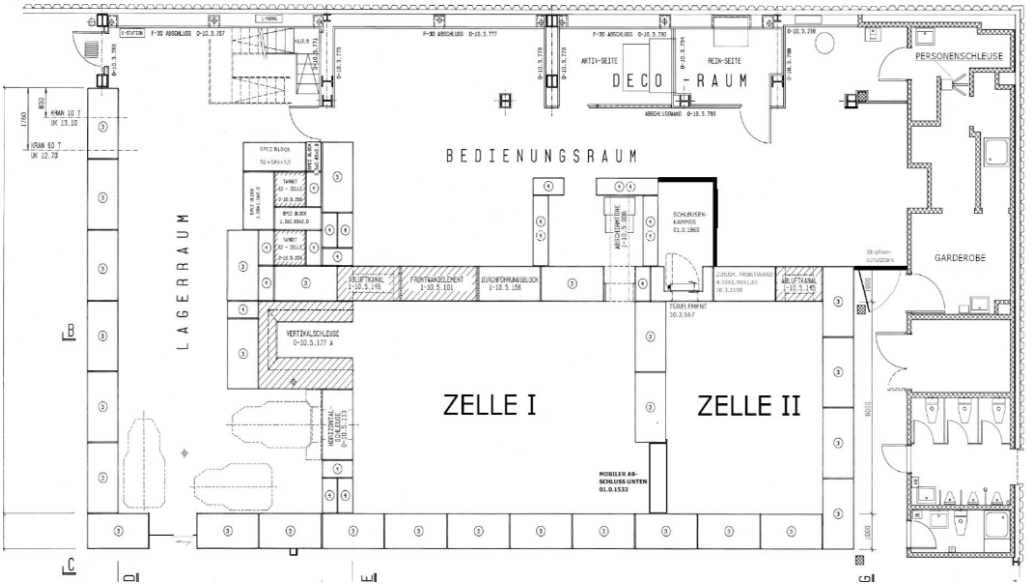

Figure 10.7: Picture showing the premises in ATEC. Shown are the service cells ("Zelle I + II"), the control room ("Bedienungsraum") and a storage room ("Lagerraum").

The changes for HIMB allow to address these issues. The new escape routes will fully comply. Additionally, the surrounding experimental areas will also feature two independent entries and exits to facilitate the escape into different directions.

The new concept shown in Figure 10.6 is a reduction of the existing situation to make it clearly structured. On the left side of the experimental hall a small courtyard will be formed as central access to the neighbouring experimental areas and for the pre-assembly of small installations. All surrounding experimental areas have their main entrance to this courtyard. This central space will become a direct passageway at ground level to the neighbouring building WBGA within a 15 m distance. This allows to be well below the legal limit of 50 m from within any of the surrounding areas. Another benefit of this passageway is the fact that equipment can be rolled in through WBGA, which reduces the overall use of the crane and results in more flexibility.

10.4 Processing and Machining of Highly Activated Parts in ATEC

The ATEC is PSI West's active facility for the treatment of highly radioactive components. During the implementation period, the ATEC is largely available for the HIMB project. In a first step, the steel shielding from Target M will be modified for reuse. Subsequently, the components that can no longer be used will be disposed of. The large containers filled with components during the dismantling process (see Section 10.5) will be opened inside the service cells and the components will then be treated remotely.

The ATEC facility is located in the southeast area of the WEHA experiment hall. The main purpose of the facility is to permit safe repair, modification and disposal of activated and contaminated components. The ATEC facility mainly receives components from the HIPA accelerator area, beam guidance systems and experimental facilities of PSI - West. The facility can be accessed from the experimental hall via a changing room and a security lock.

10.4.1 Premises in ATEC

Figure 10.7 shows the layout of the ATEC facility. The different capabilities are described below. Two service cells are classified as radiation controlled zone type IV. They are used to process contaminated or heavily activated components. The ATEC facility has two service cells, cell I has a floor area of 6 m × 9 m (54 m^2) and service cell II has an area of 6 m × 5 m (30 m^2). The infrastructure and the controls of the service cells are identical. The following devices are available in each of the two service cells:

- Power manipulator A-1000
- Hand manipulator A110, two times
- Overhead crane

- Step table
- Band saw
- Camera systems (Mirion)

All devices can be operated remotely from the control room and observed through the lead glass window and the camera system. If needed, personnel access to the service cells is possible via a security gate.

The control room summarizes all the remote controls for the devices operated in the service cells. In addition, all regularly required aids, tools, small machines and necessary radiation protection material are stored there. The service cells, the decontamination room and the storage room are accessible from the control room.

10.4.2 Accessing Material

The service cells have three options for entering and removing components due to be treated.

1. Access via the mobile roof openings
2. Access via the horizontal material lock (e.g. Target M, SINQ-Target)
3. Access via the vertical material lock (e.g. Target E)

In all three options, the components can also be transferred within a shielding bottle or exchange device.

10.5 Disassembly Process

The new HIMB facility will be installed at the position of the current Target M with the two secondary beamlines placed at 90 degrees to the proton beamline. For this reason, the current Target M and all the surrounding shielding needs to be completely dismantled.

The dismantling of the existing Target M station is an intervention in a rather complex environment. The different parts, areas and infrastructure equipment are intertwined and overlap each other. The experimental hall has continuously grown over the decades since its construction and especially in the context of older installations we are faced with sometimes significant uncertainty. Not all installations and adaptions are well documented and certain materials used are by now no longer reliable due to, e.g., embrittlement after the long period of beam operation.

10.5.1 Layout

The layout given in Figure 10.8 shows the proton beam line and shielding structures around the Target M installation. This is the region where the complete structure will be rebuilt and adapted to the new HIMB facility. The Target M with its

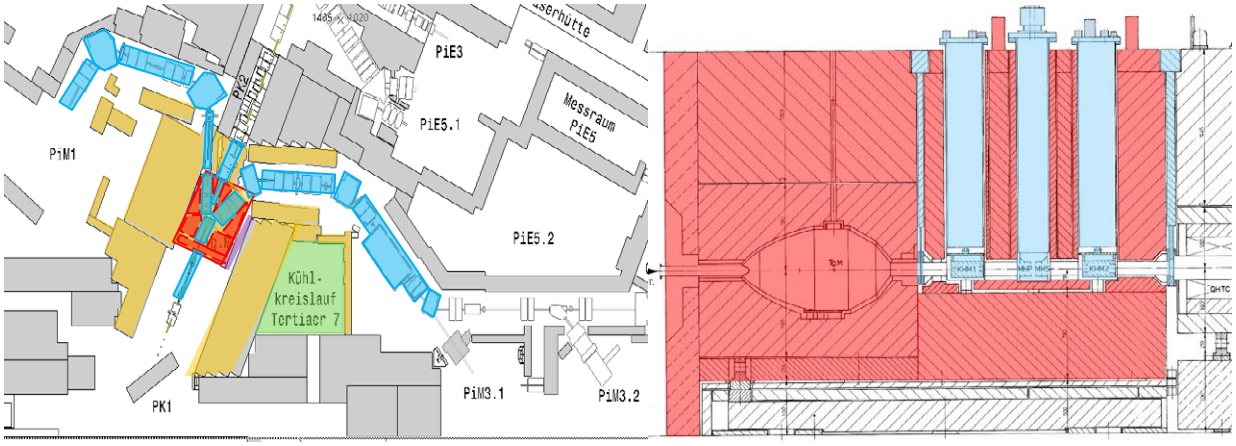

Figure 10.8: (Left) Layout of the target M region showing the items to be dismantled: Target shielding block (red), proton and muon beamlines (blue), shielding (brown), cable and piping channel (purple), and water cooling loop (green). (Right) Cross sectional view through the target shielding block showing the target vacuum chamber and the following inserts. The target block is enclosed on top with a roof made of concrete blocks (not shown here).

No.	Designation	Size	Load limit	Availability
1	Storage for proton channel concrete blocks and handling of goods	6 m×17 m = 102 m²	40 t/m²	Always
2	Storage area for light equipment	7 m×15 m = 105 m²	2.5 t/m²	Always
3	Pre-assembly area	5 m×7 m = 35 m²	40 t/m²	Always
4	Pre-assembly area	5 m×12 m = 60 m²	40 t/m²	Always
5	Pre-assembly area	5 m×9 m = 45 m²	40 t/m²	From 2024
6	Storage for activated elements	13 m×18 m = 234 m²	40 t/m²	From 2023

Table 10.1: Table showing the details of the available temporary storage and pre-assembly areas in the experimental hall. The location of these areas is shown in Figure 10.9.

primary steel shielding shown in red is located at the centre. Because of the close proximity to the Target M most of these parts are rather highly radioactive. This requires safe and remote handling during the dismantling process. The proton and secondary beam line components, such as diagnostics, magnets and vacuum chambers are coloured in blue. The main shielding block covering the whole proton beamline and target station (brown) is a complex cluster built of steel and concrete parts. The activated tertiary cooling loop (green) is situated inconveniently and will be moved. The channel for signal- and electrical cables, water pipes and air ducts is situated in between Target M and the main shielding (purple). With the dismantling of these complex structures, many uncertainties will still remain at the start of the process and the planning will need enough flexibility to be able to adapt to any potential challenges.

10.5.2 Temporary Storage and Pre-assembly Areas

The dismantling of the Target M region will require a lot of storage space as all of the parts will need to be temporarily placed somewhere before the reinstallation will take place. For this reason, we list in the following three sections the currently available temporary storage space available at PSI. Further elaborations and planning of the full dismantling steps will need to take place to assess whether this space is sufficient or whether additional space will need to be found.

10.5.2.1 Temporary Storage and Pre-Assembly Areas in the Experimental Hall

For the existing experimental hall, an overview of the available temporary storage and pre-assembly areas is given in Figure 10.9 and Table 10.1. During the preparatory phases not all of these areas will be available as they are also used for normal operation. During the long shutdown, these areas will be available and can be used for the dismantling and installation work.

Additional space for the pre-assembly of components can be created by the changes to the layout of the experimental hall described in Section 10.2. Before the completion of the central courtyard and the cavity test area a large space can be created of about 10 × 20 m² (shown in Figure 10.10) that can be used for this purpose.

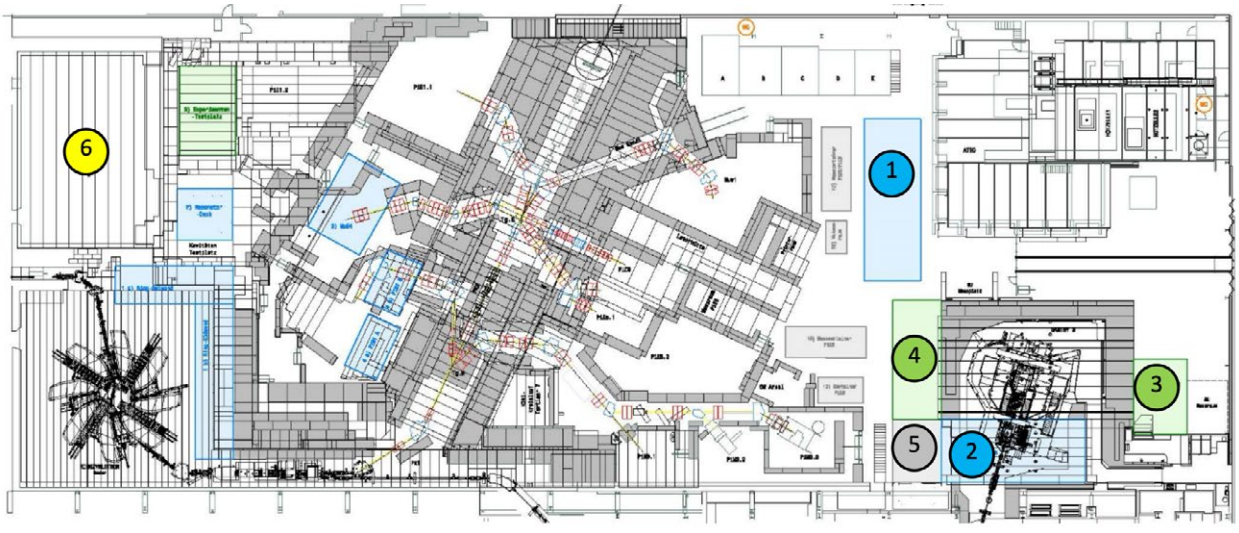

Figure 10.9: Overview of the existing temporary storage and pre-assembly areas in the experimental hall. The details according to the numbering shown are given in Table 10.1.

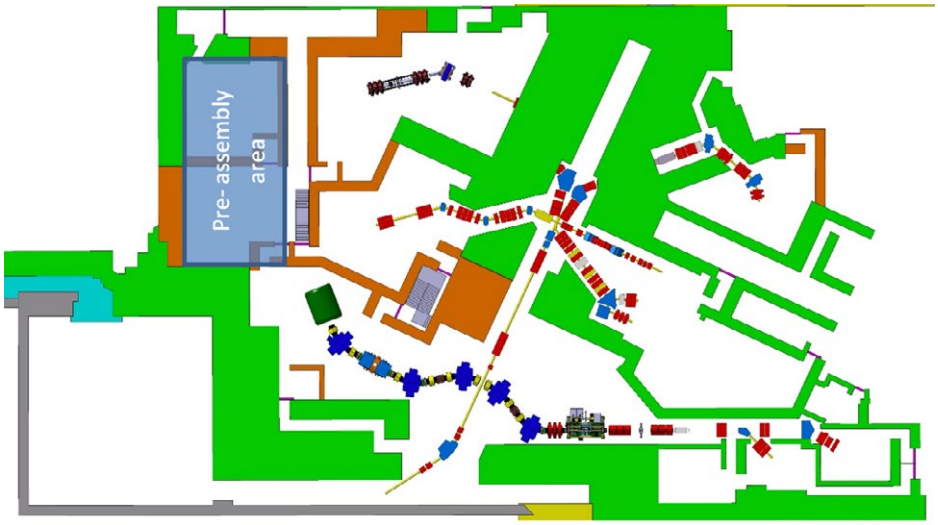

Figure 10.10: Pre-assembly area created during the changes to the layout of the experimental hall that can be used during the dismantling and installation process. This space is later converted into the central courtyard and cavity test area shown in Figure 10.4.

10.5.2.2 Temporary Outdoor Storage

Outside of the experimental hall of PSI an outdoor storage space is designated for the storage of concrete shielding blocks – see Figure 10.11. It is a designated Zone 0 according to the radiation protection regulations (see Section 11.1.1) with an overall size of about 700 m^2.

During the dismantling process we will have to temporarily store concrete blocks in this area. The final choice which of the concrete shielding blocks will be placed here, must be assessed according to radiation protection issues specified in Section 11.1.3.

The total amount of space needed for the concrete blocks being moved during the dismantling process is on the order of 1800 m^3. They are distributed in the following way: 500 m^3 from the changes to the former injector 1 experimental areas, 500 m^3 from the shielding of the secondary areas and about 800 m^3 from the shielding of the proton channel.

A large fraction of these concrete blocks will be reused during the installation process. The remaining concrete blocks will have to be disposed or stored for later use in future projects.

10.5.2.3 Additional Temporary Indoor Storage

During the dismantling process, many items in addition to the concrete blocks will have to be removed, which are later used again. Among those are control racks, power supplies, girders, platforms, magnets etc. Additionally, also the new elements that are being produced and delivered have to be stored before pre-assembly and installation. As space is at a premium in the experimental hall during the installation process, appropriate temporary indoor storage space will need be found elsewhere. As some of these items might be slightly activated, this space should be a designated radiological zone. The total space needed for these items is currently estimated at around 600 m^2.

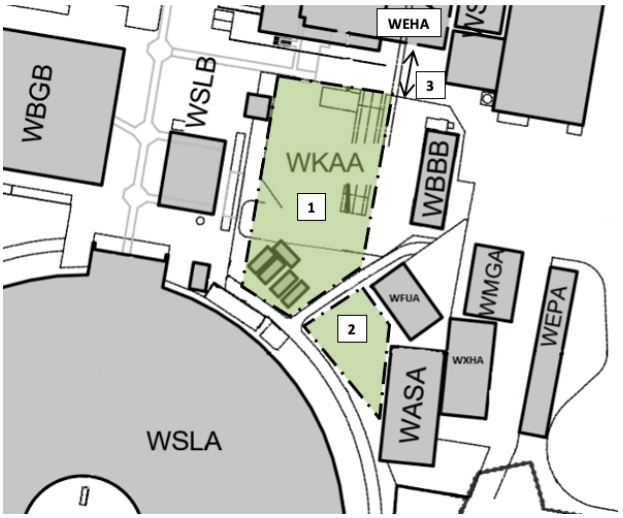

Figure 10.11: Location of the outside storage area WKAA (1) just in front of the experimental hall WEHA of PSI for dose rates ‹5 µSv/h. A second area (2) is currently being planned. Being in close proximity to the WEHA, there is good and easy access (3).

10.5.3 Universal Crane

For the handling of equipment in the proton beam channel during the dismantling process described in the next section, a new 32-ton universal crane with a length of 15 meters will be necessary. The crane will be installed under the radiation shielding. Due to the high radiation level, operation of the crane will be via remote control and a crane camera system.

10.5.4 Dismantling of the Existing Target M Region

The dismantling of the existing Target M region is a complex endeavour that is critical both in the overall planning of the shutdown of the HIPA facility and the complexity of steps that need to be undertaken in the handling of the highly radioactive parts. All the steps will of course occur following the radioprotection regulations outlined in Chapter 11 and will take place under the supervision and guidance of radiation protection officers. The following sequence describes a playbook on how the dismantling will happen, but it is also clear that still many more detailed studies need to be undertaken.

A failure-mode analysis of every step will be conducted at a later stage in order to prepare backup plans and alternatives solutions. Additionally, an inventory will track the dismantling of all the items, their activity level, storage location and re-installation (where appropriate).

At the current stage, the time needed for the complete dismantling given in the steps below is estimated at 9 months – see also Section 10.6.7.

1. *Dismantling of secondary beamlines PiM1 and PiM3*

   1.1 Removal of secondary beamline components

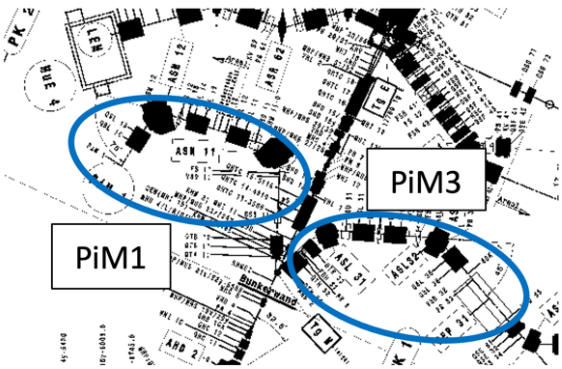

   All of the components can be accessed with the main crane of the experimental hall. This is a conventional procedure that takes place on a regular basis. The new HIMB installation has no need for most of these components. Those can be disposed, while others need to be placed in temporary storage.

   1.2 Dismantling platforms, galleries, cabinets, safety installations and local infrastructures

   A triage will take place to assess the suitability of these items for re-use or disposal

   1.3 Remove local shielding blocks in area

   These concrete shielding blocks will be placed in the outdoor storage area.

2. *Removal of Target M*

   First the concrete shielding on top is removed and brought to the outside storage. The removal of the Target M is a routine operation that is performed with dedicated exchange equipment. The activated target is transferred and stored in the ATEC facility.

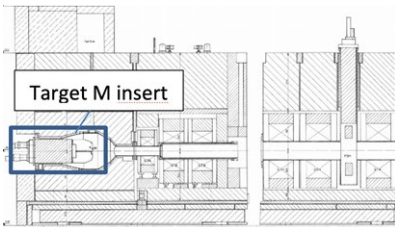

Cross-section through TgM region

TgM exchange device

3. *Removal of proton beam elements upstream of Target M (PK-1)*

   During this step the supports, guiding frames, local shielding blocks, girder with beam components, and additional infrastructure is removed and stored for reuse. After this, the area is prepared for the "contamination shielding" and the installation of the big containers used to remove the highly activated parts of the target shielding block (see step 5.4).

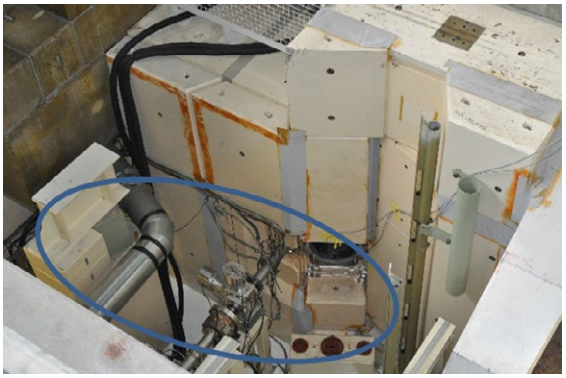

Elements upstream of the Target M region

4. *Removal of proton beam elements downstream of Target M (PK-2)*

   Various beamline components are removed with an existing exchange device. The open vacuum chambers are closed with flanges and are shielded locally. The corresponding shielding blocks are removed by crane and placed into shielding containers. The vacuum chambers themselves are bulky parts, which must be brought to and handled in an ATEC service cell.

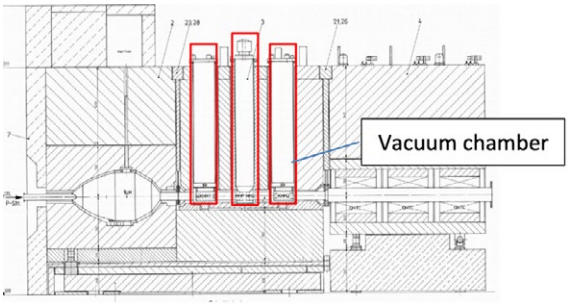

Cross-section through the Target M region showing the downstream beamline components.

5. *Preparation of the Target M station for remote dismantling*

   The picture shows the Target M region where the activation is too high such that these elements need to be dismantled remotely.

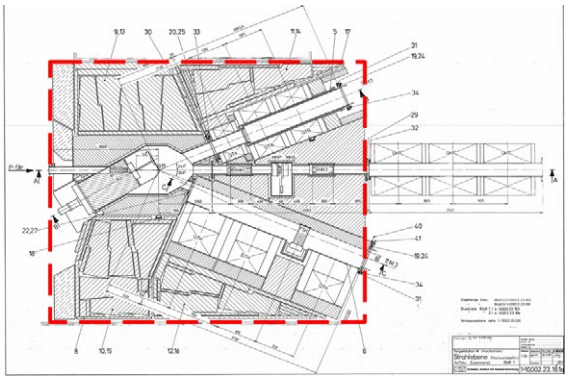

5.1 Installation of power manipulator

The power manipulator is extracted from the service cell II of ATEC and brought to the Target M station. This process and the use of this equipment was already undertaken once before in 1990/1991 during the upgrade of the Target E station.

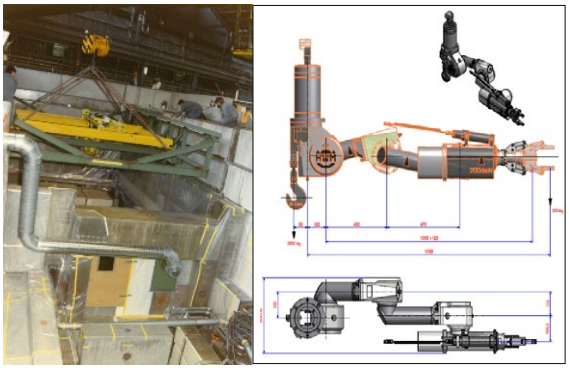

Installation of an additional crane and rail system together with a manipulator at Target E in 1990/1991.

5.2 Preparation of all the tools for the power manipulator

Grinder | Impact wrench | Drilling machine

5.3 Installation of local 32-t crane and remote camera system

32-t local crane

Remote camera system

5.4 Installation of contamination shielding with lock system

After the installation of the crane and power manipulator, a big shielding with three zones is being established around the Target M region. This is a tight and air-conditioned housing with a lock system between each zone. This lock system provides the means to safely handle the contaminated air inside the different zones. During the remote transfer of the big shielding containers, no uncontrolled escape of activated air can occur. The loaded containers are brought to ATEC for further processing and storage.

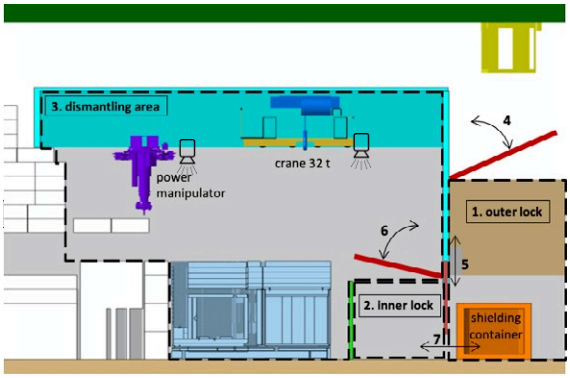

6. Dismantling process of the Target M shielding block

The dismantling plan for the different components of the target shielding block is certainly very challenging. Care needs to be taken in the sequence to optimally fill the shielding containers for an efficient process, but of course not to exceed the load limit.

The total weight of the target shielding block amounts to 360 tons. An estimated 150 t will not be suitable for re-use and will need to be prepared for long-term storage as radioactive waste.

6.1 Dismantling part 1

Shielding Target M top; Weight: 20’000 kg

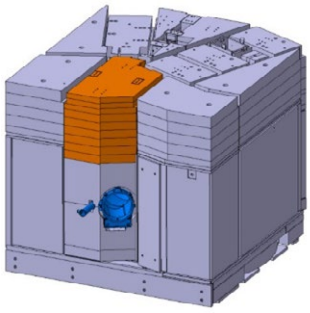

6.2 Dismantling part 2

Shielding B1 top; Weight: 15’000 kg

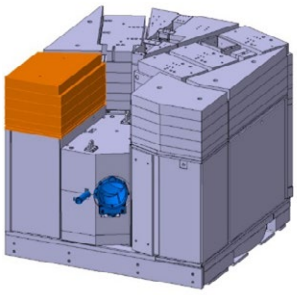

6.3 Dismantling part 3

Shielding B2 top; Weight: 12’000 kg

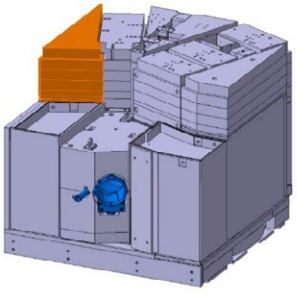

6.4 *Dismantling part 4*
Shielding B3 top; Weight: 16’000 kg

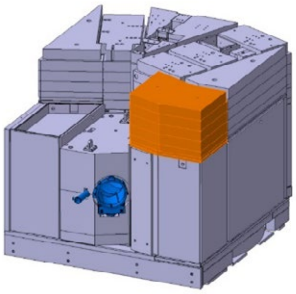

6.5 *Dismantling part 5*
Target structure; Weight: 20’000 kg

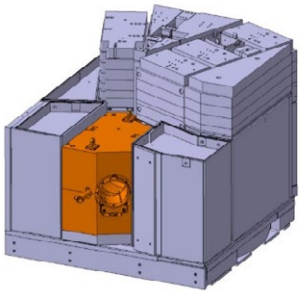

6.6 *Dismantling part 6*
Shielding PiM1 top; Weight: 11’000 kg

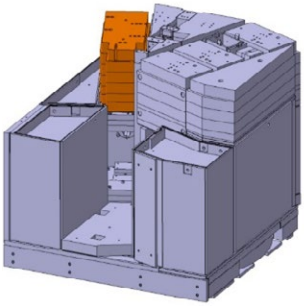

6.7 *Dismantling part 7*
Shielding B4 top; Weight: 12’000 kg

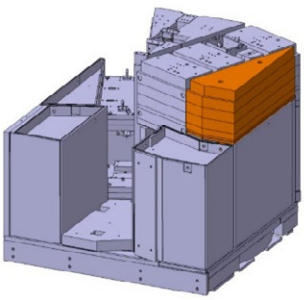

6.8 *Dismantling part 8*
Shielding PiM3 top; Weight: 40’610 kg

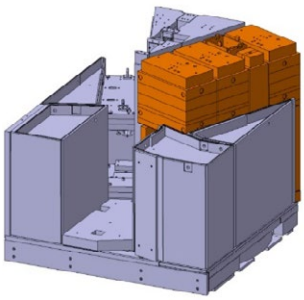

6.9 *Dismantling part 9*
Shielding collimators; Weight: 47’530 kg

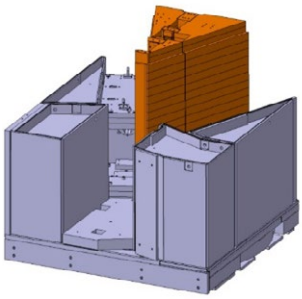

6.10 *Dismantling part 10*
Shielding B1; Weight: 24’600 kg

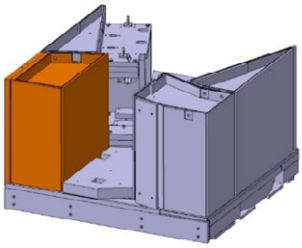

6.11 *Dismantling part 11*
Shielding PiM1; Weight:15’700 kg

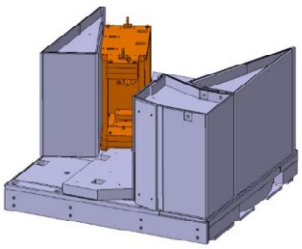

6.12 *Dismantling part 12*
Shielding B2; Weight: 27’820 kg

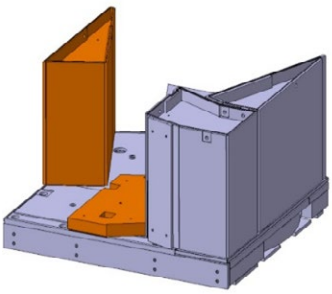

6.13 *Dismantling part 13*
Shielding B3; Weight: 23’700 kg

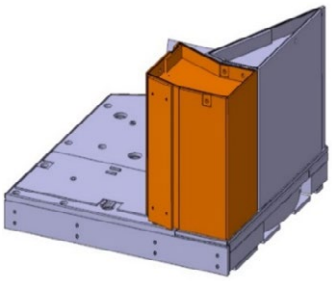

6.14 *Dismantling part 14*
Shielding B4; Weight: 17’620 kg

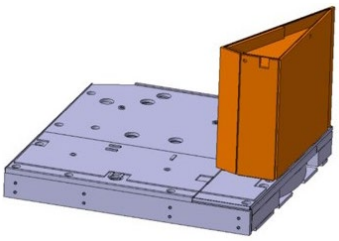

6.15 *Base plate*

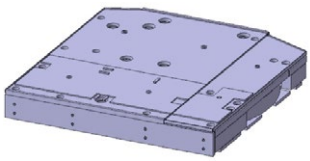

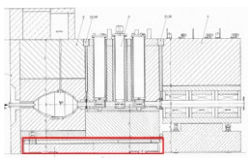

After these 14 dismantling steps only the base plate remains, which is embedded into the concrete floor. It will remain and form the basis for the installation of the new Target H.

7. *Removal contamination shielding*
After the dismantling of the target shielding block, the contamination shielding and remote handling tools are removed before proceeding with the dismantling of the main shielding.

8. *Dismantling of the main shielding*
The main shielding has a core of iron beams covered with concrete blocks; in total approximately 1’000 parts. The concrete blocks and iron beams can be moved using the standard crane of the experimental hall. Every concrete block will be checked for radiation and moved to the outside storage area. The dose rate of the blocks is expected to be low such that no special precautions or shielding should be necessary. The iron beams will need to be stored in one of the storage areas inside the experimental hall.

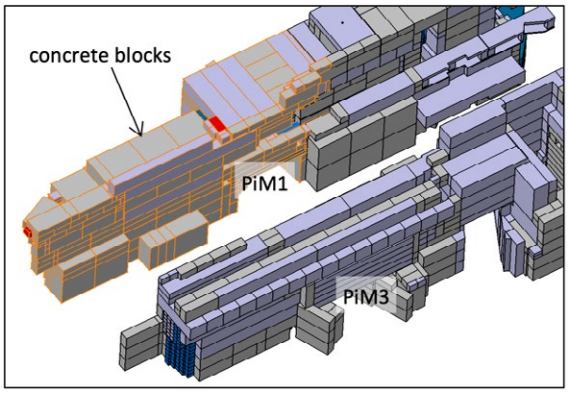

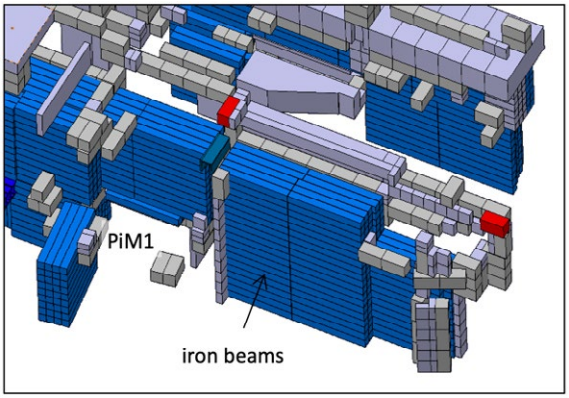

9. *Area clear for the installation of HIMB*
   At the end of all the dismantling steps, the former Target M region will look as shown above. Only the base plate remains and serves as the basis for the installation of the new Target H.
   The estimated dose rate of the base plate after 1 month of cool down is 55 µSv/h, such that only some local shielding is needed for the installation process of the new target station and secondary beamlines.

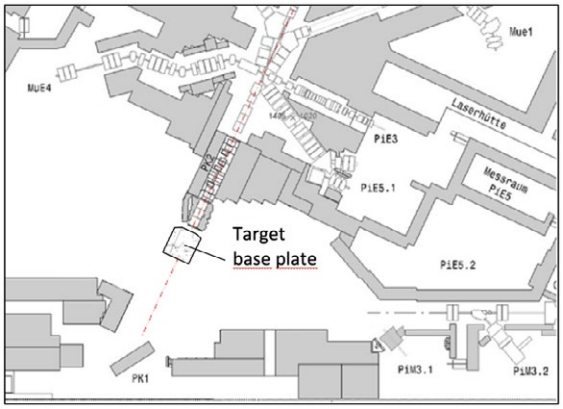

10. *Postprocessing*
    Cleaning and decontamination of all affected areas and components. Further classification and disposal of radioactive parts.

10.6 Installation Process

Since the design of the new Target H was developed at the same time as the installation process, the planning for the assembly process compared to the dismantling process has not yet been worked out at the same level of detail. The installation process section deals fundamentally with the pre-assembly of the new Target H, the planned reuse of activated material from the removal of Target M, and the subsequent installation of Target H in the proton channel.

10.6.1 Pre-assembly of Target H

Figure 10.12 shows a picture of the new Target H station and surrounding elements. The pre-assembly of the Target H station is carried out in one of the assembly areas (see Section 10.5.2) in the experimental hall WEHA as it was done in 1985 during the Target M upgrade.
The plans for the pre-assembly assume that only non-activated or weakly activated components will be used such that the work can be done with only limited restrictions from radiation protection. For the planned reuse of activated steel shielding, empty containers will be manufactured, which in a first step will serve only for structural assembly. In a next step, the containers will be filled with activated material from the removal of Target M in the ATEC facility.

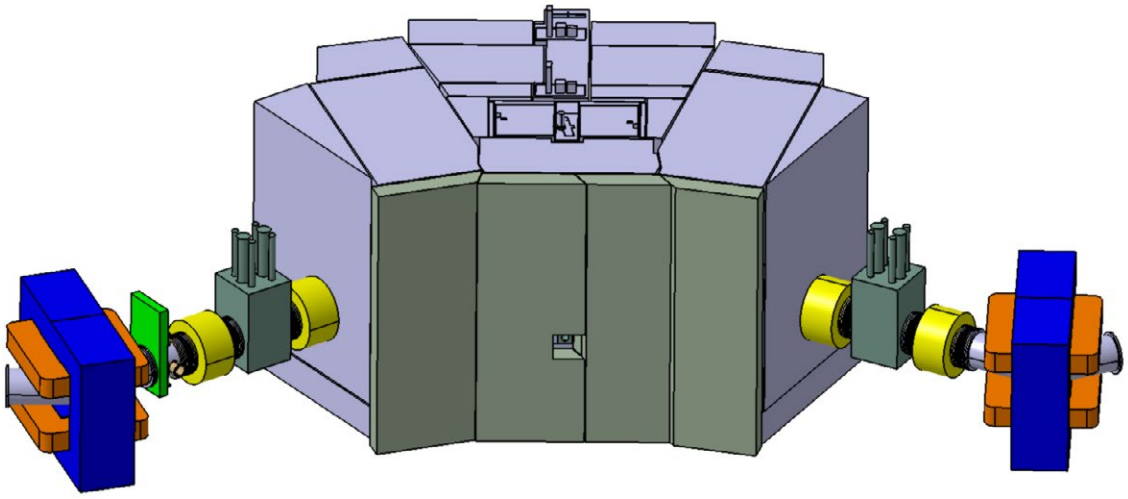

Figure 10.12: Picture of the target shielding block around the new Target H and the first part of the two beamlines MuH2 and MuH3.

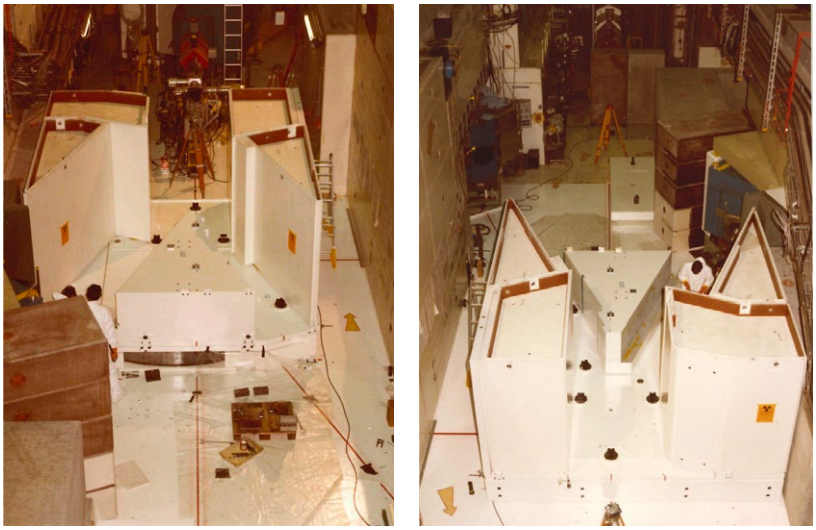

Figure 10.13: Structure of the Target M during the assembly in 1985 showing the differently shaped shielding containers.

Finally, in the pre-assembly phase, all possible system tests are carried out as well as the future remote-controlled handling of the components with the exchange devices during normal operation.

10.6.2 Reuse of Steel Shielding

The existing Target M consists of various steel shielding blocks (see Section 10.5.4 and Figure 10.13), which will be reused for the new Target H. The current planning assumes a total weight of about 200'000 kg of activated material which can be reused. The steel shielding blocks will be temporarily stored in large containers in the experimental hall after the removal of Target M. In a rolling process, the steel shielding blocks will be modified and prepared for reuse during the dismantling of Target M in the ATEC facility.

10.6.3 Integration of Target H into the Proton Beam

Figure 10.14 shows the position of the new Target H in relation to the existing shields. The layout of the shielding around the secondary beamlines has not yet been finalized and is missing in that picture. The CDR is a good basis for further planning for the construction steps of the main shielding.

10.6.4 Survey and Alignment

10.6.4.1 Alignment Concept

All components of the beamline are pre-assembled and aligned on the support structures (frames/girders). The main instrument for the alignment procedure is a laser tracker. The expected accuracy for the geometric alignment of com-

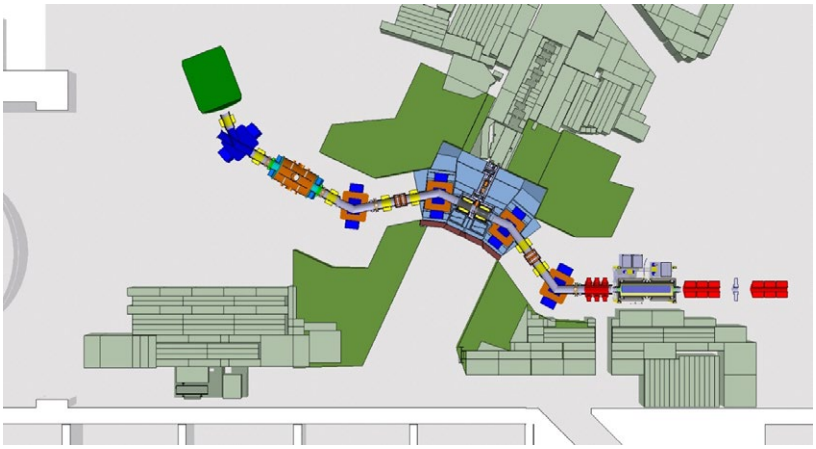

Figure 10.14: Picture of the new target station in the proton beam showing the target shielding block and main shielding. The shielding around the secondary beamlines has not yet been finalized and is thus not shown here.

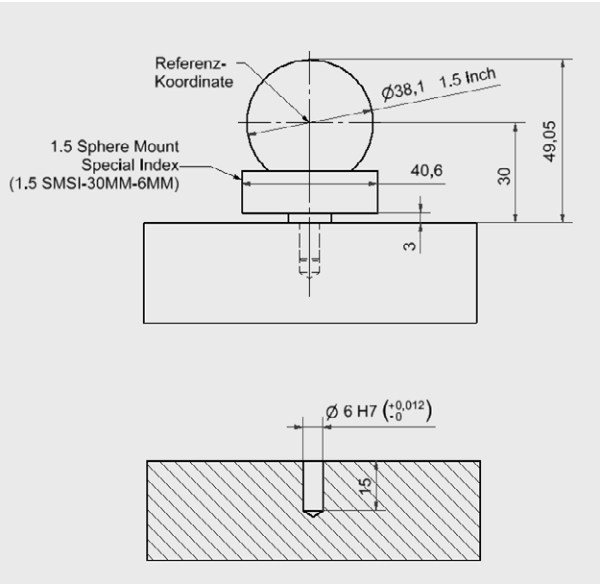

Figure 10.15 1.5: corner cube reflector used for the alignment of the different components.

ponents in a typical range of 10 m is better than 0.1 mm (σ_x, σ_y, σ_z).

It is required that each component is equipped with at least 3 or better 4 visible and well distributed reference points suitable for the placement of 1.5" corner cube reflectors (6 mm adapter) – see Figure 10.15. It is important that the relation (distances) of the coordinates of the reference mark to the physical centre is completely known. The task of fiducialisation must be done in advance. This should normally be done by the manufacturer or alternatively by the responsible PSI department.

The pre-assembled components are adjusted with the laser tracker in the final position on the basis of the 3D measurement and the new measurement network described below.

10.6.4.2 Reference Coordinate System and Network

To ensure data management and data exchange of coordinate sets, the already existing coordinate system can be used. This frame is still the basic working coordinate system for adjustment tasks. Coordinate sets of local coordinate systems are transformed by the alignment group.

A surveying network exists in the experimental hall whose fiducials are distributed throughout the entire facility. Based on these fiducials, the existing surveying network can be expanded. For this purpose, new points are installed at selected locations and newly determined.

10.6.5 Flowchart of the Installation of Target H

The following flow chart shows the installation processes in chronological order:

Pre-assembly of Target H in the WEHA experimental hall
For the pre-assembly, the complete target station is set up in the experimental hall.

Construction of the new target chamber in the proton beam on the base plate.
The current plans assume that the target chamber can be set up conventionally without remote handling.

Alignment of the target chamber

Installation of the proton & secondary beamlines
After the target chamber has been installed, the proton beamline and the first part of the secondary beamlines including alignment are set up.

Installation main shielding of target H
The main shielding consists of a core of iron beams covered with concrete blocks. The blocks and beams (about 1000 pieces) can be moved with a standard crane. The dose rate of the blocks is at a low level; no special precautions or shielding is required.

Pre-installation of infrastructure components

Installation of the activated shields
The steel shielding blocks from Target M, modified in the ATEC facility, are inserted into the target station. Here, future planning will determine whether the installation can be implemented conventionally or remote-handling is necessary.

Installation of technical connections to the new components (water, electricity, etc.)

Overall system test
Testing of all system functions and test of remote handling with the new built-in components.

Tasks during the beam period 2026	May	June	July	August	September	October	November	December
PiM3								
Removal of helium liquefaction plant above PiM3								
End of beamtime								
Remove the beamline from FS32 to QSE34								
Start remove infrastructure								
PiM1								
End of beamtime								
Remove magnet power supplies								
Remove infrastructure								
Remove ventilation system								
Remove platform / part of the walls								
Remove Beamline from QSL13 to QSL18								
MuE4								
End of beamtime								
Remove roof								
Remove infrastructure								
Remove container MuE4/PiM1/Platform								
Remove wall between MuE4/PiM1								

Table 10.2: Table showing the work that could be performed before the long shutdown in the three areas PiM3, PiM1 and MuE4.

10.6.6 Staged Start of the Long Shutdown

The HIPA facility is not only providing protons for the experimental hall. During the long shutdown, the isotope production, SINQ and UCN also have to stop.

In order to save some time during the long shutdown, a staged start could be a possibility. In this scenario the affected areas in the experimental hall stop their experimental program already somewhat earlier such that infrastructure work and the removal of non-critical shielding and components can take place in advance, while otherwise normal user operation continues.

Table 10.2 shows the work in the three areas PiM3, PiM1 and MuE4 that could potentially be completed in the three months before the start of the long shutdown.

10.6.7 Timeline for the Dismantling and Installation

Table 10.3 shows the current timeline for the dismantling of Target M and the installation of the new Target H, secondary beamlines, and experimental areas taking a total of 16 months until completion. A more detailed planning of all the steps has only just started and will of course constantly be updated and adapted based on the newest information available.

Some more detail on the steps needed for the changes to the experimental areas and infrastructure work that could potentially be done (depending on funding and manpower) before 2025 is also given in the following section.

		2027												2028			
		January	February	March	April	May	June	July	August	September	October	November	December	January	February	March	April
1	**Dismantling target M and main shielding**																
1.1	Dismantling infrastructure and concrete roof shields																
1.2	Removing Target M and Collimator KHM2																
1.3	Removing of components from proton beam section PK-1																
1.4	Prepare lock system and radiological zones for remote handling																
1.5	Remote dismantling of the target station M																
1.6	Dismantling lock system																
1.7	Dismantling main shielding																
2	**Handling of components in the ATEC**																
2.1	Modification of steel shielding from the target M																
2.2	Disposal of components target M																
3	**Installation target H & beamlines and main shielding**																
3.1	Pre-assembly target H																
3.2	Assembly of target H & beamlines in proton beam																
3.3	Assembly of main shielding																
3.4	Set-up of infrastructure for Target H																
3.5	Overall system test																
4	**Installation secondary beamlines**																
4.1	MuH2; installation new area																
4.2	MuE4; modification area																
4.3	PiE1; modification area																
4.4	MuH3; installation new area																
4.5	PiE5; restoration of area walls																

Table 10.3: Table showing the rough timeline and schedule for the dismantling of the Target M station and the installation of the new Target H, secondary beamlines, and experimental areas.

10.6.8 Optional Timeline Scenario with Anticipated Infrastructure Changes

The following tables show in more detail the work needed for the changes of the experimental areas and the work needed for the changes to the north part of the experimental hall, the helium liquefaction plant and liquid nitrogen supply (see Sections 10.2, 10.3, and Section 12.5). The baseline planning foresees these works to happen during the main funding period 2025–2028 and especially during the long shutdown 2027–2028. Depending on the availability of funding and manpower, some of this work could be performed – as assumed in these tables – already before the main funding period 2025–2028.

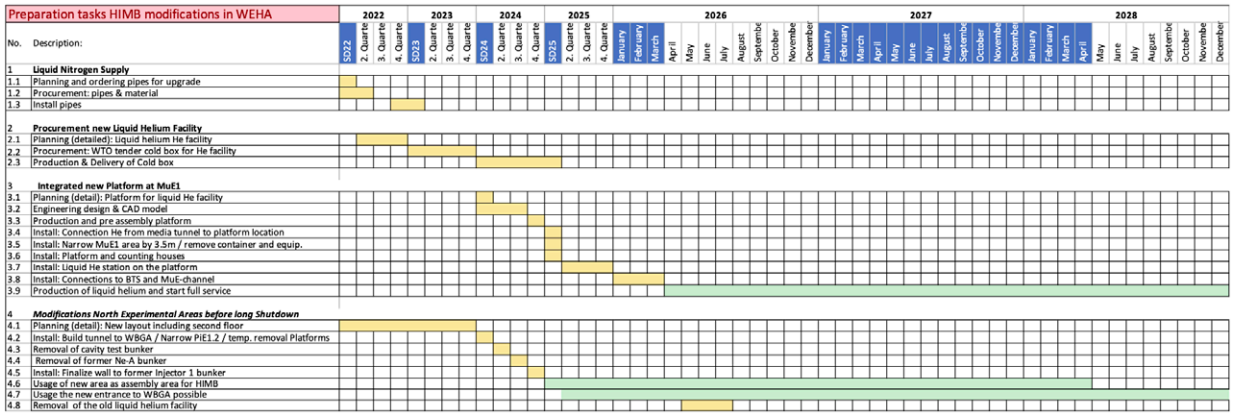

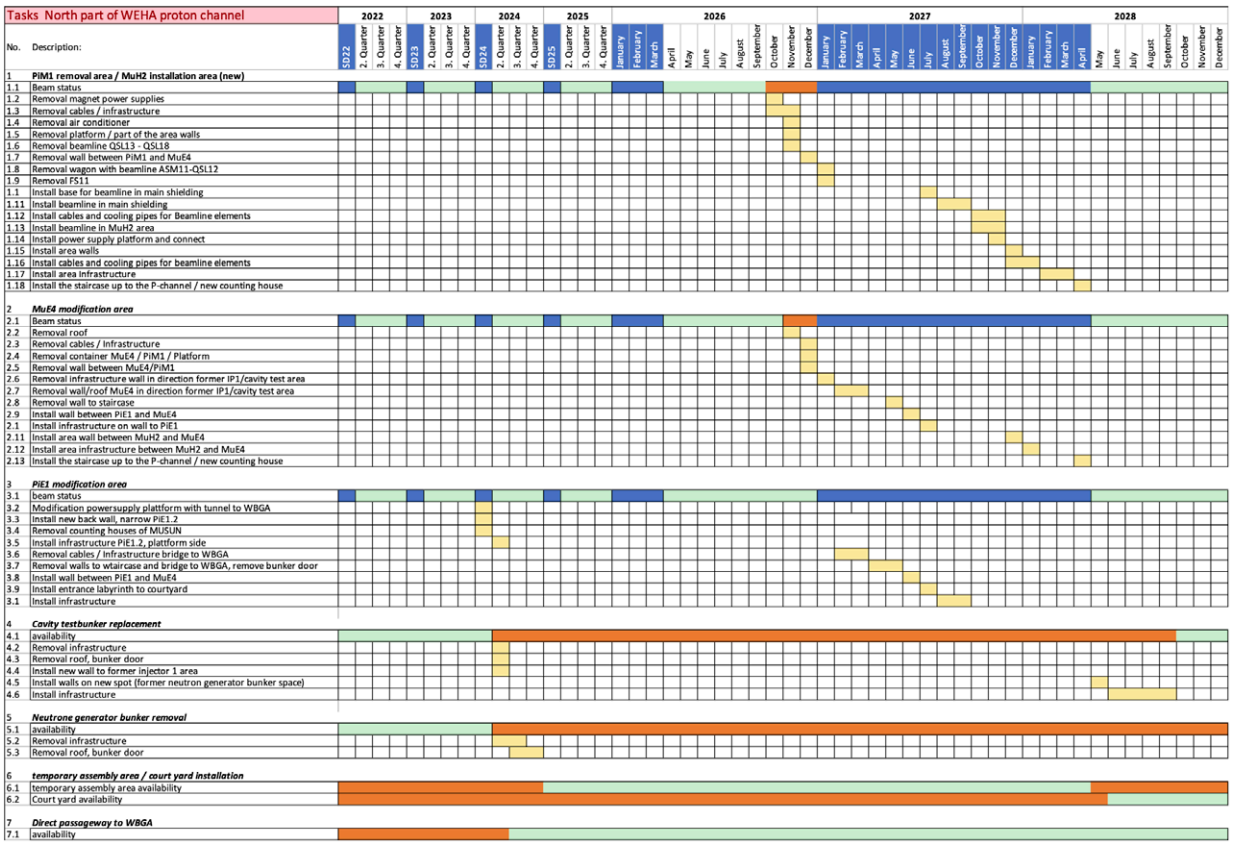

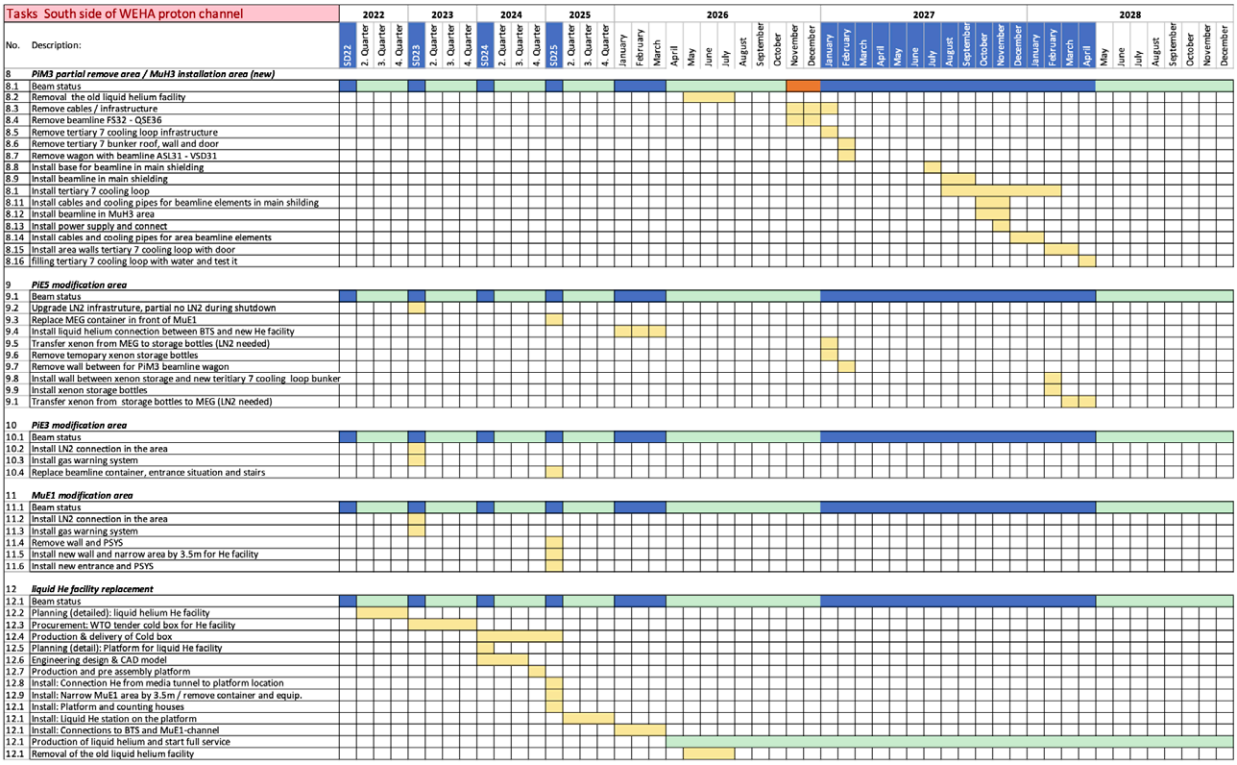
Tasks South side of WEHA proton channel
2022
2023
2024
2025
2026
2027
2028
No.
Description:
SD22
SD23
SD24
SD25
1. Quarter
2. Quarter
3. Quarter
4. Quarter
January
February
March
April
May
June
July
August
September
October
November
December
8 PiM3 partial remove area / MuH3 installation area (new)
8.1 Beam status
8.2 Removal the old liquid helium facility
8.3 Remove cables / infrastructure
8.4 Remove beamline FS32 - QSE36
8.5 Remove tertiary 7 cooling loop infrastructure
8.6 Remove tertiary 7 bunker roof, wall and door
8.7 Remove wagon with beamline ASL31 - VSD31
8.8 install base for beamline in main shielding
8.9 Install beamline in main shielding
8.1 Install tertiary 7 cooling loop
8.11 Install cables and cooling pipes for beamline elements in main shilding
8.12 Install beamline in MuH3 area
8.13 Install power supply and connect
8.14 Install cables and cooling pipes for area beamline elements
8.15 Install area walls tertiary 7 cooling loop with door
8.16 filling tertiary 7 cooling loop with water and test it
9 PiE5 modification area
9.1 Beam status
9.2 Upgrade LN2 infrastruture, partial no LN2 during shutdown
9.3 Replace MEG container in front of MuE1
9.4 Install liquid helium connection between BTS and new He facility
9.5 Transfer xenon from MEG to storage bottles (LN2 needed)
9.6 Remove temopary xenon storage bottles
9.7 Remove wall between for PiM3 beamline wagon
9.8 Install wall between xenon storage and new teritiary 7 cooling loop bunker
9.9 Install xenon storage bottles
9.1 Transfer xenon from storage bottles to MEG (LN2 needed)
10 PiE3 modification area
10.1 Beam status
10.2 Install LN2 connection in the area
10.3 Install gas warning system
10.4 Replace beamline container, entrance situation and stairs
11 MuE1 modification area
11.1 Beam status
11.2 Install LN2 connection in the area
11.3 Install gas warning system
11.4 Remove wall and PSYS
11.5 Install new wall and narrow area by 3.5m for He facility
11.6 Install new entrance and PSYS
12 liquid He facility replacement
12.1 Beam status
12.2 Planning (detailed): liquid helium He facility
12.3 Procurement: WTO tender cold box for He facility
12.4 Production & delivery of Cold box
12.5 Planning (detail): Platform for liquid He facility
12.6 Engineering design & CAD model
12.7 Production and pre assembly platform
12.8 Install: Connection He from media tunnel to platform location
12.9 Install: Narrow MuE1 area by 3.5m / remove container and equip.
12.1 Install: Platform and counting houses
12.1 Install: Liquid He station on the platform
12.1 Install: Connections to BTS and MuE1-channel
12.1 Production of liquid helium and start full service
12.1 Removal of the old liquid helium facility

11 Radiation Protection & Safety

11.1 Radiation Protection

The operation of the HIPA facility falls into the scope of Swiss legislation. Among other guidelines, beam operation must be in accordance with the Radiological Protection Act RPA [Swiss Federal Council, 1991], the Radiation Protection Ordinance RPO [Swiss Federal Council, 2017], the guideline ENSI-G12 [ENSI-G12], the approval AG-0444.12.001 [AG-0444.12.001] and PSI internal guidelines [PSI-AW-96-18-01]. In the following chapters, first general radiation protection aspects will be discussed (Sections 11.1.1, 11.1.2, 11.1.3, 11.1.4, 11.1.5) followed by specifications valid especially for the dismantling process (Sections 11.1.1.1, 11.1.2.1, 11.1.4.2).

11.1.1 Radiological Zoning Concept

The different radiological zone types are classified according to the potential expected airborne and surface contamination according to the RPO [Swiss Federal Council, 2017]. The parameters to assess the radiological zone types are the "CS", which is a nuclide-specific guidance value for surface contamination (SI unit: Bq/cm^2) and the "CA", which is a nuclide-specific guidance value for airborne contamination (SI unit: Bq/cm^3). Tabulated nuclide-specific values can be found in annex 3 of the RPO [Swiss Federal Council, 2017]. In a supervised area (zone type 0) and in controlled areas (zone types I to IV) a cumulative yearly dose for persons more than 1 mSv is possible. The classification of different zone types is illustrated in Figure 11.1.

With all installed shielding, the experimental hall is a zone type I with no expected surface contamination (less than 1 CS) and with an airborne contamination ‹ 0.1 CA.

11.1.1.1 During the Dismantling Process

To access the maintenance level, concrete shielding has to be removed and contamination can be expected. From experience at the HIPA facility, the main dominating nuclides for surface contamination at the maintenance level outside the beamline system are Be-7, Na-22, Na-24, Co-60, Co-57, Eu-152, Eu-154 and Sb-124 and for airborne contamination, when vacuum systems are opened, H-3. According to the prevalent radiological situation, which is assessed by the radiation protection personnel through contamination and dose rate mappings during service and shutdown maintenance work, the radiological zone is adapted. When vacuum systems are opened, additional aerosol measurements for H-3 are performed. From experience, the maintenance level in the Target M region is assessed as zone type III while at the experimental beam lines a zone type II is expected. The dress code is set appropriately according to the directives of the radiation protection personnel [PSI-AW-96-99-04]. During the dismantling of the Target M shielding, a zone type IV will be defined which is only accessible with full-body protection suits and under supervision by the radiation protection personnel. When highly activated components must be handled, this zone must only be accessible by remotely controlled manipulators due to the expected high dose rates and contaminations.

Zone type	Surface contamination C_S	Airborne contamination C_A
0	$C_S < 1 \cdot CS$	$C_A < 0.05 \cdot CA$
I	$C_C < 1 \cdot CS$	$0.05 \cdot CA \leq C_A < 0.1 \cdot CA$
II	$1.CS \leq C_S < 10.CS$	$0.05.CA \leq C_A < 0.1.CA$
III	$10.CS \leq C_S < 100.CS$	$0.1.CA \leq C_A < 10.CA$
IV	$C_S \geq 100.CS$	$C_A \geq 10.CA$

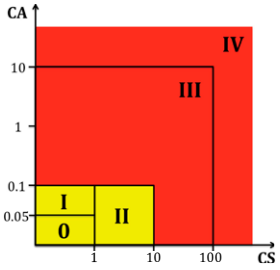

Figure 11.1: Radiological zoning concept according to [Swiss Federal Council, 2017]

11.1.2 Lower Pressure Staging

According to ENSI-G12 guideline chapter 6.4 [ESNI-G12], a lower pressure staging and a directed air flow from a lower to a higher zone must be guaranteed. Between the environment and a zone type III or IV, a permanent lower pressure of at least 50 Pa must be established. This holds for the whole proton beam line channel. The air from the proton beam line channel must be filtered and led through the monitored exhaust air channel where aerosol measurements take place.

11.1.2.1 During the Dismantling Process

During the dismantling of the Target M region, a permanent lower pressure of at least 50 Pa between the experimental hall (zone type I) and the zone type IV must be established. Additionally when beam components are dismantled, the beamline must be sealed to ensure that surface contamination stays inside the beam system. When the vacuum system is opened, a directed airflow due to lower pressure into higher zones must be established. This is achieved for example by connecting a "filter mobile" directly to the primary vacuum system where air is extracted and filtered through the filter mobile. The filtered air from the filter mobile is led to the monitored exhaust air channel where aerosol measurement takes place. As the filter inside the filter mobile can accumulate activated particles, it is essential to place the filter mobile including the attached hoses inside a zone II or higher.

11.1.3 Storage of Concrete Shielding Blocks

When the concrete shielding blocks are removed during the dismantling process, the radiation protection personnel will inspect the blocks for loose contamination and dose rate. Following radiological criteria must be fulfilled in order to store the blocks inside a radiological zone type 0 or I:

1. The loose surface contamination must be less than the nuclide-specific surface contamination guidance value "CS" specified in annex 3 of the RPO [Swiss Federal Council, 2017] to store the blocks at the outside storage are WKAA (zone type 0) or in the experimental hall WEHA (zone type I).
2. Additionally dose rate measurements at the surface of the blocks have to be performed.

Category of people	Quantity	Limit
Occupationally exposed to radiation Category A	effective dose	20 mSv/ year*
	skin dose	500 mSv/ year
	lens dose	20 mSv/ year **
Occupationally exposed to radiation Category B	effective dose	6 mSv/ year
	skin dose	150 mSv/ year
	lens dose	15 mSv/ year
Age 16 until 18	effective dose	6 mSv/ year
Pregnant women	effective dose for unborn child	1 mSv
General public	effective dose	1 mSv/ year
	skin dose	50 mSv/ year
	lens dose	15 mSv/ year
Personal dose outside company premises due to direct radiation	effective dose	0.1 mSv/year

* With permit of regulating authority, limit can be increased by exemption to 50 mSv/year if the cumulative dose of 5 successive years is below 100 mSv.

** For people who are occupationally exposed to radiation, the organ equivalent dose for the eye lens can be increased by exemption to 50 mSv/year, if the cumulative dose of 5 successive years is below 100 mSv.

Table 11.1: Dose Limits according to [PSI-AW-96-18-01]

1. Inside a supervised or controlled area		
	permanent working place	ADR ‹ 5 µSv/h
	places without time limitation	ADR ‹ 10 µSv/h
	no permanent stay (e.g. storage rooms)	ADR ‹ 25 µSv/h
	maintenance work under supervision by radiation protection personnel and according to the operating manual	1 m Sv/h ‹ ADR ‹ 10 mSv/h
	Only with special permit and under permanent supervision by radiation protection personnel	ADR › 10 mSv/h
2. Outside a supervised or controlled area		
inside company premises	permanent stay (170 h/week)	ADR ‹ 0.1 µSv/h
	permanent working place (40 h/week)	ADR ‹ 0.5 µSv/h
	no permanent stay (e.g. staircases or storage rooms)	ADR ‹ 2.5 µSv/h
outside company premises	permanent stay (170 h/week, e.g. guest house)	ADR ‹ 0.1 µSv/h
	no permanent stay (e.g. construction area)	ADR ‹ 0.5 µSv/h

Table 11.2: PSI requirements for ambient dose rates (ADR) for different type of zone classifications. Optimization is finalized when the dose rate does not exceed 10% of the guiding values valid for controlled areas.

a) In order to store the concrete blocks on WKAA (zone type 0), the measured ambient dose rates must be in compliance with the operating instructions of the WKAA [PSI-AW-83-18-04]. According to [PSI-AW-83-18-04], the ambient dose rate at the border of the WKAA must not exceed 100 µSv per week. To comply with this guiding value, the surface dose rate on each side of each individual block must not exceed 5 µSv/h measured at a distance of 10 cm.
b) To store the concrete blocks in dedicated areas inside the WEHA (zone type I), dose rate measurements are performed by the radiation protection personnel. According to the results, they will arrange the blocks to minimize the dose rate for freely accessible areas around the blocks and to ensure that the dose rates according to Table 11.2 are followed.

Under special circumstances and approval by the legal authority, it is possible to store potentially activated concrete shielding blocks outside company premises, e.g. at the parking lot of PSI West. Therefore two criteria according to RPO art. 106 [Swiss Federal Council, 2017] must hold and be checked before by radiation protection personnel:

1. The maximum ambient dose rate at a distance of 10 cm from the surface excluding natural background radiation must be less than 0.1 µSv/h (netto).
2. The surface contamination must be less than the nuclide-specific surface contamination guidance value "CS" specified in annex 3 of the RPO [Swiss Federal Council, 2017].

Additionally some special precautions have to be taken in account, e.g., the storage area and the material stored has to be marked clearly.

11.1.4 Dose Limits

For a planned radiological exposition situation according to [Swiss Federal Council, 2017], dose limits have to be assessed. These limits as given in Table 11.1 must not be exceeded.

11.1.4.1 Ambient Dose Rates

The following Table 11.2 summarizes the limits for ambient dose rates (ADR) for different types of zone classifications. These standard values guarantee that the dose limits according to Section 11.1.4 are complied with.

A PSI basic rule according to the RPO art. 4 and 60 [Swiss Federal Council, 2017] states, that radiation shielding design should result in a dose rate not exceeding 10 % of the guiding values valid for the controlled areas. The calculations for the necessary radiation shielding have to be in accordance with Swiss legislation and are described in Sections 9.4 and 9.5. If an unexpected exceeding of the limits happens, several actions can be considered: Reduction of operation time, installation of additional local shielding or reduction of beam intensity.

11.1.4.2 During the Dismantling Process

According to Table 11.1, maintenance work with an ambient dose rate ›1 mSv/h must be carried out under supervision by the radiation protection personnel. For all working steps involving the dismantling process, a detailed radiation protection planning will be performed in collaboration with other sections.

11.1.5 Emission Limits

According to Table 11.3, following emission limits for PSI in total must not be exceeded.

Issue	Quantity	Limit
Exhaust air and sewage water	Dose guidance value related to source term ("quellenbezogener Dosisrichtwert"), effective dose for the population in a worst case scenario	0.15 mSv for anual rate
		0.2 mSv per incident for short-term emission

Table 11.3: Limits for the emission of radioactive substances according to [PSI-AW-96-18-01]

11.2 Personal Safety System

Areas that are used for production and transfer of ionizing radiation have to be surveyed according to the RPO [Swiss Federal Council, 2017] and [EDI, 2017a]. This is achieved by a person-safety-system (PSYS), which ensures the absence of radiation while the area could be accessed and safely prevents access during beam operation.

The basic conditions for the PSYS will be set after an analysis of all potential risks for every area, but will have to fulfill the conditions specified in the protection concept [PSI-TM-96-03-04]. That includes the operation of the PSYS by the control room. Generally, every entrance to the areas has to be surveyed and locked during beam operation. The beam operation in every area is controlled by at least one area-specific safety element (i.e. beam-stopper) and the main beam-stopper BW2. An additional measuring device can be used to control the absence of ionizing radiation. The PSYS could also include the protection against several different dangers, i.e. moving components (e.g. robots) or laser systems.

The technical specifications of the PSYS system are discussed in Chapter 12.8.

11.3 Disposal Concept

The disposal concept comprises the radiological characterization of activated or potentially activated material which has to be cleared from mandatory licensing and supervision by the legal authority FOPH ("Federal Office of Public Health"). Therefore the concept does not comprise the handling and treatment of radioactive waste material. To achieve this, clearance measurements have to be performed according to RPO art. 106 [Swiss Federal Council, 2017] with following criteria:

- The specific activity must be below the nuclide-specific clearance limit "LL" according to annex 3 of the RPO [Swiss Federal Council, 2017]
- The maximum ambient dose rate at a distance of 10 cm from the surface excluding natural background radiation must be less than 0.1 µSv/h (netto).
- The surface contamination must be less than the nuclide-specific surface contamination guidance value "CS" specified in annex 3 of the RPO [Swiss Federal Council, 2017].

If the measurements indicate, that the material can be released according to RPO art. 106 [Swiss Federal Council, 2017] after a maximum decay period of 30 years, the activated material can be stored in decay storages according to RPO art. 117 [Swiss Federal Council, 2017]. Other disposal paths are the landfilling and the recycling. To perform the necessary measurements, PSI will have the infrastructure within a dedicated building on site (WMGA, "Freimessgebäude") including measurement equipment for total gamma measurements and in-situ gamma spectrometry. Table 11.4 lists a first estimate of the volume of the material (without concrete shielding) which has to pass through the clearance process.

Origin	Material Type	Estimated weight [t]
Dismantling of experimental areas and cooling circuit 7: pipes, valves	stainless steel	7
Ventilation pipes (pK2) and dismantling experimental areas (steel sheets, cable racks)	steel	21
Flexible hoses	plastics	2
Valves for rubber hoses	brass	1
Cable material	copper, PVC	9
installation material (steel sheets, plugs)	steel, aluminium	7

Table 11.4: Estimate of the material, which has to pass through the clearance process. The volume corresponds to a weight of about 50 tons. Note that the mentioned material does not include the concrete shielding blocks.

12 Building and Infrastructure

12.1 Present Situation

Installations in the region of Target M have grown during the past decades and now represent a complex and nested arrangement of different systems, components and infrastructure elements. For HIMB, a large part of these installations must be disentangled, dismantled and newly assembled. Replacements are inevitable, as most of the components are at end-of-life or based on legacy technology. In particular, all electrical cabling urgently needs renewal in any case. At present, the main helium liquefaction plant is mounted on top of the structure of the Target M region. This plant supplies all users within the experimental hall WEHA and neighboring SINQ building and is furthermore a contingency solution for the overall helium demand of all users on the PSI campus. Continuity of these functions and relocation of the plant will be key issues associated with the HIMB project. Figure 12.1 shows a picture of the Target M region and the helium liquefaction plant.

12.2 Basic Considerations, Requirements and Constraints

Infrastructure components within the affected area are currently not exclusively serving the Target M region. Various parts like the cryogenic helium liquefaction station support a wide range of users or areas within the building. Initial project planning included temporary or alternative supply solutions. Meanwhile, a decision for a long shutdown was made. With some exceptions, e.g. the supply of electric power, these alternative solutions are therefore no longer necessary.

Overall constraints are the very tight space in the affected area, and the dismantling and handling of activated and partly contaminated parts and components.

12.3 Electrical Installations

12.3.1 Power Distribution and Energy Supply

The currently installed power in the experimental hall WEHA is sufficient. The main energy distribution for the WEHA building will remain at its present position. Because of the new building planned for TATTOOS, two existing transformers have to be relocated and will be installed on a new podium. During the 2022 shutdown, one power distribution infrastructure (WEHA Westside) will be renewed.

For the HIMB project, new power distributions in each of the new experimental areas have to be installed. The existing main distributions need to be updated based on the new area and infrastructure design.

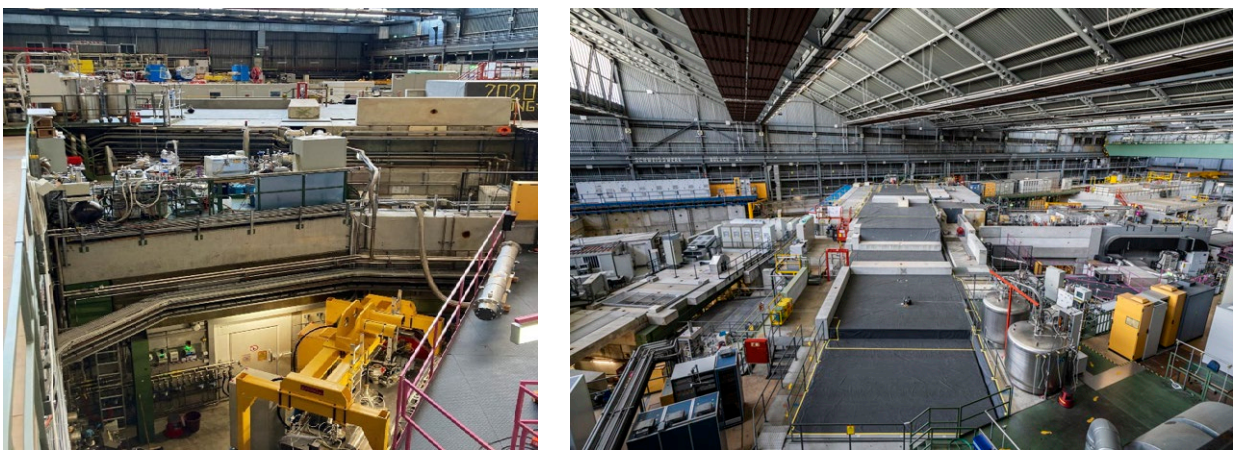

Figure 12.1: (Left) View of the Target M region. (Right) Helium liquefaction plant on top of the Target M shielding.

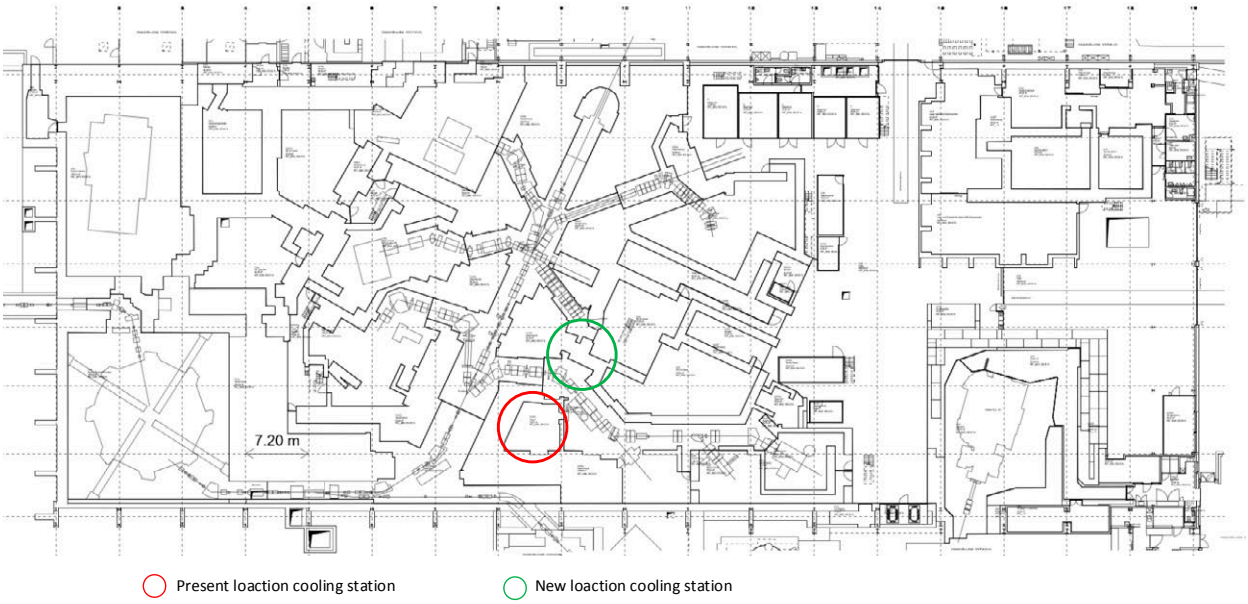

Figure 12.2: Present and new location of the water cooling installation.

12.3.2 Cabling and Installation

A high number of existing cables need to be replaced. Many cable trays, some cables and other infrastructure components have to be adapted to the new layout of the affected area.

All cables associated with the new areas and beamlines have to be changed or replaced and need to be shielded according to EMC requirements. This results in an increase of cabling volume by approximately 1/3 for the new muon beamlines, and respective requirements for additional space on the cable trays.

For a planning based on resilient data, the inventory of existing cables will be verified during the 2022 shutdown.

12.4 Cooling System

In order to obtain space for the adapted systems, components and building infrastructures, extensive dismantling and relocation work in the area of the cooling system is necessary. In general the cooling station has to move as the new muon beamlines cross the space of the existing installation; see Figure 12.2. Most of the components have been in service for approximately 15 years; selected components may have a residual life of further 15 to 20 years.

For the HIMB project, a new and tailored cooling infrastructure has to be designed. Focus is set on the beam path components, the beam dump and the experimental facilities. The new cooling system is planned and built taking energy and efficiency optimizations into consideration. As far as possible, the existing cooling circuits and components will be reused or modified. The existing cooling supply of the Target M is assigned to the cooling circuit tertiary no. 7 and the existing cooling water distributions are reassigned. The connections for cooling of the consumers are renewed. Due to space constraints, the tertiary cooling circuit no. 7 is being rebuilt at a new, suitable location as shown above. The existing, well-preserved main components such as pumps, heat exchangers, filters, control valves are partially activated or contaminated and will be reused to minimize waste. As part of the energy optimization and the move, the existing 20-year-old control system will be replaced and redesigned according to the current state of the art and the electrical cabling will be completely exchanged.

12.5 Cryogenic System

The main topic in terms of cryogenic systems is the reuse or replacement of the 1990 Sulzer helium liquefaction plant at a new location in the WEHA and the installation of a second liquid nitrogen (LN2) feed to increase supply reliability.

12.5.1 Solution a) Reuse of Existing Plant

The reuse of the existing plant at a new location in the WEHA may be considered. The cost of adapting the infrastructure at the new location are comparable to the cost of installing a new plant. This solution would be financially interesting, but involves certain risks that must be clarified in detail in advance.

The plant will be about 40 years old when HIMB goes into operation. In order to ensure continued high-availability operation, various components will have to be renewed. However, we know that some critical components in the coldbox can no longer be manufactured identically due to a lack of documentation from the manufacturer. In addition, the unit already had a crack in the vacuum envelope about 10 years ago.

12.5.2 Solution b) New Plant

The new liquefaction plant can be built in the WEHA even before the HIMB implementation. This, and the procurement of a new plant instead of relocating the old one, will allow PSI to maintain the redundant supply of liquid helium during the conversion. It will only be briefly interrupted during a shutdown when the old plant is switched off and the new one is connected.

12.5.3 Upcoming Work on the Liquefaction Plant

- The procurement of a new plant would require a WTO tender for the new liquefaction plant, which is expected to take > 9 months. A new liquefaction plant has a delivery time of about 18 months.
- A multi-storey steel structure must be designed and manufactured, on which the liquefaction plant will be installed.
- A breakthrough has to be laid from the supply tunnel under the WEHA to the new location in order to lead the helium lines from the compressors in the building WKSB and the required infrastructure to the liquefaction plant.
- The two existing 2000L and a new additional 2000L dewar must be installed with three new transfer lines.
- For the helium transfer into the mobile dewars three new transfer lines have to be designed and installed.
- Two new transfer lines to the experiments MuE1 and BTS must be planned, manufactured and installed.

12.5.4 Other Upcoming Work

- The cold head overhaul workshop, which is currently located around the existing liquefaction plant, has to be built and installed at the new location in the premises under the new liquefaction plant.
- The LN2 lines in the WEHA, which are currently fed from only one tank at the building WBGB (T2), will have to be partially renewed and extended. The tank located next to SINQ (T1) is also to be connected to this network to ensure a redundant supply to the WEHA. For this purpose, approx. 180 m of new LN2 lines have to be planned, manufactured and installed.

12.5.5 Conclusions

The comparison of the existing cryogenic system with the planned upgrades and changes is shown in Figure 12.3 and Figure 12.4. These changes will lead to a redundant and more reliable supply of liquid nitrogen and easier handling and modernized infrastructure for the distribution of liquid helium.

12.6 HVAC

The HVAC system consists of an air cooling system above the steel shielding of the proton channel and an air extraction in order to maintain a certain level of underpressure in the channel. The installation will reach end-of-life and therefore a total replacement of the present system including controls is foreseen. The existing components have to be removed and decontaminated if required..

The existing air cooling system of PiM1 will be replaced and re-sized according to the required cooling load.

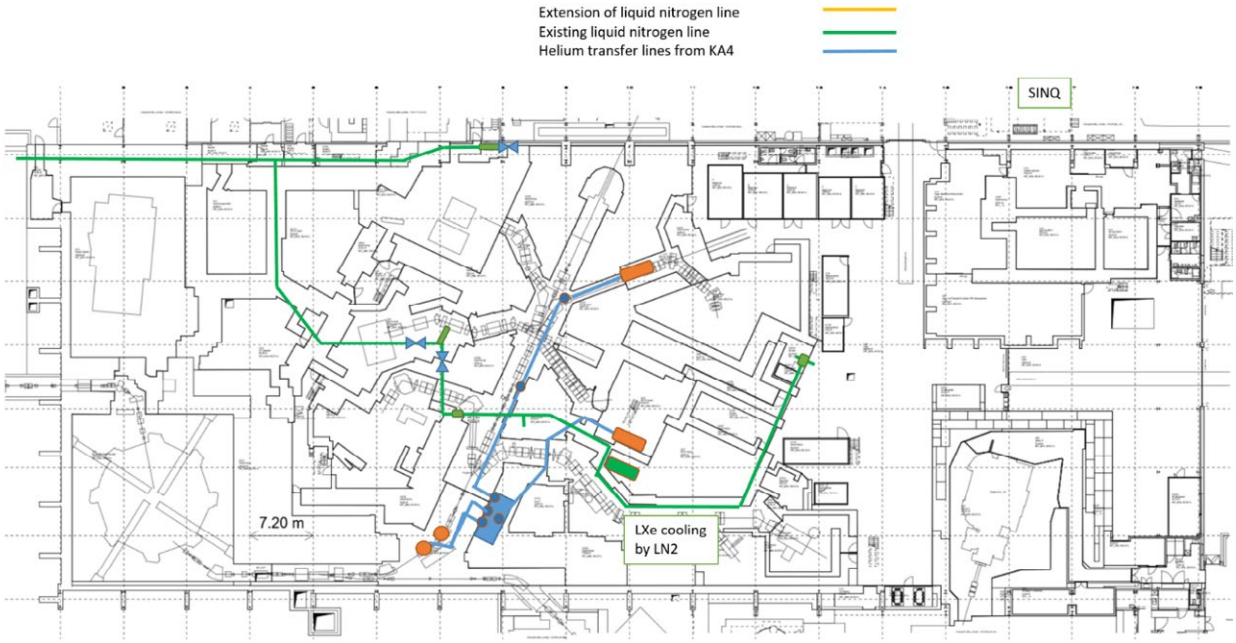

Figure 12.3: Existing liquid nitrogen and helium distribution in the experimental hall.

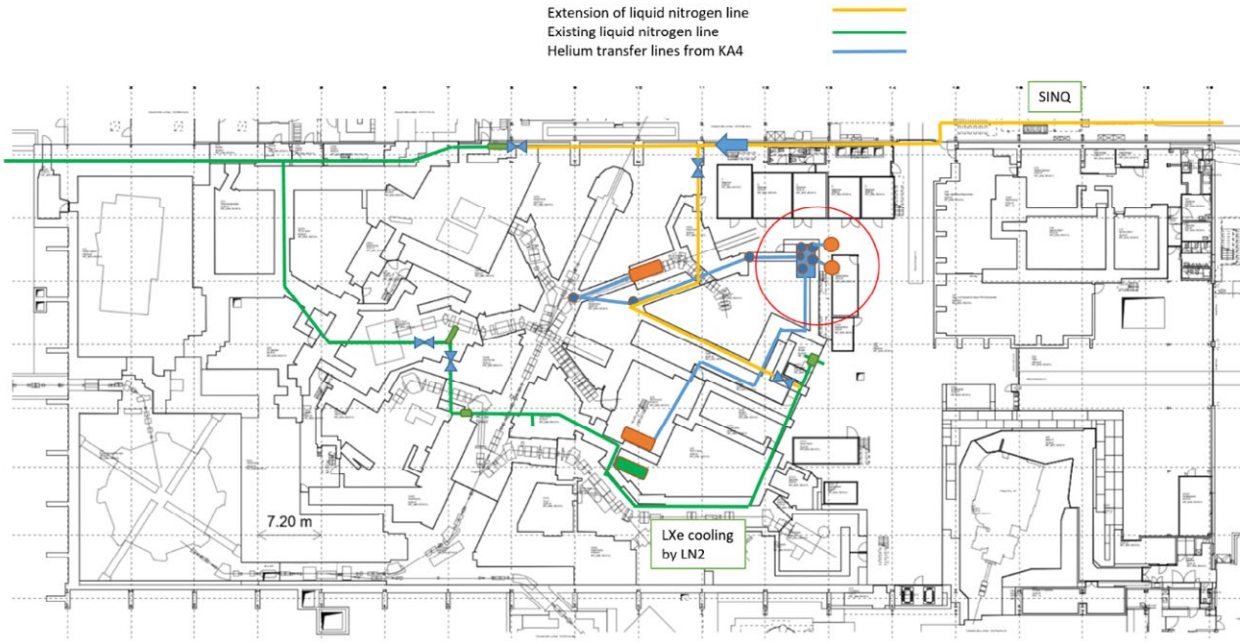

Figure 12.4: Overview of the liquid nitrogen and helium distribution in the experimental hall after the planned upgrades and changes to the infrastructure.

12.7 Compressed Air

Pressurized air will be fed by the existing campus wide network with industrial standard pressurized air with a nominal pressure of 6 bar. Various quick coupling connections will be installed.

12.8 PSYS

The Personnel Safety System (PSYS) controls access to the experimental areas, so that no people can enter the area if dangerous levels of radiation (or other hazards) can occur and ensures that no potentially harmful manipulations can be executed if people are present.

The reconstruction of the experimental areas in the WEHA for the HIMB project requires a new personnel safety system in one area and adjustments of the layout in some other areas. In particular, additional side and escape doors have to be added to comply with current regulations.

Except for one area (the current PiM3), all affected systems are equipped with modern safety PLCs. The control of the three-part area PiM3 was built up with discrete logical components, that date back to the 1970s. This control will be updated to a state-of-the-art system with a safety PLC system.

12.9 Central Bldg. Control System (GLS)

The HVAC and cooling systems are connected to the technical building control system in order to monitor the systems and to alert the service unit in case of failure. In case of extensions and replacements of control systems, the interfaces and schematics have to be adapted, implemented and tested. Generally, the system allows to archive all the monitored data points and to trace back the status of the controlled systems as required.

12.10 IT Networks

12.10.1 Network Overview

Network at PSI is based on a general purpose Network Architecture providing network isolation for large scale research facilities and trusted boundaries to other network security zones, see Figure 12.5. Beamline and machine networks within a facility are logically separated, having routing / switching network throughput within a dedicated network security zone, even if distributed across the campus. If a network security zone traversal is needed, 40Gpbs single flow bandwidth is available through the firewall.

Due to requirements and security audits, it is necessary for PSI IT department (AIT) to provide the entire network envi-

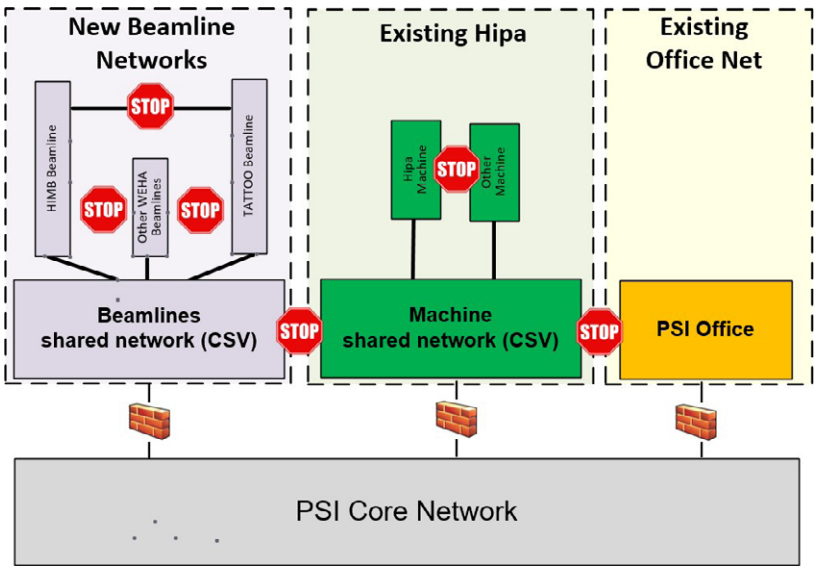

Figure 12.5: PSI Network Architecture.

ronment. Routers, switches or other network devices outside the responsibility of AIT are not allowed.

12.10.2 Machine Network

For IMPACT (HIMB & TATTOOS) it is planned to use the existing machine network zone from HIPA (1204hpanet). The current network (vlan 288) is already heavily populated. If necessary, new networks will be created in the HIPA machine network security zone. IP directed broadcast will be enabled analog to SwissFEL and SLS2.0 to help EPICS forward broadcast over network boundaries. For Gateways the responsibility is within PSI's Controls department (AWI).

12.10.3 Beamline Networks

Presently, beamlines either are within the office network (1000-psigen) or separated by customer infrastructure such as gateways, none official PSI network ranges and none PSI switches.

In general, the beamline network is the standard network for all devices at a specific beamline. Each beamline network is separated from other beamline networks. A common shared network called CSV (Central Service Virtual private network) is accessible directly from every beamline network and is targeted to access IT resources shared among beamlines, e.g. file servers, storage, acquisition servers, monitoring system and many more. This architecture approach is currently used at SINQ, SLS, SwissFEL and foreseen for SLS 2.0 as well.

For the future, next generation networking hardware will be used to meet expectations in regards of performance, scale and automation and security for the next 6-8 years. There will be no filtering and firewalling within the beamline and beamline security zone including beamline shared network. Copper 1G and 10G Ethernet network speed will be provided within the beamline for nodes and consoles. Additional ports for cameras and detectors via fiber and 10G/25G/100G will be available.

12.10.4 Network Security

There will be a hard separation of machine and beamline networks as already implemented today at SINQ, SLS and SwissFEL. Furthermore, it will not be allowed to have a node in more than one network security zone. Every service or solution needing such a configuration needs to be discussed and approved by the Central Network Team together with IT-Security. In addition, all Network devices have to be authenticated and authorized through PSI's Network Access Service (802.1X).

II – TATTOOS
(Targeted Alpha Tumour Therapy and Other Oncological Solutions)

13 Introduction and Overview to TATTOOS

13.1 Introduction

Part II of this CDR is devoted to the production of radionuclides via high-energy spallation utilizing PSI's high-energy proton beam. Radionuclides perform an important role in the diagnosis and therapy of disease, particularly, that of cancer. While its beginnings were relatively crude and rudimentary, the last 50 years have seen marked improvements to pharmaceutical targets, as well as technology towards the production of radionuclides. As a result, more radionuclides are being developed and made available to preclinical and clinical researchers in the attempt to improve imaging capability and therapeutic efficacy.

While the cyclotron was first designed and built in the 1930's, by the mid-1960's there were still only two cyclotrons situated in medical centres worldwide [Anderson et al., 2019]. The first commercial cyclotron towards medical isotope production was a 28 MeV machine sold by Phillips in 1966. Today, according to the International Atomic Energy Agency (IAEA), there are over 1500 cyclotrons worldwide – most of them situated at a clinic or hospital [IAEA, 2021]. The machines have been manufactured towards the production of specific radionuclides, for example, the 18 MeV device is generally for the production of fluorine-18 and the 11 MeV device for the production of carbon-11 – both nuclides used for Position Emission Tomography (PET). Generally, gases or liquids are used as target material, thus, these compact cyclotrons may not have been designed with solid targets in mind. As research/interest in the use of radiometals for imaging of disease has rapidly increased over the last couple of decades, so too, the design and installation of solid target stations has increased. Often, enriched target material is used to produce positron-emitting radionuclides for PET, utilizing the limited proton energy on hand, via the (p,n) nuclear reaction.

The cyclotron has been utilized towards making radionuclides that are predominantly used for diagnosis of disease, with Single Photon Emission Computed Tomography (SPECT) and Positron Emission Tomography (PET). Very few radionuclides with emissions for therapeutic purposes are produced with a cyclotron. Most therapeutic nuclides require neutron irradiation of target material, which is where research reactors are important. Lutetium-177 is an important therapeutic radionuclide on the rise worldwide, being labelled to various ligands to treat various forms of cancer. SINQ (Swiss Neutron Source) at PSI has been instrumental in the development of terbium-161, a novel therapeutic radionuclide in which the medical world is showing great interest, and the nuclide is being produced in larger activities using research reactors. Due to the political climate, however, research reactors are not in vogue and many facilities are being shut down, due to age, with fewer new facilities being built to take their place.

Paul Scherrer Institute (PSI) is steeped in history when it comes to the development and production of radionuclides for medical purposes. The facility, as Federal Reactor Research Institute (EIR) on the East site, had two reactors installed where radionuclides and radiopharmaceuticals were produced, both for medical and research fraternities and even sold commercially [Wildi, 2003] [Alder, 1957].

As the Swiss Institute for Nuclear Research (SIN), adjacent to EIR, just across the Aare River on the West site, the High Intensity Proton Accelerator (HIPA) facility was built for accelerator-based nuclear physics research, along with radionuclide production. SIN began their radionuclide production programme in 1974/75 [Weinreich, 1985], before the two institutions were united and renamed Paul Scherrer Institute in 1988. Initially, the Injector I cyclotron was utilized for commercial radionuclide production (vast activities of ^{123}I, along with ^{82}Sr) [Weinreich, 1985] [Walter, 1994] before Injector II was installed as part of HIPA in 1985 and Injector I was used for physics research until its retirement [Grundler, 2020].

The IP2 irradiation station was designed and built in the early 1980's and was put into service in 1986 [Walter, 1994]. The station was designed to handle 100 µA proton beam intensity and would receive beam, parasitically, from Injector II [Maag and Weinreich, 1991]. In the late 1990's commercial radionuclide production was stopped and research towards the development of novel radionuclides for PET pursued instead.

Previously, the station was used to produce the likes of ^{18}F [Schwarzbach, 1993] and ^{124}I [Weinreich, 1995], by utilizing its higher beam energy, as well as ^{67}Cu [Schwarzbach et al., 1995] [Schwarzbach, 2001] [Novak-Hofer, 2002], ^{82}Sr, ^{52}Fe [Smith-Jones, 1990], ^{76}Br [Ryser, 1999] and ^{68}Ge, but these

activities were halted a good two decades ago. With the increased popularity of PET for the diagnosis of cancer, as a result of its superior image resolution over Single Photon Emission Computed Tomography (SPECT), the strategy of the station's use was adjusted to meet the growing demand for new positron-emitting radionuclides, which included adjusting the targetry technology to handle small, enriched targets and beam degradation. Radionuclides developed and produced using this concept include ^{44}Sc [van der Meulen, 2015] [van der Meulen, 2020], ^{43}Sc [Domnanich, 2017b], ^{64}Cu [van der Meulen, 2019] and ^{165}Er [Gracheva, 2020]. Currently IP2 gleans ~50 µA protons from Injector II, by means of a beam splitter placed along the beam line between Injector II and the Ring cyclotron [van der Meulen, 2019]. The use of the Swiss Neutron Source (SINQ) at PSI assists with the development of neutron-rich radionuclides, such as ^{161}Tb [Lehenberger, 2010] [Gracheva, 2019] and ^{47}Sc [Domnanich, 2017a] towards preclinical application. Once developed, these proofs-of-principle can then be put into practice at partner facilities [van der Meulen, 2020] [Gracheva, 2020] [Grundler, 2020].

It is important to highlight that novel radionuclide and subsequent radiopharmaceutical production development requires a multidisciplinary approach involving nuclear physics, radiochemistry, material science, engineering, pharmacology, medical physics, radiobiology, immunology, structural biology, health physics, oncology, etc. [Talip, 2020]. To date, only a limited number of therapeutic and diagnostic radionuclides are available for routine clinical targeted radionuclide therapy (e.g. yttrium-90, lutetium-177, iodine-131, radium-223) or imaging (e.g. iodine-123, gallium-67, gallium-68). On the other hand, some radiometals have reached the manufacturing point of Good Manufacturing Practice (GMP), however, have not necessarily been registered with the authorities, for example, copper-64 and zirconium-89.

13.2 Goals & Scope

The main goal is the production and delivery of isotopically and radiochemically pure radionuclides for radiopharmaceutical use. The production route over nuclear spallation reactions using the world most powerful proton accelerator allows for unprecedented activities of a broad spectrum of radionuclides, thereby, potentially facilitating clinical studies with novel radionuclides. The aim of this venture is to utilize and expand production facilities at PSI, such that an Isotope Separation On-Line (ISOL) facility is built and installed to enable collection, as well as chemical separation of novel promising radionuclides in unprecedented activities, e.g. ^{149}Tb and ^{152}Tb or even ^{225}Ac. These can be introduced into the GMP facility on site (at Center of Radiopharmaceutical Sciences – CRS), used for labelling of biomolecules and the resultant radiopharmaceutical will be transported to imaging and therapy centres for patient application. The unique option at PSI to produce and process radionuclides at the same site, will be particularly important for the relatively short-lived ^{149}Tb ($T_{1/2}$ = 4.1 h).

PSI will become the only facility worldwide to produce radionuclides by means of proton and neutron activation, as well as spallation reactions followed by mass separation – along with the radiochemical means to obtain the desired product, as well as produce radiopharmaceuticals therefrom. The concept will cover basic research and development therefrom as part of a "bench-to-bedside" principle. The offline operation of the mass separator in downtimes of the accelerator facility will allow for assessing radionuclidic pure products from classical production routes involving low-energy protons (from cyclotrons) and neutrons (research reactors) of material irradiated elsewhere, in collaboration with nuclear reactor and accelerator facilities worldwide.

13.3 Structure of PART II

This part intends to guide the reader through the scientific and technical challenges related to the construction of the TATTOOS facility at PSI. Chapter 14 describes final performance goals, as well as the design strategy and borders of the required design to achieve the intended performance goals. Technical descriptions start in Chapter 15, with the required changes in the existing high-energy proton beam line of HIPA to peel off the intended 100 µA proton beam and guide it onto a solid spallation target. The following chapter is fully dedicated to the development of the target and the target structure, including thermal considerations, activation, production of radionuclides, shielding, radiation protection and storage and disposal. In Chapters 17 and 18 a first beam dump design is evaluated for its thermal parameters and activation. Furthermore, the strategy of removal of target and beam dump components is presented. The ion generation, extraction and mass separation, including the ion sampling, is sketched in Chapter 19. The radionuclidic and chemical purity of the mass-separated products, collected in foils, will require chemical separation towards clinical application. In Chapter 20 the radiochemical purification is detailed, including the required shielded cells to protect the working personnel. The relevant principles and guidelines of radiation protection and safety are demonstrated in Chapter 21. Based on all these assessments, the TATTOOS facility needs to be placed in a specially designed building with limited access and all the required infrastructure. These topics are elucidated in Chapter 22.

14 Design Strategy and Parameter Choice

14.1 Outline of the TATTOOS Science Case

Terbium is a unique element in that it presents four interesting radioisotopes for all modalities in diagnostic and therapeutic nuclear medicine: ^{155}Tb emits γ-radiation suitable for SPECT, while ^{152}Tb decays by the emission of β^+-particles useful for PET. ^{161}Tb emits low-energy β^--particles, but also a significant number of Auger/conversion electrons, which presents a powerful combination for therapeutic purposes. Finally, there is ^{149}Tb, the "flagship" nuclide for this project, which has promising properties for α-radionuclide therapy [Müller, 2012]. The existence of four radioisotopes that allow preparation of chemically identical radiopharmaceuticals, with equal pharmacokinetic profiles, is a unique situation that could serve the concept of personalized medicine, thereby, offering diagnostic tools and various therapy options for cancer patients in future. While ^{161}Tb can be produced via a research reactor [Lehenberger, 2011] [Gracheva, 2019], the others are more challenging to obtain and spallation, followed by mass separation and collection is necessary (also known as Isotope Separation OnLine, or ISOL).

To date, the use of an ISOL system has been limited to applying for beam time at a user lab (CERN) to be able to produce limited activities of ^{152}Tb [Müller, Vermeulen, Johnston, 2016], ^{155}Tb [Müller, Fischer, 2014] and ^{149}Tb [Müller, Reber, 2014] [Müller, Vermeulen, Köster, 2016] [Beyer, 2004] [Umbricht, 2019]. Some promising results for these radionuclides have been obtained and published, however, such that it has prickled the interest of the medical fraternity [Müller, 2019] [Baum, 2017].

Actinium-225 has also taken the world of radionuclide therapy by storm recently and the nuclear medicine fraternity is particularly interested in utilizing this alpha emitter for tumour therapy, particularly as the alpha decay is devastating to the killing of tumours, due to the high Linear Energy Transfer (LET) of alpha emitters [Kratochwil, 2016]. Accessibility to this nuclide is scarce, as the world relies predominantly on legacy supply (as waste from nuclear weapons manufacture), however, high-energy proton irradiation of thorium targets to produce Ac-225, along with over 200 radioisotopes, has been recently reported [Engle, 2018] [Fitzsimmons, 2019] [Fitzsimmons, Griswold, 2019]. A side product using this method is that of Ac-227, which has a long half-life (~21 years) and is undesirable for use in the clinic. With the use of a uranium carbide target, it is possible to produce radioisotopically pure Ac-225 via the ISOL route. It is possible to utilize the mass-separation technique at PSI's HIPA infrastructure with the construction of an ISOL facility (TATTOOS) to foster this new research area based on novel, emerging medical radionuclides. The aim is to provide improved access to new medical radionuclides, which are difficult to obtain via more conventional methods. The use of online mass separation ensures collection of radionuclides of specific mass that can, subsequently, be chemically separated. Offline mass separation can be applied to radionuclides containing radionuclidic impurities, as it has the potential of producing no-carrier-added product, not otherwise obtainable in some cases. The development of radiopharmaceuticals, notably with the rise of targeted therapies and the theragnostic approach (where one can image and treat a tumour with radioisotopes of the same element), is on the increase. Targeted radionuclide therapy (TRT) is constantly under development and new ligands being developed demand radionuclides with specific decay characteristics. The choice of radionuclides is key towards the success of the nuclear medicine application in question. Radiolanthanides, in particular, are being favoured by researchers: they have similar chemical properties and can offer the widest possible spectrum of physical properties towards nuclear medicine application. Production of sufficient activities of high-quality radiolanthanides requires systematic research in target preparation, irradiation and extraction process, radiochemical separation procedures and quality control.

14.2 Requirements of the User Community

More radionuclides have been developed and made available to preclinical and clinical researchers over the last two decades, in the attempt to improve imaging capability and therapeutic efficacy. To date, the use of radionuclide therapy has been focused on patients with no other alternative after various other forms of therapy. The tide is beginning to change, however, as medical practitioners are making efforts to use radionuclide therapy as an initial form of cancer therapy, due to its minimal side effects when compared to the likes of chemotherapy. There is a need for a greater variety of radionuclides to fit the ligands being developed, for diagnosis but, particularly, for therapeutic purposes. Radiolanthanides are a challenge to produce as radionuclidic pure (or no-carrier-added; n.c.a.) product and it is expected that the use of mass separators (online or offline) to produce n.c.a. radionuclides towards nuclear medicine applications become more attractive in future. Many therapeutic radionuclides that researchers are interested in are difficult to produce and there are very few facilities worldwide that can meet the demand. Some facilities, particularly to meet the ISOL means of producing radionuclides, are being built, but the concept for medical purposes is still in its infancy.

14.3 Overview, Layout and Design Parameters

TATTOOS is based on the Isotope Separation On-line (ISOL) principle, which was pioneered at CERN ISOLDE ([Catherall, 2017], https://isolde.cern). A target, containing a high-atomic-number element, is irradiated by a high-energy (600MeV-1GeV), low intensity, proton beam. The high energy of the incident particles produces spallation reactions - the most common nuclear reactions occurring in the target material. Thus, a broad plethora of elements, mainly with a lower atomic number (Z) compared to the one of the target, are produced. Nuclear stability aspects drive the product spectrum obtained in multi-nucleon evaporation and fragmentation reactions. Using a Ta target, large production rates are expected for isotopes of lanthanide elements. Terbium, as one of the initial main production goals of TATTOOS [Umbricht, 2019] belongs to the lanthanide series. Using UCx targets, the likes of Ac and Ra, as well as fission products, belong to the main products [Ballof, 2020]. Here, e.g., Actinium-225 is one of the products of high interest for oncological applications [Morgenstern, 2018].

The general layout of the TATTOOS (Targeted Alpha Tumour Therapy and Other Oncological Solutions) facility is shown in Figure 14.1. The facility is located in parallel to the existing Ultra-Cold Neutron Facility (UCN). Up to 100 μA protons are split from the main proton beam of HIPA (1). The beam is guided through a dedicated beam line with beam shaping components, as well as diagnostic components and a fast shutting valve (2) onto a heavily shielded target (3). There, the high-energy nuclear reaction (spallation) occurs and the beam energy is degraded from an initial 590 MeV to roughly 300 MeV. The rest of the beam is "dumped" into the beam dump (4). The irradiated target (3) is heated by the deposited beam energy either only or, additionally, by external electrical Jules heating. The target can be exchanged by moving the entire target chamber through a specially-designed channel (5) on rail tracks into the target exchange shielded cell (6). The spallation products, depending on their chemical properties, diffuse through the hot target material (up to 2800 K) towards the inner surfaces of the target and effuse in the open areas in the target setup towards a transfer tube and orifice intentionally left open. The intention of TATTOOS

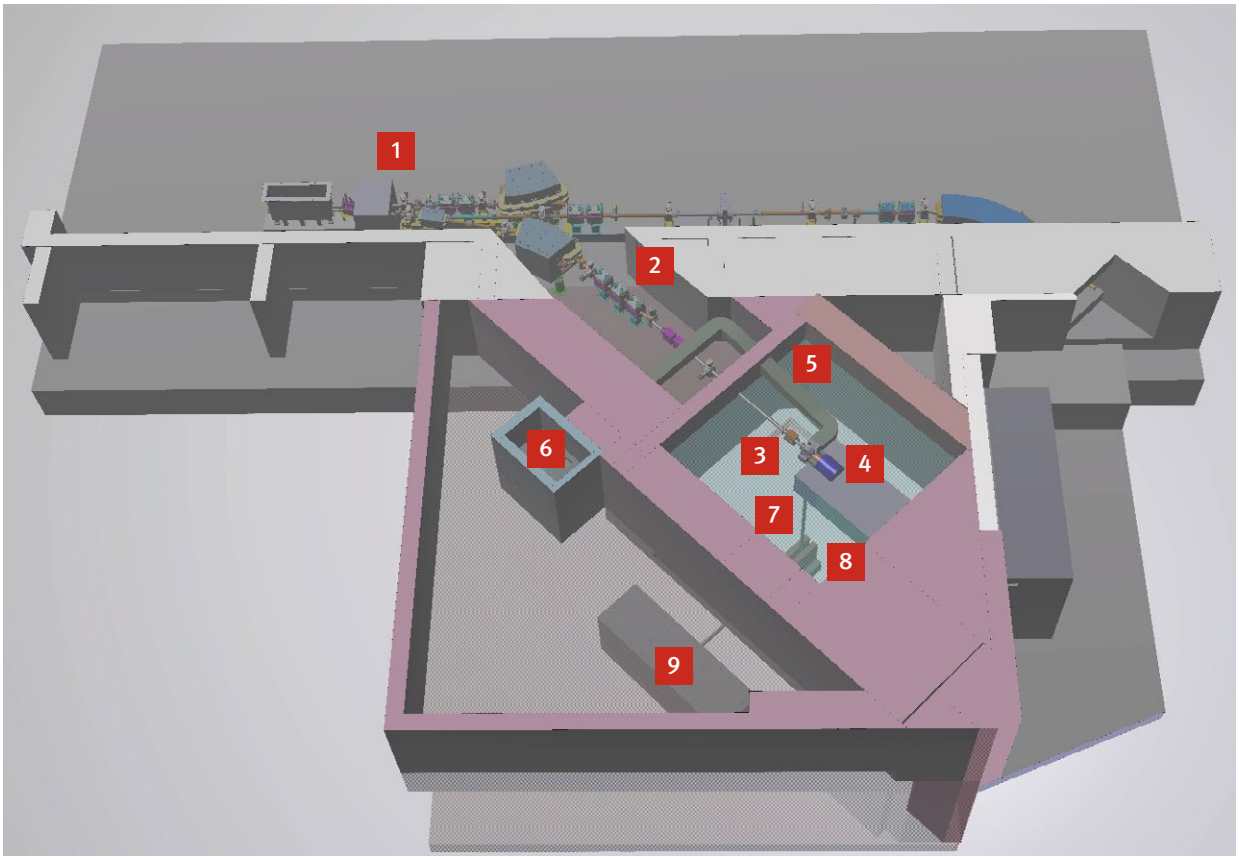

Figure 14.1: CAD overview of the TATTOOS facility. Note, the transparent floor of the ground floor to visualize the mass separator (8) and radiochemical shielded cell complex (9) in the basement.

is to apply mass separation, in conjunction with radiochemical separation, to obtain radioisotopically and radiochemically pure products for medical applications. Mass separation requires an initial ionization step of the atoms produced. Hence, in the transfer tube and orifice the high surface temperatures lead to selective surface ionizations for elements with lower ionization potential (‹6 eV) with efficiencies of up to 20 % [Kirchner, 1996]. Recently, the method of Resonance Laser Ionization (RILIS) was developed, where the introduction of an combination of intense laser pulses at dedicated tuneable wavelengths lead to selective isotope ionizations with efficiencies up to 40 % and more [Wendt, 2003; Fedosseev, 2017]. As a result, TATTOOS intends to use both ionization schemes. The ionized atoms are extracted from the target held at high potential (+30 kV) by an extraction lens, held at ground potential, and are subsequently guided electrostatically (7) towards a mass separator (8) consisting of a dipole magnet. There, the ions are separated according to their mass-to-charge ratio. Thus, only selected masses reach the outlet at the focal plane of the dipole magnet. These separated ions are guided towards an implantation station bearing a selected catcher material inside shielded cells (9). After the implantation sampling, the catcher material is extracted from the vacuum sampling station and dissolved for further radiochemical separation and purification. The challenges and novelties of the project are related to the considerable higher proton beam intensity if compared to ISOLDE and MEDICIS, scaling up by almost a factor of 50 and, thus, allowing for the production of purified radionuclides in unprecedented activities, which are essential for systematic clinical studies.

14.4 Realization Strategy, Boundary Conditions and Legacies

The timing for construction of the TATTOOS facility is a particular challenge in conjunction with the operational schedule of the HIPA facilities and connected experiments. The aim must be to minimize interferences with the regular research programs. The reconstruction of the high-energy proton beam line requires a long shut-down period, where the entire reconstruction related to the IMPACT project have to be accomplished. The identified optimum area for the placement of the facility with respect to the close proximity of high-energy proton beam lines, as well as already existing shielding and infrastructure of the PSI-UCN facility, provides limited space. Therefore, some challenges are met, related to the reuse of infrastructure, movement and replacement, which is dedicated to one of the PSI-flagship experiments, namely, the PSI-UCN facility. Therefore, both the preparation of the construction site including the required elevation of the building can be done only partly in a time-period of full HIPA operation. The technological aspects of the TATTOOS facility are addressed based on the experiences with high-power high-energy proton beam lines and targets at PSI in conjunction with the demonstrated and well documented work by world-wide ISOL facilities, with the pioneering contribution of CERN-ISOLDE. Thus, there is confidence that from the fundamental physics and technology point of view there are no showstoppers. The main challenge is related to the considerable unprecedented power upscale of the beam and the corresponding target technology.

15 Proton Beamline

15.1 Present Situation

The PSI high intensity proton accelerator (HIPA) generates a continuous wave (50.6 MHz) frequency, 590 MeV, 2 mA, 1.3 MW beam, [Seidel, 2010]. A schematic of the accelerator complex is shown in Figure 15.1.

The proton beam extracted from the ring cyclotron is normally transferred to the targets M, E and SINQ via the main proton channel. UCN (Ultra Cold Neutron), a second spallation source, runs concurrently to these targets. UCN is driven by macro-pulses kicked into the UCN beamline by means of a fast kicker magnet [Reggiani, 2009] that diverts the full-intensity beam towards UCN.

The maximum pulse length is 8 seconds, while the duty cycle, initially set to 1%, has been gradually increased over the last years to 3%. For special measurements or tests, a small portion of the beam (up to 60 µA) can be peeled off the main beam and continuously sent to the UCN target by means of an electrostatic splitter (EHT) located immediately downstream of the kicker magnet, see also Section 15.3.

Fast beam position monitors (BPMs, 50 kHz sampling rate) allow the beam trajectory to be checked and, if needed, corrected during a 7 ms pilot pulse. At the same time, several beam loss monitors can trigger an interlock in less than 1 ms.

In the UCN beamline a beam dump has been placed which can absorb the full (2000 µA) beam for 10 ms, or 20 µA continuously. This enables to test the kicking procedure and the beam diagnostics independently from UCN operation.

The UCN spallation source typically runs round-the-clock except during some week-long periods (about three times per year) during which the D2 moderator crystal needs to be reconditioned after undergoing degradation by the proton beam. A comprehensive description of the UCN source can be found in [Becker, 2015].

15.2 Basic Considerations, Requirements and Constraints

The TATTOOS beamline will guide 100 µA protons, peeled off the main beam by means of an electrostatic splitter (Section 15.3), towards the TATTOOS target.

The TATTOOS beamline and target will be located next to the UCN target area. Two options for the junction of main beamline, UCN beamline and TATTOOS beamline are presented in Sections 15.2.1 and 15.2.2. A CAD drawing of the proposed beamline layout is shown in Figure 15.3.

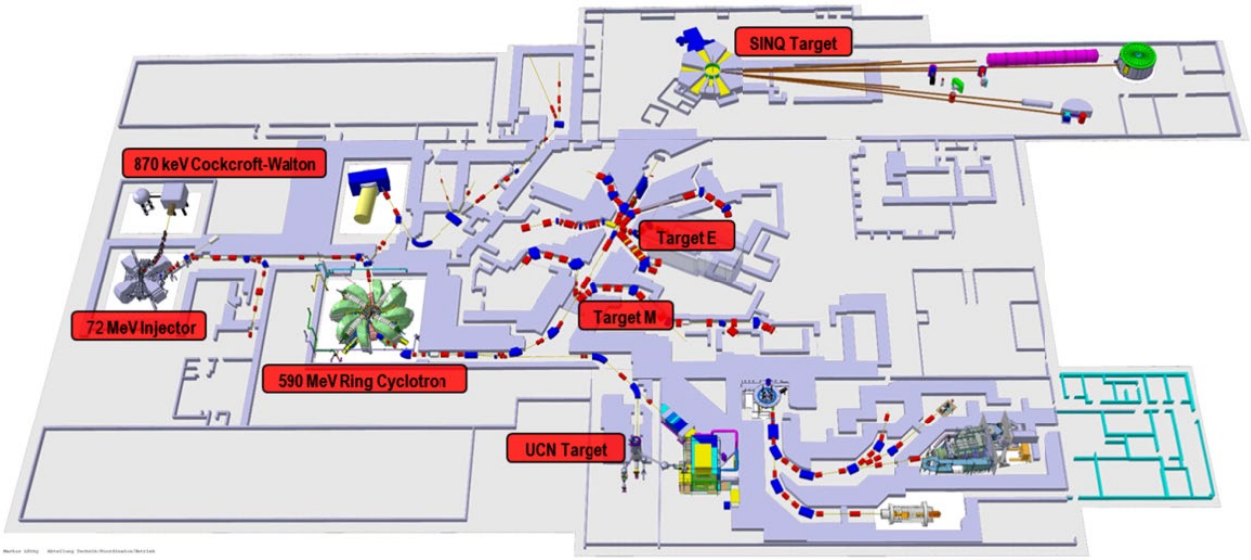

Figure 15.1: Overview of the PSI high intensity accelerator facility.

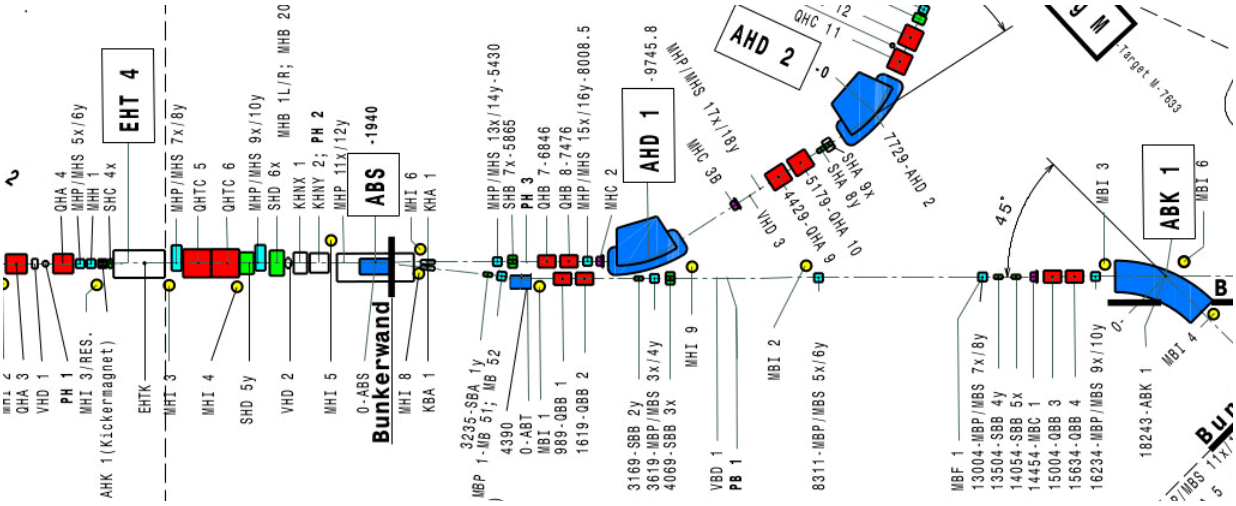

Figure 15.2: Current layout of the HIPA beamline in the TATTOOS region.

As indicated in the drawing, an existing building wall needs to be opened for the new TATTOOS beamline. While the building pillars, perpendicular to the building wall, are crucial for the building stability and cannot be moved or altered, the necessary cut-out in the wall does not present a problem. The tight space constraint, however, remains a general challenge.

The requirements on the TATTOOS beamline itself are modest: to transport the beam without large losses, and to provide means for adjusting the beam shape at the target. For steering the beam towards the target, a few vertical steering magnets are needed besides the several bending magnets that can be used for adjusting the horizontal position. Additionally required are some continuous beam

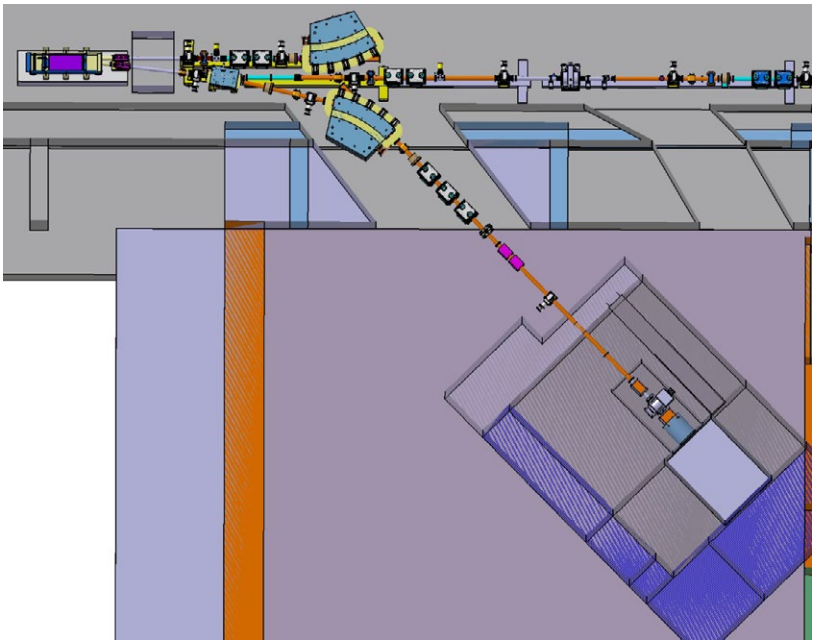

Figure 15.3: Overview of the TATTOOS beamline design (without shielding).

position monitors for automated steering, beam loss monitors to ensure beam transport with low losses, and a beam current monitor to provide an independent current measurement for target protection.

Beam shaping on the target will be facilitated by a quadrupole triplet providing an adjustable beam spot size on the target. A few profile monitors are envisioned for verification. No further quadrupoles are needed since the beamline is short and the incoming beam is only slightly diverging.

Since in its current design the target is not able to withstand a 100 µA Gaussian beam profile (see Chapter 16), the beam profile will be spread with fast dipole magnets (called "wobblers") that rotate the beam on the target (see Section 15.4.1) such that the beam is more evenly distributed on the target. For the most effective beam spreading the distance from the wobblers to the target needs to be several meters without other magnetic elements in between. Furthermore, the wobblers can be used to center the beam on target.

There are two proposed layouts for the beamline junction, one where UCN and TATTOOS share the same septum magnet and need to share the beam time, and one where UCN and TATTOOS each have a separate beamline and can operate in parallel. These two options are described in more detail in this section.

15.2.1 Alternating Beam Operation

The simplest way to integrate the new TATTOOS beamline within the present configuration is as follows: Peel off the portion of beam needed for TATTOOS by means of the EHT splitter; use the ABS septum to divert the split beam onto the trajectory of the UCN beam; steer the split beam out of the UCN trajectory towards TATTOOS by a new bending magnet, which will be ramped up for TATTOOS beam operation, see Figure 15.4.

The advantage of this scheme is that this operational mode is already well known and tested, since splitter and septum are already part of the beamline. The only point of concern is the amount of beam current that could be split: tests have shown that a current up to 30 µA can be reached, but this is still far away from the TATTOOS nominal proton beam current (100 µA). The main critical point connected to this scheme is however the fact that, during TATTOOS operation, the UCN spallation source cannot be in operation (and vice versa). TATTOOS and UCN would have to come to an agreement about the respective running time. Assuming that TATTOOS would run for 50 % of the available beam time, this would have a great impact on UCN operation.

A possible solution to this issue would be to run TATTOOS every time between two UCN pulses. The typical time between two subsequent UCN kicks is 300 seconds. After each 8 s UCN pulse, the beam is kicked back to the TgM-TgE-SINQ beamline. In order to reduce thermomechanical stress in the SINQ target, just before kicking the beam back to SINQ the beam current is reduced to roughly 50 % of its nominal value. It takes about 30 s to ramp up again the beam current. This time could be used to power the bending magnet, which would divert the beam from the UCN to the TATTOOS beamline. After this operation, the EHT splitter would need to be

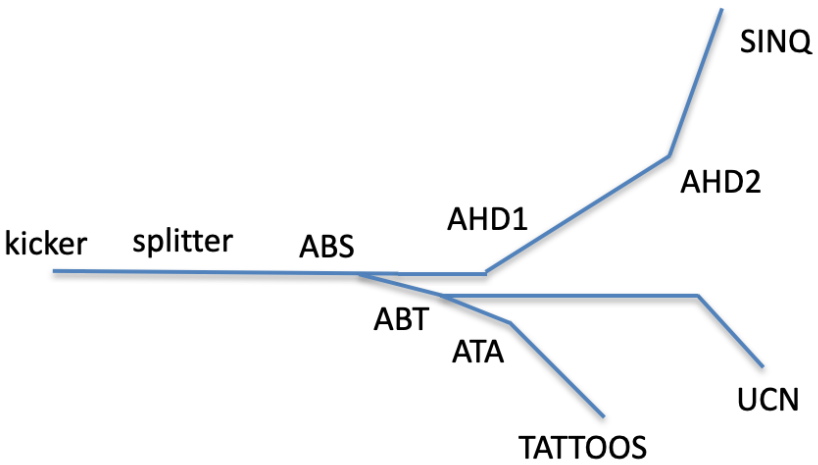

Figure 15.4: Schematic layout of the alternating beam operation.

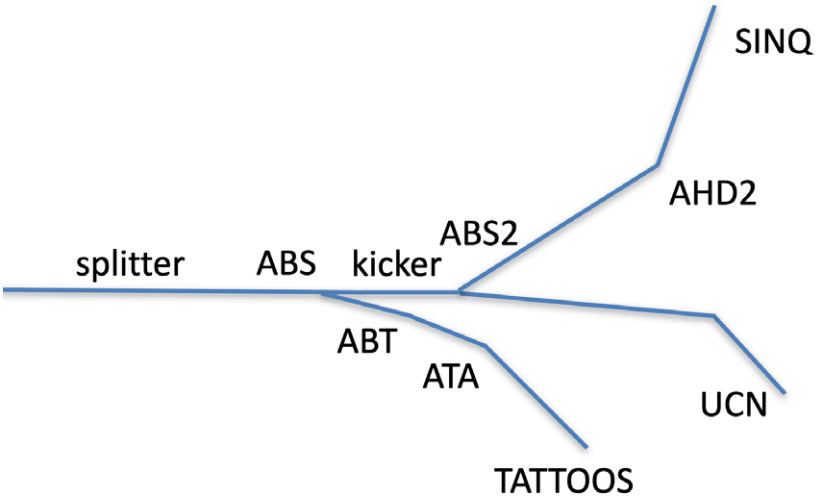

Figure 15.5: Schematic layout of the parallel beam operation.

moved into the beam. At the end of this procedure, the TATTOOS target would be irradiated with 590 MeV, 100 µA protons until the next UCN pulse. Assuming each splitter move takes 15 s and considering that the whole UCN kicks procedure (short kick + time between short and long kick + long kick) takes some 20 s, the TATTOOS target would be irradiated for 240 s every 320 s (75 % duty cycle).

In order to divert the beam into the new TATTOOS beamline, the existing bending magnet ABT could be used. This magnet is located downstream of the ABS septum and currently bends the UCN beam to the left hand side by 6.5 degrees into the separate UCN beamline, see Figure 15.4. The idea is to ramp up the magnet to the same field but with opposite polarity. This way, the net effect of the ABS septum and the ABT magnet would be a 13-degree bend towards TATTOOS. An additional dipole (ATA) located in the TATTOOS beamline downstream of ABT would bend the beam further by 32 degrees, bringing the total bending angle (ABS + ABT + ATA) to 45 degrees. To make space for the TATTOOS beamline, the QBB1 and QBB2 quadrupoles in the UCN beamline will be moved a few meters downstream. It has been verified by simulation that this will not have a detrimental effect on the UCN operation. The ABT ramping time will have to be short enough in order to make it possible to power the magnet right after the UCN kick before the beam current reaches its nominal values (roughly 30 s). It is still not clear whether the existing ABT meets this requirement. However, the design and manufacturing of a new ABT would not have a significant impact on the TATTOOS project.

15.2.2 Parallel Beam Operation

To be able to operate TATTOOS and UCN in parallel, the TATTOOS and UCN beamlines would need to be completely separated. Therefore, an additional septum magnet is needed and the kicker and the electrostatic splitter need to be set apart. Furthermore, the UCN kicker magnet should be placed after the TATTOOS septum since otherwise the kicker magnet will influence the TATTOOS beam.

The TATTOOS beamline layout will stay as discussed in the alternating beam operation. It is no longer needed to have the possibility to ramp the ABT dipole magnet quickly with both polarities and a fixed dipole magnet of 13 degrees can be used.

The proposed layout is schematically shown in Figure 15.5. In this case, the complete UCN beamline would have to be moved and reinstalled. In place of the existing bending magnet AHD1, a new septum, called ABS2, would be installed to branch off the UCN beamline from the TgM-TgE-SINQ beamline (see Section 15.2.2.1). The kicker magnet would be moved upstream after the current ABS septum. Since the distance from the kicker to the ABS2 septum will be shorter than before a new more powerful kicker magnet has to be designed, see Section 15.2.2.2 for more details.

The advantage of this scheme is that both TATTOOS and UCN can be operated fully independently of each other. Therefore, no beam time needs to be shared, which means the operation mode of splitting the beam in between two UCN pulses proposed in the previous section, is no longer needed. Also the splitter does not need to be moved in and out, which

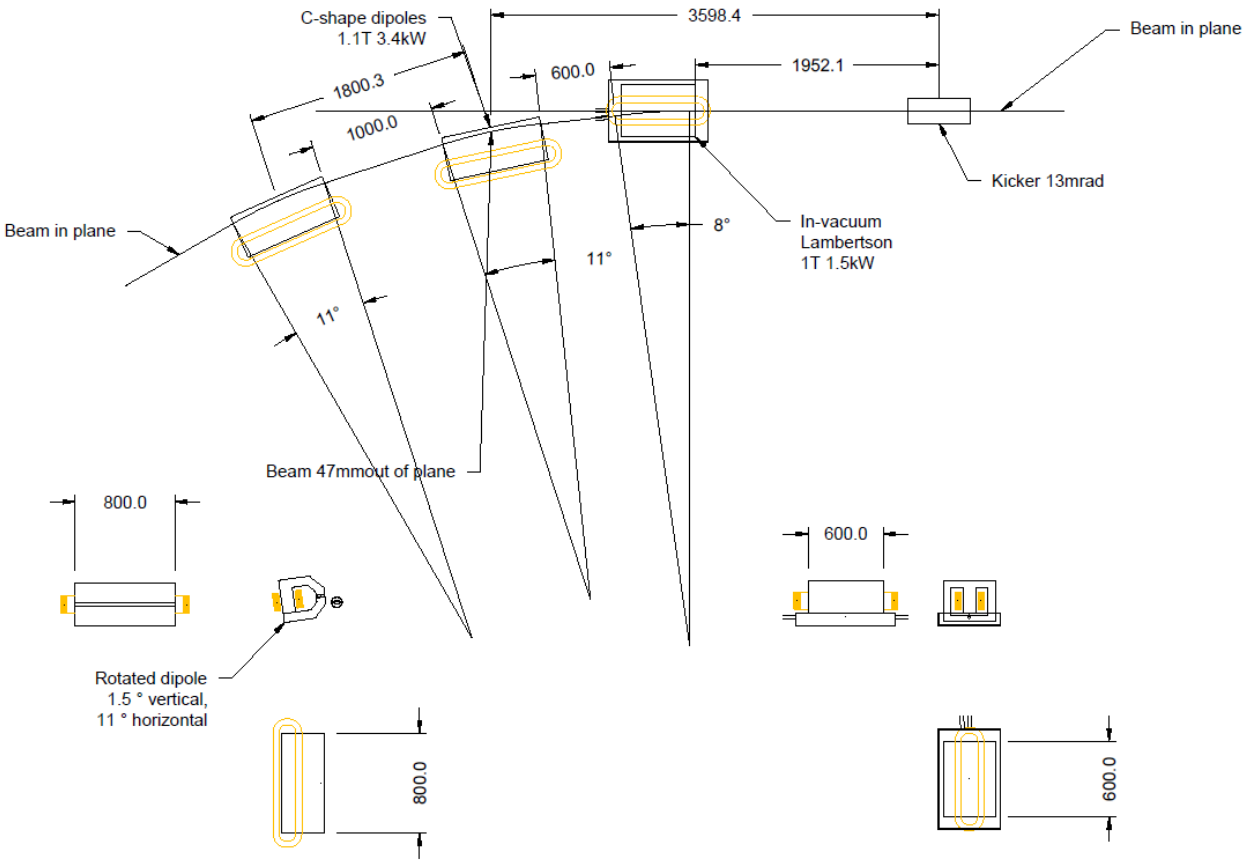

Figure 15.6: First concept of a septum magnet for the parallel option for the UCN beamline.

will relax the specifications of the motorized mechanism and increase its lifetime.

On the other hand, the disadvantages of this scheme are clear. Two new state-of-the-art beamline elements, a strong 30-degree septum magnet and a stronger kicker magnet, need to be designed and built, see below for details.

In addition, the existing beamline needs to be rebuilt, and possibly existing beamline elements need to be removed to make space for the kicker magnet, see Section 15.2.2.2 for details. The commissioning of the new elements and new operational mode will be a potential risk to the UCN experiment, and could delay its restart.

Furthermore, additional shielding will also be needed, since during the kicker's rise time the beam will be swept across the vacuum chamber at the beamline junction. In the current situation a shielding wall directly after the septum is in place ("Bunkerwand" in Figure 15.2), for the new situation similar shielding will have to be added.

For the above reasons, we judge the alternating beam operation scheme as simpler, cheaper and more practical, and identify it as our preferred option. However, if the required operation modes for TATTOOS and UCN are reconsidered, the parallel beam operation is also a viable alternative.

15.2.2.1 Septum Magnet

For the parallel beam operation option a new DC septum will be installed in place of AHD1. This septum needs to separate the main beamline from the UCN beamline. The septum needs to bend the main beam by 30 degrees and let the UCN beam pass straight through.

Since this is a challenging bending angle, to maximize the field and achieve a low leakage field, the magnet gap must

be minimized as much as possible to the point that the magnet is being heated by radiation. For DC septa, there is a compromise to get a reasonably low leakage field [Ull, 2019] [Taniuchi, 2020]. In rough terms, 1 parts per trillion leakage field with 30 mm separation from the septum conductor would be a typical value. Of advantage is that the vertical beam size is on a waist at that location, about 2-3 mm for 1 sigma. Therefore, a minimal vertical gap of about 20 mm would be feasible. The horizontal dimension would be similar, so in either direction the kicker must give 20 mm separation plus the thickness of a septum conductor of about 5-10 mm.

A first concept has been achieved, which can be seen in Figure 15.6. It is a Lambertson in-vacuum design, because this permits the smallest possible kicker deflection. Since the kicker is also in the vertical direction, this unfortunately adds the complication of lifting the beam orbit out of the horizontal plane, so the Lambertson is followed by two dipoles with drift space between them to rotate the beam back into the horizontal plane.

15.2.2.2 Kicker Magnet

Since in case of the full parallel option the kicker position will have to be located after the TATTOOS septum, the distance between the kicker and the septum will be shorter and the kicker strength will have to be increased. The proposed kicker strength is 13 mrad. This would require a new design since the existing kicker [Anicic, 2005] is designed for 6 mrad. For a double deflection, one can either double the current (i.e. double the field), double the amount of windings or double the length, or a combination of these.

Doubling the field by doubling the current will influence the rise time. A power supply upgrade could provide the required parameters. The existing magnet is designed to operate at a current of maximally 200 A, with nominal operation presently at 170 A. A further field increase would probably need a new design due to cooling issues.

Doubling the amount of windings will be difficult. The current coil is already rather complex and the same setup with twice the amount of windings might be complicated. In addition, a bigger coil changes the inductivity and will increase the rise time.

Doubling the length would be the simplest approach, but requires sufficient beamline space. The current beamline footprint is 40 cm (36 cm for the magnet itself). Both the profile monitors MHP13/14, which are redundant with MHP 15/16, and the horizontal steering magnet SHB7X, which can be made redundant by tuning the new septum magnet, could be removed to provide the needed space for the kicker magnet.

15.3 Beam Splitter

To peel off the TATTOOS beam from the main beam, an electrostatic beam splitter will be used.

Currently, an existing splitter called EHT is part of the beamline and occasionally used [Olivo, 1998]. It consists of 179 tungsten alloy strips, electrically grounded. These strips all have the same dimensions and are 50 µm thick and 3 mm wide. The strips are separated, in beam direction, by a 3 mm gap, except for the first, a few in the middle and the last three gaps that measure 9 mm each instead. In total, this amounts to a length of 1107 mm. Each strip is tensioned by a pair of springs. The EHT features two cathodes, both at a negative voltage of -172 kV. This creates two electric fields

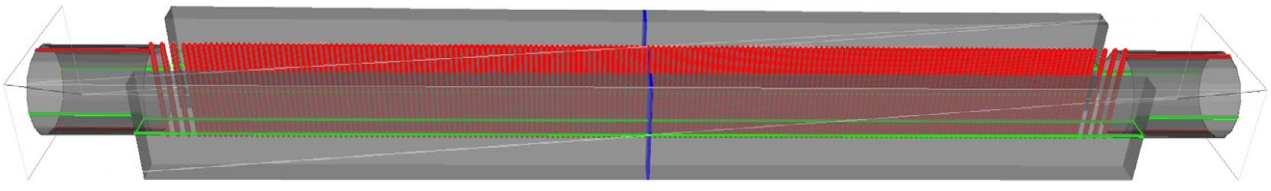

Figure 15.7: Schematic geometry of electrostatic splitter used in the BDSIM simulation.

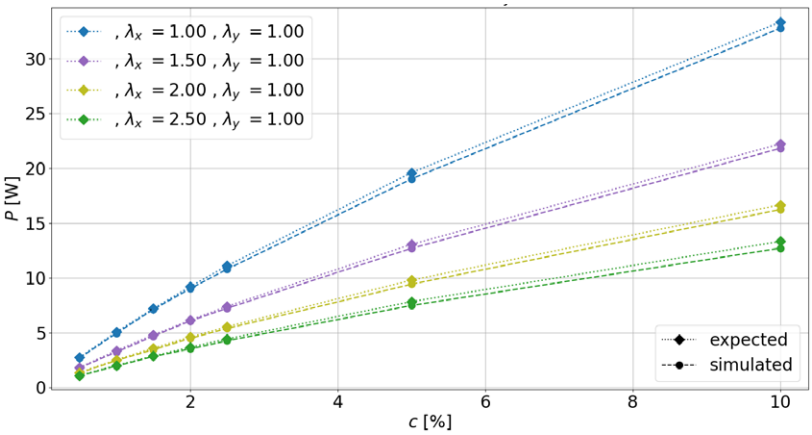

Figure 15.8: The losses on the first strip as function of the split current beam in percentage of the main beam (2 mA), 5 % corresponds to 100 µA. Different horizontal beam sizes (indicated with the relative factors λ_x) are simulated. The simulated values are close to the values from analytic considerations.

on each side of the strips, effectively splitting the protons away from the strips by 3 mrad at the end of the splitter for each beam. Two additional steering magnets, called SHC4X, on each side of the splitter compensate for the effect on the main beam (each imparts a 1.5 mrad bend) and the peeled beam gets a 6 mrad bend.

The current EHT splitter has been originally designed to peel off 20 µA [Olivo, 1998]. Peeling off more, means moving the whole device, such that the strips are more into the central part of the beam distribution and the thermal heat load, especially on the first strips is increased. The splitter can be rotated around its center to minimize the thermal heat load. Due to the unknown material properties of the strips, specifically the thermal emissivity, it is not clear if the strips can handle the power deposition.

Detailed beam simulations have been performed with BDSIM [Nevay, 2020], a Geant4 based program to simulate both the transport of particles in an accelerator and their interaction with the accelerator material, see Figure 15.7 for the 3D Geant4 model. A detailed electric field map with a resolution of 25 µm by 3000 µm by 500 µm has been obtained with ANSYS. To achieve this accuracy and reduce computing power the geometry of the EHT was simplified and split in eight parts along its symmetry axes, where only one part was used to create a realistic field map.

The BDSIM simulations, see Figure 15.8, show that the power deposit on the first strip for a split beam of 100 µA (5 % mark) is about 20 W for the nominal beam parameters and a current of 2 mA. Thermal simulations show that depending on the material properties, notably a very conservative emissivity of 0.04 was assumed, the first strip can reach a temperature of more than 2000 degree Celsius, which would be too high. To avoid inelastic deformation, the maximal temperature should be significantly lower than the melting temperature (about 3680 K). A maximum value of approximately 1500 degree Celsius should be used for design purposes.

The power deposition can be decreased if the beam width is increased horizontally at the location of the splitter. In addition, a vertical beam width increase is beneficial, as this will spread the power deposit along the strip. Beamline simulations and measurements have shown that the beam width in both directions can be increased by about 30 % with respect to the nominal beam size with the same focusing on target M without increased losses. This reduces the temperature to about 1500 degree Celsius, which is around the acceptable limit.

However, a new design for the EHT splitter is foreseen, since for the preferred alternating beam operation the splitter needs to be moved in and out of the beam for about 10 times per hour. The motor mechanism has not been designed for such frequent movements and will be revised. In addition, the splitter is already 25 years old, and a risk for a reliable and continuous operation.

15.4 New Beamline Components & Magnets

For the TATTOOS/UCN alternating beam operation, the TATTOOS beamline would need the following elements, see Figure 15.4:

- Fast ramping magnet: this dipole magnet has to bend the TATTOOS beam by a couple of degrees (6.5 in the

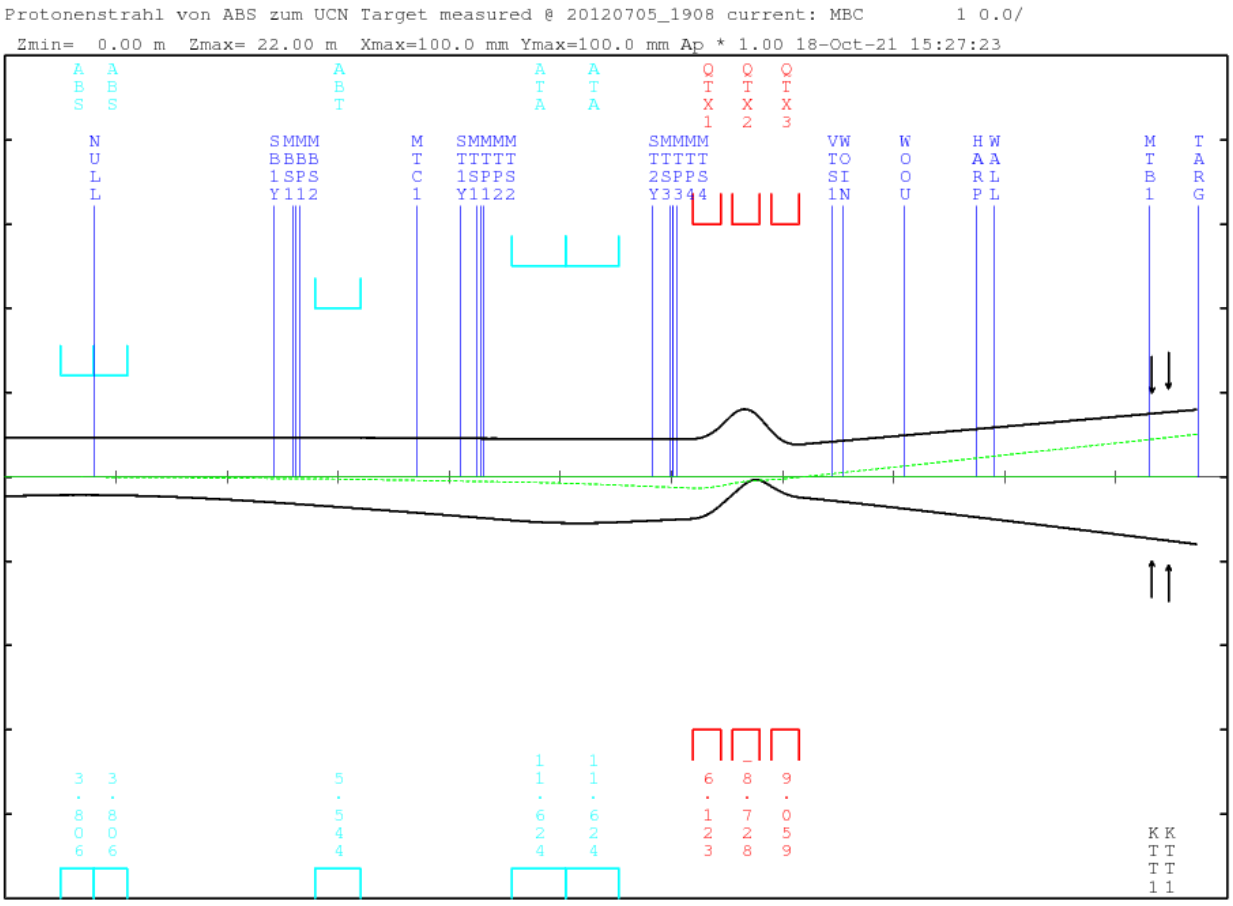

Figure 15.9: Schematic of the beamline and beam optics (two sigma envelope) as simulated in TRANSPORT.

present design) in order to separate it from the UCN beamline before it enters the next larger bend. This magnet will have to be ramped up after each UCN long kick in order to allow TATTOOS beam operation. A ramping speed of less than 30 s is required. In the present design, the fast ramping magnet coincides with the ABT dipole (effective length 823 mm, pole tip field 5.54 kG). This magnet bends the UCN beam towards the left hand side by 6.5 degree. It has to be clarified whether the present ABT can be modified to bend the beam in the opposite direction. If not, a new ABT will have to be designed and manufactured.

- Strong bend (ATA): this magnet is located some 4 m downstream of the ABT (center to center). It gives the beam the final bend (32 degree) towards the TATTOOS target. In the present design, it has 2042 mm effective length and a pole tip field of 11 kG.
- Quadrupole triplet to shape the beam on target: this is a regular triplet. In the present design, each quadrupole has an effective length of 500 mm whereas the pole tip field reaches 9 kG in the third magnet. Figure 15.9 shows the TATTOOS beamline optics simulated with Transport [Rohrer (TRANSPORT)]. The beam is only slightly diverging until it reaches the quadrupole triplet. At the TATTOOS target the beam has a circular shape with a Gaussian distribution with a sigma of 8 mm.
- Steering magnets: in order to steer the beam in the vertical plane, two steering magnets are foreseen in addition to the one already present upstream of the ABT dipole. Presently the location chosen for the pair of new steering magnets is in front of the ATA dipole and between ATA and the quadrupole triplet respectively.
- Wobbler magnets (see Section 15.4.1 below)

15.4.1 Wobbler

In order to avoid overheating of the TATTOOS target it is foreseen to flatten the beam footprint. For this a beam wobbler immediately downstream of the quadrupole triplet will be installed. The wobbler will constitute of two fast dipole magnets (Figure 15.10) driven by AC current with a frequency of around 30 Hz. The current in the two magnets will be such that the beam will draw a circle on the TATTOOS target with a radius of 9 mm. The 1 sigma width of the transverse distribution of the rotating beam will be reduced to 6 mm in both planes (from 8 mm for the static beam). Figure 15.11 shows a comparison of the transverse distribution of static and rotating beam (both areas are normalized to 1). Thanks to the wobbler, the beam current density in the center of the TATTOOS target will be reduced to roughly 60 % of the one given by the static beam. Note that instead of a circle, with a more complicated Lissajous curve and a more focused beam the profile can be flattened further if required.

15.4.2 Collimation System for Beam-Target Centering

The target protection will be achieved with a collimator preceded by a four segment aperture foil in front of the target. The 30 cm copper, or possibly Densimet®, collimator will be equipped at the front with four segments of thin-sheet metal (100 µm Ni) that provide beam halo measurements in four directions. A collimator with Densimet does not need to be cooled, while in case of copper it would look similar to the one described in Section 8.4.3. A left-right or up-down asymmetry can be detected with the aperture foil and helps steering the beam. These measurements will provide the signals for the machine protection system to protect the target and the collimator itself. Aperture foils are in use for several collimators and beam dumps in HIPA.

The collimator needs to be designed in a way that it can be exchanged by the exchanged flask planned particularly for the highly activated beamline components buried in the target shielding (see Chapter 18).

The target centering will be achieved with harps monitors, see next section.

15.4.3 Diagnostics

The TATTOOS beamline will need the following diagnostics elements (Figure 15.12):

- Two beam current monitors, one relative RF resonator [Reimann, 1975] and one absolute Bergoz monitor [Bergoz, 2021]. The absolute measurement can be used to calibrate the relative monitor, which in turn provides more stability over time.
- Two beam loss monitors, one after each bend in the vicinity of the beam pipe. Air-filled ionization chambers will be used, sensitive enough to detect beam losses in the sub-nA level [Zichy, 1975] [Dölling, 2005]. These will be coupled to the machine protection system.

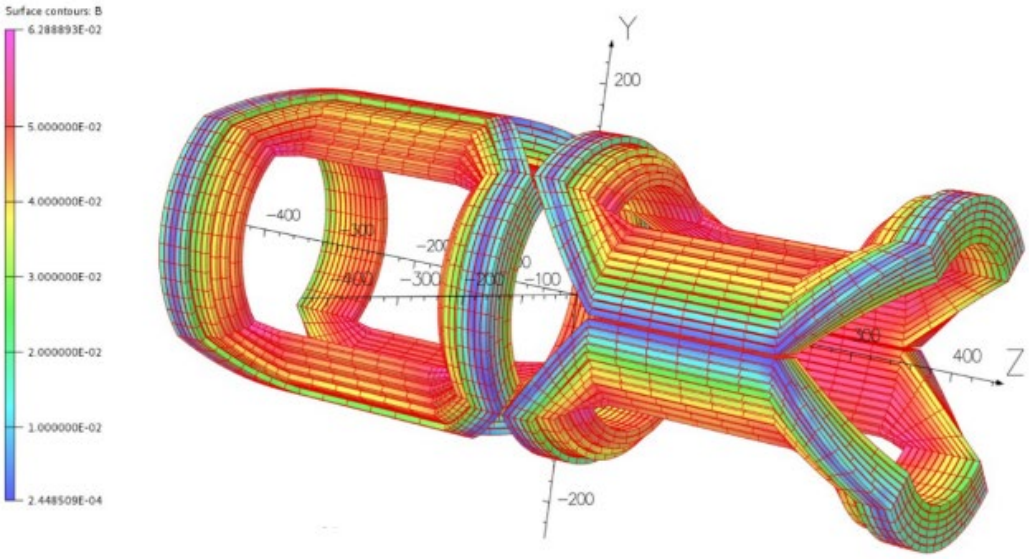

Figure 15.10: Model of the two wobbler magnets, one for each direction.

Figure 15.11: The beam profile on the target. Effect of wobbling the beam can be seen.

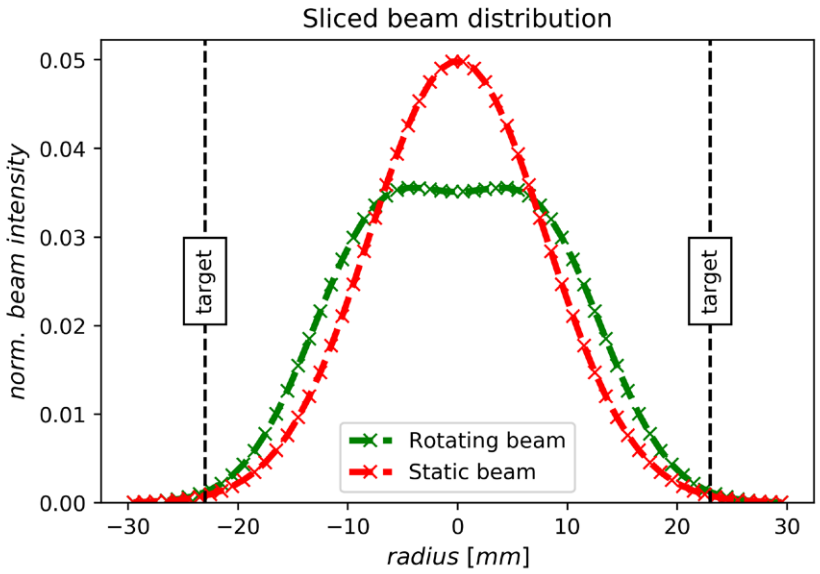

- Four beam position monitors (BPM) (see Section 8.5.4), two in each plane, will be used in addition to the one already present after the ABS septum magnet. They are located after each bend and will provide the means to steer the beam through the beamline. Their resolution at 2.0 mA is in the order of 0.2 mm [Keil, 2006].
- Four profile monitors (see Section 8.5.4) at the locations of the BPMs measure and verify the optics. Profile monitors will be a new in-house development. Each pair of profile monitor and BPM will be placed together in the same vacuum chamber, as it is already custom at HIPA.
- A harp for each plane before the target chamber measures both the beam profile and the position in a continuous manner. Such a measurement is already in use for the UCN target. Experience was also gained with LISOR at lower energy, but further development and testing will be needed [Dölling, 2002].

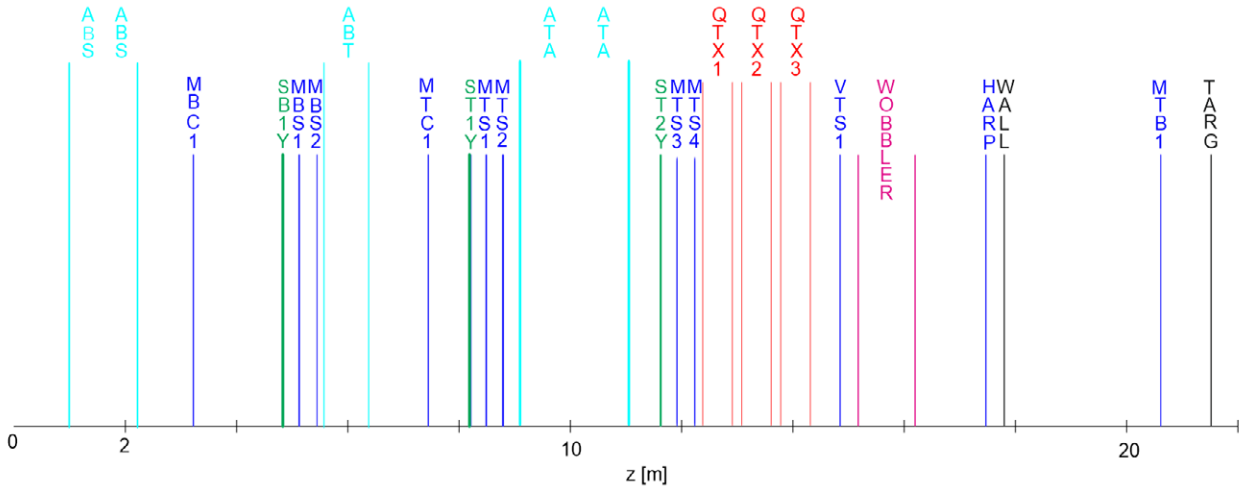

Figure 15.12: Main components along the TATTOOS beamline. Dipole bending magnets in cyan; (vertical) steerer magnets in green; diagnostic elements in blue; quadrupoles in red; shutter valve (VTS1) in blue; wobbler in magenta; collimator MTB1 in blue; shielding wall and target in black.

It is a big advantage to have access to the diagnostic elements for replacement and repair, which can be done much faster than using an exchange flask with subsequent repair in the shielded service cell due to high activation. In addition, repairs with manipulators is limited and the design of the diagnostic elements would have to support such operation. Therefore, all diagnostic devices in the current beamline layout are before the shielding (Figure 15.3) and easy access to the TATTOOS beamline is warranted.

15.5 Power

The standard power supplies in use at HIPA are double power supplies that can provide 2 × 500 A / 160 V. These will be used to power the standard magnets in the TATTOOS beamline.
For the kicker magnet in parallel operation (Section 15.2.2.2) and the wobbler magnet (Section 15.4.1) special power supplies will be needed.

15.6 Cooling System

Except for the magnets, the beamline components in front of the target shielding block do not need to be cooled. The collimator in front of the target will be water-cooled in case it is made from copper. Therefore, tungsten or Densimet® is preferred. Concerning the cooling system, no conceptual changes are expected with respect to the present situation in the other HIPA beamlines (see Section 12.4).

15.7 Vacuum System

Concerning the vacuum system, no conceptual changes are expected with respect to the present situation in the other HIPA beamlines. See Section 8.5.6 for more details.
To protect the TATTOOS beamline components from being destroyed in case the beam window (see next section) breaks, a fast closing shutter will be installed after the quadrupole triplet. The distance to the target is about 6.5 m, which is sufficient for a 12 ms VAT shutter [VAT, 2021].

15.8 Beam Windows

The beam window separates the proton beamline from the target area, which could be contaminated with alpha emitting isotopes and is therefore secured by two target windows described in Section 16.4.2. There will be one beam window in front of the target area, and one after the target area before the beam dump. The upstream beam window is located between the secondary target containment chamber (see Figure 16.38 in Section 16.4) and the upstream beam tube. The downstream beam window is between the secondary target containment and the vacuum chamber of the beam dump. This means that during normal beam operation there is no large pressure difference on the beam window. However, if the beam window would break, then the beam tube would be connected to the large volume of the secondary target containment chamber and the channel containing the rail system, which is held at fore-vacuum conditions of 10^{-2}-10^{-3} mbar. Therefore, the vacuum pressure in the beamline would suddenly increase to fore-vacuum pressure and the fast closing shutter would close. At the same time, the beam is switched off by an interlock.
When the target has to be exchanged, the secondary target containment chamber is filled with nitrogen (to avoid moistening) at normal pressure. In this case, the beam window has to stand the pressure difference of 1 bar. During this operation, the vacuum valve in front of the target block will be closed to avoid further damage, if the beam window should break.

15.8.1 Materials

The material for the foil to be used as window should keep its ductility and integrity after proton irradiation. Good experience exists with carbon, aluminum and nickel but also with molybdenum. These materials are used as e.g. safety shroud at the spallation target SINQ, as four segment aperture foils or as wires in the harps. However, none of them has been used so far as a vacuum window.

15.8.2 Cooling, Sealing & Exchange

The power deposit in 1 mm aluminum for a 590 MeV, 100 mA proton beam is 55 W, for nickel it is about three times more. Since the beam distribution is already flattened to avoid

overheating of the target, the temperature is expected to be around 100 °C for aluminum. To avoid active cooling with water a material with higher melting point is preferred. In addition, radiation decreases the thermal conductivity, which leads to higher temperatures. Nickel could be cooled also by thermal radiation as it stands high temperatures. However, the emissivity of nickel is small but could be increased by coating or oxidation.

The foil could be placed in a flange, which is sealed by a metal seal. Left and right from this an inflatable metal seal is fixed to tighten the connection to the beam tube and the target containment chamber. As the life time of the foil is not known it is important that the foil can be exchanged. This will be done with the exchange flask (see Chapter 18). Since the inflatable seals are expensive and radioactive waste should be reduced as much as possible, keeping in mind that the insert is equipped with a massive shielding plug, it is important that in case of a failure of the foil just the flange containing the foil needs to be replaced. Due to the high dose rate of about 1 Sv/h this operation has to be performed during the service in the shielded service cell ATEC (see Section 10.4).

15.9 Control System

The control system is already described in Section 8.5.7.

15.10 Machine Protection System

The philosophy of the TATTOOS machine protection will not differ substantially from the one already implemented at HIPA.

Aims of protection

The machine protection system (MPS) [Mezger, 2010] [Reggiani, 2018] should prevent on the one hand material damage and operational interruptions, and on the other hand prevent excessive activation of accelerator elements. The MPS is an extensive system that processes thousands of signals that represent the status of single elements, both active elements like magnets and HF systems, and passive elements like collimators and ionization chambers. These signals are evaluated and if in an unacceptable situation, the beam is turned off within a few milliseconds. It is essential that this time is being kept to an absolute minimum to reduce the chances of damage.

Most important for TATTOOS is to prevent target damage. The target can be overheated or damaged in case the beam is off-centered, over-focused or too much current is peeled off by the splitter. Such beam properties must be detected fast enough to prevent damage.

Also the TATTOOS beam pipe and beamline components as, e.g., the collimators, can be overheated and damaged or overly activated by accidental beam loss, caused by an off-axis or broad beam or misplaced components. Large beam loss must be detected, while lower beam losses can be tolerated temporarily, but the beam has to be switched off automatically after some time to limit the dose for service personnel.

15.10.1 Target Protection

The target protection will be achieved by:

- The four-segment aperture foil in front of the collimator will be able to detect if the beam is off-centered or has an asymmetry. This system will also be able to detect if the beam is over-focused by comparing the beam current to the expected halo.
- Until the MPS responds, the collimator in front of the target will act as a shielding for the target in case the beam is off-center.
- The harps measurement before the target will provide the measurement for the beam trajectory feedback to keep the beam position stable within 0.1 mm tolerance with an update rate of 10 Hz. Beam width and center position will be evaluated and compared to expected values. An interlock signal is generated if needed.
- The beam current monitors will provide a fast measurement that will trigger the interlock system if too much current is peeled off by the splitter.

In all cases, signal evaluation is done in the diagnostics electronics. Interlock requests to the MPS are generated according to implemented rules. The new loss monitor electronics under development will allow a broader variety of tailored algorithms.

There is no need to resolve the beam rotation generated by the wobbler. Since the rotation will have a time scale that the target does not react to, it is sufficient to be able to measure the average beam profile and position.

15.10.2 Beamline Protection

The protection of the beamline itself is less stringent. The BPMs and the already mentioned beam trajectory feedback system will keep the beam position stable within 0.2 mm and will transport the beam with low losses to the target. In addition, the beam loss monitors will provide a fast and sensitive measurement that is connected to the MPS, in case losses occur. These measures will also prevent activation of the beamline area.

In addition, each power supply will be surveilled: In case a power supply of a magnet fails, the beam can be missteered or change its focus. Each power supply will be connected to the MPS, as is already currently the case in HIPA.

15.11 Emergency Scenarios

The following emergency scenarios and protective measures are considered:

- If the beam window breaks, the fast closing shutter will protect the rest of the TATTOOS beamline from contamination. Since the shutter is installed upstream of the harps, these will unfortunately not be protected and might get damaged. This means that there should be spares for the harps to allow fast recovery after the beam window is replaced.
- In case one of the strips of the splitter, typically the one in front, breaks due to overheating or mechanical wear, the two ends of the strip will be pulled out by the tensioning system. The splitter will still be able to function correctly and can be adjusted by increasing the applied voltage slightly. These strips can be replaced in the yearly long shutdown period.
- If so many strips break that the splitter voltage cannot be increased anymore, the splitter will need to be exchanged with the available spare splitter, and the broken strips can be replaced. Since the operating voltage is about 172 kV and the expected maximum voltage is about 180 kV, after about 8 broken strips (there are 179 strips) the splitter needs to be exchanged.
- If the movement mechanism of the splitter fails, the motor repair or exchange can be done in the beamline.
- In case the wobbler system is not functioning, the beam shape can be widened by the quadrupoles and the target can be radiated with a reduced current.
- Almost all diagnostic devices have a redundant partner system and it is expected that with operational experience the breakdown of a single diagnostic sensor will not cause downtime. These devices can typically be repaired or replaced in the period of a service week or target exchange.

15.12 Commissioning and Operation

The commissioning of the beamline is planned in four stages:

1. The first stage will commission the splitter and the ABT magnet. The beam will be steered onto the UCN target or the UCN beam dump. Maximum intensities possible are 60 µA for the UCN target, and 20 µA for the UCN beam dump.
2. A dummy TATTOOS target made of graphite will be placed instead of the real target. With full current, the real optics and the wobbler system can be tested. The graphite target should be more beam tolerant as it absorbs not so much beam and has an emissivity of 0.7 instead of 0.4 for tantalum. However, a larger fraction of the beam, which is less divergent, will hit the beam dump. A beam dump design, which can operate under these conditions, should be feasible.
3. Commissioning of the real target with low current. With the target heating system, the first isotopes can be produced at a low beam current. The beam current can be slowly increased towards its final current of 100 µA.

HIPA operation can in general be divided into three distinctive types: a startup phase after the yearly shutdown or a short service, continuous operation, and beam development studies. For TATTOOS during its target exchanges additional downtime periods are expected.

After a single interruption by the MPS, the HIPA operation is automatically ramped up, usually without problems. The

beam splitter will be moved out of the beam before being able to ramp up again. This has to be included into the automatic ramp-up procedure.

Only if the interruption occurs again an operator in the accelerator control room needs to intervene and the automatic ramp is disabled. In most cases, the cause can be understood and the malfunction solved with few clicks and some adjustments. However, there are instances in which help from the PSI expert groups is required, as in the case of complete or partial failure of components. For this purpose, there is always a member from each specialty domain (for example RF, vacuum, etc.) available on call. This proven procedure keeps the beam availability high, for HIPA larger than 90 %.

For TATTOOS, the existing operational tools that are in use for HIPA can be applied without problems but need to be extended, e.g. the display for the diagnostic elements, the beam trajectory feedback system or the current feedback. Special care needs to be taken for the alternating beam operation. The fully automated UCN kick procedure needs to be extended with the splitter movement and the ramping of the ABT magnet.

16 Target

16.1 Radionuclide Production via Spallation

16.1.1 Calculation Method

To compute the nuclide inventory and the gamma dose rate, the SP-FISPACT/CINDER [Petrovic, 2001] codes and the accompanying PSI activation script [Gallmeier, 2015] were used. Having determined the nuclide inventory, a subsequent MCNP6.2 [Pelowitz, 2013] run with the so-obtained gamma source was done. The aim of the last run was to compute the resulting gamma dose rate, by folding the photon spectrum with the appropriate flux to dose conversion factors. For the uranium carbide (UCx) case, a special version of INCL4.6+ABLA capable of accurately treating polonium production in heavy elements was used. The accurate polonium production reaction rates modeled by INCL4.6 were validated using experimental data, [Ferrari, 2016]. For the tantalum target case, where polonium production is practically absent the standard high-energy module of MCNP6.2 - CEM03 was used. In addition, the SP-FISPACT results for the UCx target were observed to be unphysical and were therefore disregarded. This was attributed to the fact, that the total decay heat production in the target, as well as the H-3 production rate were unphysically high. In addition, the gamma source did not obey the typical exponential decay law.

The currently used PSI activation script uses a two-step calculation scheme. The Monte Carlo calculation yields the spectrum for neutrons with energy less than 20 MeV and the production rates of the residual nuclides caused by neutrons of energy larger than 20 MeV or other particles like protons and pions of any energy. In the energy range below 20 MeV, the nuclear reactions in MCNP are taken from tabulated cross sections (ENDF/B-VIII), whereas reactions of neutrons above 20 MeV and with all other particles are taken from models, here CEM03.03 or INCL4.6+ABLA.

In either SP-FISPACT or CINDER the neutron tabulated nuclear data are superimposed with the neutron flux computed by MCNP6.2 to produce flux weighted reaction rates. Together with the production rates of the residual nuclides obtained by models in MCNP these reaction rates are subsequently used as input parameters for solving the Bateman system of equations in either SP-FISPACT or CINDER. For this, the inventory codes SP-FISPACT and CINDER need the irradiation and cooling history of the piece of interest as input.

Having determined the concentrations of the activation and the spallation products, a gamma source term is derived. This source term is subsequently used to determine the remnant gamma dose rate.

16.1.2 Nuclide Inventory and Dose Rates of the Ta and UCx Target

To estimate the production of radionuclides dedicated to clinical studies as well as the complete nuclide inventory for the disposal of the targets, the above described methods were applied first to the spallation targets made of Ta and UCx. Further, for the handling of the target, particularly during the exchange as well as later for storage and finally for the disposal, the dose rate of the targets is taken into account when designing the shielding. Since we are interested in long-lived isotopes regarding the disposal ($T_{1/2}$ › 100 days), the irradiation period was chosen to be 28 days, the time interval anticipated to replace the target with a fresh one. This approach intentionally yields a conservative result since the irradiations might be interrupted and thus the long-lived activities will not reach production-decay-equilibrium in reality.

The results of these calculations for the tantalum and UCx targets regarding the nuclide inventory are plotted in Figure 16.1 and Figure 16.2. The Ta (UCx) target is assumed to be 20 cm long filled with 10 (15) cm equivalent of Ta (UCx) material in the form of plates yielding all together about 3.67 kg (2.57 kg) Ta (UCx). Evident from the UCx case is the pronounced fission peak (the mid-section of the plot) and the production of high mass transuranic elements via neutron capture and at the evaporation stage of the nuclear cascade (upper right corner of the plot). On the contrary, having a smaller number of protons, tantalum is much more likely to undergo evaporation than high-energy fission, hence, the peak in the upper right corner of the plot. The plots shown hereafter follow the neutron number on the abscissa (N) vs. atomic number (Z) on the ordinate representation, typical for nuclide charts.

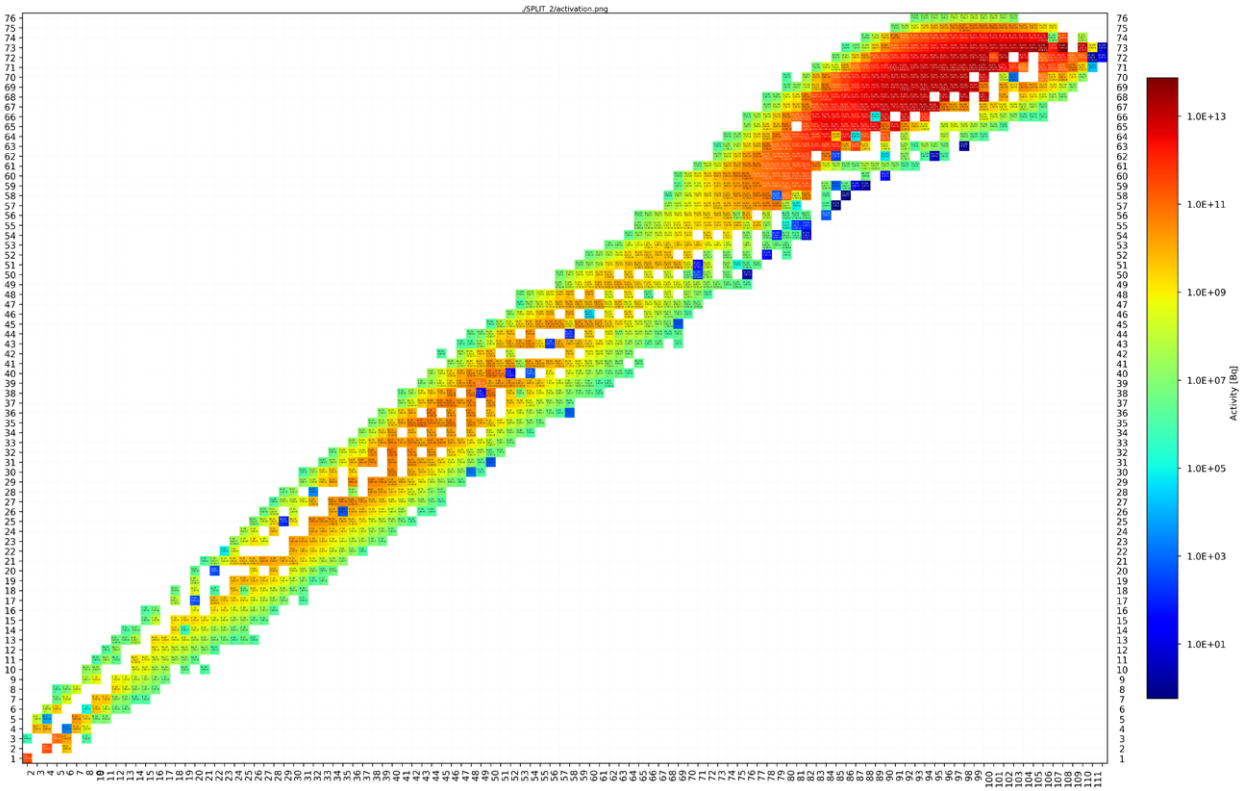

Figure 16.1: Activation and spallation products for the Ta target at shutdown following 28 days of irradiation. The results were computed with CEM03 and CINDER. Shown on the abscissa is the number of neutrons and on the ordinate the number of protons.

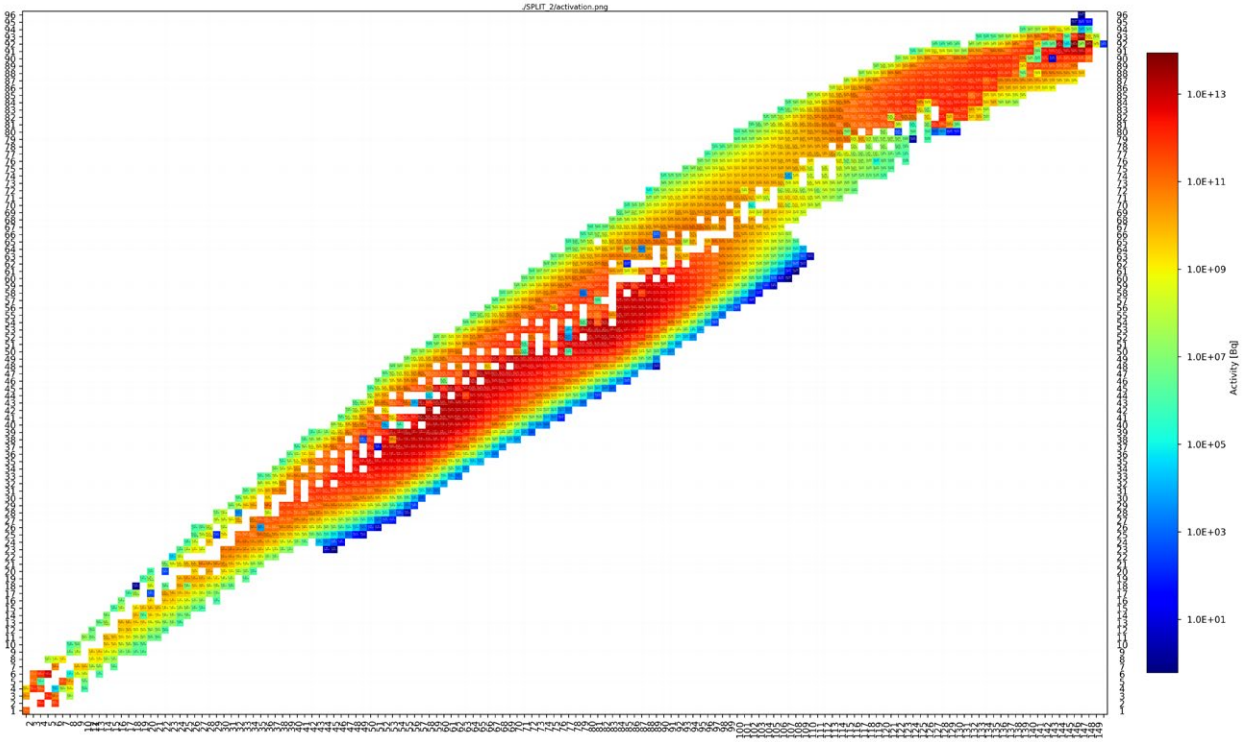

Figure 16.2: Activation and spallation products for the UCx target at shutdown following 28 days of irradiation. The results were computed with INCL4.6-ABLA and CINDER. Shown on the abscissa is the number of neutrons and on the ordinate the number of protons.

Being embedded in an intense neutron field, a significant amount of Ta-182 with a half-life of 114 days is produced via neutron capture in Ta-181. Ta-182 determines the long-term remnant dose rate. Therefore, the tantalum target is a source of a very significant gamma dose rate, which can be as high as 1000 Sv/h in 3 cm distance to the target after 12 h of cooling time. The contributions of the isotopes in Ta to the dose rate for 12 h, 24 h and 365 days as well as immediately after shutdown of the beam are shown in Table 16.1. The resulting distribution of the remnant dose rates in the vicinity of the tantalum target is shown in Figure 16.3.

Shown in Figure 16.4 is the remnant dose rate of the UCx target following 28 days of irradiation. Unlike the tantalum case, significant amounts of minor actinides and alpha emitters are produced.

An example of nuclides produced during the evaporation stage of the nuclear cascade, as well as via neutron capture are shown in Table 16.2.

Shutdown		+12h		+24h		+365d	
Lu170*	6.04	Lu170*	19.86	Lu170*	22.65	Ta182	69.46
Ta176	5.48	Tm166*	13.97	Tm166*	15.67	Lu172*	21.13
Lu163*	4.96	Ta182	9.51	Ta182	11.98	Lu173*	2.94
Tm166*	4.29	Ta176	7.57	Lu171*	6.64	Hf175	1.94
Lu166*	3.03	Lu171*	5.4	Lu169*	5.01	Ta179	1.38
Lu168m*	2.99	Lu169*	5.07	Ho160	4.25	Hf172	1.17
Ta182	2.72	Ho160*	4.34	Ta176	3.45	Gd153*	0.31
Tm162*	2.71	Ta175	3.47	Lu172*	3.04	Eu146*	0.29
Ta171	2.48	Hf171	3.18	Tm165*	2.86	Dy159*	0.27
Tm163*	2.47	Hf173	3.01	Hf173	2.71	Y88	0.17
Ta172	2.34	Tm165*	2.99	Ho160m*	2.45	Pm143*	0.16
Ta175	2.16	Lu172	2.51	Hf171	2.02	Tm168*	0.11
Lu165*	2.06	Ho160m*	2.5	Ta175	1.99	Eu149*	0.09

Shutdown		+12h		+24h		+365d	
I134*	2.44	I132	12.42	I132*	14.51	Nb95	19.35
I132*	1.92	La140	10.19	La140	13.17	Ag110m*	16.12
Cs138*	1.68	U237	5.89	U237	7.33	Rh102	9.94
Tc104	1.64	Sb128	3.6	Np239	3.32	Rh106	9.03
Mo101	1.59	Nb97	3.48	I133*	2.91	Zr95	8.67
La144	1.56	Nb97m	3.35	Nb97	2.77	Tl208*	6.42
La142	1.28	I133	3.32	Nb97m	2.67	Sb125*	6.27
I135*	1.28	Np239	2.94	I131*	2.63	Y88	6.15
La140	1.27	I135	2.91	Ru103	2.4	Cs134*	4.19
Nb102	1.13	Ag112	2.42	Sb127*	2.25	Ba137m*	1.85
Tc106	1.09	I131	2.1	Zr95	2.09	Sb124*	1.76
Sr85m*	1.07	Sb127	1.88	Ag112*	2.08	Pr144*	1.16
Sb128*	1.03	Ru103	1.85	Bi206*	2.03	Pm144*	0.86

Table 16.1: Relative contribution in % of the dominant gamma emitters as a function of the cooling time after 28 days of irradiation. First table Ta target, second table UCx target. Volatile products are marked with a star.

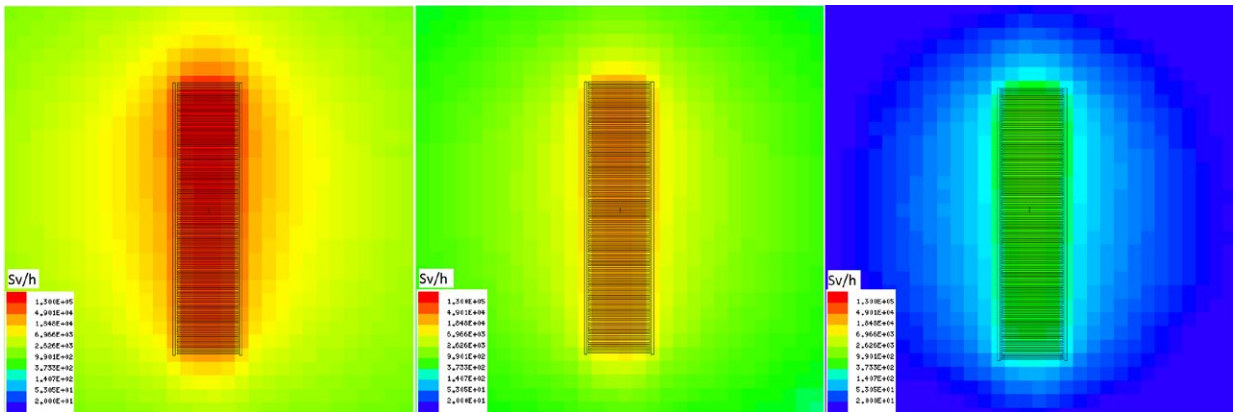

Figure 16.3: Remnant gamma dose rate of the tantalum target following 28 days of irradiation with 100 µA proton beam. The left plot shows the shutdown dose rate, whereas the plot to the right shows the gamma dose rate after 12 hours and 100 days of cooling time. The scale of the plot is 30x30cm.

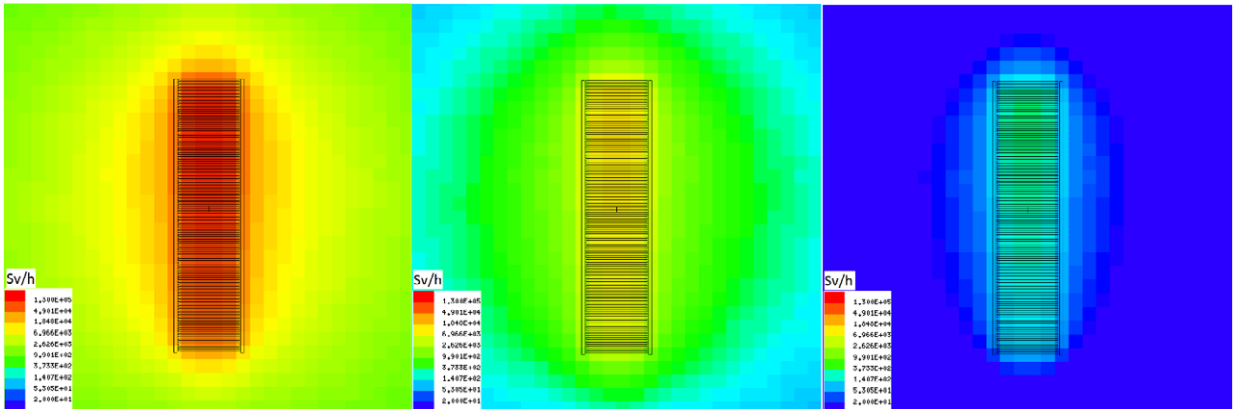

Figure 16.4: Remnant gamma dose rate for the UCx target following 28 days of irradiation with 100 µA proton beam. The left plot shows the shutdown dose rate, whereas the plot to the right shows the gamma dose rate after 12 hours and 100 days of cooling time. The scale of the plot is 30x30cm.

Radionuclide	Activity [Bq]
Po-208	2.06E+10
Po-209	7.38E+08
Po-210	2.05E+11
Pb-210	2.35E+09
Ra-226	5.49E+06
Pa-231	3.66E+06
Th-228	3.35E+10
Th-229	1.06E+07
Th-230	1.04E+06
U-228	3.57E+09
U-232	1.84E+09
U-233	9.41E+05
U-234	1.59E+06
U-236	4.17E+04
Np-237	8.24E+05
Total Pu	3.5E+08

Table 16.2: Example of alpha-decaying radionuclides relevant for disposal ($T_{1/2}$>100 d) formed via evaporation and neutron capture in the entire UCx target (2.57kg) after 28 days of irradiation.

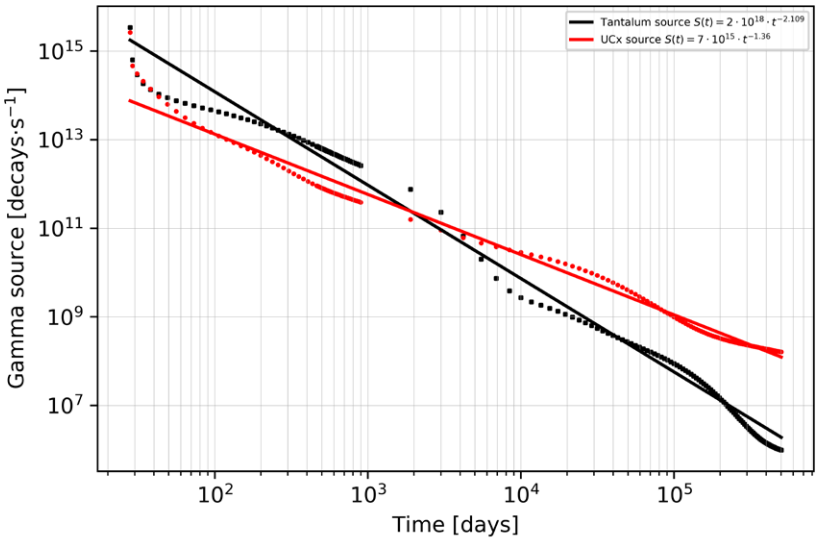

Figure 16.5: Integral decay gamma source strength as a function of the cooling time, following 28 days of irradiation, for the Ta and UCx targets. Judging based on the fit curves, the gamma source of the tantalum target decay rate is about 65% higher than the gamma source of the UCx target. Note that due to the rapid decay of the short lived activation and spallation products, the power function doesn't fit the data well for the first 10 days of cooling time.

Due to the longer half-live of the dominant gamma emitting fission products Cs-137, Cs-134, the gamma source retains its intensity for a longer period of time, when compared to the tantalum case. This effect is shown graphically in Figure 16.5, where the gamma source strength as a function of time is shown. To appreciate the effect in a quantitative manner, the data were fitted using a power function.

The dose rate of the target as a function of time is shown in Figure 16.9.

16.1.3 Release of Radionuclides from Ta and UCx

The thermal release of radionuclides from target materials is driven by thermodynamic and kinetic properties connected to the different chemical character and affinity of the corresponding target/tracer atom pair. While the kinetics of the release is of minor importance considering the high target temperature and the rather long half-lives of the intended radionuclides the thermodynamics is highly relevant for the obtainable product amount as well as for the disposal. For

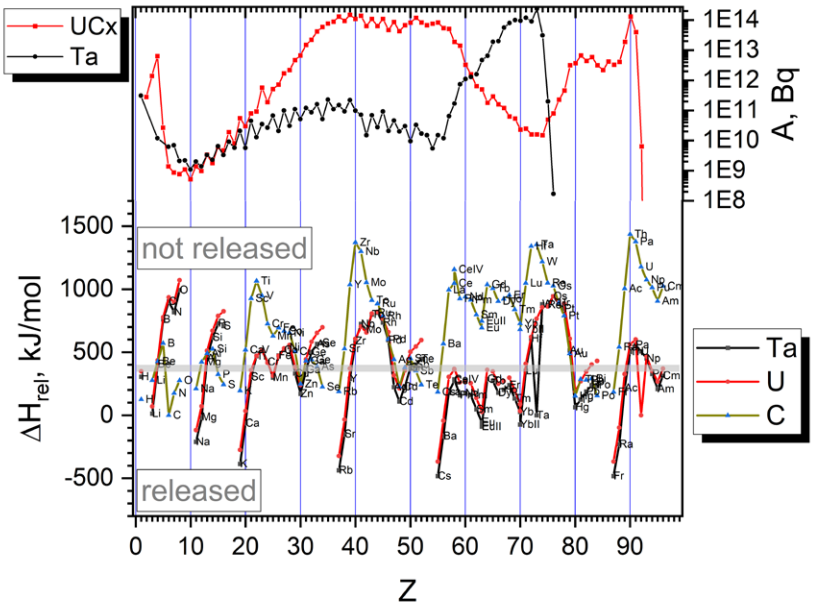

Figure 16.6: The production of elements with the atomic number Z (upper panel) and their release enthalpies (lower panel) out of Ta, U and C matrices. The grey line divides the elements with reasonably easy release (lower ΔH_{rel}) from the elements with expected lower release efficiency (higher ΔH_{rel}). Note, the UCx target is assumed a mixture of various stoichiometric compositions including phases of pure carbon the amount of which will determine the release for some carbide-forming elements.

the assessment of the release thermodynamics experience data from CERN-ISOLDE [Ballof, 2020] (https://isoyields2.web.cern.ch) and from [Kirchner, 1992] as well as from an independent integral assessment over the semi-empirical macroscopic Miedema model [Miedema, 1975; Miedema, 1976] is used. The Miedema model allows for an estimation of the enthalpy of solid solution of an atomic metallic species at infinite dissolution in a solid. In conjunction with the desublimation enthalpy [CRC Handbook, 2021] this enthalpy of solid solution allows deducing a release enthalpy the thermodynamic parameter relevant for the transfer from the solid solution into the gas phase. Figure 16.6 shows the release of all elements of the periodic table from a tantalum matrix as well as from graphite and uranium serving as model for an UCx target material. The resulting release predictions are in reasonable agreement with the isotopic yields obtained for the long-lived isotopes at CERN ISOLDE [Ballof, 2020] (https://isoyields2.web.cern.ch), where kinetic considerations do not play an important role. It is quite obvious that e.g. elements forming stable carbides are hardly released from carbon containing matrices. Otherwise, the elements with high sublimation enthalpies are not easily released. The goal products of TATTOOS Tb as well as Ac and Ra are well released from Ta and U. Ac is already shown in ISOLDE experiments to be not well released from carbon bearing materials. However, ^{225}Ra (half-life 11 d) can be produced and released in large quantities to serve as a generator nuclide for the production of the highly relevant ^{225}Ac.

From these considerations, also the nuclide vector remaining in the targets are estimated for developing disposal concepts of the used targets.

16.1.4 Disposal of Ta and UCx Targets

The disposal of the targets poses a particular challenge given the high concentration and the spectrum of isotopes produced is non-negligible amounts (see Section 16.1.2). Compare with the Ta-targets the UCx is even more challenging due to traces of fissile isotopes produced during irradiation as well as due to radiolysis, which requires a chemical processing before disposal. Since UCx is only foreseen for the second phase of TATTOOS and it needs a complex new disposal concept, we will mainly focus on the Ta targets but also mention some facts about the UCx target.

In general, the disposal of radioactive waste has to comply with numerous constraints, the comprehensive discussion of which goes beyond the scope of this chapter. For this reason a waste package type (WPT) is written, which describes the full disposal path in all aspects. The WPT needs approval by the Swiss authorities ENSI and the support of NAGRA. In the following, we concentrate mainly on the following aspects:

- The amount of targets to be disposed of per year.
- The dose rate outside of the waste container has to be below 2 mSv/h in 10 cm distance.
- The LSA-II (Low Specific Activity) index has to be ‹ 10^{-4} for the industrial package-II (IP-II) waste container called KC-T12 or KC-T30, which is used for most solid radioactive waste originating from the operation of the accelerators and related facilities.
- The nuclide inventory.

Although the lifetime of the targets is yet unknown and cannot be predicted due to the harsh conditions induced by irradiation and high temperature, the expected lifetime according to experience based on the ISOLDE facility at CERN is about 1 month. Therefore, the irradiation period of one target is set to 28 days for the following considerations. According to Section 16.3.6.2 this is a conservative assumption. It should be noted that a two times longer lifetime will reduce the volume of waste by a factor 2, but the nuclide inventory regarding the isotopes relevant for radioactive waste disposal, i.e. with half lifes › 100 days will not change significantly. Together with the fact that one target weights only a few kilograms, the number of targets per year does not need to be exactly known. Hereafter we assume a production of 10 targets per year to be disposed.

16.1.4.1 Tantalum Targets

In the following calculations, the mass of each Ta target is set to about 3.67 kg, including a cylindrical shell. In addition, the disposal of the target chamber might have to be considered as well. The target chamber however is made of stainless steel and has relatively low weight, scenario covered by the WPT already approved for operational waste from the accelerator facilities. To remove the alpha contamination inside the target chamber a dedicated decontamination has to be conducted.

The time until the LSA criteria are matched will determine how long the targets need to be stored before disposal. The LSA criteria have to be fulfilled for the full content of the container including the non-radioactive mortar for conditioning as well as the non-radioactive additional shielding. Therefore two existing containers, 091 and 635, filled with operational waste form the accelerator facilities were considered as a model. The first one is a type KC-T30, the second KC-T12 container. The outer dimension of the concrete container, reinforced with steel, are the same but its wall thickness is 30 cm and 12 cm respectively. In the 091 container the activated shield of a recent SINQ target is placed, which amounts to a LSA of 6.3 10^{-8} excluding mortar, whereas container 635 contains a variety of waste, from the accelerator facility with a 6 times lower LSA. The weight of the waste content amounts to about 6 t for both containers, where normal steel is the main component. Since the 091 has a smaller net volume the mortar amounts to 1 t whereas 635 is filled with 3 t mortar. To these two model container 10 Ta targets were added assuming decay times between 0 (no cooling time) and almost 3 years. Since the two containers serve as a model for a typical container to be disposed every year, the radioactive content was not decayed during the time the targets were stored. The nuclide inventory for the Ta targets was calculated using the method described in Section 16.1.1 and presented in Section 16.1.2.

The results for the LSA index for 10 Ta target in both containers is presented in Figure 16.7. The LSA criteria is fulfilled below the horizontal red line in Figure 16.7. As the nuclide inventory of the Ta targets differs using the two codes CINDER and SP-FISPACT, the LSA index varies by a factor of about 2. The difference in the LSA index due to the different content in the two containers is in the same order of magnitude compared to the difference using different codes. The calculations demonstrate that after 700 to 900 days of temporary storage 10 irradiated targets can be disposed of in containers filled with radioactive waste from the accelerator facilities. The storage of the targets is described in Section 16.3.6.3. It is recommended to reserve space in the storage area for at least 30-40 targets and to be able to store for 3 years 10 targets every year. The first badge of 10 targets would then be disposed of after 3 years of storage. This would contain targets with cooling times between 2 and 3 years.
Ta is known for its high decay heat, when it is used as cladding for tungsten in spallation target stations like ISIS. Therefore, the decay heat was calculated as a function of decay time in Figure 16.8. As can be seen, the decay heat is high in the very beginning directly after irradiation, but after 2 years the decay heat amounts to $3 \cdot 10^{-5}$ W/g. For 37 kg Ta material, i.e. 10 targets, this results to 1 W. This is tolerable in the waste container. For the disposal of SINQ target a maximum decay heat of 40 W is allowed.

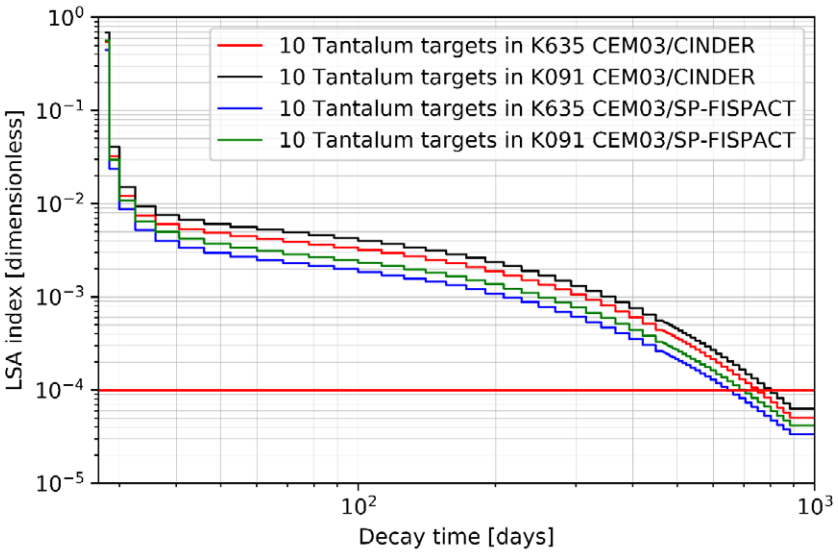

Figure 16.7: LSA index for the two model containers as a function of the time 10 Ta targets are stored. Two built-up and decay codes as indicated as used.

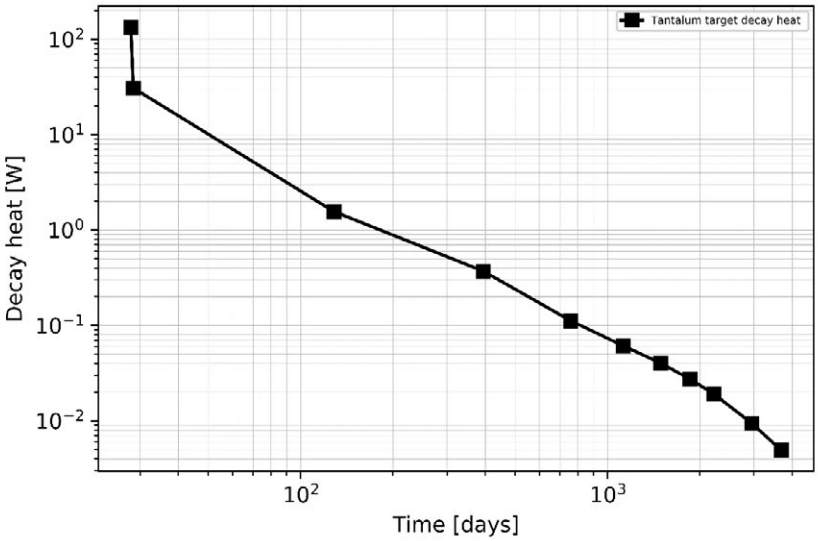

Figure 16.8: Decay heat of one Ta target as a function of storage time after irradiation.

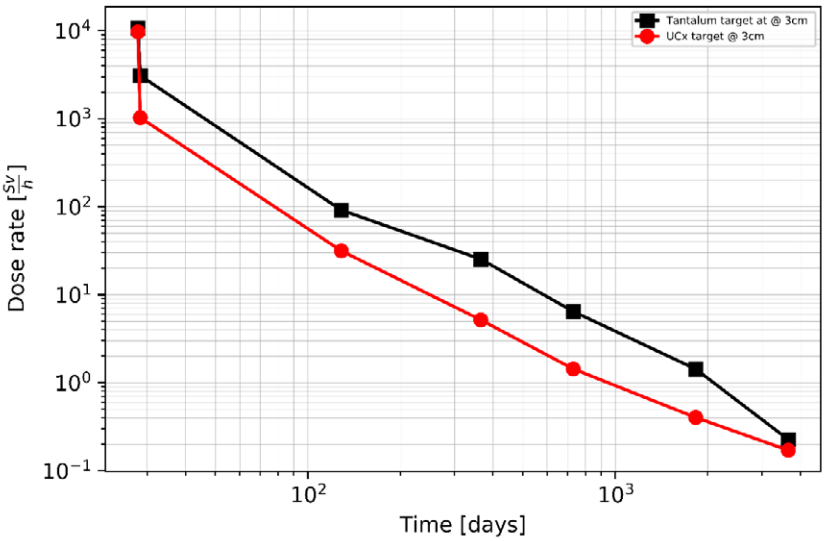

Figure 16.9: Decay gamma dose rate for both the UCx and the Ta targets. The gamma dose rate was computed on the target midplane at 3 cm distance. The higher dose rate of the Ta target can be attributed to the activation product Ta-182.

To fulfil the dose rate criteria outside of the container the dose rate of one Ta target was calculated with decay time in Figure 16.9. Shown in the same plot is also the decay gamma dose rate of the UCx target.

After 1 year (3 years) the dose rate of one Ta target is 20 Sv/h (~ 6 Sv/h). For 10 targets these values have to be multiplied by 10 since self-shielding is negligible. The dose rate is mainly driven by Ta-182 with a half life of $T_{1/2}$ = 114 days. To save space in the waste container the shielding should be as compact as possible. Materials like lead with high Z are well suited for shielding. A so called primary box shielded with 15-20 cm lead around this kind of waste reduces the dose rate by a factor of 10^5. The badge of 10 targets can be shielded even more effective, if casted with liquid metal like LBE (Lead-Bismuth Eutectic) as it is performed in the shielded service cell ATEC at PSI for the SINQ targets. LBE has the same good shielding properties but a lower melting point and is therefore preferred compared to pouring lead. Still, the primary container will be shielded with a lead wall, which can be thinner in the second case. Besides shielding such a pre-conditioning has the advantage that the targets are well encapsulated ensuring a safer handling during transport or storage. The pouring of the LBE would be done in the shielded target exchange cell (see Section 16.3.6.1). The targets can be preconditioned in primary containers on a regular basis to free space in the storage location.

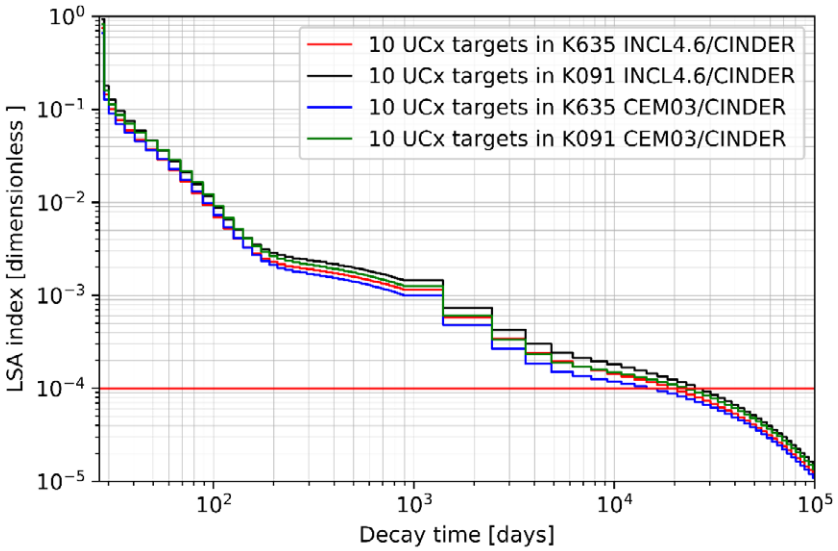

Figure 16.10: LSA index for the two model containers as a function of the time 10 UCx targets are stored. Two cross section models were used in connection with the built-up and decay code CINDER.

The nuclide inventory (see Section 16.1.4) was compared to the WPT for the disposal of SINQ targets. The nuclide inventory for Ta and the Pb-Zr SINQ target is quite similar as expected from the vicinity of Ta and Pb in the nuclide chart. Except for one radioisotope, Gd-148, the 10 Ta targets after a decay of 2 year are already within the limits of maximum activity stated in the WPT. Although quite some radioisotopes are released from the Ta during operation at 2500 °C (see Section 16.1.3), it will be conservatively assumed for the disposal concept that they are still present in the targets. A revision of the WPT for SINQ targets is planned in 2-3 years and an integration of the TATTOOS targets will be considered. Due to the considerations above, we are confident that we can find a disposal concept for the Ta targets, which will be accepted by the Swiss authorities.

16.1.4.2 Uranium Carbide (UCx) Target

The UCx target is an interesting target option for the second phase. Therefore, its disposal concept is not decisive for the beam permit and operation of TATTOOS during the first years. The dose rate of one UCx target after 1 year of decay is 4 Sv/h (see Figure 16.10) which is 5 times lower than for the Ta target and does not pose a problem. The lower dose rate compared to Ta can be attributed to the energetic gamma rays emitted by the activation product Ta-182.

Repeating the calculation of the LSA Index for 10 UCx targets in the two concrete container types KC-T12 and KC-T30, it turned out that the targets would need to decay for more than 50 years until the limit of the LSA of 10^{-4} is reached. Therefore, it is clear that for such targets a container certified for higher activated waste will be needed. A possibility would be to dispose the targets together with waste from the hot laboratory at PSI, which examines spent fuel rods from the Swiss nuclear power plants on a regular basis. In addition, the carbon has to be separated from the UCx by chemical methods. For this the infrastructure of the hot laboratory has to be used anyway. The reason for the need of separation of carbon from uranium is that due to the alpha emission of the uranium activation products, the chemical bound between C and U is broken. The ionized carbon then bounds to oxygen to form CO_2. The release of gas in the final repository has to be avoided, if possible. The practical aspects of this process has to be worked out and the disposal concept is not yet clear. However, CERN ISOLDE has already a stock of irradiated UCx targets and is searching for a disposal concepts as well. First trials started already in the hot laboratory at PSI. Therefore, we are confident that we can profit from this initiative and that in a few years the disposal concept will be consolidated.

16.2 Biological Shielding

16.2.1 Calculation Method

For the shielding calculations, the Discrete-Ordinates (S_N) code DENOVO and the Monte-Carlo transport code MCNP6.2

were used. The S_N solution was used at the initial shielding design stage and for speeding up the Monte Carlo calculation.

S_N codes lack in accuracy when compared to MC codes, but are able to deliver quick global flux solutions, uninfluenced by statistical variance, and in this manner provide quick means for accessing the shielding efficiency. ADVANTG [Mosher, 2015] was used also for preparing variance reduction parameters for MCNP6.2. Using this strategy, it was possible to concentrate on the improvement of the variance of the Monte-Carlo calculation in the spatial regions of interest (e.g. the areas with personnel access). This optimization is also performed in the energy domain, by exploiting the fact that high-energy neutrons have much higher chance, when compared to thermal neutrons, to escape the shielding. In this manner, the Monte Carlo calculation was organized by priority, thereby reducing significantly the computer runtime [Wagner, 1998].

16.2.2 Radiation Protection Constraints

According to Sections 11.1 and 22.1 places without time limitation should have a prompt and residual dose rate of 10 mSv/h. This must also include potential dose rate components coming from other nearby beamlines, e.g. the proton beam line parallel to the TATTOOS area, called PK1. This limit is also valid in front of the shielded cells. A PSI basic rule according to the RPO art. 4 and 60 states, that radiation shielding design should result in a dose rate not exceeding 10 % of the limits valid for the controlled areas mentioned in Table 11.2 in Section 11.1. Regions not accessible during irradiation could have higher dose rates, if there is no leaking or "shining" into an area accessible during irradiation. These non-accessible regions will be protected by a PSYS-system. In the office building adjacent to the TATTOOS area (no supervised or controlled area) the dose rate limit is 0.5 µSv/h for a permanent working place.

16.2.3 Conceptual Shielding Design

As many high energetic particles, particularly neutrons, are produced in the target as well as in the beam dump, these area needs to be well shielded for the access of people during beam permit. At the same time the shielding will protect personnel from the high remnant dose rate at the target (see Section 16.1.2).

High energy, proton-induced spallation reactions produce neutrons and photons within an energy range spanning many orders of magnitude. The high energy tail of the neutron spectrum stretches up to the initial proton beam energy. Therefore, the shielding should comprise significant volumes of steel and concrete. The role of steel is to slow down the high energy neutrons via inelastic reactions with iron. From this point further, concrete is used to additionally lower the neutron energy and absorb the thermal neutrons. This concept is illustrated in Figure 16.11. The iron shielding (black

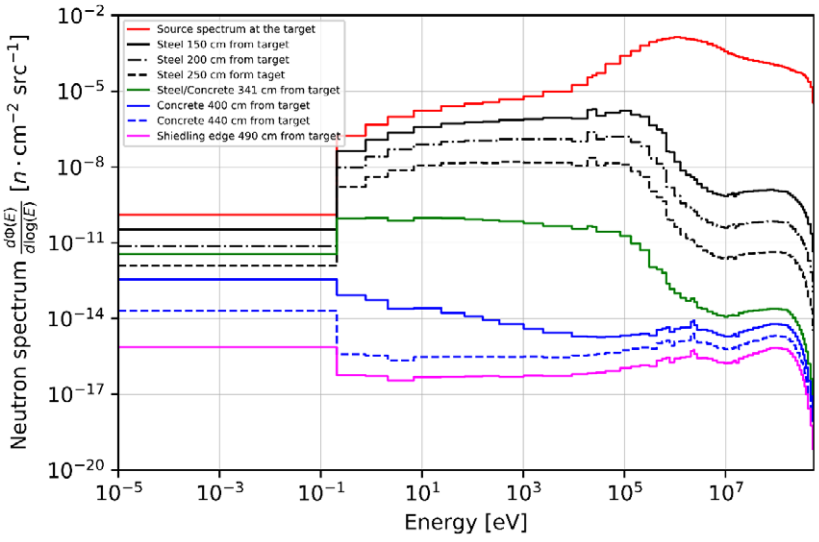

Figure 16.11: Neutron spectra at various positions within the lateral shielding volume calculated with the transport code DENOVO. The normalization is to one source neutron.

curves) suppresses the high energy part of the flux above 1 MeV. Subsequently the concrete shielding moderates the epithermal neutrons shifting the neutron spectrum to thermal energies, where neutrons are easily absorbed. Careful observation shows that the spectral shape deep into the shielding remains constant, for a given material (i.e. the shape of the curves stay the same and only the amplitude is reduced). This is the well-known equilibrium spectrum [Bell, 1970].

A 3D rendering of the TATTOOS shielding and the already existing UCN shielding is shown in Figure 16.12. The TATTOOS beamline will be positioned at a 45 degrees angle with respect to the PK1 beamline. In this manner, the TATTOOS shielding monolith will be docked to the already existing UCN shielding. The advantages of this design are twofold: First, the amount of bending magnets needed for steering the beam will be reduced compared to a concept with a 90° bend, which can only be realized by two 45° conventional magnets, impossible due to space limitations. Second, the high-energy component of the neutron flux, which is strongly forward peaked, will be directed towards a large volume of the already existing UCN shielding. In this manner, the amount of additional shielding needed for suppressing the high-energy cascade neutrons will be reduced.

The area behind the shielding in the upper corner of Figure 16.12 will not be accessible during irradiation but could serve

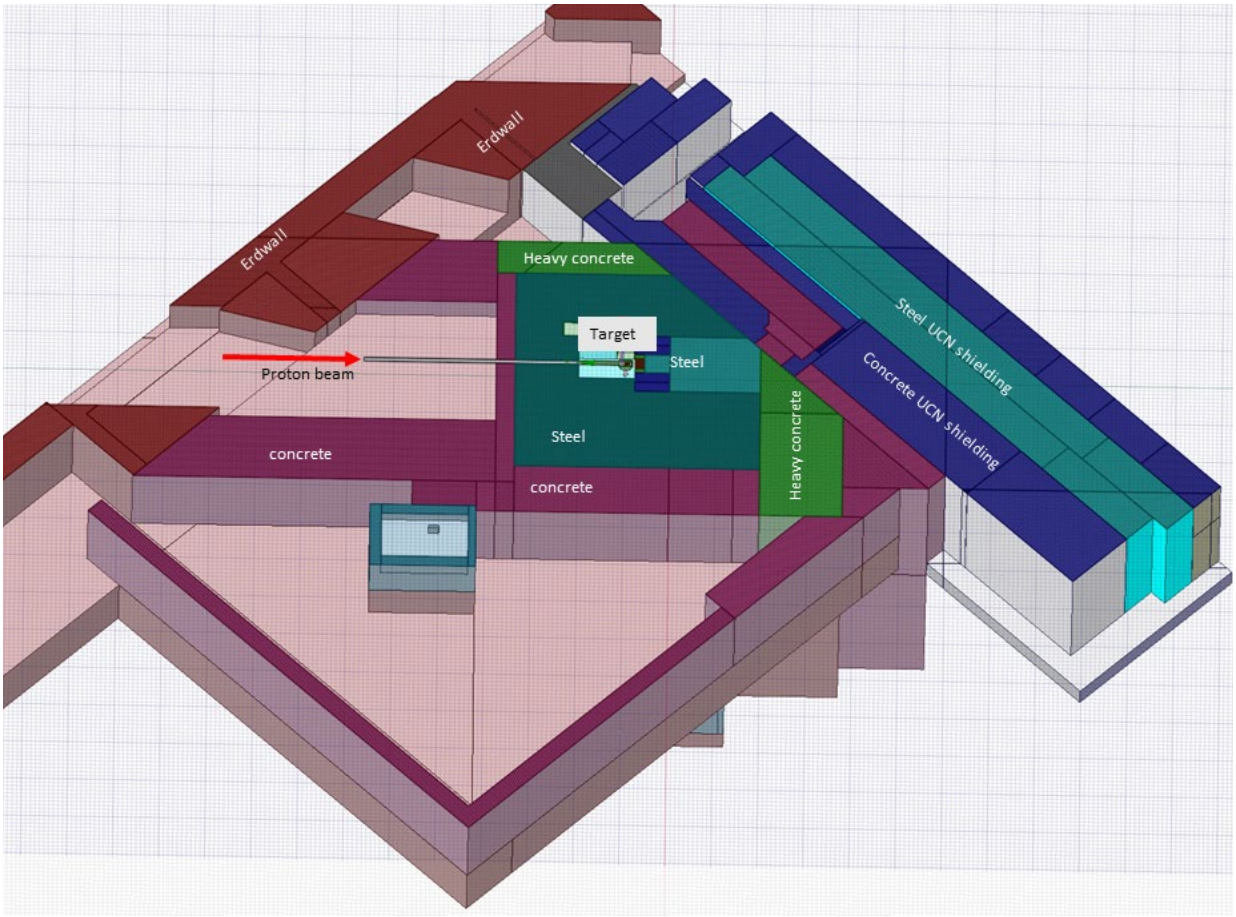

Figure 16.12: Overview of the TATTOOS target shielding and the adjacent, already existing, UCN shielding. The background mesh has a dimension of 1×1 metres.

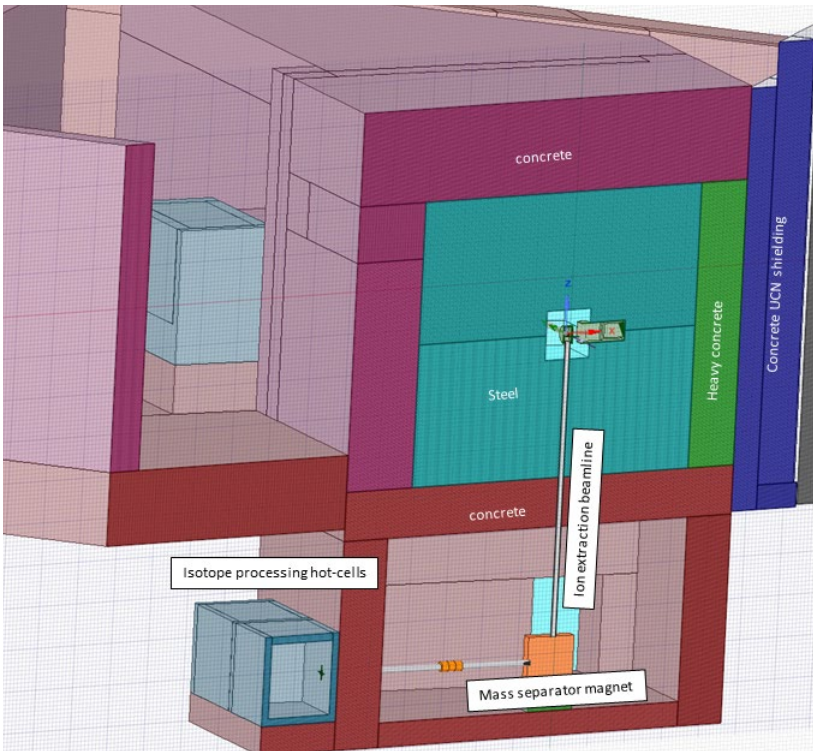

Figure 16.13: Vertical cross section of the TATTOOS shielding showing the ion extraction beamline and the shielded cells located at the subterranean level below the target shielding monolith. The background mesh has a dimension of 1×1 metres.

as emergency exit from the areal of the UCN target station on the right side of the TATTOOS target block in Figure 16.12. In this case a PSYS-door at the entrance through the UCN shielding would prevent people to enter the area during irradiation. In case of an emergency, in which case the door would be opened, an interlock would inhibit beam on the TATTOOS target. The immediate gamma dose rate permits the passage of personnel. A stairway to the basement would be needed to get the people out of the area. Alternatively, there could be stairways to cross over the shielding block. To save space, the ion extraction beamline, the excitation laser, and the corresponding hot cells are located in the basement 7 m under ground level. A 3D rendering of this level is shown in Figure 16.13.

The prompt dose rates computed with MCNP6.2 ENDFB-VIII data are shown in Figure 16.14 to Figure 16.17. As can be seen deduced from these plots, the total gamma + neutron prompt dose rate is less than 5 µSv/h for all areas with personnel access.

In the above plot the prompt dose rates are shown. The remnant dose rate at the surface of the shielding was calculated to be less than 0.1 µSv/h. Therefore, this contribution is not shown here. According to Figure 16.14 the dose rate in the triangle space is around 1 mSv/h already. This area could be used for the water supply for target and beam dump. Shown in Figure 16.18 is the prompt neutron and in Figure 16.19 the prompt gamma dose rate on the subterranean level of the TATTOOS facility. A significant neutron flux leaks into

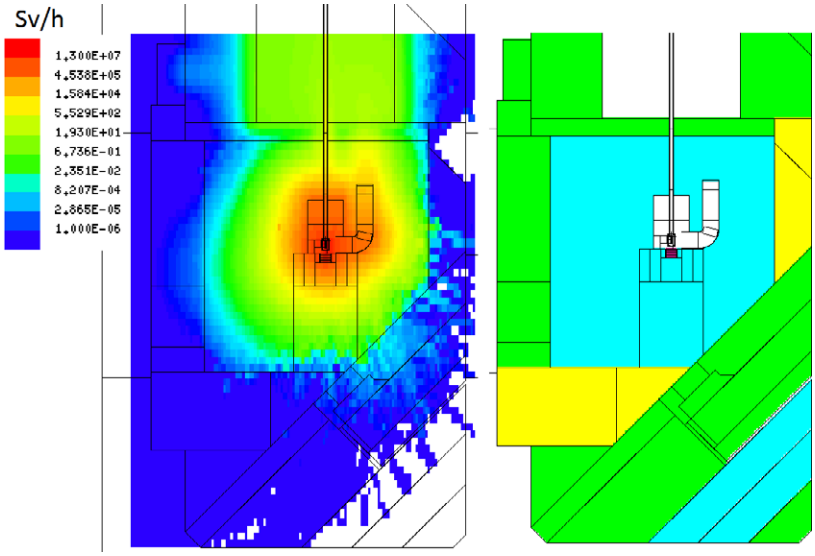

Figure 16.14: Prompt neutron dose rate top view. The uniform blue color corresponds to maximal dose of 1 µSv/h. Shown on the right hand side is the corresponding geometry. Assumed is a proton beam of 590 MeV at 100 µA intensity impinging on the target.

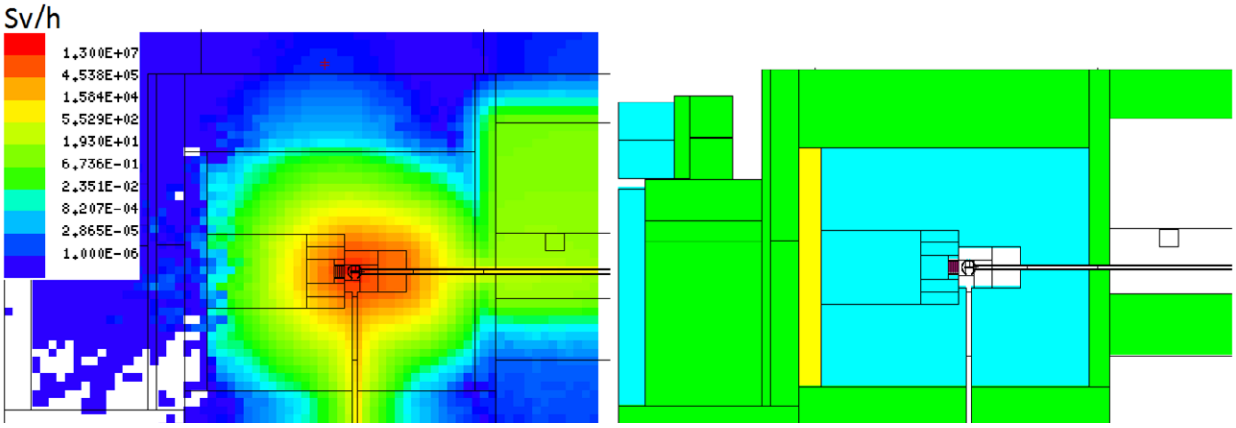

Figure 16.15: Prompt neutron dose side view. The uniform blue colour corresponds to maximal dose of 1 µSv/h. Shown on the right hand side is the corresponding geometry. Assumed is a proton beam of 590 MeV at 100 µA intensity impinging on the target.

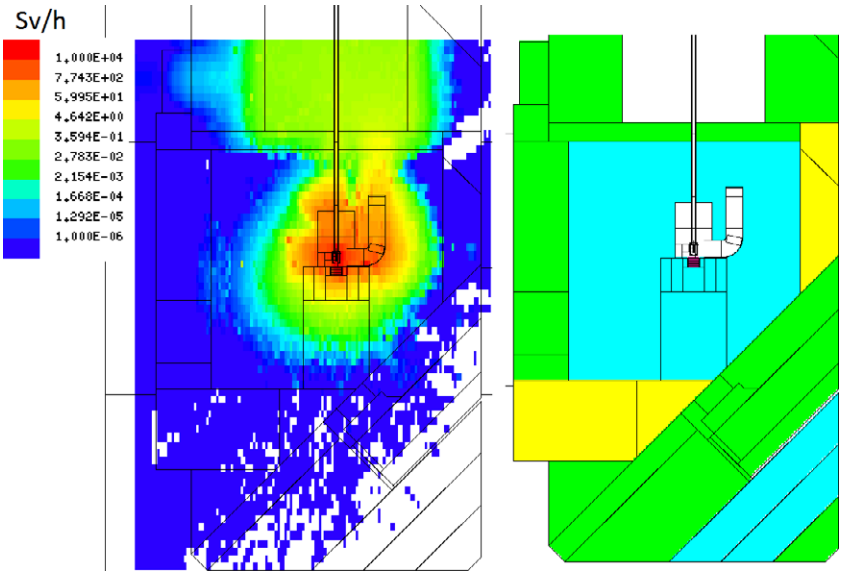

Figure 16.16: Prompt gamma dose rate top view. The uniform blue colour corresponds to maximal dose of 1 µSv/h. Shown on the left hand side is the corresponding geometry. Assumed is a proton beam of 590 MeV at 100 µA intensity impinging on the target.

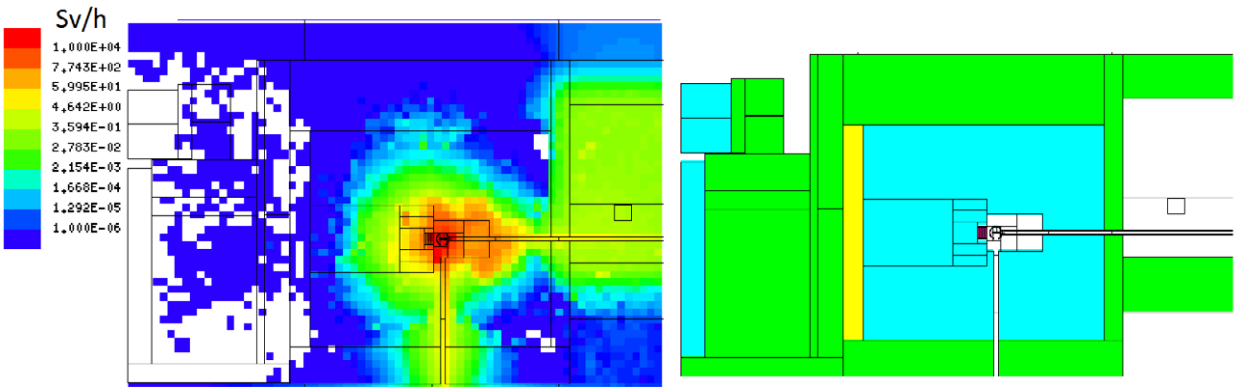

Figure 16.17: Prompt gamma dose rate top view. The uniform blue colour corresponds to maximal dose of 1 µSv/h. Shown on the left hand side is the corresponding geometry. Assumed is a proton beam of 590 MeV at 100 µA intensity impinging on the target.

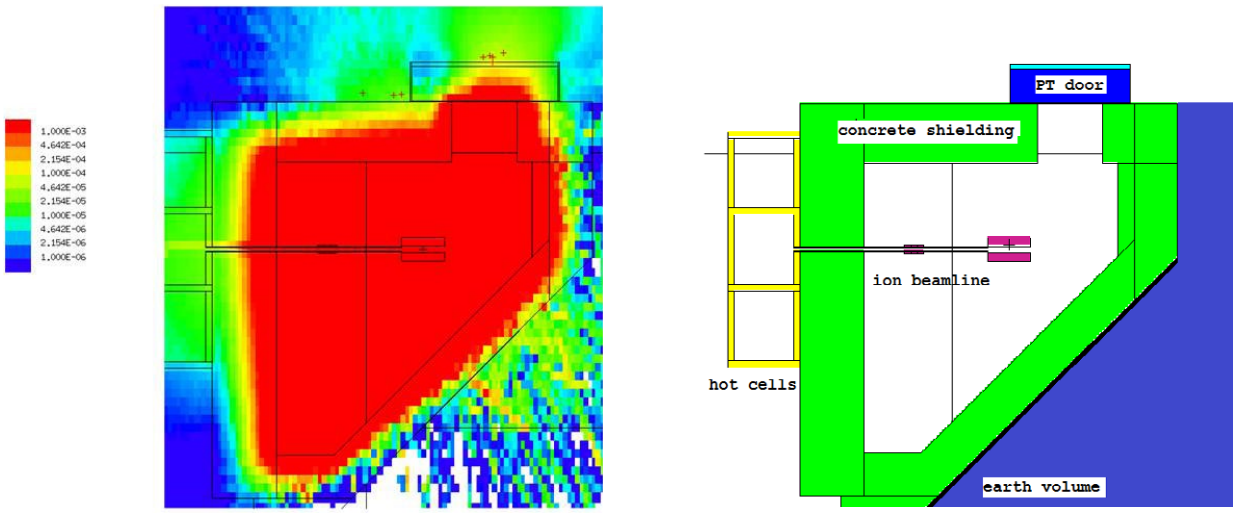

Figure 16.18: Prompt neutron dose rate on the subterranean level of the TATTOOS. Assumed is a proton beam of 590 MeV at 100 µA intensity impinging on the target.

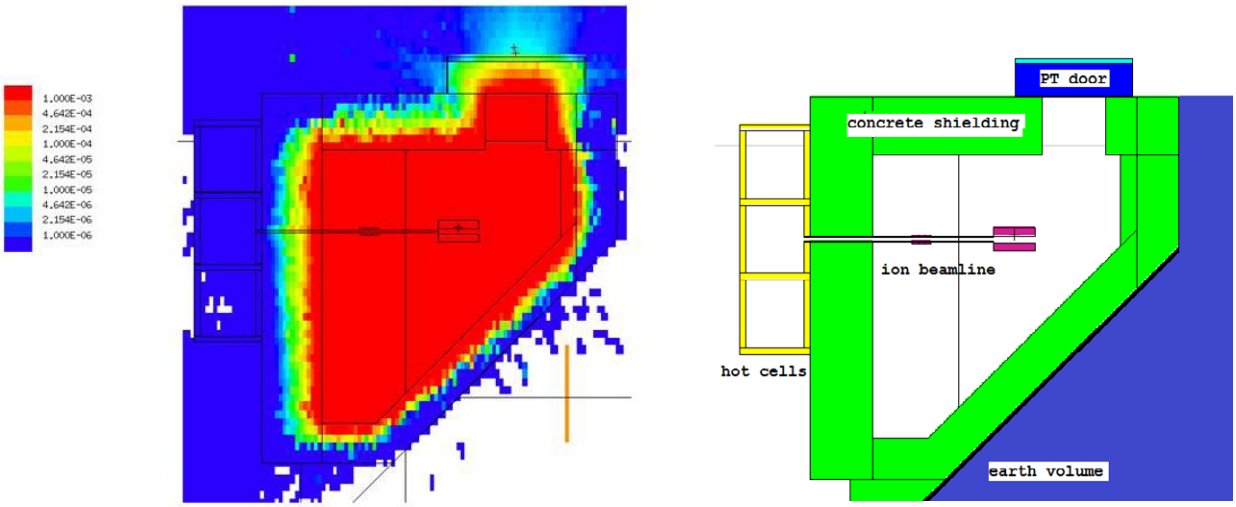

Figure 16.19: Prompt gamma dose rate on the subterranean level of the TATTOOS. Assumed is a proton beam of 590 MeV at 100 µA intensity impinging on the target.

that region via the ion extraction beamline, which is directly connected to the irradiation target. From the above plots it becomes apparent, that the polyethylene shielding door is not sufficient to suppress the both the dose rate. The maximal total gamma + neutron prompt rate in that region amounts to 50 µSv/h. This issue is to be addressed later by either installing local shielding or increasing the thickness of the door, which in the current design is chosen to be 80 cm. In addition, the door has a 3 cm thick steel case and an 8 cm thick steel front panel to serve both as a support structure and as a gamma shield. It should be noted, that the area in the vicinity of the bunker door is not intended as permanent working place and will serve as storage. In addition, it is to be declared restricted personnel access area during irradiation.

It should be noted, that due to the low dose rate of 1 µSv/h penetrating into the surrounding earth volume, activation of the earth can be excluded.

An optimization of the shielding for saving space and cost will be performed in a later stage taking into account the complete installations of all components inside the shielding block.

16.3 Layout of the Target

The principal design of the target was introduced and subsequently developed in the pioneering work performed at CERN ISOLDE [Kjelberg, 1970; Andrighetto, 2007; Noah, 2012]. For the purpose of upscaling the power on the target by a factor of 50 in IMPACT the required design parameters had to be elaborated which are important for the irradiation scheme, beam energy deposition, radiative heat emission and the achieved maximum temperatures in the target. Particularly of interest is the temperature of the target, which needs to be well below the melting temperatures of Ta (3017 °C) and UCx (2300-2500 °C), but high enough (›2400 °C for Ta, and ›2000 °C for UCx) to achieve the experimentally proven reasonable release efficiencies of radionuclides from the target materials.

16.3.1 Beam Energy Loss and Power Deposition

To access the thermal behavior of the target, first the power deposition is calculated. The target setup consists of a tantalum cylinder, which contains a stack of round tantalum disks divided by ring-shaped spacers yielding a target thickness-equivalent to 10 cm solid tantalum metal. The aim of having this amount of target material in the beam is related to the energy loss of tantalum for 590 MeV protons, since below 300 MeV only unwanted by-products would be

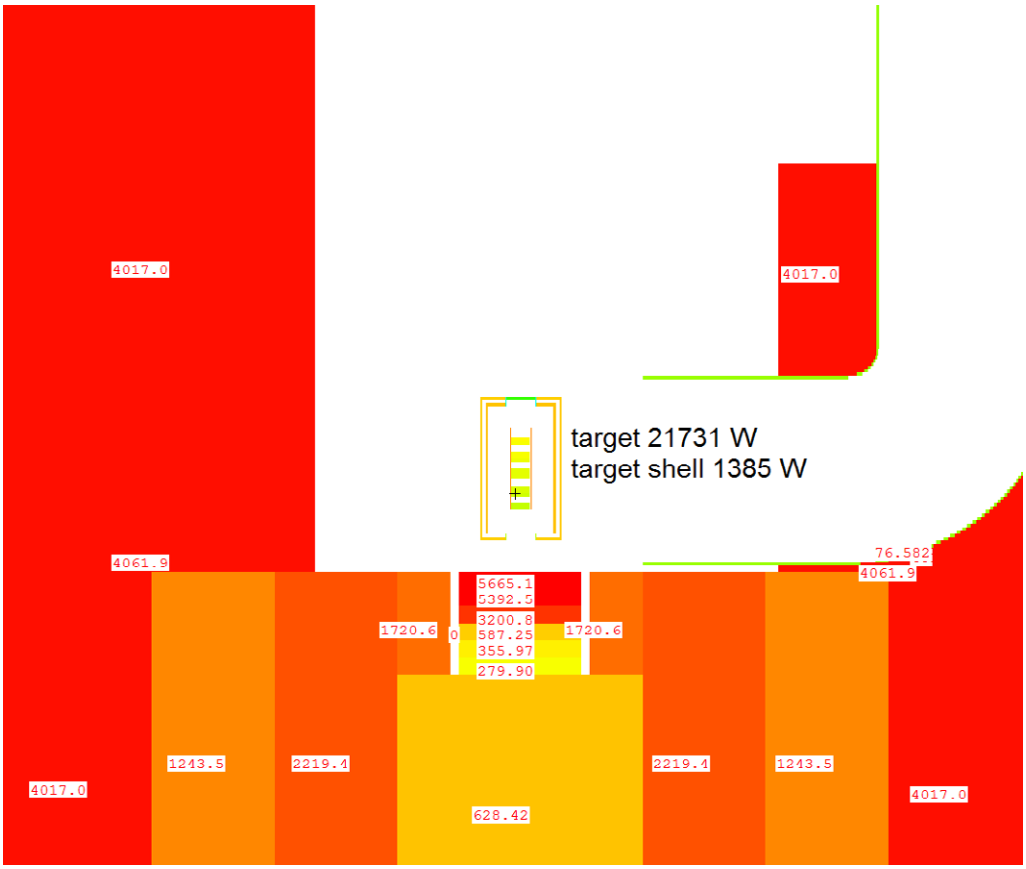

Figure 16.20: Energy deposition in [W] by both the initial proton beam and the subsequently produced secondary particles for the Ta-disc target case. Shown are the values for the beam dump and all the surrounding structures. Repeating numbers are used to denote different regions of a single extended object (also apparent from the colour coding).

produced and considerably more heat deposition and damage would occur. Thus, 10 cm integral tantalum target thickness, i.e. 160 g/cm^2, was chosen which degrades the proton energy from initially about 590 MeV to 300 MeV. For UCx the density is 25 % lower, which leads to an optimum effective target material length of 15 cm.

As shown in Figure 16.20 the main share of the power is deposited on the target and on the beam dump, the object directly behind the target. The beamdump is a 25 cm long copper cylinder with a radius of 15 cm. In the case of tantalum, from a total of maximum 59 kW about 15.5 kW is deposited on the beam dump and about 21 kW on the target. The rest of the power is mainly distributed by wide-angle inelastically scattered protons as well as fast neutrons and gamma rays in the bulk of the surrounding steel shielding. In the vacuum chamber around the target less than 1 kW is deposited. The power deposition on a solid 10 cm long tantalum cylinder having identical radius was also computed. The power deposition in this case was 26 kW. This can be attributed to the particle leakage being hindered by the solid cylinder.

Due to the degraded proton energy after passing the target, the main portion of the energy deposited on the beam dump is concentrated in the first half, facing the target.

Shown in Figure 16.21 is the energy deposition distribution for the UCx target case. Similarly, the main share of the power

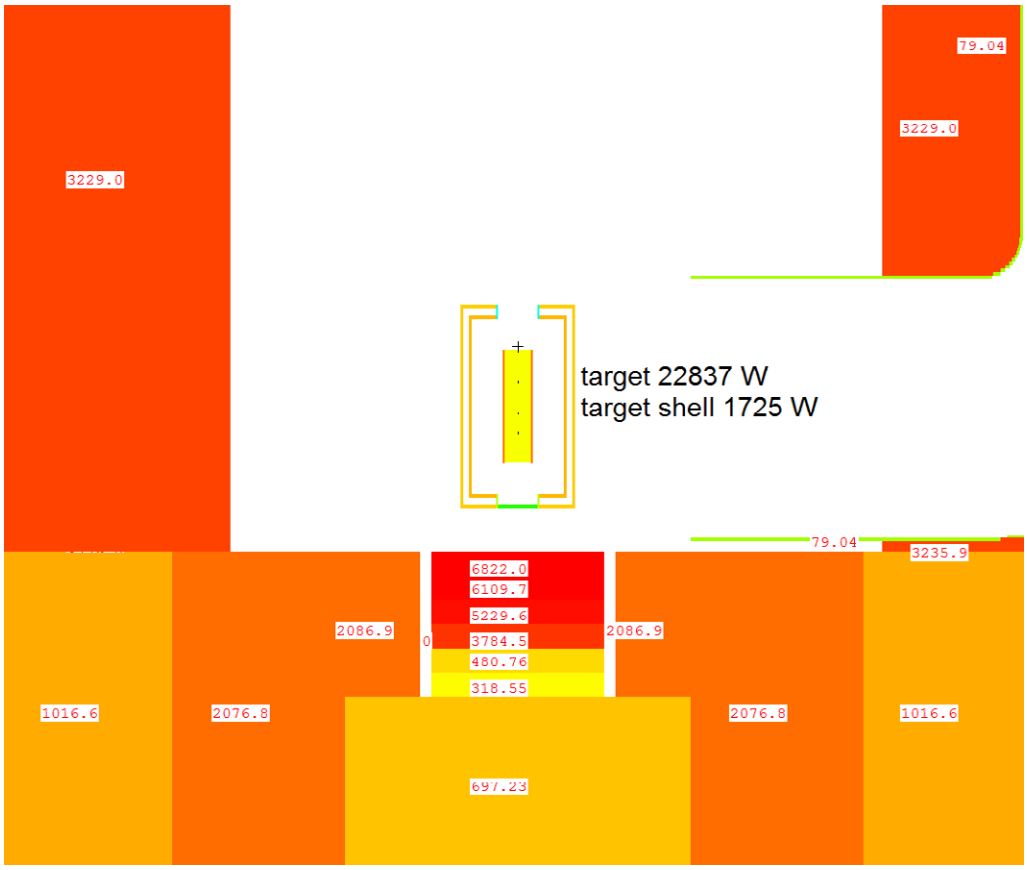

Figure 16.21: Energy deposition in [W] by both the initial proton beam and the subsequently produced secondary particles for the UCx disc target case. Shown are the values for the beam dump and all the surrounding structures. Repeating numbers are used to denote different regions of a single extended object (also apparent from the colour coding).

is deposited on the target and on the beam dump, the object located immediately behind the target. From a total of 59 kW about 22.7 kW is deposited on the beam dump and about 21.7 W on the target. The energy deposition is less compared to a monolithic Ta target (26 kW) due to multiple scattering. Due to the lower density of UCx, more particles are transmitted through the target and subsequently collide with the beam dump, increasing the local power deposition. In addition, the fast fission of U-238 increases further the energy generated in the volume of the UCx target.

Shown in Figure 16.22 is a 2D plot of the energy deposition in the Ta and the UCx targets as a function of the target length. The proton beam's point of entry is on the left. Both curves show typical 'thick target' energy deposition profiles observed for large amounts of material passed by the beam [Filges, 2009] [Barashenkov, 1972]. At 590 MeV the inelastic scattering length is energy independent and the protons loose the main part of their initial energy in inelastic nuclear cascade reactions before the stopping range is reached. Therefore, an initial increase of the energy deposition due to high-energy inelastic reactions is followed by a particle multiplicity decrease as the particles born in the inelastic reactions are less energetic and, in addition, lose their energy not in the target but in the surrounding. From this point further even a greater fraction of the protons and other secondary particles start to dissipate their energy as ionization losses. The majority of the neutrons produced during the spallation/evaporation process leave the target and are stopped in the surrounding shielding. The tantalum target case exhibits a sharper peak, since the inelastic scattering length is inversely proportional to the target density. Because both targets consist of individual 1 mm thick discs separated by a pitch of 1 mm, particle leakage plays an additional role in forming the power deposition profile. Due to a smart choice of target-disc thicknesses and distances, the energy distribution could be further smoothened.

16.3.2 Thermal Design Considerations

For the dimensioning of the target, a 1D model for the heat distribution has been created according to the geometry in Figure 16.23. With this model, the target temperature could be estimated as a first fast approximation for varying dimensions of the components. Further, it serves as general check for the ANSYS simulations. Except for the vacuum chamber cooled by water pipes (Figure 16.39), both made from stainless steel, all parts are fabricated from tantalum. As structure of lowest complexity, the tantalum target cylinder is surrounded by a tantalum tube of 2 mm wall thickness.

Figure 16.24 shows a simplified longitudinal cut through the target model of Figure 16.23. The thermal and mass fluxes flowing in and out of the target are plotted in the scheme as vectors. The thermal fluxes mainly consist of conduction and radiation. In addition, there are two heat sources, one caused by the proton beam, the other is a resistant heater

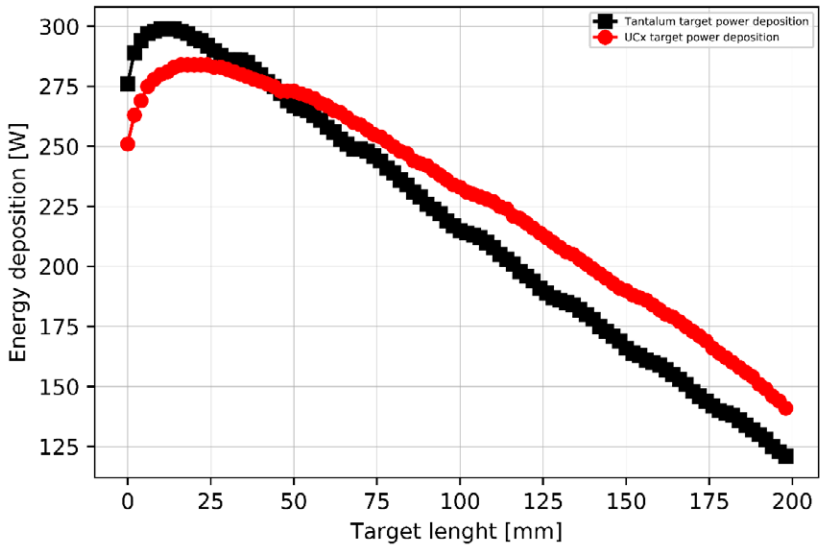

Figure 16.22: The energy deposition in the Ta and the UCx targets as the function of the target length. Each point on the plot correspond to the energy deposition in a single 1 mm thick pellet.

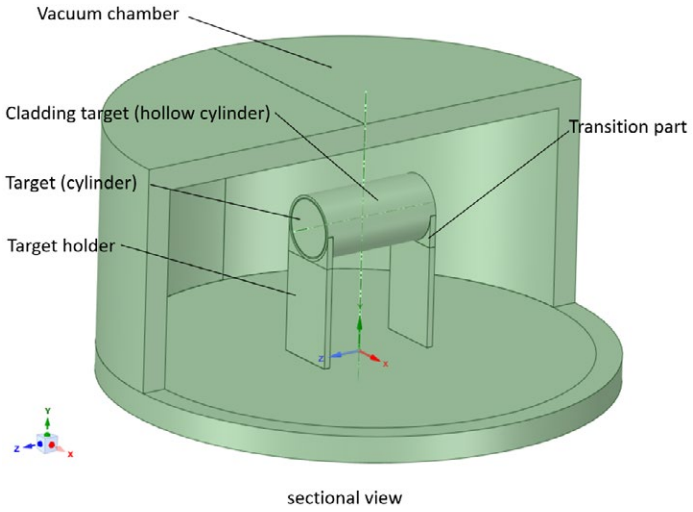

Figure 16.23: Simplified 3D-CAD-Modell of the tantalum target and its vacuum chamber. It consists of a solid tantalum cylinder, surrounded by a thin tantalum foil (hollow cylinder), the interface as well as the support made of tantalum and the vacuum chamber from stainless steel having roughly 300 mm inner diameter and 150 mm height.

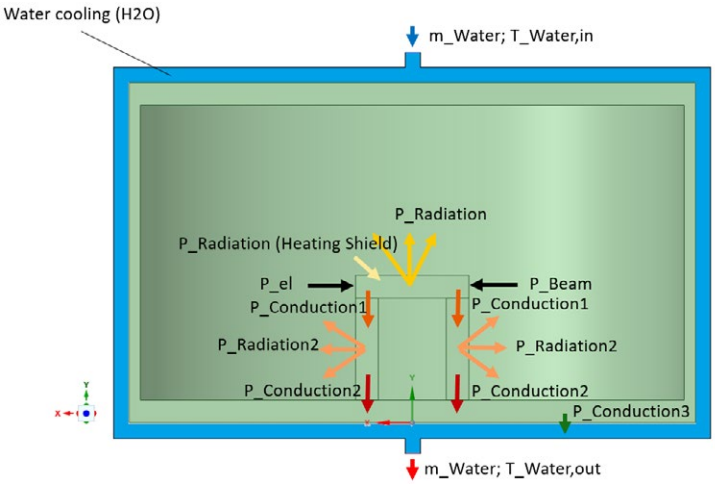

Figure 16.24: Schematic side view of the CAD model with the input and output powers and mass flows.

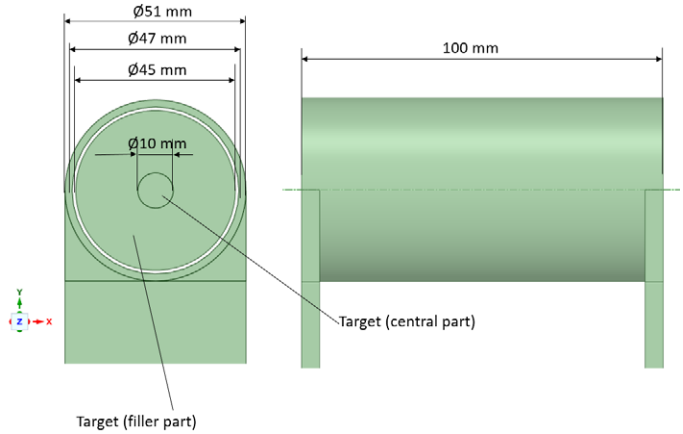

by electrical power for additional heating of the target. The main heat sink is the water-cooled steel chamber.
The following basic equation is used to balance the powers, which are flowing into and out of a component, P_{in} and P_{out}. Their difference is equal to the change of the thermal energy E_{th} with time. This equation is applied separately to each component shown in Figure 16.23:

$$P_{in} - P_{out} = \frac{dE_{th}}{dt}$$

In the first consideration, the 10 cm solid tantalum cylinder is balanced. The proton beam with the power P_Beam hits the target. This supplied power is given off in the form of heat. The tantalum target consists of several components according to Figure 16.23. In the model, the tantalum target is divided into a target central and a filler part. Dimensions are given in Figure 16.25. The central part corresponds roughly to the beam diameter, i.e. to the hottest part of the target. The beam power of 26 kW is deposited in central part. The filler part corresponds to the surrounding of the central part. However, both components correspond to one solid tantalum block, making-up the target. The division into central and filling part shall increase the accuracy of the 1D calculation. The surrounding tantalum tube is designed with a small gap towards the tantalum filler part. The power transmission from the tantalum takes place only via thermal radiation. The surrounding tantalum tube can be heated electrically.

Figure 16.25: Dimensions of the tantalum target parts.

16.3.2.1 Target (Central Part)

The needed variables for the power balance of the central part are shown in Figure 16.26.

For the power balance of the target central part, the deposit beam power (P_{Beam}), the radiation power ($P_{rad\text{-}side}$) on the front and back side of the cylinder and the conduction power (P_{cond}) to the enveloping material are taken into account. The difference between the power supplied P_{in} and the power dissipated P_{out} leads to a change in the thermal energy content over time [Scherf, 2007].

$$P_{Beam} - 2 * P_{rad-side0} - P_{cond0} = \frac{dE_{th}}{dt}$$

The change in energy takes place via the specific heat capacity (c_{Ta}), the mass (m_c) and the change in temperature (T_{c1}) of the central part.

$$\frac{dE_{th}}{dt} = c_{Ta} * m_c * \dot{T}_{c0}$$

The radiation power is defined by the emissivity ε, the radiation constant (C_s) of a black body, the area (A_c) and the temperature (T_{c0}).

$$P_{rad-side0} = \varepsilon * C_S * A_c * T_{c0}^4$$

The conduction power (P_{cond}) is determined by the thermal conductivity (λ), the penetrating distance (s), the area (A_c) and temperatures of the tantalum central (T_{c0}) and the tantalum filling (T_{f0}).

$$P_{cond} = \frac{\lambda}{s} * A_c * (T_{c0} - T_{f0})$$

The previous definitions are inserted into the balancing equation, which is then solved for the temperature change of the tantalum target (central part). The temperature is determined with the corresponding model equation in Matlab Simulink [The MathWorks, 2019].

$$\frac{P_{Beam} - 2 * P_{rad-side} - P_{cond0}}{c_{Ta} * m_c} = \dot{T}_{c0}$$

All derived equations of the target components, the vacuum chamber as well as the water itself were implemented in a Matlab Simulink model. With this model it is possible to change geometrical dimensions very fast for an estimate of the necessary dimensions of the tantalum target. This model is a tool to calculate the dimensions for different target material like uranium carbide (UCx). The program is adapted during the development of the target for a more and more accurate calculation. It will be extended to be quickly applied for different target materials for rapid estimations.

The Table 16.3 shows the deposited power in the modelled components. Radiation between the bodies is not listed in the table but it is taken into account in the modelling.

The Table 16.4 shows the calculated temperatures in the different components of the target and the allowed melting temperature. For the central part the beam power is assumed to be 26 kW, which is according to Section 16.3.1 the maximum power deposition summed up over central and filler,

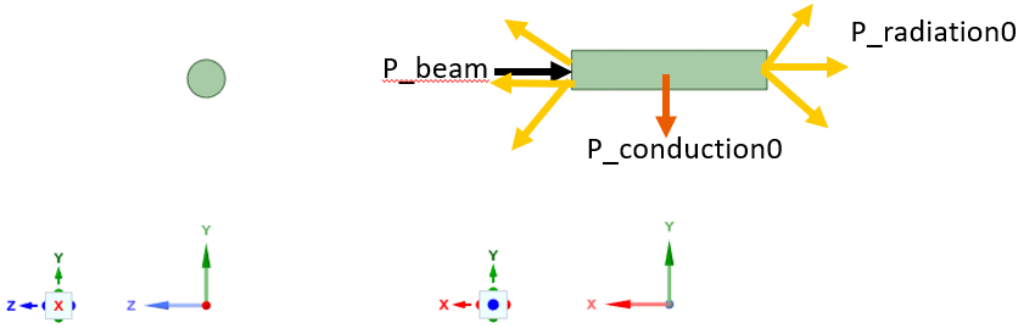

Figure 16.26: Schematic view of the tantalum target with the thermal flows in and out of the target.

Transferred power	Body	Case 2900 °C	Unit	
P_Beam	Targt central part	25	kW	
P_rad0	Target central part	1.138	kW	*
P_cond0	Target central part	23.86	kW	
P_rad0a	Target filler part	24.33	kW	*
P_el	Cladding tube/target	1	kW	
P_rad1	Cladding tube/target	13.59	kW	*
P_cond1	Cladding tube/target	0.612	kW	
P_rad2a	Transistion part	–	kW	Towards per target holder
P_cond2a	Transistion part	0.306	kW	Towards per target holder
P_rad2b	Target holder	0.174	kW	Towards per target holder
P_cond2b	Target holder	0.132	kW	Towards per target holder
P_cond3	Vacuum chamber	26	kW	
P_water	Water	26	kW	

Table 16.3: Deposited Power in the tantalum target and pipe with according to the MCNP calculation.

* Radiation only to the outside in the direction of the vacuum chamber.

so that the temperature for the central is overestimated. With a wider and more flat beam distribution provided by wobbling of the beam, the temperature in the central should be reduced. With the Matlab Simulink calculation a necessary water mass flow rate of 0.311 kg/s is obtained for efficient cooling. Keeping in mind the approximations and uncertainties of the calculation related to heat transfer between phases, a more conservative estimate for a minimum water flow is 1 kg/s.

	Temperature / °C	Unit	Melting Temperature of used material
$T_{Central\ part}$	3547	C	3017°C
$T_{Filler\ part}$	2881	C	3017°C
$T_{Cladding\ target}$	2293	C	3017°C
$T_{Transition\ part}$	927	C	3017°C
$T_{Target\ holder}$	756	C	3017°C
$T_{Vacuum\ chamber}$	45	C	1400°C
T_{Water}	30	°C	
Mass flow rate	0.311	kg/s	

Table 16.4: The temperatures and cooling water mass flow rate calculated using with the developed Matlab Simulink Model.

16.3.2.2 Material Data

For precisely predicting the temperatures and stresses in a component, the temperature-dependent material properties are required. We focus here on the target material tantalum only as all other materials like water, stainless steel etc. are widely used and their properties are taken from the ANSYS Fluent und ANSYS APDL material libraries. In order to be able to determine the temperature distribution of the tantalum target, the temperature-dependent material properties are necessary. In the following the temperature-dependent density, specific heat capacity, the thermal conductivity, the spectral emissivity, and the hemispherical total emissivity are shown. The material properties have been collected from different sources.

Temperature T in K	Density ρ in kg/m³
273.15	16650
300	16660

Table 16.5: Material data of tantalum - Density [MatWeb] [Rasor, 1960]

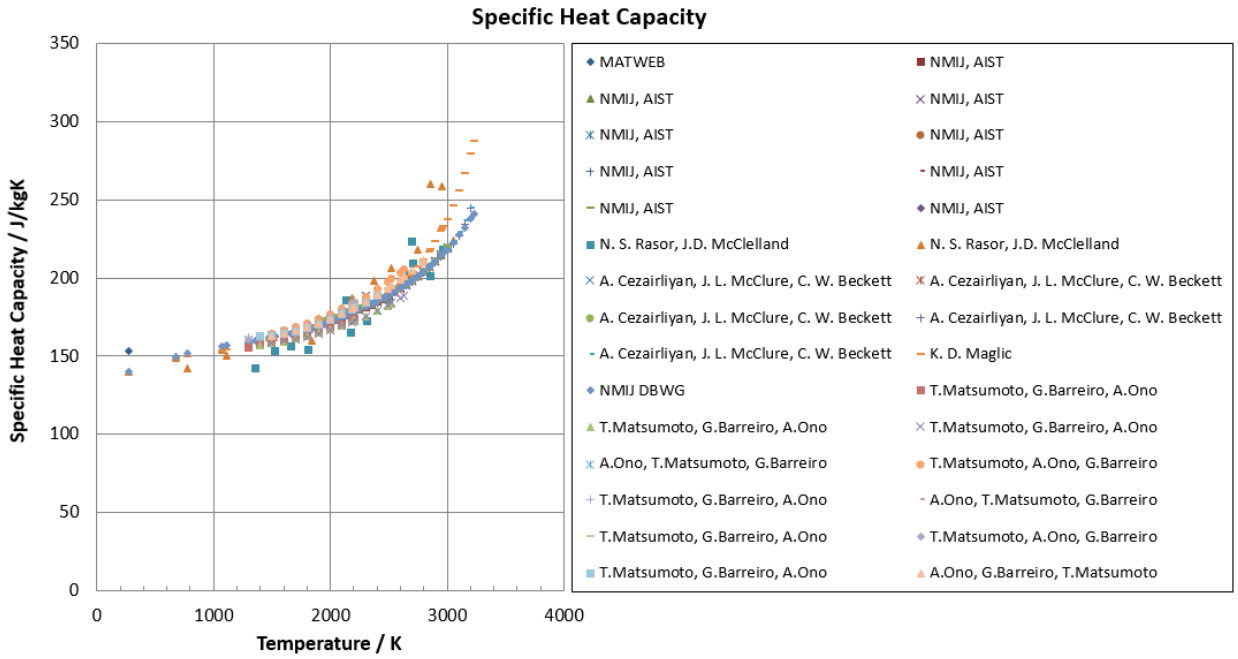

Figure 16.27: Material data of Specific Heat Capacity of tantalum
[MatWeb; NMIJ, AIST; Cezairliyan, 1971; Maglic, 2003; NMIJ, DBWG; Matsumoto, 2000]

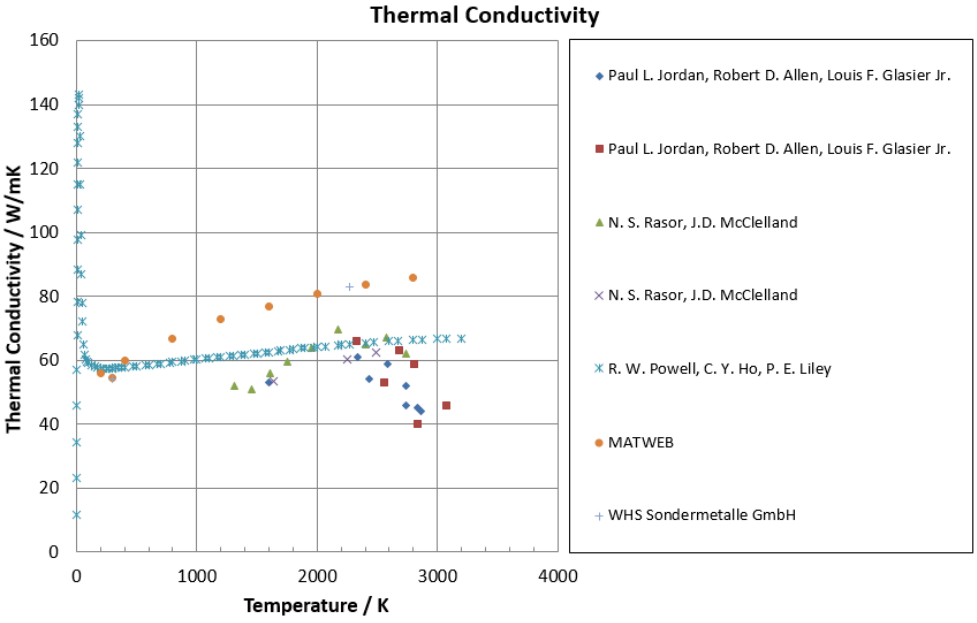

Figure 16.28: Material data of Thermal Conductivity of tantalum
[MatWeb; WHS Sondermetalle GmbH, 2021; Jordan, 1960; Rasor, 1960; Powell, 1972]

For the thermal simulations, the Specific Heat Capacity from [Powell, 1972] and Thermal Conductivity from [MatWeb] and [NMIJ, AIST] were used.

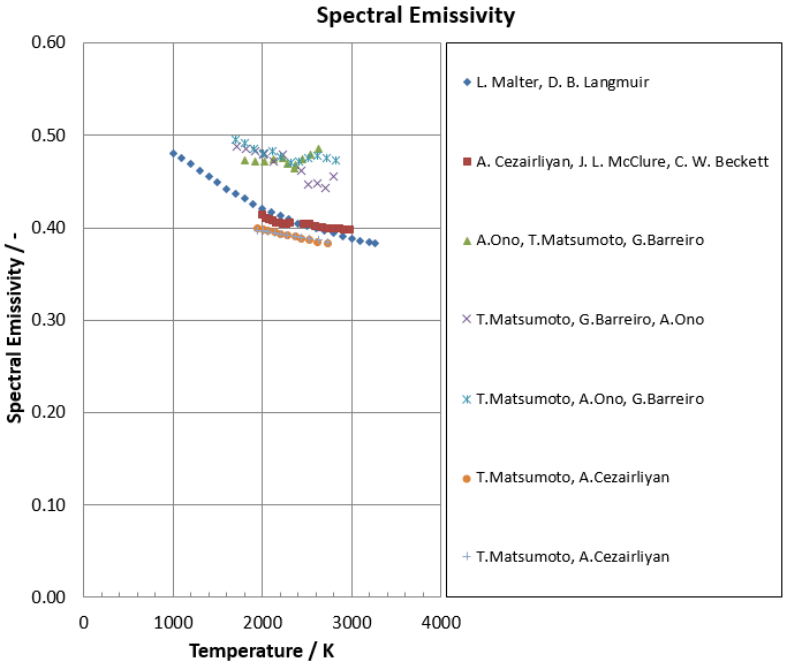

Figure 16.29: Material data of tantalum – Spectral Emissivity
[Malter, 1939; Cezairliyan, 1971; Matsumoto, 2000; Matsumoto, 1997]

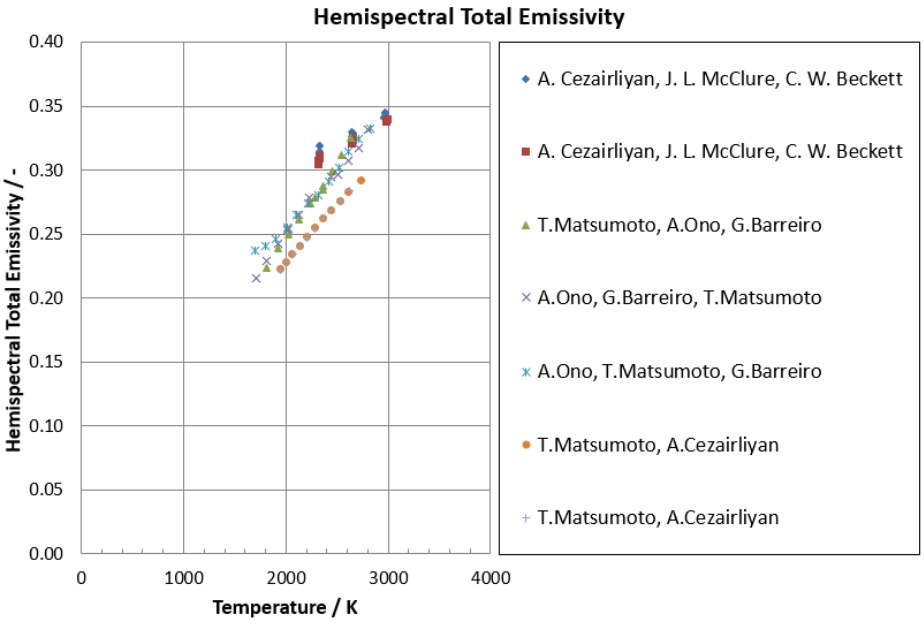

Figure 16.30: Material data of tantalum – Hemispherical Total Emissivity from Emissivity
[Cezairliyan, 1971; Matsumoto, 2000; Matsumoto, 1997]

16.3.3 Thermal Simulation

The simulation for the temperature distribution in the tantalum target was performed with two different solvers, ANSYS Fluent and ANSYS APDL, for comparison. The power deposition was taken from MCNP (see Section 16.3.1) and introduced in a spatially resolved deposition. While heat radiation can be taken into account directly with the APDL Solver, this is not possible with the Fluent Solver. In order to calculate the thermal radiation anyway, it is necessary to define a flow control space around the object. In this case, air is used as the surrounding medium and the material properties of the air were changed accordingly to a vacuum behaviour in order to simulate a vacuum in the chamber. This flow control space was used together with the Discrete Ordinates (DO) radiation model. The emissivity chosen for tantalum is and the same material data for tantalum (see Table 16.5) were used for both models. The inner walls of the vacuum chamber were exposed to 300 K. With the APDL model, the heat radiation from surface-to-surface is also taken into account, while with Fluent this takes place via the flow control space.

The APDL simulation shows slightly overestimated temperatures of 4211 °C, but this is due to the fact that the power deposition in the target is too high (Table 16.6). In the Fluent simulation, the summed-up power deposition had to be corrected to the input value from MCNP as it was drastically underestimated before. The reason for this deviation in the solvers lies in the fact that the resolution of the input data from MCNP has not a high-enough spatial resolution. A comparison of the power deposition is shown in Table 16.6. A comparison with different geometries shows how the target should be changed in order to shift the temperature of the solid body well below the melting temperature of tantalum of around 3017 °C. The specified length of 10 cm resulted in a solid material of about 4100 °C. The most important parameter to reduce the temperature is the thermal

	MCNP	Fluent	APDL
	W	W	W
Cladding target	210.85	210.81	9.12
		0	-201
Target	26331	26322	26659
		-9	+328
Temperature T in °C		4091	4211

Table 16.6: Deposited power in the tantalum target and pipe with the derivation from the MCNP calculation.

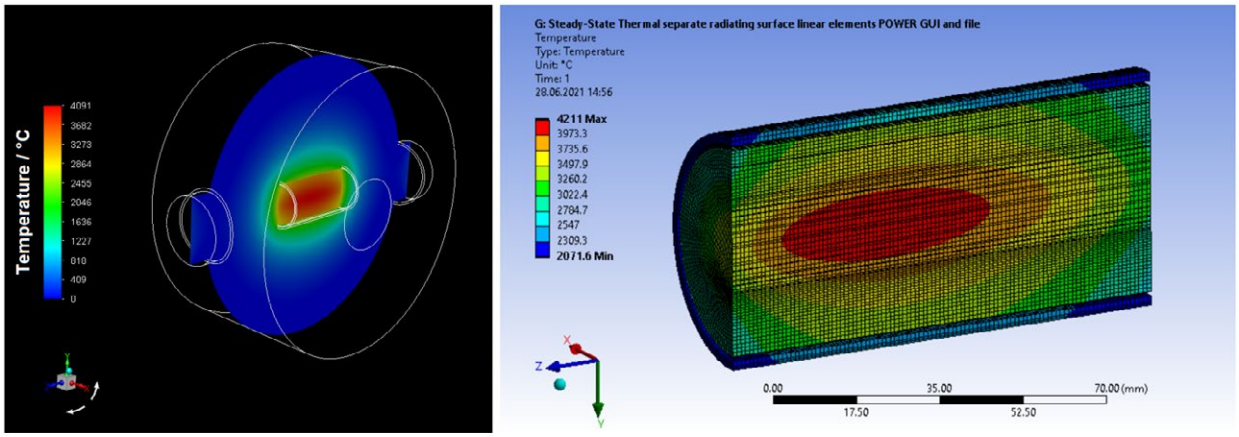

Figure 16.31: Comparison of numerical simulation of the tantalum target with ANSYS Fluent (left) and ANSYS APDL (right).

	Geometry 1	Geometry 2	Geometry 3	Geometry 4
	mm	mm	mm	mm
Thickness of disc	100	1	5	10
Spacer gap	0	1	5	10
Number discs	1	50	10	5

Table 16.7: Dimensions of the discs and spacers for the different target geometries.

radiation, i.e. increasing the radiative emission surface. This can be accomplished by increasing the radius of the cylinder as well as by introducing the tantalum target in the form of discs separated by spacers. For this design study these discs were tested with different thicknesses and spacer gaps between the discs.

Table 16.7 shows the disc thickness of the different geometries and the spacer gap between the discs.

In order to have a better comparison, the four cases have been provided with a uniform temperature scale. Figure 16.32 shows that the geometry 3 and 4 have the temperature distribution with the lowest maximum temperature. It is interesting to note that the maximum temperature is almost identical, i.e. it shows a kind of saturation. Although geometry 2 uses also discs, its temperatures are much higher. This is caused by the gap between the blades, which is too small so that the radiation heats up the adjacent discs again. With geometry 3 and 4 the gap is sufficiently large. In the case of the geometry 3, less energy is deposited in the individual target discs than in comparison to the thicker discs from geometry 4. In order to assess the real performance with 100 µA beam current, the tantalum target needs to be extended to 20 cm length. These calculations assumed a Gaussian beam profil with 9 mm (2 σ) diameter. In order to further lower the temperature, it is foreseen to rotate the beam in front of the target using a wobbler. With this rotation the energy deposition is more evenly distributed over the target.

In Table 16.8 the results from the different cases are collected. The comparison shows the different temperatures and energy depositions in the target. Here it is noted, that in the Geometry 2, 3 and 4 only half of the expected full energy is deposited, since the model was representing only

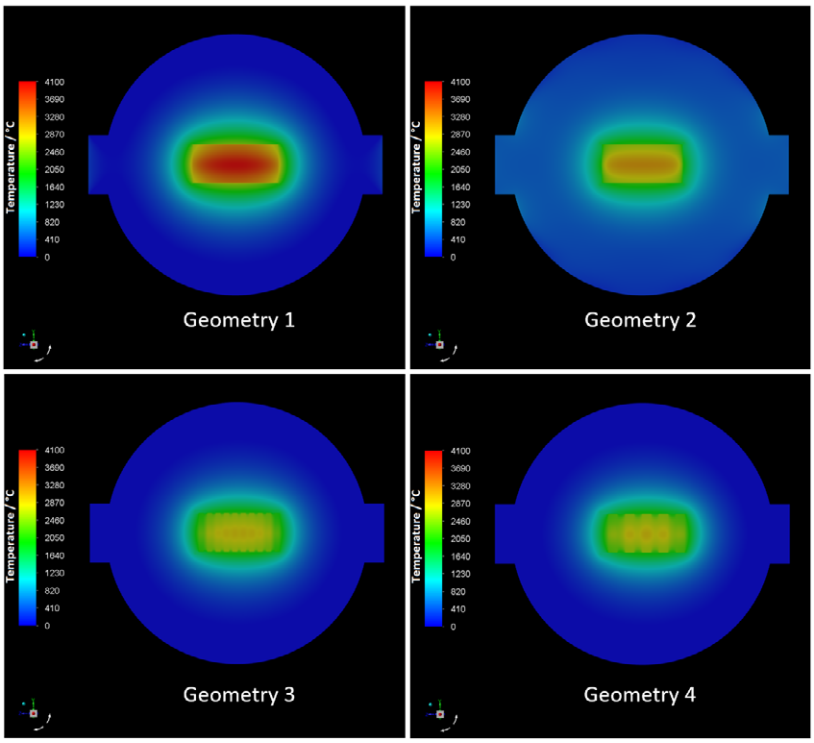

Figure 16.32: Comparison of the temperature distribution for different geometries with different disc thicknesses and spacer gap distances at the inner wall temperature of 300 K.

	MCNP	Fluent	Fluent	Fluent	Fluent
Geometry	Original	Geometry 1	Geometry 2	Geometry 3	Geometry 4
	W	W	W	W	W
Cladding target	210.85	210.81	183.28	183.28	183.28
		0	-28	-28	-28
Target	26331	26322	11749	11752	11748
		-9	-14582	-14578	-14583
Temperature T in °C		4091	3248	2978	2998

Table 16.8: Deposited power in the tantalum target and cladding target with the derivation from the MCNP calculation.

first half of the intended target where the highest power deposition occurs. With the configurations 2, 3 and 4 listed in Table 16.7 less than half of the mass of Geometry 1 is used, since in the disc target less energy is deposited (see Section 16.3.1). This explain the reduced power deposition from Table 16.8.

Figure 16.33 shows a more detailed simulation of the tantalum target with a 20 cm long cladding target and 1 mm discs and spacers. For this simulation the vacuum chamber with the beam entrance and exit windows are included. And the outer wall temperature is set to 300 K. The energy deposition is implemented with a wobbled beam with the energy deposition from Table 16.9. The simulation shows also that the tantalum target with the new calculated beam profile is heated up to around 3450 °C.

A comparison of the Case 1 (10 cm long target with a non-wobbled beam) and Case 2 (20 cm long target with 1 mm discs and spacer with a wobbled beam) are shown in Figure 16.34. It is clearly seen that with the new design and the wobbled beam it is possible to reduce the temperature.

	MCNP	Fluent
	W	W
Cladding target	1385.6	1385.6
Target	21731.63	21731.63
Beam entrance window	21.484	21.484
Beam exit window	14.331	14.331
Temperature T in °C		4154

Table 16.9: Deposited power of a wobbled beam in the tantalum target, the cladding target, and the beam windows with the derivation from the MCNP calculation.

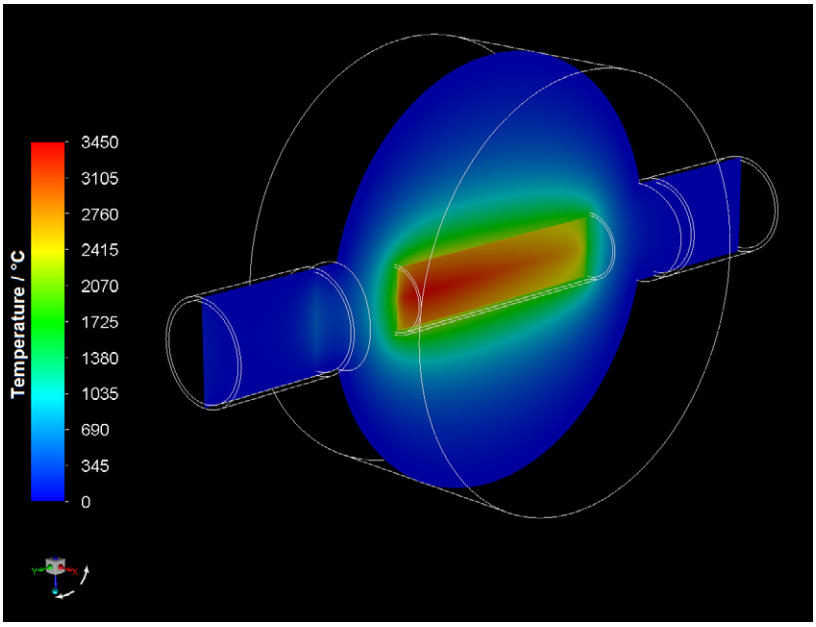

Figure 16.33: Temperature distribution for a wobbled beam for a 20 cm cladding target with 1 mm discs and spacers. The chamber walls are assumed to behave as ideal heat sink at 300 K.

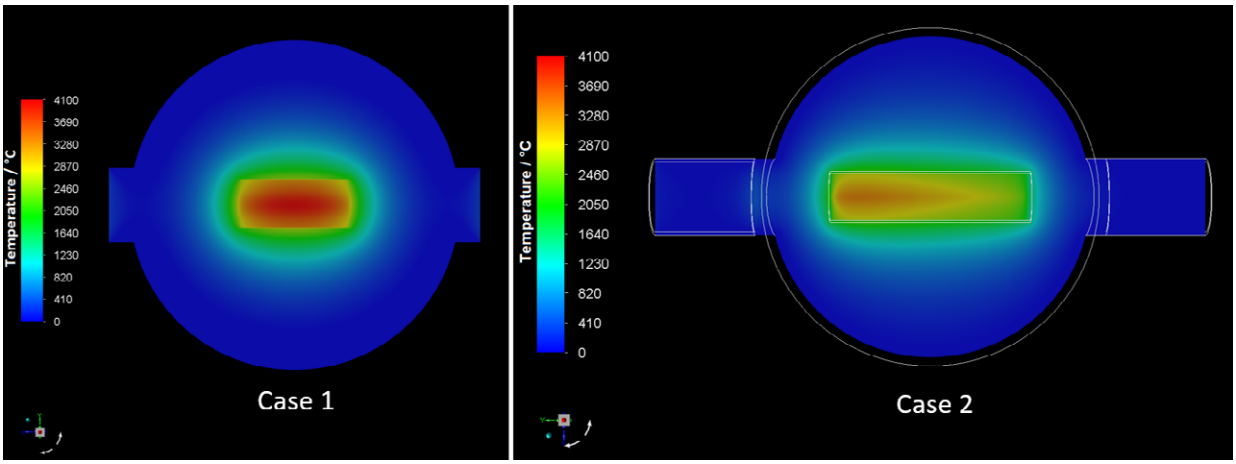

Figure 16.34: Comparison of different target design and beam profile: Case 1 (10 cm long target with a non-wobbled beam with around 26 kW) and Case 2 (20 cm long target with 1 mm discs and spacer with a wobbled beam with around 23 kW).

16.3.4 Electrical Heating

In case of beam intensity loss, the target heating has to be supported by electric Joule heating. The thermal emission of the target was assessed previously in Section 16.3.2.2. At 2600 K the thermal loss is about 26 kW which has to be compensated by the electrical resistance heating. Therefore, the two target connectors at both ends of the target cylinder are connected electrically to a water-cooled copper contact. Power equilibration is obtained at (DC) 5.55 V and 5875A. Using DC current is advised due to considerable impedance losses when using AC current. Due to space concerns, water-cooled line connections will be foreseen to provide the electrical power to the remote target inside of the heavy shielding. If copper conductors with a total cross section of 250 mm^2 are used a conduction loss of about 8 kW has to be removed by water cooling. This inherent resistance leads to an additional voltage drop at the target of 1.2 V that has to be considered. Thus a power supply grade of 0-6000A and 0-6V will be needed to provide the required heat for efficient release of the radioisotopes from the target in case of beam loss. A dedicated DC power supply will be built. The water-cooling can be connected to the same cooling loop of the target chamber. Since the targets electrical heating will inevitably be also directly connected to the high voltage potential on the target needed for the ion extraction (see Section 1.1.1.2), special care will be taken during the dedicated power supply design to warrant the proper insulation. The same electrical heating system is needed for the off-line-source, which is used for target testing, stable isotope enrichment and further development of the RILIS technology of dedicated ionizations.

Electrical conductivity and thermal emissivity data from [CRC Handbook, 2021] where used for these estimations.

16.3.5 High Voltage Supply

The extraction of the ions from the target outlet tube requires a stabilized high voltage of minimum +30 kV (10 mA) on the target side. The extraction lens is thus, connected to ground. Therefore, the target block has to be electrically insulated from the surrounding vacuum chamber and the ion beam line. Note here, the electrical Joule heating system will have to remain at the high potential too. An isolating AC transformer of 400V 150A as input for the DC power supply will be used for the high power heating to superimpose the high DC voltage safely with the secondary 6V/6000A. Hence, the high voltage potential can be provided over the heating line, thus, but putting higher isolation constraints to these connecting power lines. These power supplies will be located in an HV-rated cage with HV-interlock door to prevent access while in HV operation, including a ground stick to remove

the potential before service work in this area. Regulators connected via fiber optical connectors providing safe HV-insulation will operate the power supplies.

16.3.6 Target Exchange & Radiation Safety

The target exchange is naturally a major recurring procedure during the operation of TATTOOS. The target area will not be accessible in reasonable time scales after shut down of the beam, due to heavy activation of the surroundings of target and beam dump. Therefore, a remote target exchange system is suggested based on a rail track (see Figure 16.35, left) with a moving vehicle, where the primary target chamber is mounted to. The vehicle will be driven remotely using a chain track. Ideally, it can be retracted, when the target is in its final position. Thus, the target chamber can be entirely transported into the target exchange box after irradiation. A waiting time of minimum 12 h is needed for the target to cool down thermally. Also the main radiation dose from the short-lived activities will have decayed after this time period (see Chapter 18). The target can be moved after the vacuum surrounding the target and the primary target chamber is broken. Inside the target exchange box the irradiated target will be dismounted and a tested new target will be installed using manipulators. Therefore, special care has to be taken, when designing the mounting clutches to be operated using manipulators connecting the target to the electrical feed-through contacts for the target heating (see Figure 16.35, right). The inflatable metal seal on the bottom of the chamber (towards the ion beam line) as well as the graphite beam entrance and exit windows can be always checked during the target exchange, and, if needed, they can be replaced. Subsequently, the entire target chamber is transported back by the vehicle and placed exactly into its original position. Since the positioning of the target outlet with respect to the extraction lens in the ion beam line (see Figure 16.35, right) is crucial, this procedure needs the development of a robust and very sensitive mechanical positioning system.

The dose level of the target if irradiated for four weeks at no release is calculated with a 10 h cooling time as 6 µSv/h and 4.3 µSv/h for the Ta and UCx targets, respectively assuming a 300 mm Pb equivalent shielding which implies a 750 mm lead glass thickness (see Figure 16.36) [Magill, 2021]. Thus, the shielded cell for target exchange must be designed accordingly.

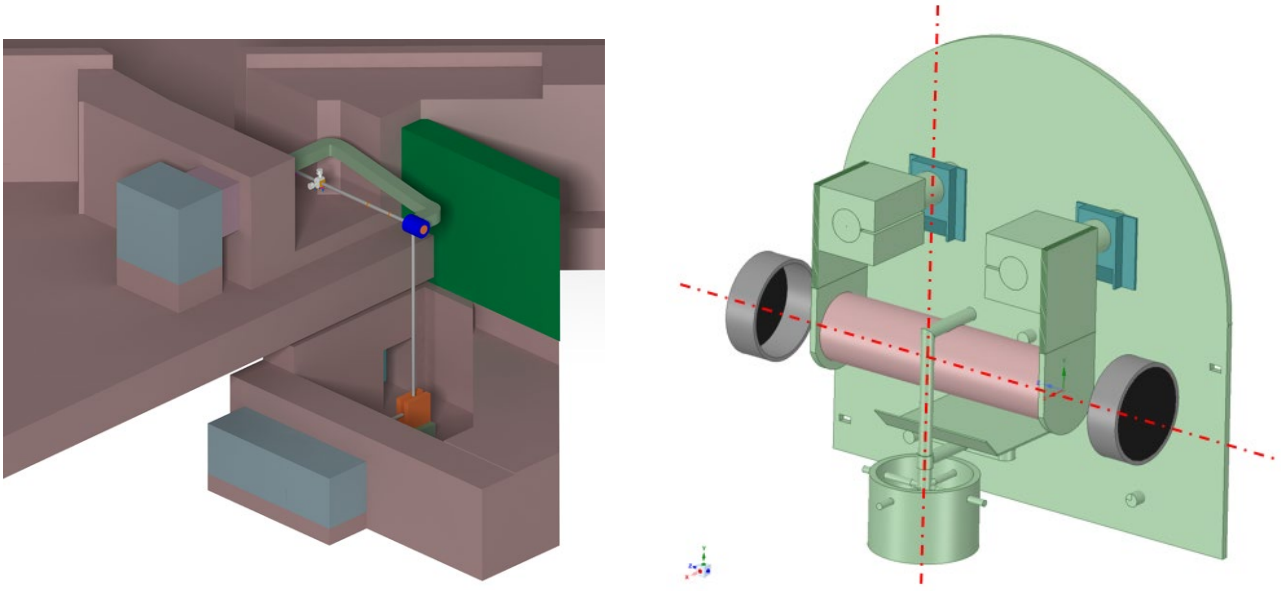

Figure 16.35: The cut out of the principal CAD design showing the rail track form the target into the target exchange cell. The two-axes position of the target chamber towards the proton beam line and towards the inlet of the ion beam line (right side, red line) has to be fixed, exactly.

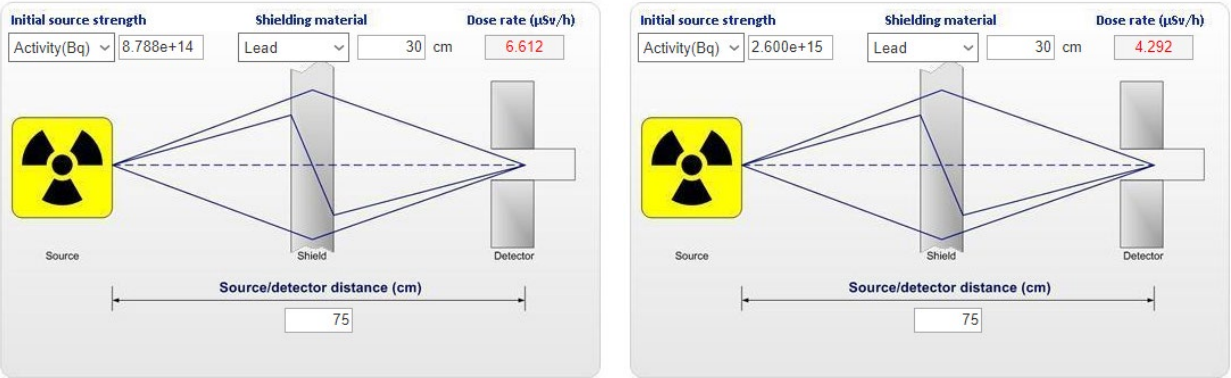

Figure 16.36: Result of the shielding calculations for the Ta and UCx targets after 4 weeks irradiation and 10 h cooling time yield with the suggested shielded cell construction dose rates below 10 µSv/h in front of the cells.

16.3.6.1 Shielded Target Exchange Cell

Two connected shielded cells, containing manipulators and different ports, will be installed in the alpha zone area for the installation of the ISOL target and the storage of other targets (on the ground floor of the building complex). This cell complex is named in the following *Target exchange cell* and consists of two parts (SC1 andf SC2) (see Figure 16.37). The shielded cell (SC1) containing the target, will have direct connection to the beam line, while the other cell (SC2) will have space for target storage (paternoster) to let irradiated targets decay before disposal.

The target exchange cell will be designed and built by an external manufacturer, who specialize in the construction of custom-designed cells. The service will include FAT (Factory Acceptance Test), SAT (Site Acceptance Test) as well as instruction and training of operating personnel.

The proposed arrangement of the two cells has the narrow side of the SC2 abut the rear wall of SC1 (External dimensions of the line: greatest width: approx. 2350 mm × greatest depth 3300 mm). The minimum height of the cell complex is 3400 mm. The exact dimensions are to be determined in the design phase, however, the projected total weight is ~130 t. The arrangement will consist of a robust, welded steel frame with its surfaces powder-coated. The shielded cell interior will be non-GMP-compliant made of stainless steel (1.4301). The proposed dimensions and attributes of the shielded cells is described below:

Shielded Cell 1

(W × D × H) approx. 1500 × 1200 × 1350 mm. It will contain Master-Slave manipulators in gas-tight design on the operating side, type HWM A202; a removable acrylic front panel behind the front lifting door; energy-saving LED lighting, glare-free, horizontal sliding door on the right side, electrically operated, with safety shut-off by safety contact strip. The cell will be shielded with lead as follows:

- 300 mm: front, rear, left, right and ceiling;
- 100 mm: under the worktop;
- 200 mm: Free space under the shielded cell (apron);
- 1 large lead-glass window size (W × H) ~ 300 × 400 mm, lead equivalent 200 mm;
- Each door of the three airlocks shielded with 200 mm lead.

Shielded Cell 2

(W × D × H) approx. 700 × 800 × 2800 mm. The cell is intended to contain 18 storage locations, consisting of 2 paternoster magazines for 9 targets each. The load compartments for target carriers/target plates to have a dimension of 100 × 100 × 100 mm. There will be a maintenance opening behind the lead bricks of SC2, which is screwed and sealed. The cell will be shielded with 200 mm lead on all sides, except for the partition to SC1.

There will be shielded airlocks between the two cells, size (W × H) ~ 200 × 200 mm and a shielded airlock to the target tunnel, size (W × H) ~ 400 × 400 mm.

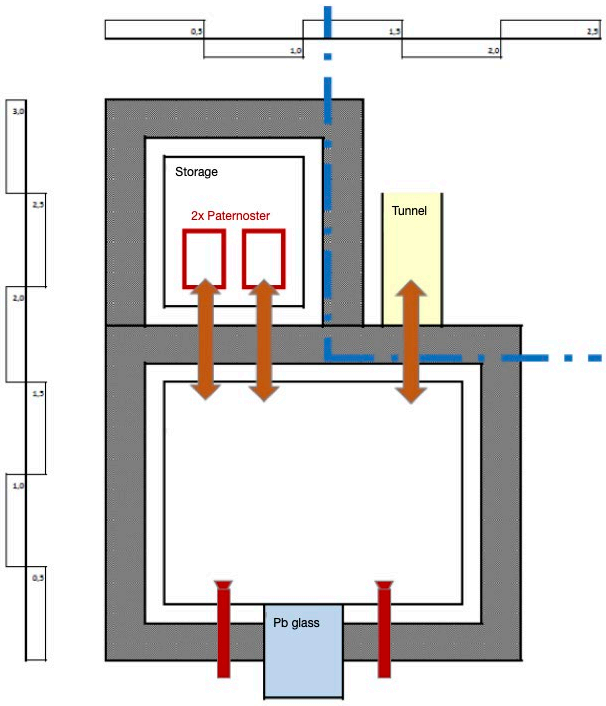

Figure 16.37: Schematic top cross sectional view of the target exchange cell and target decay storage cell.

To operate and control the system, a central electric system will be installed. Mechanical push-buttons and switches at the sides and above the doors will be available for intuitive operation of important functions, without the operator having to take his eyes off the inner cell. Along with it, there will be an additional control panel with touch display. There will be two electrical connections (240 VAC double socket (type J), splash-proof (IP44) in each cell. Three connections will be installed outside the cells (240 VAC sockets (type J); power supply: 230 V/50 Hz 16 A). An interlock circuit will be installed for all relevant doors of the shielded cell system. The shielded cells' ventilation will consist of negative pressure of at least -150 Pa, with both cells having identical air pressure level. There will be a minimum of 5 air changes/hour filtration and one HEPA 13 (DIN 1822) filter per cell. The exhaust air system will consist of a combination of HEPA 13 (DIN 1822) + active carbon filters (type Delbag DKD). The exhaust air filters will be shielded with lead (50 mm circumferential). The ventilation will be prepared for subsequent use of bag-in/bag-out filters.

A dose rate monitor (ALMO-3 1 sensor each for: - operating side, outside SC1 & SC-2) will be provided and installed.

16.3.6.2 Lifecycle Considerations

The possibility of recovering target material has to be assessed after a post-irradiation examination of the first targets after their initial storage for decay. Therefore, we intend to collaborate with the PSI Hotlab facility, which has the required knowhow and equipment for a post-irradiation examination of highly radioactive fuel [Degueldre, Bertsch and Martin 2016]. The operation time of minimum 28 days per target is deduced from the experiences at CERN ISOLDE. Since the intended radionuclides have half-lives of more than one hour, the need for ultra-fast release is marginal. Therefore, retention processes observed at CERN ISOLDE targets by beam induced sintering of the target and restructuring of the material shall not prevent an efficient production of these isotopes over longer times. Beam induced embrittlement and structural material changes due to gas development shall be topics addressed by the post-irradiation examination. These will be decisive for the long-term operation of targets, which would be beneficial because of the substantial cost of the target, and it would reduce the amount of needed storage space and disposal volume at a similar activation level.

16.3.6.3 Storage and Decay

The target is expected to have a minimum lifetime of 700 full operation hours. Beam related sintering and structural damage will occur and at some point (to be defined experimentally) prevent efficient production and particularly release from the target even for longer-lived radionuclides. Therefore, we expect a target exchange every month of full operation i.e. about 8 targets per year. In the shielded target exchange cell a temporary decay storage for up to 18 targets is foreseen. The targets will be afterwards moved towards a separate storage place to be prepared inside the building for storage before final disposal (see Section 16.1.4). Using the Nucleonica on-line calculator for the Ta target we expect a cooling after 24 hours from 180 W to not more than 30 W decay heat. For UCx the calculations yield a cooling after 24 hours from initially 876 W to 52 W decay heat. Hence, the target storage is equipped with an air cooling.

16.4 Target Station

All the components of the beam line are accessible from top using the exchange-flask technology well established at PSI accelerators. For the dimensioning of these flasks suitable for the exchange of beam dump, media column, target chamber and collimator as well as cushion seals of the proton beam line see Chapter 15. A principle sketch of the removable collimator, target and beam dump chambers is given in Figure 16.38. The target station contains five components: 1.) The target containment chamber with a shielding plug; 2) The insert called media support to supply cooling water, heating current, high voltage, pressurized air to the target chamber; 3) The inflatable metal seals containing the beam window, which seal the chamber to each other; 4) The beam dump with shielding plug and four-segment aperture; 5) The collimator with shielding plug and four-segment aperture.

The target chamber exchange works normally over a rail system, however in case of an emergency situation it could be also removed with the exchange flask through the vertically chamber no. 1 of Figure 16.38 containing the target shielding plug. When the target chamber is in beam position, it is also locked to the target-shielding plug. The exchange flask will grab with the lifting hook of the shielding plug and lift it together with the target chamber inside the exchange flask. Each of the five insert is placed inside a vacuum chamber. Around the chamber shielding is placed to protect the environment. When the target chamber stops at beam position, at the same moment it couples with this insert over plug-in couplings to connect to the media. The inserts, no. 3, has a flexible metal ring (see yellow ring on Figure 16.38), which is blown up by pressurized air and in this way it is tightening the vacuum chambers to each other. Beam dump, no. 4, is described in Chapter 17 and the collimator, no. 5, is designed similar to the beam dump.

The primary target chamber surrounding the spallation target itself is designed as a double walled water-cooled steel chamber with 5 mm thick steel walls avoiding deformation due to the vacuum (see Figure 16.39). The beam enters into and exits out of this chamber through carbon windows of 50 mm diameter (inlet) 75 mm diameter (outlet) with both 1 mm thickness (see Section 16.4.1). They are mounted directly onto this chamber using metal sealing and their dimensioning is based on experience enabling to withstand beam and shock waves in case of vacuum breaches. The target chamber is mounted onto a cart that is moved together with the irradiated target into the shielded target exchange cell dedicated for target exchange (see Section 16.3.6). The primary target chamber is surrounded by a secondary target chamber, which provides the media support, i.e. cooling water, heating current, high voltage, pressurized air (see Figure 16.38). The entire volume of the secondary target containment is directly connected to the rail path channel. This volume is separated hermetically in operations mode and held at fore-vacuum conditions of 10^{-2}-10^{-3} mbar. Thus, on the one hand air activation is avoided between the beam-line window, the target box and the beam

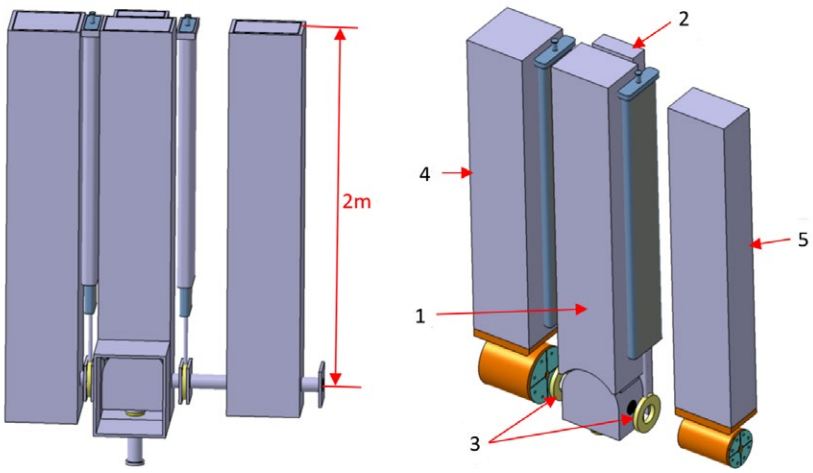

Figure 16.38: Left: Vacuum chambers and beam tubes of the TATTOOS target area, where the beam enters from the right. Right: Side view showing the collimator, target chamber and beam dump.

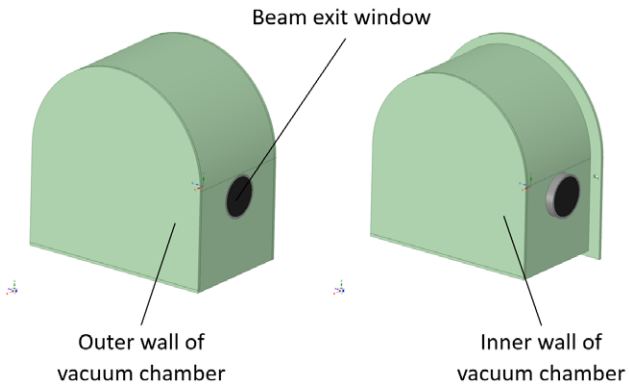

Figure 16.39: First design of the target chamber with surrounding water-cooling channels.

dump. On the other hand the absolute hermetical sealing of the inflatable metal seals is not required for reaching high vacuum in the target region which is needed for efficient ion transport and mass separation.

As the target chamber has to be cooled by water, water channels from stainless steel are needed for fluxes higher than 2 l/s due to erosion. Otherwise also copper tubes can be used or have to be implemented into the chamber walls (Figure 16.39). If more efficient cooling of the large heat load is required, instead of tubes the cooling-water flow can be fed in a directed flow between the chamber walls using diffusers. A similar construction was introduced in the cooling of the outer SINQ-safety hull.

Further, to exchange the target quickly via a manipulator one lid needs to be opened easily. Due to the high radiation

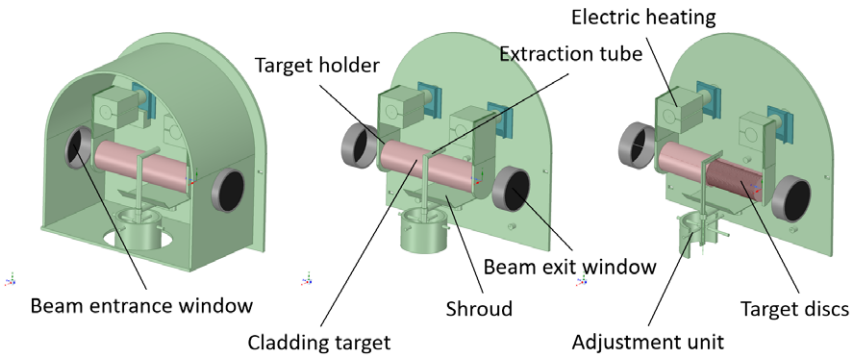

Figure 16.40: First design of the target chamber with the target, the cladding target, the target holder, the electric high voltage heating and the extraction tube pipe for collecting the isotopes from below.

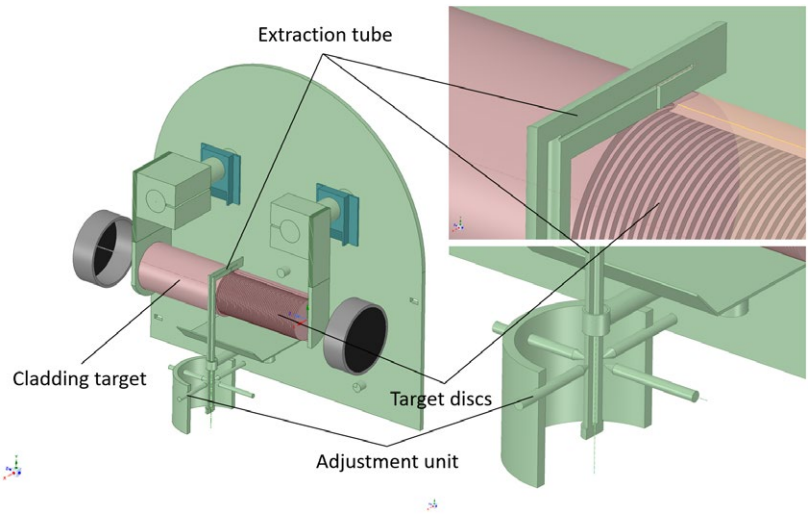

Figure 16.41: Development of the target chamber with the extraction tube for collecting the isotopes at the bottom side.

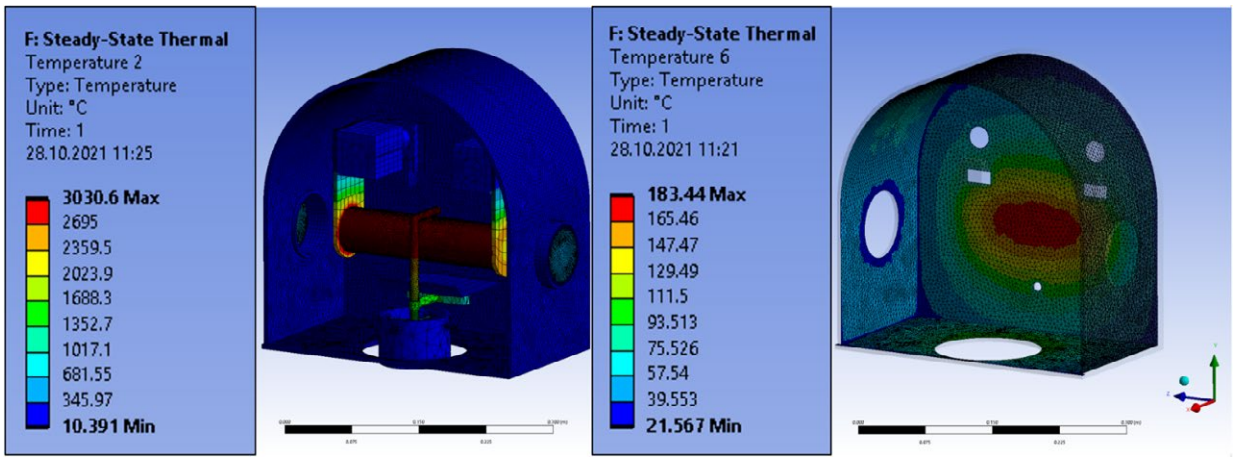

Figure 16.42: Temperature distribution of the target and the back wall of the target chamber.

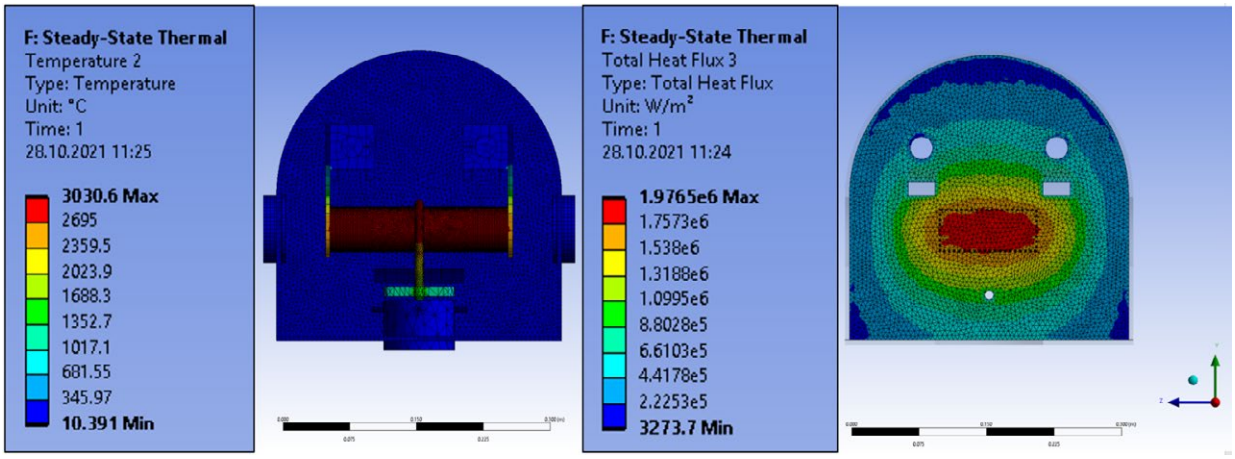

Figure 16.43: Temperature distribution and heat flux at the chamber wall from the side view (marked area of maximum heat flux).

area metal seals have to be used and fixed by screws. A particular challenge here is aligning the 1-3 mm wide extraction tube at the target within 0.1 mm to the extraction lens and the associated laser beam. This means, a highly reproducible and simple mechanism is necessary.

Figure 16.40 and Figure 16.41 shows a schematic view of the target chamber with the ion extraction beam line towards the bottom. The target chamber has to be sealed by an inflatable seal to the top flange of the ion extraction beam line. This has to be positioned within 0.1 mm with the adjustment unit.

A first calculation of the first design of the target chamber (Figure 16.42) with stainless steel (default in ANSYS-FEM) shows the target temperature and the chamber wall temperature. In this simulation the target is set to 3000 °C and the radiation and conduction are used. The outside wall is set to 300 K as ideal heat sink. The chamber wall reaches the expected temperature of around 183 °C. It is also seen that the temperature is at highest at the projected screen. A detailed view to this projected screen (Figure 16.43) shows a heat flux of around 1.9765 MW/m^2. For a check the heat flux is calculated for the marked area. In this surface area

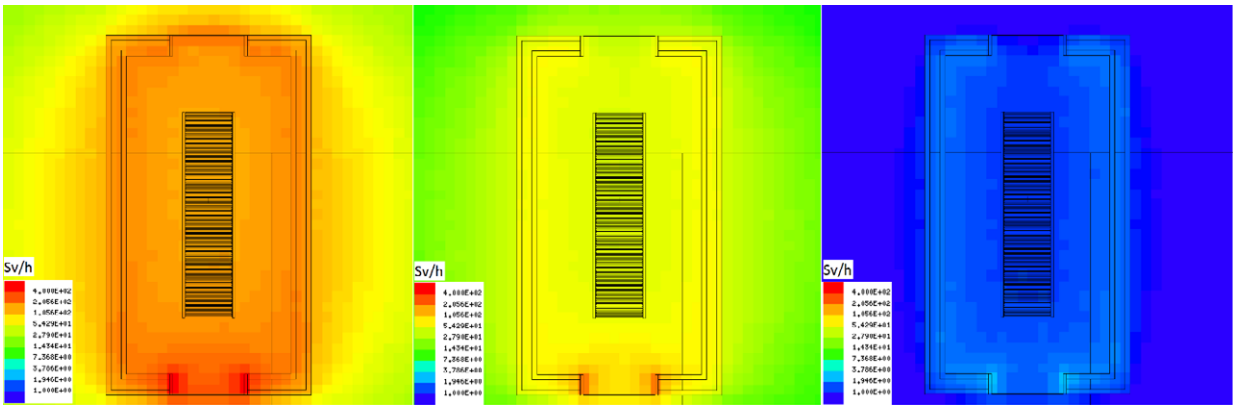

Figure 16.44: Remnant dose rate following 28 days of irradiation with 100 µA proton beam. Starting from left to right shown are the dose rate distributions at shutdown, 12h and 1 year of cooling time. It should be noted, that the gamma source from the target itself is suppressed on these plots and the target volume was voided.

around 10 kW radiation heat are deposited. This corresponds well to the 1D-Modell calculation. To reduce the heat-load on the back-wall of the chamber, the size of the chamber could be slightly increased. For example the increase of 50 mm towards the back and front-side leads to an estimated decrease of the maximum wall temperature to 120 °C.

16.4.1 Dose Rate of Target Chamber and Window

As the target chamber is made from stainless steel, the main dose rate induced in the target chamber is caused by typical activation products like Mn-54, Co-56, Co-57,Co-58 and Co-60. For the activation calculation, the same representative stainless steel material composition was applied as it is regularly used for the waste characterization of radioactive waste via calculation. To filter the contribution of the target chamber alone, the strong gamma source of the tantalum target was switched off and the target replaced with a void dummy. The activation of the target chamber appears to be uniform with the exception of the lower plenum facing the beam dump. There, due to the divergence of the proton beam following the target, a significant number of protons and secondary particles collide as can be seen in the maps of the dose rate in Figure 16.44. Therefore, it is recommended to enlarge the downstream window to avoid a hot spot on the vacuum chamber, which would later need a thick extra shielding in the waste container. This is particularly important as the target chamber is expected to be exchanged from time to time, mainly due to scratches in the sealing flanges, as high vacuum conditions are required.

Due to their small mass, the gamma rays emitted from the two windows are completely overshadowed by the rest of the chamber. At shutdown the dose rate at contact of the graphite window was determined to be 80 Sv/h. Within 12 hours of cooling time the dose rate at the same point of the graphite window falls to 0.6 Sv/h, which can be attributed to the rapid decay of C-11 with a half-life of 20 min. Following 1 year of cooling time, the dose rate of the graphite window at point of contact was determined to be 3 mSv/h. The dominant gamma-emitting isotopes, following 12 h of cooling time, for the graphite and the aluminum windows are respectively Be-7 and Na-22, Na-24. Where relevant for the long term behavior of the dose rate are only Be-7 and Na-22 having the corresponding half-lives of 53 days and 2.6 years. However, as it is shown in Section 16.4.2.1 the downstream window will be made from graphite as well due to the heat radiation from the target. Although as expected and as shown in Figure 16.3, the dose rate of both components is negligible compared to the activated steel parts of the target chamber.

16.4.2 Target Entrance and Exit Windows

16.4.2.1 Cooling

In the model the entrance window is made of graphite. Graphite is used for both meson production targets and good experience with it exist at PSI. At high temperature graphite is cooled effectively by irradiation due to its high emissivity. To check potential materials, in this calculation the exit window was assumed to be out of aluminum. Further, in comparison to the simulation with a wobbled beam (Figure 16.43), in the first design (Figure 16.45) the target is set to a constant temperature of 3000 °C as a conservative assumption. The radiative thermal emission of the target is included. With the wobbled beam the center part of the target has a temperature of around 3450 °C and at the cladding of the target (Figure 16.41, left side) the temperature is around 2350 °C (Figure 16.33/Figure 16.34). For the case with a constant temperature of around 3000 °C the entrance and

exit windows shows a temperature of 715 °C for the entrance window (graphite) respectively to 646 °C for the exit window (aluminum). From this result it is clear that only graphite windows can be used.

16.4.2.2 Sealing and Exchange

Due to the high irradiation area the windows have to be sealed with a metal seal to the target chamber. At PSI a HELICOFLEX® metal seal is used in such cases successfully with a long life time. In case the window or seal get leaky, breaks or for preventive maintenance, it is foreseen to change the graphite windows via manipulators in the shielded target exchange cell. Therefore, the mounting of the window has to be simple. To avoid handling of the 1 mm thick window with the manipulators the window has to be already pre-assembled in a flange. This flange is then fixed with screws of size M6 or larger, preferably with an INBUS key specially made for handling with manipulators as it is used in the shielded service cell ATEC at PSI. The metal seal should be also already fixed on the pre-assembled window flange. Then the window flange with seal can be safely mounted vertically on both sides of the target chamber.

16.4.2.3 Radiation Safety and Disposal

If a window needs to be exchanged in the shielded target exchange cell, contamination of the graphite with alpha particles evaporating from the target can be expected. Therefore, the window will be packed into a plastic bag and put into a shielded flask for disposal. Since it is 1 mm thick only and irradiated with just 100 µA protons the dose rate of 0.6 Sv/h after 12 h is smaller than for PSI's meson production target (Target E) which consists of 40 mm thick graphite hit by 2 mA of protons and has a dose rates up to 3 Sv/h. However, after a few years of storage the dose rate decreases to the µSv/h level as the dominant isotope is Be-7 with a half-life of 53 days. Important is the purity of graphite since otherwise the dose rate is finally determined by radionuclides formed from impurities like Na or Hf. Since there is good experience with the graphite grade used for target E, also from the point of view of radiation hardness, it is planned to use the same grade material. Disposal campaigns will be performed from time to time and can be scheduled together with the disposal of the meson production targets E and H.

To avoid extra stress on the graphite window during operation, the target chamber and its containment will be pumped down slowly to pre-vacuum. In this case the window does not need to withstand a pressure difference of 1 bar. However, it will be tested to safely stand a 1 bar pressure difference in case there is e.g. a vacuum leak in the target chamber. As safety check it is planned to evacuate the target chamber after exchange of the target via the inflatable seal on the bottom to check the tightness of all seals and the integrity of the chamber.

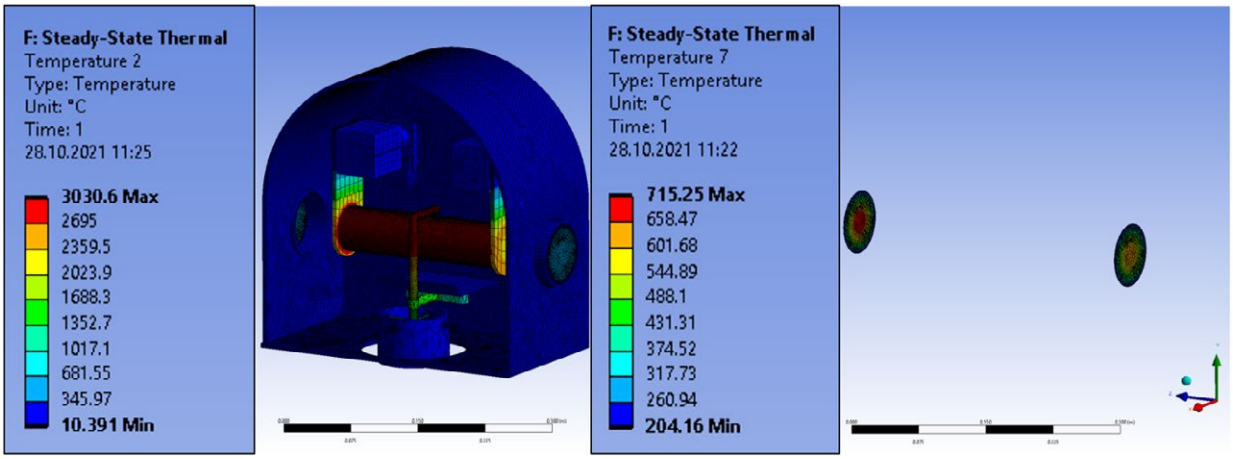

Figure 16.45: Temperature distribution of the beam entrance and exit window.

17 Beam Dump

For proof-of-concept, we assume a cylindrical beam dump that consists of six identical stacked discs of copper with a total length of 25 cm and a diameter of 30 cm. The beam dump is collinear with the target and the incoming proton beam.

The beam dump will be made of high purity oxygen free copper (Cu-OFE), which has different material properties compared to normal copper and its alloys. The reason of using Cu-OFE is the possible build-up of water in activated copper due to the production of hydrogen from spallation. This water may lead to cracks at elevated temperatures. Another reason is the brazing procedure demanding oxygen-free copper.

The beam dump will require water-cooling. An example is shown in Figure 17.12.

17.1 Activation

Significant activation is induced in the beam dump. The main contributor to the long-term remnant gamma dose rate of the beam dump is Co-60. Since the beam dump is located within the line of sight of the fast neutrons direction (collinear with the proton beam), Co-60 is mainly produced via fast neutron (n,α) reactions with Cu-63. Additional secondary mechanism for Co-60 production is neutron absorption in Co-59, present as typical impurity in copper.

For the calculations presented here, the representative copper material composition routinely used for waste calculations at PSI was assumed for the activation calculations. In addition, to test the sensitivity towards the initial Co-59 concentration, the activation of an artificial material composition with 5 ppm of Co-59 was compared to a 0.5 ppm Co-59 composition, under the same irradiation conditions. The buildup of Co-60 differed by 2 %, confirming that the main production mechanism of Co-60 are (n,α) reactions with Cu-63. In Cu-OFE, which will be used for manufacturing, impurities of cobalt are negligible.

The resulting remnant dose rates of the beam dump are shown in Figure 17.1. After 35 years of constant irradiation with a 70 µA proton beam on target the dose rate of the beam dump is already in radioactive equilibrium, i.e. represents the maximum dose rate in the life time of the beam dump. The averaged value of 70 µA for the proton current

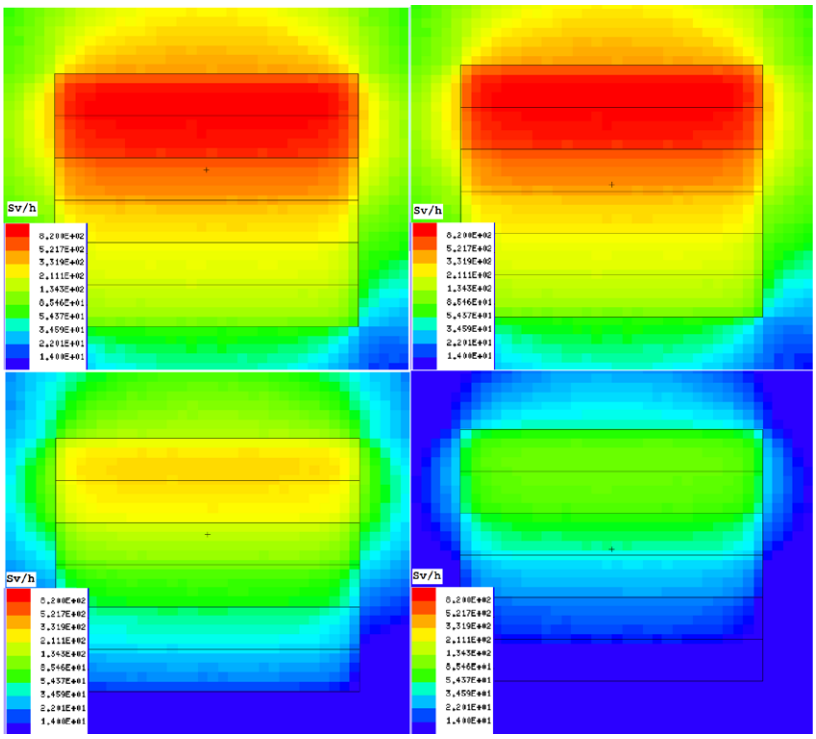

Figure 17.1: Remnant dose rate following 35 years of irradiation with an averaged proton current of 70 µA on the tantalum target impinging from the top. Shown from left to right: on the top row is the gamma dose rate at shutdown and at 1 day. Shown on the bottom row starting from left to right is the shutdown dose rate at 7 days and at 1 year of cooling time. These results were computed using the tantalum target. It should be noted, that all the geometry other than the beam dump itself was suppressed, i.e. the beam dump is surrounded by vacuum.

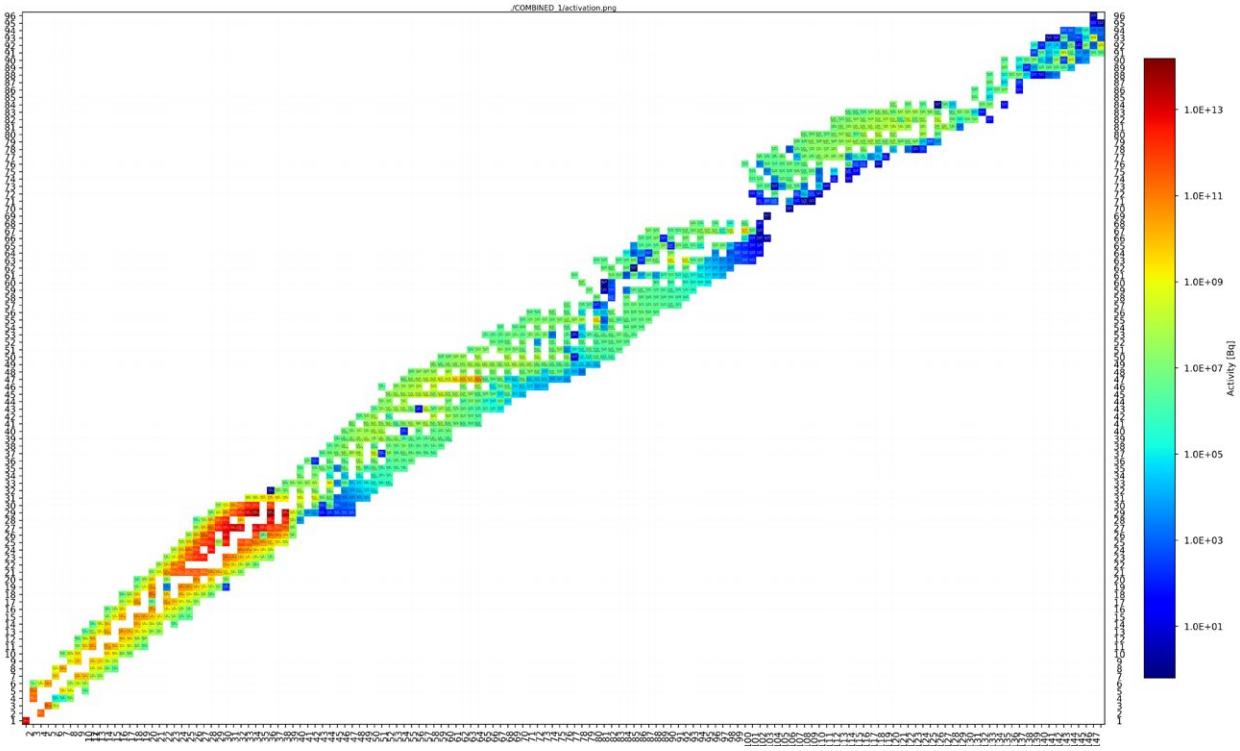

Figure 17.2: Activation and spallation products in the beam dump following 35 years of irradiation with an averaged proton current of 70 µA on the tantalum target. The heavy isotope tail (upper right corner) is due to lead and other impurities in the initial composition.

was chosen to take into account the potential shutdown/maintenance periods of the TATTOOS facility. The maximum dose rate of around 500 Sv/h appears in front of the beam dump. Following one year of cooling the dose rate within the vicinity of the beam dump drops to about 100 Sv/h. For comparison, the collimator KHE2 between Target E and the HIPA beam dump, which was exchanged a few years ago, was handled after 2 months of cooling. The dose rates of KHE2 were measured in the PSI shielded service cell ATEC at 500 Sv/h (close to contact dose rate).

The distribution of the produced radionuclides in the beam dump is shown in Figure 17.2. They cover almost the entire nuclide chart due to impurities in the material definition of the copper. The isotopes above Cu will be significantly reduced using high purity copper. Therefore, the dose rates are a conservative estimate.

17.2 Power Deposit by Proton Beam

The power deposit in the beam dump is dominated by the protons escaping the target losing their energy, mainly due to ionization. The power deposition on the beam dump by the primary proton beam and by secondary particles produced in the target is shown in Figure 17.3. Since the range of 300 MeV protons behind the Ta target is about 12 cm in copper, most of the power is deposited over the first segments of the beam dump. Therefore, the power drops between the third and the fourth disc. Due to the lower density of UCx, the energy of the protons exiting the target is about 400 MeV. This enables a deeper penetration of the power distribution into the beam dump. Unlike the tantalum case, even the fourth ring of the beam dump gets significant power deposition.

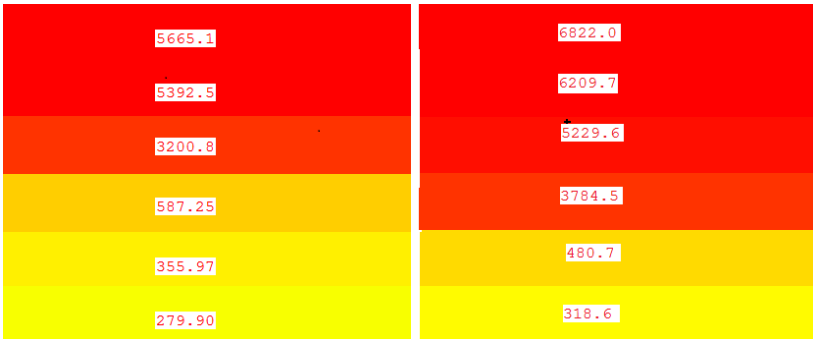

Figure 17.3: Power deposition on the beam dump tallied in several equal segments along the beam direction [W]. The length of each segment is 4.2 cm. Shown on the left is the tantalum case and on the right the UCx case.

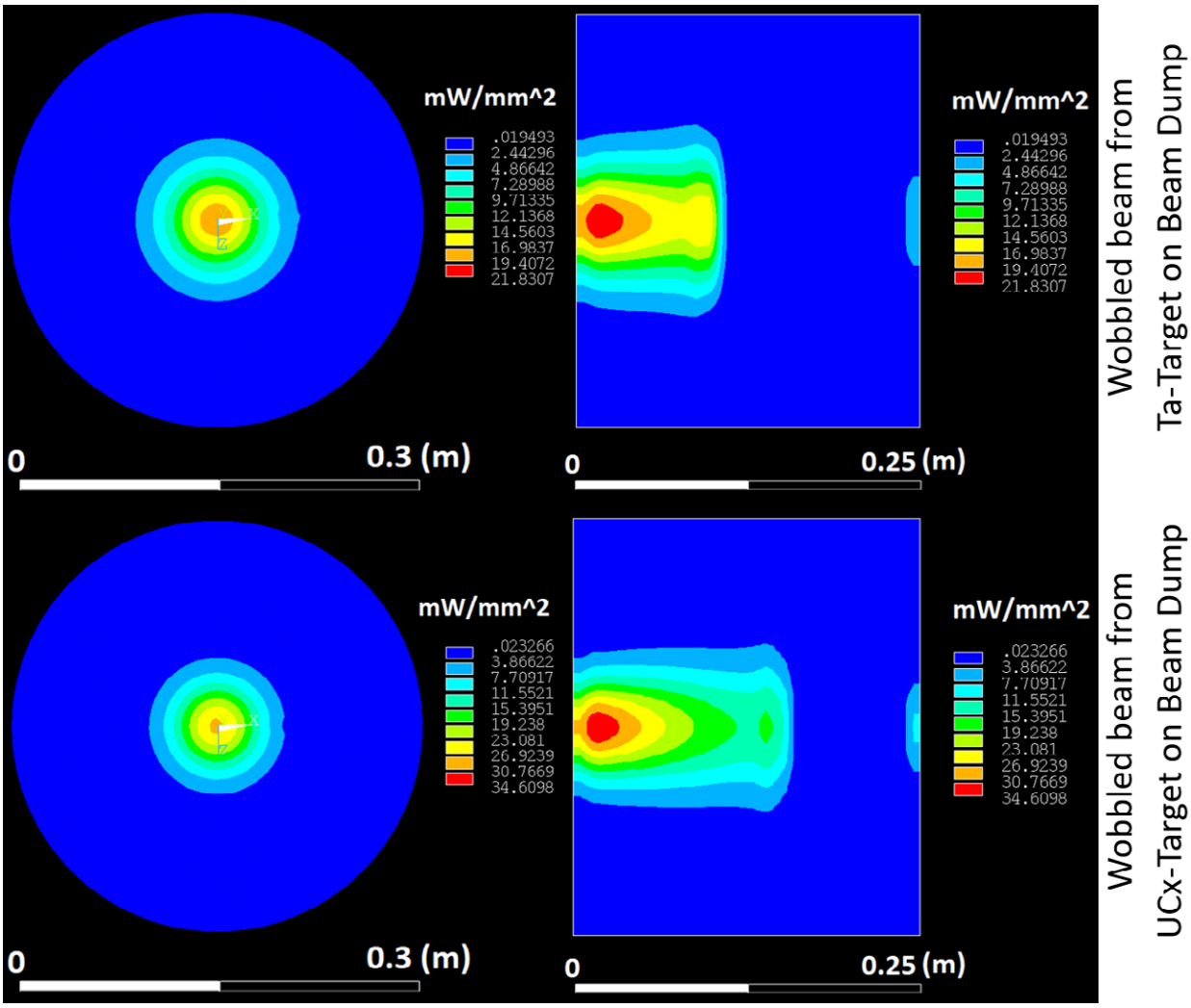

Figure 17.4: Power area density distribution in the beam dump for a wobbled beam from a Ta target (top) and an UCx target (bottom).

In addition, due to their large mass, protons see little deflection from their initial trajectory. This is why the power distribution and the temperature peak in the center of the beam dump and represent the initial proton beam distribution entering the beam stop (see Figure 17.4).

17.3 Temperature Distribution

17.3.1 Material Data

Table 17.1, Figure 17.5 and Figure 17.6 contains the material data of oxygen-free copper (Cu-OFE) required for thermal calculations and simulations.

17.3.2 Thermal Simulation

The front side where the beam hits the beam dump is allowed to radiate the heat in the simulation with an emissivity of 0.8 for oxidized copper [Fluke Process Instruments, 2021]. The back side is set to adiabatic boundary condition.

The surrounding walls are set to the linearly increasing water temperature from the first beam dump disc (BD1) with inlet water temperature of around 20 °C to the BD6 with an assumed outlet water temperature of around 40 °C (Figure 17.7).

The power deposition in the beam dump is implemented via mesh profiles with space-resolved power depositions. A similar procedure was applied to the power deposition in the target. Overall values are around 13 kW for a constant beam, 15 kW for a wobbled beam with Ta-Target, respectively, and 23 kW for a wobbled beam with UCx-Target.

Temperature T in K	Density in kg/m³
293.15	8940
1356.15	8330
1357.15	7980

Table 17.1: Material data of copper-OFE [Deutsches Kupferinstitut, 2005]

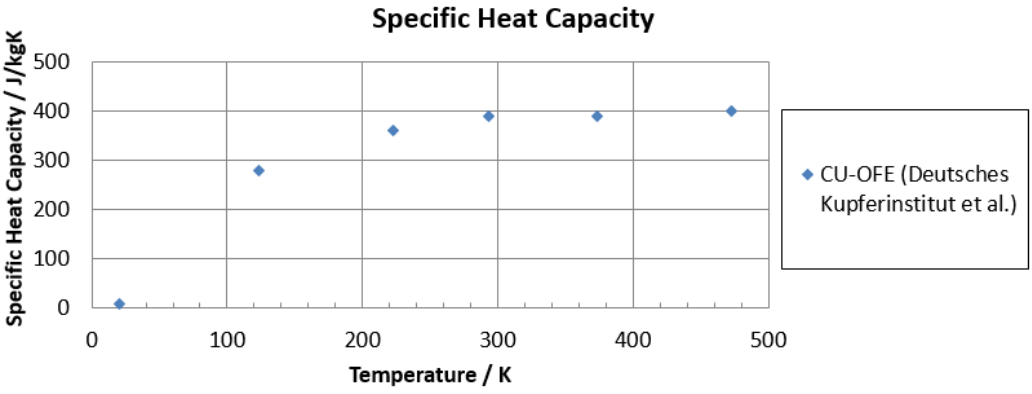

Figure 17.5: Material properties of copper-OFE: Specific Heat Capacity [Deutsches Kupferinstitut, 2005]

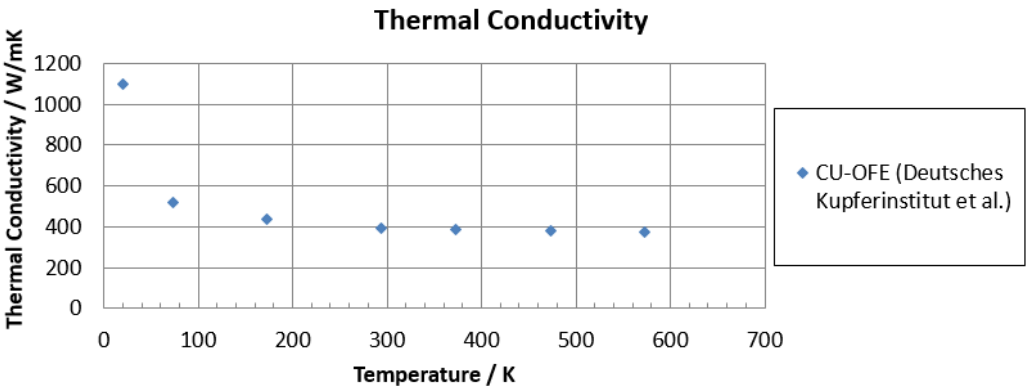

Figure 17.6: Material properties of copper-OFE: Thermal Conductivity [Deutsches Kupferinstitut, 2005]

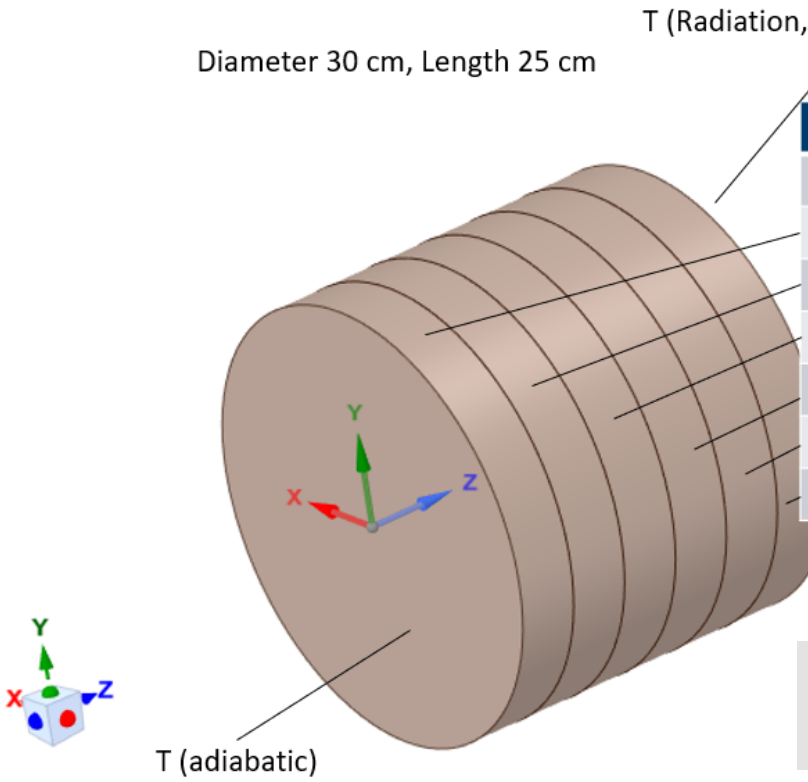

	Temperature
	°C
T-Wall (BD1)	39
T-Wall (BD2)	35,5
T-Wall (BD3)	32
T-Wall (BD4)	28
T-Wall (BD5)	24
T-Wall (BD6)	20

Figure 17.7: Boundary conditions of the beam dump for the simulation with ANSYS Fluent and APDL.

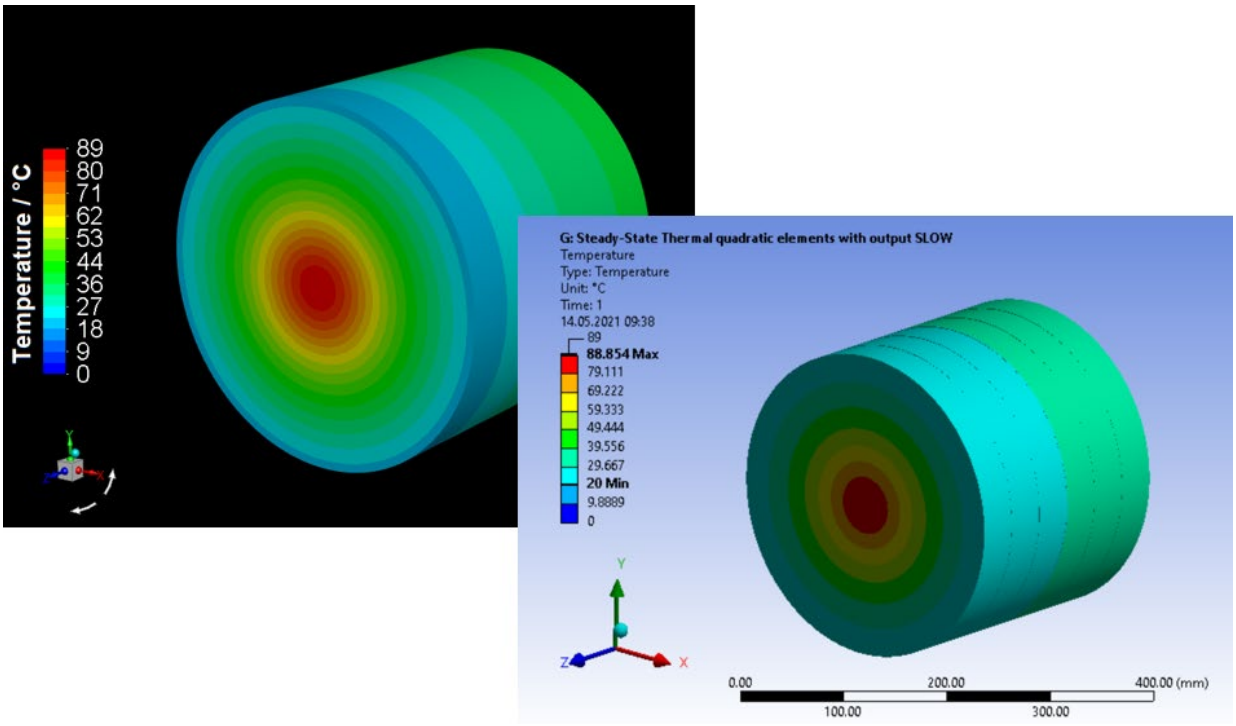

Figure 17.8: Comparison of the beam dump simulation with two different solvers: ANSYS Fluent (left) and ANSYs APDL (right).

The comparison of two different solvers, ANSYS Fluent and ANSYS APDL, is shown in Figure 17.8. Both simulations show the same maximum temperature at the entrance of the beam dump. The maximum temperature of around 89 °C is found in the central part of the first beam dump component. The temperature distribution indicates that the diameter of the beam dump can be reduced.

Figure 17.9 shows a cut through the Beam Dump along the beam direction.

The temperature distribution in this sectional view shows that the temperature is very low in the last two slices. Considering only the temperature distribution during normal operations, these last two slices could be abandoned.

Figure 17.10 shows the influence of the emissivity. The previously assumed emissivity of around 0.8 corresponds to an oxide layer on the surface; the emissivity of around 0.0653 [Cagran, 2004] to a polished surface. The comparison shows that the influence is very small, because of the low temperature of less than 100 °C.

Figure 17.11 shows the comparison of the wobbled beam on the Ta target and the UCx target with an emissivity of 0.0653.

With the wobbled beam on the Ta target a maximum temperature of around 89 °C is obtained, while with the wobbled beam on the UCx target a maximum temperature of around 110 °C is predicted.

17.4 Manufacturing

The manufacturing of the beam dump follows the description in Section 8.5.3 for the collimators. The present simulations indicates (see Section 17.3.2) that the design will be similar to the third part of the 590 MeV beam dump behind target E (see Figure 17.12 and Figure 17.13). It will, however, have a larger diameter of 300 mm instead of 140 mm due to the spread of the beam in the massive target and a length of actually 250 mm due to the reduced energy of the beam after the target. In the present, non-optimized design there is no opening in the center of the copper block. Four slits, slanted to the beam direction, equalize the thermal stress, when the heated-up material expands.

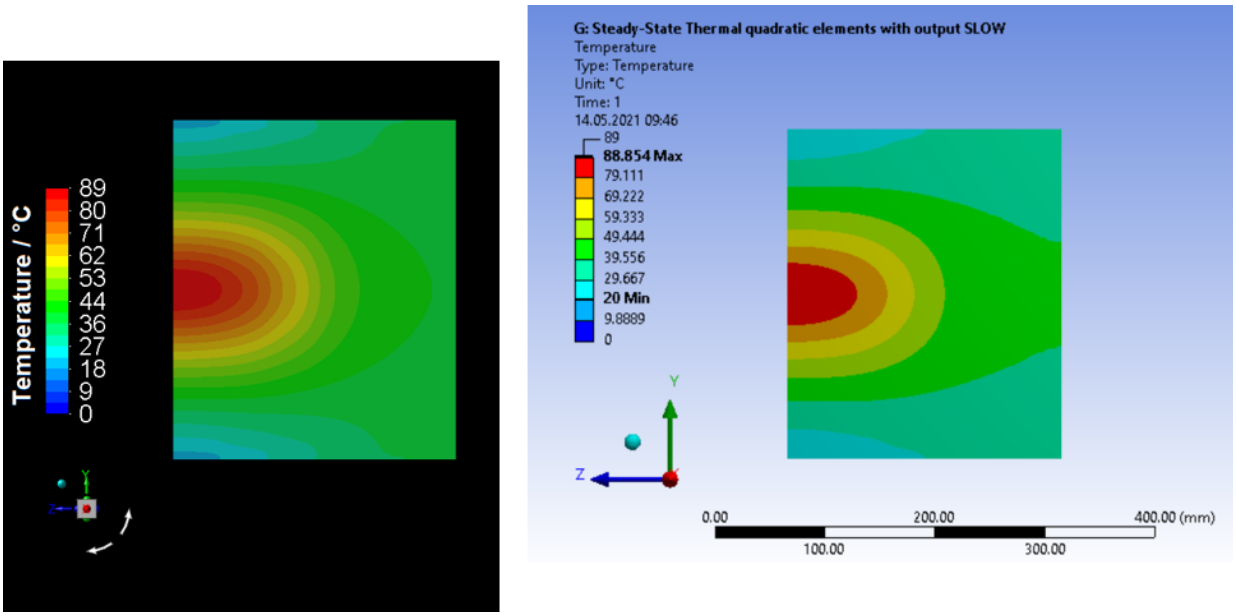

Figure 17.9: Cut-through figure of the beam dump with the temperature distribution in the beam dump caused by the proton beam profile. ANSYS Fluent (left) and ANSYS APDL (right).

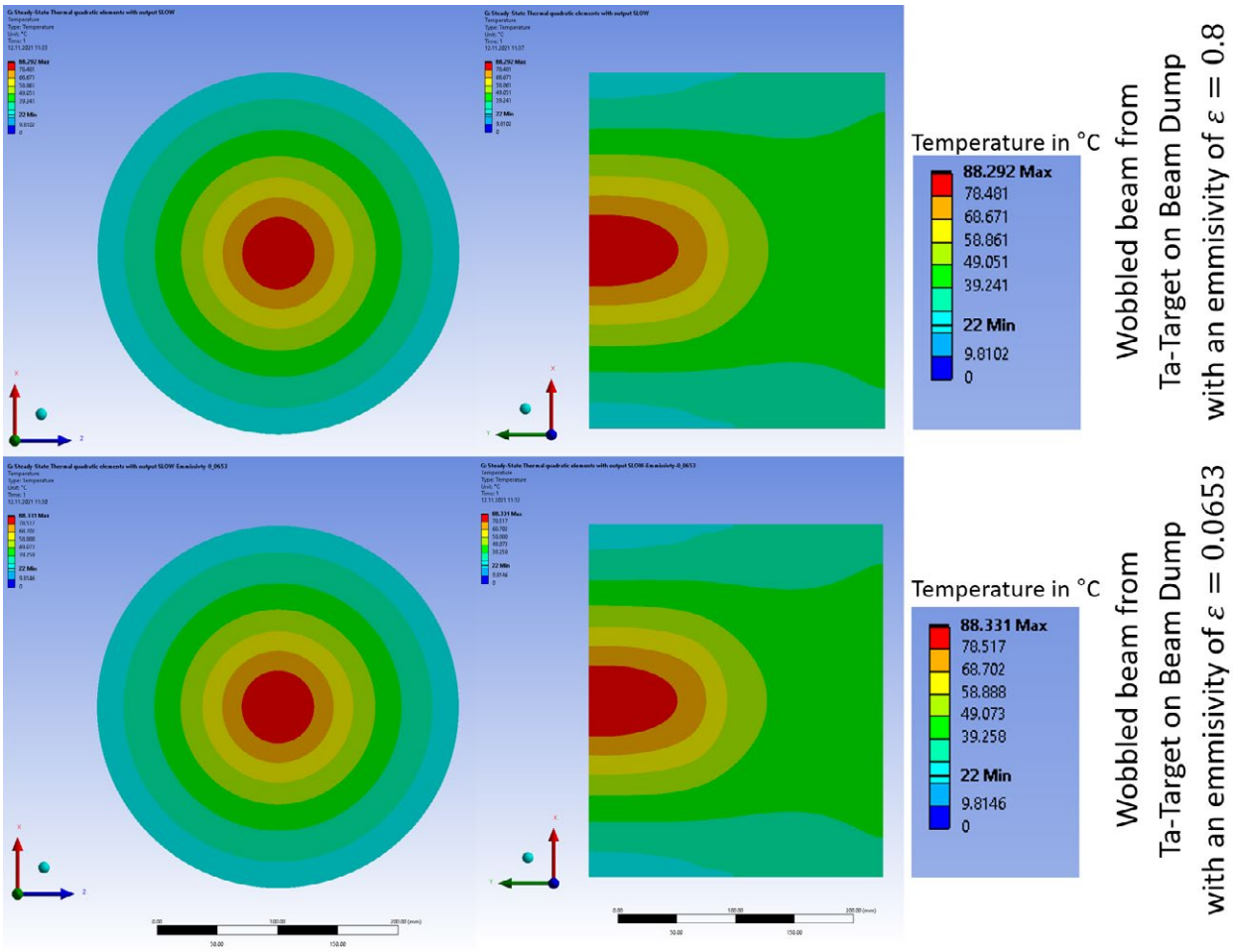

Figure 17.10: Comparison of the temperature distribution on the beam dump from a wobbled beam from a Ta-target with an emissivity of 0.8 (top) with an emissivity of 0.0653 (top). The left side shows the temperature on the front of the beam dump and the right side the cut through the beam dump, both calculated with ANSYS APDL.

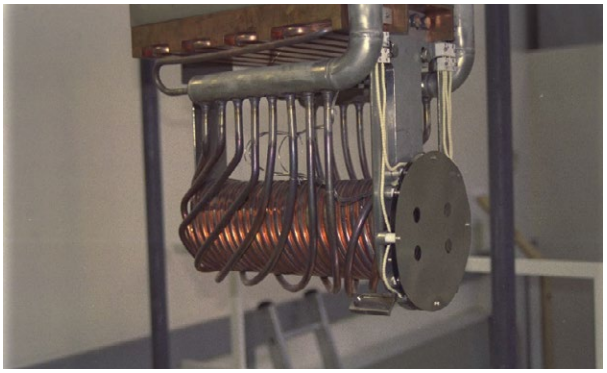

Figure 17.12: Beam dump 3 with aperture

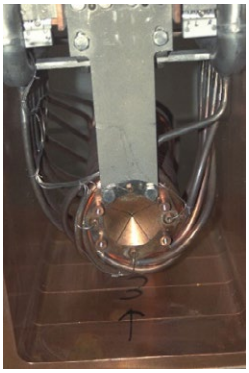

Figure 17.13: Beam dump 3 without aperture

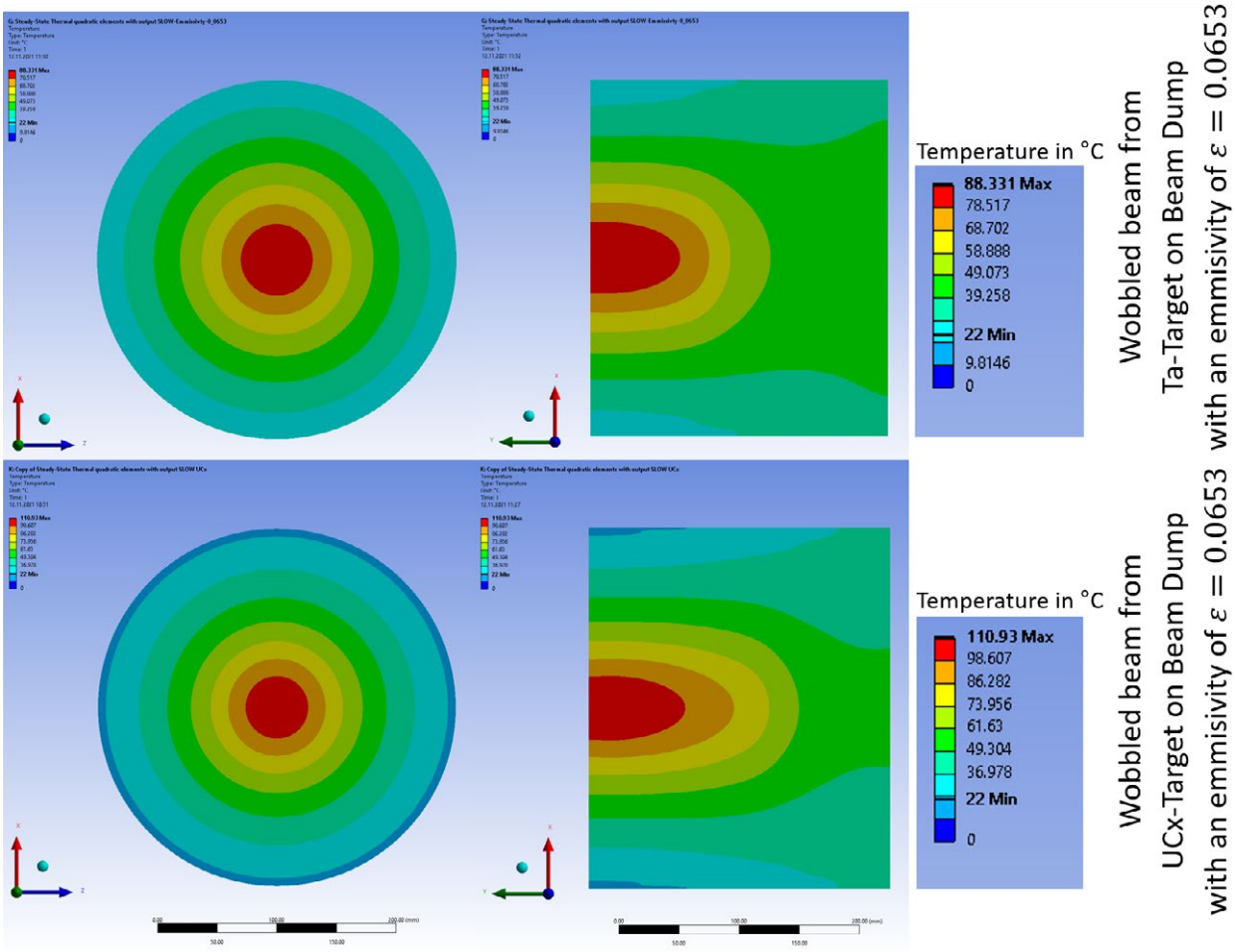

Figure 17.11: Comparison of the temperature distribution on the beam dump with a wobbled beam on a Ta target (top) and an UCx target (bottom). The left side shows the temperature distribution on the front of the beam dump and the right side the cut through the beam dump, both calculated with ANSYS APDL.

17.5 Exchange & Storage

Since the beam dump gets highly activated to several hundred Sv/h (see Section 17.1), a well shielded exchange flask is required, if the beam dump needs to be taken out of the beamline in case of failure or disposal. For this, the shielding blocks above the beam dump up to its top have to be removed with the crane installed in the TATTOOS area. The subsequent procedure is very similar to the exchange of target E or H or another high-activated component in the proton beamline described in Section 9.3.1. The difference is that the TATTOOS area is locally separated from the shielded service cell ATEC as well as from the parking slots (see Section 9.3.2 and figures therein) where the beam dump can be stored. This means that the exchange flask cannot be transported with the crane inside a radiological zone but needs to be transported on a heavy load trailer. Therefore, along with other constraints described in Section 18.1, a new exchange flask is required for the TATTOOS beamline components.

In case of an exchange the beam dump will be transported to a free parking slot or directly to the sluice of ATEC for inspection or disposal. The new beam dump will be pulled into the exchange flask and transported to the TATTOOS area.

18 Exchange Flask

18.1 Basic Considerations, Requirements and Constraints

Exchange flasks are used for handling components that are considerably activated or contaminated, to remove these components from or insert them into the beamline or storage compartment, and to provide containment and shielding during transport. The to-be-designed TATTOOS exchange flask will need to accommodate the beam dump, the collimator in front of the target, the two beam windows and the media supply. In addition, the exchange flask shall provide a back-up solution for exchanging the target chamber including the target (possible only after cool-down).

Inside the TATTOOS hall, the exchange flask will be maneuvered by means of the indoor crane. The weight of the TATTOOS exchange flask including its payload must therefore not exceed the maximum crane capacity of 40 t. Another constraint is the height of the TATTOOS hall, which is currently just 8 m.

The transport of the exchange flask from the TATTOOS hall into the experimental hall has to be performed outside the radiological controlled zone, crossing a few hundred meters of open-air, fenced PSI premises. A concept without recourse to a crane has to be worked out for this part of transport. During transport, the dose rate outside of the flask has to be less than 2 mSv/h and no contamination on the outer surfaces is allowed.

The Target E exchange flask will serve as a blueprint for the TATTOOS exchange flask. From operational experience, the Target E flask has never been contaminated outside and only once inside. Considering the dose rate of the most activated part to be lifted in routine operation, i.e. the TATTOOS beam dump, the TATTOOS flask will require about 40 cm steel shielding. The same amount of shielding is used in the Target E flask, which however weights already 42 t unloaded. Careful optimization of the shielding will be required to comply with the 40 t gross weight restriction indicated above Nevertheless, to exclude spreading of alpha emitters, the already existing target E flask must not be used in the TATTOOS area, due to possible alpha contamination, which could be carried to the non-alpha radiological zone.

18.2 Layout

The present concept of the TATTOOS exchange flask (see Figure 18.1 and Figure 18.2) is based on the target E exchange flask. The exchange flask has a frame, on which the hoisting mechanic, the rails to guide the hook and the movable rails are mounted (see Figure 18.3). On this frame the shielding of the flask is attached. On top of the flask is a mechanic to lock the hock of the hall crane with the exchange flask. Like in the target E exchange flask a sliding door at the bottom will hermetically close-up the inner part.

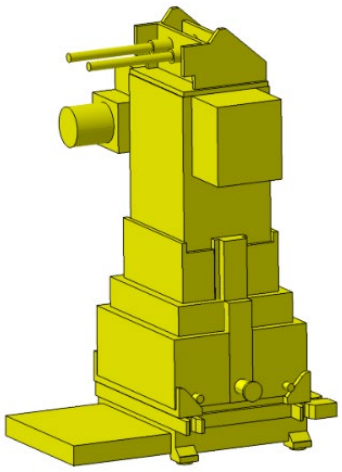

Figure 18.1: Outside view of the TATTOOS exchange flask

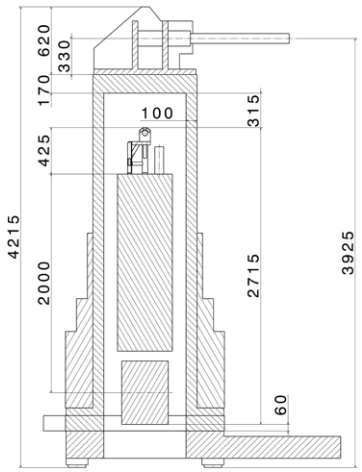

Figure 18.2: Cut of the exchange flask with beam dump

Figure 18.3: Target E exchange flask from inside

Based on this blueprint, the height of the future TATTOOS exchange flask may be estimated. Currently, a height of 4.5 m is expected, whereof 2.7 m is attributable to the total length of the insert, and 1.8 m to the shielding plug. The length of the shielding plug is determined by the acceptable dose rate on top of it, which should allow short manual interventions. The exchange flask has to be positioned on top of the insert whose lower part is centered at 1.5 m beam height. This means that the hook of the exchange flask in Figure 18.1 is at a height of 8.2 m, which is already above the current roof of the building at 8 m. Taking into account the installation of the 40 t crane the roof has to be lifted to about 10 m.

18.2.1 Transport Options

When docked to the shielding plug of the insert, the exchange flask will be in upright position. For transport on the open-air stretch of way, i.e. outside the radiological controlled area, two options are considered: transport in horizontal (lying) and transport in vertical (upright) position.

18.2.1.1 Transport in Horizontal Position

In this case, the exchange flask has to be brought from a vertical to a horizontal position. Figure 18.4 and Figure 18.5 display images of the SINQ exchange flask during assembly in the past. The exchange flask is latched to a turning support and can thus be brought by means of a crane from a vertical to a horizontal position or vice versa. Since the material lock of the ATEC service cell (see Section 10.4) is also in a horizontal position, the SINQ exchange flask has a special hoisting mechanic that allows pushing the target out of the flask. Normal hoisting system are just made to lift a load. At the time when the SINQ exchange flask was designed, it was a difficult task to solve this push mechanic. However, this will be not needed for the TATTOOS exchange flask as the sluice for such components is in vertical position.

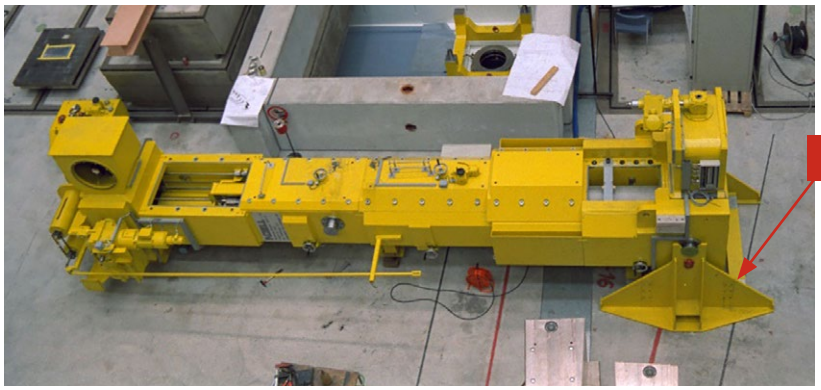

Figure 18.4: SINQ exchange flask when it was assembled

Figure 18.5: SINQ exchange flask when it was assembled: No 1 points to the turning support.

Figure 18.6: SINQ exchange flask with gripper rack for horizontal position

An additional crane rack is needed to lift the flask at horizontal position (see Figure 18.6).

18.2.1.2 Transport in Vertical Position

The exchange flask could be moved on a specially designed low-loading trailer, which is equipped with a motor and a steering unit. Such a concept is going to be realized at GSI for an exchange flask of similar height (almost 4 m) and weight (30 t). The advantage would be that additional shielding could be carried on the trailer. This would allow reducing the shielding and therefore the weight of the exchange flask to meet the weight limits of the TATTOOS crane, and at the same time having enough shielding during transport to meet the 2 mSv/h maximum dose rate requirement. This shielding would also stabilize the flask during transport and prevent it from tilting over. The disadvantage is that the respective gates have to be about 5 m high. While the gate for the new TATTOOS area can be planned accordingly, the existing gate of the experimental hall would have to be replaced to allow approach to the ATEC facility.

18.3 Safety Measures

The concept has to anticipate and remediate any potential problematic situation, including the failure of a sensor or of the motor, or the jamming of the hoisting. One key part is the gripper inside the flask that has to bear the whole weight in every situation. The mechanism has a fail-safe design, i.e. the gripper must always be in a closed position if there is a load on it (see Figure 18.7).

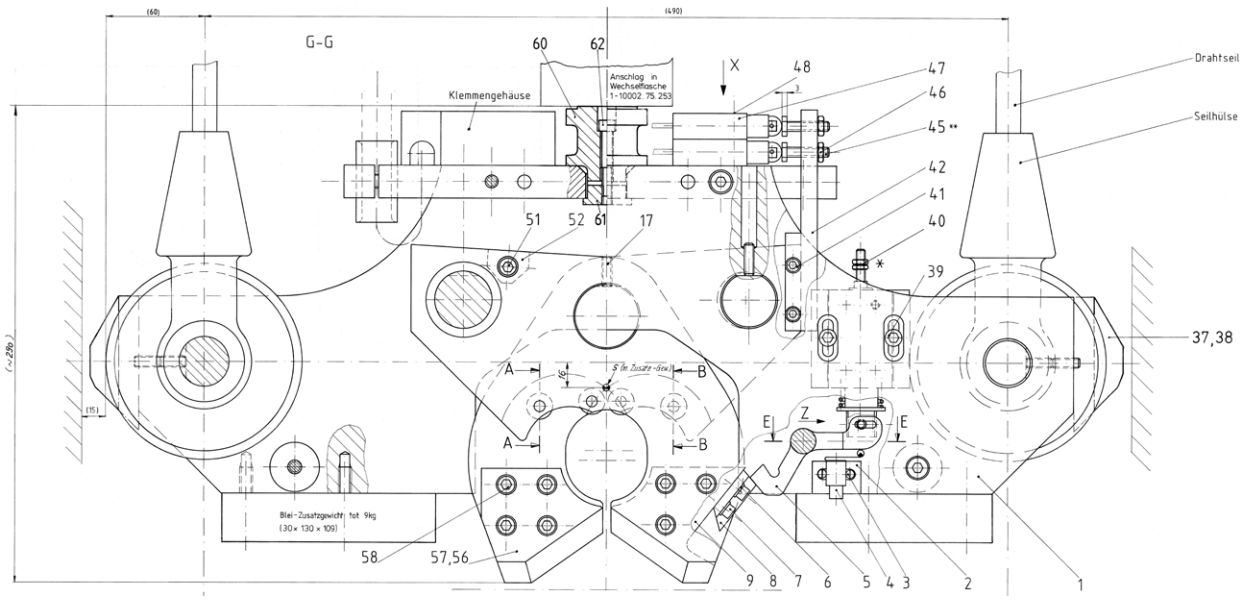

Figure 18.7: Gripper of the exchange flask

Figure 18.8: Worker with protection clothes

A risk analysis is needed for the operation of the exchange flask. GSI is currently manufacturing two large exchange flasks; the final construction phase includes such a risk analysis. There is close collaboration between the GSI technicians and the group at PSI, which will be responsible for the exchange flask.
During flask operation, i.e. an exchange of a beamline component, the same safety precautions as described in Section 9.3.1 will be applied. All workers (see Figure 18.8) are closely supervised and radiologically monitored by radioprotection experts to avoid contamination and incorporation, in particular of Tritium.

18.4 Operation

The exchange flask will be operated in the same way as described in the Section 9.3.1, except for the transfer between the TATTOOS hall and the experimental hall, which does present an additional challenge.
With the flask in upright position, the beam dump or other beamline component will be pulled into the flask with the gripper. The flask is then moved to the area close to the door of the TATTOOS hall where it is checked for contamination and dose rate. The next step depends on the solution implemented (upright vs lying position during transfer, see Section 18.2.1). The exchange flask will either be brought into a horizontal position first, by means of a turning support, or it will be lifted directly onto the low trailer in upright position. The trailer will be moved through the PSI West area into the experimental hall. There, the beamline component will be transferred to ATEC for maintenance or disassembling into a waste container, either directly or after temporary storage inside a parking slot.
If the target has to be lifted, a contamination protection will be installed like in case of the graphite target E (see Figure 18.9). In addition, an air flow towards the beam line prevents spreading of contamination.

Figure 18.9: Installation of the contamination protection on the so-called bridge, where later the exchange flask will be positioned.

19 Mass Separation

19.1 Basic Considerations, Requirements and Constraints

The mass separation is designed according to the experiences from the pioneering works at CERN ISOLDE [Catherall, 2017] and at the RISIKO Separator at Mainz University, Germany [Wendt, 1997]. The principle is tested for single charged ion beams with intensities of up to 1 micro Ampere (6.25E12 Ions/s). The quality and yield of mass separation depends clearly on the selectivity of the ionization process and on the ion beam quality at the entrance of the analyzing magnet. The highest selectivity of ionization is achieved by the RILIS technique described below. Non-specific surface ionization has to be considered on tantalum at temperatures above 2000 °C.

19.2 Ion Generation

19.2.1 Laser Ionization vs. Surface Ionization

19.2.1.1 Resonance Laser Ionization (RILIS)

Recently, the principles and current state of Laser Resonance Ionization (RILIS) in conjunction with mass separation was reviewed in [Fedosseev, 2017; Gadelshin, 2020]. A principle sketch of RILIS is shown in Figure 19.1.

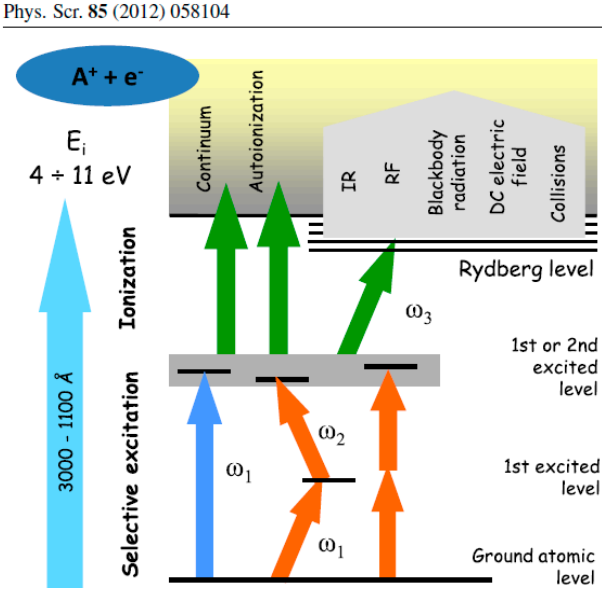

The neutral atoms emerging at the exit of the irradiated target due to thermal release are hit by a photon of laser-light of a defined frequency to selectively excite the atoms into an metastable excited state according to the atomic physics data available for almost all elements. The required resonance ionization schemes for the intended primary product spectrum of IMPACT, i.e. Tb and Ac exist [CERN-ISOLDE]. A second laser photon with a second freqency is ionizing those metastable excited atoms. Even a three photon ionization can be achieved to reach higer selectivity. However, the main advantage of RILIS above surface ionization is the elemental selectivity and higher achievable efficiencies. In Figure 19.2 a sketch of the laser equipment is given needed for RILIS.

The RILIS scheme requires commercially available laser systems with a power of about 10 W in the red spectral range and up to 5 W in the blue spectral range to be able to produce ions for most of the elements [Wendt, 2003]. This requires driver laser powers of up to 100 W (Table 19.1).

Existing RILIS designs can be used as operational examples to be rebuild for IMPACT in [Fedosseev, 2017; Gadelshin, 2020] (see Figure 19.2). A laser hut will be installed close to the mass separator to guide the composed laser pulses into the outlet tube of the target via a dedicated prism and mirror system. Alternatively, the laser light can be redirected through a second mirror system directly through the quadrupole switch in the mass separator beamline straight into the off-line ion source described in Section 19.4.2

19.2.1.2 Surface Ionization

The surface ionization follows the fundamentals given by the Saha-Langmuir law [Dresser, 1968]. This method is successfully used experimentally at the JAEA ISOL-facility, Tokai-mura, Japan [Sato, 2013] (see Figure 19.3) or at the CERN MEDICIS Facility [Gadelshin, 2019], [Martinez Palenzuela, 2021] for elements with low ionization potential (‹6 eV), i.e. alkaline, earth-alkaline elements and some lanthanides.

Figure 19.1: Schematic of the RILIS ionization principle with a multi-photon excitation [Fedosseev, Kudryavtsev, and Mishin, 2012]

Laser	Function	Wavelength	Power, max.	Pulse width
Nd:YAG *Edgewave CX16III-OE*	Dye pumping Dye pumping	532 nm 355 nm	100 W 20 W	8 ns 11 ns
Nd:YAG *Photonics Industries DM-60–532*	Ti:Sa pumping	532 nm	60 W $M^2 < 30$	170 ns
$Nd:YVO_4$ *Coherent Blaze 532–40-HE*	Non-resonant ionization/ Ti:Sa and dye pumping	532 nm	40 W $M^2 < 1.3$	17 ns
Dye laser *Sirah Credo*	Resonance atomic excitation, Spectroscopy 9 GHz linewidth	390–860 nm 270–390 nm 210–270 nm	20 W (fundamental) 2.5 W SHG 0.2 W THG	7 ns 6 ns 5 ns
(NB-)Dye laser *DMK MSS*	Resonance atomic excitation, (NB) spectroscopy 15 GHz (0.8 GHz)	390–860 nm 270–390 nm 210–270 nm	10 W (fundamental) 1 W SHG 0.2 W THG	10 ns
(NB-)Ti:Sa laser CERN/Mainz	Resonance atomic excitation, (NB) spectroscopy 5 GHz (0.8 GHz)	680–950 nm 340–475 nm 210–315 nm	6 W (fundamental) 1 W SHG 0.15 W THG,FHG	30–50 ns

Table 19.1: Design parameters for the laser system required for RILIS [Rothe et al., 2016]

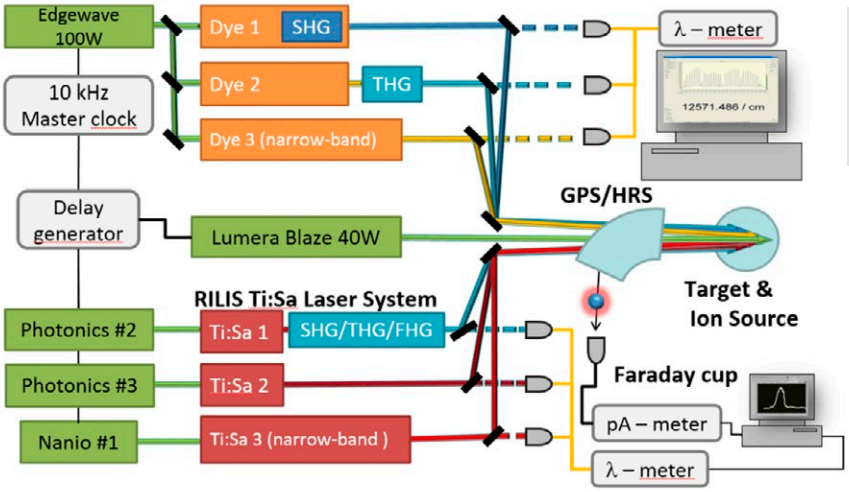

Figure 19.2: Schematic layout of a RILIS Laser system used for RILIS@ISOLDE [Fedosseev, Kudryavtsev and Mishin, 2012]

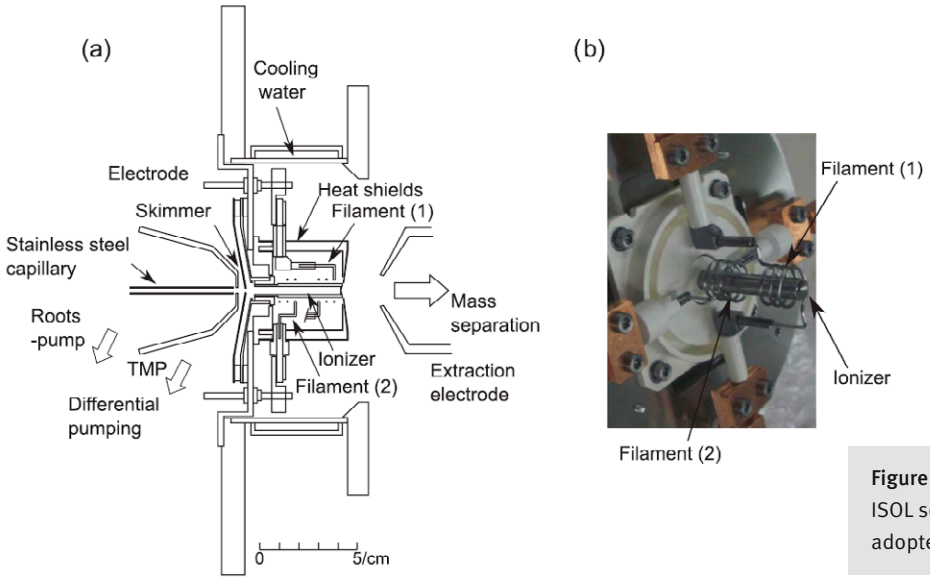

Figure 19.3: The surface ionization ISOL source operated at JAEA, adopted from [Sato, 2013]

The ionization efficiency depends mainly on the surface temperature, the electron work function of the surface material and on the ionization potential of the atoms. The plasma formation effects on the surfaces have to be considered if larger amounts of various species are simultaneously inside the surface ion source. High electron work function materials, such as tungsten, tantalum or rhenium are preferred. A further chemical separation can be achieved based on the adsorption properties of the atoms on the surface [Kirchner, 1992].

19.3 Ion Extraction

19.3.1 HV-Extraction

The entire Ta-target is powered to the desired extraction voltage of about 30 kV. The particular shaping of the extraction tube (left in Figure 19.4) and extraction lens (see e.g. Figure 19.3) with 10 mm diameter helps to provide a linear extraction behavior with a homogeneous electric field at the extraction aperture. The distance between the extraction lens and the transfer line emerging from the target can be adjusted during the commissioning process. Figure 19.4 shows the emittance and phase space of ions extracted by an extraction cone 5 mm inner diameter (at ground potential) from the target exit tube of inner diameter of 1 mm (at potential +30 kV).

The extraction of the Tb-Ions was modelled assuming that the partial pressure of Tb atomic gas drops linear from the target-side to the extraction-side. A distribution of Tb-Ions following such a linear density distribution was tracked through the extraction potential in order to obtain an estimate of the emittance and divergence of the Tb ion beam (see Figure 19.4). The calculations were performed using ANSYS/Maxwell 2D and RELAX3D [Houtman, 1994]. For larger ion currents, space charge effects will broaden the ion emittance form the source. So far, best extraction results have been obtained with ion currents below 100 nA at CERN ISOLDE. One possibility that is foreseen to be checked in simulations is to position the optical extraction directly into the target chamber. This would allow for a shorter transfer-ionizer tube connected to the target with a higher temperature on its entire length. This approach would facilitate

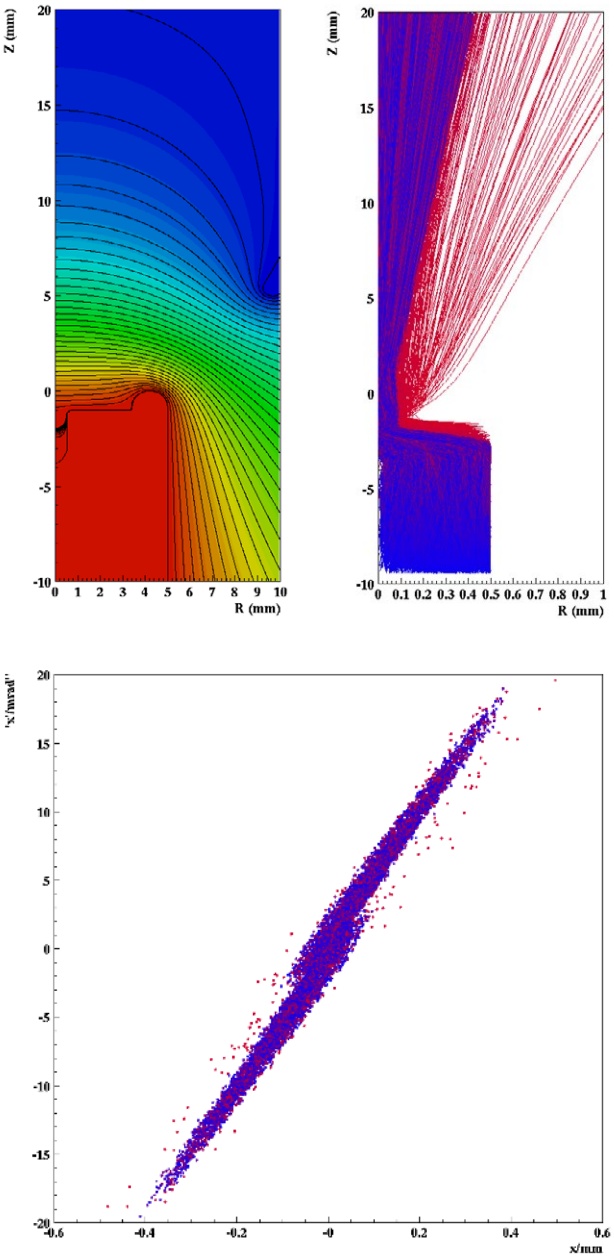

Figure 19.4: Upper left: Electrostatic equipotentials in polar coordinates. Upper right: Randomized trajectories starting in the volume of the extraction tube. The colour indicates the depth within the tube where the respective ion originates. Lower: Density weighted phase space plot of extracted ions. The calculated emittance is 0.072 π mm mrad (unnormalized) at 30 keV, and the rms beam size (divergence) is about 0.12 mm (6 mrad) using 1σ.

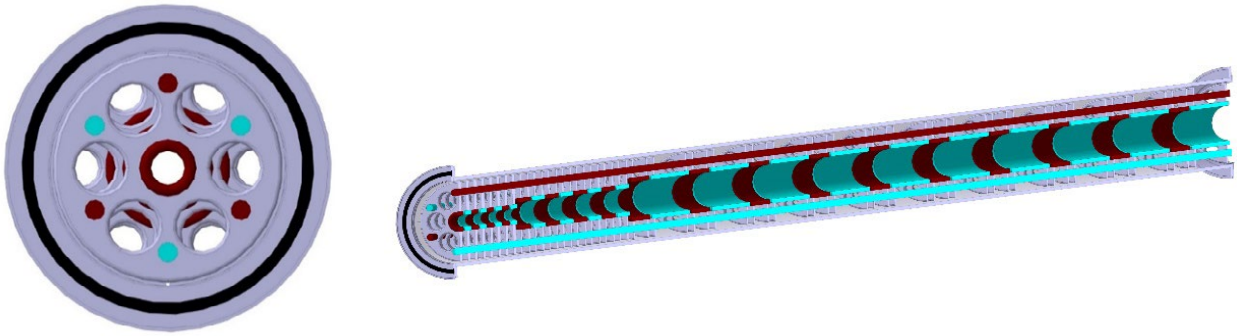

Figure 19.5: The CAD-schematic for the extraction and ion-transport beam line from the target through the inaccessible shielding towards the mass separator. Gate interlock entrance into the mass separator cave will be in place to ensure the high-voltage safety upon access to the device. Non-conducting vacuum beam-line parts will ensure the safe operation of the high voltage extraction system.

the atomic transfer through the tube for atoms with lower volatility and thus larger adsorption interaction potential.

19.3.2 Ion Guide

The ions extracted from the source are guided through a DN100 vacuum tube within the radiation shielding from the target. The tube will be equipped with an electrostatic XY-steerer shortly after the extraction electrodes to compensate possible misalignments (see Figure 19.5). One or more electrostatic einzel-lenses are used to obtain an almost parallel beam at the entrance of the mass separator. The use of a set of several lenses instead of a single lens allows to keep the required voltages of the einzel-lenses in the extraction tube below 10 KV. This reduces the risk of discharges. The beam envelope in this extraction optics and mass separation was assessed using the software packages MinT and TRANSPORT and are shown in Figure 19.6. For the mass separator magnet system commercial products are available (see Section 19.4). For this simulation an idealized magnetic field was assumed. This field bends the Tb beam by 90° into the horizontal direction. An electrostatic quadrupole duplet after the mass separation is then used to achieve good focus and separation at the sampling station. For the mass of 150 AMU a separation of 15 mm for +/– 1 AMU is achieved. A slit after the mass separator can help to stop wrong masses before entering the shielded cells with the sampling station.

The mass separator will be insulated from the ion guiding part using non-conductive vacuum parts. Commercially

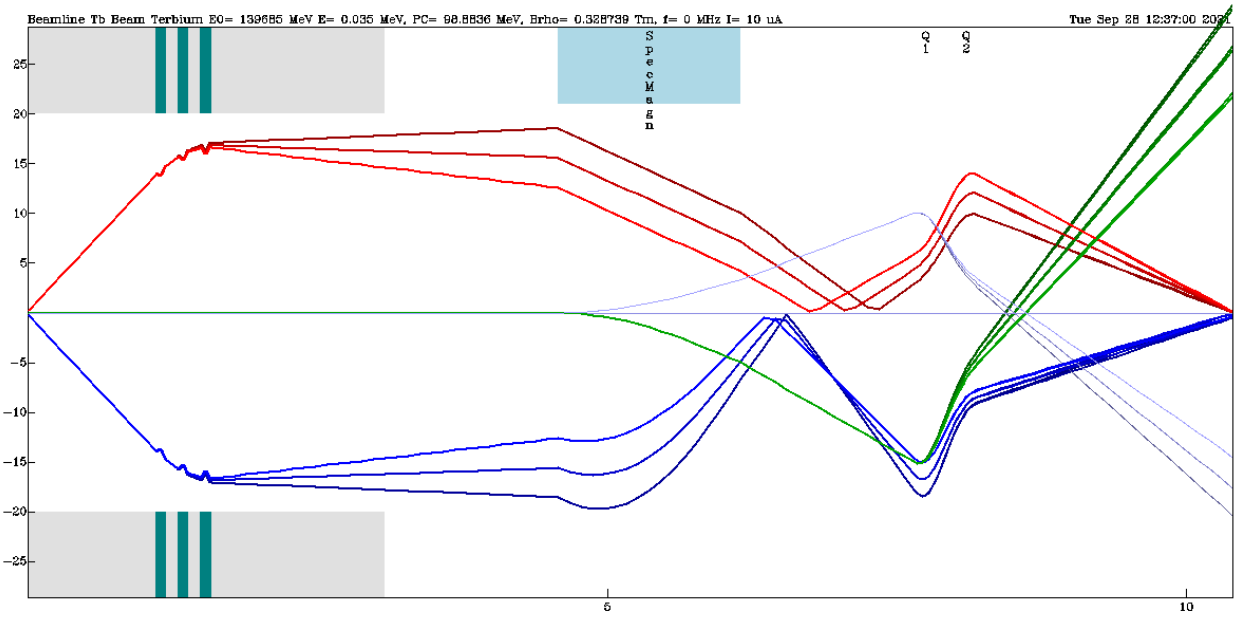

Figure 19.6: The extraction and beam transport optics from target (left) for ^{149}Tb up to the sampling chamber in the shielded ion-sampling cell. The blue lines symbolize the horizontal beam size (2 σ) , the red line show the vertical beam size, the green lines show the dispersion in mm for 0.5 % momentum deviation and the thin blue lines the beam center for a mass difference of 1 AMU from ^{149}Tb. Shown are the envelopes for 5.75, 6 and 6.25 kV voltage for the einzel-lenses shown in Figure 19.5. Horizontal axis in m, vertical axis in mm.

Figure 19.7: Commercial ion beam diagnostic element (UniBeam25-D by D-pace, https://www.d-pace.com)

available, stabilized HV power supplies will be used. An HV interlock system will be installed for safe access into the bunker below the target towards the ion beam line, the mass separator and to the electrical power supply for the target. The ion sampling station will be electrically isolated inside the shielded cells via suitable non-conductive ceramic/glass vacuum parts. The laser injection is provided through an isolated remotely operated mirror systems outside of the shielding block and view ports, thus not connected to the high voltage. The same design of the ion extraction and ion guide will be devised on the offline ion source. Therefore, the HV interlock door/cage system will be provided for the controlled access to this source too.

19.3.3 Diagnostics

Standard devices like commercially available slits are used to collimate the ion beam in front of the mass separator and a faraday cup is used behind the mass separator to diagnose the ion beam intensity. A beam diagnostic element, similar to e.g. the Unibeam25-D (see Figure 19.7) will be used for ion beam visualization and fine-tuning.

19.4 Mass Separator

19.4.1 Design & Separation Quality

We intend to acquire the mass separator with dm/m = 1/1500 mass resolution for the mass separation task as described recently in [Martinez Palenzuela, 2021].

Analyzing Magnet System with Resolution 1:1500 AMU

This design note prepared by D-Pace describes the technical characteristics of such an analyzing magnet, vacuum box, stand, power supply and DC cables as well as relevant ion-optical considerations for the system. The Faraday Cup and Entrance/Exit Slits are separate standard D-Pace products documented elsewhere, however, their specifications are included herein, as they influence the design of the Analyzer System. The technical design parameters are presented in Table 19.2.

TECHNICAL DESIGN PARAMETERS

A plan view cross-sectional layout for the analyzer magnet is shown in Figure 19.8.

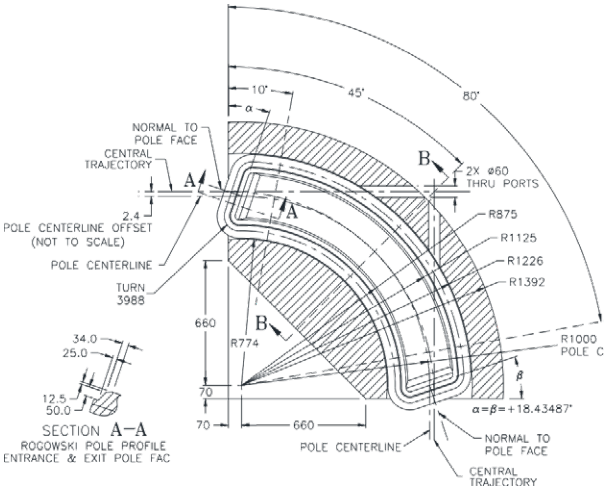

Figure 19.8: Analyzer Magnet plan view cross-section. Dimensions in mm.

1	**Magnet**
	Type: Analyzing Dipole Mass Resolution: Δm/m = 1/1500 Maximum Bend Angle: 90° Bend Direction: Bend Right (for positive charges) Nominal Bend Radius: 1000 mm Magnet Gap: 50 mm Entrance Pole Angle: 18.43487° Exit Pole Angle: 18.43487° Pole Type: Rogowski (on Entrance & Exit surfaces) Iron: C1006 Max Magnet Gap Flux Density: ~1.25 Tesla Peak Yoke Magnetic Flux Density: ≈1.4 Tesla (avoids general iron saturation, local saturation can be tolerated in corners and near holes) Calculated Field Flatness: ±0.001% over good-field region, with 250 mm wide flat pole Cooling Technique: Water-Cooled Maximum Inlet Pressure = 90 psi Nominal Inlet Temperature = 20° Centigrade Coil Maximum Temperature: ‹ 72° Centigrade Thermal Switches: Qty = 1 per coil pancake, located in an accessible region. Alignment: ±25 mm all directions, Spherical Mounted Reflector and Laser Tracker
2	**Power Supply**
	Power Supply Manufacturer & Model: Danfysik 9100 AC Input: 360-440 VAC (400V ± 10 %), 3 phase + neutral, 47-63 Hz DC Output Voltage: 60 V maximum DC Output Current: 200 A maximum DC Current Setting Resolution: 20 bit DAC DC Current Reproducibility: ±10 ppm Current Control Range: 1 – 100 % Remote Control Interface: RS232 ON/OFF Command, Reset Command, ON/OFF Status, Remote Status Output Current, Output Voltage, I Set Value, V Set Value Interlock Status: Over Voltage, Over Current, Over Temperature, Fan Fault, Earth Leakage, AC Fault, Out of Regulation Cooling Technique: Water and/or Air Cabling Cable type: A.W.G. 0000 Rubber Insulation (i.e. Welding Cable)
3	**Slits (D-Pace Standard Product)**
	Nominal Entrance Slit Aperture: 1 mm Horizontal, 50 mm Vertical Nominal Exit Port Slit Aperture: 1 mm Horizontal, 50 mm Vertical Max Beam Power Per Slit: 50 Watts Slit Locations Relative to Magnet: 1500 mm Alignment: Spherical Mounted Reflector and Laser Tracker Technique Technology: Adjustable with Maximum Horizontal Slit Aperture 20 mm. UHV design with 120 °C bake-out followed by dry Nitrogen treatment and blank-off.
4	**Faraday Cup (D-Pace Standard Product (TRIUMF Licensed)**
	Cup Inner Diameter: 50 mm with slit location proximate to cup entrance. Max Cup Beam Power: 50 Watts Stroke Length: 75 mm Technology: UHV design with 120C bake-out followed by dry Nitrogen treatment and blank-off.
5	**Vacuum Box**
	Vacuum capability: Ultra High Vacuum (UHV) Material: SS316, 3 mm wall thickness. Flange Type: Conflat with metals seals. Entrance, Exit and Through Port Flange centers located at 2.4 mm positive “x” relative to pole centers to account for Rogowski Fringe Field. Vacuum Chamber vertical gap: 42 mm clear gap, 48 mm outside height dimension Through Port: Qty = 2, Located at 180° to Entrance/Exit Port with Conflat flanges. Bake-Out: 300C followed by dry Nitrogen Treatment followed by blank-off. Blank-Offs: Each port blanked-off for transportation Beampipe/Bellows: Integrated SS316 beampipe/bellows required at magnet upstream and downstream to connect magnet vacuum box to upstream and downstream slits. UHV vacuum technology, conflat flanges with metal seals, 300 °C bake-out followed by dry Nitrogen treatment & blank-off. Baffles: Constructed with SS316 and to be included in interior of magnet vacuum box. One baffle to protect inner radius wall of vacuum box, other baffle to protect outer radius wall of vacuum box. Baffles are to have spot-welded fins to stop any ion grazing-angle reflections. Baffles are to be remove-able for cleaning purposes, and then re-locatable.
6	**Support Structure**
	Concept: A single support structure shall be designed to support the magnet with ±25 mm adjustability in all directions. Separate structures to support Slits and Faraday Cup shall also be designed with ±25 mm adjustability in all directions. The key aspects are the high precision alignment of the slits relative to the magnet. This alignment shall be accomplished with a Spherically Mounted Reflector technique and a Laser Tracker. The Slit apparatus, Faraday Cup apparatus and the Magnet shall be provided with accurately machined flats for precisely located mounting of the Spherically Mounted Reflectors.

Table 19.2: Technical design parameters of the analyzing magnet and power supply of the mass separator

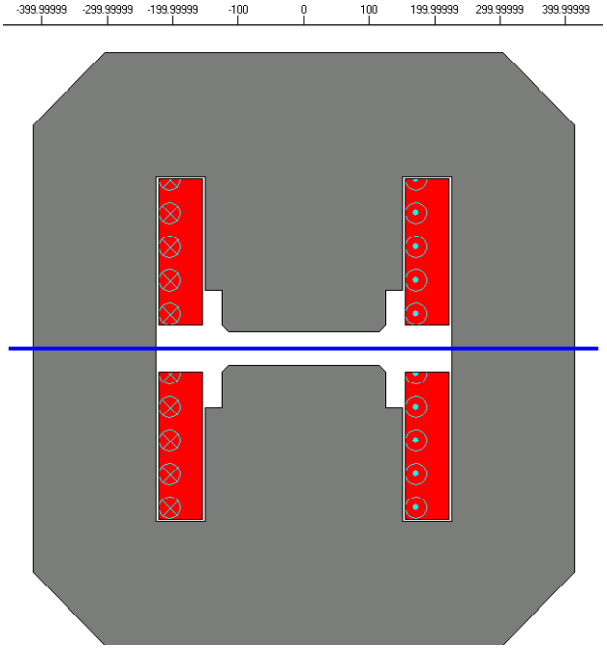

Figure 19.9: Analyzer Magnet 2D Magnetic Model. Dimensions on top are in mm. Gap 50 mm, pole width 250 mm, and yoke widths proportioned to accommodate flux as near as possible to that of 3D operation.

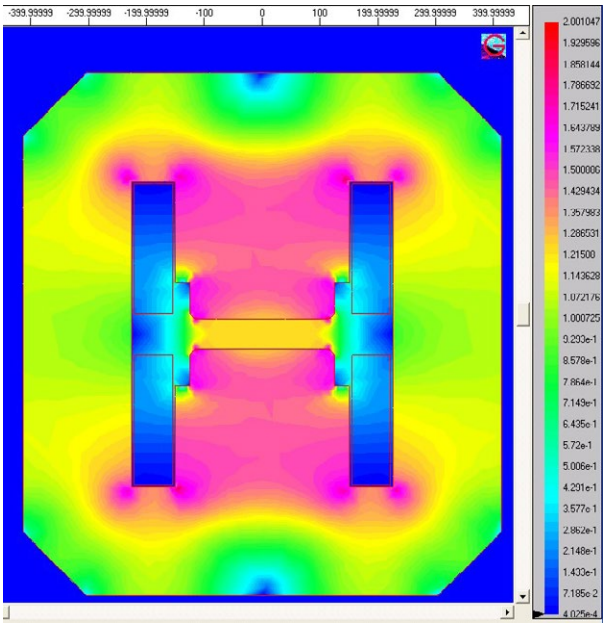

Figure 19.10: Magnetic Flux in Color with the color scale in Tesla, $B_{Max\text{-}A1nrs}(0,0,0)$ = 12468.5 Gauss, $I_{Max2D\text{-}A1nrs}$ = 187.065 Amps. Notice that the central pole is just entering into saturation at ~1.5 Tesla.

2D MAGNETIC FIELD MODELING

Figure 19.9 and Figure 19.10 illustrate the magnet entrance and results of 2D Magnetic field modeling in a side view using the software product used is called *Gemini* from Infolytica.

3D MAGNET FIELD MODELING

The Analyzing Magnet was modeled using the 3D Magnet Modeling code called "OPERA" from Vector Fields (see Figure 19.11). It is immediately evident that the Rose Shims were not required as the field is extremely flat within ±22 mm

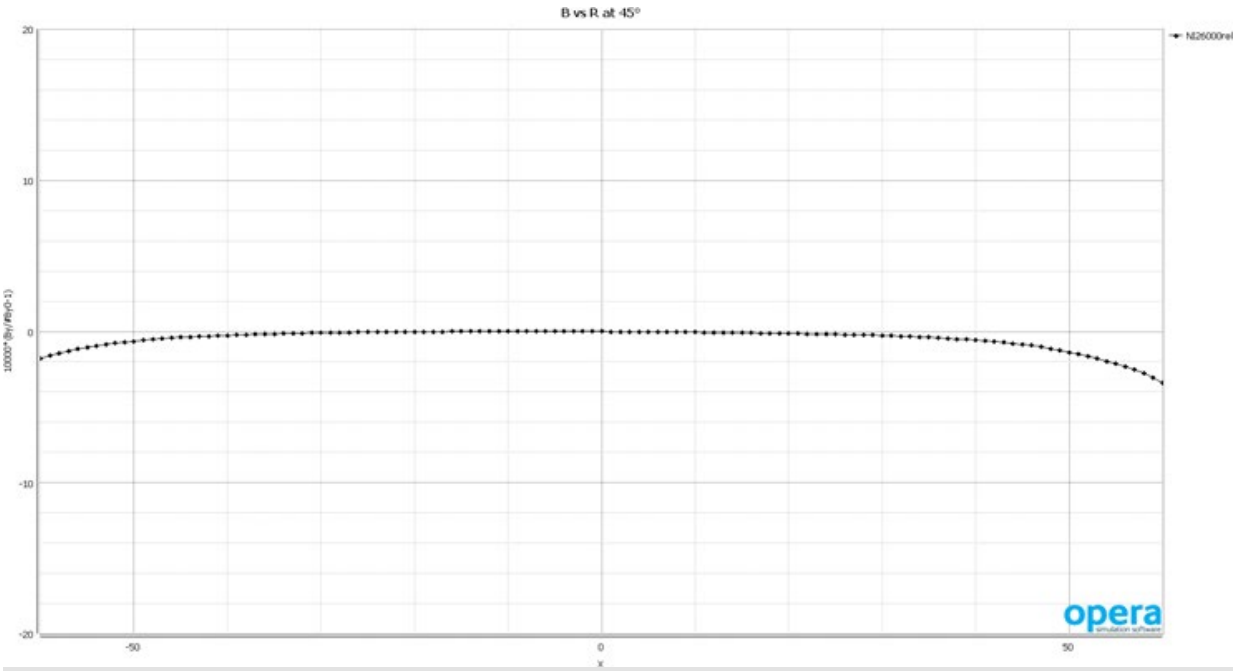

Figure 19.11: Magnet field plotted in the radial direction in the bend plane at the 45-degree bend point. Y-axis is 10000*(By(R)/By(0) – 1), and X-axis is in the radial direction transverse to the beam in mm. Note that the field is very flat over the good field region and is flat to ± 0.001% over ± 30 mm.

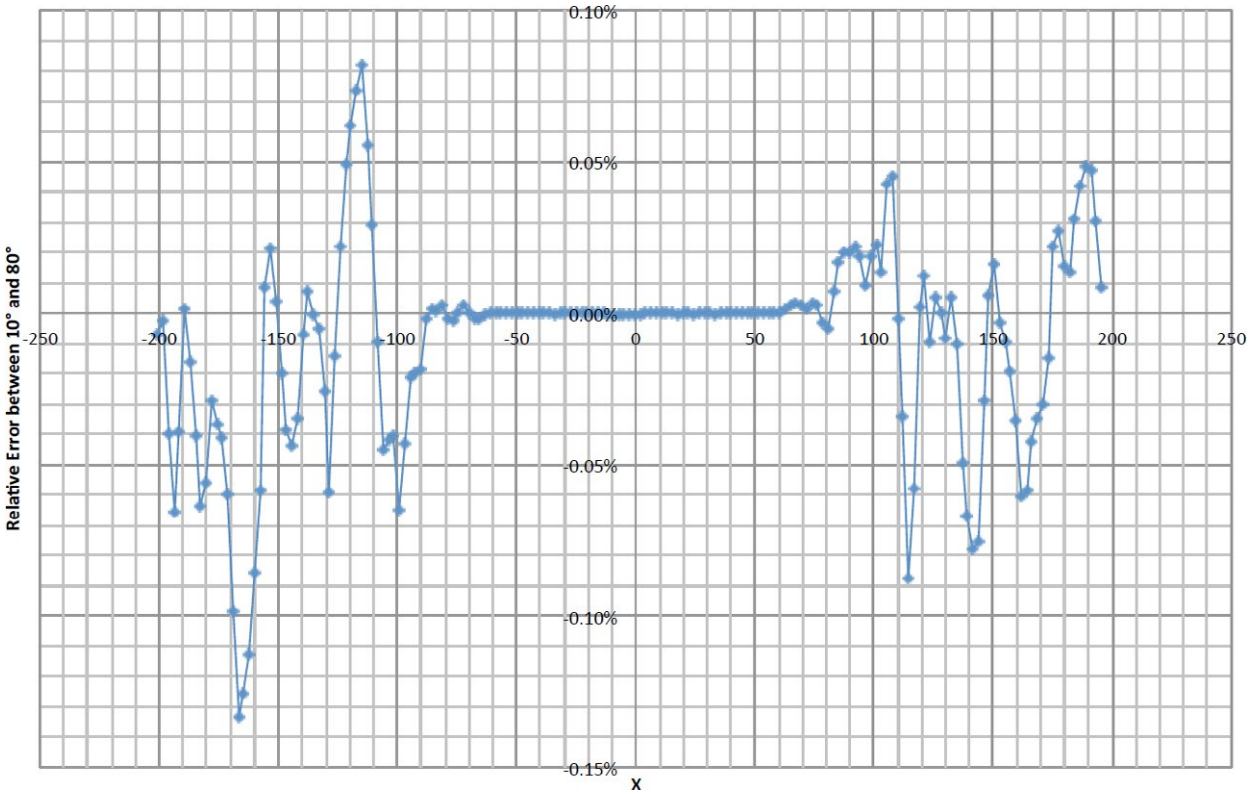

Figure 19.12: The relative error between numerical solutions for the magnetic field at the 10° and 80° angular bend points. The X axis is transverse to the central trajectory and in the bend plane. Dimensions are in mm.

transverse to the central trajectory in the bend plane. Figure 19.11 shows the difference between magnetic fields at transverse radial distances between ± 60 mm and the central magnetic field at the 45° bend point (i.e. at the center of the magnet). This plot shows that the field is flat to within 0.001% at distances transverse to the central trajectory of up to ± 30 mm. Figure 19.12 shows the relative error between field plots at the 10° and 80° angular bend points through the magnet. There is excellent agreement in the magnetic field solutions between ± 60 mm transverse to the central trajectory.

Figure 19.13 shows the 1500 AMU 50 keV central trajectory tracked through the 3D magnetic field. The entrance and exit beamline central axes must be offset by 2.4 mm transverse to the pole centers in the positive x direction in order to follow the nominal radius of curvature as closely as possible (this effect is due to the exit/entrance fringe fields and is typical).

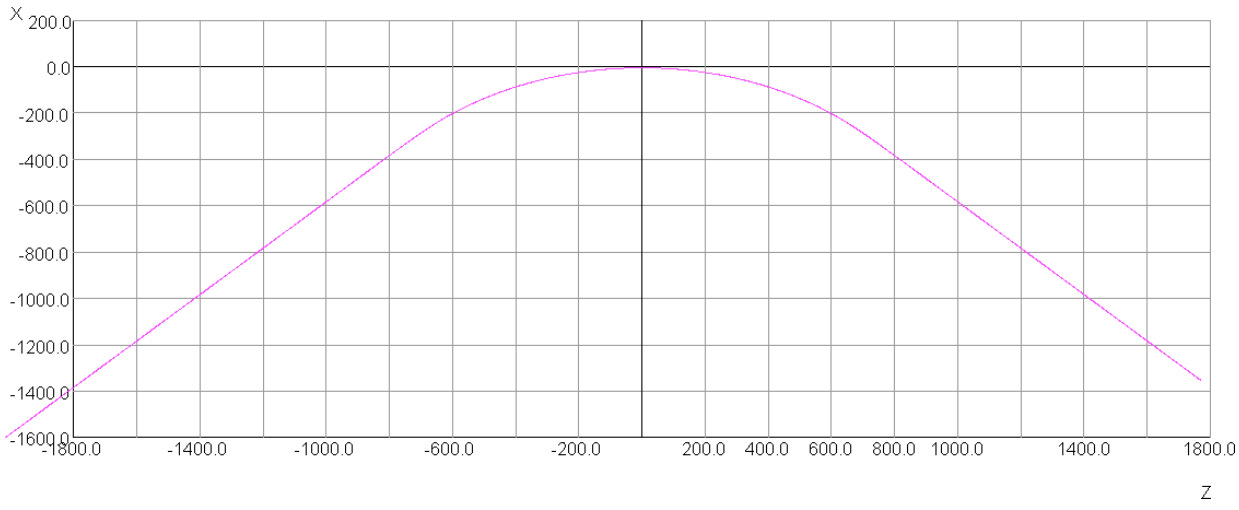

Figure 19.13: Analyzer Magnet plot showing the central trajectory in the median plane as particle tracked through the 3D magnetic field model in the software "Opera".

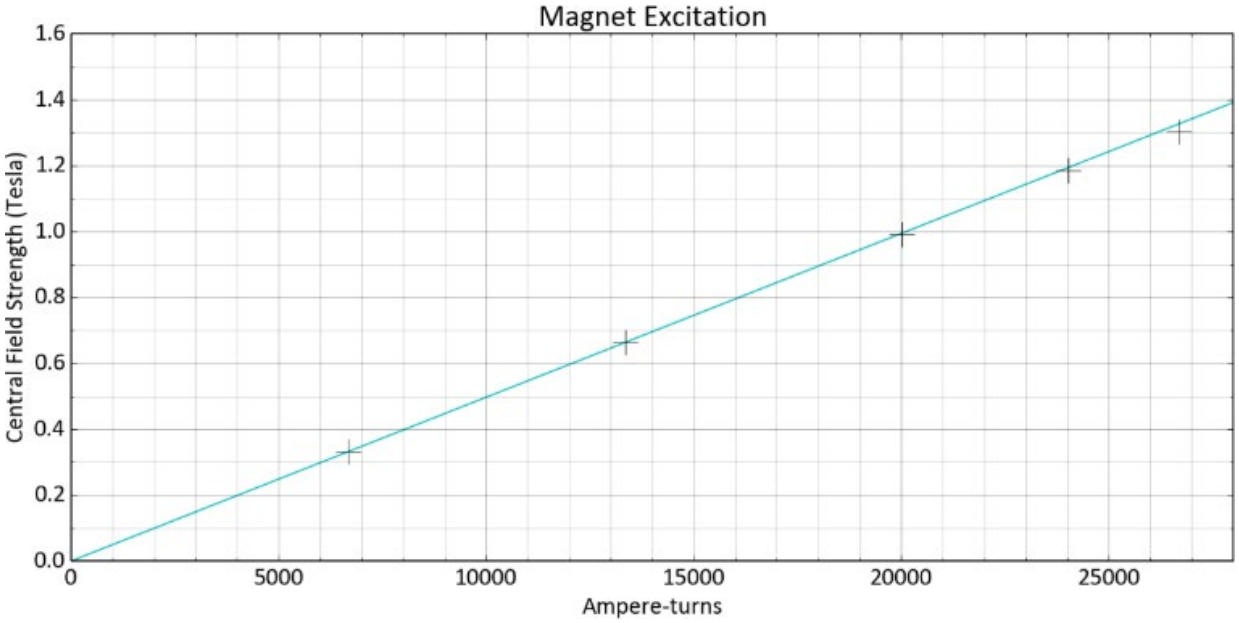

Figure 19.14: Analyzer Magnet plot showing the B0 excitation of the magnet using 3D Magnetic Field Modeling. The Y axis is the field at the centre of the magnet in units of Tesla, and the X axis is in Amp-Turns.

EXCITATION

Figure 19.14 shows the field strength at B0. The value of B0 = 1.24685 Tesla must be achieved for a 1500 AMU 50 keV molecule, and this is achieved with 25427.3 Amp- Turns. This excitation plot from "Opera" 3D Magnetic Field Modeling shows that the peak field necessary for 1500 AMU can easily be achieved.

The peak B0 can be achieved well within the power supply specifications of Vpsmax = 60 VDC, and Ipsmax = 200 Amperes. The magnet power consumption is reasonable. This is a good choice based on 3D magnetic field modeling in OPERA.

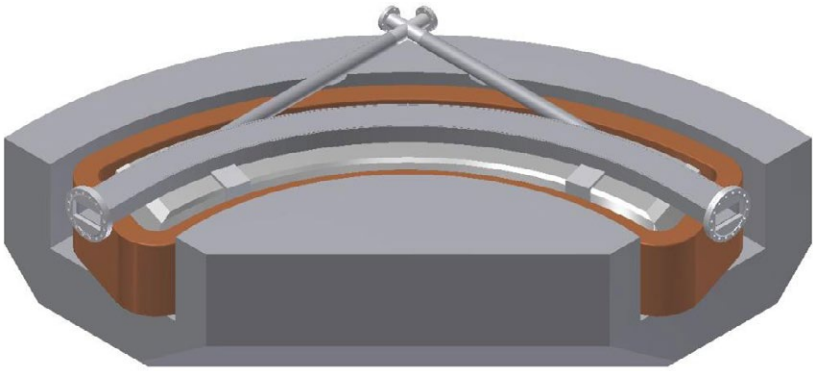

Figure 19.15: Analyzing Magnet. Isometric View of bottom half of magnet iron (C1006), and also showing the SS316 UHV vacuum box with conflat flanges. Remove-able (for cleaning) baffles to protect the inner radius wall, and outer radius wall, respectively, are installed inside of the vacuum box.

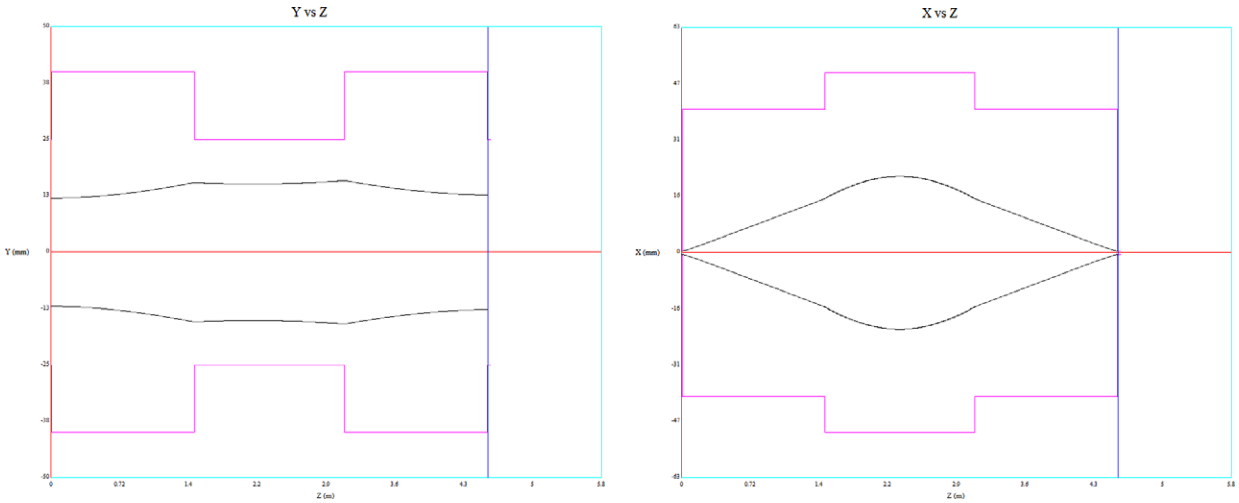

Figure 19.16: The most divergent beam that the system can analyze in the horizontal plane at a resolution of 1:1500 is shown. Input is (x = 0.5 mm, x' = 0.01 radians) at entrance slit. Right: The largest beam specifications in size and divergence that the system can transport in the vertical plane while at the same time analyzing the beam in the horizontal plane at 1:1500. Input is (y = 12 mm, y' = 0.0065 radians) at entrance slit. 1500 mm drift distance between entrance slit and analyzing magnet and between analyzing magnet and exit slit have been determined as key as well as +18.43487° for the analyzing magnet entrance pole face rotation angle as well as exit pole face rotation angle.

VACUUM CHAMBER

A stainless steel vacuum chamber is featuring viewports for introducing the collinear laser excitation parallel to the ion beam into the hot ion-source cavity (see Figure 19.15).

ION-OPTICAL CALCULATIONS

Charged Particle Beam

Ion Mass:	Up to 1500 Atomic Mass Units
Ion Charge State:	+1
Maximum Kinetic Energy:	50 keV
Maximum Beam Power:	50 Watts
Beam axis height:	1500 mm above floor level

Figure 19.16 (left) shows the most divergent beam that the system transports and analyzes in the horizontal bend plane at a resolution of 1:1500. The entrance slit is set with a horizontal opening of 1.0 mm, and the exit slit is also set

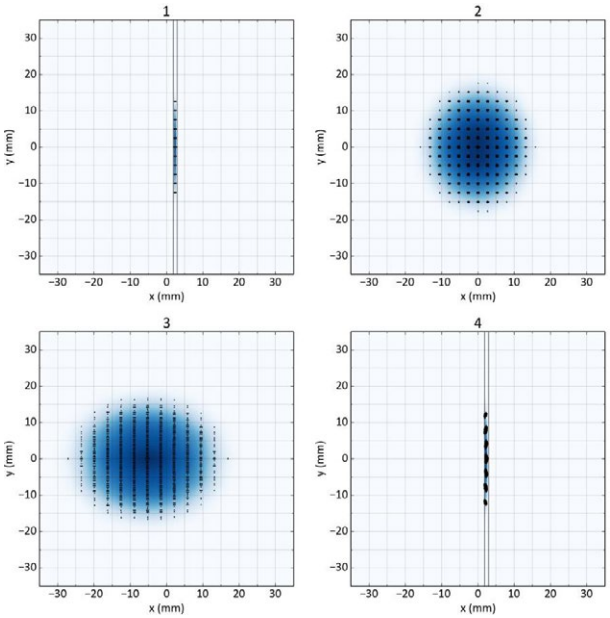

Figure 19.17: Beam Specification at Entrance Slit: (x = ± 0.5 mm, x' = ±10.5 mrad, y = ± 15 mm, y' = ± 6.8 mrad) at 1500 AMU and 50 keV. Locations : [1] The Entrance Slit 1500 mm upstream of effective edge of magnet, [2] The magnet entrance at the effective edge, [3] The magnet at the mid-point or 45 degree bend point, [4] The Exit Slit 1500 mm downstream of the effective edge of the magnet.

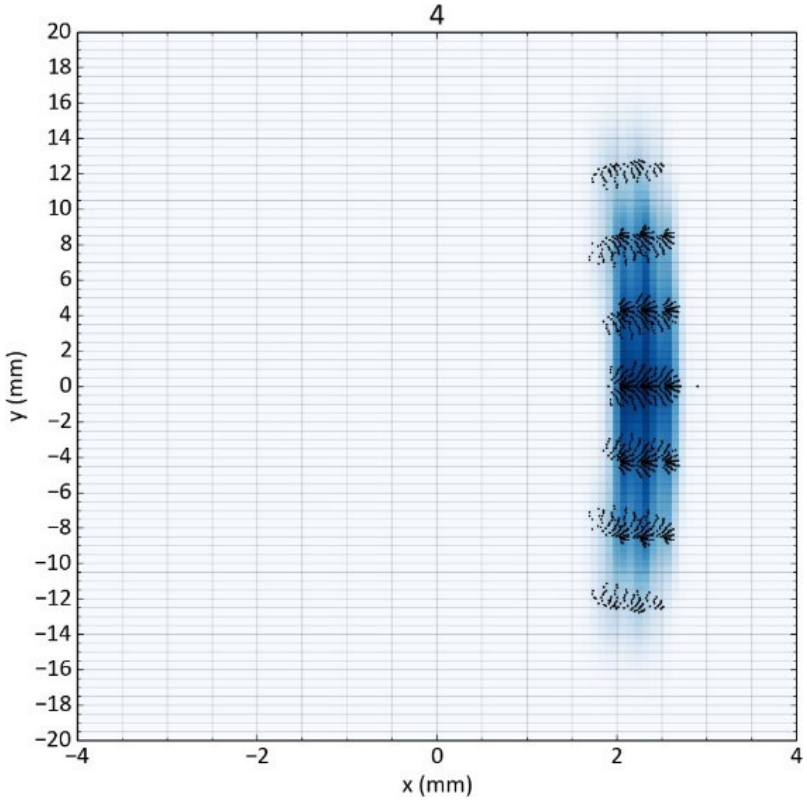

Figure 19.18: Beam Specification at Entrance Slit: (x = ± 0.5 mm, x' = ±10.5 mrad, y = ± 15 mm, y' = ±6.8 mrad) at 1500 AMU and 50 keV. Location [4]: The Exit Slit 1500 mm downstream of the effective edge of the magnet.

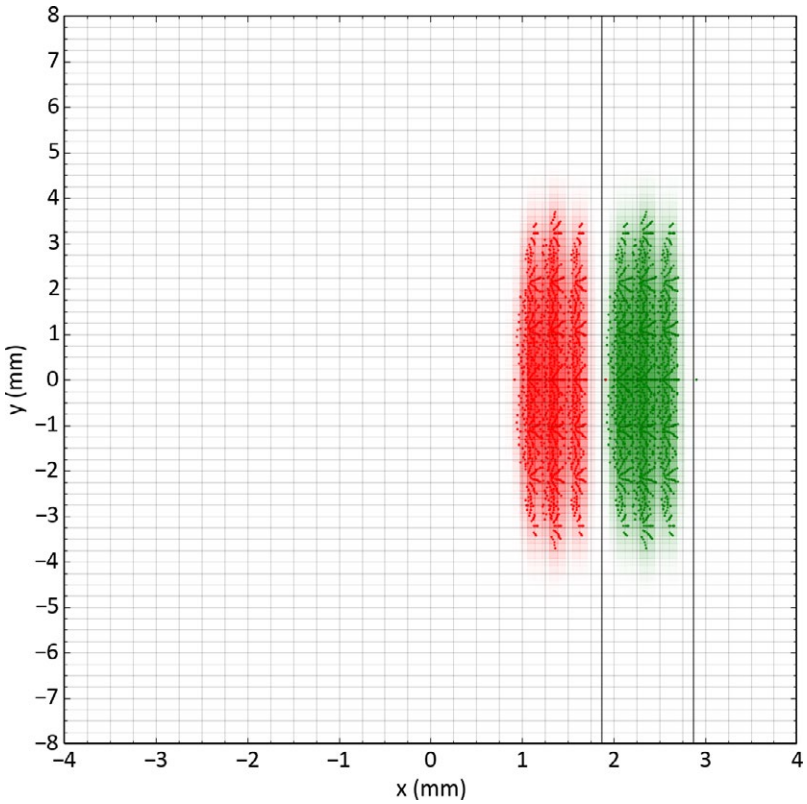

Figure 19.19: Green Beam Specification at Entrance Slit: (x = ± 0.5 mm, x' = ±10.5 mrad, y = ± 15 mm, y' = ±6.8 mrad) at 1500 AMU and 50 keV. Green Beam Specification at Entrance Slit: (x = ± 0.5 mm, x' = ±10.5 mrad, y = ± 15 mm, y' = ±6.8 mrad) at 1499 AMU and 50 keV. Location: The Exit Slit 1500 mm downstream of the effective edge of the magnet. Note the separation of two masses will be improved using an additional drift length.

with a 1.0 mm horizontal opening. The largest beam extents that we are permitting in the horizontal plane are ±22 mm within the magnet. This defines the horizontal good field region. Figure 19.16 (right) reveals the largest beam dimensions that the system can transport in the horizontal plane, respectively, while maintaining 1:1500 resolution. This vertical good field region is ±16 mm.

"OPERA" PARTICLE TRACKING THROUGH 3D MAGNETIC FIELDS
A 1500 AMU 50 keV beam was particle tracked through the 3D "OPERA" Magnetic Field Model see Figure 19.13. The beam was represented in two ways, which are overlaid on top of each other in each plot. These were: (1) The phase space of the entrance slit beam was represented as a grid of discrete "black" beamlets populating the phase space, and (2) the phase space of the entrance slit beam was also represented as a Gaussian distribution with intensity varying as shades of blue. One can see that the beam is contained within a 1 mm slit at the exit slit position. The entrance and exit slit are offset by 2.4 mm relative to the pole center. Figure 19.18 shows the 1500 AMU 50 keV beam at the exit slit position in larger detail.
Figure 19.19 establishes that the magnet resolves a 1500 AMU 50 keV molecular ion beam from a 1499 AMU 50 keV molecular ion beam that passes through a 1 mm entrance slit aperture (in the horizontal plane) 1500 mm upstream of the effective edge of the magnet entrance, and a 1 mm exit slit aperture (in the horizontal plane) 1500 mm downstream of the effective edge of the magnet exit.

19.4.2 Offline Operation of Mass Separation

The installation of the additional offline ion source is highly desirable for commissioning and ion beam development. Installation of a 1:1 copy of the thermal ion source including RILIS is intended to exercise the source operation offline without activation products, but by injecting low-level radioactive tracers to be able to determine the yield balances for the ionization and mass separation including the sampling. The ions are transported from this source to a 90° quadrupole bend (see Figure 19.20) placed in the entrance ion beam line of the mass separator in front of the entrance slit. Thus, if the quadrupole is switched on, the ion beam from the off-line source is bent and injected into the separator. For normal on-line operation the quadrupole will stay switched off to pass the on-line generated ions to the mass separator. Thus, the mass separation can operated off-line particularly in shut down periods also for the highly desired enrichment of stable target isotopes for isotope production

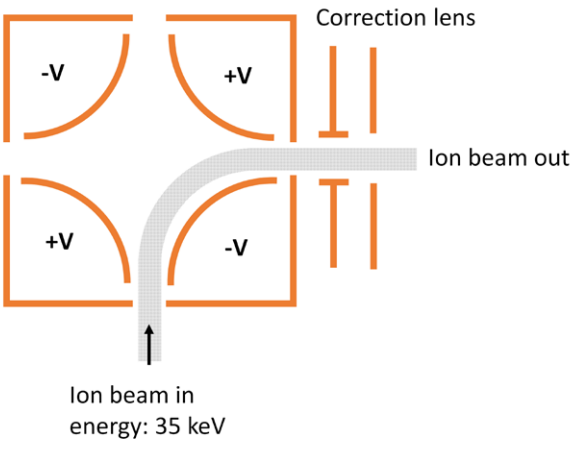

Figure 19.20: Example 30 kV quadrupole switch from DreeBit (https://www.dreebit-ibt.com/beam-optics.html).

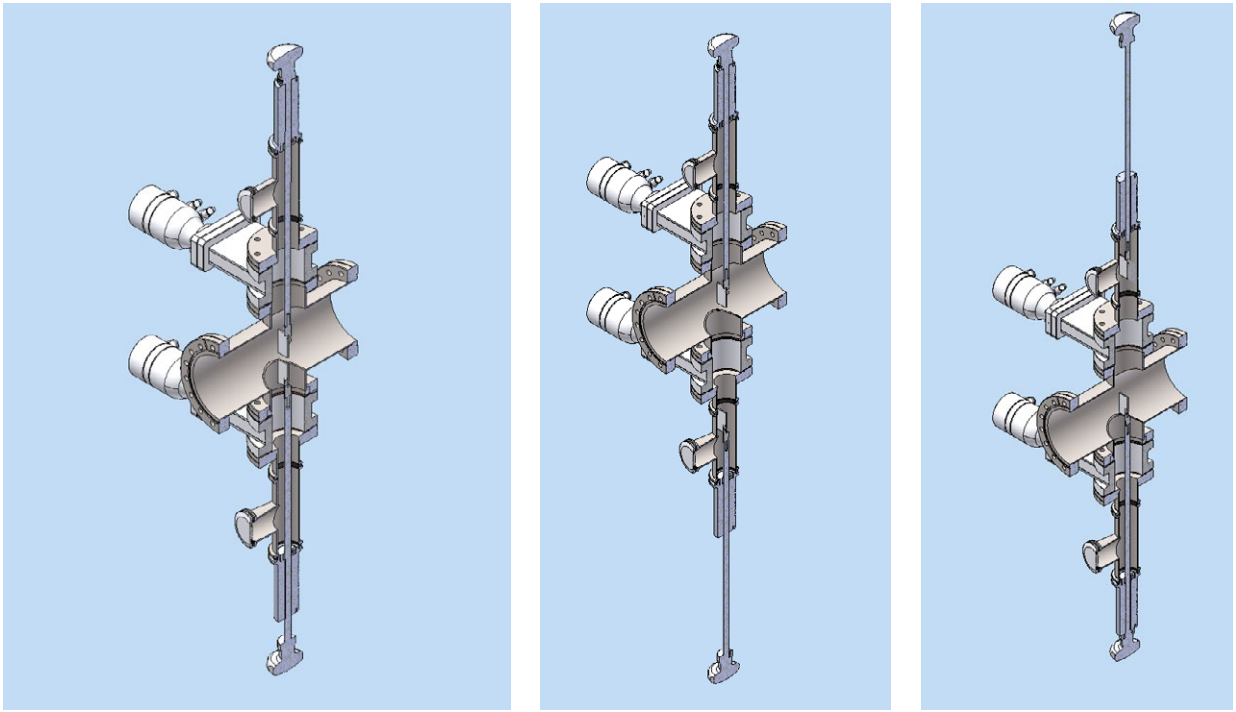

Figure 19.21: Principle scheme of the on-line ion sampling stage with two implanters (both in and in & out position) placed upstream behind the faraday cup (that is used for magnet and ion beam tuning) in the ion beam line behind the mass separator exit. This stage is placed in the shielded cell dedicated for ion sampling.

using the IP2 72 MeV protons and the SINQ Neutron Irradiation Facilities (NIS). For this part the extraction high voltage, the electrical heating, the ion guide principle and, thus, the safety measures are the same as for the on-line source.

19.4.3 Sampling Station

The mass-separated ions will appear at the focal plane of the mass separator divided into lines of 1 cm length and 1 mm width (see Figure 19.19). The ions are guided to the central shielded cell, which is dedicated entirely for sampling/collection purposes (see shielded cells Chapter 20). Thus, the available room for the ion implantation station shall be enough. The ions arrive at 30 keV energy, with a maximum intensity of 1 µA current. Thus, a maximum power of 3 mW is deposited on an area given by the ion-optical design of the magnet and the final distance between the sampling cell and the magnet. According to the experiences at CERN ISOLDE the implanter is subject to heavy sputtering and thus to losses of separated material [Sigmund, 1981]. Therefore, further materials research is needed to avoid these effects. However, the compatibility of the materials with the chemical separation is another limiting factor. Hence, physical barriers preventing sputtering or for sampling the sputtered material will have to be developed, particularly when scaling-up the production and thus increasing ion currents. For a dedicated controlled sampling of the activities several water-cooled implanter stages are foreseen to be mounted in the sampling position inside the beam line vacuum for periodic batch-wise sampling and on-line exchange (principle see e.g. Figure 19.21). Each sampling side can be retracted, be vented, and evacuated separately to remove the sampled activities from the vacuum and place a new sampling foil. Not shown is the typical sandwich structure of the implantation sampling, providing a collimator for the product beam and a potential to collect the delta electrons for an exact ion current determination.

19.5 Commissioning of TATTOOS

Apart from the commissioning of the TATTOOS beam line that is described in Chapter 15 the commissioning experiments of TATTOOS are performed in five steps, which can partly be overlapping with the beam line commissioning (D) and also done in parallel (A&B&C).

A: Commissioning of the mass separator with surface ionization and RILIS at the offline ion source;
We will produce samples of radioactive isotopes of Tb in proton induced reactions on Gd targets at PSI's IP2 target station. These irradiated lanthanide samples will be included into a Ta target equivalent to the on-line target and this target will be heated electrically to the temperatures expected for the real target. With simple surface ionization the transport and injection of ions into the mass separator and their collection after mass separation in the collection chamber can be commissioned. Later on, using the commissioned laser RILIS setup the yield increase due to selective RILIS ionization can be demonstrated using the same scheme.

B: Commissioning of the target operation and handling (irradiation & electrical heating & target exchange);
The target operation has to be trained well before beam operation with full access to the target chamber and target environment. Here, the exact and reproducible positioning of the movable target exchange vehicle and its remote docking to the media connections of water cooling, pressurized air and electric connection has to be addressed as well as the scale of vacuum achievable in the target chamber. The handling of targets (mounting, dismounting, storage, extraction) has to be trained in remote handling procedures using the manipulators inside the shielded target exchange cell.

C: Commissioning of the radionuclide sampling station and the radiochemical purification procedure;
Using the mass separated samples produced in commissioning step A the principle operation scheme and procedures will be trained for the discharge of the collected samples from the sampling chamber, the transfer of samples to the radiochemical cells and the remotely operated radiochemical separation. The products will be handled the same way as later the final products including the quality control and labeling procedures using GMP-modules.

D: Online Experiments with pure surface ionization, mass separation and sampling;
If the commissioning procedures A-C reach sufficient reproducibility and safe operation procedures are established first on-line tests can be performed using the on-line target at low beam intensities. These on-line tests could be part of the beam-line commissioning experiments with very low intensities of proton beam. First separations of lanthanide ions will be performed using surface ionization schemes as well as Laser RILIS. On-line radionuclidic yields will be measured to assess the performance of the entire production, release and mass separation scheme. First estimations of true achievable yields will be possible. Further improvements can be deduced and introduced if needed.

20 Radiochemical Separation

20.1 Present Status, Requirements and Constraints, Shielded Cells, Access and Operation

The concept of producing Tb radioisotopes by means of ISOL was demonstrated via spallation of a tantalum target using high-energy protons, followed by ionization of the spallation products and online mass separation [Müller, 2012]. This procedure was performed several-fold at the ISOLDE facility, CERN, Geneva, Switzerland [Müller, Fischer, 2014; Müller, Reber, 2014]. The mass-separation process enabled the production of the desired product, along with its isobaric side bands. Chemical processing was, therefore, necessary to separate the desired product from the collection matrix, as well as isobar and pseudo-isobar impurities. Due to laboratory restrictions and internal guidelines, only limited activities were produced at ISOLDE. In principle, this production route at TATTOOS could ensure the making of terbium radioisotopes available in significantly larger quantities.

Chemical separation of ^{149}Tb, ^{152}Tb and ^{155}Tb (see Figure 20.1) produced at ISOLDE, CERN, was experimentally demonstrated and published in 2012 [Müller, 2012] and, subsequently, improved. The radionuclides were separated from the collection matrix (zinc layer sputtered on gold foil) as well as isobaric impurities using a single-column system to provide the desired radionuclide in α-hydroxyisobutyric acid (αHIBA) at pH 4.7. This formulation enabled the use of the terbium radionuclides for direct radiolabelling by adding the targeting agent (e.g. DOTA-folate) to the formulation of the radionuclide in question. Later, the option of employing a similar separation concept as previously developed for ^{161}Tb [Gracheva, 2019] was also shown to be feasible for the separation of ^{149}Tb to enable its formulation in dilute hydrochloric acid (0.05 M HCl) [Gracheva, 2020], suitable for radiolabelling procedures [Umbricht, 2019].

The concept has had its limitations, as the irradiation, spallation process and radioisotope collection would be performed at ISOLDE, CERN, after which the collection foils were shipped to PSI for chemical separation. Taking short half-lives and physics experimental halls into consideration, limited activities could be obtained and processed for preclinical evaluation. The concept of TATTOOS will have all the necessary steps on one site. It is envisaged to develop effective separation methods to produce radionuclides in high yields, based on the vast experience and expertise available at PSI. A laboratory, as part of this proposed facility, will be located close to the site of collection, containing shielded cells to chemically separate the desired product. The production of Tb radiopharmaceuticals under GMP conditions is planned to be performed at PSI and the use of the new

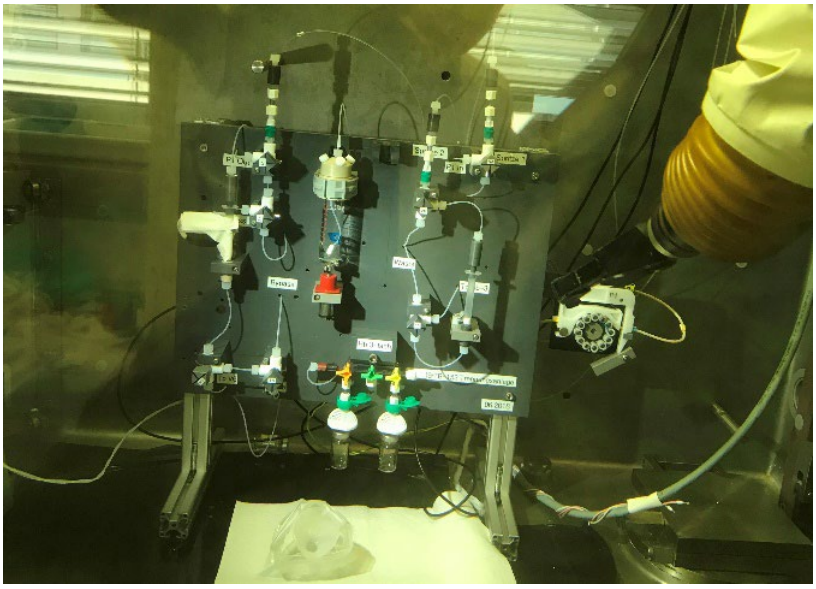

Figure 20.1: Tb-149 chemical separation system within a shielded cell and handled by manipulators.

Existing facilities for medical radionuclides in CH	Institution	Diagnostic radionuclides	Therapeutic radionuclides
18 MeV cyclotrons	USZ, HUG, Insel/Uni Bern, ETHZ	^{11}C, ^{13}N, ^{15}O, ^{18}F, ^{44}Sc, ^{61}Cu, ^{68}Ga	
Injector II	PSI	$^{43/44}Sc$, ^{64}Cu, $^{155}Tb^{+}$	$^{67}Cu^{+}$, ^{165}Er, ^{167}Tm
SINQ	PSI		$^{47}Sc^{+}$, ^{161}Tb, ^{169}Er, ^{175}Yb
IMPACT/TATTOOS including online and offline mass separation	PSI	^{152}Tb, ^{155}Tb	^{149}Tb, ^{167}Tm, ^{211}At, ^{223}Ra, ^{225}Ac, ^{225}Ra (for $^{225}Ra/^{225}Ac$ generators). ^{153}Sm*, ^{175}Yb*, ^{169}Er*, ^{67}Cu, ^{47}Sc

Table 20.1: List of radionuclides produced at sites in Switzerland, along with those proposed as part of the IMPACT/TATTOOS proposal.

* requires offline mass separation

\+ nuclides produced elsewhere that can be purified by offline mass separation in TATTOOS during down-times of the accelerator.

laboratory at Center for Radiopharmaceutical Sciences can be utilized for this purpose. The Tb-radiopharmaceutical can then be shipped to clinics throughout Switzerland or neighbouring countries. The radionuclides currently of interest, as part of this proposal, are listed in Table 20.1, with the calculated expected production yields (extraction and adsorption losses as well as losses during ionization and ion transport not taken into consideration) listed in Table 20.2.

			TATTOOS 100 µA, 590 MeV	
Radionuclide			A, GBq	A, GBq
Element	M	$T_{1/2}$	Production 12 h Ta	Production 6 d UC_x
Tb	149m+g	4.2 m/4.118 h	2630	12.5
Tb	152	17.5 h	625	44
Tb	155	5.32 d	67.3	20
Tm	165	30.06 h	2930	20.8
Er	165	10.36 h	977	30.3
Ac	225	9.92 d		150
Ra	225	14.9 d		30.3
Ac	225	9.92 d		175
Ra	225	14.9 d		26.26
At	211	7.214 h		500
Ra	223	11.43 d		80
Rn	211	14.6 h		500
Cu	67	61.83 h	2.58	278
Sc	47	3.3492 d	1.2	16.60
Sc	48 - g	43.67 h	1.56	13.60
Sm	153	46.284 h	520.00	522.00

Table 20.2: Calculated production yields (100 µA, 590MeV proton beam) for a selection of medically relevant radionuclides to be obtained from TATTOOS using a tantalum (12 h irradiation) and a uranium (6 d irradiation) target, respectively.

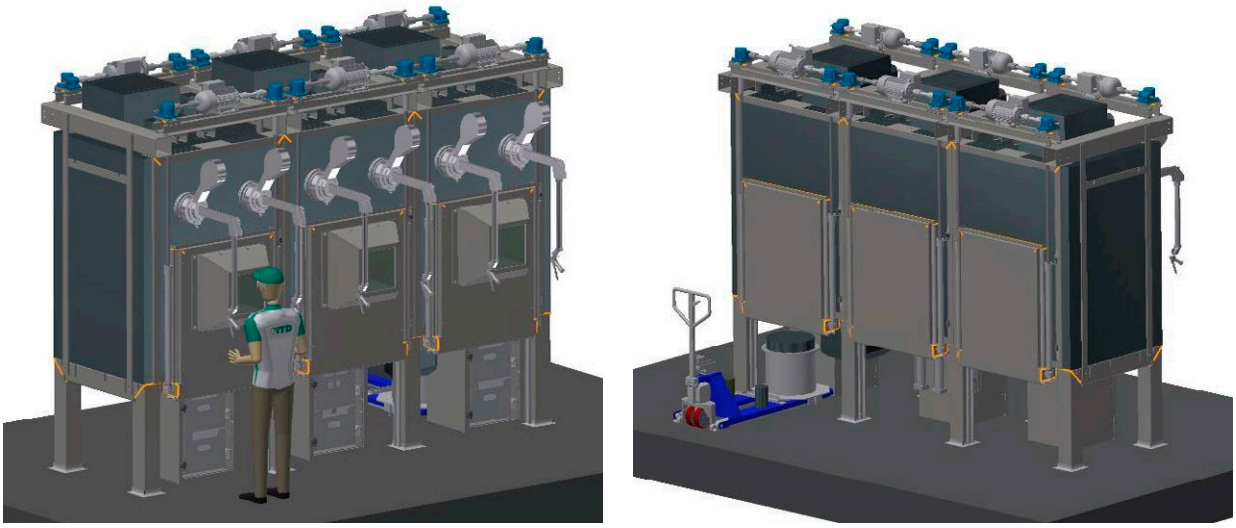

Figure 20.2: Sketch of the three shielded cells used for ion collection (middle) and radiochemical processing (left and right).

20.2 Radionuclide Transport

The radionuclidic product will be transferred to the GMP laboratory (which will require 2 × 5 cm Pb shielded containers), where the activity will be dispensed for particular requests/orders from clinics or research facilities. The dispensing will involve the radiolabelling of the radionuclide in question to a specific ligand and sending the product out as a radiopharmaceutical. Pharmaceuticals are sent out in vials, which are packed in Pb pots, encased in an Al container (or using a W-shielded pot instead of Pb), and placed in a Type A box. This box will be sent out to the users. Should 1 GBq Tb-149 (one patient dose shipped over a long distance) be shipped in a W-shielded pot and sent in a Type A box,

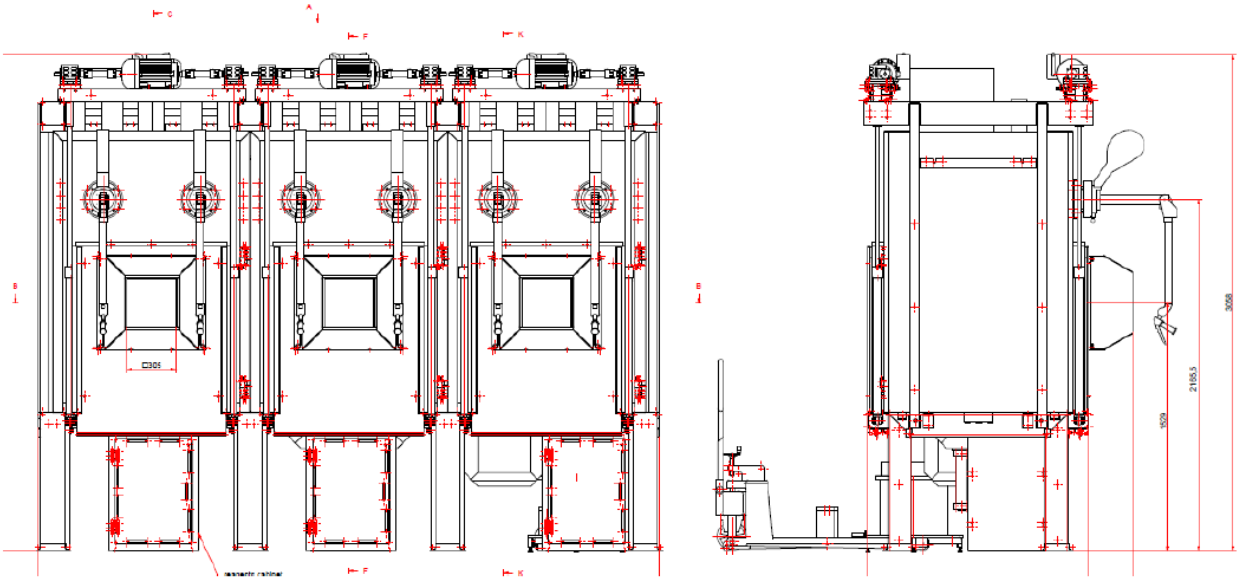

Figure 20.3: The dimensions of the shielded cells used to estimate the space requirements.

the dose rate is ‹10 uSv/h at 1m distance, indicating Yellow II shipping conditions, with a Transport Index of ‹1. The logistics will be handled in-house, with staff specifically trained in this regard. Dangerous Goods forms are filled in and the radioactive transport regulations (ADR) adhered to when transporting by road or air. Based on current regulations, a maximum activity of 800 GBq Tb-149 may be transported as a Type A package.

20.3 Shielded Cells for Chemical Processing

Three shielded cells, connected in series, containing manipulators and different ports, will be installed in the alpha zone area for the installation of the ISOL collection and the chemical processing of the collected radionuclides (on the lower ground floor of the building complex). The center shielded cell will be the collection cell and have direct connection to the beam line from the mass separator. The other two cells, connected to the collection cell on either side, will be utilized for the chemical processing of the radionuclides.

The shielded cells will be designed and built by an external manufacturer that specializes in the construction of custom-designed cells. A principle sketch of the shielded cell concept is presented in Figure 20.2.

The shielded cell complex will consist of the following:

- 3 cells, 150mm lead shielding, with the exception of the collection cell, which is shielded with 200 mm lead;
- The external dimensions of the shielded cell complex (see Figure 20.3) is (WxD) ~5600 × 2300 mm, with a total weight of ~80 t. The exact dimensions will be re-determined in the final design phase.
- Cells interconnected via double-door locks;
- Shielded interim storage positions;
- Shielded ionization chamber beneath the floor of the cell;
- Non-shielded external ventilated cabinet;
- Each cell will be equipped with a front sliding door (on the operation side (see Figure 20.4)), electrically operated, with safety shut-off by safety contact strip, shielded with 150 mm lead, including a “cold” preparation door (acrylic) and glove ports;
- Each cell will be equipped with a large sliding rear door for maintenance (hinged door is also an option);
- Master-slave manipulators (2 per cell), with gas-tight design, will be installed on the operation side of each shielded cell.

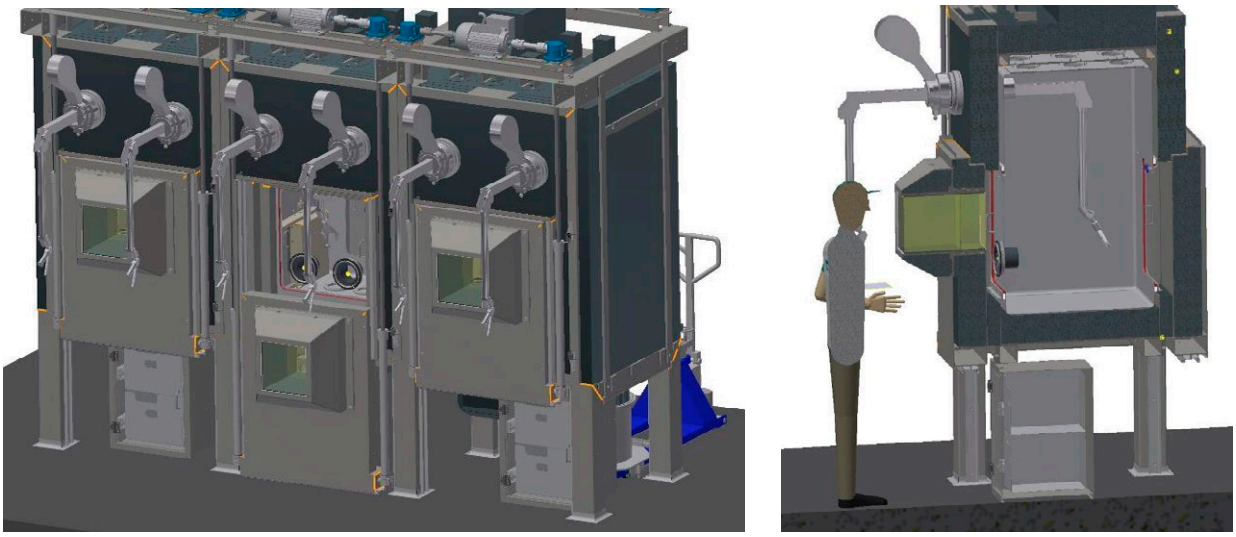

Figure 20.4: Shielded cell, with front sliding door, “cold” preparation door with gloves and master-slave manipulators. Side view for estimated space requirements during operation.

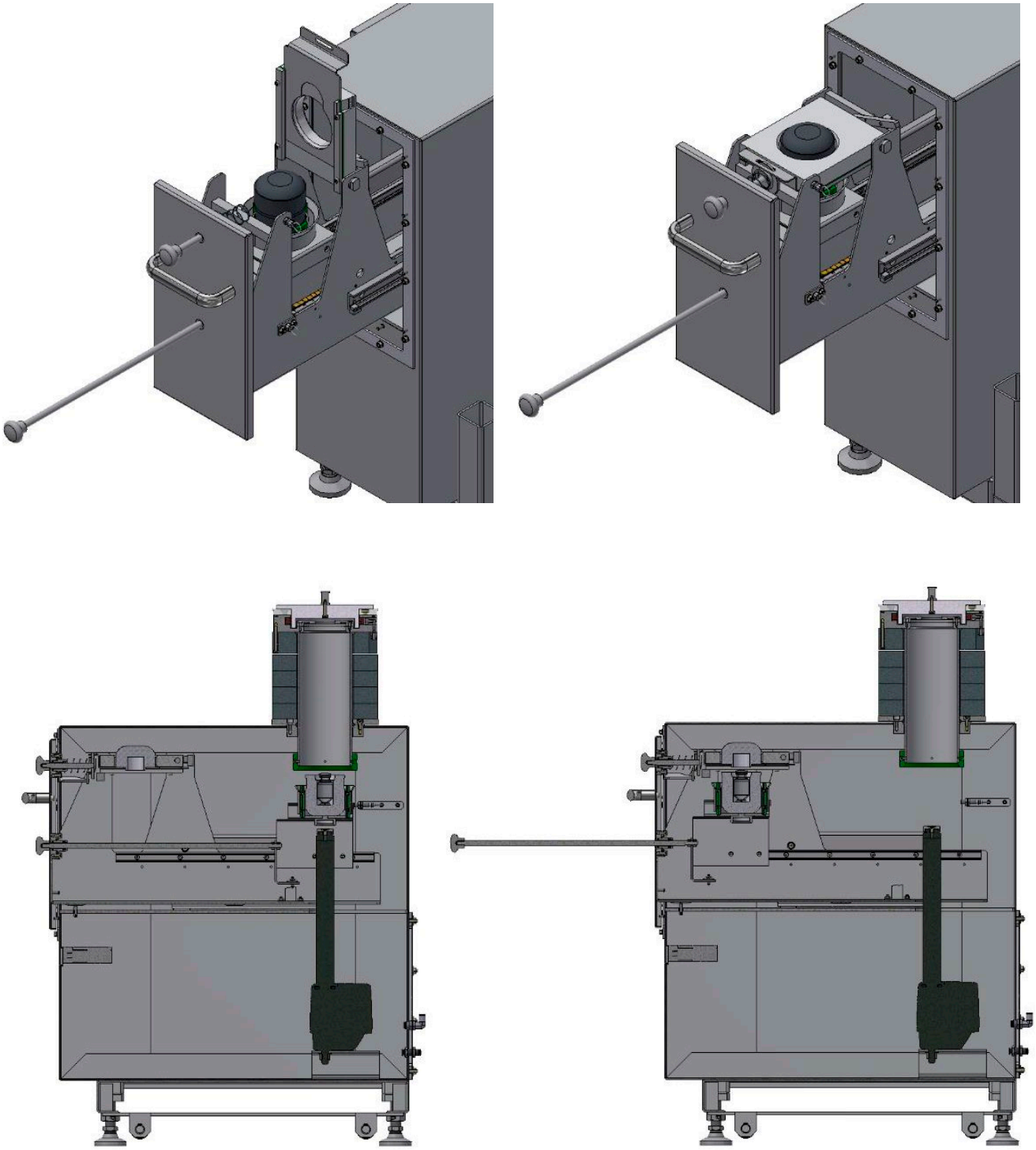

Figure 20.5: Substructure module allowing manual insertion and removal of the lead pots, with a pneumatic lift.

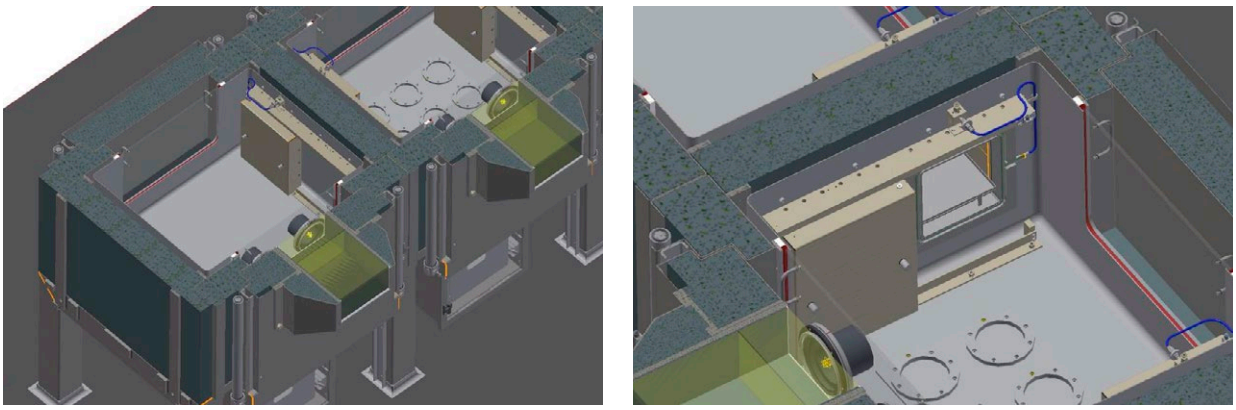

Figure 20.6: Detailed view illustrating the double door lock system and lead glass window.

- The two chemical processing cells will be able to discharge vials into light lead pots below the cell chamber;
- A substructure module below the chemical processing cell will allow manual insertion and removal of the lead pots, with a pneumatic lift for the lead pots (see Figure 20.5). The pots are sealed in the module - Module is connected to the inner cell - Vials are inserted into the lead pots via the manipulators, while the pot is lifted up.
- Reinforced shielding of the collection cell will be 200 mm instead of 150 mm, with 200 mm lead shielding of the double-door locks (see Figure 20.6). The lead-glass window will have a lead equivalent of 200 mm.
- The inner cells will be made of stainless steel (1.4301) internally coated with HALAR (ECTFE). The working area in the cells (W × D × H) is ~1500 × 1200 × 1350 mm. The frame will be robust, welded steel, with the surfaces powder-coated. Removable acrylic front panels will be installed behind the front lifting doors, with 2 glove ports per cell. Energy-saving LED lighting, glare-free, ›500 lux, will light the inner cells. Adjacent cells will be interconnected via shielded double-door locks (2 pcs.), size (W × H) ~500 × 500 mm.

The two external chemical processing cells (left and right) will be equipped with:

- Alpha port, 105 mm in diameter, in the bottom for the docking of heavy lead containers from below.
- Alpha port, 105 mm in diameter, in the respective outer wall for docking light plastic containers for the introduction of consumables. The internal part will contain an additional shielded airlock door.
- Waste disposal (1 each) for solids and liquids into shielded containers.
- Each cell will be equipped with a liquid connection (for the transfer of solutions to the separation system) from above.
- Each cell will be shielded with 150 mm lead on all sides and have 1 large lead-glass window installed, size (W × H) ~ 300 × 300 mm, lead equivalent 150 mm. Each door of the two double-door airlocks will be shielded with 75 mm lead (total: 150 mm). Lateral alpha ports will be shielded with one sliding 150 mm lead door each.

The three shielded cells will have:

- Dose rate monitoring (ALMO) in all 3 cells;
- The cell will contain a shielded ionization chamber, situated beneath the floor, for the activity measurement of the product (see Figure 20.7);
- A central electrical system for operation and monitoring of the line;
- Mechanical push-buttons and switches on the sides and above the doors for intuitive operation of important functions, without the operator having to take his eyes off the inner cell;

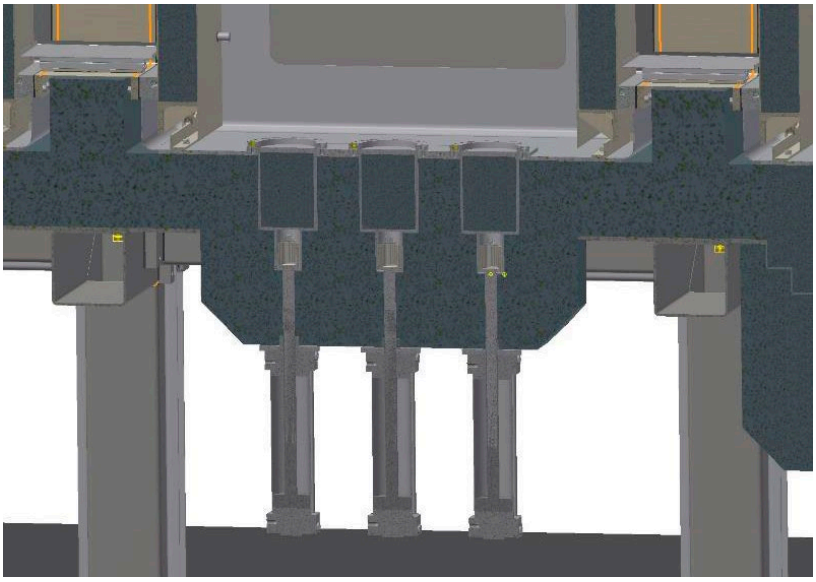

Figure 20.7: Shielded ionization chamber under the shielded cell floor for activity measurements.

- Additional control panel with touch display;
- Electrical connections in each cell: 2 × 240 VAC double socket (Schuko), splash-proof (IP44);
- Three electrical connections outside the line of the cell (240 VAC sockets (Schuko));
- Power supply: 230 V/50 Hz 16 A;
- Interlock circuit for all relevant doors;
- The shielded cells' ventilation will consist of negative pressure of at least -50 Pa, with all cells having identical air pressure level. There will be a minimum of 5 air-changes/hour filtration and one HEPA 13 (DIN 1822) filter per cell. The exhaust air system will consist of a combination of HEPA 13 (DIN 1822) + activated carbon filters. The exhaust air filters will be shielded with lead. Ventilation will be prepared for subsequent use of bag-in/bag-out filters; no laminar flow.

20.4 Radiochemistry Facilities at UZH

In 2021, UZH Chemistry moved into new buildings on Irchel campus (UZI-5). The facilities include purpose-built radiochemistry laboratories (Class B) that are designed and optimized for handling open sources of radionuclides (Figure 20.8). Separate laboratories have been designed for radiochemistry using nuclides that decay *via* different mechanisms including beta- and alpha-decay for synthesizing radiotherapeutic compounds, as well as higher-energy positron emitters and gamma-ray emitters for developing diagnostic radiopharmaceuticals for imaging with positron emission tomography (PET) and single-photon emission computed tomography (SPECT). The radioactive laboratories include 20 chemical fume hoods, two glove boxes for working with air-sensitive materials, and a BSL1 tissue culture facility for performing radioactive studies in combination with human cancer cell lines. State-of-the-art radioanalytical tools are available to perform the full suite of chemical and biological tests on developed radiopharmaceuticals. Dedicated space is assigned for animal housing and imaging (Class-C radioactive labs equipped for biological safety level 2 [BSL2] experiments) evaluate radiopharmaceutical performance in vivo.

The chemistry and radiochemistry laboratories at UZH are distinct from the facilities at PSI. Specifically, PSI is equipped to handle much higher radionuclide activities. UZH Operation with lower levels of radioactivity provides UZH with the flexibility to perform a very large number of experiments in parallel. This flexibility is essential when developing new chemical reactions or optimizing radiochemical methods.

As part of IMPACT, the radiochemistry laboratories at UZH Chemistry would acquire a new state-of-the-art PET/SPECT/CT camera system and a new UHPLC-MS chromatography tool for analysis of radioactive materials. These devices will expand existing capabilities and allow to study the biolog-

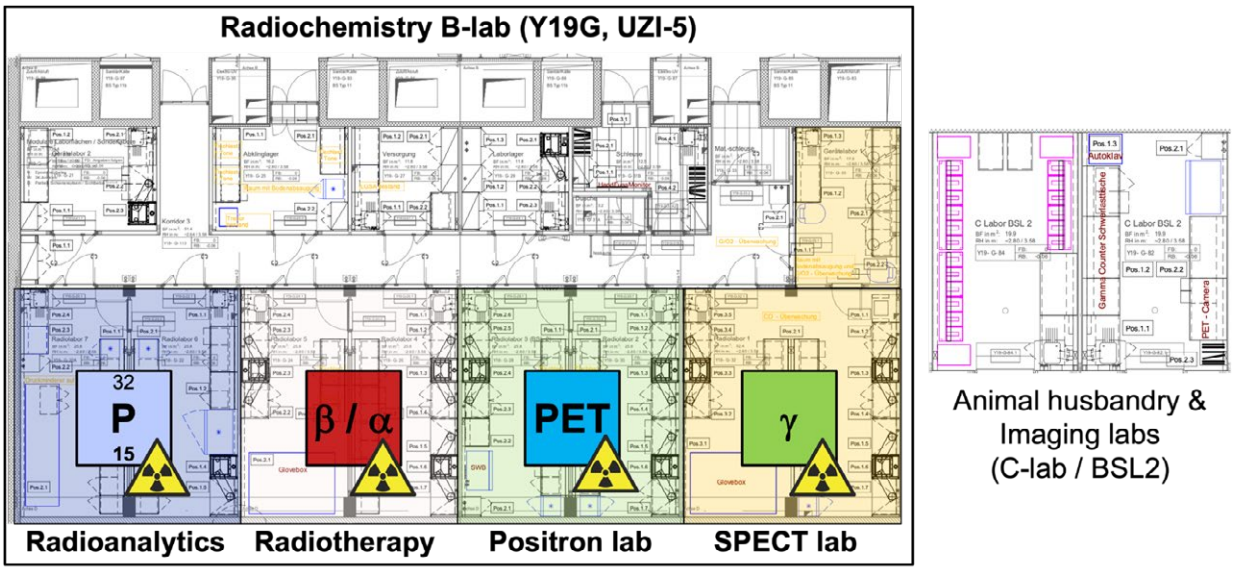

Figure 20.8: Overview of the new UZI-5 radiochemistry research facilities in the Department of Chemistry at UZH Irchel.

ical potential of our radiopharmaceuticals using the new radionuclides produced at PSI. Importantly, existing equipment is unsuitable for detecting many of the new radionuclides that could be made by the mass isotope separator. Installation of a multi-modality device will speed up the preclinical evaluation of radiopharmaceutical research and facilitate translation to the hospital. Many different camera systems exist and as an example, the Bruker Albira SI (https://www.bruker.com/en/products-and-solutions/preclinical-imaging/nmi/albirasi.html and Figure 20.9) provides high-resolution detection with whole body imaging in rodent models. This device is currently state-of-the-art in preclinical radionuclide imaging.

As part of the IMPACT project, UZH Chemistry would provide in-kind access, on a collaborative basis, to researchers from across Switzerland who have a specific need to use radiochemistry in the research studies. In addition, UZH would provide access to expert advice, materials, and tools for performing research using the new radionuclides produced from the PSI.

Figure 20.9: The Bruker Albira: a preclinical imaging device that would fit spatially at the new UZH Chemistry building on the Irchel campus.

20.5 Facilities at USZ

Production of radionuclides and PET-radiopharmaceuticals, and their application in humans is a highly complex and interdisciplinary process, requiring scientists from (radiation-) physics, engineering, chemistry, molecular biology, pharmacy as well as medical doctors and lab technicians. The translation of an innovative novel scientific radiopharmaceutical from the bench to its clinical application, therefore, must be planned with utmost care and requires means to an easy-to-access facility. The construction of the new PET radiopharmacy facility at the Wagi campus in Schlieren, Zurich, serves as an ideal starting point to plan an infrastructure that can enable this translation (see Figure 20.10). The new building will see the installation of a (second) cyclotron, with all the necessary accoutrements associated with a clinical facility. The first floor is organized such that the three "Hot Labs" with shielded cells can be flexibly used for research and preclinical development. Two of the laboratories will be equipped to accommodate USZ work, while one Hot Lab and an office are reserved for the UZH project. Early experiments with radionuclides coming from the Wagi PET Radiopharmacy can also be carried out in labs outside this facility on the Wagi campus at large (provided appropriate radiation protection for lower dose activities is available in such labs), as radionuclides in lower doses can be delivered from the cyclotron/PET- radiopharmacy facility to such laboratories.

USZ will provide two fully Swissmedic-certified clean rooms on the first floor of the building for the preparation of research tracers for clinical use. The necessary equipment will be installed in this room. The equipment of the two other rooms be will be provided, which means that shielded cells and the necessary automated synthesis units needed specifically for the various users will not be covered by IMPACT.

While the finer details of the equipment cannot be defined at this point, the research rooms will need to be equipped with:

1. Four shielded cells and dispensing units (cost approx. 1.05 Mio CHF)
2. Synthesis systems for the production of radiopharmaceuticals from radionuclides and cold tracers (cost depending on the user requirements, approx. 0.5 Mio CHF)
3. Analytical chemistry equipment such as Gas Chromatography, HPLC, gamma-counters etc. to establish a QC lab (cost approximately 1.0 Mio CHF.)

The construction and operational costs of the new radiopharmacy will be covered by USZ. Users will need to pay for:

1. Cyclotron beam time (per hour);
2. Infrastructure use (possibly rental basis);
3. Personnel linked to the production of clinically used tracers for human studies. This comprises production technician hours, QC assurance personnel, radiation protection personnel.

Figure 20.10: The floor plan of the new infrastructure at USZ Wagi campus in Schlieren.

21 Radiation Protection & Safety

Concerning radiation protection & safety for TATTOOS the same legislation and guidelines are valid and will be applied as depicted in Chapter 11. Please refer to Chapter 11 and the sections about radiation protection (11.1), personal safety system (11.2) and disposal concept (11.3) for the applicable classifications, limits and ordinances.

21.1 Radiation Protection Considerations for TATTOOS

21.1.1 Laboratory Type Classification

According to the activity of the radioactive materials handled per operation or per day, laboratories are classified as type A, B or C:

- Type C: 1 LA until 100 LA
- Type B: 1 LA until 10'000 LA
- Type A: 1 LA until upper limit defined in the licensing procedure.

The licensing limit is the nuclide-specific absolute activity above which handling of this material is subject to mandatory licensing. These values are listed in annex 3 column 10 of the RPO (Swiss Federal Council, 2017).

21.1.2 Requirements for Laboratory Type A

According to the designated amount of handled activity, the TATTOOS laboratory will be classified as type A. Additionally α-emitting nuclides (e.g. Tb-149) will be produced and handled there. Therefore the laboratory will have to have the necessary radiological measurement equipment for these kind of nuclides. Structural properties as well as metrological requirements can be found in UraM [EDI, 2017b]. Some important features include the lower pressure staging (Chapter 21.1.3), the usage of surface materials, which can easily be decontaminated, showers and washing facilities for decontamination purposes, at least five air changes within one hour, filtering of the fume hood and room exhaust air, etc. A more detailed listing can be found in Annex 5 and 6 of the UraM [EDI, 2017b].

21.1.3 Lower Pressure Staging

According to ENSI-G12 guideline chapter 6.4 [ENSI, 2020], a lower pressure staging and a directed air flow from a lower to a higher zone must be guaranteed. Between the environment and a zone type III or IV, a permanent lower pressure of at least 50 Pa must be established. This holds for the whole proton beam line channel and also inside the fume hoods. The air from the proton beam line channel must be filtered and led through the monitored exhaust air channel where aerosol measurements take place. According to [EDI, 2017], the air from the fume hoods must have a nuclide-specific filtering in the vicinity of the hood.

21.1.4 Dose Limits

For a planned radiological exposition situation according to [Swiss Federal Council, 2017], dose limits have to be assessed. These limits as given in Table 11.1 in Chapter 11 must not be exceeded.

21.1.4.1 Ambient Dose Rates

Table 11.2 in Chapter 11 summarizes the limits for ambient dose rates (ADR) for different types of zone classifications. These standard values guarantee that the dose limits according to Section 21.1.4 are complied with.

A PSI basic rule according to the RPO art. 4 and 60 [Swiss Federal Council, 2017] states, that radiation shielding design should result in a dose rate not exceeding 10 % of the guiding values valid for the controlled areas. The calculations for the necessary radiation shielding have to be in accordance with Swiss legislation. If an unexpected exceeding of the limits happens, several actions can be considered: Reduction of operation time, installation of additional local shielding or reduction of beam intensity.

According to Table 11.2, maintenance work with an ambient dose rate ›1 mSv/h must be carried out under supervision by the radiation protection personnel. *For all working steps involving the dismantling process, a detailed radiation protection planning will be performed in collaboration with other sections*.

21.1.5 Emission Limits

Emission limit values corresponding to new exhaust emergency facilities will have to be calculated according to the PSI principles documented in the paper describing program ESS41 [PSI-TM-96-10-09]. The fixed nuclide and emission site-specific intervention thresholds are based on an

artificial dose limit of 0.05 mSv corresponding to the quarter of the dose guide value attributed to PSI for short emissions.
The emission limits for PSI according to Table 11.3 in total must not be exceeded.

21.1.6 Accounting for Radioactive Volatile Isotopes

According to the Paul Scherrer Institut (PSI) exhaust "Reglement" [BAG, et al., 2018], PSI has to prove that the artificially induced environment dose falls under the annual limit of 0.15 mSv or the limit for short emissions of 0.2 mSv. To achieve this, radioactive volatile isotopes have to be surveyed and accounted for at the different emission points. In normal operation, those emissions are balanced as a mixture at the already existing stations of Stack North and South. Both stations have been renewed in 2019.
The future operation of the new TATTOOS facility needs the implementation of a supplementary emergency stack and therefore the accounting for and the surveillance of radioactive volatile isotopes in the upstream airflow within a new sampling station.
The requirements for the new measuring and balancing system of radioactive substances in the emergency exhaust air are determined in the guideline ENSI-G13 "Measuring equipment for ionizing radiation" of the Swiss Federal Nuclear Safety Inspectorate [ENSI, 2015]. In addition, the design of the sampling system has to take into account the currently valid international standard ISO 2889: 2010 [DIN, 2012] as well as the rules of the German nuclear committee KTA 1503.1 [KTA, 2016] and KTA 1502 [KTA, 2017]. Thereby the emphasis is set on the testing before operation of the new system. Mainly it has to be demonstrated that the aerosol distribution at the sampling location is representative, that the aerosol transfer to the sampling filter of aerosols from different sizes are fulfilling the requirements and that the sampling loop has no leakage. On top of that, it must be proven mathematically that the balancing system is securely mounted against earthquakes.

21.2 Personal Safety System

Please refer to Section 11.2 for considerations and aspects concerning the personal safety system.
The technical specifications of the PSYS system are discussed in Section 12.8.

21.3 Disposal Concept

Please refer to Section 11.3 for considerations and aspects of the disposal concept.

22 Building and Infrastructure

22.1 Present Situation

The institute is located in the canton of Aargau on the grounds of the municipalities of Villigen and Würenlingen, on both sides of Aare river. All buildings and installations in the west area are located in the parcel of land 588, which is dedicated to industrial use (see Figure 22.1).

The perimeter of the new building to be constructed is in a closely overbuilt area between the experimental hall (WEHA), towards the east, and the WMFA building towards the west, as well as the connected UCN hall (WNAB) (see sketch in Figure 22.2). The existing cooling facilities and large helium compressors for UCN will be renewed in 2023 and rebuilt in another area. The old compressors then have to be removed from the construction site. The tank facility on the steel grid on the roof of the existing building will have to be removed for the construction and will be rebuilt above the new building.

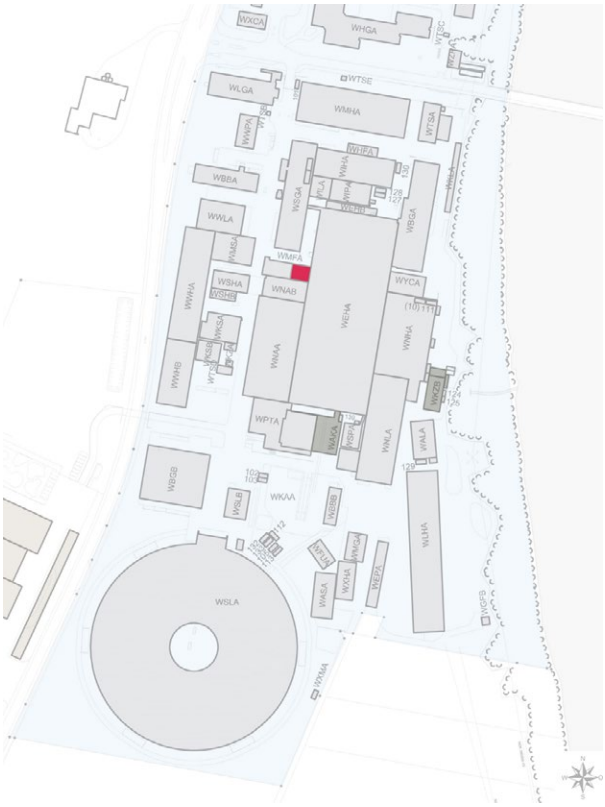

Figure 22.1. Site plan PSI West (land parcel 588).

22.2 Building Structure

The planned structure of the new building consists of a hall on the ground floor with a height of 10 m. Below, a basement is planned for the laboratory, which will have a height of 4 m. For the collection of liquid radioactive waste, a secondary basement with a tank room is foreseen, which will have a clearance of 2.5 m (see Figure 22.3).

Ground area total: ca. 488 m^2
Ground floor: ca. 232 m^2
Basement 1: ca. 232 m^2
Basement 2: ca. 24 m^2

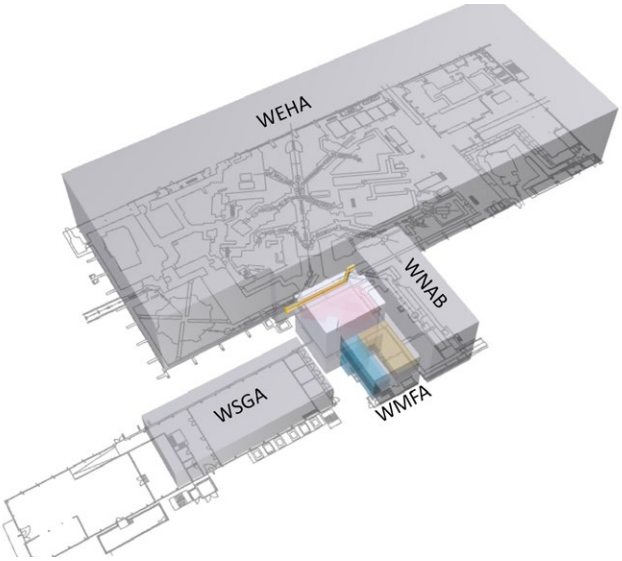

Figure 22.2: Sketch of the building structure.

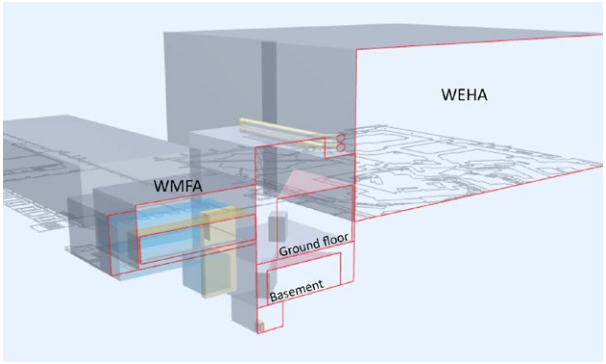

Figure 22.3: Cross sectional view of the building structure.

For the placement of further infrastructure, parts of the ground floor and basement of the adjacent WMFA building will have to be reconstructed. A technical supply area is planned in the region above the area, close to the WEHA hall, to deliver space for further technical installations, particularly that of ventilation.

22.3 Statics / Structural Engineering

Since the planned basement of the new building is around 5.5 m below the finished floor level (FFL) (see Figure 22.4) a construction pit with a full pit safeguard is needed [MWV Bauingenieure AG, 2021]. Furthermore, the sideways weights and foundations of the adjacent buildings have to be taken into account and stabilized accordingly.

As a construction pit closure, a sprouted retaining wall is foreseen, which enables an economical and efficient way of pit safeguarding in the narrow space conditions of the site.

The retaining wall consists of vertical beams and intermittently-placed infill of shot concrete and reinforcement nets. The supports of the retaining wall are about 11.5 m long and, thus, reach a minimum of 4.5 m into the ground. These supports are prepared in pre-drilled holes of about 80 cm in diameter, filled by a steel profile beam. The retaining wall supports are placed systematically every 2.4 m. During and after each excavation campaign, the infill between the supports will be done. Before the next excavation towards the following level, the retaining wall will be supported all around by a longarine made of steel profiles. Three sprout wall levels are foreseen. These three levels and longarines

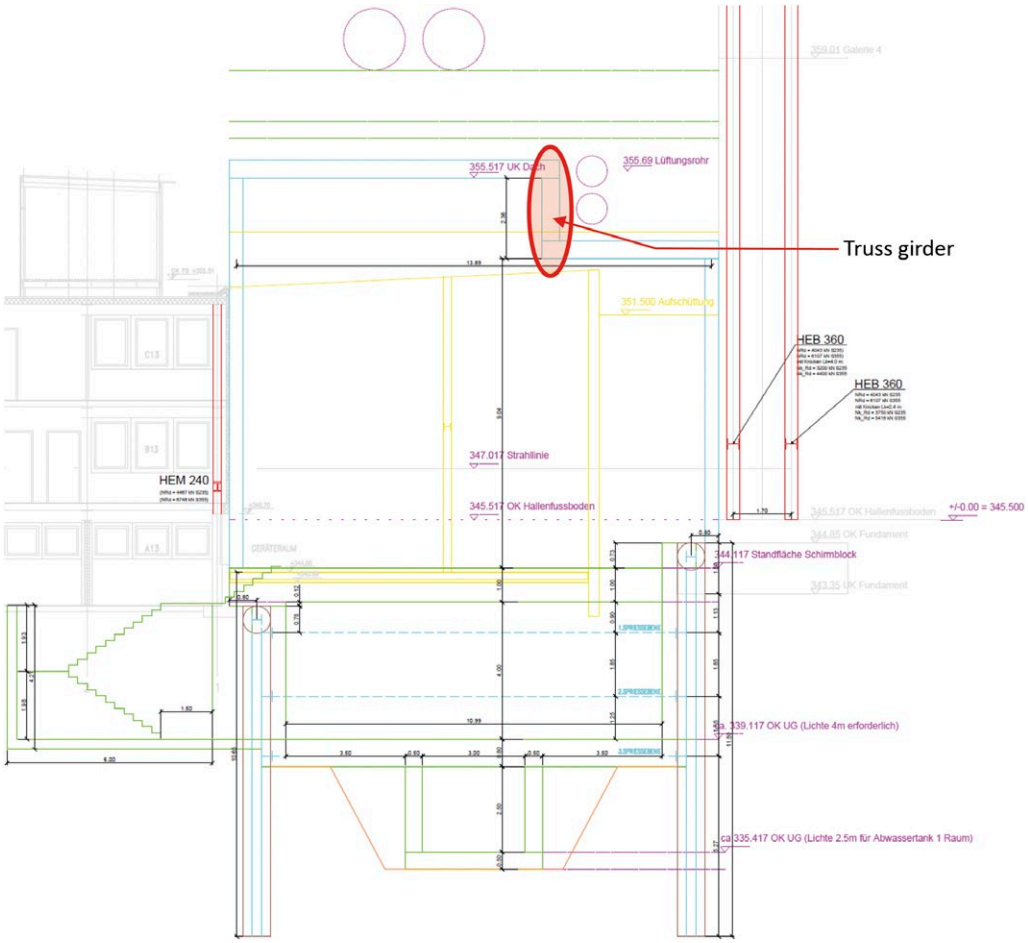

Figure 22.4 : Structure cross section (side view).

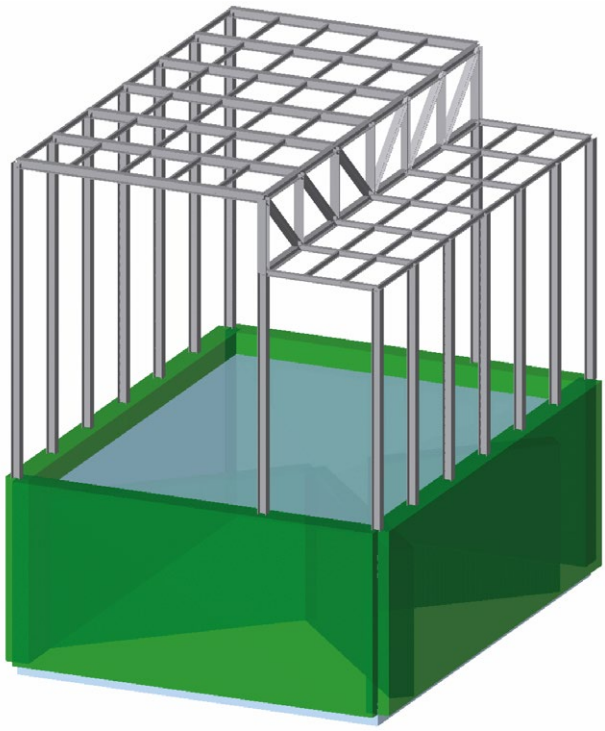

Figure 22.5: Structural steelwork.

are connected by horizontal beams to stabilize them vertically. Thus, the entire construction pit is secured from inside and does not require any intervention from the adjacent buildings.

The entire hall construction is planned as steel work (see Figure 22.5). The access to the newly constructed building will be located in the existing WMFA building over a new staircase. The corresponding well for the staircase will be introduced using either a caisson or a similar retaining wall, as explained before. The entrance from the staircase into the new building will be between two support beams of the main retaining wall of the excavation pit to minimize additional efforts of retention.

22.4 Layout / Allocation Program

On the ground floor, a proton beam line will be introduced from the WEHA accelerator complex into the new facility (see Figure 22.7). There, the target is located in a massive shielding block of about 2000 t made of steel and surrounded by concrete. In an adjacent heavy target-exchange shielded

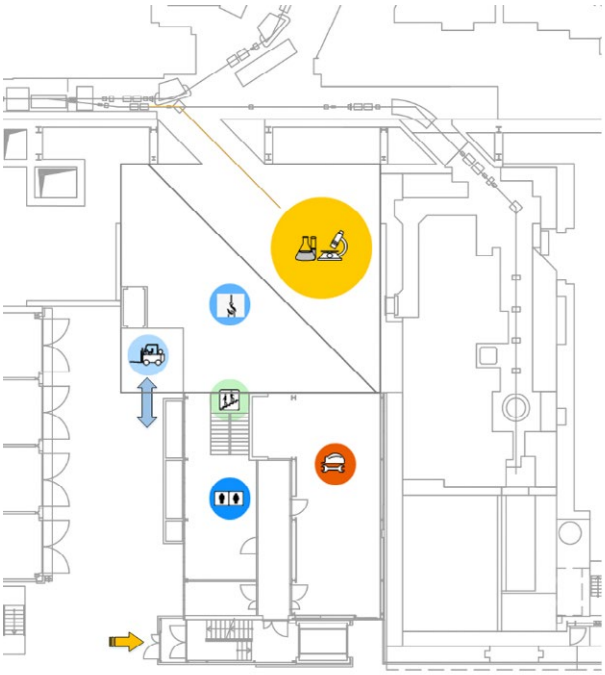

Figure 22.6: General allocation plan.

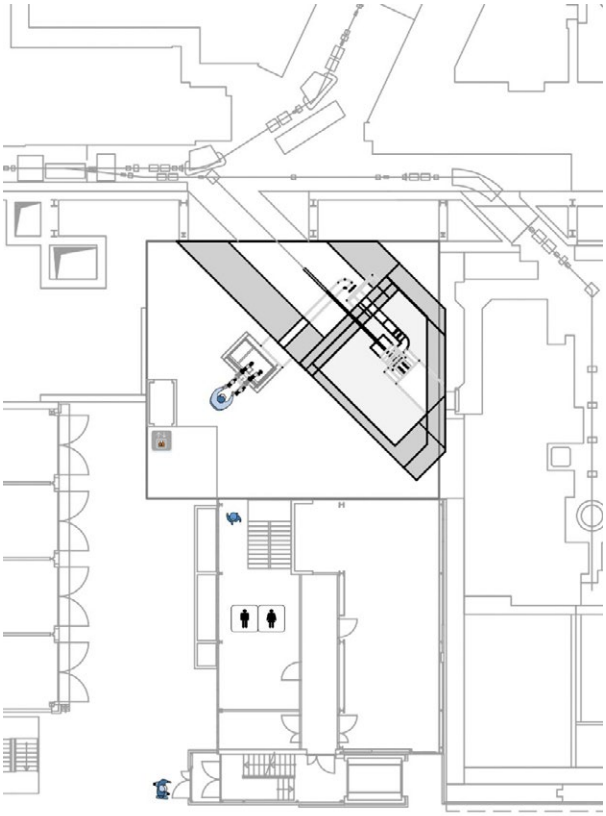

Figure 22.7: Ground floor allocation plan.

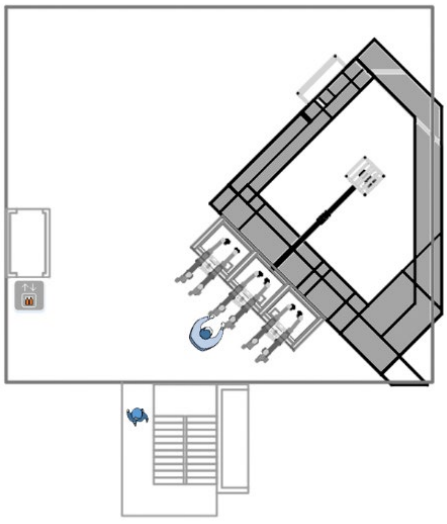

Figure 22.8: Basement 1 allocation plan.

cell, irradiated targets can be handled and exchanged. A material lock at the north-west side of the building ensures the introduction and removal of materials to prevent radioactive spread. A heavy crane below the ground floor ceiling is used for the exchange and handling of heavy components of the beam line and shielding, as well as the exchange flasks for targets and beam stop replacements, repair and replacement. An opening is foreseen in the floor of the ground floor, to introduce heavy materials into the basements when necessary, which can be closed with a heavy plate.

The mass separator is located in the basement, where it separates the product ions emitted by the target and guides them into the three shielded cells dedicated for the collection of ions and their radiochemical purification. The mass separator magnet, having direct view on the target during the irradiation, will have to be heavily shielded. These shielded walls are also intended to have a carrying function for the shielding on the ground floor above. The purified final radioactive products will be packed into corresponding transport containers and moved towards the material lock using a service elevator (see Figure 22.8, left side).

22.5 Personnel Movement and Material Flow

22.5.1 Entrance & Access (Personnel)

The entrance for personnel is located in the adjacent building WMFA. On the ground floor, as well as in the basement, there will be personnel locks (Figure 22.9), which are required for the controlled access into A-class laboratories and zones.

Vertical access is granted over the staircase in the WMFA building that connects the personnel lock with the working area in the basement, as explained previously.

22.5.2 Removal and Disposal of Material

The material entering the controlled zone will mostly pass through the material lock. Material leaving the controlled zone are required to pass through the material lock, where they are checked for contamination and dose levels. The material lock is located in the north-west corner of the building. The ground floor and basements are connected

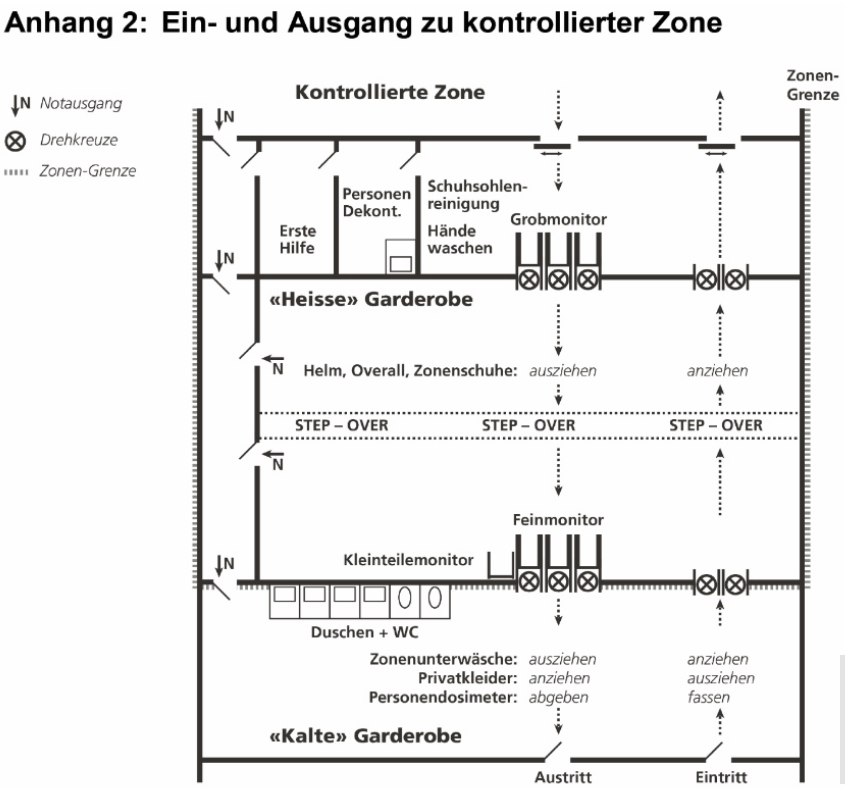

Figure 22.9: Principal scheme of a personnel lock as required by the Swiss regulator ENSI [ENSI, 2021].

via a service elevator for material transfer, directly connected to the material lock. To keep the radioactive zones separate, a separate lock structure has to be installed at the entrance and exit of the service elevator.

22.5.3 Cranes and Lifting Tools

A new overhead crane will be installed. The main purpose is to lift the shielding blocks and other heavy components. Local lifting tools may be needed in the regions closer to the building walls.

22.6 Technical Infrastructure of the Building

22.6.1 Electrical Installations

22.6.1.1 Power Distribution and Energy Supply

The installed electrical power should be sufficient. As a result of the new TATTOOS building, two existing transformers need to be replaced on a new podium. These two transformers are connected to the WEHA building. In principle, the energy supply in the WEHA building stay at their existing positions.

TATTOOS requires the installation of new power distributions for building infrastructure and the new part of the beamline. There are existing power distributions in the WMFA Building for power, UPS and emergency lights. These must all be transferred to another location.

For all electric connections to the new TATTOOS beamline, the new building and the new shielded cells, a new electric supply room is necessary to be placed in the service area of the existing WMFA building. On the first floor of WMFA, two rooms can be used for all electric racks, power supplies and the new power distributions (see Figure 22.10).

22.6.1.2 Cabling and Installation

Many existing cabling installation parts will have to be dismounted. Many cable trays, some cables and infrastructure components have to be replaced as a result of the new area design and project, particularly, the installation needed for the beamline to UCN and the UCN target station as well as the existing building.

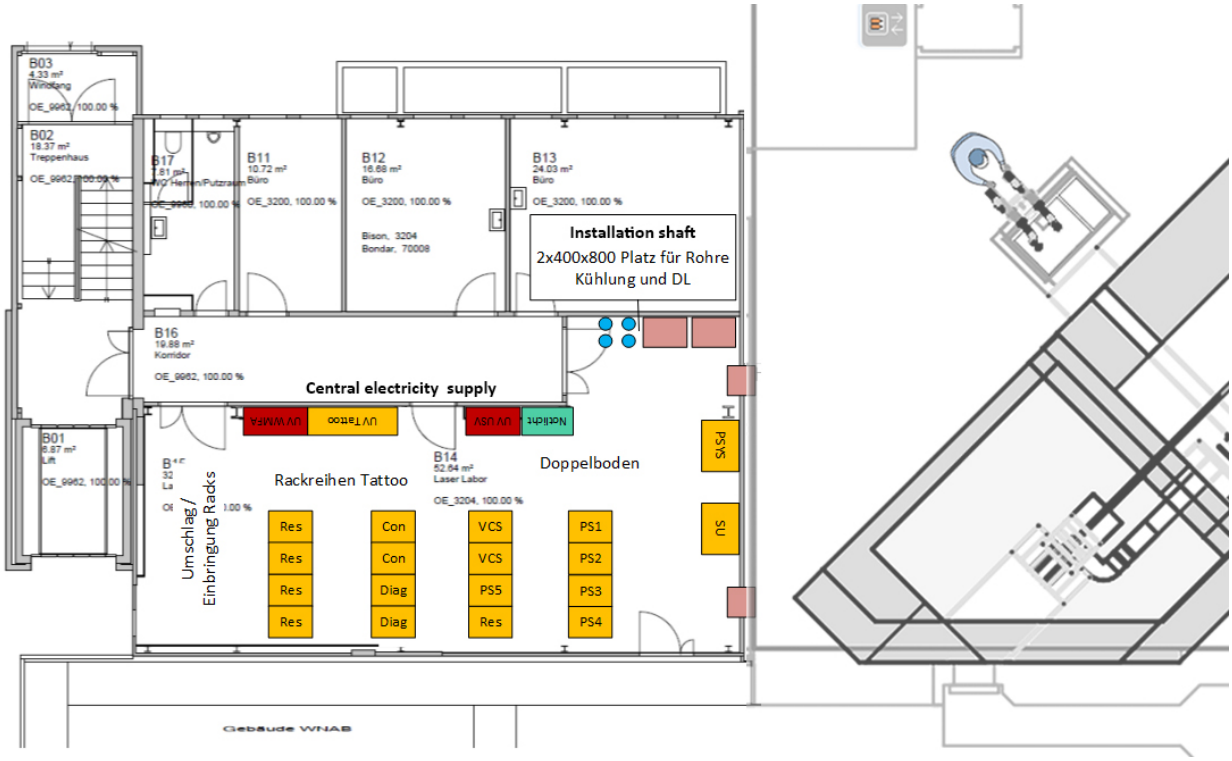

Figure 22.10: Sketch illustrating the potential location of the electric power installations in WMFA.

All cables have to be changed or renewed for the newly designed areas, as well as the beamline. In the case of EMC, the cables must be all shielded. That also means that more space is needed in the cable trays.

22.6.2 Cooling System

The stringent space limitations require a thorough planning of the process cooling installations in parallel to the other systems, components and internal building infrastructures. Extended reconstructions are needed. These works are to be coordinated with the HIPA operation planning. The legal authorization processes will have to be started early, in collaboration with the PSI radiation safety group and the governmental authorities from the Bundesamt für Gesundheit (BAG).

A new, automated independent collection system for radioactive aqueous waste, containing alpha-decaying radionuclides, has to be built as part of the TATTOOS project. This collection system will be constructed to be able to handle aqueous waste released in operation of the radiochemical procedures within the shielded cells, as well as potential cooling water breaks in accident scenarios.

For the process cooling of the beam line and beam dump, the existing cooling loop «Tertiär 4» will be moved and reconstructed (see Figure 22.11). The well-maintained components such as pumps, heat exchangers, filters, regulation valves are contaminated, but will be reused to minimize the radioactive waste. The modern regulation system will need only marginal updates to bring it to the PSI standard state of the art (see Figure 22.11). The cabling will have to be replaced. New plumbing and tubing is needed to provide the cooling into the newly designed TATTOOS areas and will have to be designed and built.

The target cooling is a special case. Similar to the principle of the isotope production target at the 72 MeV proton beam line (IPII), the TATTOOS target cooling will be planned as a separate cooling loop with minimized cooling media volume. To retain the activation products in this water loop, a locally

Figure 22.11: Components of the «Tertiär 4» cooling loop that will be reused for TATOOS.

shielded retention system based on mixed-bed anion/cation exchange, which will be accessible for service and repair, will have to be designed.

22.6.3 HVAC

The ventilation and air conditioning systems will ensure the required air exchange, room pressure cascade, temperature, humidity (laser room) and cleanliness. The sizing and ventilation design will follow the regulatory guidelines [EDI, 2021], such that air exchange rate, as well as the necessary air filtration at the air exhaust to atmosphere, is adhered to. The ventilation systems will be installed in a new ventilation room, which is planned for the roof of the WMFA building. It will consist of one supply air unit, and two separate exhaust air units for room and shielded cells, each with a 100 % redundancy unit including a special filter bank to allow

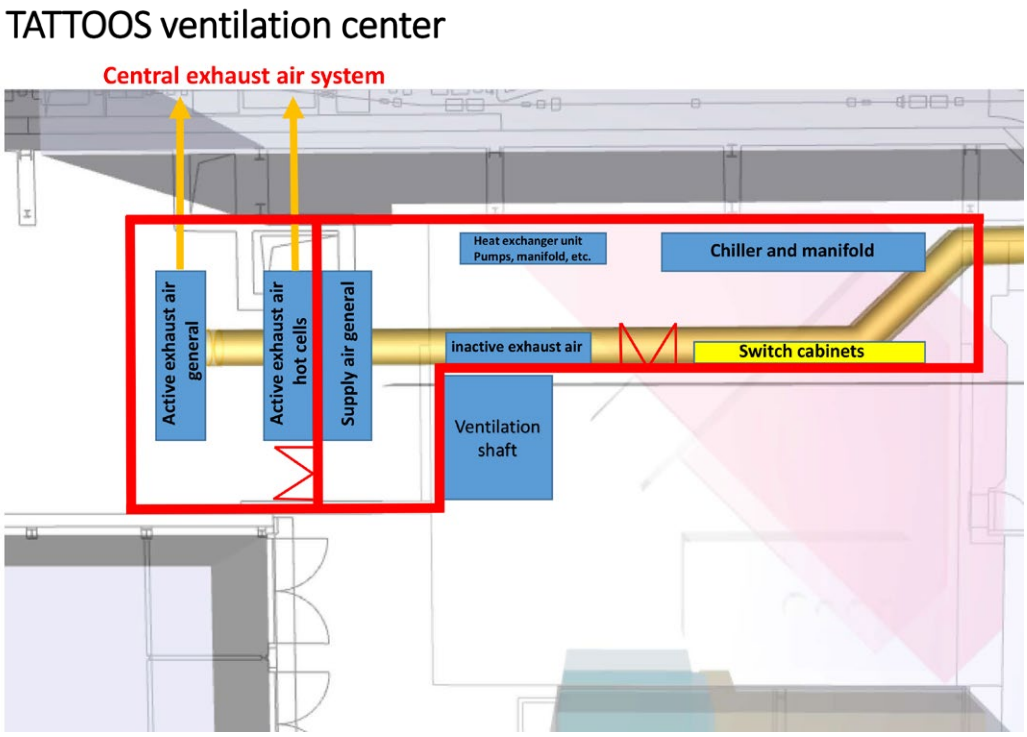

Figure 22.12: Central ventilation unit.

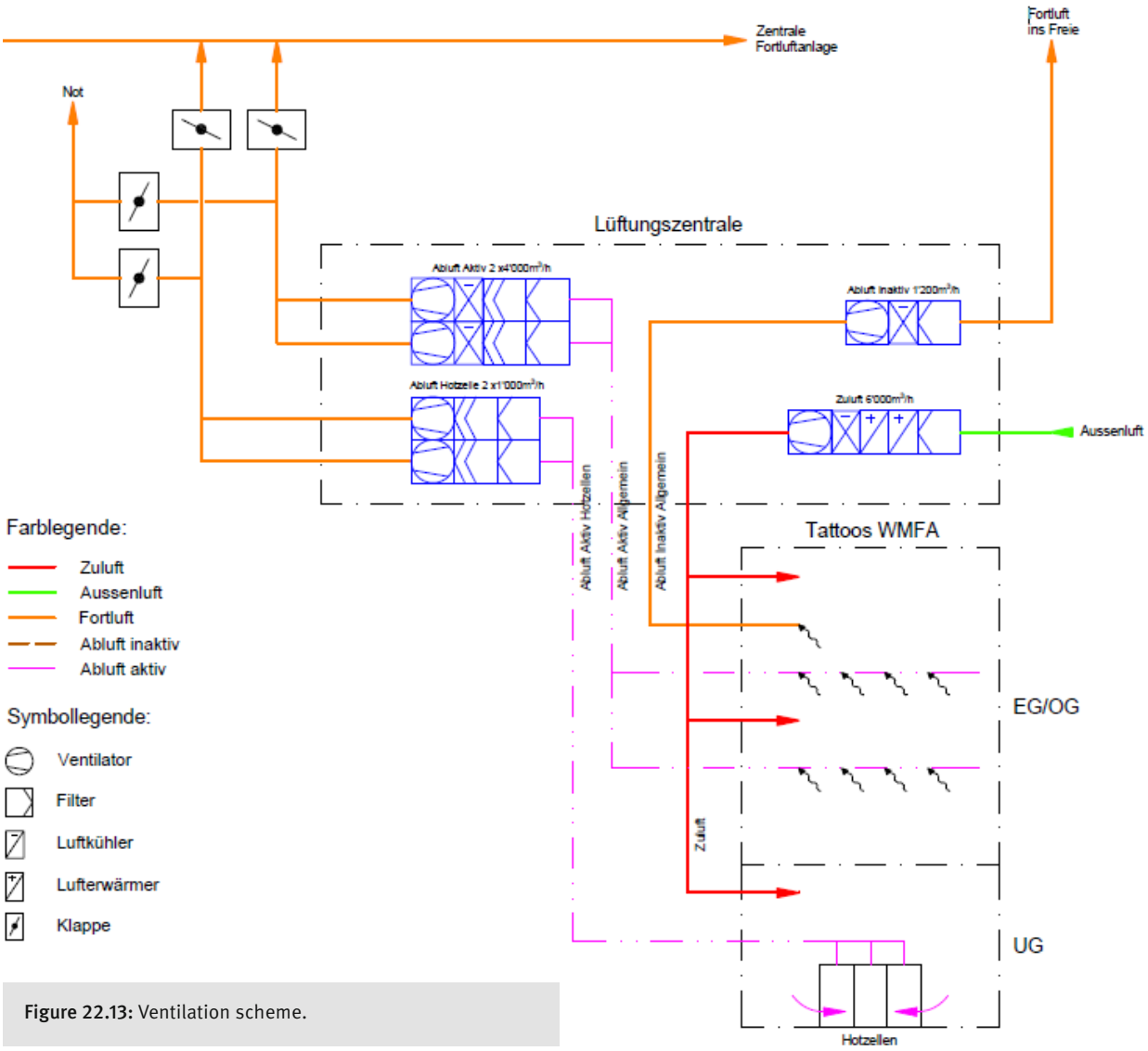

Figure 22.13: Ventilation scheme.

contamination-free filter exchange. The exhaust air is led into the existing central exhaust air system which is radiologically controlled. In addition, emergency exhaust air will be ducted to the outside. Cooling water for air conditioning is produced by a 35-kW chiller with air cooled condenser. For heating purposes, four local heating fan units will be installed.

22.6.4 Compressed Air

Pressurized air will be fed by the existing campus network, with industrial standard pressurized air at a nominal pressure of 6 bar. Various quick-coupling connections will be installed.

22.6.5 IT Networks

IT network access will be installed according to PSI standards. No special requirements are needed.

22.6.6 Central Building Control System (GLS) and PSYS

The building control system will be implemented into the PSI control system. The access to the building will be limited to authorized personnel only.

22.7 Preparation of Site

22.7.1 Removal of He-Cryostat & Compressors

Dismantling of the Sulzer helium refrigeration plant, including both compressors and both compressor foundations, will be necessary.

22.7.1.1 Dismantling of the Helium Refrigeration Plant (Coldbox):

The refrigeration plant, consisting of the coldbox, the valve panel and the two compressors, has to be dismantled after the new plant (NewTwo project) has replaced it. It can be performed during beam operation.

Upcoming work on the coldbox:

- Flushing the coldbox with compressed air;
- Dismantling of all pipes leading to and from the coldbox;
- Clearance measurements of all components by SU;
- Removal and disposal of pipe components and coldbox;
- Re-routing of nitrogen line (gaseous) and helium recovery if necessary.

22.7.1.2 Dismantling of the Compressors and the Compressor Foundations

The external concrete-block wall towards the experimental hall needs to be taken down. Susequently, the foundations of the compressors made from concrete must be sawn into pieces (‹ 10 t), by a specialized company inside the building, i.e. on-site. The pieces will then be lifted out of the hall, with a temporary crane, and disposed. Ideally, this work, as well as the removal of the compressors is carried out at the same time as all the other planned construction-related adjustments. It can only be done during a shutdown period.

Upcoming work on the compressors and the foundations:

- Open building (dismantle front) above shielding stone wall;
- Remove shielding stone wall and store stones (temporarily);
- Erect temporary crane;
- Dismantle all pipes leading to and from compressors;
- Clearance measurement of all components by SU;
- Remove and dispose of piping components, compressors, heat exchangers, and ventilation;
- Saw foundations into pieces;
- Clearance measurement of all foundation pieces by SU;
- Remove and dispose of foundation pieces;
- Remove temporary crane.

22.7.2 Displacement of Electric Installations of the UCN Facility

Electrical power installations dedicated to the UCN facility are located on a steel platform inside the area foreseen for TATTOOS (see Figure 22.14). These have to be relocated to the WMFA building.

Figure 22.14: Electrical installations of UCN to be moved to WMFA.

22.7.3 Cabling and New Feeds for UCN

Electrical as well as media supplies of water or gases have to be relocated to free space for the construction at the new site, as well as in parts of the WMFA building. This work is scheduled for the shutdown periods before the construction of the new building is scheduled to begin.

22.7.4 Removal of Existing Buildings and Removal of the Mound at WEHA

The land parcel 588 in Villigen is listed in the cantonal cadastre of burdened sites (KbS) under the number AA4121.0145 as operational site with the status AltlV, i.e., as burdened but not surveyed and no restoration work required.

The parcel is completely overbuilt. The building and mound on the west side of WEHA experimental hall will be removed during the construction phase.

For the buildings built before 1990, a general suspicion for building pollutants is given. Therefore, the duty of clarification is given by the regulator according to article 16 VVEA, which governs the clarification of the amounts and place of contaminants as well as the development of a disposal concept, if needed (article 17 VVEA).

The intention is to start these clarification processes, as well as the check of the construction ground, long before the construction phase to be able to plan potentially time-consuming and elaborate disassembly and disposal work timeously (see Table 22.1).

Table 22.1: The schedule of the TATTOOS building construction.

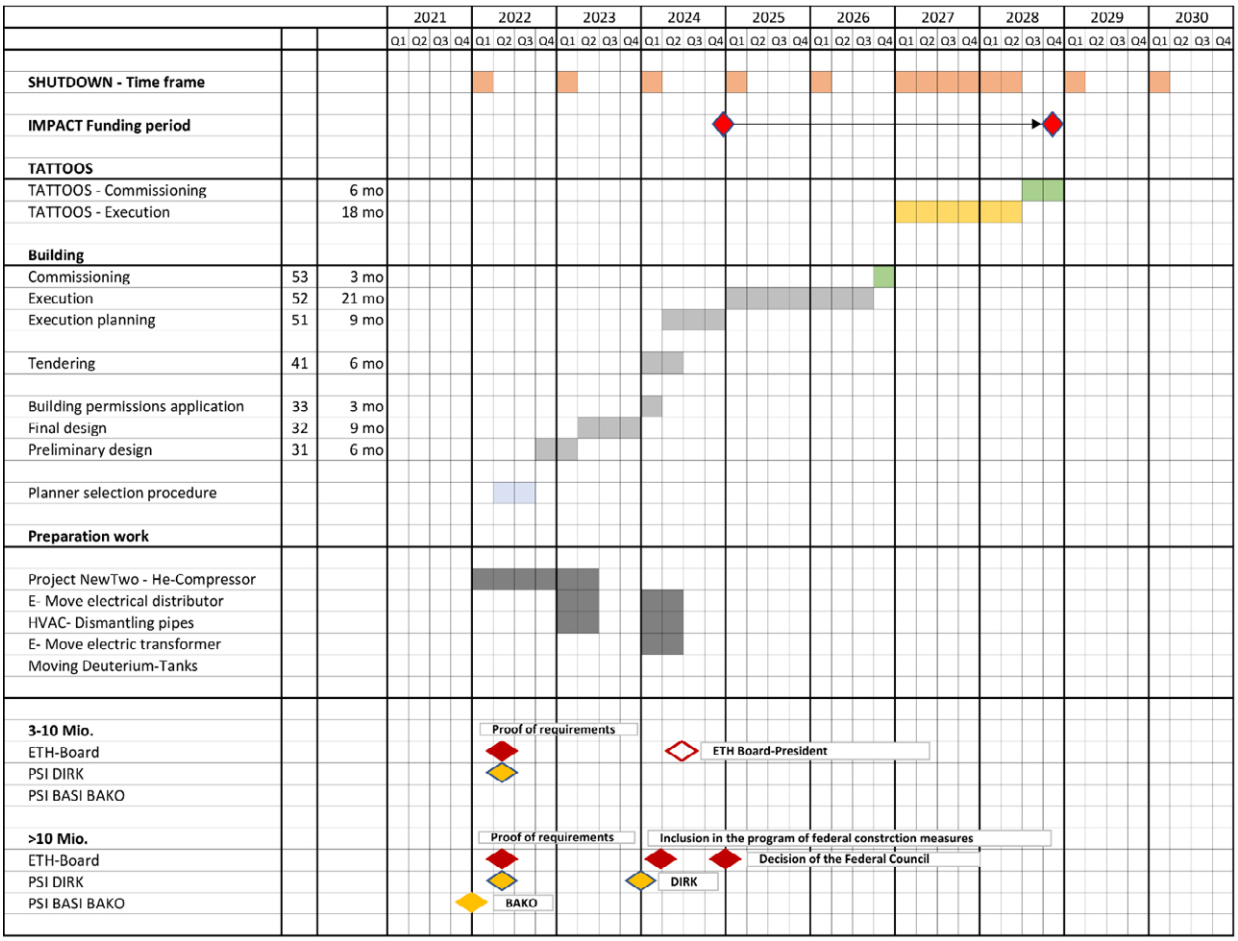

Bibliography

Abela, R. et al. 2021. Photon Science Roadmap for Research Infrastructures 2025–2028 by the Swiss Photon Community. *Swiss Academies Reports 16 (5)*, doi:10.5281/zenodo.4588917

Abi, B. et al. 2021. Measurement of the Positive Muon Anomalous Magnetic Moment to 0.46 ppm. *Phys. Rev. Lett., 126:141801, 4*, doi:10.1103/PhysRevLett.126.141801.

AG-0444.12.001. Bewilligung für den Umgang mit ionisierender Strahlung vom 27. Januar 2021: HIPA und Experimentierareale.

Agostinelli, S. et al. (GEANT4 Collaboration), 2003. GEANT4: A Simulation Toolkit. *Nucl. Instrum. Methods A, 506(3), p.250-303*, doi.org/10.1016/S0168-9002(03)01368-8.

Aiba, M. et al. 2021. Science Case for the new High-Intensity Muon Beams HIMB at PSI. *arXiv:2111.05788*, https://www.arxiv.org/abs/2111.05788.

AIDAInnova. aidainnova.web.cern.ch. Supported by European Union Horizon 2020 Research and Innovation program, under grant 101004761.

Akhmetshin, R. et al. 2020. COMET Phase-I technical design report. *PTEP Vol. 2020, Issue 3, 033C01*, doi.org/10.1093/ptep/ptz125.

Alder, F. et al. 1957. Alder, F., A. Colomb, A. Fritzsche, P. Schmid, F. Staub, and W. Zuenti. "Description of the Swiss Research Reactors." Wuerenlingen: Reaktor AG Wuerenlingen. 1957.

Allkofer, Y. et al. 2008. Design and performance of the silicon sensors for the CMS barrel pixel detector. *NIMA 584, 25*.

Amato, A. 1997. Heavy-fermion systems studied by μSR technique. *Rev. Mod. Phys., 69:1119– 1180, 10*, doi:10.1103/RevModPhys.69.1119.

Amato, A. et al. 2009. Probing the ground state properties of iron-based superconducting pnictides and related systems by muon-spin spectroscopy. *Physica C: Superconductivity, 469(9):606–613*, doi:10.1016/j.physc.2009.03.017.

Amhis, Y. S. et al. 2021. Averages of b-hadron, c-hadron, and τ-lepton properties as of 2018. *Eur. Phys. J. C, 81(3):226*, doi:10.1140/epjc/s10052-020-8156-7.

Anderson, C.J. et al. 2019. Anderson, C.J., Ling, X., Schlyer, D.J., Cutler, C.S.. 'A Short History of Nuclear Medicine.' in Jason S. Lewis, Albert D. Windhorst and Brian M. Zeglis (eds.), Radiopharmaceutical Chemistry (Springer International Publishing: Cham). 2019.

Andrighetto, A. et al. 2007. The SPES direct UCx target. *The European Physical Journal Special Topics, 150: 273-74*.

Anicic, D., et al. 2005. A fast kicker magnet for the PSI 600MeV proton beam to the PSI ultra-cold neutron source. *Nuclear Instruments and Methods in Physics Research Section A: Accelerators, Spectrometers, Detectors and Associated Equipment, 2005. Vol. 541, 3*.

ANSYS, Inc., 2016. *ANSYS Mechanical APDL Theory Reference. 2016*.

ANSYS, Inc. Structural Analysis Software. [Online] https://www.ansys.com/products/structures.

Arndt, K. et al. 2021. Technical design of the phase I Mu3e experiment. *Nucl. Instrum. Meth. A, 1014:165679*, doi:10.1016/j.nima.2021.165679.

Asner, D. M. et al. 2013. Project X: Broader Impacts. *arXiv:1306.5024*, arxiv.org/abs/1306.5024.

Atchison, F. 2001. PWWMBS: A computer based book-keeping system for radioactive waste from PSI-West accelerator complex. *PSI Report AN-96-01-20*. 2001

Augustin, H. et al. 2021. The Mu3e Data Acquisition. *IEEE Trans.Nucl.Sci 68*, 1833.

Baartman, R., 2014. Space charge limit in separated turn cyclotrons. *CYCLOTRONS 2013 – Proceedings of the 20th International Conference on Cyclotrons and their Applications. Vol. 5*, p. 305-309.

BAG, 2018. REGLEMENT für die Abgabe radioaktiver Stoffe und die Überwachung von Radioaktivität und Direktstrahlung in der Umgebung des PAUL SCHERRER INSTITUTS (PSI). *Federal Office of Public Heath und ENSI, Swiss Federal Nuclear Safety Inspectorate. BAG 438.0012-20, ENSI 22/1363*. Switzerland, January 2018.

Balaprakash, P. et al. 2018. DeepHyper: Asynchronous hyperparameter search for deep neural networks. *2018 IEEE 25th International Conference on High Performance Computing (HiPC)*, Bengaluru, India, doi.org/10.1109/HiPC.2018.00014.

Baldini, A. M. 2020. Charged Lepton Flavor Violations (CLFV). *Proceedings, 28th International Symposium on Lepton Photon Interactions at High Energies (LP17), Guangzhou (Guangdong), China, August 7-12, 2017*, W. Wang and Z.-z. Xing, Eds., Singapur:WSP, pp. 142–153.

Baldini, A. M. et al. 2016. Search for the lepton flavour violating decay $\mu^+ \dashrightarrow e^+\gamma$ with the full dataset of the MEG experiment. *Eur. Phys. J. C, 76(8):434*, doi:10.1140/epjc/s10052-016-4271-x.

Baldini, A et al. (MEG II Collaboration) 2018. The design of the MEG II experiment. *Eur. Phys. J. C, 78(5), 380*, doi.org/10.1140/epjc/s10052-018-5845-6.

Baldini A. M. and Mori T. 2021. MEG: Muon to Electron and Gamma. *SciPost Phys. Proc., 5:019*, doi:10.21468/SciPostPhysProc.5.019.

Ballof, J. et al. 2020. The upgraded ISOLDE yield database – A new tool to predict beam intensities. *Nuclear Instruments and Methods in Physics Research Section B: Beam Interactions with Materials and Atoms, 463: 211-15*. 2020.

Barashenkov, V. and Toneev, V. 1972. *Interaction of High Energy Particles and Nuclei with Atomic Nuclei. Moscow : Atomizdat*, 1972.

Bartoszek, L. et al. 2015. Mu2e Technical Design Report. *arXiv:1501.05241*, arxiv.org/abs/1501.05241.

Baum R. P. et al. 2017. Clinical evaluation of the radiolanthanide terbium-152: first-in-human PET/CT with ^{152}Tb-DOTATOC. *Dalton Transactions, 46(42):14638–14646*, doi:10.1039/c7dt01936j.

Baumgarten, C., 2021. MinT User Guide. Available at: https://gitlab.psi.ch/baumgarten/mint-src/-/blob/master/TeX/mint_user.pdf.

Becker, H. et al. 2015. Neutron production and thermal moderation at the PSI UCN source. *Nuclear Instruments and Methods in Physics Research Section A: Accelerators, Spectrometers, Detectors and Associated Equipment, 777*. 2015.

Bell, G.I. and Glasstone, S. 1970. *Nuclear Reactor Theory*. [Eds.] Van Nostrand Reinhold Company. 1970.

Bellgardt, U. et al. 1988. Search for the Decay $\mu \dashrightarrow eee$. *Nucl. Phys. B, 299:1–6*, doi:10.1016/0550-213(88)90462-2.

Bennett, G. W. et al. 2006. Final Report of the Muon E821 Anomalous Magnetic Moment Measurement at BNL. *Phys. Rev. D, 73:072003*, doi:10.1103/PhysRevD.73. 072003.

Berg, F. et al. 2016. Target studies for surface muon production. *Phys. Rev. Accel. Beams, 19(2), 024701, p.1-13*, doi.org/10.1103/PhysRevAccelBeams.19.024701.

Berg, F. et al. 2020. A quasi-non-invasive ultra-thin luminophore foil detector system for secondary beam monitoring. *Nucl. Instrum. Methods A, 955, 163298*, doi.org/10.1016/j.nima.2019.163298.

Bergoz. 2021. Non-destructive DC beam current measurement. [Online] Bergoz Instruments, 2021. [Cited: 11 3, 2021.] https://www.bergoz.com/products/npct/.

Bernstein, R. H. 2019. The Mu2e Experiment. *Front. in Phys., 7:1*, doi:10.3389/fphy. 2019.00001.

Bertl, W. H. et al. 2006. A Search for muon to electron conversion in muonic gold. *Eur. Phys. J. C, 47:337–346*, doi:10.1140/epjc/s2006-02582-x.

Berz, M. and Makino, K. 2006a. COSY INFINITY Version 9. *Nucl. Instrum. Methods A, 558, p.346-350*, doi.org/10.1016/j.nima.2005.11.109.

Berz, M., Makino, K. and Young-Kee, K. 2006b. Long-Term Stability of the Tevatron by Verified Global Optimization. *Nucl. Instrum. Methods A, 558, p.1-10*, doi.org/10.1016/j.nima.2005.11.035.

Bespin, C. et al. 2020. DMAPS Monopix developments in large and small electrode designs. *NIMA 978, 164460*.

Beyer, G.J. et al. 2004. Targeted alpha therapy in vivo: direct evidence for single cancer cell kill using ^{149}Tb-rituximab. *Eur J Nucl Med Mol Imaging, 31*. 2004.

Blank, H., Brossmann, G. and Kemmerich, M. 1962. ZWEI- UND MEHRSTOFFSYSTEME MIT PLUTONIUM. *Karlsruhe: Kernforschungszentrum Karlsruhe*, 1962.

Brönnimann, C. et al. 2006. Development of an indium bump bond process for silicon pixel detectors at PSI. *NIMA 565, 303*.

Brown, K.L. and Iselin, F.C., 1974. DECAY TURTLE (Trace Unlimted Rays Through Lumped Elements): A computer program for simulating charged-particle beam transport systems, including decay calculations. *CERN-74-02. Geneva: CERN, 1974. 51 p*. DOI 10.5170/CERN-1974-002. Available at: http://cds.cern.ch/record/186178.

Buller, R. et al. 2021. Chemistry Roadmap for Research Infrastructures 2025–2028 by the Swiss Chemistry Community. *Swiss Academies Reports, 16*, doi:10.5281/zenodo.4572642.

Cagran, C. 2004. Untersuchung des Emissionsverhaltens flüssiger Metalle mittels Photopolarimetrie und Mehrwellenlängenpyrometrie. *Graz: Institut für Experimentalphysik der Technischen Universität Graz*, 2004.

Calibbi, L. and Signorelli, G. 2018. Charged Lepton Flavour Violation: An Experimental and Theoretical Introduction. *Riv. Nuovo Cim., 41(2):71–174*, doi: 10.1393/ncr/i2018-10144-0.

Caminada, L. and Starodumov, A. 2009. Building and commissioning of the CMS pixel barrel detector. *JINST 4, P03017*.

Campbell P., Moore I. D., and Pearson M. R. 2016. Laser spectroscopy for nuclear structure physics. *Progress in Particle and Nuclear Physics, 86:127–180*, doi:10.1016/j.ppnp.2015.09.003.

Catherall, R. et al. 2017. The ISOLDE facility. *Journal of Physics G: Nuclear and Particle Physics, 44(9):094002*, doi:10.1088/1361-6471/aa7eba.

CDA, 2010. THE COPPER ADVANTAGE A Guide to Working With Copper and Copper Alloys. *Copper Development Association*. A1360.

Cengel, Y.A. 2003. *Heat Transfer: A Practical Approach*. New York: McGraw-Hill, 2003.

CERN-ISOLDE. 2021. RILIS Database. [Online] http://isolde.cern/rilis

Cezairliyan, A., McClure, J.L. and Beckett, C.W. 1971. High-speed (subsecond) measurement of heat capacity, electrical resistivity, and thermal radiation properties of tantalum in the range 1900 to 3200 K. *Journal of research of the National Bureau of Standards-A. Physics and Chemistry*. 1971.

Choi, J. et al., 2020. Disentangling Intertwined Quantum States in a Prototypical Cuprate Superconductor. https://arxiv.org/abs/2009.06967

CHRISP Swiss Research Infrastructure for Particle Physics. https://www.psi.ch/ltp/facilities. Accessed: 2021-12-14.

CMS collaboration 2021. The CMS Phase-1 Pixel Detector Upgrade. *JINST 16, P02027*.

Cost, J. R., Janowski, K. R. and Rossi, R. C. 1968. Elastic properties of isotropic graphite. *The Philosophical Magazine: A Journal of Theoretical Experimental and Applied Physics*. 1968, Vol. 17, 148.

Correia J. G., Johnston K., and Wahl U. 2012. Nuclear radioactive techniques applied to materials research. *Radiochimica Acta, 100(2):127–137*, doi:10.1524/ract.2011.1873.

CRC Handbook. 2021. CRC Handbook of Chemistry and Physics. Ed. 102. CRC Press. [Online] Accessed 21.11. https://hbcp.chemnetbase.com/faces/documents/12_09/12_09_0001.xhtml.

Crivellin, A. et al. 2017. Renormalisation-group improved analysis of $\mu \dashrightarrow e$ processes in a systematic effective-field-theory approach. *JHEP, 05:117*, doi:10.1007/JHEP05(2017)117.

Damerell, C. 2021. Tracking the rise of pixel detectors. *CERN Courier, Volume 61, Number 4*, p.39.

Das, D. et al. 2021a. Probing the superconducting gap structure in the noncentrosymmetric topological superconductor ZrRuAs. *Physical Review B, 103: 144516*, doi:10.1103/PhysRevB.103.144516.

Das, D. et al. 2021b. Unconventional Pressure Dependence of the Superfluid Density in the Nodeless Topological Superconductor α-$PdBi_2$. *Physical Review Letters, 127:217002*, doi:10.1103/PhysRevLett.127.217002.

Degueldre, C., Bertsch, J. and Martin, M. 2016. Post irradiation examination of nuclear fuel: Toward a complete analysis, *Progress in Nuclear Energy, 92: 242-53*. 2016.

Daum, M. 1982. A surface muon beam at SIN. *Nucl. Instrum. Methods, 192(2), p.137-141*, doi.org/10.1016/0029-554X(82)90815-1.

Deniau, L. et al., 2021. The MAD-X Program (Methodical Accelerator Design): Reference Manual. [online] https://mad.web.cern.ch/mad/webguide/manual.html.

Deutsches Kupferinstitut. 2005. Deutsches Kupferinstitut. [Online] 2005. [Cited: 04 29, 2021.] http://www.kupferinstitut.de.

DIN. 2012. Probenentnahme von luftgetragenen radioaktiven Stoffen aus Kanälen und Kaminen kerntechnischer Anlagen (ISO 2889:2010). *DIN ISO 2889*. Germany, July 2012.

Dölling, R., et al. 2002. Profile Measurement Of Scanning Proton Beam For LiSoR Using Carbon Fibre Harps. *AIP Conference Proceedings, 2002. Vol. 648, 361.*

Dölling, R. et al., 2005. Beam diagnostics at the high power proton beam lines and targets at PSI. *7th European Workshop on Beam Diagnostics and Instrumentation for Particle Accelerators, DIPAC 2005*. p. 228-232.

Dölling, R. et al., 2019. DEVELOPMENT OF MODULAR SPARE PARTS FOR THE PROFILE AND POSITION MONITORS OF THE 590 MeV BEAM LINE AT HIPA. *Proc. 8th Int. Beam Instrumentation Conf. (IBIC'19), Malmö, Sweden, Sep. 2019*, pp. 402-406. doi:10.18429/JACoW-IBIC2019-TUPP035.

Dölling, R. et al., 2020. PROGRESS OF PROFILE MEASUREMENT REFURBISHMENT ACTIVITIES AT HIPA. *Proc. 9th Int. Beam Instrumentation Conf. (IBIC'20), Santos, Brazil, Sep. 2020*, pp. 179-183. doi:10.18429/JACoW-IBIC2020-WEPP33.

Domnanich, K. A. et al. 2017a. Domnanich, K.A., C. Müller, M. Benešová, R. Dressler, S. Haller, U. Köster, B. Ponsard, R. Schibli, A. Türler, and N. Van der Meulen. ^{47}Sc as useful β^--emitter for the radiotheragnostic paradigm: a comparative study of feasible production routes. *EJNMMI Radiopharmacy and Chemistry, 2*.

Domnanich, K. A. et al. 2017b. Domnanich, K.A., R. Eichler, C. Müller, S. Jordi, V. Yakusheva, S. Braccini, M. Behe, R. Schibli, A. Türler and N. van der Meulen. Production and separation of ^{43}Sc for radiopharmaceutical purposes. *EJNMMI Radiopharmacy and Chemistry, 2: 14*.

DORA. Digital Object Repository At PSI. https://www.dora.lib4ri.ch/psi/. Accessed: 2021-12-12.

Dresser, M. J. 1968. The Saha-Langmuir Equation and its Application. *Journal of Applied Physics, 39: 338-39*.

EDI. 2017a. *Verordnung des EDI über den Strahlenschutz bei nichtmedizinischen Anlagen zur Erzeugung ionisierender Strahlung. SR 814.501.51* Switzerland, 4. April 2017.

EDI. 2017b. *UraM, Verordnung des EDI über den Umgang mit radioaktivem Material (UraM). SR 814.554* Switzerland, 26. April 2017.

EDI. 2021. *Verordnung des EDI über den Umgang mit radioaktivem Material (UraM)*. s.l. : Eidgenössische Departement des Innern (EDI), 2021. 814.554.

Eichler R. and Grab C. 2021. The SINDRUM-I Experiment. S*ciPost Phys. Proc., 5:007*, doi:10.21468/SciPostPhysProc.5.007.

Engle, J.W. 2018. The Production of Ac-225. C*urr Radiopharm. 2018, 11(3):173-179*. doi: 10.2174/1874471011666180418141357.

ENSI. 2015. *Messmittel für ionisierende Strahlung. ENSI-G13* Switzerland, October 2015.

ENSI. 2020. *Anlageninterner Strahlenschutz. ENSI-G12* Switzerland, April 2020.

ENSI-G12. Eidgenössische Nuklearsicherheitsinspektorat. Anlageninterner Strahlenschutz. 01. November 2021.

ENSI. 2021. *Richtlinie für die schweizerischen Kernanlagen*. Brugg: ENSI, 2021. ENSI-G12 (Annex 2).

European Strategy 2020. Update of the European Strategy for Particle Physics. CERN Council, Geneva. doi:10.17181/ESU2020.

Fedosseev, V.N., Yu Kudryavtsev, and V.I. Mishin. 2012. Resonance laser ionization of atoms for nuclear physics. *Physica Scripta, 85*. 2012.

Fedosseev, V. et al. 2017. Ion beam production and study of radioactive isotopes with the laser ion source at ISOLDE. *Journal Of Physics G-Nuclear And Particle Physics, 44(8)*, doi:10.1088/1361-6471/aa78e0.

Ferrari, A. et al. 2016. *Po-production in lead: A benchmark between Geant4, FLUKA and MCNPX*. SATIF-13, 2016.

Filges, D. and Goldenbaum, F. 2009. *Handbook of Spallation Research: Theory, Experiments and Applications. Wiley*, 2009.

Fischer, O. et al. 2021. Unveiling Hidden Physics at the LHC. arXiv:2109.06065.

Fitzsimmons, J., Foley, B., et al. 2019. Optimization of Cation Exchange for the Separation of Actinium-225 from Radioactive Thorium, Radium-223 and Other Metals. *Molecules, 24: 1921*. 2019.

Fitzsimmons, J., Griswold, J., et al. 2019. Defining Processing Times for Accelerator Produced ^{225}Ac and Other Isotopes from Proton Irradiated Thorium. *Molecules, 24: 1095*. 2019.

Fluke Process Instruments. 2021. *https://www.flukeprocessinstruments.com*. [Online] 05 28, 2021. https://www.flukeprocessinstruments.com/en-us/service-and-support/knowledge-center/infrared-technology/emissivity-metals.

Fobes, D. M. et al., 2017. Versatile strain-tuning of modulated long-period magnetic structures. *Applied Physics Letters, 110, 192409*.

FORCE11. The FAIR Data Principles. https://www.force11.org/group/fairgroup/fairprinciples. Accessed: 2021-12-12.

Forrest, R. A. and EURATOM/UKAEA 2007. FISPACT-2007: User manual. *Technical Report UKAEA FUS 534. EURATOM/UKAEA Fusion Association*. Abington, UK.

Frosch, R. 1980. PSI Internal Report TM-37-14. 1-12. Paul Scherrer Institut, Villigen, Switzerland.

Frosch, R. 1995. PSI Internal Report TM-11-95-01. 1-7. Paul Scherer Institut, Villigen, Switzerland.

Gadelshin, V.M. et al. 2019. Measurement of the laser resonance ionization efficiency for lutetium. *Radiochimica Acta, 107: 653-61*. 2019.

Gadelshin, V.M. et al. 2020. MELISSA: Laser ion source setup at CERN-MEDICIS facility. Blueprint. *Nuclear Instruments and Methods in Physics Research Section B: Beam Interactions with Materials and Atoms, 463: 460-63*. 2020.

Gallmeier, F. X. et al. 2007. An environment using nuclear inventory codes in combination with the radiation transport code MCNPX for accelerator activation problems. *Proc. of the 8th Int. Topical Meeting on Nuclear Applications and Utilization of Accelerators (AccApp'07), Pocatello, USA, July 29–August 2, 2007*, pp. 207–211.

Gallmeier, F. and Wohlmuther, M. 2015. The Residual Nuclei Patch of MCNPX 2.6.0 and 2.7.0. *TM-85-15-03*. PSI, 2015.

Garcia-Sciveres, M. and Wermes, N. 2018. A review of advances in pixel detectors for experiments with high rate and radiation. *Rep. Prog. Phys. 81, 066101*.

Geue, T. et al. 2021, SINQ - performance of the new neutron delivery system, *Neutron News, 32(2)*, p.37-43.

Goorley, T. et al., 2017. Initial MCNP6 Release Overview - MCNP6 version 1.0. *Nuclear Technology, 180:3*, p.298-315. DOI 10.2172/1086758. Available at : https://www.osti.gov/biblio/1086758.

Gracheva, N. et al. 2019. Gracheva, N., Müller, C., Talip, Z., Heinitz, S., Köster, U., Zeevaart, J.R., Vögele, A., Schibli, R. and N. van der Meulen. Production and characterization of no-carrier-added ^{161}Tb as an alternative to the clinically-applied ^{177}Lu for radionuclide therapy. *EJNMMI Radiopharmacy and Chemistry, 4: 12*. 2019.

Gracheva, N. et al. 2020. Gracheva, N., Carzaniga, T.S., Schibli, R., Braccini, S. and N. van der Meulen. ^{165}Er: A new candidate for Auger electron therapy and its possible cyclotron production from natural holmium targets. *Applied Radiation and Isotopes, 159: 109079*. 2020.

Gracheva, N. 2020. Development of Terbium and Erbium Radiolanthanides for Radiopharmaceutical Application. *ETH Zurich*. 2020.

Grange, J. et al. 2015. Muon (g-2) Technical Design Report. *arXiv:1501.06858*, arxiv.org/abs/1501.06858.

Graverini, E. 2019. Flavour anomalies: a review. *J. Phys. Conf. Ser., 1137(1):012025*, doi:10.1088/1742-6596/1137/1/012025.

Grillenberger, J., Baumgarten, C., and Seidel, M. 2021. The High Intensity Proton Accelerator Facility. *SciPost Phys. Proc., 5:002*, doi:10.21468/SciPostPhysProc.5.002.

Grinenko, V. et al. 2021a. Unsplit superconducting and time reversal symmetry breaking transitions in Sr_2RuO_4 under hydrostatic pressure and disorder. *Nature Communications, 12:3920*, doi:10.1038/s41467-021-24176-8.

Grinenko, V. et al., 2021b. Split superconducting and time-reversal symmetry-breaking transitions in Sr_2RuO_4 under stress. *Nat. Phys. 17, 748*.

Grundler, P.V. et al. 2020. The Metamorphosis of Radionuclide Production and Development at Paul Scherrer Institute. *CHIMIA, 74(12):968–975, 2020*. doi:10.2533/chimia.2020.968.

Guguchia, Z. et al. 2017. Signatures of the topological s^{+-} superconducting order parameter in the type-II Weyl semimetal T_{d-} $MoTe_2$. *Nature Communications, 8:1082*, doi:10.1038/s41467-017-01066-6.

Guguchia, Z. 2020a. Unconventional magnetism in layered transition metal dichalcogenides. *Condensed Matter, 5(2)*, doi:10.3390/condmat5020042.

Guguchia, Z. et al., 2020b. Using Uniaxial Stress to Probe the Relationship between Competing Superconducting States in a Cuprate with Spin-stripe Order. *Phys. Rev. Lett. 125, 097005*.

Guguchia Z. et al. 2021. Multiple quantum phase transitions of different nature in the topological kagome magnet $Co_3Sn_{2-x}In_xS_2$. *npj Quantum Materials, 6:1–8*, doi:10.1038/s41535-021-00352-3.

Guillou, A. et al. 2020. Light-induced synthesis of protein conjugates and its application in photoradiosynthesis of ^{89}Zr-radiolabeled mono-clonal antibodies. *Nature Protocols, 15(11)*, doi:10.1038/s41596-020-0386-5.

Heidenreich, G. 2009. Zusammenfassung einiger Ergebnisse zur Weiterentwicklung des Kollimators KHE2/3 für höhere Ströme. PSI, 2009.

Heidenreich, private comm., Heidenreich, Gerd, private communication.

Hicks, C. W. et al., 2017. Piezoelectric-Driven Uniaxial Stress Apparatus for Muon Spin Rotation. *Proceedings of the 14th International Conference on Muon Spin Rotation, Relaxation and Resonance (μSR2017)*, 10.7566/JPSCP.21.011040.

Higman R., Bangert D., and Jones S. 2019. Three camps, one destination: the intersections of research data management, FAIR and Open. *Insights-The UKSG Journal, 32*, doi:10.1629/uksg.468.

HIMB 2021. HIMB Physics Case Workshop, April 6-9, 2021. https://indico.psi.ch/event/10547/. Accessed: 2021-12-12.

Houtman, H., Jones, F.W. and Kost, C.J. 1994. Laplace and Poisson equation solution by relax3d. *Computers in Physics, 8: 469-73*. 1994.

Huang, L. et al. 2016. Spectroscopic evidence for a type II Weyl semimetallic state in $MoTe_2$. *Nature Materials, 15:1155–1160*, doi:10.1038/nmat4685.

IAEA. 2021. IAEA Database of cyclotrons for radionuclide production. [Online] 2021.

Ikedo, Y. 2013. Positron separators in Superomega muon beamline at J-PARC. *Nucl. Instrum. Methods B, 317*, p.365-368, doi.org/10.1016/j.nimb.2013.07.060.

ISOLDE Yield Database. https://isoyields2.web.cern.ch/. Accessed: 2021-12-16.

Janoschek M. and Khasanov R. 2020. ExtremeP: A Joint Pressure Capability for Complementary Neutron and Muon Experiments on Quantum Materials. *SNF R'Equip Project 198101*, https://data.snf.ch/grants/grant/198101.

Japan 2017. Final report of the committee on Future Projects in High Energy Physics, Japan. http://www.jahep.org/files/20170906-en.pdf. Accessed: 2021-12-11.

Jordan, P.L., Robert, A.D. and Glasier Jr., L.F. 1960. Spectral Emissivity, Total Emissivity, and Thermal Conductivity of Molybdenum, Tantalum, and Tungsten above 2300 K. *Journal of Applied Physics*. 1960.

Kästli, H.-C. et al. 2006. Design and Performance of the CMS pixel detector readout chip. *NIMA 565, 188*.

Keil, B., Duperrex, P.A. and Mueller, U., 2006. Commissioning of a new digital BPM system for the PSI proton accelerators. *Proceedings, 10th European Conference, EPAC 2006, Edinburgh, UK, June 26-30, 2006*, p.1226-1228

Kenney, C.J. et al. 1994. A prototype monolithic pixel detector. *NIMA 342, 59*.

Kettle, P.-R. 2019. HiMB Technical Note. Paul Scherrer Institut, Villigen, Switzerland. 2019.

Khasanov, R. et al. 2016 High pressure research using muons at the Paul Scherrer Institute. *High Pressure Research, 36(2):140–166*, doi:10.1080/08957959.2016.1173690.

Kirchner, R. 1992. On the release and ionization efficiency of catcher-ion-source systems in isotope separation on-line. *Nuclear Instruments and Methods in Physics Research B, 70: 186-99*. 1992.

Kirchner, R. 1996. Ion sources for radioactive beams and related problems (Review) (invited). *Review of Scientific Instruments, 67: 928-33*. 1996.

Kiselev, D. et al. 2015a. D. Kiselev, P. Otiougova, T. Reiss, V. Talanov, and M. Wohlmuther. Estimate of the total decommissioning radioactive waste of the high intensity proton accelerator (HIPA) facility at PSI. *In Proc. of ARIA 2015, Knoxville, Tennessee, 2015*.

Kiselev, D. 2015b. Key parameters for the calculation of the temperature at Target E. PSI, 2015.

Kiselev, D. et al., 2021a. Progress and Challenges of the PSI Meson Targets and Relevant Systems. *Proc. of the 3rd J-PARC Symposium (J-PARC2019). JPS Conf. Proc. 33, 011102 (2021)*. DOI 10.7566/JPSCP.33.011102.

Kiselev, D., et al. 2021b. The Meson Production Targets in the high energy beamline of HIPA at PSI. *SciPost Phys. Proc. 5, 3*, 2021, doi.org/10.21468/SciPostPhysProc.5.003.

Kiselev, D. et al. 2021. The Meson Production Targets in the high energy beamline of HIPA at PSI. *SciPost Phys. Proc., 5:003*, doi:10.21468/SciPostPhysProc.5.003.

Kjelberg, A. and Rudstam, G. 1970. The ISOLDE Isotope Separator On-Line Facility at Cern. *Geneva: CERN ISOLDE*. 1970.

Kolano, A. et al., 2018. Intensity limits of the PSI Injector II cyclotron. *Nuclear Instruments and Methods in Physics Research Section A: Accelerators, Spectrometers, Detectors and Associated Equipment. Vol. 885*, p. 54-59. ISSN 0168-9002. DOI https://doi.org/10.1016/j.nima.2017.12.045.

Kratochwil, C. et al. 2016. ^{225}Ac-PSMA-617 for PSMA-Targeted α-Radiation Therapy of Metastatic Castration-Resistant Prostate Cancer. *Journal Of Nuclear Medicine, 57(12):1941–1944*, doi:10.2967/jnumed.116.178673.

Kronfeld, A.S. et al. 2016. Project X: Physics Opportunities, *arXiv:1306.5009*, arxiv.org/abs/1306.5009.

KTA. 2016. Überwachung der Ableitung gasförmiger und an Schwebstoffen gebundener radioaktiver Stoffe, Sicherheitstechnische Regel des KTA. *KTA1503.1* November 2016.

KTA. 2017. Überwachung der Aktivitätskonzentrationen radioaktiver Stoffe in der Raumluft von Kernkraftwerken, *Sicherheitstechnische Regel des KTA. KTA1502* November 2017.

Kugathasan, T. et al. 2020. Monolithic CMOS sensors for sub-nanosecond timing. *NIMA 979, 164461*.

Lehenberger, S. 2010. Evaluation and application of the low energy electron emitter ^{161}Tb. *PhD Dissertation. Technischen Universität München*. 2010.

Lehenberger, S. et al. 2011. The low-energy β– and electron emitter ^{161}Tb as an alternative to ^{177}Lu for targeted radionuclide therapy. *Nuclear Medicine and Biology, 38: 917-24*. 2011.

LMU 2021. SμS Instruments. LMU website www.psi.ch/en/lmu/instrumentation.

Luetkens, H. et al. 2009. The electronic phase diagram of the $LaO_{1-x}F_xFeAs$ superconductor. *Nature Materials, 8: 305–309*, doi:10.1038/nmat2397.

Lugaro, M et al. 2016. Origin of the p-process radionuclides ^{92}Nb and ^{146}Sm in the early solar system and inferences on the birth of the Sun. *PNAS, 113:907-912*, doi:10.1073/pnas.1519344113.

Maag, R. and Weinreich, R. 1991. Four years experience with a polyvalent 72 MeV target station. *IVth International Workshop on Targetry and Target Chemistry, edited by Regin Weinreich*. Paul Scherrer Institut, Villigen, Switzerland. 1991.

Maglic, K.D. 2003. Recommended specific heat capacity functions of group VA elements. *International Journal of Thermophysics*. 2003.

Magill, J. 2021. Nucleonica. *Nucleonica GmbH*. [Online] 21.11.21. www.nucleonica.com.

Malter, L. and Langmuir, D.B. 1939. Resistance, emissivities and melting point of tantalum. *Physical Review*. 1939.

Marciano W. J., Mori T. , and Roney J. M. 2008. Charged Lepton Flavor Violation Experiments. *Ann. Rev. Nucl. Part. Sci., 58:315–341*, doi:10.1146/annurev.nucl.58.110707.171126.

Martinez Palenzuela, Y. et al. 2021. The CERN-MEDICIS Isotope Separator Beamline. *Front Med (Lausanne), 8: 689281*. 2021.

Matsumoto, T. and Cezairliyan, A. 1997. A Combined Transient and Brief Steady-State Technique for Measuring Hemispherical Total Emissivity of Electrical Conductors at High Temperatures: Application to Tantalum. *International Journal of Thermophysics*. 1997.

Matsumoto, T., Barreiro, G. and Ono, A. 2000. Measurements of Specific Heat Capacity and Hemispherical Total Emissivity of Refractory Metals Using a Feedback-Controlled Pulse-Heating Technique. *TPDS-web Thermophysical Properties Database System*. [Online] 29.04.2021 https://tpds.db.aist.go.jp/tpds-web/index.aspx?MaterialID=107.

MatWeb. MatWeb Material Property Data. *MatWeb Material Property Data*. [Online] 29. 04 2021 http://www.matweb.com/.

Meier, B. 2011. CMS pixel detector with new digital readout architecture. *JINST 6, C01011*.

Mendels, P. et al. 2007. Quantum Magnetism in the Paratacamite Family: Towards an Ideal Kagome Lattice. *Physical Review Letters, 98:077204*, doi:10.1103/PhysRevLett.98.077204.

Méot, F., 1999. The ray-tracing code Zgoubi. *Nuclear Instruments and Methods in Physics Research Section A: Accelerators, Spectrometers, Detectors and Associated Equipment. Vol. 427*, p. 353-356. ISSN 0168-9002. DOI https://doi.org/10.1016/S0168-9002(98)01508-3.

Mezger, A.C. and Seidel, M., 2010. Control and protection aspects of the megawatt proton accelerator at PSI. *HB 2010 - 46th ICFA Advanced Beam Dynamics Workshop on High-Intensity and High-Brightness Hadron Beams*. p.281-285.

Miedema, A.R. 1975. On the heat of formation of solid alloys. *Journal of the Less-Common Metals, 41:283-298*. 1975.

Miedema, A.R. 1976. On the heat of formation of solid alloys II. *Journal of the Less-Common Metals, 46:67-83*. 1976.

Mihara. S. et al. 2013. Charged Lepton Flavor-Violation Experiments. *Ann. Rev. Nucl. Part. Sci., 63:531–552*, doi:10.1146/annurev-nucl-102912-144530.

Mokhov, N. 2021. Personal communication.

Morenzoni, E. et al. 2014. Low-Energy Muons at PSI: Examples of Investigations of Superconducting Properties in Near-Surface Regions and Heterostuctures. *JPS Conf. Proc. 2, 010201*, doi:10.7566/JPSCP.2.010201.

Morgenstern, A. et al. 2018. An Overview of Targeted Alpha Therapy with ^{225}Actinium and ^{213}Bismuth. *Curr Radiopharm. 2018, 11(3):200-208*. doi:10.2174/1874471011666180502104524.

Morgenstern A., Apostolidis C., and Bruchertseifer F. 2020. Supply and clinical application of actinium-225 and bismuth-213. *Seminars in Nuclear Medicine, 50(2):119–123*, doi:10.1053/j.semnuclmed.2020.02.003.

Moritsu, M. 2021. The COMET Experiment: Search for Muon-to-Electron Conversion. *JPS Conf. Proc., 33:011111*, doi:10.7566/JPSCP.33.011111.

Mosher, S.W. et al. 2015. ADVANTG An Automated Variance Reduction Parameter Generator. *ORNL/TM-2013/416 Rev. 1, United States: N. p., 2015*. Web. doi:10.2172/1210162.

Müller, C. et al. 2012. Müller, C., K. Zhernosekov, U. Köster, K. Johnston, H. Dorrer, A. Hohn, N. T. van der Walt, A. Türler, and R. Schibli. A unique matched quadruplet of terbium radioisotopes for PET and SPECT and α- and β^--radionuclide therapy: An in vivo proof-of-concept study with a new receptor-targeted folate derivative', *J Nucl Med, 53: 1951-9*. 2012.

Müller, C., Fischer, E. et al. 2014. Future prospects for SPECT imaging using the radiolanthanide terbium-155 - production and preclinical evaluation in tumor-bearing mice. *Nucl Med Biol, 41 Suppl: e58-65*. 2014

Müller, C., Reber, J. et al. 2014. Folate receptor targeted alpha-therapy using terbium-149. *Pharmaceuticals (Basel), 7:353-65*. 2014.

Müller, C., Vermeulen, C., Johnston, K. et al. 2016. Preclinical in vivo application of 152Tb-DOTANOC: a radiolanthanide for PET imaging. *EJNMMI Research, 6:35*. 2016.

Müller, C., Vermeulen, C., Köster, U. et al. 2016. Alpha-PET with terbium-149: evidence and perspectives for radiotheragnostics. *EJNMMI Radiopharmacy and Chemistry, 1:5*. 2016.

Müller, C. et al. 2019. Preclinical investigations and first-in-human application of Tb-152-PSMA-617 for PET/CT imaging of prostate cancer. *EJNMMI Research, 9*, doi:10.1186/s13550-019-0538-1.

Muons Inc. 2019. G4beamline (version 3.06). http://www.muonsinternal.com/muons3/G4beamline

MWV Bauingenieure AG. 2021. *Machbarkeit Neubau TATTOOS-Gebäude*. Baden: 2021.

Nevay, L.J. et al., 2020. BDSIM: An accelerator tracking code with particle–matter interactions. C*omputer Physics Communications. Vol. 252*, p. 107200. ISSN 0010-4655. DOI https://doi.org/10.1016/j.cpc.2020.107200.

NMIJ, DBWG. Equation derived from NIST-JANAF Thermochemical Tables Fourth Edition. *TPDS-web Thermophysical Properties Database System*. [Online] NMIJ AIST. 29.04.2021. https://tpds.db.aist.go.jp/tpds-web/index.aspx?MaterialID=107.

NMIJ, AIST. *TPDS-web. TPDS-web Thermophyscal Properties Database Systems*. [Online] Thermophysical Properties Research Group, Research Institute for Material and Chemical Measurement, NMIJ, AIST. 29.04.2021. https://tpds.db.aist.go.jp/tpds-web/index.aspx?MaterialID=107.

Noah, E. et al. 2012. Post-irradiation analysis of the tantalum container of an ISOLDE LBE target. *Journal of Nuclear Materials, 431: 60-65*. 2012.

Novak-Hofer, I. and Schubiger, A.P. 2002. Copper-67 as a therapeutic nuclide for radioimmunotherapy. *European Journal of Nuclear Medicine and Molecular Imaging, 29: 821-30*. 2002.

NTOF. NTOF Public web: https://twiki.cern.ch/NTOFPublic. Accessed: 2021-12-16.

NuPECC 2017. NuPECC Long Range Plan: Perspectives of Nuclear Physic. http://www.nupecc.org/pub/lrp17/lrp2017.pdf. Accessed: 2021-12-11.

Olivo, M., Mariani, E. and Rossetti, D. 1998. An electrostatic beam splitter for the PSI 590 MeV - 1MW proton beam line. *EPAC, 1998*.

Oram, C. et al. 1981. Commissioning of a new low energy π-μ at TRIUMF. *Nucl. Instrum. Methods, 179(1)*, p.95-103, doi.org/10.1016/0029-554X(81)91166-6.

P5 2014. Building for Discovery - Strategic Plan for U.S. Particle Physics in the Global Context. https://science.osti.gov/-/media/hep/hepap/pdf/May-2014/FINAL_P5_Report_053014.pdf. Accessed: 2021-12-11.

Paolozzi, L. et al. 2019. Characterization of the demonstrator of the fast silicon monolithic ASIC for the TT-PET project. *JINST 14, P02009*.

Parker, C. et al. 2013. Alpha emitter radium-223 and survival in metastatic prostate cancer. *New England Journal of Medicine, 369(3):213–223*, doi:10.1056/NEJMoa1213755.

Patra, M. et al. 2019. Photochemical conjugation and one-pot radiolabelling of antibodies for immuno-pet. *Angewandte Chemie International Edition, 58(7):1928–1933*, doi:10.1002/anie.201813287.

Pelowitz, D. B. 2013. MCNP6 User's Manual Version 1.0. *LA-CP-13-00634*. LANL. Los Alamos, United States.

Peric, I. et al. 2013. High-voltage pixel detectors in commercial CMOS technologies for ATLAS, CLIC and Mu3e experiments. *NIMA 731, 131*.

Petrovic, C. 2001. *SP-FISPACT-2001: A computer code for activation and decay calculations for intermediate energies. A connection of FISPACT with MCNPX*. ENEA-RT/ERG, 2001.

Pifer, A., Bowen, T. and Kendall, K. 1976. A High Stopping Density μ^+ Beam. *Nucl. Instrum. Methods, 135(1)*, p.39-46, doi.org/10.1016/0029-554X(76)90823-5.

Poco Graphite, Inc. 2001. *Properties and Characteristics of Graphite for Industrial Applications*. 2001.

Powell, R.W., Ho, C.Y. and Liley, P.E. 1972. Thermal Conductivity of the Elements. *Journal of Physical and Chemical Reference Data*. 1972.

Prokscha, T. et al. 2008. The new μE4 beam at PSI: A hybrid-type large acceptance channel for the generation of a high intensity surface-muon beam. *Nucl. Instrum. Methods Phys. Res., Sect. A 595(2)*, p.317-331, doi.org/10.1016/j.nima.2008.07.081.

PSI. 2010. SwissFEL. Conceptual design report. [Ed.] Roman Ganter. Villigen PSI, Switzerland: Paul Scherrer Institut, 2010. 130 p.

PSI-AW-01-07-02. PSI Weisung. Sicherheit, Gesundheitsschutz und Umweltschutz am PSI.

PSI-AW-22-04-01. PSI Weisung. Betriebsvorschriften für das Gebäude WIPA.

PSI-AW-81-18-01. PSI Weisung. Betriebsvorschriften HIPA.

PSI-AW-81-20-434. PSI Weisung. Allgemeine Vorschriften für den Betrieb der PSI Beschleunigeranlagen.

PSI-AW-83-18-04. Betriebsvorschrift für den „Kontrollierten Abstellplatz West" (WKAA und WALB) auf dem PSI-Westareal.

PSI-AW-96-18-01. PSI Weisung. Allgemeine Weisung für den Strahlenschutz am Paul Scherrer Institut.

PSI-AW-96-19-176. PSI Weisung. Arbeitssicherheit und Gesundheitsschutz am PSI.

PSI-AW-96-19-198. PSI Weisung. Prozess „PSYS Entwicklung".

PSI-AW-96-99-04. PSI Weisung. Betriebsstrahlenschutz: Merkblätter für das SU-Personal.

PSI-PB-9670-214. PSI Prozessbeschreibung. Einsatz und Betrieb von am PSI hergestellten und eingesetzten Geräten und Anlagen zu Forschungszwecken.

PSI-RL-11-14-01. 2014. Risikomanagement am PSI. *RL-11-14-01.* 2014.

PSI-TM-96-03-04. PSI Technische Mitteilung. Schutzkonzept der Personensicherheitssysteme der HIPA-Beschleunigeranlage des PSI-West.

PSI-TM-96-10-09. Beschreibung des Programms ESS41 zur Berechnung von Dosisumrechnungsfaktoren und Dosen aus den Aktivitätsabgaben über die Fortluft des PSI. 23. May 2011.

PSI Data Policy. https://www.psi.ch/en/science/psi-data-policy (under revision). Accessed: 2021-12-14.

PSI Guest House. https://www.psi.ch/en/guesthouse. Accessed: 2021-12-12.

PSI User Office. https://www.psi.ch/en/useroffice. Accessed: 2021-12-12.

Raidal, M. et al. 2008. Flavour physics of leptons and dipole moments. *Eur. Phys. J. C, 57: 13–182*, doi:10.1140/epjc/s10052-008-0715-2.

Rasor, N.S. and McClelland, J.D. 1960. Thermal properties of graphite, molybdenum and tantalum to their destruction temperatures. *Journal of Physics and Chemistry of Solids*. 1960.

Reggiani, D., et al. 2009. A Macro-Pulsed 1.2 MW Proton Beam for the PSI Ultra Cold Neutron Source. *Vancouver, Canada: PAC, 2009*.

Reggiani, D., et al. 2018. Improving machine and target protection in the SINQ beam line at PSI-HIPA. *Vancouver, Canada: IPAC, 2018*.

Reggiani, D. et al., 2020. Improving beam simulations as well as machine and target protection in the SINQ beam line at PSI-HIPA. *Journal of Neutron Research. Vol. 22*, p. 325-335.

Reimann, R. and Rüede, M. 1975. Strommonitor für die Messung eines gepulsten Ionenstrahls. *Nuclear Instruments and Methods, 1975. Vol. 129, 1*.

Rohrer, U. (TURTLE). PSI Graphic TURTLE Framework by U. Rohrer based on a CERN-SLAC-FERMILAB version by K.L. Brown et al., aea.web.psi.ch/Urs_Rohrer/MyWeb/turtle.htm.

Rohrer, U. (TRANSPORT). PSI Graphic TRANSPORT Framework by U. Rohrer based on a CERN-SLAC-FERMILAB version by K.L. Brown et al., aea.web.psi.ch/Urs_Rohrer/MyWeb/trans.htm.

Rohrer, U., 2002. A NOVEL METHOD TO IMPROVE THE SAFETY OF THE PLANNED MEGAPIE TARGET AT SINQ. *Scientific and Technical Report 2001, Vol. VI, Large Research Facilities, PSI*. p.34-35. ISSN 1423-7350. Mar 2002.

Rohrer, U., 2004. FIRST BEAM TESTS WITH THE NEW SLIT COLLIMATOR IN THE PROTON BEAM LINE TO SINQ. PSI Annual Report. 2004.

Rohrer, U., 2005. THE MULTILEVEL PROTECTION SYSTEM FOR THE VACUUM CHAMBERS OF THE HIGH-INTENSITY 590 MEV PROTON BEAM LINES. 2005.

Rothe, S. et al. 2016. Laser ion beam production at CERN-ISOLDE: New features – More possibilities. *Nuclear Instruments and Methods in Physics Research Section B: Beam Interactions with Materials and Atoms, 376: 91-96*. 2016.

Rønnow, H. M. et al. 2021. Neutron Science Roadmap for Research Infrastructures 2025–2028 by the Swiss Neutron Science Community. *Swiss Academies Reports 16 (7)*, doi:10.5281/zenodo.4637661.

Ryser, J.E. et al. 1999. [76Br]bromodeoxyuridine, a potential tracer for the measurement of cell proliferation by positron emission tomography, in vitro and in vivo studies in mice. *Nuclear Medicine and Biology, 26: 673-79*. 1999.

Sato, T. K. et al. 2013. First successful ionization of Lr (Z = 103) by a surface-ionization technique. *Rev Sci Instrum, 84: 023304*. 2013.

Scherf, H.E. 2007. Modellbildung und Simulation dynamischer Systeme. *München: Oldenbourg Wissenschaftsverlag GmbH. 978-3-486-58277-2*. 2007.

Schöning, A. et al. 2019. MuPix and ATLASPix - Architectures and Results. *PoS Vertex 2019, 024*.

Schumann D., Maugeri E., and Dressler R. 2020. Exotic Radionuclides - What are they good for? *Chimia, 74(12):932–938*, doi:10.2533/chimia.2020.932.

Schwarzbach, R. et al. 1993. Production of ^{18}F from Sodium-metal-target. *Fifth International Workshop on Targetry and Target Chemistry (WTTC). Brookhaven National Laboratory, Upton, New York*. 1993.

Schwarzbach, R. et al. 1995. Development of a simple and selective separation of ^{67}Cu from irradiated zinc for use in antibody labelling: A comparison of methods. *Applied Radiation and Isotopes, 46: 329-36*. 1995.

Schwarzbach, R. et al. 2001. A comparison of ^{67}CU production by proton (67 TO 12 MEV) induced reactions on NATZN and on enriched 68ZN/70ZN. *Journal of Labelled Compounds and Radiopharmaceuticals, 44:S809-S11*. 2001.

SCNAT CHIPP, 2021. CHIPP Roadmap for Research Infrastructure 2025-2028 and beyond by the Swiss Particle Physics Community. *Swiss Academies Reports 16 (6)*. doi.org/10.5281/zenodo.4637623. https://scnat.ch/en/uuid/i/a4a1b2d1-5483-5229-aa88-699c00c366d2-CHIPP_Roadmap

SCNAT Photons, 2021. Photon Science Roadmap for Research Infrastructures 2025-2028 by the Swiss Photon Community. *Swiss Academies Reports 16 (5)*. doi.org/10.5281/zenodo.4588917 https://scnat.ch/en/for_a_solid_science/networks_and_infrastructures/research_infrastructures/uuid/i/4aac4b50-e8a0-5681-97dd-315aaf5345c7-Photon_Science_Roadmap

SCNAT Neutrons, 2021. Neutron Science Roadmap for Research Infrastructures 2025-2028 by the Swiss Neutron Science Community. *Swiss Academies Reports 16 (7)*. doi.org/10.5281/zenodo.4637661 https://scnat.ch/en/uuid/i/23635943-a35c-5447-a0a3-f8a5ba5d823b-Neutron_Science_Roadmap

SERI State Secretariat for Education, Research and Innovation. Preparations for 2023 Swiss Roadmap for Research Infrastructures. https://www.sbfi.admin.ch/sbfi/en/home/services/publications/data-base-publications/s-n-2021-3/s-n-2021-3d.html. Accessed: 2021-12-11.

Seidel, M. et al. 2010. Production of a 1.3 MW beam at PSI. *IPAC, 2010*.

Shang T. and Shiroka T. 2021. Time-reversal symmetry breaking in Re-based superconductors: Recent developments. *Frontiers in Physics, 9:270*, doi:10.3389/fphy.2021.651163.

Sigmund, P. 1981. Sputtering by ion bombardment theoretical concepts. *doi: 10.1007/3540105212_7. In Behrisch, R. (ed.), Sputtering by Particle Bombardment I. Topics in Applied Physics (Springer: Berlin, Heidelberg)*. 1981.

Signer A., Kirch K., and Hoffman C. 2021. Review of Particle Physics at PSI. *SciPost Phys. Proc., 5*, doi:10.21468/SciPostPhysProc.5.

SINQ Swiss Spallation Neutron Source. https://www.psi.ch/sinq. Accessed: 2021- 12-14.

Smith-Jones, P., Schwarzbach, R. and Weinreich, R. 1990. The Production of ^{52}Fe by Means of a Medium Energy Proton Accelerator. *Radiochimica Acta, 50: 33*. 1990.

SµS Swiss Muon Source. https://www.psi.ch/smus. Accessed: 2021-12-14.

Snider, E. et al., 2020. Room-temperature superconductivity in a carbonaceous sulfur hydride. *Nature 586, 373*.

SR-814.50. Bundesrecht. Strahlenschutzgesetz (StSG) vom 22. März 1991.

SR-814.501. Bundesrecht. Strahlenschutzverordnung (StSV) vom 26. April 2017.

SR-814.501.51. Bundesrecht. Verordnung des EDI über den Strahlenschutz bei nichtmedizinischen Anlagen zur Erzeugung ionisierender Strahlung (SnAV) vom 26. April 2017.

SR-814.554. Bundesrecht. Verordnung des EDI über den Umgang mit radioaktivem Material (UraM) vom 26. April 2017.

SR-822.11. Bundesrecht. Bundesgesetz über die Arbeit in Industrie, Gewerbe und Handel (Arbeitsgesetz, ArG) vom 13. März 1964.

SR-822.113. Verordnung 3 zum Arbeitsgesetz (ArGV 3) (Gesundheitsschutz) vom 18. August 1993.

SR-832.30. Bundesrecht. Verordnung über die Verhütung von Unfällen und Berufskrankheiten (Verordnung über die Unfallverhütung, VUV) vom 19. Dezember 1983.

SR-930.11. Bundesrecht. Bundesgesetz über die Produktesicherheit (PrSG) vom 12. Juni 2009.

Stammbach, T., 2001. The PSI 2 mA beam and future applications. p.423-427. DOI 10.1063/1.1435294.

Steinegger, P. et al. 2016. Vacuum Chromatography of Tl on SiO_2 at the Single-Atom Level. *Journal Of Physical Chemistry C, 120(13):7122–7132*, doi:10.1021/acs.jpcc.5b12033.

Streun, Andreas. 2017. SLS-2. Conceptual design report. *Report No. 17-03. p.158*. Villigen PSI, Switzerland: Paul Scherrer Institut, 2017.

Swiss Federal Council. 1991. *Radiological Protection Act (RPA). SR 814.50* Switzerland, 22. March 1991.

Swiss Federal Council. 2017. *Radiological Protection Ordinance (RPO). SR 814.501* Switzerland, 26. April 2017.

Talip, Z. et al. 2020. A Step-by-Step Guide for the Novel Radiometal Production for Medical Applications: Case Studies with ^{68}Ga, ^{44}Sc, ^{177}Lu and ^{161}Tb. *Molecules, 25: 966*. 2020.

Taniuchi, T. et al. 2020. DC septum magnet based on permanent magnet for next-generation light sources. *Physical review accelerators and beams, 23, 012401*. 2020.

TATTOOS 2021. TATTOOS Mini Symposium, April 26, 2021. https://indico.psi.ch/event/11148/. Videos of the Presentations: https://youtube.com/playlist?list=PL0b-ynhMVTd-5qQXsjfVaV_ChrS0jkkBI-. Accessed: 2021-12-12.

Teshima, N. 2020. Status of the DeeMe Experiment, an Experimental Search for µ-e Conversion at J-PARC MLF. *PoS, NuFact2019:082*, doi:10.22323/1.369.0082.

The MathWorks, Inc. 2019. *Simulink Release Notes R2016 to R2019a*. [Matlab Simulink] The MathWorks, Inc., 2019.

Tortaiada, A. et al. 2021. Latest Developments and Results of Radiation Tolerance CMOS Sensors with Small Collection Electrodes. *JPS Conf. Proc. 34, 010009*.

TRIUMF. www.triumf.ca/. Accessed: 2021-12-16.

Turchetta, J. et al. 2001. A monolithic active pixel sensor for charged particle tracking and imaging using standard VLSI CMSO technology. *NIMA 458, 677*.

Ukleev V. et al. 2021. Frustration-driven magnetic fluctuations as the origin of the low-temperature skyrmion phase in $Co_7Zn_7Mn_6$. *npj Quantum Materials, 6:1–8*, doi:10.1038/s41535-021-00342-5.

Ull, A.S. 2019. Optimized design of magnetic septa for the Future Circular Collider. *Eindhoven: Technical University Eindhoven*. 2019.

Umbricht, C. A. et al. 2019. Alpha-PET for Prostate Cancer: Preclinical investigation using Tb-149-PSMA-617. *Scientific Reports, 9*, doi:10.1038/s41598-019-54150-w.

U.S. Department of Energy 1993. DOE fundamentals handbook: Chemistry. Volume 2 of 2. DOE-HDBK-1015-2-93. Washington, DC.

UZH Data Policy. Universtiy of Zurich - Open Science Policy. https://www.openscience.uzh.ch/en/definition/policy.html. Accessed: 2021-12-14.

van der Meulen, N.P. et al. 2015. van der Meulen, N.P., M. Bunka, K.A. Domnanich, C. Müller, S. Haller, C. Vermeulen, A. Türler and R. Schibli. Cyclotron production of ^{44}Sc: from bench to bedside. *Nucl Med Biol, 42*. 2015.

van der Meulen, N.P., Eichler, R. et al. 2019. van der Meulen, N.P., R. Eichler, P.V. Grundler, R. Hasler, W. Hirzel, S. Joray, D.C. Kiselev, R. Sobbia, A. Sommerhalder, Z. Talip and H. Zhang. The use of PSI's IP2 beam line towards exotic radionuclide development and its application towards proof-of-principle preclinical and clinical studies. *22nd International Conference on Cyclotrons and their Applications (Cyclotrons 2019). Cape Town, South Africa: JACoW Publishing*. 2019.

van der Meulen, N.P., Hasler, R. et al. 2019. van der Meulen, N.P., Hasler, R., Blanc, A., Farkas, R., Benešová, M., Talip, Z., Müller, C., and R. Schibli. Implementation of a new separation method to produce qualitatively improved ^{64}Cu. *Journal of Labelled Compounds and Radiopharmaceuticals, 62(8):460-470*. doi:10.1002/jlcr.3730. 2019.

van der Meulen, N.P. et al. 2020. van der Meulen, N.P., R. Hasler, Z. Talip, P.V. Grundler, C. Favaretto, C. Umbricht, C. Mueller, G. Dellepiane, T.S. Carzaniga and S. Braccini. The Development of ^{44}Sc Towards Implementation at a Medical Cyclotron. *Molecules, 25:4706*. 2020.

Van der Schaaf, A. 2021. SINDRUM II. *SciPost Phys. Proc., 5:008*, doi:10.21468/SciPostPhysProc.5.008.

Vasudevamurthy, G. and Nelson, A.T. 2021. Uranium carbide properties for advanced fuel modeling – A review. *Jornal of Nuclear Materials, 558:153145, ISSN 0022-3115,* doi 10.1016/j.jnucmat.2021.153145. 2021.

VAT. 2021. 77.3 UHV Fast Closing Shutter. [Online] VAT, 2021. [Cited: 11 3, 2021.] https://www.vatvalve.com/series/ultra-high-vacuum-fast-closing-slot-shutter.

Wagner, J. and Haghighat, A. 1998. Automated Variance Reduction of Monte Carlo Shielding Calculations Using the Discrete Ordinates Adjoint Function. *Nuclear Science and Engineering*. p.186-208. 1998.

Wallny, R. et al. 2021. CHIPP Roadmap for Research and Infrastructure 2025- 2028 and beyond by the Swiss Particle Physics Community. Swiss Academies Reports, 16, doi:10.5281/zenodo.4637623.

Walter, H.C. 1994. *User's guide: Accelerator facilities*. Villigen and Wuerenlingen: Paul Scherrer Institut, 1994.

Wauters, F. 2021. The Mu3e experiment. *SciPost Phys. Proc., 5:020*, doi:10.21468/SciPostPhysProc.5.020.

Weinreich R., Knust E. J. 1995. Quality control of ^{124}I. *6th International Workshop on Targetry and Target Chemistry, 84. Vancouver, Canada*. 1995.

Weinreich, R. et al. 1985. Large-scale production of radioisotopes on the SIN cyclotron facilities. *Radiopharmaceuticals and labelled compounds (IAEA: Tokyo)*. 1984.

Wendt, K. 1997. Rapid Trace Analysis of ^{89,90}Sr in Environmental Samples by Collinear Laser Resonance Ionization Mass Spectrometry. *Radiochimica Acta, 79: 183-90*. 1997.

Wendt, K. D. A. et al. 2003. Nuclear Instruments & Methods In Physics Research Section B- Beam Interactions With Materials And Atoms, 204:325–330, doi:10.1016/S0168-583X(02)01936-5

WHS Sondermetalle GmbH. 2021. Tantal. *ob der Tauber: WHS Sondermetalle GmbH*. 2021.

Wiescher M., Kaeppeler F., and Langanke K. 2012. Critical Reactions in Contemporary Nuclear Astrophysics. *Annual Review of Astronomy and Astrophysics, 50:165–210*, doi:10.1146/annurev-astro-081811-125543.

Wildi, T. 2003. Der Traum vom eigenen Reaktor. *University of Zurich. doi:10.3929/ethz-a-004459704*. 2003.

Wittwer, D. et al. 2011. The thermal release of scandium from titanium metal - a simple way to produce pure Sc-44 for PET application. *Radiochimica Acta, 99(3):193–196*, doi:10.1524/ract.2011.1832.

Young, W.C. and Budynas, R.G. 2002. *Roark's Formulas for Stress and Strain*. New York: McGraw-Hill, 2002.

Zichy, J., Markovits, C. and Rezzonico, L. 1975. The design, assembly and performance of the SIN beam transfer line. *Proc. 7th International Conference on Cyclotrons and their Applications, Zurich, Switzerland, 19-22 August 1975. Cyclotrons*. 1975.

ZORA. Zurich Open Repository and Archive. https://www.zora.uzh.ch. Accessed: 2021-12-12.

PSI in brief

The Paul Scherrer Institute PSI is a research institute for natural and engineering sciences, conducting cutting-edge research in the fields of matter and materials, energy and the environment and human health. By performing fundamental and applied research, we work on sustainable solutions for major challenges facing society, science and economy. PSI develops, constructs and operates complex large research facilities. Every year more than 2500 guest scientists from Switzerland and around the world come to us. Just like PSI's own researchers, they use our unique facilities to carry out experiments that are not possible anywhere else. PSI is committed to the training of future generations. Therefore about one quarter of our staff are post-docs, post-graduates or apprentices. Altogether PSI employs 2100 people, thus being the largest research institute in Switzerland.

Imprint

Design and Layout
Christoph Schütz

Printing
Paul Scherrer Institut

Available from
Paul Scherrer Institut
Events and Marketing
5232 Villigen PSI, Switzerland
Tel. +41 56 310 21 11

Villigen PSI, January 2022

Paul Scherrer Institut :: 5232 Villigen PSI :: Switzerland :: Tel. +41 56 310 21 11 :: www.psi.ch